

THE UNIVERSITY *of* EDINBURGH

This thesis has been submitted in fulfilment of the requirements for a postgraduate degree (e. g. PhD, MPhil, DClinPsychol) at the University of Edinburgh. Please note the following terms and conditions of use:

- This work is protected by copyright and other intellectual property rights, which are retained by the thesis author, unless otherwise stated.
- A copy can be downloaded for personal non-commercial research or study, without prior permission or charge.
- This thesis cannot be reproduced or quoted extensively from without first obtaining permission in writing from the author.
- The content must not be changed in any way or sold commercially in any format or medium without the formal permission of the author.
- When referring to this work, full bibliographic details including the author, title, awarding institution and date of the thesis must be given.

The East Australian, Tasmantid and Lord Howe Volcanoes: Exploring the origins of three, contemporaneous, parallel chains of volcanism

Amelia Douglas née Smethurst



Thesis submitted for the degree of Doctor of Philosophy
to The University of Edinburgh
2022

0.1 Abstract

At greater than 3000 km long, and 500 km wide, the East Australian volcanic chain is one of the largest intraplate volcanic regions in the world and is represented by over 50 individual provinces, which erupted during the period 84–0 Ma. Some of these provinces show clear age-progression north to south from 34–6 Ma (Cohen et al., 2013; Wellman et al., 1970), whilst others show no age-progression at all. Offshore to the east lie the Tasmantid and Lord Howe volcanic chains which formed coevally with the age-progressive continental volcanoes, 56–7 Ma, and 28–7 Ma, respectively (Kalnins et al., 2015; Seton et al., 2019a; Mortimer et al., 2010; Quilty, 1993; McDougall and Duncan, 1988). Broad patterns in age, lithosphere thickness, major element concentrations, trace element concentrations, isotope ratios, and volume have allowed the identification of three distinct forms of intraplate volcanism operating across the three chains. These include: (1) oceanic, age-progressive volcanism from a deep, EMI-type mantle plume; (2) continental, age-progressive volcanism from the same plume mixed with melts from the metasomatised subcontinental lithospheric mantle (SCLM); and (3) continental, non-age-progressive volcanism related to passive melting of the depleted mantle and the metasomatised SCLM.

A deep plume source is particularly evident through analysis of Tasmantid samples which lie along the extinct Coral and Tasman Sea spreading ridges. As seafloor spreading ceased around 52 Ma, the Tasmantid seamounts were emplaced onto progressively older and thicker oceanic lithosphere. Ratios of any incompatible element (Nb, Sr, Th, LREE, P) versus any garnet-compatible element (Y, V, Sc, HREE) increase moving south through the seamount chain, in accordance with this increase in lithosphere thickness. These changes are adequately modeled by melting of a deep, garnet-lherzolite source, where the degree of melting varies along the chain and is controlled by lithosphere age and thickness. Isotopic results from the Tasmantids show that increasing degrees of melting correlate with greater isotopic enrichment (high $^{87}Sr/^{86}Sr$ and $^{206}Pb/^{204}Pb$, and low εNd) and lower Nb/La. This suggests the source of the Tasmantids is a deep, EMI-like plume, with relatively low Nb compared to other OIBs.

On the continent, the most extreme HFSE and LILE enrichments are found in the age-progressive leucitite samples, which lie on the thickest continental lithosphere. These are most likely produced from melting of the SCLM, which has been previously enriched through metasomatism. SCLM involvement is evident from $K > Na$, which cannot be achieved through partial melting of normal mantle or fractional crystallisation alone, and phlogopite phenocrysts, up to 5mm long, coupled with Th-U depletions, and Rb, Ba, K enrichments, which probably reflect melting of a phlogopite-rich source i.e., not the convecting mantle. On a plot of Nb/Y versus Zr/Y all continental, age-progressive provinces fit well with mixing between the same SCLM source as the leucitites and the EMI-plume source of the Tasmantids. Other factors pointing towards SCLM involvement in the age-progressive continental volcanoes include the fact that the highest enrichments are only observed in continental samples and that there are good correlations between the most extreme enrichments and the most primitive continental samples containing lithospheric xenoliths and plagioclase megacrysts.

Volume estimates of each province have been calculated using a number of methods that include data from multispectral satellites, boreholes, magnetic surveys, geological maps, and high-resolution digital elevation models. A comparison of these volumes with each other and also with geochemical results, suggest that the lava fields consistently represent lower volume, small degree melts and the central volcanoes consistently represent higher volume, high degree melts. The Tasmantid seamounts represent higher degrees of melting still, which is to be expected due to their location on thinner oceanic lithosphere.

The results of this thesis show that age-progressive intraplate volcanism in eastern Australia can be well explained by mixing of a two-component source; a deep, EMI-type mantle plume, and a varyingly metasomatised SCLM. Sr-Nd-Pb isotope data for all non-age-progressive, continental provinces fit with mixing between the depleted mantle and components of EMI, EMII and HIMU reservoirs. Such observations are most easily explained by passive melting of the upper mantle once again mixed with melts from the metasomatised SCLM.

0.2 Lay Summary

This thesis contributes to the understanding of how volcanoes form and why they are only found in certain locations. In eastern Australia, and just off the coast, there exists three chains of volcanoes (one on land and the other two in the ocean) that have similar ages and were probably created at the same time. The chains all progress in age from older in the north to younger in the south. Interspersed with the chain of volcanoes on land are more volcanoes that were not erupted at the same time but were instead erupted sporadically throughout the last 60 million years. The two types of volcano erupt lavas that tend to have different composition that must relate to how they were created. The age-progressive chains of volcanoes, both on land and in the ocean, are probably created by a mantle plume. That is, an area of particularly hot mantle that rises up from just above the Earths core and remains stationary with respect to the Earths rotation axis forming a local hotspot. As it approaches the surface, the top of the plume will melt, and the melt will travel through the tectonic plate to create a volcano and as the tectonic plate moves over the stationary hotspot, more volcanoes are created to form a chain. The other volcanoes, those that have been erupting in seemingly random locations over the past 60 million years, are created in a different way. These have formed by the melting of the lower part of the tectonic plate. Tectonic plates are made up of mantle and overlying crust and form a rigid slab called the lithosphere. The passage of magmas and fluids through the lower lithosphere over millions of years will change its composition and may make it locally more susceptible to melting. An increase in temperature caused by the arrival of a mantle plume at the bottom of a tectonic plate may warm the plate and any minerals which have a low melting point will melt. The molten rock will then make its way through the crust, to the surface and form a volcano.

In this work, the two types of volcano have been identified through the study of basalt rock samples. Basaltic magma is the first thing to form when the mantle melts and the concentration of certain elements within the basalt magma will reflect how and where the mantle has melted. Some elements prefer to be incorporated in certain minerals, and other do not. For example, the element yttrium, prefers to remain in the mineral garnet; it is said to be compatible in garnet. Garnet is found relatively deep in the mantle (more than about 70 km) and when the mantle melts at this greater depth, the basaltic melt produced will contain less yttrium. Other elements, such as lanthanum, do not have this affinity with garnet or with any other mantle minerals, and are said to be incompatible. So, when the mantle melts lanthanum will readily enter the melt and the resulting basalt will have a higher lanthanum concentration. We can use the relative concentration of a number of elements of varying compatibility, to estimate the depth at which a basalt rock sample might have originated, and what might have happened to it on its way to the surface. In this study we find basalt rocks across eastern Australia are sourced from both the deep mantle via a mantle plume, and from the lower portion of the lithosphere forming the Australian tectonic plate.

0.3 Declaration

I declare that this thesis has been composed solely by myself and that it has not been submitted, either in whole or in part, in any previous application for a degree. Except where otherwise acknowledged, the work presented is entirely my own.

Amelia Douglas
January 2022

0.4 Acknowledgements

I would like to thank the following people, who without, this thesis would definitely not have been possible! Firstly, to my three supervisors Lara Kalnins, Godfrey Fitton and Ben Cohen. Lara, for setting a real example for me to follow, for keeping me on track, for copious editing, and for patiently listening to all my complaints. Godfrey, for his wonderful, thought-provoking discussions, unlimited passion and motivation. Ben, for his unrivaled knowledge of east Australia's volcanoes, and assistance with all my field work and sample selection. I would also like to thank Linda Kirstein, whose has always been there as an ear and whose advice has proven invaluable throughout my PhD.

Next, my tireless field assistant, Aki Suganuma, thank you for accompanying me around Australia and your excellent skills with a rock hammer. I would not have been able to do all that work without you. I would also like to thank the whole crew of the RV Investigator for their general merriness whilst at sea, and in particular Saskia Ruttor for kindly lending me her isotope results. It would also not have been possible to collect any of these samples without the help of the Australia State Geological Surveys and National Parks and to who I am very grateful in giving me permission to collect the samples.

From the University of Edinburgh Geoscience Department, I would like to thank Laetitia and Nic for all their help with my laboratory XRF and ICP-MS prep, I will bug you no longer! Thank you to The Natural Environment Research Council Doctoral Training Partnership who funded my work. Finally, I would like to thank my friends and family who have supported, encouraged and motivated me in achieving my goals. In particular to my parents and to my husband, Sandy, who have been the rocks I relied on to get me though quite a long four years. I dont think any of them ever expected to be as involved in this project as they were, and thank you for all for your help.

Contents

0.1 Abstract . . . 2
0.2 Lay Summary . . . 3
0.3 Declaration . . . 4
0.4 Acknowledgements . . . 5

1 Introduction **14**
1.1 Intraplate Volcanism . . . 15
1.2 Mechanisms . . . 18

2 Literature Review **20**
2.1 Geological History of Eastern Australia . . . 21
2.2 East Australian Intraplate Volcanism . . . 21
2.2.1 Central Volcanoes . . . 24
2.2.2 Leucitites . . . 25
2.2.3 Lava Fields . . . 26
2.2.4 Seamounts . . . 27
2.3 Cenozoic Tectonics . . . 28
2.3.1 Seismic Tomography . . . 34
2.4 Current Stress Regime . . . 39
2.5 Igneous Geochemistry . . . 42

3 Methods **43**
3.1 Geochemistry . . . 44
3.1.1 Sample Collection . . . 44
3.1.2 Major and Trace Elements . . . 44
3.2 Volume Calculations . . . 46
3.2.1 Preserved mapped extents . . . 48
3.2.2 Preserved remote sensing extents . . . 48
3.2.3 Original volcanic extents . . . 61
3.2.4 Local minima baseline . . . 62
3.2.5 Masked interpolation baseline . . . 63
3.2.6 Ridgeline resurfacing . . . 65
3.2.7 Pyramidal reconstruction . . . 65
3.2.8 Simple conical estimate . . . 67

4 Volcanic Sources **68**
4.1 Introduction . . . 69
4.2 Results and Discussion . . . 70
4.3 Conclusions . . . 92

5 The Leucitite Chain **94**
5.1 Introduction . . . 95
5.2 Results and Discussion . . . 96
5.3 Conclusions . . . 104

6 Volume Estimates **105**
6.1 Introduction . . . 106
6.2 Results and Discussion . . . 106
6.2.1 Remote Sensing . . . 106
6.2.2 Continental Volumes . . . 127
6.2.3 Recent Northern Queensland Volcanism . . . 130
6.2.4 Leucitites, Macedon & the NVP . . . 144
6.2.5 Age Progressive Volcanism . . . 150
6.2.6 Prolonged 60–10 Ma Volcanism . . . 188
6.2.7 Older, Multi-phase Volcanism . . . 214
6.2.8 Tasmania . . . 229
6.2.9 Seamounts . . . 231
6.3 Conclusions . . . 233

7 Summary **235**
7.1 Conclusions . . . 236
7.2 Future Work . . . 242

A Thin Sections **263**

B Fieldwork Samples **426**

C Study Samples **441**

D Major and Trace Element Results **446**

E XRF Standards **486**

F ICP-MS Standards **488**

G ICP-MS Duplicates **494**

H Distribution Coefficients **500**

I Volumes **502**

List of Figures

1.1 The Glasshouse volcanoes, Queensland. . . . 14
1.2 Map of Australia's three intraplate, Cenozic volcanic chains . . . 15
1.3 Primarily Quaternary occurrences of four basaltic rock types . . . 16
1.4 Schematic cross section showing the subduction of oceanic crust . . . 17

2.1 The Undara lava tube, McBride volcanic province, far north Queensland. . . . 20
2.2 The six main units of the Tasman Fold Belt . . . 21
2.3 Individual volcanic provinces within the five volcanic suites . . . 23
2.4 Depiction of a stagnant slab and schematic of undulating lithosphere thicknesses . . . 24
2.5 $^{40}Ar/^{39}Ar$ results of silicic rocks from the east Australian central volcanoes . . . 25
2.6 Sr-Nd-Pb isotope data from lava fields across Eastern Australia . . . 26
2.7 The principle features of the northeastern Australian Plate and neighbouring plates . . . 28
2.13 Present-day plate boundaries including the dominant forces acting upon them . . . 39
2.14 Distribution of $M > 4$ historical earthquake epicenters and directions of maximum horizontal compression . . . 40
2.15 1955–2014 seismicity across Eastern Australia . . . 41
2.16 Lithospheric structure of East Australia from seismic surface wave tomography and horizontal shear wave speeds . . . 42
2.17 Lithospheric thickness . . . 42

3.1 Sleeping koala, Magnetic Island, Queensland. . . . 43
3.2 New samples collected during fieldwork in 2019 . . . 44
3.3 Ba and Nb plotted against LOI for each volcanic sample . . . 45
3.4 Correlation of elements cross analysed by XRF and ICP-MS. . . . 45
3.5 MODIS, ASTER, Landsat-7, -8, and Sentinel-2 bands, atmospheric transmission, and wavelength 49
3.6 Reflectance spectra from the USGS spectral library . . . 53
3.7 Measured emissivity of pure quartz and emission of typical igneous rocks . . . 54
3.8 Present-day DEM of the Warrumbungle and Liverpool Range provinces . . . 62
3.9 Cross section across the Warrumbungle volcano . . . 62
3.10 Warrumbungle local minima baseline and masked interpolation . . . 63
3.11 Warrumbungle masked interpolation baseline . . . 64
3.12 Warrumbungle ridgeline resurfacing . . . 66
3.13 DEM of Warrumbungle volcano with reconstructions . . . 66

4.1 Sailing the Coral Sea aboard the RV Investigator. . . . 68
4.2 Ba and Nb plotted against LOI for each volcanic sample . . . 69
4.3 Ages and locations of valcanic rocks collected from literature sources and this study . . . 70
4.4 Tectonic reconstructions of the east Australian plate . . . 71
4.5 Total alkali-silica (TAS) diagram of samples analysed in this study . . . 72
4.6 Primitive mantle (PM)-normalised multi-element plot of incompatible elements . . . 73
4.7 PM-normalised multi-element plots of incompatible elements . . . 73
4.8 SSI versus La, Gd, and Yb for each suit . . . 74
4.9 Ni and CaO/Al_2O_3 plotted against MgO for each volcanic sample . . . 75
4.10 Typical thin-section photomicrographs of each suite taken with crossed polars (XP) . . . 75
4.11 Tasmantid sample showing Ar-Ar ages and Tb/Yb against latitude and lithosphere thickness . 76
4.12 Strongly incompatible/garnet-compatible element ratios versus estimated lithosphere thickness 77
4.13 Lithosphere thickness versus La/Yb concentration for each suite . . . 78

4.14 Map showing the largest central volcano alongside the largest Tasmantid seamounted and plot of La/Yb versus estimated lithosphere thickness . . . 79
4.15 Map showing the locations of the Tasmantid seamounts and central volcanoes with high volumes and correspondingly low La/Yb and a plot of La/Yb versus lithosphere thickness . . . 80
4.16 Nb/Y versus Zr/Y for all samples coloured by suite, age, SSI, and MgO content . . . 81
4.17 Chronology of volcanic eruptions within the East Australian chain ordered by decreasing latitude 82
4.18 Chronology of volcanic eruptions within the East Australian chain ordered by decreasing latitude 83
4.19 Volcanic provinces split by the six groups . . . 84
4.20 Groups identified in Figures 4.19 and 4.18 on a plot of Nb/Y versus Zr/Y . . . 85
4.21 TAS diagrams for data from the various geographical groups defined in Figure 4.19 . . . 86
4.22 ΔNb vs Nb/La and (b) Nb/Y vs Zr/Y highlighting all samples from age-progressive provinces including the continental age-progressive group, the NVP, the leucitites, and the Tasmantids. . 88
4.23 $^{206}Pb/^{204}Pb$ versus $^{208}Pb/^{204}Pb$ and εNd versus $^{87}Sr/^{86}Sr$ for all samples split by groups . . 89
4.24 Map showing the Tasmantid samples and plotted showing an increase in Gd/Yb with increasing $^{208}Pb/^{204}Pb$, and increasing εNd . . . 90
4.25 εNd versus $^{87}Sr/^{86}Sr$ and ΔNb vs Nb/La showing the Tasmantid samples analysed by Ruttor (2021) . . . 91
4.26 $^{206}Pb/^{204}Pb$ versus $^{238}U/^{204}Pb$ calculated for the Ruttor (2021) Tasmantid samples and corrected for degree of melting and $^{206}Pb/^{204}Pb$ versus uncorrected $^{238}U/^{204}Pb$ calculated for other age progressive provinces. . . . 92
4.27 Nb/Y versus Zr/Y showing three of the main groups identified in this study as having different sources . . . 93

5.1 Leucitite sample from Byrock Quarry, NSW. Visible phlogopite phenocrysts up to 9mm in length. 94
5.2 The Cosgrove hotspot track from Davies et al. (2015) . . . 95
5.3 Location of the leucitite, Macedon-Trentham central volcano and Newer Volcanic lava field samples . . . 96
5.4 Primitive mantle (PM)-normalised multi-element plot of incompatible elements for leucitite and Victoria samples . . . 97
5.5 Chondrite-normalised REE plot for leucitite and Victoria samples. Normalising values and average composition of OIB and EMORB from Sun and McDonough (1989). . . . 97
5.6 Na_2O vs Al_2O_3, K_2O vs Al_2O_3, TiO_2 vs MgO, Nb vs SSI, Rb vs Al_2O_3, and Ba vs Al_2O_3; each showing the five groups identified in Figure 5.3 . . . 98
5.7 $^{206}Pb/^{204}Pb$ versus $^{208}Pb/^{204}Pb$ and εNd versus $^{87}Sr/^{86}Sr$ for the five groups identified in Figure 5.3 . . . 99
5.8 $^{207}Pb/^{204}Pb$ versus $^{206}Pb/^{204}Pb$ plotting each of the five groups alongside the Geochron, growth curves ($\mu = 8, 8.35, 9$), and the Northern Hemisphere Reference Line. . . . 100
5.9 Figure 5.6 with additional data added . . . 101
5.10 Location of the five groups identified in Figure 5.3 alongside Mount McIntyre, Southern Highland and Tasmania . . . 102
5.11 εNd versus $^{87}Sr/^{86}Sr$ again showing the five groups identified in Figure 5.3, alongside samples from Tasmania, the Southern Highlands province, and Mount McIntyre in SA. . . . 102
5.12 The six main units of the TFB, modifed after Crawford et al. (2003). . . . 103
5.13 Cr vs vs Al_2O_3, Ti vs V, and Ti vs Zr/Y; each showing the five groups identified in Figure 5.3, Tasmania, Southern Highlands, and Mt McIntyre samples (MgO > 7 wt% and LOI < 3 wt%). . 103
5.14 Nb vs Ca/Na for each of the five groups identified in Figure 5.3, as well as Tasmania and Mt McIntyre samples (MgO > 7 wt% and LOI < 3 wt%). . . . 104

6.1 Cape Hillsborough National Park, Queensland. . . . 105
6.2 Landsat-8 band 1 mean and median reduction over the full age range . . . 106
6.3 Landsat-8 band 1, TIR band 10, ASTER band 1 median reduction over a variety of age ranges 107
6.4 K-means clustering on Landsat band 1 with k set to 5 groups, 10 groups and 20 groups. . . . 108
6.5 K-means clustering on ASTER-GED band 10 with k set to 5 groups, 10 groups and 20 groups. 108
6.6 Dominant lithologies of the Warrumbungle central volcano province. . . . 109
6.7 Dominant lithologies of the McBride lava field province. . . . 109
6.8 Warrumbungle province k-means clustering on Landsat-8 bands (a) B1 (b) B2 (c) B3 (d) B4 (e) B5 (f) B6 (g) B7, and (h) ASTER-GED B10. . . . 111

6.9 Warrumbungle province k-means clustering on ASTER-GED bands (a) B11 (b) B12 (c) B13 (d) B14, including images of (e) DEM (f) slope (g) FAA (h) TMI. . . . 112
6.10 McBride province k-means clustering on Landsat-8 bands (a) B1 (b) B2 (c) B3 (d) B4 (e) B5 (f) B6 (g) B7, and (h) ASTER-GED B10. . . . 113
6.11 McBride province k-means clustering on ASTER-GED bands (a) B11 (b) B12 (c) B13 (d) B14, including images of (e) DEM (f) slope (g) FAA (h) TMI. . . . 114
6.12 Warrumbungle Landsat-8 reflectance spectra gathered from geological polygons. . . . 115
6.13 Warrumbungle ASTER-GED emissivity spectra gathered from geological polygons. . . . 116
6.14 McBride Landsat-8 reflectance spectra gathered from geological polygons. . . . 117
6.15 McBride ASTER-GED emissivity spectra gathered from geological polygons. . . . 117
6.16 The Landsat-8 7–6–3 FCC, the Sentinel-2 12–11–2 FCC and the ASTER 10–11–12 FCC for the Warrumbungle and McBride provinces. . . . 118
6.17 The Landsat-8 6/7 ratio used to highlight clays, the Landsat-8 6/2 ratio used to isolate epidote and chlorite and the Landsat-8 2/5 ratio used to supress vegetation in the Warrumbungle and McBride provinces. . . . 119
6.18 The Landsat-8 FCC 6/7–6/2–5, the ASTER empirical index of SiO_2 (%) and the ASTER Mafic Index at Warrumbungle and McBride. . . . 120
6.19 Warrumbungle Landsat-8 and ASTER composite images . . . 122
6.20 McBride Landsat-8 and ASTER composite images . . . 123
6.21 Tuning results for the Warrumbungle province, showing the validation accuracy of the classification versus the number of decision trees specified in the random forest operator. . . . 124
6.22 Tuning results for the McBride province, showing the validation accuracy of the classification versus the number of decision trees specified in the random forest operator. . . . 124
6.23 Warrumbungle and McBride GEE classification and dominant geology map. . . . 125
6.24 Individual volcanic provinces within the five volcanic suites . . . 129
6.25 Age data for the Piebald province. . . . 130
6.26 The Piebald volcanic province. . . . 131
6.27 Age data for the Maclean province. . . . 132
6.28 The Maclean volcanic province. . . . 133
6.29 Age data for the Atherton province. . . . 134
6.30 The Atherton volcanic province. . . . 135
6.31 Age data for the McBride province. . . . 136
6.32 Age data for the Wallaroo province. . . . 137
6.33 The McBride volcanic province. The 3D baseline by Ransley et al. (2020) has been created using the results of a drilling program conducted by the Queensland Government Department of Environment and Science in 2017–2018 (Hansen et al., 2020) . . . 137
6.34 Age data for the Chudleigh province. . . . 138
6.35 The Chudleigh volcanic province. . . . 139
6.36 Age data for the Nulla province. . . . 140
6.37 The Nulla volcanic province. The red dot shows the location of the only freely available borehole from Queensland Government (2022). The 3D baseline by Ransley et al. (2020) has instead been created using the results of a drilling program conducted by the Queensland Government Department of Environment and Science in 2017–2018 (Hansen et al., 2020). . . . 141
6.38 Age data for the Sturgeon province. . . . 142
6.39 The Sturgeon volcanic province. . . . 143
6.40 Age data for the Leucitite chain. . . . 145
6.41 Northern and Central Leucitite volcanic provinces. . . . 145
6.42 Age data for the Macedon-Trentham province. . . . 146
6.43 The Macedon-Trentham volcanic province. Red dots show the locations of freely available borehole data obtained from Victoria State Government (2022). . . . 147
6.44 Age data for the Newer Volcanic Province. . . . 148
6.45 The Newer Volcanic Province. Red dots show the locations of freely available borehole data obtained from Victoria State Government (2022). . . . 149
6.46 Age data for the Cape Hillsborough province. . . . 150
6.47 The Cape Hillsborough volcanic province. . . . 151
6.48 Age data for the Nebo province. . . . 152
6.49 The Nebo volcanic province. Red dots show the locations of freely available borehole data obtained from Queensland Government (2022). . . . 153

6.50 Age data for the Peak Range province. . . . 155
6.51 The Peak Range volcanic province. . . . 155
6.52 Age data for the Springsure province. . . . 156
6.53 The Springsure volcanic province. Red dots show the locations of freely available borehole data obtained from Queensland Government (2022). . . . 157
6.54 Age data for the Buckland province. . . . 158
6.55 The Buckland volcanic province. . . . 159
6.56 Age data for the Fraser Island province. . . . 160
6.57 The Fraser Island volcanic province. . . . 161
6.58 Age data for the Bauhinia province. . . . 162
6.59 The Bauhinia volcanic province. . . . 163
6.60 Age data for the Mitchell province. . . . 164
6.61 The Mitchell volcanic province. Red dots show the locations of freely available borehole data obtained from Queensland Government (2022). . . . 165
6.62 Age data for the Noosa province. . . . 166
6.63 Age data for the Glasshouse-Maleny province. . . . 167
6.64 The Glasshouse-Maleny-Noosa volcanic province. . . . 167
6.65 Age data for the Bunya province. . . . 168
6.66 The Bunya volcanic province. The red dot shows the location of the only freely available borehole obtained from Queensland Government (2022). . . . 169
6.67 Age data for the Toowoomba province. . . . 170
6.68 The Toowoomba volcanic province. Red dots show the locations of freely available borehole data obtained from Queensland Government (2022). . . . 171
6.69 Age data for the Main Range province. . . . 172
6.70 The Main Range volcanic province. The red dot shows the location of the only freely available borehole obtained from Queensland Government (2022). . . . 173
6.71 Age data for the Tweed province. . . . 174
6.72 The Tweed volcanic province. Red dots show the locations of freely available borehole data obtained from New South Wales Government (2022). . . . 175
6.73 Age data for the Belmore province. . . . 176
6.74 The Belmore volcanic province. . . . 177
6.75 Age data for the Ebor province. . . . 178
6.76 The Ebor volcanic province. . . . 179
6.77 Age data for the Comboyne province. . . . 180
6.78 The Comboyne volcanic province. . . . 181
6.79 Age data for the Nandewar province. . . . 182
6.80 The Nandewar volcanic province. Red dots show the locations of freely available borehole data obtained from New South Wales Government (2022). . . . 183
6.81 Age data for the Warrumbungles province. . . . 184
6.82 The Warrumbungles volcanic province. The red dot shows the location of the only freely available borehole obtained from New South Wales Government (2022). . . . 185
6.83 Age data for the Canobolas province. . . . 186
6.84 The Canobolas volcanic province. Red dots show the locations of freely available borehole data obtained from New South Wales Government (2022). . . . 187
6.85 Age data for the Mingela province. . . . 188
6.86 The Mingela volcanic province. . . . 189
6.87 Age data for the Brisbane province. . . . 191
6.88 The Brisbane volcanic province. The red dot shows the location of the only freely available borehole obtained from Queensland Government (2022). . . . 191
6.89 Age data for the Doughboy province. . . . 192
6.90 The Doughboy volcanic province. . . . 193
6.91 Age data for the Walcha province. . . . 194
6.92 The Walcha volcanic province. The red dot shows the location of the only freely available borehole obtained from New South Wales Government (2022). . . . 195
6.93 Age data for the Barrington province. . . . 196
6.94 The Barrington volcanic province. . . . 197
6.95 Age data for the Liverpool Range province. . . . 198

6.96 The Liverpool Range volcanic province. Red dots show the locations of freely available borehole data obtained from New South Wales Government (2022). . . . 199
6.97 Age data for the Kandos province. . . . 200
6.98 The Kandos volcanic province. Red dots show the locations of freely available borehole data obtained from New South Wales Government (2022). . . . 201
6.99 Age data for the Sydney province. . . . 202
6.100 The Sydney volcanic province. . . . 203
6.101 Age data for the Grabben Gullen province. . . . 204
6.102 The Grabben Gullen volcanic province. Red dots show the locations of freely available borehole data obtained from New South Wales Government (2022). . . . 205
6.103 Age data for the Southern Highlands province. . . . 206
6.104 The Southern Highlands volcanic province. Red dots show the locations of freely available borehole data obtained from New South Wales Government (2022). . . . 207
6.105 Age data for the Snowy Mountains province. . . . 208
6.106 The Snowy Mountains volcanic province. . . . 209
6.107 Age data for the South Coast province. . . . 210
6.108 The South Coast volcanic province. . . . 211
6.109 Age data for the Monaro province. . . . 212
6.110 The Monaro volcanic province. Red dots show the locations of freely available borehole data obtained from New South Wales Government (2022). . . . 213
6.111 Age data for the Rockhampton province. . . . 215
6.112 The Rockhampton volcanic province. . . . 216
6.113 Age data for the Hoy province. . . . 217
6.114 The Hoy volcanic province. . . . 218
6.115 Age data for the Monto province. . . . 219
6.116 The Monto volcanic province. . . . 220
6.117 Age data for the Bundaberg province. . . . 221
6.118 The Bundaberg volcanic province. . . . 222
6.119 Age data for the New England province. . . . 223
6.120 The New England volcanic province. Red dots show the locations of freely available borehole data obtained from New South Wales Government (2022). . . . 224
6.121 Age data for the Dubbo province. . . . 225
6.122 The Dubbo volcanic province. Red dots show the locations of freely available borehole data obtained from New South Wales Government (2022). . . . 226
6.123 Age data for the Older Volcanic Province. . . . 227
6.124 The Older Volcanic Province. Red dots show the locations of freely available borehole data obtained from Victoria State Government (2022). . . . 228
6.125 Age data for the Tasmania province. . . . 229
6.126 The Tasmania volcanic province. Red dots show the locations of freely available borehole data obtained from Mineral Resources Tasmania and Tasmanian Government (2022). . . . 230
6.127 Age data for the Tasmantid chain. . . . 231
6.128 Age data for the Lord Howe chain. . . . 232
6.129 Graphical depiction of central volcano and lava field preferred original volume estimates. . . . 233
6.130 Estimated paths of age-progressive plumes. . . . 234

7.1 Noosa National Park, Queensland. . . . 235
7.2 Individual volcanic provinces within the five volcanic suites 237
7.3 Chronology of continental volcanic eruptions ordered by decreasing latitude 238
7.8 Nb/Y versus Zr/Y showing three of the main groups identified in this study as having different sources 241

List of Tables

2.1 Major tectonic events taking place along the boundary of the Australian plate since 100 Ma. Palaeogeographic reconstructions from Schellart et al. (2006) with Cenozoic intraplate volcanoes shown in red. A continuous palaeogeographic reconstruction can also be viewed at EarthByte (2006). 29

3.1 XRF and ICP-MS standard results 46

4.1 Distribution coefficients with 1σ errors 78

6.1 Confusion matrix for the Warrumbungle random forest classification. 126
6.2 Confusion matrix for the McBride random forest classification. 126

C.1 Locations and catagories of all samples used in this study. 441

D.1 Major and trace element data for volcanic rocks analysed in this study. 446

E.1 XRF standard analyses 486

F.1 ICP-MS standard analyses 488

G.1 ICP-MS duplicate samples analyses. 494

H.1 Distribution coefficients (D) used in this study 500

I.1 Results of volume analyses for each province discussed in this study. 502

Chapter 1

Introduction



Figure 1.1: *The Glasshouse volcanoes, Queensland.*

1.1 Intraplate Volcanism

Since the development of the plate tectonic theory in the late 1960s, volcanism at plate boundaries has been explained through adiabatic partial melting at mid ocean ridges and lowering of the solidus at subduction zones. Volcanism at intraplate settings however, remains more of a mystery. Hotter-than-ambient mantle rising up from a thermal boundary layer may explain large-scale melting, like that seen in Hawaii and Iceland. However, with more than 70,000 isolated seamounts in the Pacific Ocean alone, not all intraplate volcanism can be a product of relatively deep mantle plumes. Despite there being numerous examples worldwide, we still do not know how the majority of this magmatism is sourced. The East Australian, Tasmantid, and Lord Howe volcanoes represent three, linear, volcanic chains that formed coevally between 56 and 0 Ma in an intraplate setting (Wellman and McDougall, 1974a; Cohen et al., 2013; Kalnins et al., 2015). Although the chains are separate, the geographical proximity, sub-parallel tracks, and equivalent ages suggest they are closely related. This unique ensemble gives us an excellent opportunity to assess both continental and oceanic, and both age-progressive and non-age-progressive, forms of intraplate volcanism.

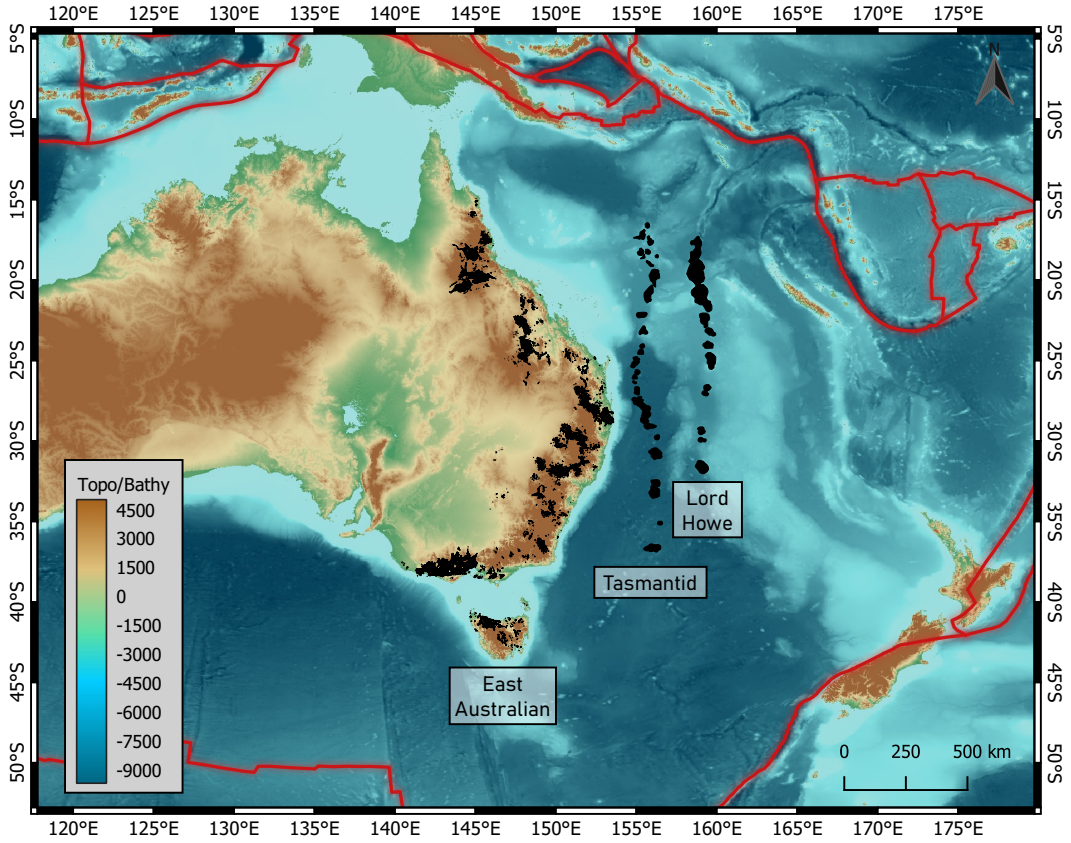

Figure 1.2: *Map of Australia's three intraplate, Cenozoic volcanic chains shown in black: the East Australian chain and associated continental lava field volcanoes, the Tasmantid Seamount chain, and the Lord Howe Seamount chain which lies on a drowned continental fragment. Tectonic plate boundaries (red solid lines) by Bird (2003). Topographic and bathymetric grid by GEBCO (2020).*

For this study, the major and trace element and radiogenic isotope results of basalts, *sensu lato*, have been gathered to produce the most widespread geochemical dataset of east Australian Cenozoic volcanism to date. As the initial product of mantle melting, the composition of basalts provide an indirect measurement for the composition of the mantle from which they are sourced. Because of this, they are often indicative of the tectonic province that they originate from and may be split into four primary groups; mid-ocean ridge basalt (MORB), arc basalt (AB), ocean island basalt (OIB) including oceanic plateaus, and continental basalt (CB) including those lying on submerged continental crust (Sun and Hanson, 1975; Ringwood, 1974; Zindler and Hart, 1986; Sun and McDonough, 1989) (Figure 1.3). MORB can be split further into normal mid-ocean ridge basalt (N-MORB) and enriched mid-ocean ridge basalt (E-MORB) (Schilling, 1973; Sun and McDonough, 1989). Figure 1.3 shows Quaternary examples of the four groups. Intraplate volcanism, taking place away from plate boundaries, encompasses both OIB and some non-arc CB, which are chemically very similar.

Like other intraplate provinces, Cenozoic volcanic rocks across eastern Australia almost always have com-

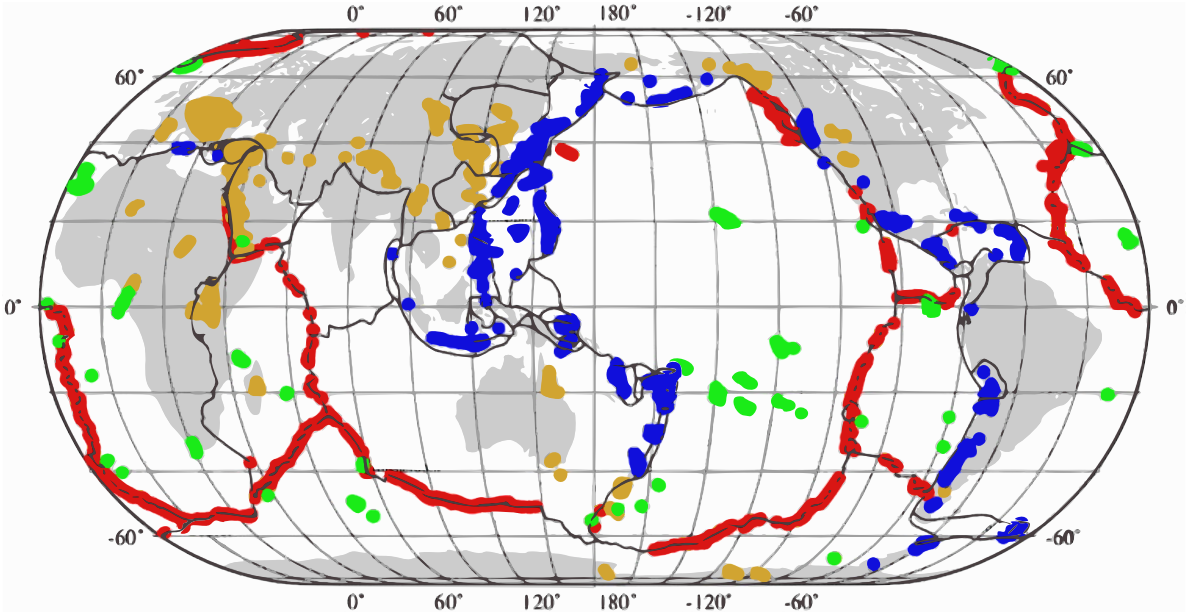

Figure 1.3: *Map modified from Iwamori and Nakamura (2015) showing primarily Quaternary occurrences of the four basaltic rock types. Mid-ocean ridge basalts (MORB, red), arc basalts (AB, blue), ocean island basalts (OIB, green), and continental basalts (CB, orange). Solid lines indicate tectonic plate boundaries by Bird (2003).*

positions similar to OIB (Ewart et al., 1988; Johnson, 1989; O'Reilly and Zhang, 1995). Unfortunately, the occurrence of OIB-like basalts does not pertain to a single process of formation (Fitton, 2007). In fact, given spatial and temporal relationships, it is very difficult to account for all volcanoes across the three Australian chains with just one process alone. The source of OIB volcanism, primarily in Australia but with implications globally, is the main focus of this study.

OIB and N-MORB differ from primitive mantle (PM) by an enrichment and depletion, respectively, in elements incompatible in mantle phases (Hofmann, 1997). Work by Gale et al. (2013) suggest N-MORB is the "most likely composition of basalt encountered along spreading ridges >500 km from hotspots" and is moderately depleted in incompatible elements. Values of N-MORB used in this thesis refer to those by Sun and McDonough (1989), which have been shown by Gale et al. (2013) to represent the most depleted end of the MORB compositional spectrum. Whichever definition is used, it is clear N-MORB contains at least some portion of a depleted mantle component and as mid-ocean ridges are known to form through the passive upwelling of asthenosphere, N-MORB is taken to derive from depleted zones, or layers, within the upper mantle. Simple mass balance equations give rise to the conventional view that the relative depletion of incompatible elements observed in N-MORB is largely due to the extraction of continental crust via partial melting (Armstrong, 1968; McKenzie and O'Nions, 1991). The lack of this depletion in OIBs has led to the hypothesis that OIBs are sampling mantle reservoirs separated from the bulk upper mantle (Allegre, 1982).

In addition to this, the long-lived, age-progressive nature of some intraplate volcanic chains has been suggested as evidence that the source of some OIB volcanism must be deep within the mantle, decoupled from the overriding lithospheric plate and confined to a localised zone. Such zones may be termed hotspots, where magmatism occurs outside the context of plate tectonics. In an attempt to explain this, the plume theory was developed (Morgan, 1971), where anomalously hot, less depleted mantle is brought to the surface in a convective plume arising from the core-mantle boundary or other discontinuities within the Earth e.g., 660 km. Deep mantle reservoirs are thought to be enriched by incorporating components of subducted and dehydrated oceanic crust or veined, metasomatised lithosphere (Hofmann and White, 1982; White, 2015; Niu and O'Hara, 2003; Pilet et al., 2008) (Figure 1.4). The plume hypothesis works well to explain large-scale partial melting, like that seen in the Hawaii, Galapagos, and Reunion islands, but it is difficult to relate to small, isolated seamounts, or non-age-progressive chains such as the Cameroon line (Fitton and Dunlop, 1985). Further problems are introduced where proposed plume locations lack evidence of precursory uplift, large igneous provinces (LIPs) assumed to represent the plume head or detectable seismic anomalies at depth beneath present-day hotspot locations (Courtillot et al., 2003; Foulger, 2010).

The occurrence of more enriched MORB (E-MORB) in localities such as Iceland has predominantly been explained through the interaction of a deep-seated plume with a depleted upper mantle source (Schilling, 1973). However, globally there are a number of E-MORB segments that are not proximal to plumes suggesting

that at least some, minor, enriched zones must exist in the upper mantle itself and may also contribute to some OIB volcanism globally (Gale et al., 2013). A second explanation for OIB volcanism is therefore that streaks of incompatible-element-enriched material occupy the depleted upper mantle where enrichment is again introduced through subducted oceanic crust or lithosphere, but also from plumes, continental foundering and low degree metasomatic melts (Fitton and James, 1986; Niu and O'Hara, 2003; Langmuir et al., 2005). Smaller degrees of melting would preferentially sample the enriched components to produce OIB-like melts whilst larger degrees of melting would homogenize the two to produce N-MORB-like melts (McKenzie, 1989; Ito and Mahoney, 2005). Unlike the plume model, this hypothesis struggles to explain prolonged, large-scale hotspot trails.

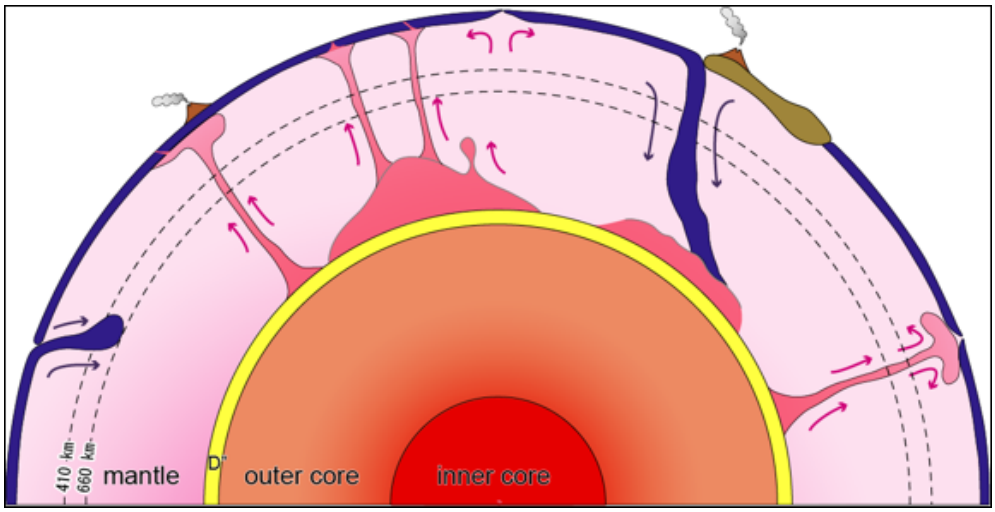

Figure 1.4: *Schematic cross section showing the subduction of oceanic crust to the 660 km discontinuity and the core-mantle boundary alongside mantle plume volcanism (Fitton, 2018).*

Adding to this complexity, and contradictory to both the plume and the streak models, continental rifts (e.g., the Scottish Midland Valley, the East African Rift) thought to be produced by large-scale melting of the upper mantle frequently erupt OIB-type lavas where one would expect N-MORB-type lavas (Fitton, 2007). Again, such volcanism occurs in both age-progressive and non-age-progressive forms and for this reason, the role of the continental and oceanic lithosphere in contributing to OIB volcanism also needs to be assessed.

Lithospheric mantle is thought to be enriched through the process of metasomatism which occurs where low degree silicate or carbonate melts, or water-rich or CO_2-rich fluids interact with and chemically alter mantle rocks close to the lithosphere-asthenosphere boundary (LAB) (McKenzie, 1989; Ionov et al., 2002; Luth, 2003; Pilet et al., 2011). Such fluids may originate from a number of sources including the convecting asthenospheric mantle (Class and Goldstein, 1997; Niu and O'Hara, 2003), along the periphery of mantle plumes (Halliday et al., 1995; Wyllie, 1988), or from subducted oceanic lithosphere (Churikova et al., 2001; Downes, 2001). As the fluids ascend through the lithosphere they interact with the surrounding rock, forming veins of altered and enriched peridotite as they cool (Pilet et al., 2011; Harte et al., 1993; McKenzie, 1989). Dissolution and deposition of new minerals occur simultaneously and the result expresses itself as three main forms: (1) modal metasomatism where new, often hydrous, minerals are formed in the surrounding rock i.e., apatite; (2) cryptic metasomatism where the composition of pre-existing minerals are changed; and (3) stealth metasomatism which introduces more phases indistinguishable mineralogically from common mantle phases i.e., garnet (O'Reilly and Griffin, 2013; Lloyd and Bailey, 1975; Dawson, 1984).

Old lithospheric mantle may therefore record multiple metasomatic events that have repeatedly overprinted, variably depleted mantle resulting in heterogeneity on scales of microns to terranes (O'Reilly and Griffin, 2013). This alteration significantly decreases the solidus temperature of lherzolite and as such these fertile zones will be the first things to melt with increased temperature from a mantle plume or decompression via extension (McKenzie, 1989; Pilet et al., 2011). The resultant enriched, alkali melts are believed to contribute significantly to OIB volcanism globally (Menzies and Wass, 1983; Zhang et al., 2001; O'Reilly and Griffin, 2013). Given the time associated with generating and transporting melts, metasomatised lithosphere is most prevalent in Archean cratons but may also be present in very old oceanic plates, although enrichment here is likely to be volumetrically lower (McKenzie, 1989). It is also possible that the subduction of metasomatised oceanic lithosphere or delamination of metasomatised continental lithosphere may contribute to the source of some OIB rocks.

In this study, I use the major element, trace element and isotopic characteristics of basalts from eastern Australia to assess the contribution of lithospheric versus asthenospheric melt in each volcanic province. I also assess what geodynamic mechanisms might have been in operation throughout the Cenozoic Era to produce the array of volcanic rocks found there today.

1.2 Mechanisms

As an alternative to the Plume Theory, a complex array of plate-related processes and mechanisms have been used over the years to explain, particularly non-age-progressive, intraplate volcanism. Some of the more popular explanations include the Plate Theory, Gravitational Instability, Small-scale Sub-lithospheric Convection (SSC), Edge-Driven Convection (EDC), and Shear-Driven Upwelling (SDU) (e.g. Ballmer et al., 2009; Conrad et al., 2010; Petersen et al., 2018; Davies and Rawlinson, 2014; Demidjuk et al., 2007; Finn et al., 2005; Oostingh et al., 2016; Rawlinson et al., 2017; Sutherland et al., 2012).

The Plate Theory

The Plate Theory refers to the notion that all intraplate volcanism may be explained by lithospheric extension, where changes in plate stresses permit pre-existing partial melt to escape to the surface (Foulger, 2005; Anderson, 2007). If this extension is sufficient to thin the lithosphere, additional magma may form through decompression melting, and if this extension evolves spatially, age-progressive volcanism may develop (Anderson, 2002). Lithospheric stress fields are a product of plate-boundary forces, plate temperature, lithospheric flexure, and topography (Zoback and Zoback, 1989) and changes to any one of these factors may have influenced intraplate volcanism within eastern Australia. From $\sim$95 Ma onward the eastern edge of the Australian Plate has been subject to numerous changes in plate boundary configurations as well as major topographic changes with the emplacement of the Great Dividing Range (Hall, 2002; Crawford et al., 2003; Johnson, 1989; Vasconcelos et al., 2008). Part of this thesis assesses any significant tectonic events that may have aided the initiation of intraplate volcanism in eastern Australia by altering the stress regime of the plate.

Gravitational Instability

Gravitational instability (or Rayleigh-Taylor instability) occurs where the lower continental lithosphere becomes denser than the mantle underlying it, causing removal and sinking of the lithosphere (e.g. Bird, 1979; Houseman and Molnar, 1997; Le Pourhiet et al., 2006; Gorczyk et al., 2012). This leads to three processes that may induce melting underneath the continent: (1) convection in the resulting lithospheric void; (2) hydrous fluids entering the asthenosphere from the falling lithosphere; and (3) melting of the falling piece of lithosphere (Elkins-Tanton, 2007). For instability to occur the lower lithosphere must be both denser than the material underlying it but also have a viscosity low enough to flow (Conrad and Molnar, 1997; Morency et al., 2002; Elkins Tanton et al., 2002). Density variations may arise from compositional differences, such as buoyant mantle residuum beneath the lithosphere (Elkins-Tanton, 2007), through cooling or mechanical thickening of the lithosphere (Houseman and Molnar, 1997; Conrad, 2000), or through the occurrence of denser minerals in the lithosphere (Elkins-Tanton, 2007). One problem with this theory is that the high density required for lithosphere to sink is relatively difficult to achieve and given the vast distance over which Cenozoic volcanism has erupted in eastern Australia it is unlikely to all be the product of gravitational instability.

Small-scale Sub-lithospheric Convection (SSC)

Small-scale Sub-lithospheric Convection (SSC) develops where the cold thermal boundary layer (TBL) at the base of mature oceanic lithosphere reaches a critical thickness (Bonatti and Harrison, 1976; Haxby and Weissel, 1986; Van Hunen and Zhong, 2006; Ballmer et al., 2009). At this point, convection, rather than conduction, becomes a more efficient mechanism for transporting heat through the mantle and the lithosphere base develops elongate rolls, roughly 200–300 km apart, which are aligned parallel to plate motion (Richter and Parsons, 1975; Ballmer et al., 2007). As convection commences, it first removes the depleted harzburgite layer and subsequently brings fresh, warm asthenospheric mantle into shallower depths, resulting in decompression melting (Ballmer et al., 2007). Melting is then self-perpetuated by the positive density anomalies of partially molten peridotite (Tackley and Stevenson, 1993; Raddick et al., 2002; Hernlund et al., 2008). The degree of melting generated by SSC depends on: (1) the effective viscosity in the asthenosphere, and (2) the amount of pre-existing lateral density heterogeneity (Huang and Zhong, 2005; Korenaga and Jordan, 2002; Dumoulin et al., 2005). The duration of melting generated by SSC is then constrained by cooling of the asthenosphere

as it mixes with the cold thermal boundary (Ballmer et al., 2007). The resultant volcanic chains are not expected to be age-progressive but SSC could explain long-lasting, coeval volcanism occurring over large distances (Ballmer et al., 2007).

Edge Driven Convection (EDC)

Edge Driven Convection (EDC) is an instability that develops at the boundary between thick lithosphere i.e., an Archean craton, and thinner lithosphere i.e., an oceanic plate (King and Anderson, 1998; King and Ritsema, 2000). Cratonic roots and oceanic plates represent relatively fixed, boundaries compared with the underlying asthenosphere, and as such, both will evolve to a point where they are nearly the same temperature (King and Anderson, 1998; King and Ritsema, 2000). At this point, the vertical temperature variation along the edge of the cratonic root will be almost uniform leading to the cooler craton being juxtaposed against warmer asthenosphere (King and Anderson, 1998; King and Ritsema, 2000). This vertical thermal boundary is an unstable condition and will generate small-scale flow, but only in the absence of other upper-mantle instabilities or large-scale plate flow (King and Anderson, 1998; King and Ritsema, 2000). The flow is expected to adopt a horizontal wavelength similar to the depth (Turcotte and Schubert, 2002; King and Anderson, 1998; King and Ritsema, 2000). Therefore it is reasonable to expect that weak upwellings 600–1000 km from the craton boundary are from EDC (King and Anderson, 1998; King and Ritsema, 2000). In all models, EDC melting happens soon after beginning the model and for only a short time span, so any significant magmatism resulting from EDC beneath mature oceanic lithosphere is unlikely (Córdoba and Ballmer, 2021).

Shear-Driven Upwelling (SDU)

Shear-Driven Upwelling (SDU) is the asthenospheric equivalent of shear-driven cavity flow, an engineering principle in which shear flow in a channel induces circulatory flow within an adjacent fluid-filled cavity, or step (e.g. Shankar and Deshpande, 2000; Conrad et al., 2010). In the mantle, shear develops from the relative motion between the rigid lithosphere and the convective asthenosphere (Conrad et al., 2010; Till et al., 2010; King and Anderson, 1998). All previous mechanisms discussed i.e. gravitational instability, small-scale convection, edge-driven convection, and even plume impingement, rely on density heterogeneity between the lithosphere and asthenosphere to create instabilities. SDU however, invokes lateral viscosity heterogeneity and vigorous asthenospheric shear to drive upwelling flow and decompression melting (Conrad et al., 2010). One of the main requirements in the development of SDU is vigorous shearing between the lithosphere and asthenosphere which has been observed in the Basin and Range province of North America where other mechanisms have failed to explain the occurrence of intraplate volcanism (Humphreys and Dueker, 1994; Silver and Holtz, 2002; Van Der Lee and Frederiksen, 2005; Conrad et al., 2007), but it is not a condition frequently observed in eastern Australia, so how big a role this mechanism might play in inducing volcanism across the three Australian chains is unknown.

It is entirely likely a combination of a number of mantle reservoirs and processes contribute, in varying amounts, to intraplate volcanism globally. Lying on both continental and oceanic lithosphere and consisting of both age-progressive and non-age-progressive volcanism, the East Australian, Tasmantid, and Lord Howe volcanoes offer an excellent opportunity to test each of the hypotheses discussed above. The primary aim of this study is to use geochemical and volumetric observations to assess which of these mechanisms best fit the data and which can most feasibly, and most simply, explain the assortment of basaltic rocks found here. Some of the more specific objectives of this thesis include:

- The collection of major and trace element data to assess the depths and degrees of partial melting of each volcanic suite and thus analyse the contribution from the deep asthenosphere, shallow asthenosphere, and the sub-continental lithospheric mantle (SCLM).
- The comparison of continental samples to the oceanic Tasmantid samples to further distinguish whether the SCLM plays a significant role in inducing geochemical differences within these rocks. To date, the latter have only been studied by two authors (Eggins et al., 1991; Ruttor et al., 2018).
- The collation of isotopic work to assess the contributions of depleted mantle (DM), enriched mantle I (EMI), enriched mantle II (EMII), and high U/Pb (HIMU) mantle reservoirs to establish whether or not each volcanic suite shares a common source.
- The topographic extrapolation of present-day volcanic outcrops to estimate the original volumes of each province, in turn concluding what the most plausible mechanisms may be for creating the volume and the geochemical array of intraplate volcanoes observed across eastern Australia today.

Chapter 2

Literature Review



Figure 2.1: *The Undara lava tube, McBride volcanic province, far north Queensland.*

2.1 Geological History of Eastern Australia

Australia has an extensive and complex geologic history dating back to the Archean. Very broadly speaking, rocks young from west to east across the continent. The Yilgarn, Pilbara and Gawler cratonic shields in western Australia are some of the oldest rocks in the world and are bounded by a number of Proterozoic foldbelts and epicratonic sedimentary basins (Johnson, 1989; Myers et al., 1996). In eastern Australia, Proterozoic outcrops are found only in the Georgetown and Coen Inliers of Northern Queensland, as well as the Rocky Cape and Tyennan Blocks of Tasmania. These are all separated from Phanerozoic rocks further east by the Tasman Line (Shaw et al., 1996) (Figure 2.2). Throughout the Paleozoic and much of the Mesozoic, the eastern edge of the Australian landmass underwent successive orogenic cycles of subduction, compression and arc volcanism that defines much of the crust today, and subsequently, the subcontinental lithospheric mantle which underlies it (Veevers, 1984; Johnson, 2009). These are collectively known as the Tasman Fold Belt, the main elements of which are (1) the Cambro-Ordovician Kanmantoo Fold Belt; (2) the early to mid Paleozoic Lachlan Fold Belt; (3) coeval with the Thompson Fold Belt; (4) the early to mid Paleozoic Hodgkinson-Broken River Fold Belt; (5) the Permo-Triassic Sydney-Bowen Basin; and (6) the mid to late Paleozoic New England Fold Belt (Figure 2.2). The Paleozoic-Mesozoic Tasman Fold Belt is variably overlain by a cover of Mesozoic-Cenozoic sedimentary and igneous rocks, which includes the East Australian volcanic chain.

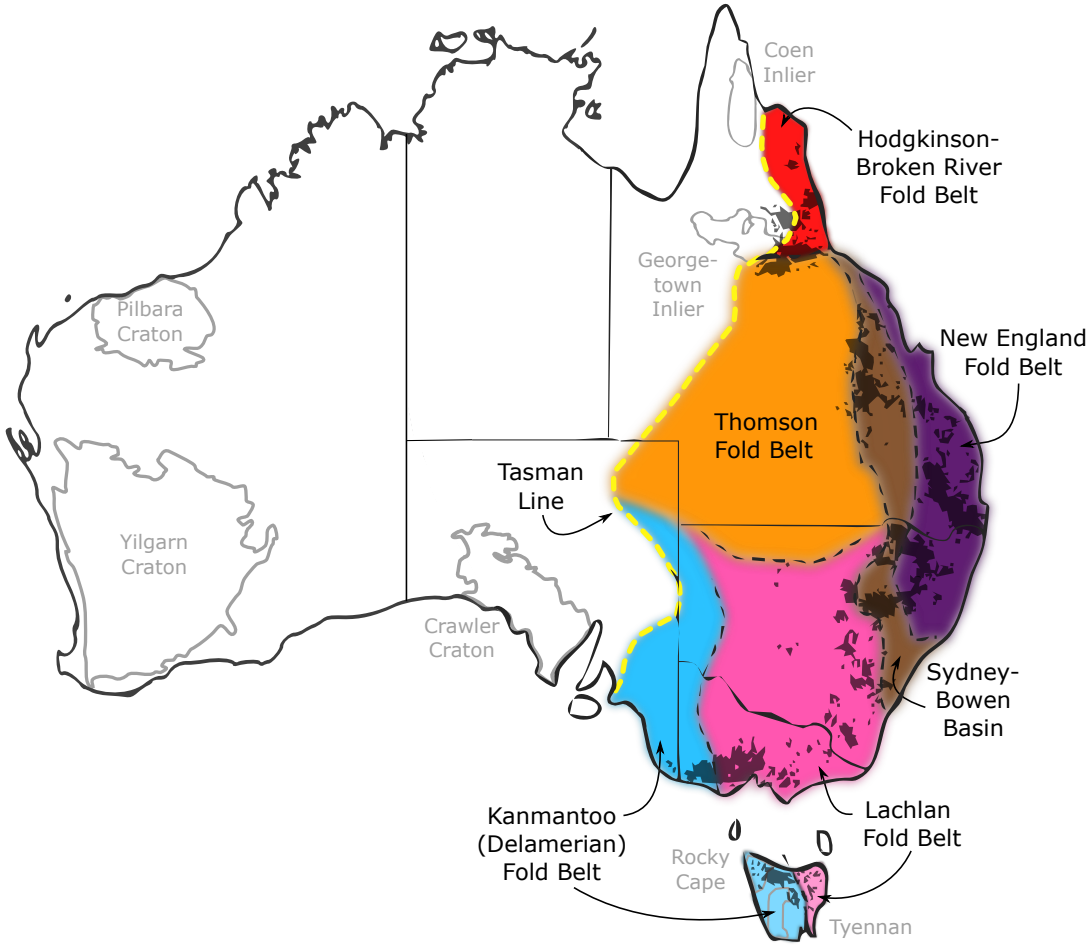

Figure 2.2: *The six main units of the Tasman Fold Belt, modifed after Crawford et al. (2003) with the east Australian intraplate volcanoes in black.*

2.2 East Australian Intraplate Volcanism

Intraplate volcanism in eastern Australia extends over 3000 km through Queensland, New South Wales, Victoria, South Australia, and Tasmania, and at roughly 500 km wide, it is one of the most extensive regions of intraplate volcanism in the world (Wellman and McDougall, 1974a; Davies et al., 2015). Magmatism here

occurred from the late Mesozoic, around 84 Ma, with the opening of the Tasman Basin, and continued up to the Holocene (Johnson, 1989). Offshore to the east, the Tasmantid chain stretches over 2400 km and sits primarily on oceanic lithosphere (McDougall and Duncan, 1988). Volcanism along the chain took place between 56 and 7 Ma and seamount morphology appears to be strongly governed by lithospheric faults inherited from the extinct Tasman mid ocean ridge (Richards et al., 2018) which ceased spreading around 52 Ma (Crawford et al., 2003). Results from the Louisiade Plateau at the northern end of the Tasmantid chain suggest that it is composed of basalt of the correct age to be a large igneous province (LIP) formed by the impact of the proposed Tasmantid plume head reaching the lithosphere (Kalnins et al., 2015). However, this hypothesis is still in it's infancy and a detailed study of the entire plateau would need to be undertaken to confirm or deny this. The Lord Howe volcanoes, which cover a similar length but offset to the northeast, lie on a drowned continental fragment that rifted away from the Australian mainland approximately 84 Ma (Gaina et al., 1998; Veevers et al., 1991). Many authors have drawn comparisons between the three chains in terms of age, longevity and surface signature. Geochemically speaking, volcanism from these three areas can be split into five distinct suites (Figure 6.24):

1. **Central volcanoes:** continental volcanoes, chemically bimodal, slightly undersaturated to saturated mafic lavas with some felsic intrusions and flows. Primarily composed of olivine basalt and hawaiite, with some tholeiitic basalt, mugearite, benmoreite, trachybasalt, trachyte, comendite, and rhyolite (Wellman and McDougall, 1974a; Ewart et al., 1988; Grenfell, 1984; Shao et al., 2015; Crossingham et al., 2018). Age analyses for the central volcanoes show a strong age progression from 34–6 Ma, younging southward (e.g. Wellman and McDougall, 1974a; Cohen et al., 2013).

2. **Leucitites:** continental volcanoes, volumetrically negligible, leucite-phlogopite-bearing minor intrusions and flows that are found only in central New South Wales and Victoria (Wellman and McDougall, 1974a; Cundari, 1973; Nelson et al., 1986; Paul et al., 2005). K/Ar and $^{40}Ar/^{39}Ar$ results from the leucitite suite are contemporaneous with the central volcanoes (Wellman et al., 1970; Cohen et al., 2008).

3. **Lava fields:** continental volcanoes, mafic, often strongly undersaturated, generally thin and extensive in area. Primarily composed of olivine basalt, with some hawaiite, nephelinite, melilitite, and basanite (Wellman and McDougall, 1974a; Ewart et al., 1988; McDonough et al., 1985; O'Reilly and Zhang, 1995; Oostingh et al., 2016). Emplaced between 84 and 0 Ma, the lava fields exceed the duration of central volcano and leucitite volcanism but show no age progression (Vasconcelos et al., 2008). The most recent lava field eruptions were 7000 years ago in northern Queensland, and 4300 years ago in South Australia, at opposite ends of the East Australian chain (Cohen et al., 2017).

4. **Tasmantids:** the Tasmantid seamount chain which consists of saturated tholeiitic to transitional alkali-olivine basalt, with very few undersaturated examples (McDougall et al., 1981). $^{40}Ar/^{39}Ar$ data for the Tasmantids exhibit a younging trend north to south from 56–7 Ma, concurrent with the age progression of the continental chain (Kalnins et al., 2015; McDougall and Duncan, 1988).

5. **Lord Howe:** the Lord Howe seamount chain also consists of saturated tholeiitic to transitional alkali-olivine basalt, with very few undersaturated examples (Eggins et al., 1991) and $^{40}Ar/^{39}Ar$, K/Ar and biostratigraphic dating results from the Lord Howe chain also show southward younging ages from around 28–7 Ma, coeval with the Tasmantids, central volcanoes and leucitites (Seton et al., 2019a; Mortimer et al., 2010; Quilty, 1993).

Over the past couple of decades, a number of mechanisms have been proposed to try and explain the origins of each of the suites, for example: (1) three independent deep seated hotspots (Johnson, 1989); (2) interaction with a remnant oceanic slab beneath the Tasman Sea (Kalnins et al., 2015) (Figure 2.4); (3) diffuse flow of the Pacific mantle (Finn et al., 2005); (4) edge-driven convection (EDC) (Davies and Rawlinson, 2014; Rawlinson et al., 2017). Mechanisms from other regions that may be applicable to eastern Australia include: (5) a plume pooling at the 660 km discontinuity with separate conduits to the surface (Saki et al., 2015; Ballmer et al., 2013); and (6) small-scale convection (SSC) beneath the lithosphere (Ballmer et al., 2009, 2011). This is not an exhaustive list and it is likely that more than one mechanism is needed to explain the variety of volcanism occurring over the east Australian continent and adjacent oceanic crust. An example of how a few of these processes might develop and interact beneath Eastern Australia is given in Figure 2.4.

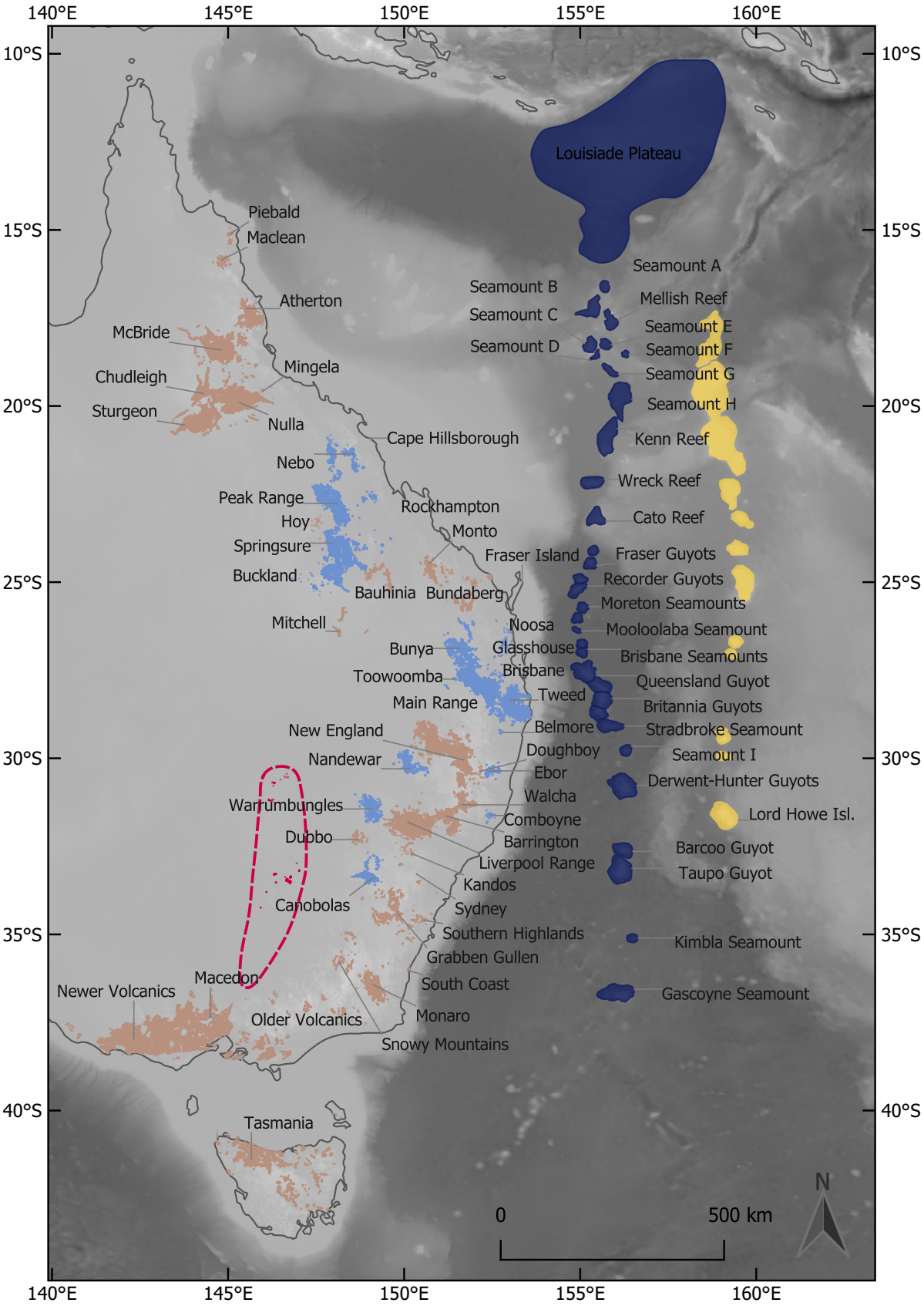

Figure 2.3: *Individual volcanic provinces within the five volcanic suites. Tasmantid seamounts marked in navy; Lord Howe seamounts in yellow; central volcanoes in light blue; lava fields in tan; and leucitites within the dashed crimson area. Topographic and Bathymetric grid from GEBCO (2020).*

Broad spatial and temporal patterns, as well as changes in chemistry between each of the five suites are all likely to reflect the area of the mantle from which they are sourced. Chemically, heterogeneous mantle reservoir exists in the form of primitive mantle (PM), depleted mantle (DM), and enriched mantle (EM); including high U/Pb mantle (HIMU), enriched mantle I (EMI), and enriched mantle II (EMII) (e.g. Zindler and Hart, 1986; Hart et al., 1992; Hofmann, 1997). Enriched components may be derived from the lower asthenospheric mantle, the upper asthenospheric mantle or the subcontinental lithospheric mantle (SCLM), which may be further enriched via mantle metasomatism. This becomes ever more complicated when source heterogeneity is intertwined with secondary processes such as magma mixing, differentiation by partial melting, fractional crystallisation, crustal contamination, and surface alteration (e.g. DePaolo, 1981; McKenzie and O'Nions, 1991). Below I summarise some of the key findings to date relating to the possible heterogeneous mantle sources and secondary processes operating to form these intraplate volcanoes. For ease, interpretations have been split between the five suites.

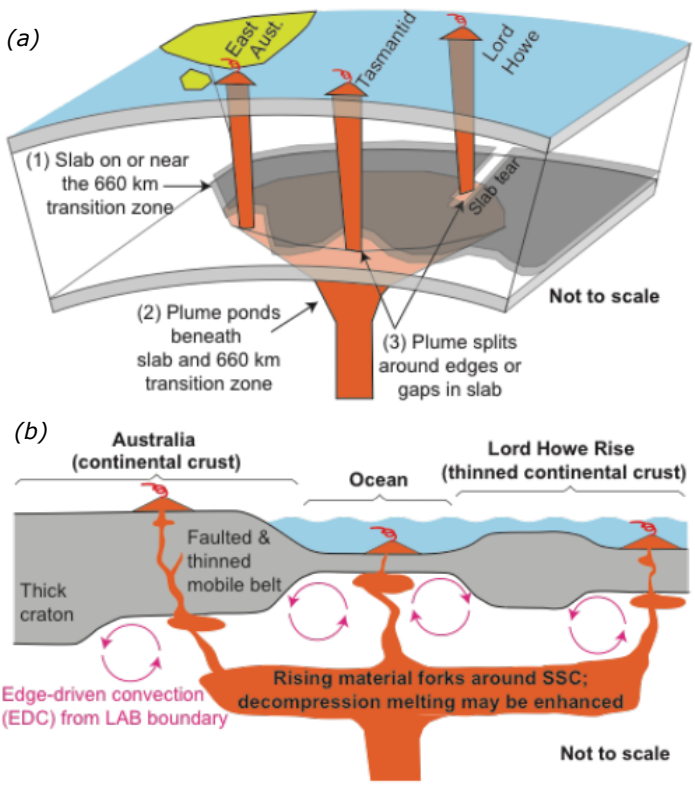

Figure 2.4: *(a) Depiction of a stagnant slab at the 660km discontinuity, intersected by a mantle plume which then splits into 3 distinctly smaller plumes (Kalnins et al., 2015) (b) Schematic of how undulating lithosphere thicknesses creating SSC may result again in the splitting of a mantle plume (Cohen, 2018; Kalnins et al., 2020).*

2.2.1 Central Volcanoes

Despite the considerable volume of central volcanoes across Australia, they have been relatively understudied when compared with coeval lava fields. A deep asthenospheric plume has long been considered as the dominant source of central volcano magmatism, although this appears primarily to be due to reported OIB-like trace element patterns, Sr-Nd-Pb-isotope ratios indicating an EMI-like source, and the observed southward younging age trend (e.g. Crossingham et al., 2018; Sun and McDonough, 1989; Ghorbani and Middlemost, 2000; Jones et al., 2020) (Figure 2.5). This age progression suggests the central volcano source is decoupled from the lithosphere and present-day heat flow, seismological and residual P-wave data point towards melting deep within the mantle beneath the Bass Strait where the inferred East Australian Plume would sit today (O'Neill et al., 2003; Quigley et al., 2010; Montelli et al., 2004). However, complications with this theory arise where central volcanoes of similar ages form hundreds of kilometers apart, such as the Buckland and Glasshouse volcanoes which are the same age but separated by a distance of ~500 km (Figure 2.5), or where geochemical analyses with non-age-progressive lava fields show considerable similarities (Figure 2.6). Also, the influence of the SCLM on the central volcanoes has been discussed by Crossingham et al. (2018) who suggest pronounced negative K anomalies in some central volcano basalts may be due to melting within the presence of a residual K-rich phase such as amphibole and/or phlogopite in the lithospheric mantle (Class and Goldstein, 1997).

The most distinguishable feature of the central volcanoes is that they are bimodal and significantly more fractionated than other provinces (Ewart et al., 1980, 1988). The importance of fractional crystallisation in controlling the evolution of the magmas is clear from major element chemistry with dual patterns of progressive element enrichment (e.g., Pb, Th) and depletion (e.g., Mg, V, Ni, Cr, Sr, Ba, Eu). Modeling of central volcano basalts by Ewart et al. (1988) show that overall Ni-MgO depletion trends are consistent with extensive olivine crystallisation alongside pyroxene and plagioclase phases. Trachytes and peralkaline rocks are shown to be residual magmas generated by further fractional crystallisation (Ewart, 1982; Cohen, 2002), and peraluminous rhyolites are probably the result of crustal melting following magmatic influx and underplating (Cohen, 2002; Shao et al., 2015).

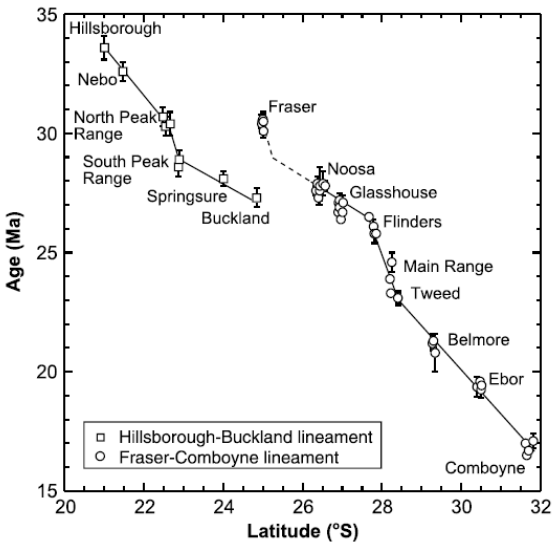

Figure 2.5: *$^{40}Ar/^{39}Ar$ results of silicic rocks from the east Australian central volcanoes, showing a southward decrease in age (Cohen et al., 2013).*

Minor occurrences of olivine and feldspar accumulation, shown by positive anomalies in MgO-Ni-Cr and Ba-Sr-Eu, respectively, have also been observed in this suite, although rarely. This includes trachyte and mugearite lavas from the Nandewar central volcano (Stolz, 1985) and trachybasalt and trachyte lavas from the Warrumbungle and Comboyne central volcanoes (Crossingham et al., 2018). In both studies, rocks thought to be affected by accumulation are extremely limited and the vast majority of samples are more consistently modeled through fractional crystallisation alone. Analysis of heterogeneous mantle sources throughout this study has not focused on commonly considered mobile elements (Mg, Ni, Cr, Ba, Sr, Eu) but primarily on immobile trace elements. No studies have detailed petrographic or geochemical evidence of magma mixing in any of the east Australian central volcanoes (e.g., evidence of recycled minerals). However, to date, few studies of individual volcanoes have actually been conducted when compared to the lava fields (e.g. Crossingham et al., 2018; Sun and McDonough, 1989; Ghorbani and Middlemost, 2000; Jones et al., 2020).

Mild assimilation of crustal material during fractional crystallisation (AFC) has also been described by a couple of authors with regards to the central volcanoes. A few tholeiitic basalts have been found to exhibit small positive Pb and K anomalies, relatively high Ba/Nb and La/Nb ratios, relatively high $^{87}Sr/^{86}Sr$, moderate $^{206}Pb/^{204}Pb$, and low ε_{Nd} which can all, in theory, be modeled by contamination with arc-like crust (e.g. Ewart et al., 1988; Price et al., 1997; Crossingham et al., 2018). However, the same values may just as easily be modeled by various degrees of partial melting of heterogeneous mantle sources, particularly derivation from subduction-modified lithosphere which may mimic a crustal signature (Ewart et al., 1988). This has been examined further in this thesis but due to the relative difficultly in altering magma chemistry through crustal interaction as oppose to partial melting of the lithospheric mantle (e.g. Lum et al., 1989; Kempton et al., 1991; Wedepohl, 1995), the latter is presumed to have had a greater influence. Also, since SCLM enrichments are observed in the most primitive central volcano samples as well as in other continental rocks (see later Chapters), these would also be expected to be present in the less primitive central volcano magmas and may, more simply, explain the geochemical signatures that have been described as being inherited from AFC processes. If assimilation of crust were to play a role in inducing some chemical variation across the suite, it is expected to be fairly limited and certainly not observed frequently enough to explain the full range of central volcano samples. Throughout this work, any analyses focusing on heterogeneous mantle sources have only used the most primitive rocks (MgO >7 wt%) which are unlikely to have been significantly affected by any assimilation or contamination of upper or lower crustal material.

Most evidence presented here suggests that accumulation, magma mixing, and crustal assimilation are very unlikely to explain the main isotopic and trace element trends of, particularly the most primitive, central volcanoes within eastern Australia. Whilst fractional crystallisation is presumed to account for most of the magmatic differentiation across the region (Ewart et al., 1988; Johnson, 1989), modeling of this can still not account for the broad scatter within geochemical data. Therefore, variation is more likely to reflect melting of heterogeneous mantle sources and differing degrees of partial melting. As decompression partial melting of a mantle plume occurs close to the base of the SCLM it is often interwoven with partial melting of the upper asthenosphere itself (White and McKenzie, 1989) and partial melting, through thermal perturbation, of metasomatised layers in the SCLM (Zhang et al., 2001). It is therefore, not unusual for primitive continental basalts to record the signatures of at least three major mantle reservoirs and each of these will need to be analysed in this work. For this study, as I am interested in source compositions, analysis will focus entirely on the less evolved volcanic rocks, with $SiO_2 < 55$ wt%, and primarily on immobile trace elements (e.g. Nb, Zr).

2.2.2 Leucitites

The leucitite suite of continental volcanoes outcrop throughout central NSW and into Victoria (Cundari, 1973; Nelson et al., 1986; Ewart et al., 1988). With around 10 times as much Na in the mantle compared with

K, prolonged lithospheric interaction is generally required to produce K > Na, as is the case for the leucitites. However, given a clear age-progression coeval with the central volcano and seamount chains, recent work by Cohen et al. (2008) and Davies et al. (2015) have shown the leucitites may be directly linked to the central volcanoes, implying a plume origin. However, if an asthenospheric plume is the primary source, it was suggested that at least two plumes would be needed to explain the southward migration of both the leucitites and central volcanoes, separated by a lateral distance of ∼300 km. Some authors have discounted a direct plume origin because Pb isotope systematics differ from the inferred "plume" component of the central volcanoes (Nelson et al., 1986; Ewart et al., 1988). They instead associate age-progressive volcanism with thermal reactivation of the SCLM and partial melting following passage over a hotspot, although this is difficult to model without material input from the hotspot itself. Nelson et al. (1986) concluded that the source of the leucitites was contaminated by a isotopic component typical of the Dupal anomaly region of Hart (1984), which is also found in some central volcanoes and lava fields in Victoria and Queensland (Ewart et al., 1988). Through analysis of major and trace element concentrations the lithospheric versus asthenospheric origin of the leucitites is discussed in Chapter 5 of this thesis. This is followed by an isotopic analysis of the suite in comparison to the central volcanoes, lava fields, and seamounts. What role the Dupal anomaly region might play in the formation of the east Australian volcanoes is also assessed.

2.2.3 Lava Fields

Historical interpretation of the lava fields has been consistent with an upper mantle derivation as opposed to the deep-plume model of the central volcanoes, primarily due to the lack of any observed age-progression (Johnson, 1989). However, as with the central volcanoes, incompatible element and Sr-Nd-Pb isotope results vary between rock types and show complex patterns possibly representative of a number of mantle sources including: (1) a deep asthenospheric plume-like component (e.g. Davies et al., 2015; McDonough et al., 1985); (2) a shallow asthenospheric MORB-like component (e.g. Zhang et al., 2001; Sutherland, 2003); and (3) a metasomatised SCLM component (e.g. Ewart et al., 1988; Zhang et al., 2001) (Figure 2.6). The predominantly undersaturated, high-Mg, lava fields are believed to exhibit much less contamination by crustal components, and much less fractional crystallisation than the central volcanoes (Ewart et al., 1988).

Work by Zhang et al. (2001) shows that assimilation of continental crust is expected to be low in the lava fields based on: (1) high SiO_2 and low MgO basalts have some of the lowest concentrations of elements typically found in the felsic upper crust (e.g. Pb, K, Rb); (2) primitive magmas within single provinces display broadly positive but different SiO_2–K/Nb trends suggesting any homogeneous enrichment from the crust is insignificant; (3) Sr/La ratios appear too low to have been derived by crustal contamination; (4) many lava fields have Ce/Pb ratios within the range of most oceanic basalts (Hofmann et al., 1986) and any variation appears to be driven by changes in Ce as oppose to Pb, which is unlikely to be produced by crustal contamination but instead partial melting or source enrichment; (5) based on simple mass balance equations, the mafic nature of granulite-facies lower-crust xenoliths found within lava field provinces makes them ineffective contaminants with at least 40–80 wt% of material required to produce the recorded concentrations of SiO_2; (6) the abundance of mantle xenoliths and high-pressure megacrysts in many lava fields requires fast transportation to the Earth's surface and precludes any significant interaction between magma and crustal wall rocks (Zhang et al., 2001).

The influence of a deep asthenospheric "plume" source in the lava fields has been described by Sun and McDonough (1989); McDonough et al. (1985); O'Reilly and Zhang (1995); McBride et al. (2001);

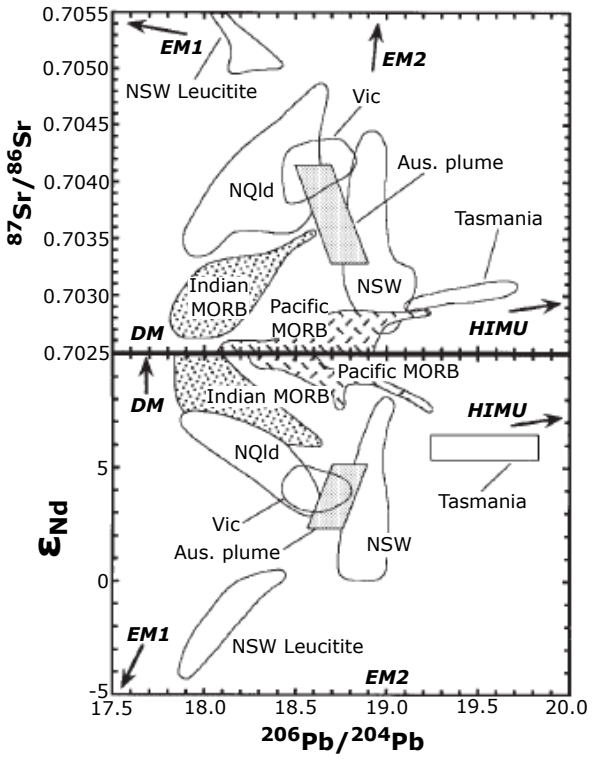

Figure 2.6: *Lava field Sr-Nd-Pb isotope data (NQld, Vic, NSW, Tasmania), including the central volcano suite (Aus. plume), and the NSW leucitite suite (Zhang et al., 2001).*

Crossingham et al. (2018); and Jones et al. (2020). Most authors have reached this conclusion based on the geochemical similarity of $^{87}Sr/^{86}Sr$, ε_{Nd} and $^{206}Pb/^{204}Pb$ isotopic data to the enriched "plume" component of the central volcanoes. Jones et al. (2020) suggest that Sr-Nd-Pb isotopic results from lava field provinces in Queensland and New South Wales (NSW), which extend from the FOZO mantle reservoir and along the EMI array are indicative of a similar plume-like origin. It should be noted however, that these results also extend into the Pacific MORB and Indian MORB isotopic fields of Ito et al. (1987). Zhang et al. (2001) and Sutherland (2003) have instead interpreted this as evidence of a shallower MORB-like source. Zhang et al. (1999) go further to suggest the Indian MORB is a widespread long-term reservoir beneath eastern Gondwana lithosphere, whilst westward migration of the Pacific MORB may be associated with Tasman Sea opening ~80–65 Ma (Veevers et al., 1991; Zhang et al., 1999). More recently, a few authors have suggested that the geochemical and geophysical characteristics of lava fields in Victoria may relate to upwelling of the asthenosphere by edge-driven convection along the boundary between continental and oceanic lithosphere (e.g., Demidjuk et al., 2007; Price et al., 2014; Davies and Rawlinson, 2014; Boyce et al., 2015). Edge-driven convection relies on steep variations in lithospheric thickness forming areas of thermal instability where cycling asthenosphere is sharply juxtaposed against cooler lithosphere (e.g., Farrington et al., 2010). Where lithospheric thickness variations are accompanied by plate motion-induced shear, convection is focused in relatively thin sections of lithosphere (Davies and Rawlinson, 2014). This mechanism goes some way to connect the geochemical characteristics of an asthenospheric source with seismic tomographic results of localized upwelling within the lava fields (Davies and Rawlinson, 2014; Rawlinson et al., 2017) but how it relates to lava field volcanism further north or central volcano volcanism is unclear.

The role of metasomatised SCLM in generating the lava fields has been a popular area of debate, although most studies agree that the SCLM exerts at least some influence on east Australia's volcanoes (e.g., Kesson, 1973; Menzies and Wass, 1983; O'Reilly and Zhang, 1995; Zhang et al., 2001; Sutherland et al., 2002; Roach et al., 2008). Metasomatism is thought to be one mechanism which introduces mobile large ion lithophile elements (LILE) and light rare earth elements (LREE) into the otherwise depleted mantle. Menzies and Wass (1983) studied trace element patterns of alkaline rocks and associated apatite-rich xenoliths from the Southern Highlands in New South Wales (NSW) to find both highly enriched in LILE and LREE. Similarly, O'Reilly and Griffin (1984) showed that Sr-isotope data from basaltic rocks in NSW correlate particularly well with amphibole-bearing xenoliths from the same region. Metasomatic replacement textures have also been reported in east Australian lherzolitic xenoliths by Wass (1980). To further this, O'Reilly and Zhang (1995) and Foden et al. (2002) analysed basalts from across South Australia, NSW and Queensland to find that incompatible trace element enrichments may correlate spatially and temporally to the tectonic evolution of the Australian lithosphere. For example, basalts in north Queensland have anomalously high $^{206}Pb/^{204}Pb$ and high $^{87}Sr/^{86}Sr$ at a given ε_{Nd} compared with other regions. These are also the only provinces to outcrop around the Hodgkinson-Broken River Fold Belt, the Thompson Fold Belt, and the Georgetown Inlier. Such regional differences may be most easily explained by the evolution of the Phanerozoic lithosphere (Zhang et al., 2001) although there are other explanations such as multiple asthenospheric sources that require testing.

The basaltic rocks of Tasmania have markedly different isotopic values compared with other provinces and Cenozoic volcanism here consists entirely of mafic lava fields, primarily melilitites and nephelinites (Johnson, 1989; Nasir et al., 2010). Numerous highly alkaline lavas exhibit a HIMU chemical composition (characterized by low $^{87}Sr/^{86}Sr$, high $^{143}Nd/^{144}Nd$, and high $^{206}Pb/^{204}Pb$) not frequently observed in lavas on the Australian mainland. These are similar to the postulated HIMU Balleny Plume in the South Pacific Ocean over which, the Tasman Sea is speculated to have opened ~84 Ma (Lanyon et al., 1993; Sutherland, 2003) but could also be related to another HIMU-creating mechanism such as lithospheric metasomatism. Meeuws et al. (2019) postulated that basalts across Tasmania may be modeled by various degrees of melting in a three-component mixture of Pacific MORB, HIMU mantle, and SCLM containing remnant Jurassic dolerite signatures.

2.2.4 Seamounts

To date, only two sets of geochemical studies have been carried out on the Tasmantid seamount chain: this includes eleven samples analysed by Eggins et al. (1991), and 32 samples analysed by Ruttor et al. (2018). Collectively, these basalts cover most of the chain from Wreck Reef in the north to Gascoyne seamount further south. Given the subaqueous nature of the Tasmantids, some geochemical characteristics may be attributed to seawater alteration such as P enrichment and anomalous Rb and K (Eggins et al., 1991). Trace element patterns match that of average OIB and the samples are petrologically similar to the central volcanoes (Eggins et al., 1991; Ruttor et al., 2018). Sr-Nd-Hf-Pb isotope ratios have FOZO-EMI-type characteristics, implying a similar plume origin to the continental chain (Ruttor et al., 2018). The only samples from the Lord Howe chain are those from Lord Howe Island itself, where major elements were analysed by McDougall et al. (1981).

Whilst many studies have focused on the origins of east Australian volcanism, few provide definitive results that pinpoint the central volcanoes, leucitites, lava fields or seamounts as originating from a plume, MORB or SCLM source. By analysing 170 new samples from across the three chains each of these hypotheses are here tested in more detail using major and trace element analyses, with a focus on immobile trace elements. Samples from the central volcanoes include 29 rocks collected by Benjamin Cohen (Cohen, 2007), 12 rocks collected during fieldwork for this thesis in 2019, and 16 rocks provided by other researchers in Australia. Eight leucitite samples were also collected during fieldwork in 2019 and one specimen was provided by another researcher. Lava field samples include 24 rocks from Cohen (2007), 36 rocks collected during fieldwork, and 12 rocks provided by other researchers in Australia. The oceanic dataset contains 17 rock samples from a dredging campaign conducted in October-November 2012 in the eastern Coral Sea aboard the RV Southern Surveyor (CSIRO, 2012), along with 15 samples from earlier dredging voyages throughout the 1980s.

2.3 Cenozoic Tectonics

In addition to a thorough geochemical assessment, it is important to document the tectonic regimes through which magmatism has taken place. For a large part of its history, around 370 million years, the Australian landmass was bound within the Gondwana supercontinent (Johnson, 2009; Blewett, 2012). However, around 180 Ma this began to fragment, and at 154 Ma rifting of the Australian continent from Gondwana started along the north west coast, progressing anticlockwise to the Tasman Sea (Gaina et al., 2003; Veevers, 1986). By 120 Ma, India had broken away from western Australia, and by the late Cretaceous this culminated in the separation of Australia from Antarctica (Gaina et al., 1998; Blewett, 2012). Ever since, the isolated Australian continent has been moving northwards (Johnson, 2009). Minor volcanism along the eastern coast began ~84 Ma with the opening of the Tasman Sea, followed by major volcanism beginning ~56 Ma and continuing up to 4300 years ago in a quiescent, intraplate setting (Vasconcelos et al., 2008). Whilst volcanism has been within-plate, from ~95 Ma onwards the eastern edge of the Australian Plate has seen a cocktail of plate boundary configurations resulting in the opening of several major and minor basins, along with the formation of many microcontinents and intra-oceanic arc systems (Hall, 2002; Crawford et al., 2003) (Figure 2.7).

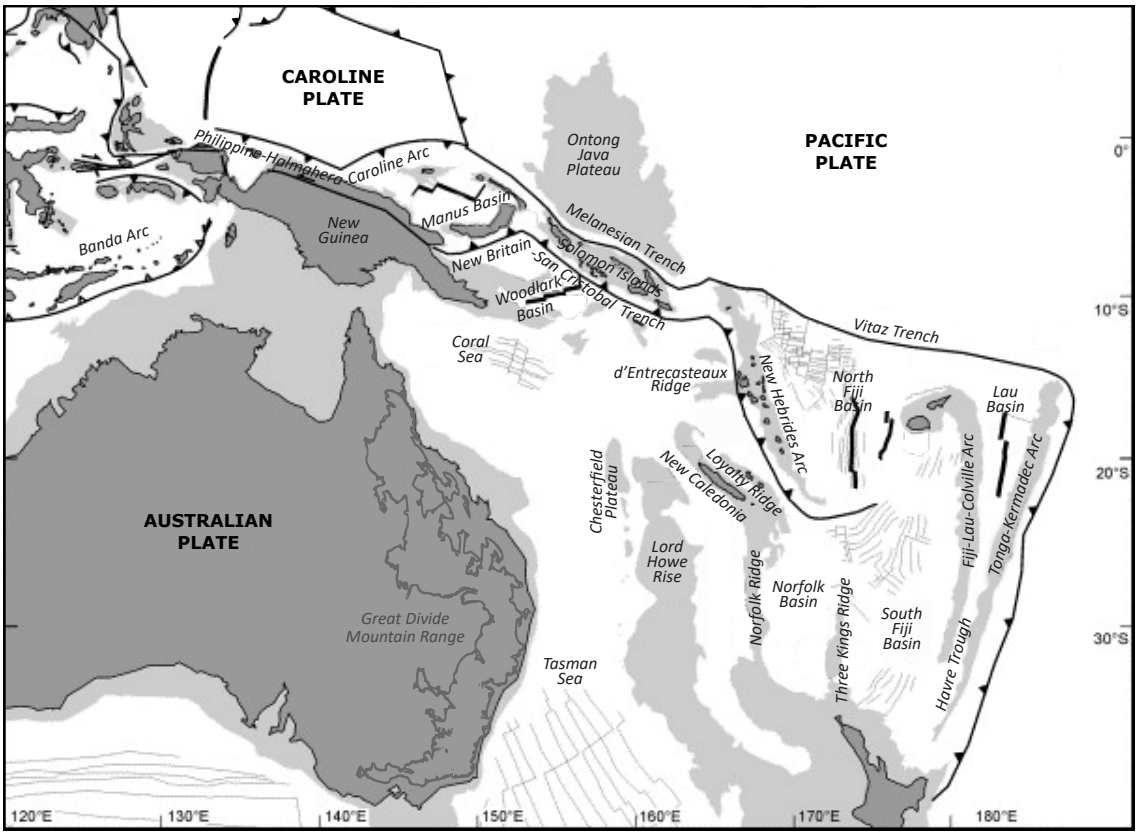

Figure 2.7: *The principle features of the northeastern Australian Plate and neighbouring plates, modified from Hall (2002). The outline of the Great Dividing Range is represented by the 300 m contour.*

Plate driving forces have a considerable effect on intraplate stresses and as such, major plate tectonic events are often accompanied by intraplate tectonic reactivation (Muller et al., 2000). Given that intraplate volcanism may be associated with high tensional stresses within a continent, it is important to evaluate the tectonic events that could have affected the stress regime within the Australian continent throughout the Cenozoic. Also, to further characterise intraplate volcanism in east Australia, Chapter 6 of this thesis focuses on modeling the volume of each volcano. Changes in extruded volumes may be attributed to variations in the volcanic source or to variations in the tectonic regime at the time of emplacement. For this reason, I have documented the primary tectonic changes operating along the northern and eastern edge of the Australian plate throughout the Cenozoic Era and these are summarized in Table 2.1 below. All palaeogeographic reconstructions within the table have been taken from Schellart et al. (2006) and modified to include Cenozoic intraplate volcanoes.

Table 2.1: *Major tectonic events taking place along the boundary of the Australian plate since 100 Ma. Palaeogeographic reconstructions from Schellart et al. (2006) with Cenozoic intraplate volcanoes shown in red. A continuous palaeogeographic reconstruction can also be viewed at EarthByte (2006).*

Age (Ma)	Tectonic Events	Palaeogeography (Schellart et al., 2006)
0	At present, westward subduction of the Pacific plate is accommodated along the Tonga–Kermadec Trench which drives back-arc extension within the Lau Basin (Schellart et al., 2006). Northwestward subduction of the Australian plate is accommodated along the New Britain–San Cristobal–New Hebrides Trench which drives back-arc extension in the North Fiji Basin (Schellart et al., 2006) and northward convergence of the Australian plate transpires as collision across the island of New Guinea (DeMets et al., 2010; Blewett, 2012). The youngest lava field volcanoes were erupted 7000 years ago in far north Queensland and 4300 years ago in Victoria (Cohen et al., 2017; Johnson, 2009). Other lava fields volcanoes in far north Queensland and Victoria were erupted primarily within the last 10 Ma.	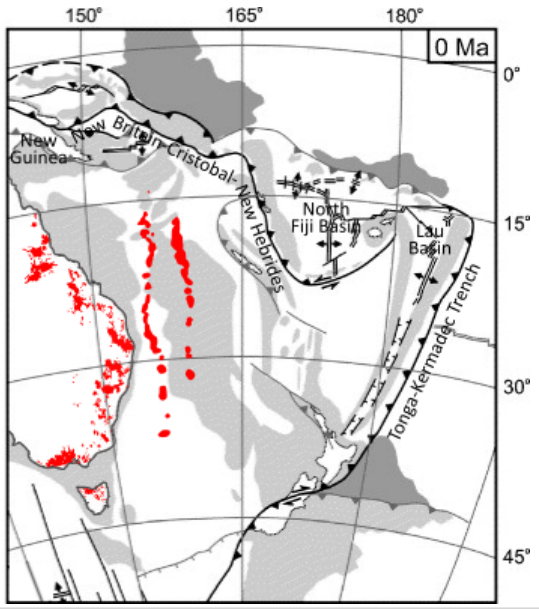
6	At this time, clockwise rollback of the New Hebrides subducting slab resulted in continued opening of the North Fiji Basin and rotation of the New Hebrides arc (Schellart et al., 2006). Further rollback of the Pacific plate resulted in spreading of the Lau Basin and Havre Trough ∼5 Ma (Parson et al., 1994), the Woodlark Basin ∼6 Ma (Taylor et al., 1995) and the Manus Basin in the Pliocene (Martinez and Taylor, 1996) (Schellart et al., 2006). The youngest central volcano is the ∼6 Ma Macedon-Trentham province in Victoria (Sutherland et al., 2014) and the majority of lava field magmatism in the Newer Volcanic Province in Victoria also occurred less than 5 Ma. This is also the age of the most recent Tasmantid and Lord Howe volcanism.	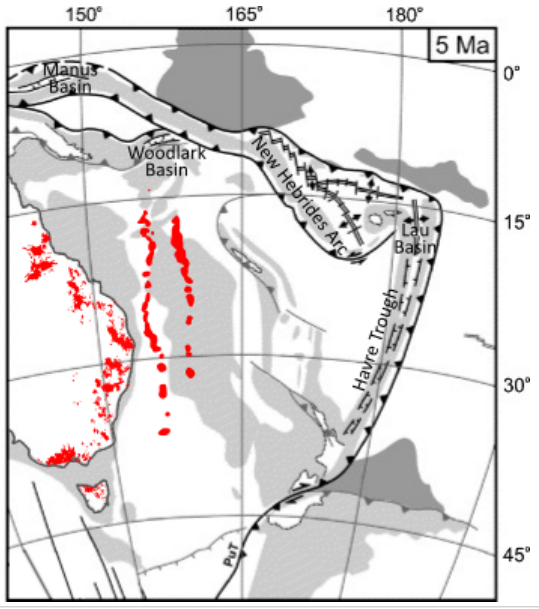

10

This is thought to be the main episode of blocking and compression following collision with the Ontong Java Plateau (OJP) (Petterson et al., 1997; Wessel and Kroenke, 2000). The result was a flip in subduction polarity across the north Australian plate. Westward subduction of the Pacifc plate continued to be accommodated along the Tonga-Kermadec Trench (Muller et al., 2000) but northeastward subduction of the Australian plate started up along the New Britain–San Cristobal–New Hebrides Trench (Yan and Kroenke, 1993). The newly formed New Hebrides Trench soon started to retreat southwestward which led to the opening of the North Fiji back-arc Basin (Schellart et al., 2006). After this time, we see a resurgence of lava field activity in far north Queensland.

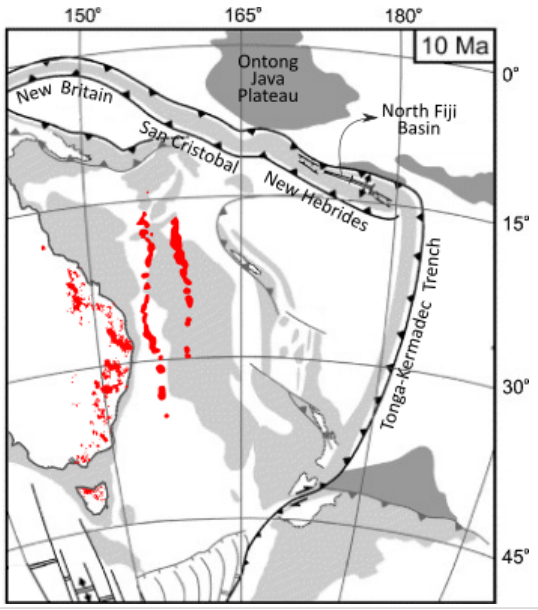

20

Subduction along the Melanesian and Vitiaz Trenches ceased following docking of the OJP (Kroenke et al., 2004). This collision also caused two new subduction zones to form; the Trobriand Trough which initiated southward subduction of the Solomon Sea, and the New Britain-San Cristobal Trench which initiated northward subduction of the Solomon Sea (Schellart et al., 2006). The rest of the Miocene was characterised by a lull in basin formation (Sdrolias et al., 2001) as the Australian plate moved northwards at ∼60 mm/yr (Zahirovic et al., 2015; Knesel et al., 2008). On the continent, lava field volcanism was considerably subdued during this period but emplacement of the central volcanoes, the leucitites and the Tasmantid and Lord Howe seamounts continued to progress southward at a steady rate.

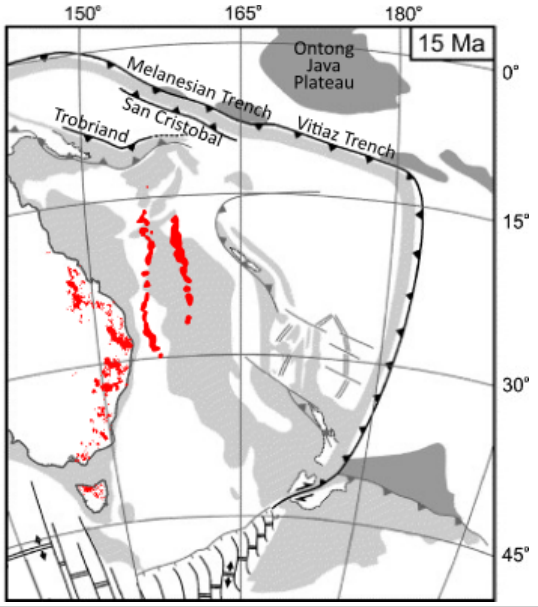

26

Between 26–23 Ma the Australian plate experienced slower migration rates (∼26 mm/yr) and a slight clockwise rotation (Knesel et al., 2008). There was also an increase in the volume and silicic content of central volcanoes around this period, consistent with prolonged crustal residence times (Duncan and Kulm, 1989; Ewart et al., 1985). Subduction along the north of the Australian plate was replaced by left-lateral strike-slip faulting (Yan and Kroenke, 1993; Hall, 2002). There are three major collisions which may have influenced this reorganization (Cohen, 2007), including: collision of Australian continental crust with the southeast Asian margin in Sulawesi (Hall, 2002); continued New Guinea passive margin collision with the Philippine-Halmahera-Caroline Arc which coincided with termination of spreading in the Solomon Sea (Hill and Hall, 2003; Pigram and Davies, 1987);

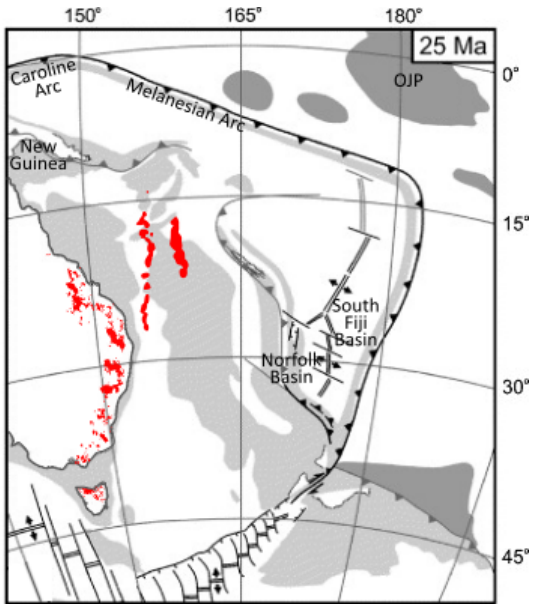

cont'd...	and collision of the OJP with the Melanesian Arc (Petterson et al., 1999; Kroenke et al., 2004). Given the OJP-Australian plate collision was oblique, this is consistent with the initiation of left-lateral strike-slip faulting (Hall, 2002). However the timing of OJP collision remains contentious (e.g. Yan and Kroenke, 1993; Petterson et al., 1999; Mann and Taira, 2004; Holm et al., 2016). A new phase of Pacific slab rollback further accommodated spreading in the South Fiji Basin and Norfolk Basin around this time (Schellart et al., 2006).	
30	Cohen et al. (2013) record a period of reduced plate velocity between 30–29 Ma, coeval with the most intense part of the Peninsular Orogeny in New Guinea with similar orogenesis in New Caledonia (jump in subduction from the east to the west side of the island (Schellart et al., 2006)) and New Zealand. The authors suggest that each of these events may have combined to halt subduction along the Melanesian Arc, reducing the northward slab-pull force of the Australian plate. There is also a considerable reduction in the number of lava fields emplaced around 30 Ma but an increase in the number of central volcanoes and Tasmantids emplaced, each moving southwards through the plate (Cohen et al., 2013). Volcanism along the Lord Howe chain began shortly after this ∼28 Ma.	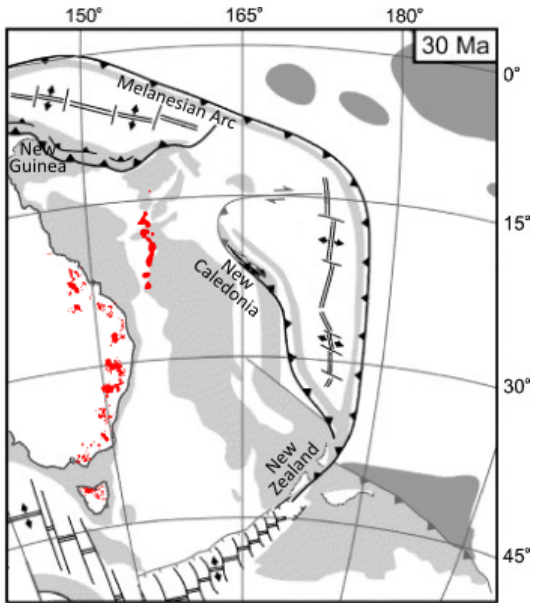
35	Australia saw full separation from Antarctica by 35 Ma (Veevers et al., 1991). Collision of the Loyalty Arc with New Caledonia resulted in choking of the subduction system along the east Australian plate boundary. This resulted in obduction of the New Caledonia ophiolite and formation of the Vitiaz Arc further east (Aitchison et al., 1995; Crawford et al., 2003; Spandler et al., 2005). Splitting of the Vitaz Arc and roll back of the Tonga-Kermadec Trench then transferred back-arc spreading to the South Fiji Basin (Crawford et al., 2003; Sdrolias et al., 2003). On the northern margin of the Australian plate, southward rollback along the Pocklington Trough resulted in formation of the New Guinea Arc and opening of the Solomon Sea as a back-arc basin (Schellart et al., 2006). ∼35 Ma New Guinea saw the onset of the Peninsular Orogeny involving passive margin collision with the Philippine-Halmahera-Caroline arc system (Hill and Hall, 2003; Quarles van Ufford and Cloos, 2005). This is also the onset of central volcano volcanism (Cohen, 2007), although it is possible that older samples exist beneath the Great Barrier Reef. Australian plate velocity also peaked ∼75 mm/yr before beginning to decline (Zahirovic et al., 2015).	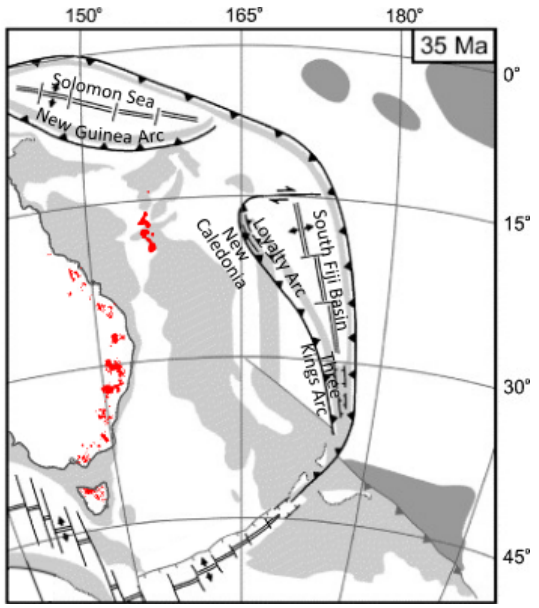

45	This period records a major reorganisation in Asia-Pacific plate boundaries, probably as a result of India–Asia collision (Veevers, 2000; Hall, 2002; Sharp and Clague, 2006; Wright et al., 2015). Australia-Antarctica separation fastened and the velocity of the Australian plate increased, reaching ∼75 mm/yr by ∼35 Ma (Zahirovic et al., 2015). The Pacific plate changed to a more westward motion and the eastern margin of the Australian plate underwent rapid convergence along the Tonga-Kermadec Trench (Muller et al., 2000; Gaina et al., 1998). The New Caledonia Subduction Zone and the Pocklington Trough also formed ∼48 Ma, initiating subduction of the Loyalty–Santa Cruz–Pocklington Basins (Schellart et al., 2006). This is also the age of the oldest lava field deposits in far north Queensland (Mingela Province).	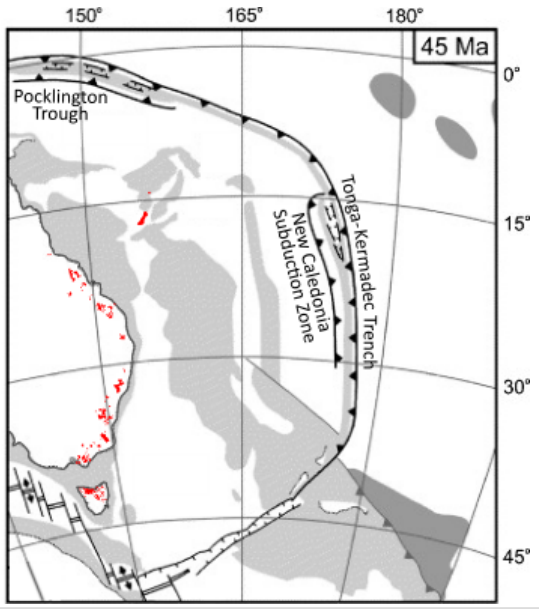
52	Rifting in the Tasman Sea, the Coral Sea, and the South Loyalty, Santa Cruz and Pocklington back-arc Basins ceased around 52 Ma (Gaina et al., 1999; Schellart et al., 2006), possibly in response to the first effects of the India-Asia collision (Crawford et al., 2003) or due to changes in Pacific plate motion. By around 50 Ma, motion of the Australian plate had decreased to just ∼5 mm/yr from ∼70 mm/yr at 55 Ma (Zahirovic et al., 2015). The Tasmantid seamounts began erupting during this period, moving southward with decreasing age. The oldest samples are ∼56 Ma from the Louisaide Plateau at the northern end of the chain. During this time, considerable lava field volcanism also continued along the east Australian coastline throughout Queensland, New South Wales, Victoria and Tasmania.	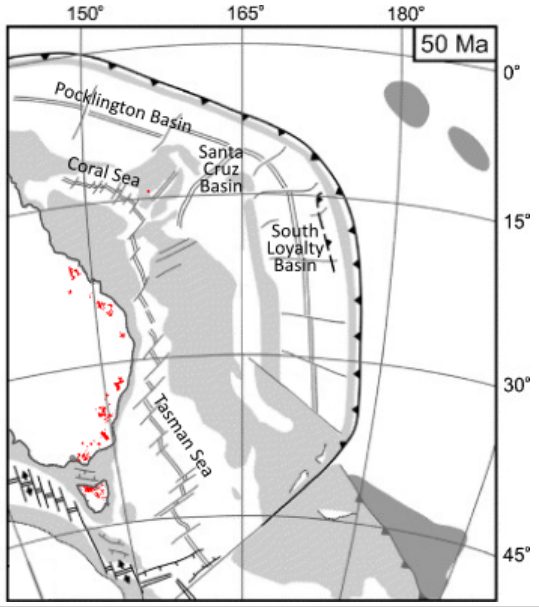
55	Crawford et al. (2003) record a major plate reorganisation event around 55 Ma, possibly due to the subduction of the Pacific-Izanagi spreading ridge in the northwest Pacific. The motion of the Pacific plate shifted to become more west-directed, and Australian plate motion switched to a northeastward trajectory. Pacific-Australian compression resumed, although insufficient evidence is available to say for certain which volcanic arcs and backarc basins were in operation east of the rift system; potential candidates include the d'Entrecasteaux-Loyalty Arc, the Loyalty Basin, the Three Kings Arc, and the Norfolk Basin (Ali and Aitchison, 2000; Sdrolias et al., 2001; Crawford et al., 2003) (Figure 2.7). This was also the beginning of the main pulse of lava field volcanism along the Australian coastline (Vasconcelos et al., 2008).	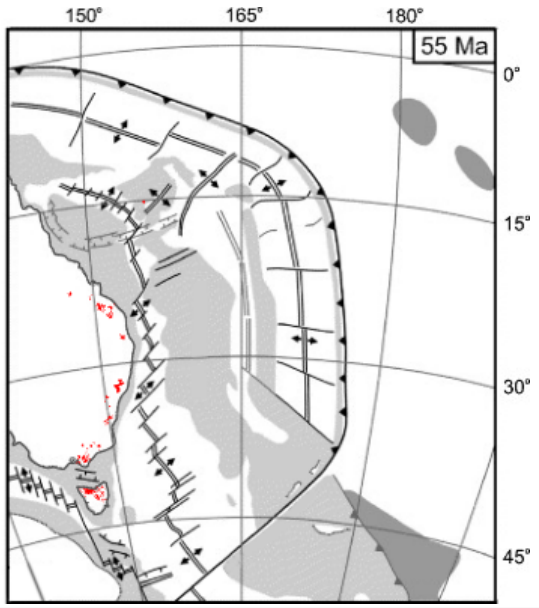

61	Opening of the Coral Sea began ∼61 Ma along with rifting of the final section of continental lithosphere from Australia, the Chesterfield Plateau ∼64 Ma (Gaina et al., 1998; Veevers et al., 1991). During this period, rollback of the Pacific slab also accommodated back-arc spreading in the New Caledonia Basin, the South Loyalty Basin, the Santa Cruz Basin, and the Pocklington Basin (Schellart et al., 2006). Motion of the Australian plate at this time was just ∼10 mm/yr (Zahirovic et al., 2015) but increased rapidly thereafter, reaching ∼70 mm/yr by 55 Ma (Zahirovic et al., 2015). Also around 61 Ma, minor lava field volcanism was taking place along the east Australian coastline but this again increased rapidly and by 55 Ma much of the lava field volcanism in New South Wales and Tasmania had initiated.	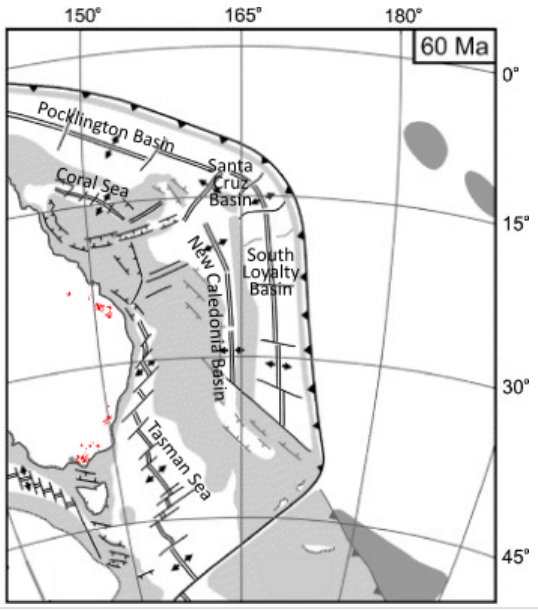
84	At ∼84 Ma rifting progressed anticlockwise and compressional tectonics from Australian-Pacific collision were succeeded by active transtension across the region (Sdrolias et al., 2001). This led to the opening of the Tasman Sea south to north and fragmentation of the continental lithosphere as the Norfolk Ridge and the Lord Howe Rise broke away from eastern Australia (Weissel and Hayes, 1977; Muller et al., 2000; White et al., 2013; Crawford et al., 2003). Both the Norfolk Ridge and the Lord Howe Rise represent submerged, variably thinned, continental crust consisting of the same Paleozoic-Mesozoic accreted terranes that are found on the east coast of the Australian landmass (Mortimer et al., 1998). ∼84 Ma is also the onset of minor magmatism throughout eastern Australia, particularly the Older Volcanic Province (OVP) in Victoria.	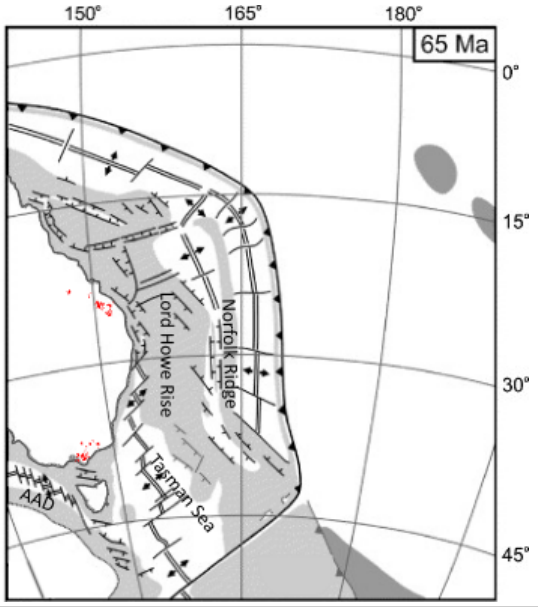
95	The break-up of east Gondwana and rifting from the Antarctic landmass along the Australian Antarctic Discordance (AAD) commenced ∼95 Ma. Australia started to move northwards at ∼15 mm/yr (Zahirovic et al., 2015; Muller et al., 2000; White et al., 2013). The formation of the Great Dividing Range is also likely to have occurred around this time although this is still under debate (e.g. Johnson, 1989; Vasconcelos et al., 2008).	
100	At ∼100 Ma, the east Australian plate was undergoing convergence with the Pacific plate (Sdrolias et al., 2004). There is possible evidence for the arrival of a major mantle plume (Balleny) beneath southern Lord Howe Rise-east Tasmania at this time (Crawford et al., 2003). There was also a change in the isotopic composition of basalts from Tasmania, New Zealand and Antarctica, to HIMU representatives (Lanyon et al., 1993).	

2.3.1 Seismic Tomography

The results of present-day topography studies may be used to assess some of the mechanisms suggested to have induced volcanism across east Australia during the Cenozoic Era, such as the interaction of a mantle plume with a stagnant oceanic slab beneath the Tasman Sea (Kalnins et al., 2015) (Figure 2.4). Based on the tectonic evolution of eastern Australia, one would expect a sizable volume of subducted oceanic crust to be present within the mantle beneath the Australian tectonic plate. This is complicated slightly because, as shown above, the exact duration of subduction zones in some places are ill constrained, partly due to the poor data coverage of seafloor ages and the subduction of several back-arc basins during the Cenozoic. This has a knock on effect in tomographic studies where it is useful to know the times at which subduction zones were active i.e., ephemeral subduction zones of young ocean floor will not be advected to depth and long-lived subduction zones result in slabs with longer residence time in the lower mantle (Matthews et al., 2012). Nevertheless, by analysing the results of authors who have forward-modeled subduction history within the region, one can make some broad observations about where subducted material is likely to exist in the mantle at present, and compare these inferences with present-day tomographic results.

Matthews et al. (2012) have completed such modeling using the plate model of Seton et al. (2012) which records a similar tectonic evolution of the southwest Pacific as described in this thesis. As the early development of back-arc basins occurred at higher latitudes compared to present-day, cross-sections by Matthews et al. (2012) have been produced at 10 °S, 20 °S, 30 °S and 38 °S in order to capture the entire mantle domain where slab material is expected to be laying (Figure 2.8). Both the model results and topographic comparisons are shown in Figures 2.9 and 2.10. The two models from Matthews et al. (2012), SWP1 and SWP2, use slightly different parameters, a temperature-dependent viscosity versus a temperature-independent viscosity, respectively, but the results from both are quite similar and broad inferences can be made using the two together. The tomographic studies used include the P-wave model MIT-P08 (Li et al., 2008) and the S-wave model GyPSum-S (Simmons et al., 2010). P-wave models provide high-resolution imaging of subduction zones due to the high concentration of receiver stations in proximity to these areas, whereas S-wave models better resolve the lower half of the mantle due to their higher amplitudes (Ritsema and Allen, 2003) (Matthews et al., 2012). Both MIT-P08 and GyPSum-S can therefore be used to assess the upper and lower mantle beneath Australia, respectively. In all topographic images the mantle directly beneath the Australian continent, east of around 150 °E, consistently displays fast seismic velocities but this is not thought to be associated with subducted oceanic crust within the late Cretaceous-Cenozoic time frame.

Most tectonic models of the region (e.g. Seton et al., 2012; Schellart et al., 2006; Crawford et al., 2003; Sdrolias et al., 2003), incorporate some level of subduction along the eastern edge of the Australian plate from around 84 Ma until present-day and based on sinking velocities these slabs are now expected to sit deep within the mantle. Modeling results by Matthews et al. (2012) (SWP1 and SWP2) show that due to this subduction, large volumes of slab material are expected to be present around the core mantle boundary, mostly along the 30 °S and 38 °S lines (Figure 2.10). In both of the 30 °S and 38 °S GyPSum-S lines (Figure 2.10), and to some extent the 20 °S line (Figure 2.9), there is a continuous band of fast seismic velocity material below 1500 km in the west and 2000 km in the east, which is the depth where the 84 Ma slabs are predicted to be located at present. Matthews et al. (2012) associate this material with Jurassic to late Cretaceous (∼200–66 Ma) west-dipping subduction of the proto-Pacific. When considering intraplate volcanism across eastern Australia, slab material so deep in the mantle is unlikely to have influenced the splitting of a mantle plume at such depths but may play a role in affecting the chemistry of the plume-like source i.e., the generation of an EMI isotopic signature in most age-progressive, plume-like basalts.

Further work by Matthews et al. (2012) predicts that slab material associated with Melanesian subduction (∼27–16 Ma) should be seen around 820–650 km depth on the 10 °S line, and slab material associated with San Cristobal-New Hebrides subduction (∼15–0 Ma) should be seen at 650–0 km on the same line (Figure 2.9). The MIT-P08 10 °S topography model shows fast seismic velocity material extending between 1000–400 km around 155–170 °E, and connects to the surface around 160–165 °E (Figure 2.9). The position of this fast seismic velocity material matches where the SWP1 and SWP2 models predicts slab material associated with Melanesian and San Cristoba-New Hebrides subduction to be. A similar anomaly at this location has been imaged by Hall and Spakman (2002) who show that because of the large lateral extent of this fast, relatively flat zone it can be identified in many other global mantle models, even with lower resolution, such as that of Laat et al. (2021). Most of this material will have been being subducted during emplacement of the age-progressive volcanoes therefore may have influenced the emplacement of the very northern volcanoes but is unlikely to have reached the extent of the continental or oceanic volcanoes and they progressed southwards i.e., most of these anomalies appear to trend much too far north to have had a significant effect on Cenozoic intraplate volcanism.

More recent subduction along the east of the Australian plate has been accommodated along the Tonga-Kermadec and New Caledonia subduction zones (e.g. Seton et al., 2012; Schellart et al., 2006; Crawford et al., 2003; Sdrolias et al., 2003). The Matthews et al. (2012) model includes west-dipping Tonga-Kermadec subduction from ∼36 Ma and contemporaneous east-dipping subduction along the New Caledonia trench. The slab subducted along the New Caledonia subduction zone is named the South Loyalty slab, after the basin with which it contained. In the tectonic model used in this study the same trenches are in operation from around 48 Ma. The SWP1 and SWP2 models from Matthews et al. (2012) predict slab material from such events to be present at relatively shallow depths on the 20 °S, 30 °S and 38 °S lines (Figure 2.9 and 2.10). On the MIT-P08 30 °S line, and to some extent the 20 °S line, fast seismic velocity material is observed at 1600 km depth between 160–180 °E, extending to the surface between 175–180 °E where the active Tonga-Kermadec trench is located (Figure 2.10). On the 38 °S line, MIT-P08 has poor resolution at this latitude due to fewer seismic receiver stations this far south (Matthews et al., 2012) (Figure 2.10). However, GyPSum-S resolves fast seismic velocity material extending from the surface to around 1500 km depth which the authors associate with New Caledonia and Tonga-Kermadec subduction.

Slab material from the New Caledonia subduction zone has also been inferred from seismic tomography by Schellart et al. (2009) who place the position of the South Loyalty slab almost continuously within the centre of the Tasman Sea from ∼48–0 Ma (Figures 2.11 and 2.12). From their study, P-wave and S-wave mantle tomography models identify a high-velocity anomaly below the Tasman Sea at around 1100 km depth, striking NW–SE and around 2200 km by 600–900 km in lateral extent (Schellart et al., 2009) (Figure 2.12). The size and position of this anomaly cannot be linked to subduction of the Pacific plate along the eastern edge of the Australian plate but when considering relative and absolute plate motions it is found presently at the predicted depth and location of the 48–15 Ma, northeast-dipping New Caledonia subduction zone (Schellart et al., 2009) (Figure 2.11). Most of this material will have been being subducted during emplacement of the age-progressive volcanoes with subduction initiating just after the first Tasmantid seamounts are emplaced. It is certainly possible the South Loyalty slab blocked the rising Tasmantid mantle plume and caused it to split into a number of smaller plumes producing the coeval (but offset) central volcanoes and Lord Howe seamounts. This may explain why the initiation of both the central volcanoes and Lord Howe seamounts appears to have occurred later than the Tasmantids i.e., 34 Ma, 28 Ma, and 55 Ma, respectively, although some earlier central volcanoes may exist beneath the Great Barrier Reef.

Given the volume of subducted material that has been imaged by both Matthews et al. (2012) and Schellart et al. (2009) it is certainly not an unreasonable assumption that these may have played a role in inducing or influencing volcanism within the east Australian plate from 90 Ma all the way to the present-day. The most likely candidates for influencing the ascent of Cenozoic melts to the surface is from the 48–0 Ma Tonga-Kermadec slab or the 45–15 Ma South Loyalty slab which are both predicted to lie between approximately 500–1500 km depth across the north (Matthews et al., 2012; Schellart et al., 2009) and centre (Schellart et al., 2009) of the Tasman Sea, respectively. The location of these two slabs inferred from seismic tomography could well act as a simple mechanism to split up a single mantle plume originating from depth into a number of smaller plumelets.

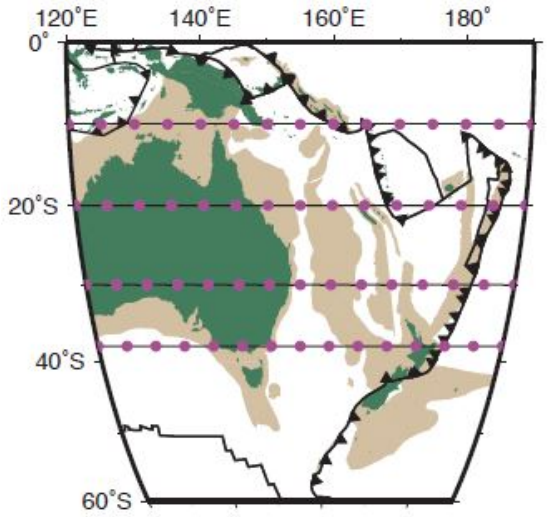

Figure 2.8: *Locations of the 10°S, 20°S, 30°S and 38°S cross-sections from Matthews et al. (2012) through the mantle temperature models SWP1 and SWP2, and seismic tomography models MIT-P08 and GyPSum-S.*

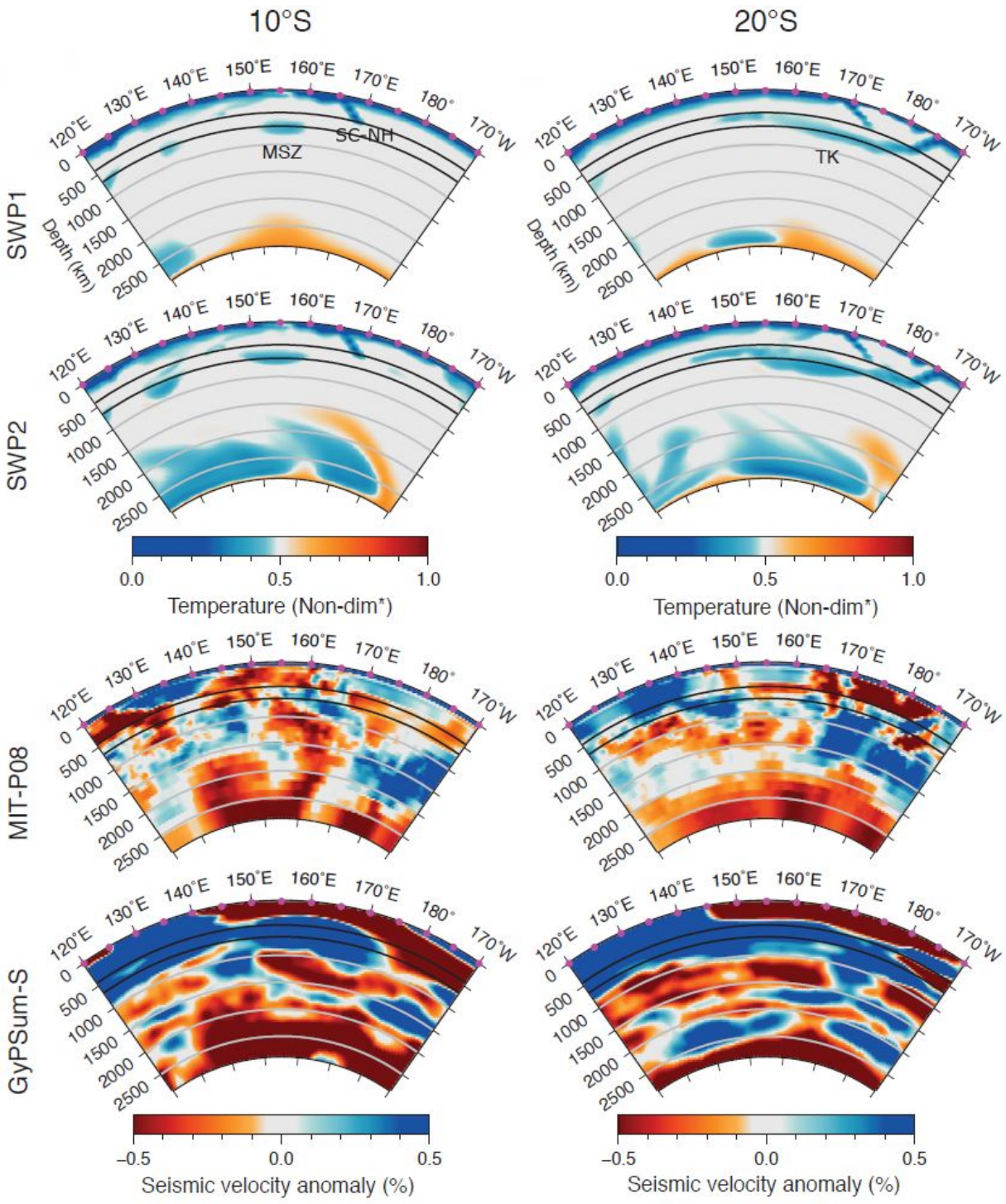

Figure 2.9: *Cross-sections from Matthews et al. (2012) at 10°S and 20°S through the predicted present-day mantle temperature models SWP1 and SWP2 (top), and seismic tomography (bottom). The MIT-P08 P-wave model, mostly used for imaging the upper mantle, is from Li et al. (2008) and the GyPSum-S S-wave model, mostly used for imaging the lower mantle, is from Simmons et al. (2010). Within the tomography images, anomalously fast seismic velocities (blue) are inferred to represent slab material (Matthews et al., 2012). MSZ, slabs from the Melanesian subduction zone; SC-NH, slabs from San Cristobal-New Hebrides subduction; TK, slabs from Tonga-Kermadec subduction. *The SWP1 and SWP2 temperature models are non-dimensionalised with a value of 1 being equivalent to 2800 K (Matthews et al., 2012).*

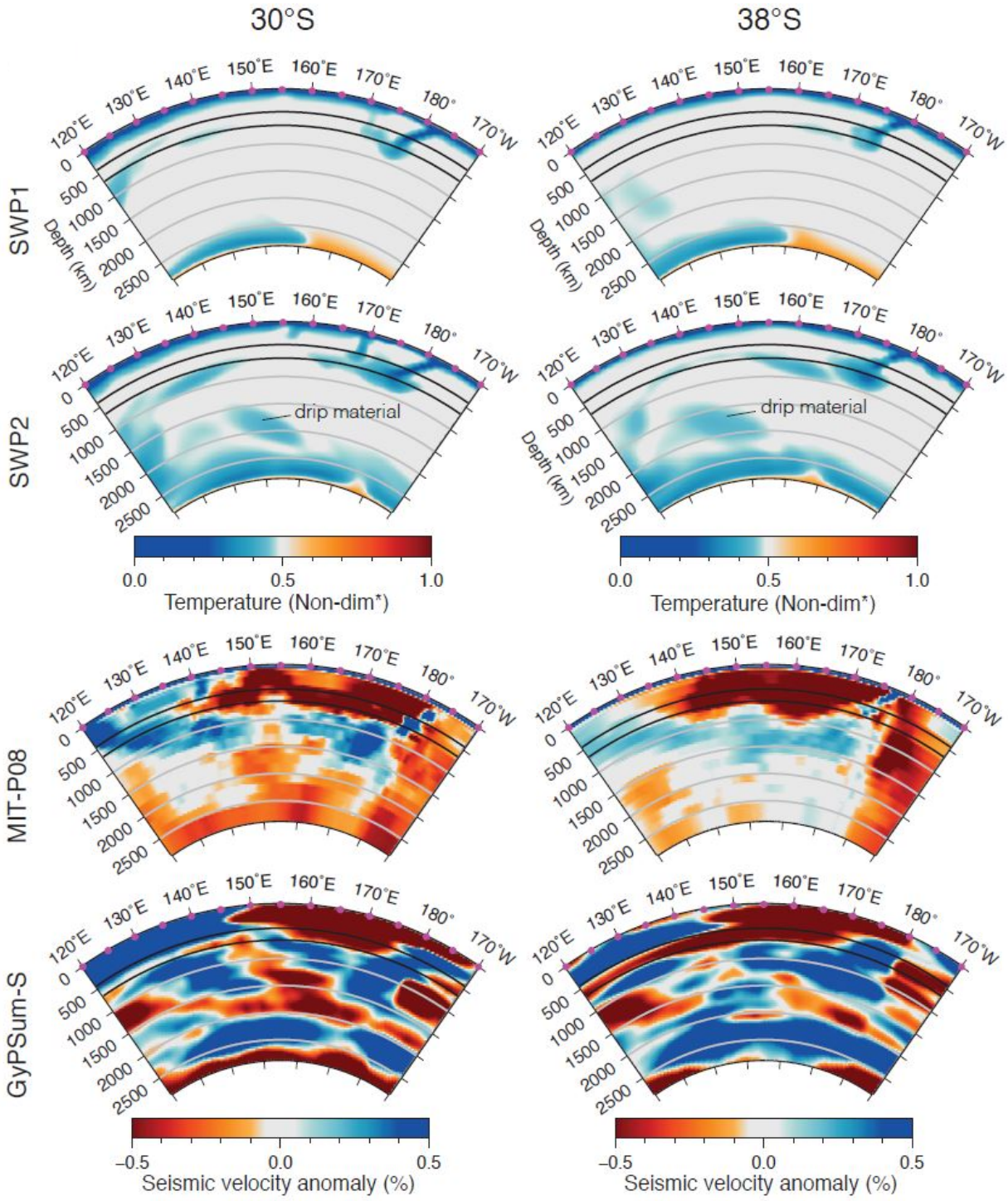

Figure 2.10: *Cross-sections from Matthews et al. (2012) at 30°S and 38°S through the predicted present-day mantle temperature models SWP1 and SWP2 (top), and seismic tomography (bottom). The MIT-P08 P-wave model, mostly used for imaging the upper mantle, is from Li et al. (2008) and the GyPSum-S S-wave model, mostly used for imaging the lower mantle, is from Simmons et al. (2010). Within the tomography images, anomalously fast seismic velocities (blue) are inferred to represent slab material (Matthews et al., 2012). *The SWP1 and SWP2 temperature models are non-dimensionalised with a value of 1 being equivalent to 2800 K (Matthews et al., 2012).*

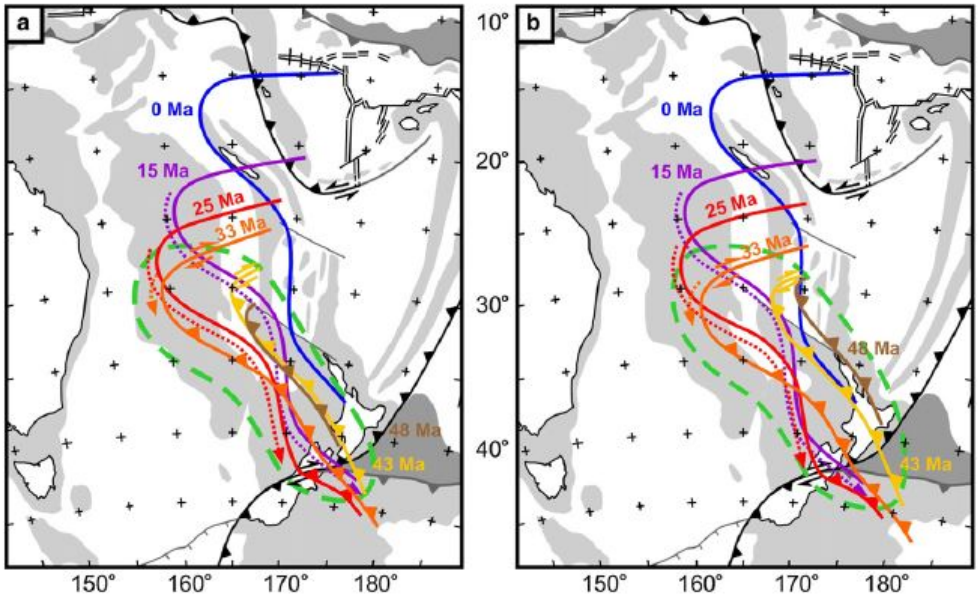

Figure 2.11: *"Migration of the New Caledonia subduction zone from 48 Ma to 0 Ma (Present) in two reference frames by combining subduction zone migration relative to Australia (Schellart et al., 2006), timing of slab detachment (Schellart, 2007) and motion of the Australian plate in (a) a global hotspot reference frame (Gordon and Jurdy, 1986) and (b) an Indo-Atlantic hotspot reference frame (Muller et al., 1993). Different trench positions are found in the two reference frames, which are small (0–100 km) from 25 to 0 Ma but amount up to 370 km at 48 Ma. Location of the subduction zone for distinct times is indicated by the blue, purple, red, orange, yellow and brown lines. Numbers indicate time in Ma. Teeth are located on the upper plate side and indicate active subduction. Dotted lines indicate detached slab while arrows indicate direction of lateral slab tear propagation. Dashed green line indicates predicted lateral extent of the detached South Loyalty slab." (Schellart et al., 2009).*

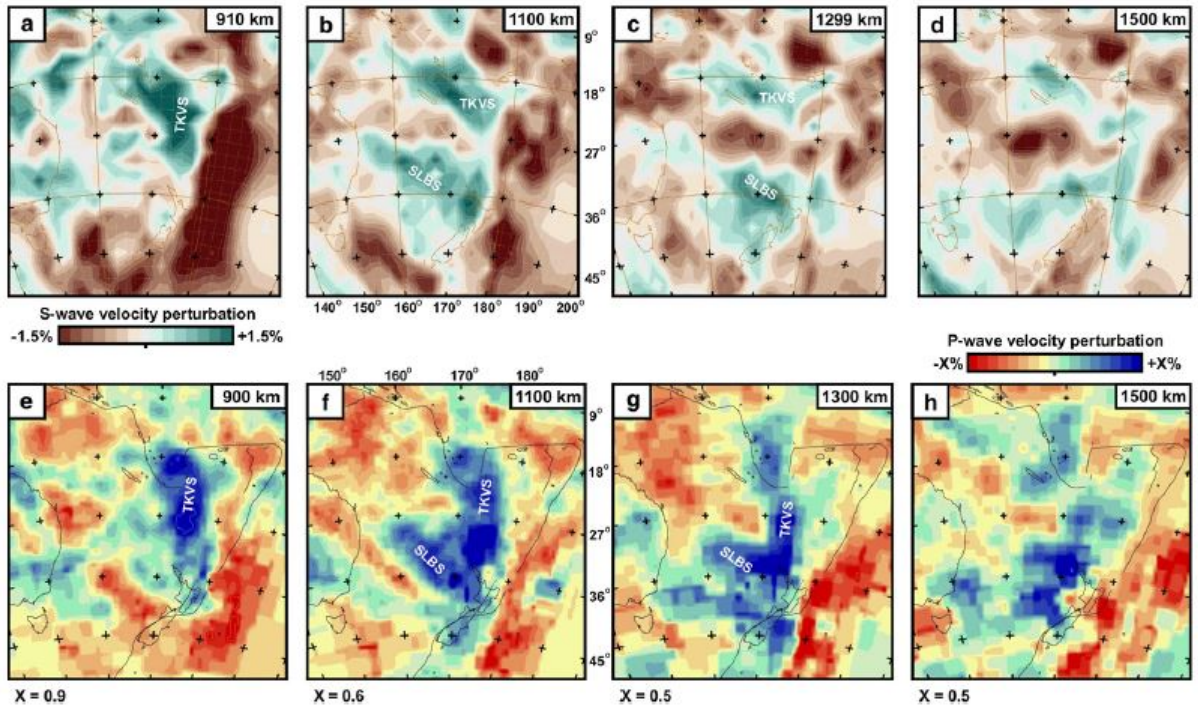

Figure 2.12: *"S-wave (a–d) and P-wave (e–h) tomographic images from the Southwest Pacific region at depths of (a) 910 km, (b) 1100 km, (c) 1299 km, (d) 1500 km, (e) 900 km, (f) 1100 km, (g) 1300 km and (h) 1500 km. The NW–SE striking fast anomaly below the Tasman Sea between New Zealand and Australia (SLBS) is interpreted as the fossil slab of the subducted South Loyalty Basin. The high velocity anomaly below the North and South Fiji basins represents the subducted Tonga-Kermadec-Vitiaz slab (TKVS)." (Schellart et al., 2009).*

2.4 Current Stress Regime

In order to consider how past boundary conditions might have played a role in defining the stress regime, heat flow, tectonic configuration, lithospheric structure, and thus magmatism of the Australian Plate, one can take a look at present-day conditions (Figure 2.13). The Australian Plate is dominated by convergence and sinistral shear relative to the Pacific Plate (Hillis and Muller, 2003). Collision to the east is marked by westward subduction of the Pacific Plate beneath the Tonga-Kermadec Arc and the North Island of New Zealand (DeMets et al., 2010; Blewett, 2012). Convergence and dextral shear characterize the boundary in southern New Zealand and the Macquarie Ridge which extend down to the Australian-Antarctic Discordance (AAD) spreading ridge (DeMets et al., 2010; Blewett, 2012). Along the northeastern margin, the Australian Plate is being subducted beneath the Pacific Plate at the New Britain–San Cristobal–New Hebrides Trench (DeMets et al., 2010; Blewett, 2012). Moving west, this convergence transpires as collision across the island of New Guinea and subduction along the Banda Arc, Java Trench and Sumatra Trench (DeMets et al., 2010; Blewett, 2012). Today, Australia is the fastest moving continent on Earth with a plate motion 23°N towards the Pacific of 67 mm/yr (Sella et al., 2002; Zahirovic et al., 2015).

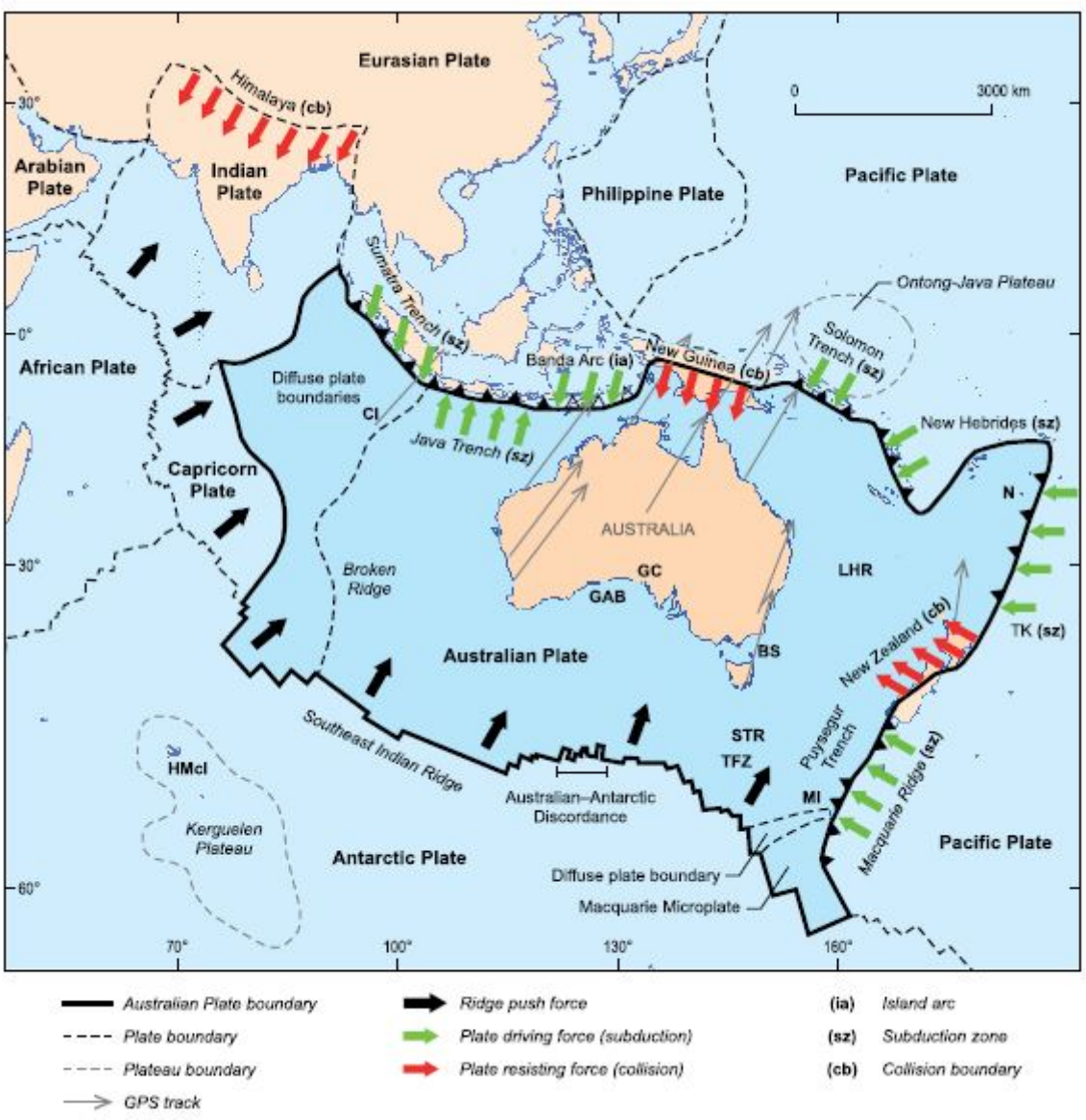

Figure 2.13: *Present-day plate boundaries including the dominant forces acting upon them, from Blewett (2012), modified after Tregoning (2003) and DeMets et al. (2010). GPS measurements show the direction that Australia is moving, at a rate of around 7 cm per year. BS = Bass Strait; CI = Cook Islands; GAB = Great Australian Bight; GC = Gawler Craton; LHR = Lord Howe Rise; HMcI = Heard and McDonald Islands; MI = Macquarie Island; STR = South Tasman Rise; TFZ = Tasman Fault Zone.*

Unlike most other continental areas, stress orientations throughout Australia are variable and do not parallel the 23°N absolute motion of the plate (Johnson, 2009). In-situ stress measurements indicate that most of Australia is subject to horizontal compressional stress. South of latitude -30°, in northern NSW, stress fields are oriented E–W to NW–SE. North of this latitude, the stress fields are closer to the present-day plate motion, oriented ENE–WSW to NE–SW (Tregoning, 2003; Hillis and Muller, 2003) (Figure 2.14). Despite not always paralleling plate motion, regional stresses are consistent with control by present-day plate dynamics (Hillis and Muller, 2003). Ridge-push force from the AAD is the dominant force which controls the magnitude and pattern of first-order stresses, which is evident in the E–W to NW–SE stress directions south of -30° and closer to the AAD (Zhao and Muller, 2003). The effect of the boundary drag forces is secondary and they mostly influence the pattern of the stress nearer to collisional boundaries, appearing more dominant north of -30° (Zhao and Muller, 2003). South of -30°, where compressional stress fields are oriented E–W to NW–SE is also the location where most recent seismicity occurs across the continent (Figure 2.14). Whether or not this change corresponds to the different forms of volcanism which are observed between Queensland and the more southerly states is considered further on in this thesis. For example, the youngest lava fields in far north Queensland, the youngest lava fields in Victoria, and the youngest central volcano and leucitite volcanoes in Victoria have all been emplaced within the last ∼10 Ma where plate boundary conditions are likely to have remained relatively stable (Table 2.1). However, geochemistry of the different suites suggests the may be derived by different mechanisms which may in turn relate to the altering stress regime across the continent.

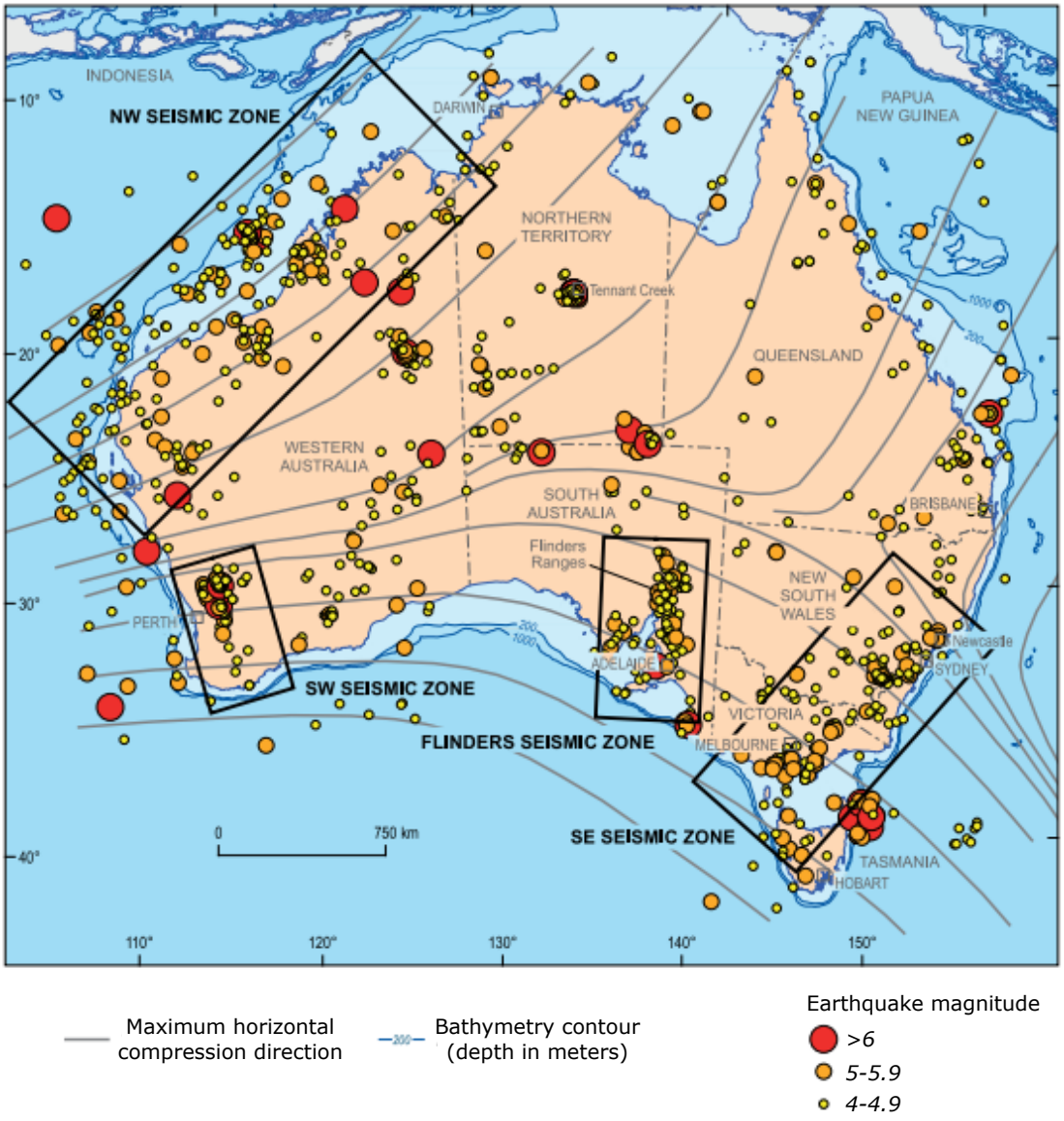

Figure 2.14: *Distribution of $M > 4$ historical earthquake epicenters (Quigley et al., 2010) and directions of maximum horizontal compression (SHmax) across the Australian continent (Hillis and Muller, 2003) from Blewett (2012).*

The north to south age progression of central volcanoes, leucitites, Tasmantids and the Lord Howe chain, as well as deflections in the oceanic chains possibly corresponding to plate motion, have all been interpreted as potential evidence of numerous mantle plumes (e.g. Cohen et al., 2013; Knesel et al., 2008; Wellman and McDougall, 1974a). The predicted present-day positions of these have been estimated by Richards (2014) to sit within the Bass Strait, and further out into the Tasman Sea (Figure 2.15). Further geophysical evidence to support the plume theory is given by (1) the relatively high seismicity in southeastern Australia, with epicenters in the Bass Strait (Quigley et al., 2010); (2) a heat flow of Quaternary volcanics in southeast Australia, around 1.5 times the world average (Johnson, 1989; O'Neill et al., 2003); and (3) slow seismic velocities extending to ∼650 km beneath the Bass Strait (Montelli et al., 2004). From Figure 2.15, earthquake clusters correspond well with the projected Tasmantid hotspot location, and partly around the East Australian hotspot although this is less clear due to high background seismicity and perhaps more visible from $M > 4$ examples in Figure 2.14. The projected location for the Lord Howe hotspot does not appear to correspond to any measured seismicity. However, comparing this projected location with Figure 2.14 it is possible the Lord Howe hotspot is now situated in a different stress regime to the Tasmantid and East Australian hotspots.

In addition to stress regime, we must also consider the lithosphere onto which each volcano has been emplaced. Deep lithospheric faults may act as conduits for magma transport through the lithosphere and following numerous arc accretion events throughout the Phanerozoic, sizable faults are observed between fold belts throughout eastern Australia. Figure 2.2 shows how each Cenozoic volcanic province relates geographically to the tectonic evolution of the Australian lithosphere. Of note, the five volcanic provinces from North Queensland (Atherton, McBride, Chudleigh, Sturgeon, and Nulla) straddle a series of major faults between the Hodgkinson-Broken River Fold Belt, the Thompson Fold Belt, and the Georgetown Inlier. Similarly, the New England Fold Belt represents a complex collage of continental margin terranes now represented by a series of fault-bound blocks in eastern Queensland and NSW (Veevers, 1984). Due to the complex nature of the belt, faulting is widespread and may relate to the abundance of Cenozoic volcanism found here (Johnson, 1989) e.g. the Bunya, Toowoomba, Main Range, and Tweed central volcanoes, as well as the Monto, Bundaberg, and New England lava fields. The majority of other Cenozoic volcanic provinces outcrop within the Lachlan-Thomson Fold Belts and the Sydney-Bowen Basin.

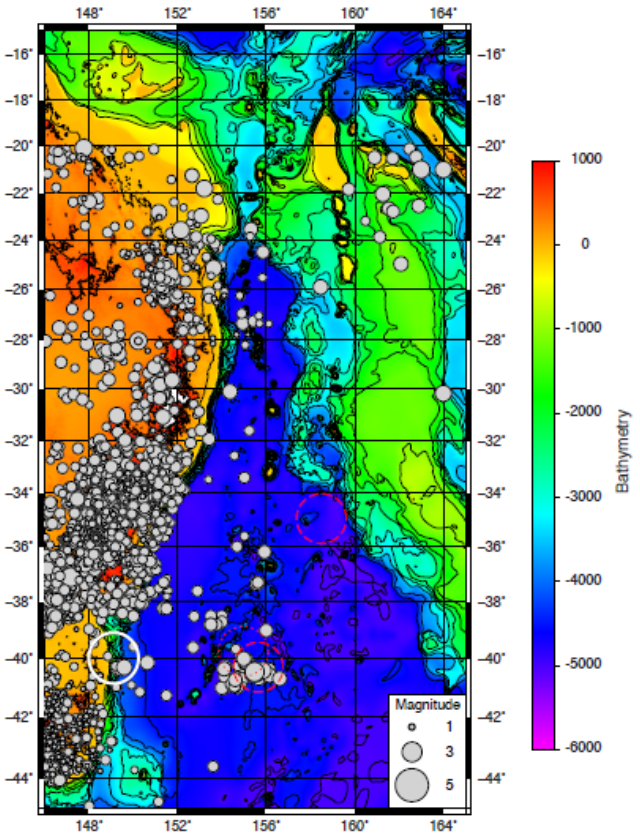

Figure 2.15: *1955–2014 seismicity across Eastern Australia from Richards (2014). Dashed red circles show projected hotspot location from plate models. Solid white circle shows inferred location of the East Australian hotspot (Knesel et al., 2008).*

To add to this complexity, a number of tomographic studies have determined that the Australian lithosphere thins in a series of abrupt steps from west to east (Fishwick et al., 2008; Davies et al., 2015; Kennett, 2003) (Figure 2.16). Lithosphere is ∼200-150 km thick beneath Proterozoic cratons, ∼100–50 km beneath Phanerozoic terranes, and moving onto oceanic lithosphere, less than 70 km beneath the Tasman Sea (Fishwick et al., 2008). Thinner lithosphere appears to correlate with higher geotherms and this is also where we find most Cenozoic volcanoes (Gaul et al., 2003). Davies et al. (2015) suggest that major variations in lithosphere thickness may explain the distinct geochemistry of the leucitite lavas, deriving from relatively small degrees of melting beneath thicker lithosphere (Figure 2.17). Whether this difference can explain the full suite of major element and trace element concentrations within the leucitites is assessed in Chapter 5 of this thesis.

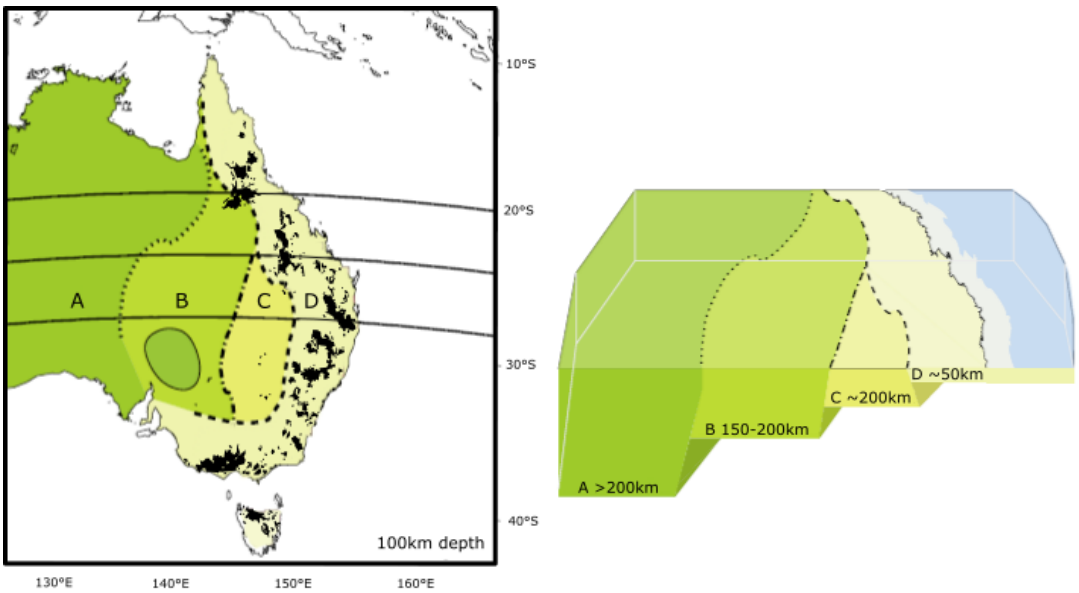

(a) (b)

Figure 2.16: *Lithospheric structure of East Australia from seismic surface wave tomography and horizontal shear wave speeds, modified after Fishwick et al. (2008) in (a) plan view and (b) cross section. Most Cenozoic volcanism is confined to level D with a thickness of ∼50 km except for leucitite samples found on level C.*

2.5 Igneous Geochemistry

Away from the continent, the role of lithosphere thickness in controlling the geochemistry of ocean islands has been assessed by numerous authors (e.g. Humphreys and Niu, 2009; Fitton et al., 2021). Rising asthenosphere is limited by the more brittle lithosphere which provides a cap on the depth at which decompression melting can occur. Beneath thin lithosphere, asthenosphere rises to shallower levels, allowing greater degrees of decompression partial melting. Beneath thicker lithosphere, asthenosphere only reaches deeper levels, producing lower degrees of decompression partial melting. This is largely noticeable due to the "garnet signature" described in detail by Wood et al. (2013). Deeper melting primarily takes place within the higher pressure, garnet stability field. Residual garnet would result in partial melts with lower Y and heavy rare earth element (HREE) concentrations relative to residual spinel or plagioclase. To date, few studies have included the East Australian, Tasmantid, or Lord Howe volcanoes in their assessment of geochemical variation via lithosphere thickness changes, so for this thesis the same hypothesis has been tested on the basaltic rocks of eastern Australia.

Just as variations in the final depth of melting affect magma chemistry, so do variations in the initial depth of melting. Fertile mantle and higher mantle potential temperatures (Tp) are also likely to influence OIB compositions globally, although these two variables have been suggested by Humphreys and Niu (2009) to exert only secondary effects to the final depth of melting. To assess these theories, Chapter 4 of this thesis uses studies by Hastie et al. (2016) and Fitton et al. (2021) to show how one can model the changes in basaltic chemistry with changes in the Tp and depth (lithosphere thickness) of mantle melting. Heterogeneous mantle sources are then assessed in Chapters 4 and 5 with an in-depth analysis of isotopic ratios across the continental and oceanic chains.

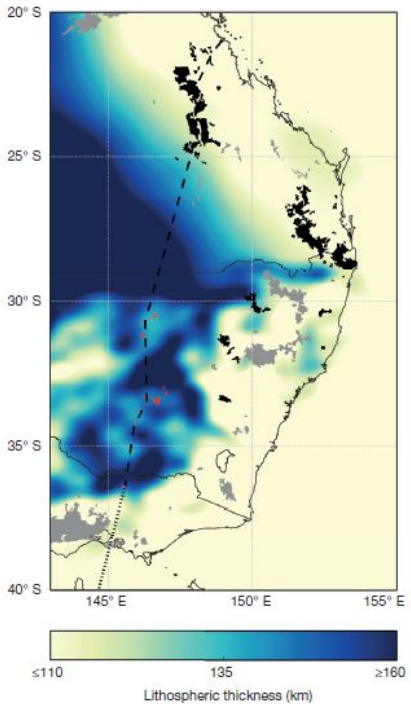

Figure 2.17: *Lithospheric thickness, after Davies et al. (2015). Volcanic centres in black, grey and red denote the central volcanoes, lava fields and leucitites, respectively. The Cosgrove hotspot track is denoted by the black dashed.*

Chapter 3

Methods



Figure 3.1: *Sleeping koala, Magnetic Island, Queensland.*

3.1 Geochemistry

3.1.1 Sample Collection

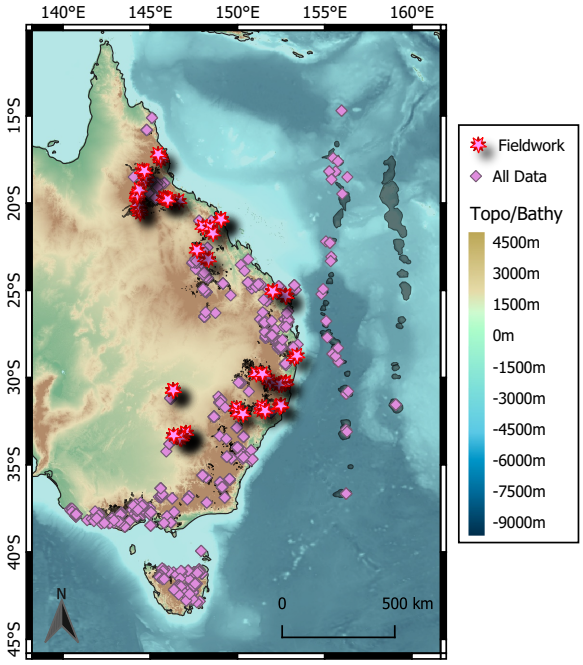

Figure 3.2: *New samples collected during fieldwork in 2019 shown as red stars. The provinces samples were collected from include, the Leucitites, Liverpool Range, Barrington, Comboyne, Ebor, New England, Tweed, Bundaberg, Peak Range, Nebo, Cape Hillsborough, Mingela, Nulla, Sturgeon, Chudleigh, McBride, and Atherton. Samples from previous studies that were used in this thesis are shown in pink.*

As the focus of this study is volcanic sources, only primitive mafic rocks have been sampled in order to minimise the contribution of fractional crystallisation and assimilation. A suite of 170 rocks have been selected from the East Australian and Tasmantid chains for major and trace analysis (Figure 3.2). This includes 57 central volcano, 72 lava field, 9 leucitite and 32 Tasmantid samples. Rocks were selected on the basis of locality, to get the most even geographic spread, and freshness. The continental dataset mostly includes samples collected by Benjamin Cohen during his PhD in 2007 and those collected during fieldwork for this thesis in 2019, along with a few specimens provided by other researchers in Australia. The oceanic dataset contains samples from a 2012 dredging voyage in the Tasman and Coral Seas, as well as samples from earlier dredging missions throughout the 1980s. Care was taken to select the freshest rocks and any samples with a loss on ignition (LOI) greater than 2 wt% were discarded from further major element interpretation which included 26 samples. LOI values give an indication of the volatile content of the rock where volatiles such as water are often associated with alteration of igneous rocks. Given that weathering and alteration can affect mobile element concentrations, these specimens have been excluded from any further mobile element interpretation (Figure 4.2). 161 rocks were large enough to be made into thin sections and analysed under the petrographic microscope. Thin section descriptions of all samples analysed in this study may be found in Appendix A. Where alteration minerals were present the composition and morphology of the phase was used to identify the original igneous mineral (e.g., iddingsite and olivine). A dataset of major and trace element and radiogenic isotope results has also been compiled from 277 central volcano, 810 lava field, 53 leucitite and 94 Seamount samples from the GEOROC database (`http://georoc.mpch-mainz.gwdg.de/georoc/`).

3.1.2 Major and Trace Elements

All 170 rock samples have been analysed for major elements and trace elements via X-ray fluorescence (XRF) spectrometry and inductively coupled plasma mass spectrometry (ICP-MS) at the University of Edinburgh, Grant Institute. To begin, samples were photographed and cut to approximately 50 g using a copper-diamond rocksaw at the Scottish Universities Environmental Research Centre (SUERC). Any significant alteration, large amygdales, manganese crusts and xenoliths were removed. 50 g of material was deemed enough to provide a homogeneous sample. Each specimen was brought to the Grant Institute and split into 5 mm chips in a tungsten-carbide jaw crusher, and where possible any remaining alteration surfaces were removed. All chippings were then ground into a fine powder using an agate-lined Tema mill.

LOIs were determined by heating 0.95 g of sample at 1100 °C for 20 minutes and recording weights before and after. Samples were then fused with 4.75 g of $LiBO_2$ flux containing La_2O_3 as a heavy absorber, at 1100 °C for an additional 20 minutes in a gold-platinum crucible. More flux was added to bring the sample up to the target weight and the crucible placed on a burner for 5 minutes. Samples were then cast to a disc. Whole rock major element concentrations were determined by running each glass disc through a Panalytical PW 2404 wavelength-dispersive sequential X-ray fluorescence spectrometer with a Rh-anode Xray tube at the Grant Institute, University of Edinburgh.

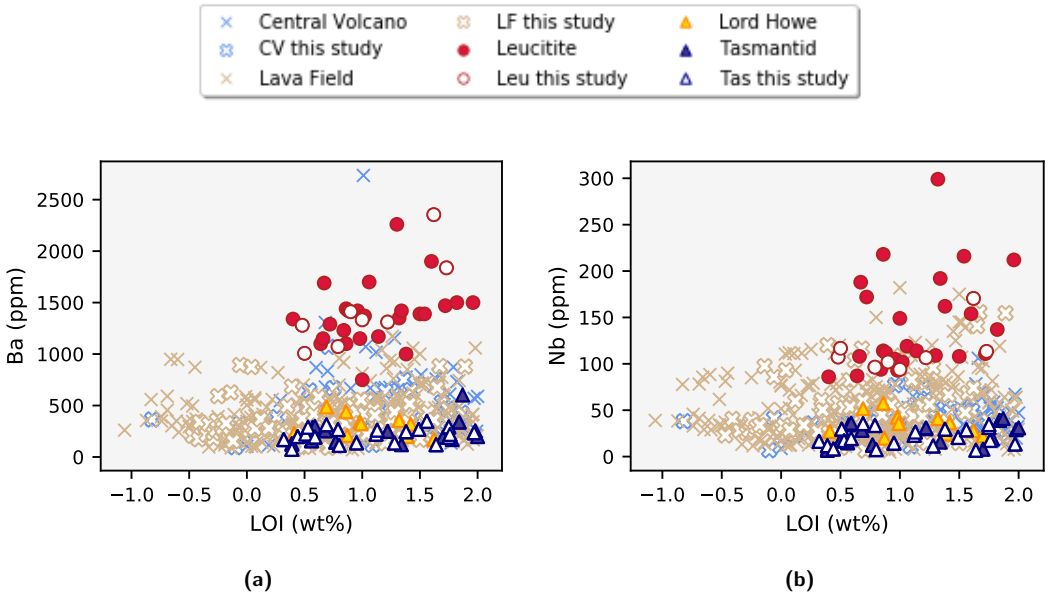

Figure 3.3: *(a) Ba and (b) Nb versus LOI. Both plots show that neither typically mobile (Ba) or immobile (Nb) elements are affected by alteration of the samples when LOI is < 2wt% i.e., no clear trends are observed in either plot.*

For XRF trace element analysis, 8 g of each powdered sample was measured out into a glass beaker and mixed with 8 drops of adhesive (dilute PVA). The mixture was poured into a 35 mm diameter aluminum cup and compressed at 8 tonnes/cm^2 in a hydraulic press to form a pellet. XRF analysis was then carried out on the pressed pellets to determine whole rock trace element concentrations using the same XRF as used for major element analyses.

Following this, all samples were analysed by ICP-MS at the Grant Institute. To prepare the specimens, 50 mg of powder was added to a Teflon vessel along with 3 ml HNO_3, 2 ml HCl and 0.5 ml HF. The lids were then attached and the vessels placed onto a hot plate for overnight digestion at around 100 °C. The vessels were checked to ensure the digestion was complete and then placed back onto the hot plate with the lids off to evaporate. Once done, 10 ml of 1 M HNO_3 was added to each vessel and returned to the hot plate for the second digestion. Finally, 0.8 ml of each sample was transferred to a vial and diluted with 3.2 ml 1 M HNO_3. Trace element concentrations were determined using an AttoM high resolution inductively coupled plasma-mass spectrometer. Drift and background were monitored using acid blanks. Trace element results from ICP-MS were then cross checked with results of elements also analysed by XRF (La, Ce, Nd). Concentrations determined by the two methods display a good correlation (Figure 3.4). Four basalt standards BIR-1, BCR-2, BHVO-1, and BE-N were also analysed by each technique to check accuracy of both major and trace element concentrations. The accuracy of all standard reference material measured by XRF and ICP-MS is within 8.5% and 8.3%, respectively, of GeoReM preferred values (`http://georem.mpch-mainz.gwdg.de/`) (Table 3.1). To calculate precision, duplicate samples were analysed by both procedures. For full analytical precision and accuracy see Appendices G, F, and E.

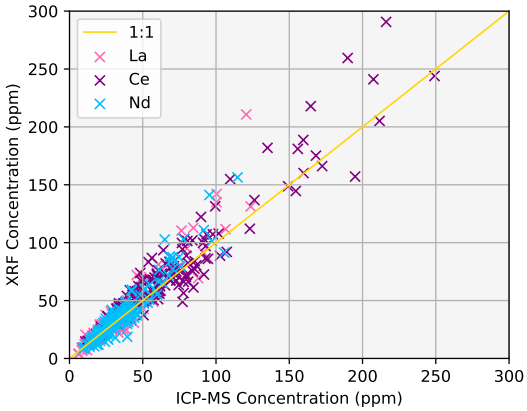

Figure 3.4: *Correlation of elements cross analysed by XRF and ICP-MS.*

	XRF								
Standard	Nb	Nb GeoRem	% diff	Zr	Zr GeoRem	% diff	Y	Y GeoRem	% diff
BIR-1	0.59	0.553	6.69	16.1	14.8	8.41	16.5	15.6	5.61
BCR-2	13.7	12.74	7.26	194.6	190.3	2.23	38.0	36.91	2.91
BHVO-1	19.4	18.53	4.59	176.1	174.6	0.86	27.4	26.23	4.36
BE-N	116.6	113.2	2.96	267.8	272.9	1.89	29.7	29.44	0.88
	ICP-MS								
Standard	La	La GeoRem	% diff	Tb	Tb GeoRem	% diff	Yb	Yb GeoRem	% diff
BIR-1	0.680	0.627	7.90	0.34	0.3623	5.02	1.58	1.631	2.91
BCR-2	23.73	25.08	5.39	1.06	1.077	1.64	3.43	3.392	1.15
BHVO-1	15.73	15.44	1.89	0.97	0.9455	3.08	2.09	1.987	5.26
BE-N	83.88	82.55	1.61	1.22	1.303	6.35	1.37	1.817	8.29

Table 3.1: *XRF and ICP-MS standard results, in ppm. All reference standards were analysed in the XRF and ICP-MS laboratories at the Grant Institute, Kings Buildings, University of Edinburgh. ICP-MS results are within 8.3% and XRF results are within 8.5% of GeoReM preferred values (GeoReM, 2005). For full analytical precision and accuracy see Appendix E.*

3.2 Volume Calculations

In conjunction with the timing of volcanic eruptions, the volume of lava emplaced is often indicative of the mechanism operating behind-the-scenes to drive volcanism. Therefore, finding the total volume of volcanic rock at each province would be beneficial in helping to identify the source of volcanism for each geochemical group. For example, large volumes of eruptive material from the Tweed and Peak Range have been correlated with a decrease in velocity of the Australian Plate (Knesel et al., 2008; Cohen et al., 2013) and an overall decrease in the magma supply rate of the central volcanoes moving southwards has been interpreted by Jones and Verdel (2015) as the northward migration of Australia over a waning mantle plume. A full age review of each volcano has been conducted and a synthesis of how these ages relate to volcanic volumes can be found in the latter half of Chapter 6.

To accurately estimate volume, one of the measurements required is the area over which the volcano flowed when it was first erupted, prior to erosion or burial of rock beneath subsequent sediments. As the East Australian volcanoes were all erupted in the Cenozoic Era, most represent surface geology and overlying units are often relatively thin covers of sediment. The most significant factor affecting the present-day extent of the volcanoes is the degree to which they have been eroded, and this needs to be accounted for in the final estimations. The original baseline of the volcano also needs to be estimated, that is, the palaeotopography onto which the volcano was erupted, taking into consideration any subsequent flexure of the lithospheric plate due to emplacement of the volcano itself. The final variable is the original height the volcano reached and what form it took, i.e., a shield-like volcano versus a flat-lying lava plain. This is the least constrained variable in the volume calculations and, at best, I can give the most-likely range over which the upper surface of the volcano extended.

The original, and most complete, calculations of the continental East Australian chain were conducted by Wellman (1971), who calculated volumes based on a simple conical shape of each volcano. The author took the base of the volcano as the area covered by the extant volcanic material and the height given by the thickest sequence still preserved. They then used a conical model to assume the outline from base to top. Where more of the volcano was preserved, the model was made to just enclose this material, still assuming a conical shape. Wellman (1971) estimated that the central volcanoes average 500 km^3, lava fields 200 km^3, and the leucitites 5 km^3. The fitting of a cone shape itself accounts for some erosion on the flanks of the volcano, however, the volume of preserved material is always less than the original volume and it is likely that the height, thickness, and extent of each volcano has here been underestimated. Many of the volcanoes are likely to have had volumetrically significant ash blankets that were quickly eroded, and in some area lavas will be obscured i.e., buried beneath alluvium. To further this, coal resource drilling has revealed basalts buried in the shallow subsurface with a cumulative thickness of up to 60 m (Jones and Verdel, 2015) which also needs to be included in the calculations.

For these reasons, the re-evaluation of three central volcanoes was undertaken by Jones and Verdel (2015), who used the same method of a simple conical shape but with the addition of a high resolution gravity and magnetic grids, borehole depths, and more precise geological maps. Jones and Verdel (2015) showed that, using the same method but with updated data, eruptive volumes are likely to be much larger than previously suggested by Wellman (1971). Results were calculated using subsurface flow thicknesses derived from drill hole data combined with thicknesses reported in Johnson (1989). These values were then used to produce a regional isopach map from a spherical kriging model. Volumes were then estimated using a simple conical calculation, with heights taken from the maximum basalt thicknesses. Jones (2018) found no obvious correlation between basalt extents and the observed aerial magnetics or gravity surveys, although no modeling was undertaken by the authors. Instead, lava extents were estimated from the isopach maps. Jones and Verdel (2015) estimated a volume of 2600 km^3, 1460 km^3, and 860 km^3 for the Peak Range, Springsure, and Buckland volcanoes, respectively. For the same volcanoes, Wellman (1971) estimated a volume of 800 km^3, 360 km^3, and 800 km^3. Results by Jones and Verdel (2015) appear to give a better estimation of overall volumes compared to that of Wellman (1971), primarily due to the incorporation of subsurface core data.

Given the difference in volcanic form between the shield-type central volcanoes and the broader low-lying lava fields, the accuracy of the simple conical model in estimating the volume of the lava fields clearly has limitations. Another author, Van den Hove et al. (2017), chose the juvenile, well preserved and exposed lava fields of the Newer Volcanic Province (NVP) to evaluate volumes. Here the extents of young basaltic rocks within the NVP were mapped using aeromagnetic anomaly maps combined with pre-existing geological maps. Volumes were then calculated using a high-resolution digital elevation model (DEM) as the upper surface and total accumulated thicknesses were derived from 1472 well logs to constrain the basal surface. This form of volume calculation is likely to be more accurate when considering the lava fields of eastern Australia, where the amount of erosion is expected to be much lower than in the shield-type central volcanoes. Van den Hove et al. (2017) estimated the volume of preserved rock in the NVP to be at least 680 km^3. For the same province, Wellman (1971) estimated an original volume of 1300 km^3.

Both the Jones and Verdel (2015) and Van den Hove et al. (2017) models may act as a good starting point to estimating volumes for the two types of volcanoes found in eastern Australia, but a number of other options are still to be explored. The calculation and analysis of volumes in this thesis have been split into three main parts; (1) uses regional geological mapping and multispectral imaging to compute the preserved volcanic area currently exposed at the surface and shallow subsurface; (2) uses extant lava-rock contacts and borehole depths to model the basal contact of each volcano; and (3) uses simple reconstructions to define and assess possible pre-erosion volcanic heights. No attempt has been made in this study to calculate erosion rates because of the difficulties in quantifying each variable and their associated error i.e. climate, lithology, and drainage changes over the entire east coast of Australia over the last 60 Ma. Because of this, erosion rates over each edifice will be very heterogeneous, so an overall mm/yr rate is not very meaningful, although I do give a general indication of the level of erosion by looking at the percentage of the original volcanic edifice remaining.

The results of all models for each of the 60+ continental volcanic provinces are discussed in Chapter 6 and give an expected range of volumes for each volcano. All remote sensing work has been completed in Google Earth Engine (GEE) which is an open-source, geospatial processing service powered by the Google Cloud Platform, and all other calculations have been completed in QGIS. The aim of this workflow was to automate each of my results so they may be easily adapted, altered, and modeled by others in the future. It also allowed me to test a much wider range of methods in order to find the most appropriate for each province and helped to give an indication of the uncertainty of the estimates. This also means the results are easier to compare between provinces where the main variables at each location will be due to the pre-existing geology and topography of the area, rather than the process. It is these factors that affect how to interpret the remote sensing, borehole, gravity and magnetic data and therefore variations in the inputs and the final results for each province are explained further in Chapter 6 of this thesis. The overall workflow involves the following steps:

1. The preserved extent of volcanic rock at each province have first been determined using polygons from regional geological mapping. For the Warrumbungle and McBride provinces these outlines have then been analysed further using remote sensing to classify volcanic rocks that may have been obscured or overlooked during mapping. The Warrumbungle and McBride provinces were chosen for this step as they are two of the most well mapped central volcanoes and lava fields in the region, therefore remote sensing results could be quickly compared to the high resolution geological maps. The area representing the original extent of volcanism i.e., prior to any erosion or burial, has then been estimated by enclosing all present-day outcrops within an envelope so each is connected. For this, three possible footprints have been created in QGIS using convex hull and concave hull geometries.

2. The baseline of each volcano has first been estimated by gridding the local minima of the digital elevation model (DEM) covering each volcanic province. For the next baseline, each volcanic footprint (calculated in the earlier step) has been masked from the present-day DEM and the topography interpolated across the gap to create an undulating surface over which most of the volcano should lie. Borehole data was also used during this process to guide the interpolation across the masked region.

3. The upper surface of each volcano has been calculated first by simply using the present-day DEM as the volcano top, to calculate the preserved volume. The eroded upper surface has then been estimated using a couple of different extrapolation methods. The first extracts points along preserved ridgelines to represent the highest points of the volcano top, a surface has then been extrapolated between these ridges and down to the base of the volcano. The second method involves the reconstruction of a simple pyramid shape at each province where the height of the pyramid is made to enclose 80, 90, and then 100% of the preserved volcanic material.

4. A final method of volume calculation applies the same simple conical estimation used by Wellman (1971) and Jones and Verdel (2015) but with updated extents to give a volume which is able to be compared more directly to the results of the two authors.

3.2.1 Preserved mapped extents

The present-day surface extent of each volcano has been defined by high resolution polygons from regional geological maps. Queensland data is from the 2018, 1:250000 Detailed Surface Geology and Detailed Solid Geology datasets by the Queensland Department of Resources. New South Wales data from the 2021, 1:250000 NSW Seamless Geology Data Package (version 2.1) by the Geological Survey of NSW. Tasmania data is from the 1995, 1:250000 Digital Geology of Tasmania data package by Mineral Resources Tasmania. Data for Victoria is from the 2014, 1:250000 Seamless Geology Data Package by Geoscience Victoria. Any gaps have been infilled using the 2012, 1:1 M Surface Geology of Australia dataset from Geoscience Australia.

3.2.2 Preserved remote sensing extents

Given the vast remoteness of much of Australia and difficulties in access due to dense shrubbery etc., most geological maps have been constructed through the combination of broad geological mapping, aerial geophysical surveys and remote sensing. The resolutions of the final digitised maps are generally much lower (around 1:250,000) than that of Britain (around 1:50,000) and in fact, notable differences are seen between these regional maps and more recent, local, high-resolution maps, for example, that by Bull et al. (2020) at the Warrumbungle volcano (1:50,000). This recent mapping project has refined the area covered by present-day lava flows of the Warrumbungle volcano, which has a knock-on effect on the overall volume of the volcano.

For this thesis, in order to try and improve the lower-resolution maps and to more precisely delineate the present-day extents of volcanism this second step uses the analysis and random forest classification of multispectral data (e.g., Landsat) on the Google Earth Engine (GEE) platform to try and image volcanic rocks. With a wealth of high-resolution multispectral bands, high-resolution airborne geophysical surveys (gravity, magnetic) and new mathematical techniques proven to isolate mafic volcanism now available, such new data can greatly enhance the accuracy of the published geologic polygons, as has already been shown by a number of authors (e.g. Gupta, 2017; Van Der Meer et al., 2012; Van den Hove et al., 2017).

Gupta (2017) defines remote sensing as "the acquisition of electromagnetic radiation data from sensors flying on aerial or space platforms, and its interpretation for deciphering ground object characteristics". One output of this is multispectral data, which consists of a number of bands which each sample the same image at differing wavelengths along the electromagnetic spectrum, from visible light to near, short wave, and thermal infrared. The advantage of this is that features on the Earth surface absorb, reflect and emit a unique amount of radiation dependent upon their physical or compositional attributes (Gupta, 2017). Various combinations of bands can therefore be merged (composited) to highlight specific geological facies such as mafic volcanism, felsic basement, basement-derived sediments and vegetation.

One of the pioneering programs in remote sensing is the NASA/USGS Landsat mission which, since 1972, has provided the longest, continuous record of spaceborne Earth imagery. Many of these earlier satellites acquired data via the Thematic Mapper (TM) and Enhanced Thematic Mapper (ETM+), which contains four bands in the Visible and Near-Infrared (VNIR) region (0.4–1.0 μm), two bands in the Shortwave-Infrared (SWIR) region (1–3 μm), and one band in the Thermal-Infrared (TIR) region (approx. 3–25 μm) (Figure 3.5). The results of these have been used for years in mapping of lithology using techniques such as band

ratioing, decorrelation stretching, saturation enhancement and principal component analysis (PCA) (Chavez et al., 1991; Van Der Meer et al., 2012).

In Landsat-8 these components were superseded by the Operational Land Imager (OLI) and Thermal Infrared Sensor (TIRS). Landsat-8 contains five bands in the Visible and Near-Infrared (VNIR), two in the Shortwave-Infrared (SWIR), and two in the Thermal-Infrared (TIR) (Figure 3.5). VNIR and SWIR bands all have a spatial resolution of 30 m and TIR bands of 100 m. For this project I have been able to focus mostly on Landsat-8 data which provides sufficient spatial coverage, resolution and image quality for the majority of remote sensing processes. However, for enhanced band resolution, and for enhanced spatial resolution, I have included data from the Advanced Spaceborne Thermal Emission and Reflection Radiometer (ASTER) and Sentinel-2 imagers.

The ASTER sensor launched on NASA's Terra satellite has provided enhanced mineral mapping capabilities since 2000 (Abrams et al., 2002; Salisbury and D'Aria, 1992; Yamaguchi et al., 1998; Hewson et al., 2001; Rowan and Mars, 2003; Kalinowski and Oliver, 2004). ASTER is designed with three bands in the Visible and Near-Infrared (VNIR) with 15 m resolution, six bands in the Shortwave-Infrared (SWIR) with 30 m resolution, and five bands in the Thermal-Infrared (TIR) with 90 m resolution (Figure 3.5). The addition of channels in the TIR has allowed the transition from mapping alteration indices to mapping mineral indices and can therefore be used to identify a greater variety of rock types, including mafic and felsic volcanism. For this study, analysis has focused on TIR bands as other bands are often affected by the cross-talk instrument problem; a type of noise caused by light reflected from band 4 optical components leaking into SWIR detectors (Abrams et al., 2002), the same noise is not present in the Landsat-8 SWIR bands.

The Sentinel-2 satellite developed by the European Space Agency (ESA), has been acquiring optical imagery at high spatial resolution (10–60 m), since 2015. Sentinel-2 collects data in 13 spectral bands from the Visible and Near-Infrared (VNIR) and the Shortwave-Infrared (SWIR) regions, much like Landsat, and has therefore been used for many of the same techniques, but with a greater spatial resolution, providing an excellent quality check to the Landsat-8 results (Figure 3.5). With most imagers, roughly the top 3 cm of the Earths surface is measured with VNIR and SWIR wavelengths and the top 10 cm with TIR wavelengths.

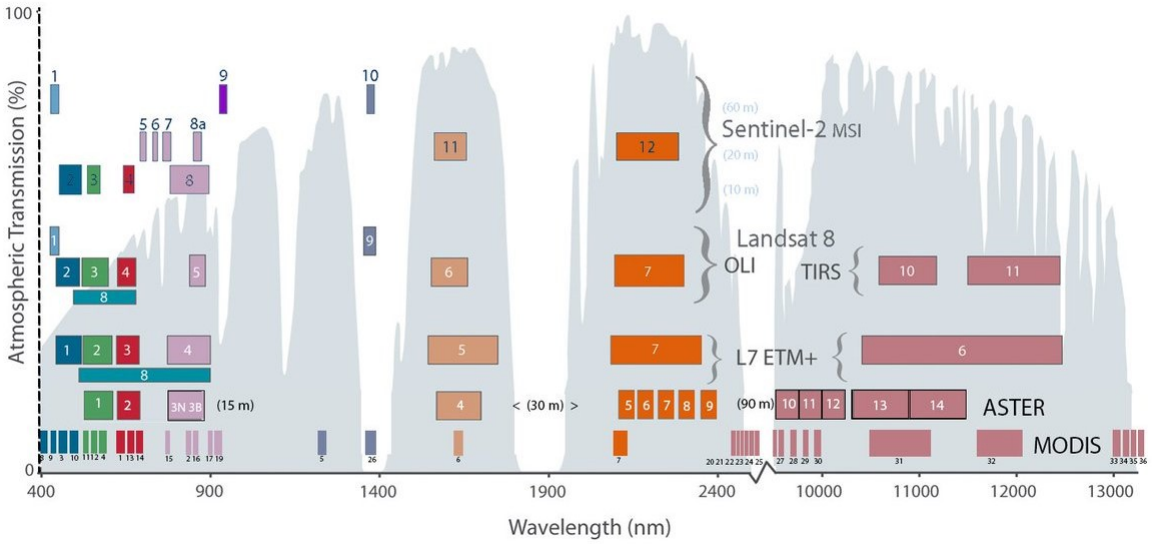

Figure 3.5: *MODIS, ASTER, Landsat-7, -8, and Sentinel-2 bands, atmospheric transmission, and wavelength (USGS Landsat Program, 2017).*

Within this thesis, the remote classification of volcanic rocks was tested at two different provinces with distinctly different climates; (1) the humid, vegetated Warrumbungle volcano and (2) the semi-arid McBride volcano, both of which have been well mapped. The remote sensing results are discussed in detail in Chapter 6 of this thesis. Unfortunately, basaltic and felsic rock types from across the two provinces proved to be difficult to isolate from adjacent mafic metamorphic rocks, older volcanics, and particularly iron-rich sediments and after difficulties in generating precise results within the time frame, it was decided not to take this process any further within the other provinces. However, the steps taken here prove that at least a large portion of the East Australian volcanoes may be better mapped using remote sensing, with a focus on basaltic products, and improvements upon this workflow would be a good area for further work. The typical workflow is as follows:

1. Load and quality check data including geophysical rasters and geological polygons.

2. Run k-means clustering on Landsat-8 Visible and Near-Infrared (VNIR) and Shortwave-Infrared (SWIR) bands.
3. Run k-means clustering on ASTER Thermal-Infrared (TIR) bands.
4. Compare expected spectra of dominant rock types to the observed spectra within polygons.
5. Create composites to highlight geological features based on observed spectra and k-means results.
6. Run principle component analysis (PCA) on all input bands including composites.
7. Normalise all PCA, terrain, gravity and magnetic bands to be used in the classification.
8. Create training data for each class using the uploaded geological polygons.
9. Tune Google Earth Engine (GEE) random forest parameters using training versus validation data.
10. Run the random forest classification and export the results.

Loading data

All data sets to be used in the random forest classification were first loaded into Google Earth Engine (GEE), including geological polygons and geophysical grids from external sources, and multispectral tiles from the platform itself. Multispectral tiles were then filtered to show only the region of interest (roi), with cloud cover less than 1% and all bands recorded by the imager present. A detailed description of all data sets included in the final workflow are given below:

- Geological polygons: the dominant rock type of each geological unit from the regional geology maps.
- Bounding boxes: boxes around each volcano, enlarged by 40 km to allow space for the re-analysis of volcanic boundaries.
- Geoscience Australia Gravity FAA A-Series (2019) 400 m: Free Air Anomaly (FAA) grid produced from a combination of ground gravity data for Australian onshore locations, gravity data derived from imager altimetry for offshore locations, and gravity data from the Earth Gravitational Model (EGM2008) for the onshore locations in countries other than Australia (Lane et al., 2019).
- Geoscience Australia Magnetics TMI VRTP (2019) 90 m: Total magnetic Intensity (TMI) grid with variable reduction to pole (VRTP). This grid only includes airborne-derived TMI data for onshore and near-offshore continental areas. The VRTP processing followed a differential reduction to pole calculation up to 5th order polynomial. Magnetic inclination and declination were derived from the International Geomagnetic Reference Field (IGRF-11) model using a data representative date of January 2005 and elevation 300 m (Poudjom Djomani and Minty, 2019).
- NASA SRTM Digital Elevation (2000) 30 m: The Shuttle Radar Topography Mission (SRTM) (Farr et al., 2007) digital elevation data is an international research effort that obtained digital elevation models on a near-global scale. This SRTM V3 product (SRTM Plus) is provided by NASA Jet Propulsion Laboratory (JPL). This dataset has undergone a void-filling process using open-source data (NASA Jet Propulsion Laboratory (JPL), 2022).
- USGS Landsat-8 Level 2, Collection 2, Tier 1 (2013–2021) 30 m: This dataset contains atmospherically corrected surface reflectance and land surface temperature derived from the data produced by the Landsat 8 Operational Land Imager (OLI) and Thermal Infrared Sensor (TIRS) sensors. These images contain five Visible and Near-Infrared (VNIR) bands and two Shortwave-Infrared (SWIR) bands processed to orthorectified Surface Reflectance (SR), and one Thermal Infrared (TIR) band processed to orthorectified Surface Temperature (ST). They also contain intermediate bands used in calculation of the ST products, as well as Quality Assessment bands. Landsat-8 SR products are created with the Land Surface Reflectance Code (LaSRC). All Collection 2 ST products are created with a single-channel algorithm jointly created by the Rochester Institute of Technology (RIT) and NASA Jet Propulsion Laboratory (JPL). Strips of collected data are packaged into overlapping scenes covering approximately 170 km x 183 km using a standardized reference grid (Google, 2022a).

- ASTER L1T Radiance (2003–2006) 15–90 m: The Advanced Spaceborne Thermal Emission and Reflection Radiometer (ASTER) is a multispectral imager that was launched on board NASA's Terra spacecraft in December, 1999. ASTER can collect data in 14 spectral bands from the visible to the thermal infrared. Each scene covers an area of 60 x 60 km. These scenes, produced by the USGS, contain calibrated at-sensor radiance, ortho-rectified and terrain corrected (Google, 2022a).
- AG100 ASTER Global Emissivity Dataset V003 (2000–2008) 100 m: The Advanced Spaceborne Thermal Emission and Reflection Radiometer Global Emissivity Database (ASTER-GED) includes the mean emissivity and standard deviation for all five ASTER Thermal-Infrared (TIR) bands, mean Land Surface Temperature (LST) and standard deviation, a re-sampled ASTER Global Digital Elevation Map (GDEM), land-water mask, mean Normalized Difference Vegetation Index (NDVI) and standard deviation, and observation count. ASTER Global Emissivity Database (ASTER-GED) Land Surface Temperature and Emissivity (LST&E) are generated using the ASTER Temperature Emissivity Separation (TES) algorithm in combination with a Water Vapor Scaling (WVS) atmospheric correction method using Moderate Resolution Imaging Spectroradiometer (MODIS) atmospheric profiles (MOD07) and the Moderate resolution atmospheric Transmission (MODTRAN) 5.2 radiative transfer model (Google, 2022a).
- Sentinel-2 MSI (2015–2021) 10–20 m: MultiSpectral Instrument, Level-1C: Sentinel-2 is a wide-swath, high-resolution, multi-spectral imaging mission supporting Copernicus Land Monitoring studies. The Sentinel-2 data contain 13 UInt16 spectral bands representing top-of-atmosphere reflectance scaled by 10000. In addition, three quality assessment bands are present where one (QA60) is a bitmask band with cloud mask information. Each tile is a 100 km x 100 km ortho-image (Google, 2022a).

All data packages used here are freely available on the Google Earth Engine (GEE) platform. The USGS Landsat-8 Level 2, Collection 2, Tier 1 product is provided as atmospherically corrected surface reflectance and land surface temperature data. The ASTER L1T Radiance product is calibrated at-sensor radiance data and the AG100 ASTER Global Emissivity Dataset V003 includes the mean emissivity of each of the five Thermal-Infrared (TIR) bands. The Sentinel-2 MultiSpectral Instrument, Level-1C product is top-of-atmosphere (TOA) reflectance data scaled by 10000. When computing spectral ratios, it is possible to use raw data (DN values), or alternatively processed data such as at-sensor radiance, top-of-atmosphere radiance, surface reflectance, radiant temperature or surface emissivity (Ninomiya et al., 2005). All data sets have been used whilst assessing band ratios, Landsat-8 has been used in the generation of surface reflectance curves and ASTER Global Emissivity Database (ASTER-GED) has been used in the generation of emissivity curves.

ASTER, Landsat-8, and Sentinel-2 imagers were chosen because they have good global coverage, good resolution, and a large breadth of bands from visible to thermal infrared. The ASTER imager has the most thermal bands, the Landsat-8 imager has the largest tile size, and the Sentinel-2 imager has the highest spatial resolution, so together they cover most bases required for this study. In order to run the classification on one single composite image, all tiles from each band, in a specified range of dates, were reduced into one image. The time of year in which the tiles were captured has a considerable effect on the final image i.e., in changes in vegetation cover, water quantity, and cloud cover. Therefore, date filters were tested on a trial and error basis to see which date range best represented geological, rather than agricultural or man-made variations. The results, including the final dates that were chosen in the filter, are given in Chapter 6. Once all multispectral tiles to be used were loaded and merged, I created terrain rasters i.e., hillshade and slope, using the Terrain algorithm within Google Earth Engine (GEE). I then masked coastal areas by applying a mask over any data at 0 m elevation. The full GEE JavaScript code used to complete each of these steps is given below.

```
// load shapefiles
var box = ee.FeatureCollection("users/ameliasmethurst/2021_bounding_box"),
    grav = ee.Image("users/ameliasmethurst/2019_grav_faa"),
    mag = ee.Image("users/ameliasmethurst/2019_mag_tmi"),
    table1 = ee.FeatureCollection("users/ameliasmethurst/simplified_Alluvium"),
    table2 = ee.FeatureCollection("users/ameliasmethurst/simplified_Sandstone"),
    table3 = ee.FeatureCollection("users/ameliasmethurst/simplified_Clay"),
    table4 = ee.FeatureCollection("users/ameliasmethurst/simplified_Dolerite"),
    table5 = ee.FeatureCollection("users/ameliasmethurst/simplified_Saprolite"),
    table6 = ee.FeatureCollection("users/ameliasmethurst/simplified_Basalt"),
    table7 = ee.FeatureCollection("users/ameliasmethurst/simplified_Syenite"),
```

```
    table8 = ee.FeatureCollection("users/ameliasmethurst/simplified_Trachyte"),
    table9 = ee.FeatureCollection("users/ameliasmethurst/simplified_mcbr_Alluvium"),
    table10 = ee.FeatureCollection("users/ameliasmethurst/simplified_mcbr_Arenite"),
    table11 = ee.FeatureCollection("users/ameliasmethurst/simplified_mcbr_Metamorphics"),
    table12 = ee.FeatureCollection("users/ameliasmethurst/simplified_mcbr_Granitoid"),
    table13 = ee.FeatureCollection("users/ameliasmethurst/simplified_mcbr_Felsites"),
    table14 = ee.FeatureCollection("users/ameliasmethurst/simplified_mcbr_Basalt"),
    pca_aster_warr = ee.Image("users/ameliasmethurst/pca_aster_warr"),
    pca_landsat_warr = ee.Image("users/ameliasmethurst/pca_lands_warr"),
    pca_aster = ee.Image("users/ameliasmethurst/pca_aster_mcbr"),
    pca_landsat = ee.Image("users/ameliasmethurst/pca_lands_mcbr");

// set location
var prov = 'Warrumbungles';

// extract roi from bounding box
Map.centerObject(box.filterMetadata('PROVINCE', 'equals', prov), 8);
var roi = box.filterMetadata('PROVINCE', 'equals', prov);

// load geophysical datasets
var dem = ee.Image('USGS/SRTMGL1_003').clip(roi);

var landsat = ee.ImageCollection('LANDSAT/LC08/C02/T1_L2')
                  .filterBounds(roi)
                  .filterMetadata('CLOUD_COVER', 'less_than', 1)
                  .select('SR_B[1-7]')
                  .reduce(ee.Reducer.median());

var sentinel = ee.ImageCollection('COPERNICUS/S2')
                  .filterBounds(roi)
                  .filterMetadata('CLOUD_COVERAGE_ASSESSMENT', 'less_than', 1)
                  .select('B[1-9]','B10','B11','B12')
                  .reduce(ee.Reducer.median());

var aster = ee.Image('NASA/ASTER_GED/AG100_003')
                  .select('emissivity_band10','emissivity_band11',
                  'emissivity_band12','emissivity_band13','emissivity_band14')
                  .clip(roi);

// create coastal mask and terrain analyses
var mask = dem.neq(0);
var slope = ee.Terrain.slope(dem);
```

K-means clustering

Curves showing the relationship between radiation intensity and wavelength are named spectral response curves and are specific to any object on the Earths surface (Gupta, 2017). Geological identification with remote sensing utilises spectral response curves and the existence of characteristic absorption and reflection bands to help recognise specific mineral assemblages (Gupta, 2017). Spectra generated from satellite images may then be compared with the spectra of known pure materials, referred to as end-members, found in libraries such as Kokaly et al. (2017); Salisbury et al. (1991); Baldridge et al. (2009). Classically, most geological remote sensing studies have focused on hydrothermal alteration deposits and mapping within the mining industry, however, a number of these findings are transferable to volcanic regions. The measured reflectance of common minerals and vegetation are shown in Figure 3.6, alongside the same spectra resampled to the spectral resolution of Landsat-8. The Figure shows that whilst a lot of data is lost in the acquisition of satellite data, a number of minerals can be identified by key features within the resampled spectra.

Spectral features in the Visible and Near-Infrared (VNIR) region are dominated by electronic processes in transition metals, particularly iron and some rare-earth elements (REE) (Rowan and Mars, 2003), and are also useful for vegetation mapping, due to the characteristic absorption of chlorophyll in photosynthesizing vegetation (Knipling, 1970). Molecular absorption features in the Shortwave-Infrared (SWIR) region are dominated by hydroxyls and carbonates (Gad and Kusky, 2007; Yamaguchi and Naito, 2003; Gupta, 2017), therefore, VNIR and SWIR ratio images can primarily identify two assemblages of minerals; iron minerals and clays (Sabins, 1999). Absorption features of ferrous and ferric iron oxides typically appear within the 0.7–1.0 μm atmospheric window (Gupta, 2017), which corresponds to the spectral region covered by Landsat-8 band 5 (Figure 3.6). FeO minerals are prevalent in all volcanic rocks, particularly mafic rocks, in pyroxenes, amphiboles and magnetite, but also make up a high component of weathered volcanic rocks due to the immobility of iron, and of many sedimentary rocks. Landsat-8 band 5 can therefore be a useful discriminator of FeO-rich rocks, where non-FeO-rich clays and vegetation should have maximum reflectance in this band. The vegetation curve generally flattens with dry long grass, and flattens further with dark soil.

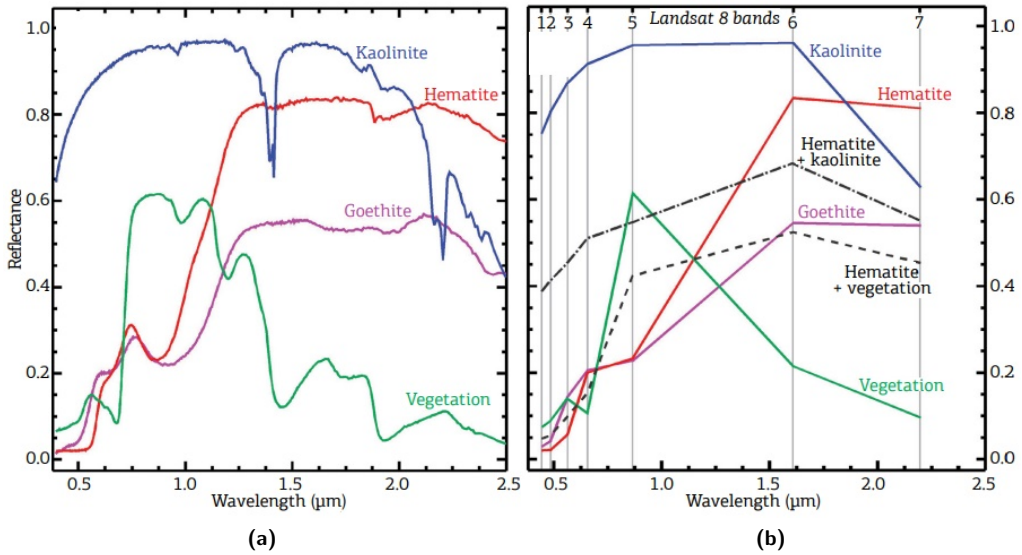

Figure 3.6: *(a) Reflectance spectra from the USGS spectral library showing typical alteration minerals and vegetation. (b) The same reflectance spectra resampled to Landsat-8 Operational Land Imager (OLI) bandwidths, from Ducart et al. (2016).*

As shown in Figure 3.6, clay minerals e.g., kaolinite, have higher reflectance in Landsat-8 bands 1–6 and absorption features are observed in the 2.1–2.4 μm region which corresponds to Landsat-8 band 7 (Gupta, 2017). This characteristic feature occurs where hydroxyl ions are found in combination with aluminium and magnesium, i.e., as Al–OH and Mg–OH, which is common in many clays and hydrated silicates. Differences between the reflectance of Landsat-8 band 7 may therefore be used to identify clay-rich rocks. The alteration of mafic minerals to iron-rich phyllosilicates such as iddingsite and chlorite, as is commonly found in the East Australian basalts *sensu lato*, (Appendix A), exhibit a similar absorption in band 7 as well as in band 5 due to high FeO contents. These bands may therefore also be combined to separate FeO-rich clays from non-FeO-rich clays.

Many important rock-forming minerals including quartz, feldspars, and olivines have no diagnostic features in the Visible and Near-Infrared (VNIR) and Shortwave-Infrared (SWIR) regions and instead lead to increased reflectance in these bands, they do however, show absorption in the Thermal-Infrared (TIR) region (Sabins, 1999). Reflectance, or emissivity, in the TIR region of the electromagnetic spectrum may therefore be attributed to a wide range of minerals. The most common being silicate minerals which show an intense absorption within the 8–12 μm atmospheric window (Salisbury and D'Aria, 1992) (Figure 3.7). Absorption in this region is sensitive to silicate structure and shifts from around 9 μm in framework silicates or felsic minerals to 11.5 μm in chain silicates or mafic minerals (Gupta, 2017). The same minerals also have a peak within this window which migrates systematically with composition, being near 7 μm for felsic minerals and 9 μm for ultramafic minerals (Gupta, 2017). The five ASTER TIR bands cover the region 8–12 μm and changes in emissivity in these bands can therefore be used to identify quartz, feldspars, olivines and pyroxenes, and to isolate felsic volcanics i.e., syenites and trachytes, from mafic volcanics i.e., basalts and dolerites, primarily in bands 10, 11, and 12. As shown in Figure 3.7a, there is quite a large gap between ASTER bands 10–11–12

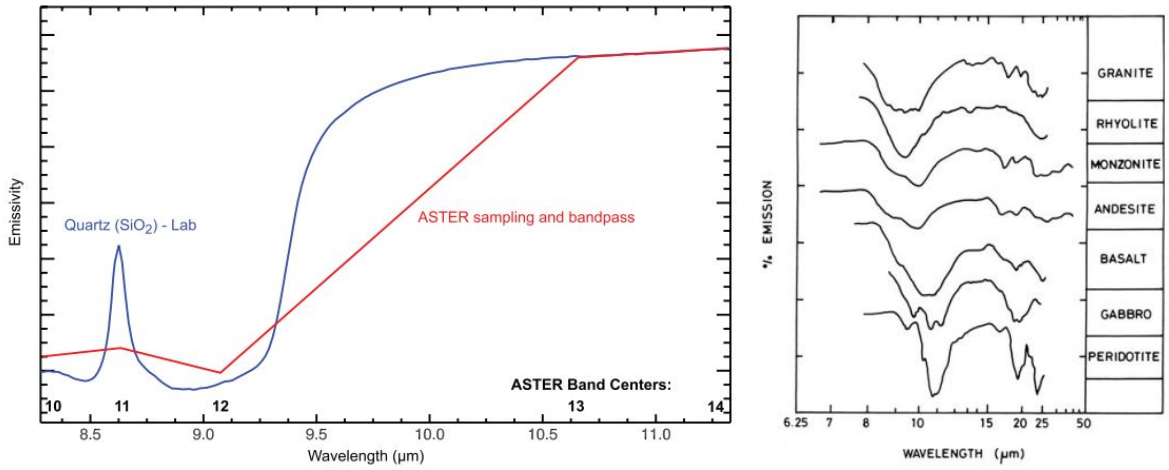

Figure 3.7: *(a) The measured emissivity of pure quartz, resampled to ASTER bandwidths (Rockwell and Hofstra, 2008). (b) % emission of typical igneous rocks with the characteristic shift in absorption between felsic and mafic mineralogy (Gupta, 2017).*

and bands 13–14 and the latter are often used more in identifying ultramafic from mafic rocks, which is less relevant to this study due to the lack of ultramafics in either study area.

Following data loading, I ran the Google Earth Engine (GEE) k-means clustering algorithm on each satellite band to identify any distinct groups within the multispectral data. Surface materials highlighted in a particular band would suggest they have a strong spectral absorption or reflectance in the wavelength range of that band i.e., the pronunciation of basaltic rocks in Landsat-8 band 5 may be an indication of strong FeO absorption. K-means clustering is an unsupervised classification and is therefore a very quick way to initially assess how the geology is interacting with specific wavelengths of electromagnetic radiation. This information can then be fed into more sophisticated image enhancement techniques to isolate that particular geological unit further. The objective of k-means clustering is to minimize the sum of squared distances between all points and the cluster center (MacQueen, 1967). The algorithm does this by selecting at random a number of points (k), the centroids. Each data point, or pixel, is then assigned to the closest centroid and the sum of squared distances computed. New centroids are then placed and the data points reassigned until the minimum distances have been reached and the algorithm is complete. Clustering was computed on Landsat-8 bands 1–7, and ASTER Thermal-Infrared (TIR) bands 10–14 as these cover all wavelength ranges of interest.

```
// define band
var composite = landsat.select('SR_B1_median').clip(roi);

// define the training region as the full image
var training = composite.sample({
  region: roi,
  scale: 30,
  numPixels: 100});

// train cluster on image
var clusterer = ee.Clusterer.wekaKMeans(10).train(training);

// cluster the complete image
var kmeans = composite.cluster(clusterer);

// display the clusters with random colours
Map.addLayer(kmeans.randomVisualizer());
```

Spectral response curves

The next step in the classification workflow was to assess the spectral response of each volcano compared to that of the surrounding geology. In an ideal situation, the characteristic absorption and reflection bands of volcanic rocks would be detected only within volcanic boundaries and easily identified in the k-means analysis, however, underlying rocks are often obscured by sediment or vegetation, with their respective spectral signatures added. Some rocks, i.e., iron-rich volcanics and sedimentary red beds will have similar spectra, and detritus eroded from altered rocks will influence the spectra of the bedrock they overlay. Also, over the same lithology, the spectral response may be quite variable, being a function of several factors including the state of weathering and moisture content (Rowan and Mars, 2003; Gupta, 2017). Despite these complexities, there are a few ways we can use spectral features to quantitatively assess the Cenozoic volcanoes of eastern Australia, particularly where clear changes in rock type also correlate with changes in terrain and vegetation. To analyse gathered spectra I have loaded geological polygons from regional geological surveys into QGIS and created up to eight distinct shapefiles based on the dominant lithology attribute of each geological unit. A comparison of the different spectra for each dominant lithology has been carried out in Chapter 6 of this thesis and the Google Earth Engine (GEE) code used to compute them is given below.

```
// create feature collection from shapefiles
var polygons = ee.FeatureCollection([
  ee.Feature(table1.geometry(), {'class': 0}),
  ee.Feature(table2.geometry(), {'class': 1}),
  ee.Feature(table3.geometry(), {'class': 2}),
  ee.Feature(table4.geometry(), {'class': 3}),
  ee.Feature(table5.geometry(), {'class': 4}),
  ee.Feature(table6.geometry(), {'class': 5}),
  ee.Feature(table7.geometry(), {'class': 6}),
  ee.Feature(table8.geometry(), {'class': 7})]);

// define chart parameters
var plotOptions = {
  hAxis: {title: 'Wavelength'},
  vAxis: {title: 'Reflectance', viewWindow: {min: 8000, max: 20000}},
  lineWidth: 3,
  pointSize: 5,
  fontSize: 20,
  series: {0: {color: 'pink'},
  1: {color: 'DarkKhaki'},
  2: {color: 'SaddleBrown'},
  3: {color: 'BlueViolet'},
  4: {color: 'LightSkyBlue'},
  5: {color: 'blue'},
  6: {color: 'orange'},
  7: {color: 'red'}
  }};
var wavelengths = [443, 482, 562, 655, 865, 1609, 2201];

// print the chart
var spectra1 = ui.Chart.image.regions(landsat, polygons, ee.Reducer.mean(), 300, '
    label', wavelengths)
        .setSeriesNames(['Alluvium','Sandstone','Clay','Dolerite','Saprolite','
            Basalt','Syenite','Trachyte'])
        .setChartType('ScatterChart')
        .setOptions(plotOptions);
        print(spectra1);
```

Composite analysis

Prior to the selection of training data, the geology at each of the two provinces was analysed further using image enhancement procedures including colour composites and band ratios. Colour composite images are created by displaying a combination of three spectral bands at once, often as red, green, and blue colours

(RGB). False colour composites (FCC) use bands other than visible red, green and blue as the RGB components, allowing interpretation of wavelengths not visible to the human eye. This effect can be enhanced further through the use of band ratioing. As already mentioned, individual minerals are identified by distinctive absorption and reflectance features i.e., reflectance minima and maxima at specific wavelengths. Ratio images can emphasise and quantify these spectral differences to isolate certain minerals or mineral groups (Sabins, 1999). They are therefore particularly useful for lithological discrimination and, advantageously, suppress topographic variation and brightness differences related to grain size variation (e.g., Gad and Kusky, 2006). A comprehensive overview of FCCs and band ratios used to detect mineral indices may be found in Kalinowski and Oliver (2004) and Gupta (2017). Those created for this study using the results of k-means and spectral response analyses and are discussed in detail in Chapter 6.

```
106 // landsat 7-6-3
107 var r = landsat.select('SR_B7_median');
108 var g = landsat.select('SR_B6_median');
109 var b = landsat.select('SR_B3_median');
110 var rgb7_6_3 = r.addBands(g).addBands(b);
111
112 // sentinel 12-11-2
113 var r = sentinel.select('B12_median');
114 var g = sentinel.select('B11_median');
115 var b = sentinel.select('B2_median');
116 var rgb12_11_2 = r.addBands(g).addBands(b);
117
118 // aster 10-11-12
119 var r = aster.select('emissivity_band10');
120 var g = aster.select('emissivity_band11');
121 var b = aster.select('emissivity_band12');
122 var rgb10_11_12 = r.addBands(g).addBands(b);
123
124 // landsat 6/7-6/2-5 (TM 5/7-5/1-4)
125 var r = landsat.select('SR_B6_median').divide(landsat.select('SR_B7_median'));
126 var g = landsat.select('SR_B6_median').divide(landsat.select('SR_B2_median'));
127 var b = landsat.select('SR_B5_median');
128 var rgb6o7_6o2_5 = r.addBands(g).addBands(b);
129
130 // 6/7 feo compared to clays or general hydroxyl
131 var rgb6o7 = landsat.select('SR_B6_median').divide(landsat.select('SR_B7_median'));
132
133 // 6/2 haematite-epdiote-chlorite compared to non feo
134 var rgb6o2 = landsat.select('SR_B6_median').divide(landsat.select('SR_B2_median'));
135
136 // 2/5 vegetation compared to minerals
137 var rgb2o5 = landsat.select('SR_B2_median').divide(landsat.select('SR_B5_median'));
138
139 // aster mafic index 12/13
140 var rgb12o13 = aster.select('emissivity_band12').divide(aster.select('
        emissivity_band13'));
141
142 // aster empirical silica index watanabe
143 var rgb_sio2 = ee.Image().expression(
144         '56.2 - 271.09 * log((em10 + em11 + em12) / 3 / em13)',
145         {'em10': ee.Image(aster.select('emissivity_band10')),
146         'em11': ee.Image(aster.select('emissivity_band11')),
147         'em12': ee.Image(aster.select('emissivity_band12')),
148         'em13': ee.Image(aster.select('emissivity_band13'))}).rename('sio2');
```

Principle component analysis

Once all input data due to be used in the classification was complied, principle component analysis (PCA) was used to reduce the size of the dataset and to segregate noise from the dataset. This is a common practice used in many remote sensing mapping studies (e.g. Abrams et al., 1983; Hassouna et al., 2015). PCA is

a statistical technique that, in its simplest form, compresses data from a large number of intercorrelated variables into fewer uncorrelated variables, or principal components (PC) (Crosta et al., 2003; Yesou et al., 1993). Multispectral bands are often highly correlated and, as shown in the k-means analysis, there is considerable crossover between bands. PCA finds the direction between all of the input bands which shows the greatest variation. It then finds a direction orthogonal to this which again shows the maximum variation, and so on until a specified number of PC directions have been identified (Eklundh and Singh, 1993; Valentine and Kalnins, 2016). Each successive PC explains decreasing variance levels, indicated by their decreasing eigenvalue percentages (Yesou et al., 1993). For this next step, before sampling training points, I ran PCA on any final composite images i.e., the images collated to include the bands which best highlighted any geological differences. >95% of the variance from the original images were captured in 3-band PCA images i.e., three bands for Landsat data, and three bands for ASTER data. Using each of these PCA bands instead of the full composite sends a stronger signal to the classifier and improves accuracy by allowing it to distinguish different classes better. The code used to compute the PCA is given below and has been adapted from Google (2022b).

```
// pca of landsat-8 and aster data
function PCA(maskedImage){
  var image = maskedImage.unmask();
  var scale = 30;
  var region = roi;
  var bandNames = image.bandNames();
  // mean center the data to enable a faster covariance reducer
  // and an SD stretch of the principal components
  var meanDict = image.reduceRegion({
    reducer: ee.Reducer.mean(),
    geometry: region,
    scale: scale,
    maxPixels: 1e9,
    bestEffort: true,
    tileScale: 16});
  var means = ee.Image.constant(meanDict.values(bandNames));
  var centered = image.subtract(means);
  // helper function returns a list of new band names
  var getNewBandNames = function(prefix) {
    var seq = ee.List.sequence(1, bandNames.length());
    return seq.map(function(b) {
      return ee.String(prefix).cat(ee.Number(b).int());});};
  // add the mean centered imagery, a scale and a roi
  // function returns the pcs in the region as a new image
  var getPrincipalComponents = function(centered, scale, region) {
    // collapse the bands of the image into a 1d array per pixel
    var arrays = centered.toArray();
    // compute the covariance of the bands within the region
    var covar = arrays.reduceRegion({
      reducer: ee.Reducer.centeredCovariance(),
      geometry: region,
      scale: scale,
      maxPixels: 1e9,
      bestEffort: true,
      tileScale: 16});
    // cast covariance to an array representing band-to-band covariance in the roi
    var covarArray = ee.Array(covar.get('array'));
    // perform eigen analysis and slice apart the values and vectors
    var eigens = covarArray.eigen();
    // P-length vector of eigenvalues
    var eigenValues = eigens.slice(1, 0, 1);
    // compute percentage variance of each component
    var eigenValuesList = eigenValues.toList().flatten();
    var total = eigenValuesList.reduce(ee.Reducer.sum());
    var percentageVariance = eigenValuesList.map(function(item) {
      return (ee.Number(item).divide(total)).multiply(100).format('\%.2f');});
    // show how many components capture most of the variance
    print('percentage variance of each component', percentageVariance);
```

```
    // PxP matrix with eigenvectors in rows
    var eigenVectors = eigens.slice(1, 1);
    // convert array image to 2D arrays for matrix computations
    var arrayImage = arrays.toArray(1);
    // left multiply the image array by the matrix of eigenvectors
    var principalComponents = ee.Image(eigenVectors).matrixMultiply(arrayImage);
    // turn the square roots of eigenvalues into a P-band image
    var sdImage = ee.Image(eigenValues.sqrt())
      .arrayProject([0]).arrayFlatten([getNewBandNames('sd')]);
    // turn the pcs into a P-band image, normalized by SD
    return principalComponents
      // throw out an an unneeded dimension, [[]] -> []
      .arrayProject([0])
      // make the one band array image a multi-band image, [] -> image
      .arrayFlatten([getNewBandNames('pc')])
      // normalize the pcs by their sds
      .divide(sdImage);};
  var pcImage = getPrincipalComponents(centered, scale, region);
  return pcImage.mask(maskedImage.mask());}

// create composite of all bands to be used in classification
var composite = landsat.select('SR_B3_median','SR_B5_median','SR_B6_median','
    SR_B7_median')
                        .addBands(rgb6o7).addBands(rgb6o2).addBands(rgb2o5);

var composite = aster.select('emissivity_band10','emissivity_band11','
    emissivity_band12')
                       .addBands(rgb12o13).addBands(rgb_sio2).toUint16();

// from printed results, 99\% of variance is captured in the first 3 pcs
var pca = PCA(composite).select(['pc1', 'pc2', 'pc3']);
```

Normalisation & training data selection

Once all input data had been created and approved, all results then needed to be normalised to values between 0 and 1 in order to aid the random forest classification. For this, I used a normalising function created in Google Earth Engine (GEE) to find the min and max of each band within each image and then divided bands by the respective difference. Following this, all normalised inputs were joined into a single composite image and the bands with which to train and classify the composite image were defined. Training data was created by taking 500 points from within each class polygons, 30% of these were then randomly selected as validation points and the other 70% were used to train the classifier. Once again, the full code is given below.

```
// normalise function
function normalise(image){
  var bandNames = image.bandNames();
  var minDict = image.reduceRegion({
    reducer: ee.Reducer.min(),
    geometry: roi,
    scale: 30,
    bestEffort: true,
    tileScale: 16});
  var maxDict = image.reduceRegion({
    reducer: ee.Reducer.max(),
    geometry: roi,
    scale: 30,
    bestEffort: true,
    tileScale: 16});
  var mins = ee.Image.constant(minDict.values(bandNames));
  var maxs = ee.Image.constant(maxDict.values(bandNames));
  var normalised = image.subtract(mins).divide(maxs.subtract(mins));
  return normalised}
```

```
245
246 // normalise landsat data
247 var norm_landsat = normalise(pca_landsat);
248 // normalise aster data
249 var norm_aster = normalise(pca_aster);
250 // normalise slope data
251 var norm_slope = normalise(slope);
252 // normalise gravity data
253 var gravity = grav.select(['b1']).rename(['grav']);
254 var norm_grav = normalise(gravity.clip(roi));
255 // normalise magnetic data
256 var magnetic = mag.select(['b1']).rename(['mag']);
257 var norm_mag = normalise(magnetic.clip(roi));
258
259 // combine all inputs into one composite
260 var composite = norm_landsat.addBands(norm_aster).addBands(norm_slope).addBands(
      norm_grav).addBands(norm_mag);
261 var bands = ['pc1', 'pc2', 'pc3', 'pc1_1', 'pc2_1', 'pc3_1', 'slope', 'grav', 'mag'
      ];
262
263 // create classes from feature collection
264 var classes = ee.Image().byte().paint(polygons, "class").rename("class");
265 Map.addLayer(classes, {min:0,max:7, palette:['pink','DarkKhaki','SaddleBrown','
      BlueViolet','LightSkyBlue','blue','orange','red']});
266 Map.addLayer(classes, {min:0,max:5, palette:['pink','DarkKhaki','LightGreen','red',
      'orange','blue']});
267
268 // filter number of points within classes
269 var stratified = classes.addBands(ee.Image.pixelLonLat())
270     .stratifiedSample({
271       numPoints: 300,
272       classBand: 'class',
273       projection: 'EPSG:3665',
274       scale: 30,
275       region: polygons.geometry()
276     }).map(function(f) {
277       return f.setGeometry(ee.Geometry.Point([f.get('longitude'), f.get('latitude')
          ])})});
278 print ('class_points', stratified.reduceColumns(ee.Reducer.frequencyHistogram(),['
      class']));
279
280 // add a random column to split points into a training and validation set
281 var stratified = stratified.randomColumn();
282
283 // take 30\% points for validation
284 var trainingStrat = stratified.filter(ee.Filter.lt('random', 0.3));
285 var validationStrat = stratified.filter(ee.Filter.gte('random', 0.3));
286
287 // display training points
288 var palette = ee.List(['pink','DarkKhaki','SaddleBrown','BlueViolet','LightSkyBlue'
      ,'blue','orange','red']);
289 var classed = ee.List([0, 1, 2, 3, 4, 5, 6, 7]);
290 var palette = ee.List(['pink','DarkKhaki','LightGreen','red','orange','blue']);
291 var classed = ee.List([0, 1, 2, 3, 4, 5]);
292 var pointStyled = ee.FeatureCollection(
293   classed.map(function(lc){
294     var color = palette.get(classed.indexOf(lc));
295     var markerStyle = { color: 'white', pointShape: 'diamond',
296       pointSize: 4, width: 1, fillColor: color};
297     return trainingStrat.filter(ee.Filter.eq('class', lc))
298                 .map(function(point){
299                   return point.set('style', markerStyle)})})).flatten();
300 Map.addLayer(pointStyled.style({styleProperty:"style"}), {});
```

Hyperparameter tuning & classification

For the training classification to run smoothly each hyperparameter, i.e., a parameter whose quantity is used to control the learning process, needs to be tuned to its optimum value. In the case of the smile random forest algorithm in Google Earth Engine (GEE), this requires a number of decision trees to be specified. Too few trees and the algorithm will miss important information out of the classification, too many and the classifier could be overtrained and the computation is likely to time out. The random forest was run with the number of trees increasing in increments of 10, from 10 to 150, and the validation points that were taken out of the calculation a few steps earlier were used to check the accuracy of the result. Where the accuracy began to level off was the point at which I selected the optimum number of trees; this was 100 for the Warrumbungle province and 60 for the McBride province. Once the optimal number of trees had been selected the classification was run on the composite image. The outputs include a classified image, a confusion matrix to show which classes have been mistaken for one another, and an overall accuracy rating where an accuracy greater than 80% was approved. A full discussion regarding how well each test has performed is given in Chapter 6.

```
// overlay points on image to train
var training = composite.select(bands).sampleRegions({
  collection: trainingStrat,
  properties: ['class'],
  scale: 30,
  tileScale: 16});

// train the classifier
var classifier = ee.Classifier.smileRandomForest(10).train({
  features: training,
  classProperty: 'class',
  inputProperties: bands});

// run .explain() to see what the classifer looks like
print(classifier.explain());

var test = composite.sampleRegions({
  collection: validationStrat,
  properties: ['class'],
  scale: 30,
  tileScale: 16});

// tune the numberOfTrees parameter.
var numTreesList = ee.List.sequence(10, 150, 10);

var accuracies = numTreesList.map(function(numTrees) {
  var classifier = ee.Classifier.smileRandomForest(numTrees)
      .train({
        features: training,
        classProperty: 'class',
        inputProperties: composite.bandNames()});

  // classify a table instead of an image
  return test
    .classify(classifier)
    .errorMatrix('class', 'classification')
    .accuracy()});

var chart = ui.Chart.array.values({
  array: ee.Array(accuracies),
  axis: 0,
  xLabels: numTreesList
  }).setOptions({
      vAxis: {title: 'Validation Accuracy', titleTextStyle: {fontSize: 40}},
      hAxis: {title: 'Number of Trees', gridlines: {count: 15}, titleTextStyle: {
          fontSize: 40}},
      pointSize: 10,
```

```
      fontSize: 30});
print(chart);

// overlay points on image to train
var training = composite.select(bands).sampleRegions({
  collection: trainingStrat,
  properties: ['class'],
  scale: 30,
  tileScale: 16});

// train the classifier
var classifier = ee.Classifier.smileRandomForest(90).train({
  features: training,
  classProperty: 'class',
  inputProperties: bands});

// run the classification and display result
var classified = composite.classify(classifier);
Map.addLayer(classified, {min:0, max:7, palette:['pink','DarkKhaki','SaddleBrown','
    BlueViolet','LightSkyBlue','blue','orange','red']});
Map.addLayer(classified, {min:0, max:5, palette:['pink','DarkKhaki','LightGreen','
    red','orange','blue']});

// use classification map to assess accuracy
var test = classified.sampleRegions({
  collection: validationStrat,
  properties: ['class'],
  scale: 30,
  tileScale: 16});

var testConfusionMatrix = test.errorMatrix('class', 'classification');
print('confusion_matrix', testConfusionMatrix);
print('test_accuracy', testConfusionMatrix.accuracy());
```

3.2.3 Original volcanic extents

The remote sensing results collected for the Warrumbungle and McBride volcanoes were not able to fully isolate the present-day footprints of volcanic rock from surrounding bedrock and alluvium and struggled particularly in areas of heavy vegetation. Due to these difficulties and due to the time required to output more accurate results, the process was not repeated at other volcanic provinces. Enhanced delineation of volcanic rocks using this process, and with a focus on basalts, is instead suggested as further work to this thesis. An alternative process was therefore required to estimate the eroded extents of each volcano. The original volcanic extent must cover all preserved outcrops but there are a number of ways in which outcrops may be joined. For this, I have used the Convex Hull and Concave Hull tools in QGIS to draw an envelope around existing volcanic rock in order to connect isolated outcrops. For each province the following footprints have been defined and an example is shown in Figure 3.8:

- Footprint 1: A tight geometry not connecting all exposures, using the concave hull tool in QGIS (number of neighbours = 3, and SNN clusters = 10) which gives a lower estimate for the volcanic footprint.
- Footprint 2: A looser geometry connecting all exposures, using the concave hull tool in QGIS (number of neighbours = 3) giving a middle estimate for the volcanic footprint.
- Footprint 3: The minimum geometry bounding all exposures, using the convex hull tool in QGIS which gives a higher estimate for the volcanic footprint.

The convex hull or convex envelope of a shape is the smallest convex geometry that fully contains it. The concave hull of a geometry represents a possibly concave geometry that encloses the input geometry and for this work it was computed using the Concave Hull plugin by Detlev Neumann. Prior to computation of the concave hull, data can optionally be divided into clusters using the Shared Nearest Neighbour (SNN) algorithm. SNN assigns points to a cluster which share a large number of their nearest neighbours. Concave

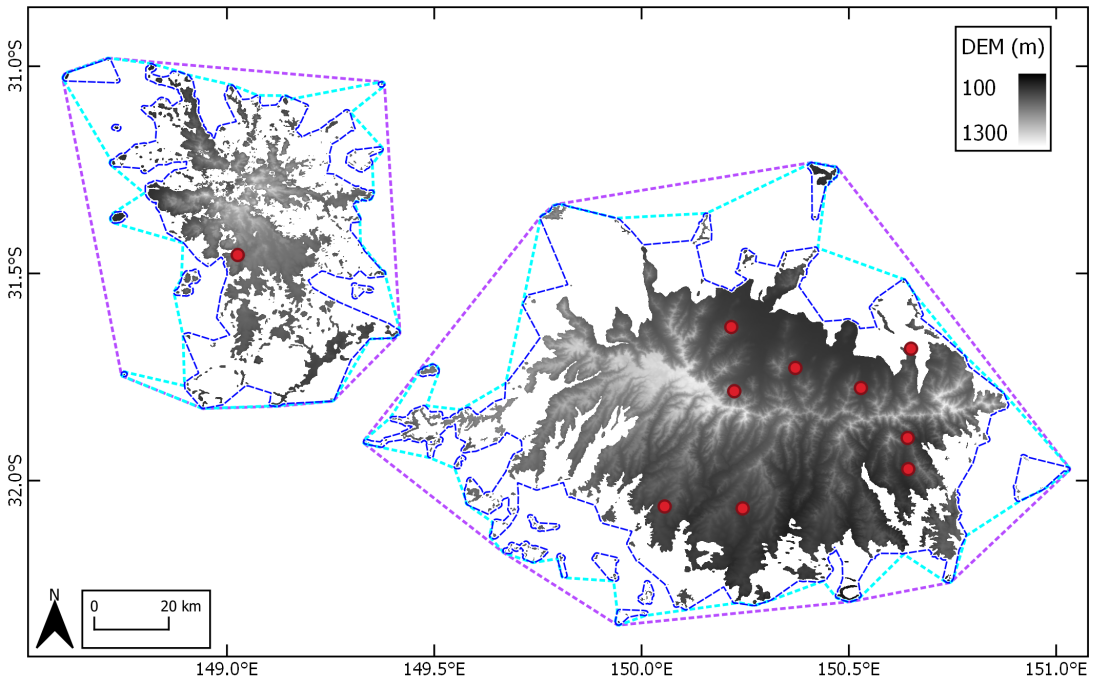

Figure 3.8: *Present-day digital elevation model (DEM) of the Warrumbungle and Liverpool Range provinces with calculated footprints 1, 2, and 3 shown in blue, cyan, and purple, respectively. Red dots are borehole locations.*

Hull in QGIS allows you to specify the number of neighbours and the neighbourhood size when searching for SNN clusters. Each of these values were tested on a trial and error basis to find a reasonable level of connectivity between volcanic deposits whilst retaining the general shape of the volcano.

3.2.4 Local minima baseline

Initial baselines were calculated by gridding local minima extracted from the digital elevation model (DEM) of each volcano. Minima points were created using the SAGA local minima and maxima tool in QGIS, and then gridded using the SAGA Multi B-Spline interpolation tool. Results for the Warrumbungle volcano are shown in Figure 3.9 in cyan and give a minimum i.e., shallow, estimate of the volcano baseline. The location of the cross section is shown in Figure 3.10. For most provinces, particularly the shield-like central volcanoes, local minima will not be representative of the volcano base but for provinces with very small, scattered exposures such as the Piebald province, this method provides a reasonable estimation for the baseline of preserved volcanic rocks.

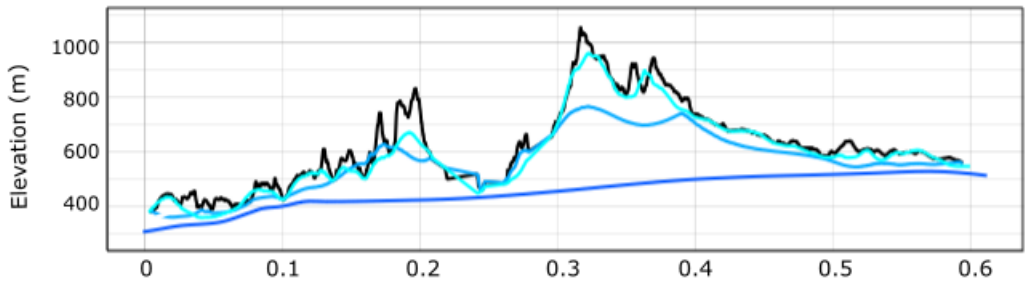

Figure 3.9: *Cross section across the Warrumbungle volcano (black) showing three baseline examples: (1) the local minima baseline in cyan, Figure 3.10a; (2) the masked interpolation across present-day extents in light blue, Figure 3.10b; and (3) the masked interpolation across footprint 1 in dark blue, Figure 3.10c.*

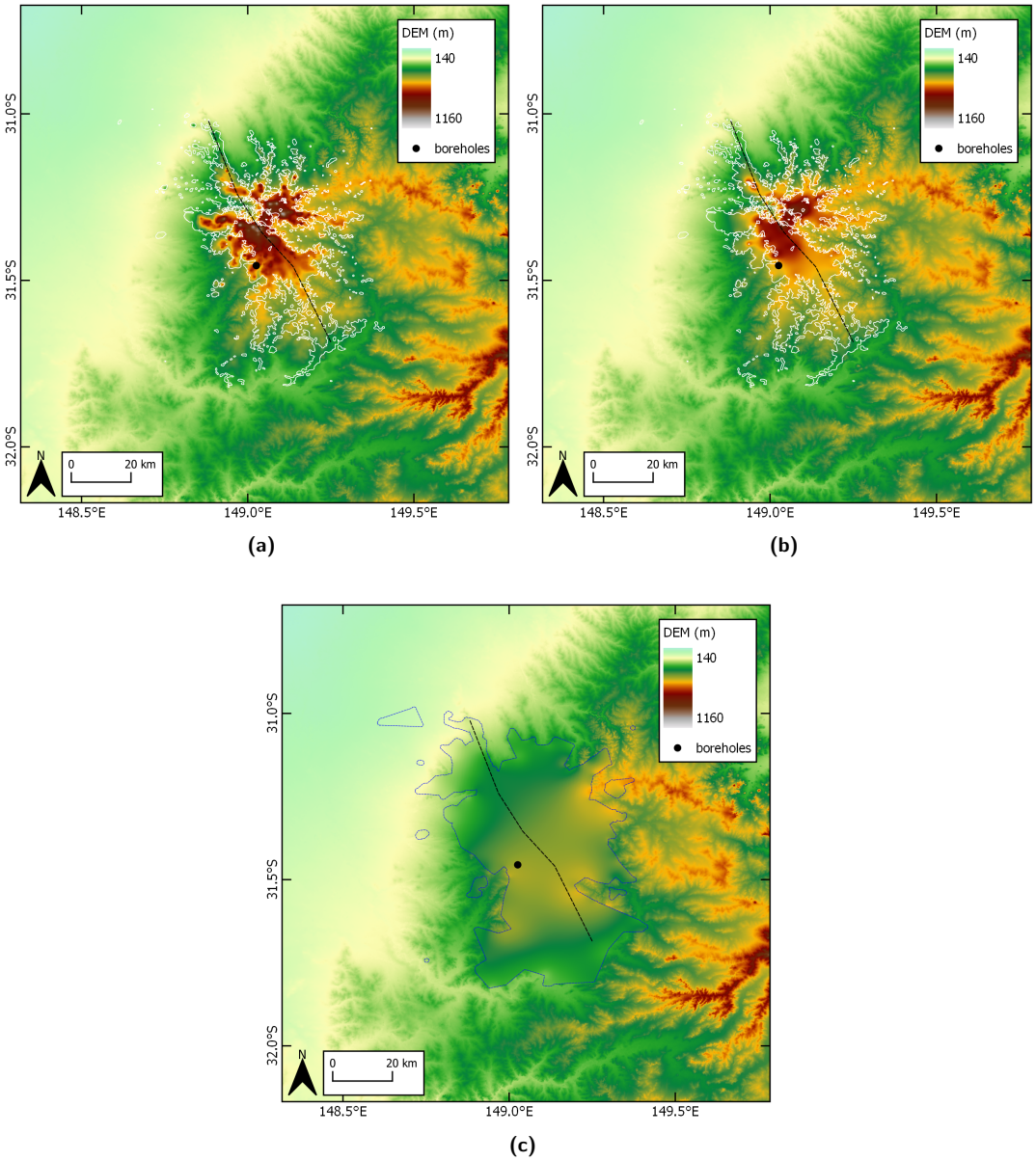

Figure 3.10: *(a) Local minima baseline. (b) Masked interpolation across present-day volcanic extents. (c) Masked interpolation across footprint 1. Black dashed line = cross section, Figure 3.9. Black dot = borehole location.*

3.2.5 Masked interpolation baseline

As shown by Figure 3.9, the local minima method closely follows the upper volcanic surface and excludes thicker lava sequences, such as that either side of the Warrumbungle vent. An improved basal surface which includes these areas is therefore required. For this, baselines were created by masking all volcanic outcrops from the DEM and gridding across the resulting hole to create a gently undulating surface, where available, borehole depths to the base of known Cenozoic lavas were included to guide the interpolation. With this process basal depths are defined by the current outline of volcanic rocks which assumes that all present-day lava-rock contacts represent the base of the volcano. This is not always the case, particularly where lava is in contact with alluvium and so the same process was repeated using the three different footprints defined previously. An example of the masked interpolation across present-day volcanic extents and across the extents of footprint 1 are shown in Figure 3.10 in light blue and dark blue, respectively. The volume of preserved volcanic rock at the Warrumbungle volcano calculated using the local minima, masked present-day extent, and masked footprint 1 baselines are 35 km^3, 65 km^3, and 171 km^3, respectively. For most volcanoes, the masked interpolation across footprint 1 is the most effective at encompassing all preserved volcanic material.

The full process is as follows: (1) using polygons as a mask, remove the volcano footprint from the original digital elevation model (DEM) raster to create a hole with which to interpolate the baseline over (2) convert the output raster to points (3) grid the resulting points using the Triangulate, Inverse Distance Weighting (IDW), and Multi B-Spline interpolations in QGIS. This is similar to the gridding method undertaken by Crossingham et al. (2018) who converted bathymetric swath map data from the Tasmantid seamounts to an ASCII file and then converted this to a triangular irregular network (TIN) file in ArcMap where any areas not representing the seamount were removed using polygons. Examples of the three gridding methods used here are shown in Figure 3.11. The Triangulate gridding algorithm resulted in odd artifacts and abrupt changes between high and low topography, which is smoothed out with other gridding methods. There is only a small difference in the final volumes from 164 km^3 with Triangulation, 178 km^3 with IDW and 171 km^3 with Multi B-Spline. Multi B-Spline gridding appeared the smoothest and for this reason was chosen for all further baseline interpolations.

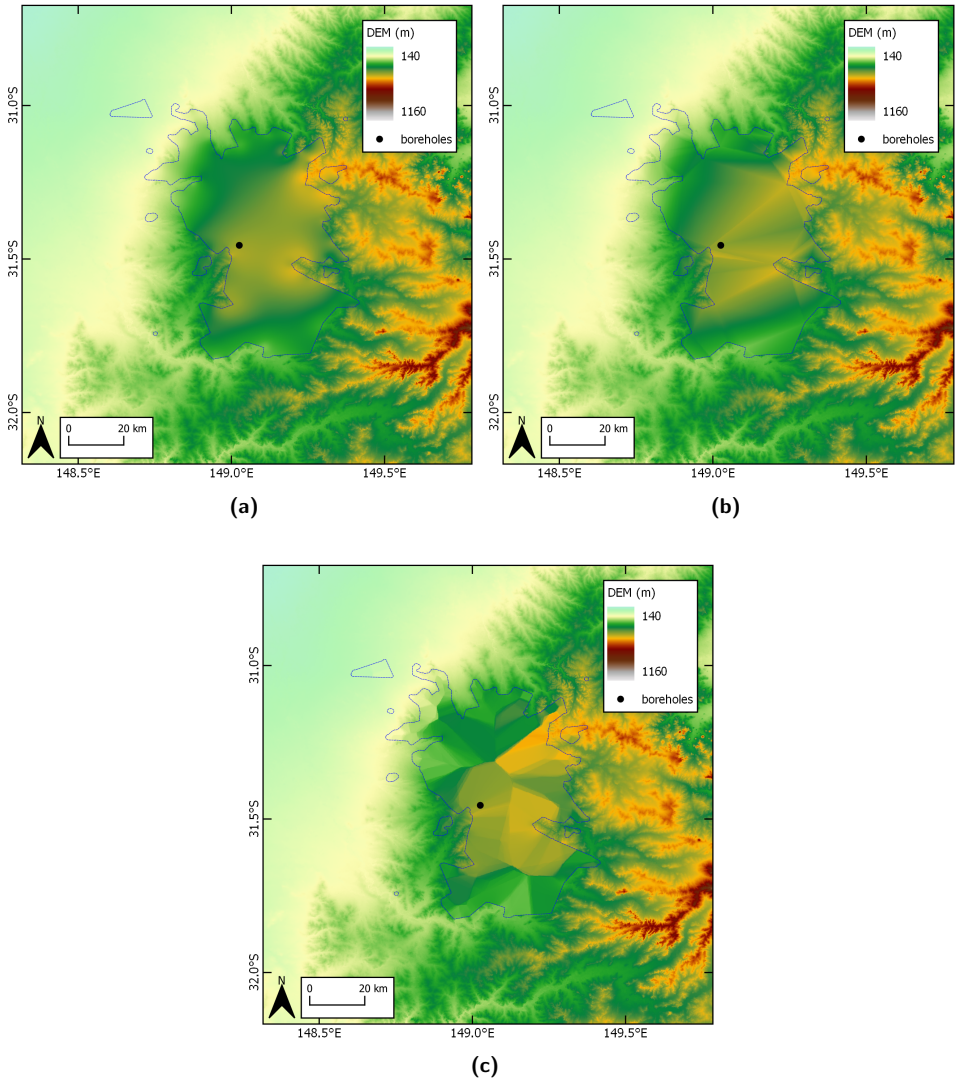

Figure 3.11: *(a) Multi B-Spline interpolation (b) Triangulate interpolation (c) Inverse Distance Weighting (IDW) interpolation. Black dot = borehole location.*

The addition of borehole data generally had the effect of decreasing the depth to the baseline and reducing the overall volume calculation, although not all volcanoes had appropriate borehole data. Boreholes intersecting volcanic provinces in Queensland were obtained from the Queensland Spatial Catalogue, Queensland Government which contained a legacy dataset with stratigraphic well tops, additional wells were obtained from the Geological Survey of Queensland Open Data Portal where one can search for wells and well completion reports (Queensland Government, 2022). Borehole data from New South Wales was acquired from MinView where drillholes and completion reports could be downloaded directly (New South Wales Government, 2022).

Victoria boreholes were obtained from Geovic, Earth Resources, where wells could be downloaded with attached stratigraphic and lithology logs (Victoria State Government, 2022). Borehole data from Tasmania was acquired from the TIGER database which again included the location of all wells and attached drilling and completion reports (Mineral Resources Tasmania and Tasmanian Government, 2022). Very few, freely available boreholes exist for the Cenozoic volcanoes in far north Queensland, however, 3D baselines have recently been created by Ransley et al. (2020) for the McBride and Nulla provinces. The surfaces have been created using the results of from a drilling program conducted by the Queensland Government Department of Environment and Science in 2017–2018 (Hansen et al., 2020).

3.2.6 Ridgeline resurfacing

Initial volume estimates were calculated using the present-day digital elevation model (DEM) as the upper surface of each volcano, which therefore do not take into account erosion. However, throughout the Cenozoic, much of Australia lay in a warm and humid climate and the volcanic cones of many of the East Australian central volcanoes were eroded away so that plugs, gabbros and other intrusives are now exposed at the surface (Johnson, 1989). Therefore, to accurately calculate volumes of the volcanoes at the time of emplacement, pre-erosive volumes must be considered. As a minimum estimate of erosion, I have infilled volumes of rock across the present-day valleys and edifices by interpolating the DEM, to create a smoother, blanket of rock across the breadth of the volcano. Surfaces which most closely represent the original top of each volcano are likely to be represented by present-day ridgelines. We can isolate these and re-grid the points to create a new surface which takes into account some level of erosion, primarily extrapolating across large valleys. In many cases, the present-day DEM is highly irregular, consisting of numerous drainage patterns and ridgelines which do not represent original surfaces. For this reason, a low pass filter has first been applied to present-day DEMs to isolate large-scale ridgelines.

The full process is: (1) resample the digital elevation model (DEM) using the SAGA resampling filter with a scale of 10 which means the original cell size is scaled by a factor of 10 and aggregated as weighted means of the cell area (2) apply the GRASS r.geomorphon tool to the resampled grid to identify broad geomorphological features (3) use the raster calculator to select the ridgelines feature i.e., result = 3 (4) convert the result from raster pixels to points (5) extract vertices from the appropriate footprint (5) merge the ridgeline points with the vertices to create a set of points (6) sample raster values from the original DEM to include height and remove any outliers that are not representing the original upper surface (7) grid the final points again using the Triangulate, Inverse Distance Weighting (IDW), and Multi B-Spline methods. For this process, the Triangulate gridding method was deemed best as it gave the smoothest result with a high tension i.e., less irregular peaks and troughs. Once again, the final volume difference between the three different methods was very minimal and so the selection of the Triangulate method is, more than anything, aesthetical. Estimated volumes for the three methods, using the interpolated footprint 1 baseline, were 334 km^3, 349 km^3, and 344 km^3, respectively.

For each of the three footprints defined earlier, volumes have been calculated using the resurfaced ridgelines as the volcano top and the masked interpolation as the basal surface. An example of the reconstructed ridgeline surface for the Warrumbungle volcano is shown in Figure 3.12 and Figure 3.13b. In some cases, generally highly eroded volcanoes now reduced to small rounded outctops, ridgelines are not well defined and the extracted ridgeline volume may be lower than preserved rock volume. For this reason, volumes have also been calculated for each of the volcanic footprints using the present-day digital elevation model (DEM) as the upper volcanic surface and the masked interpolation as the basal surface (Figures 3.12 and 3.13a).

3.2.7 Pyramidal reconstruction

A maximum case for erosion would be that each volcano, specifically the central volcanoes, were once pyramidal in shape and high enough to encompass all of the remaining outcrops. In order to model this, I have created a simple pyramid from the convex hull outline with a varying maximum height. I have then output the height that the pyramid needs to be to encompass 80, 90, and 100% of the present-day rock outcrop giving a simple low, mid and high case. The centre of each volcano was selected using the centroids tool in QGIS. The pyramids have been created again using the Triangulate gridding tool in QGIS and extrapolating from the convex hull base heights to the specified centroid height. Heights of the centroid chosen are given in Appendix I. This top surface may also be appropriate for the highly eroded shield volcanoes but for the lava fields the less extensive extrapolation across valleys and edifices is expected to be more accurate as these are known to erupt as flat, low-lying plains. An example of the 100% pyramid for the Warrumbungle volcano is shown in Figure 3.12 and Figure 3.13c.

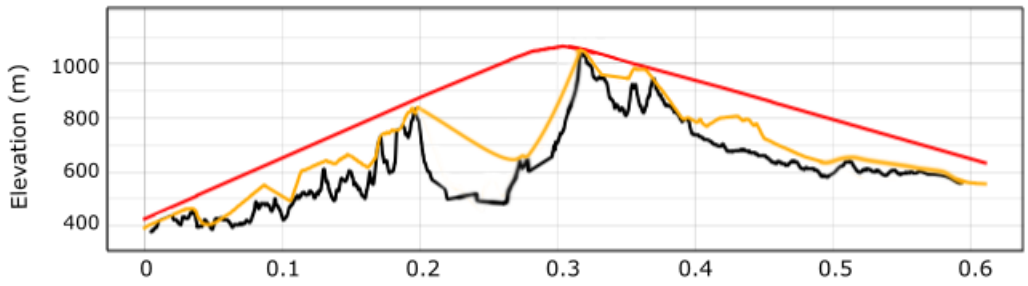

Figure 3.12: *Cross section showing three upper surface examples: (1) the present-day digital elevation model (DEM) in black, Figure 3.13a; (2) the resurfaced ridgelines in orange, Figure 3.13b; and (3) the 100% pyramidal surface in red, Figure 3.13c.*

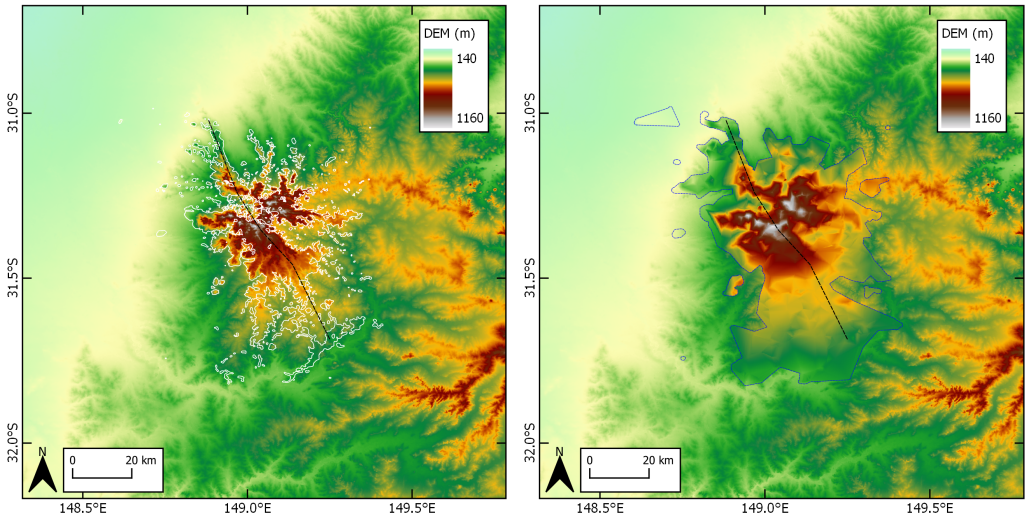

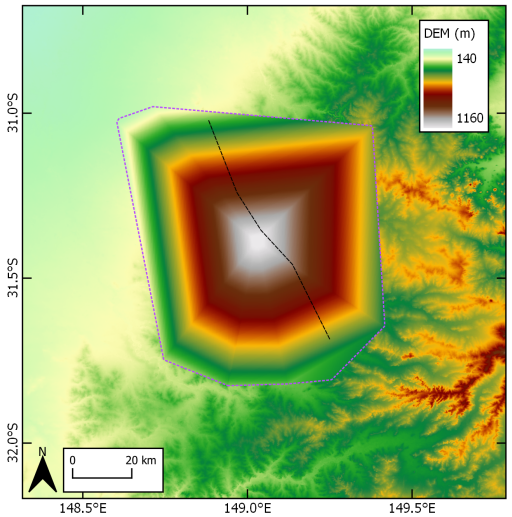

Figure 3.13: *(a) Present-day digital elevation model (DEM) of the Warrumbungle volcano. (b) Reconstructed upper surface extrapolated from ridgelines using the triangulate gridding method. (c) Reconstructed pyramidal upper surface encompassing 100% of preserved volcanic rock.*

3.2.8 Simple conical estimate

To compare the results of Wellman (1971) and Jones and Verdel (2015) with results from this thesis I have also calculated simple conical volumes using a similar method i.e., Equation 3.1, where the radius was taken from the minimum bounding geometry assuming it to be a roughly circular shape where the perimeter has been calculated from Equation 3.2, using the perimeter measurement from the convex hull shapefile. Heights (h) have been estimated from maximum thickness measurements from borehole and outcrop data. Borehole thicknesses are taken from this study and from Jones and Verdel (2015) and outcrop thicknesses are taken from Johnson (1989) and Sutherland et al. (2005). This method still represents a minimum, pre-erosive volume as it is unlikely the thickest lava sequence has been drilled and the accuracy of this method is highly dependent on the accuracy of the thickness used. More than anything, it is here used as a quick comparison to other authors. All volume results are given in Appendix I.

$$Volume_{cone} = \frac{1}{3} \times \pi \times r^2 \times h \tag{3.1}$$

$$Perimeter = 2 \times \pi \times r \tag{3.2}$$

Chapter 4

Volcanic Sources

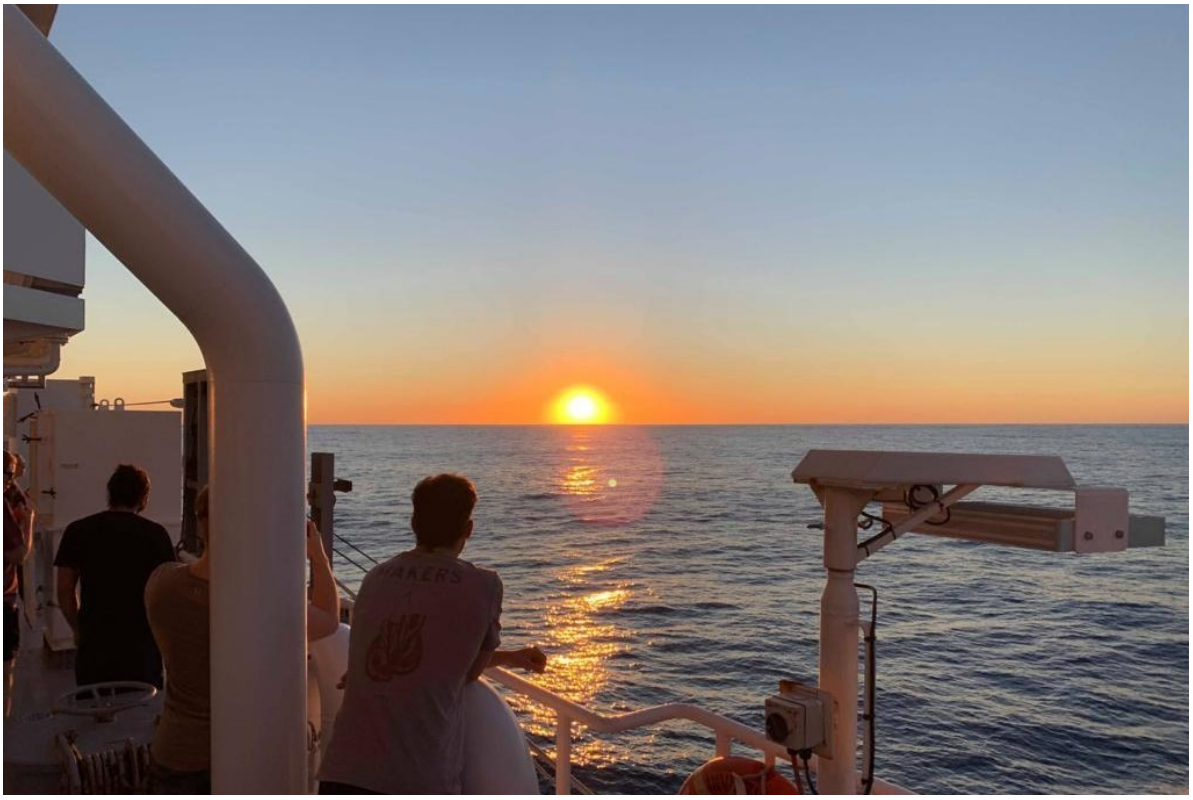

Figure 4.1: *Sailing the Coral Sea aboard the RV Investigator.*

4.1 Introduction

The central volcanoes of East Australia have classically been regarded as plume related magmatism (e.g. Crossingham et al., 2018; Johnson, 1989; Ghorbani and Middlemost, 2000; Jones et al., 2020), whilst the lava fields have primarily been explained by rift-flank volcanism associated with opening of the Tasman and Coral Seas (e.g. McDonough et al., 1985; Zhang et al., 2001; Sutherland, 2003; Ewart et al., 1988). The complexities however, of the 50+ volcanic provinces within the East Australian chain do not support each of these hypotheses in their entirety and a number of potential sources including a deep plume, shallow MORB, and a metasomatised SCLM have all been proposed for both the central volcanoes and lava fields. A similar complexity is observed in the leucitite suite with an age-progression that would imply an asthenospheric origin but a unique geochemistry that is typically only observed in continental rocks. The influence of the lithosphere versus the asthenosphere, in creating the suite of volcanoes observed on the Australian mainland is one of the primary focuses of this study and to assess this I have compared continental rocks to the analogous volcanoes of the Tasmantid and Lord Howe seamount chains which should be unaffected by influences of the SCLM.

This study uses major element, trace element, and radiogenic isotope data of basalts, *sensu lato*, to assess the contribution of heterogeneous mantle sources across the three volcanic chains. The dataset consists of 170 rocks analysed at the University of Edinburgh alongside the geochemical results of 1032 basalts, *sensu lato*, collected from the GEOROC (1999) database. At least one sample has been gathered from almost every province along the East Australian and Tasmantid chains, samples from the Lord Howe chain only include Lord Howe Island itself. To accurately assess mantle sources the degree of partial melting, fractional crystallisation, crustal assimilation and alteration of each rock first need to be resolved and are considered in the first part of this Chapter. From the samples analysed, 26 had an LOI greater than 2 wt% and these specimens have been excluded from any further mobile element interpretation e.g., K, Rb, Sr, Cs, Ba. Figure 4.2 shows that both mobile (Ba) and immobile (Nb) elements show no correlation with alteration when LOI is less than 2 wt%.

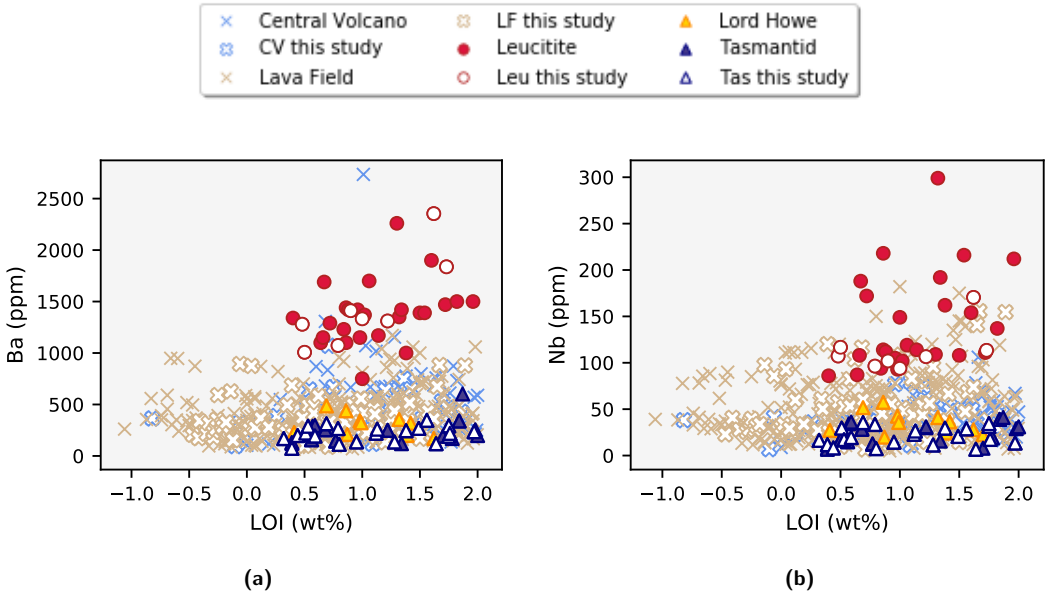

Figure 4.2: *(a) Ba and (b) Nb versus LOI. Both plots show that neither typically mobile (Ba) or immobile (Nb) elements are affected by alteration of the samples when LOI is < 2wt% i.e., no clear trends are observed in either plot.*

Temporal relationships can tell us a lot about the mechanism responsible in producing volcanism i.e. short-lived age-progression is typical of plume magmatism, whilst long-lived non-age-progression is more typical of passive upper mantle processes. Because of this, a thorough age review of each volcanic province has also been undertaken to aid my interpretations. Age data from across the continental chain has been complied using a database provided by Cohen (2018) updated with the most recent published age data. Ages for the Tasmantid and Lord Howe seamount chains come primarily from recent studies by Kalnins et al. (2015), Mortimer et al. (2010), and Seton et al. (2019b). The middle section of this Chapter therefore uses the most up-to-date chronology of Cenozoic volcanism in East Australia to assess how mantle source characteristics have varied over time, with a particular focus on immobile trace element concentrations. The final part of the Chapter looks at the isotopic results of each volcano and what contribution DM, EMI, EMII, HIMU, and PREMA type mantle has played in the generation of each province.

4.2 Results and Discussion

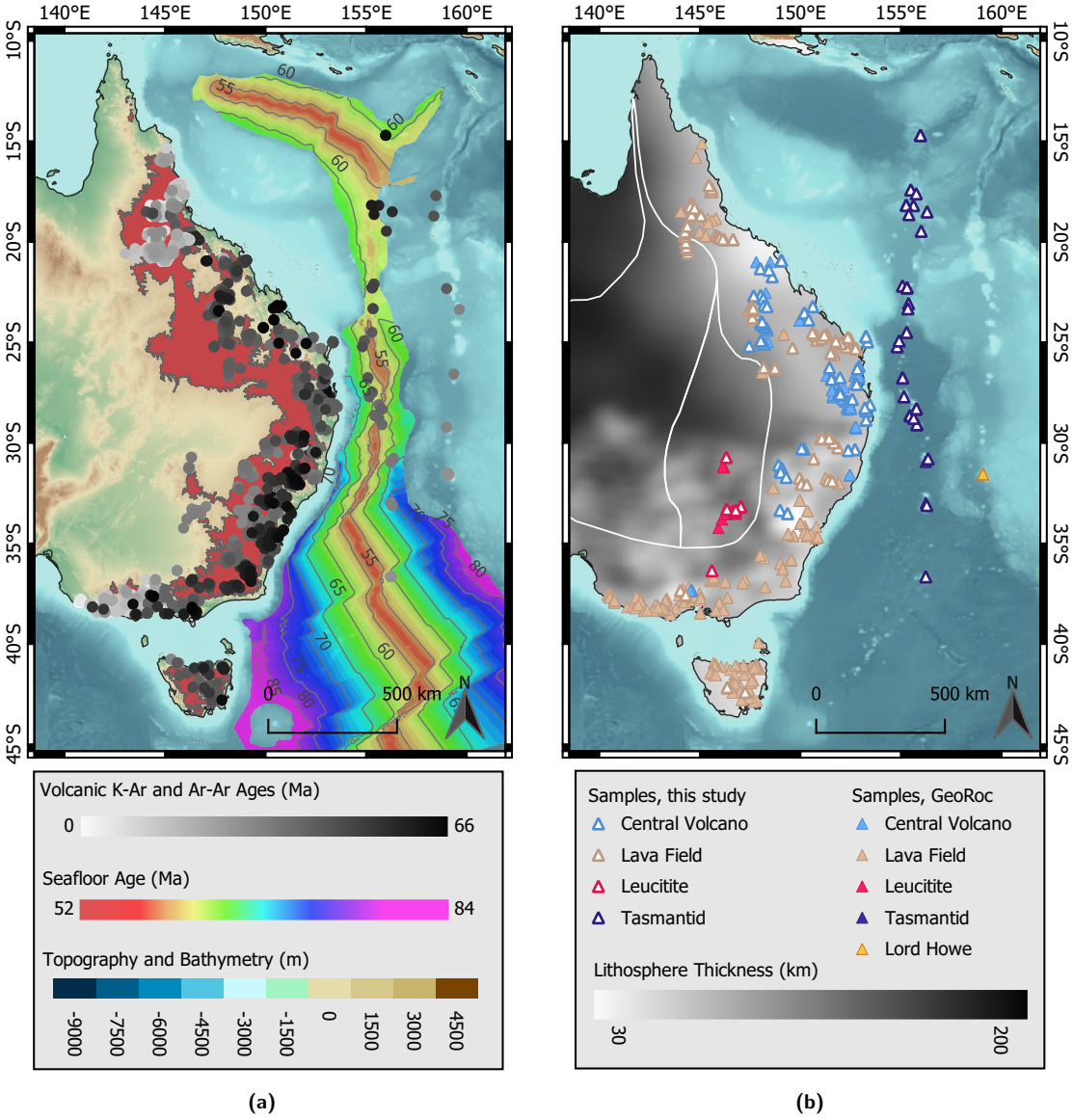

Figure 4.3: *(a) Ages of volcanic rocks collected from literature sources. The Tasmantid Seamounts, Lord Howe Seamounts, and central volcanoes show a clear age progression north to south whilst the most recent volcanism is located at both north and south extremities. The Mesozoic to Early Cenozoic Great Dividing Range (defined by the 300 m contour) is shown in red. Tasman and Coral seafloor ages are from Muller et al. (2000). (b) Locations of mafic rock samples analysed in this study are marked as open triangles. Sample locations for geochemical data collected from GEOROC (1999) are marked as filled triangles. Lithosphere thickness estimates (depth to the lithosphere-asthenosphere boundary, LAB) are derived from body wave tomography by Rawlinson et al. (2017). White lines mark distinct changes in lithospheric velocity (Vh) as denoted by horizontal velocity gradients through the surface wave model of Fishwick et al. (2008). These probably relate to changes in age and composition of the underlying lithosphere. Of note, the northernmost leucitites lie on the thickest continental lithosphere whilst the Tasmantid seamounts lie on oceanic lithosphere. All central volcanoes and lava fields lie between these two end-members. The topographic and bathymetric grid used on both plots is from GEBCO (2020).*

Reported K-Ar and Ar-Ar ages of all four volcanic suites are shown in Figure 4.3a. The most recent Ar–Ar data for the Lord Howe, Tasmantid, central volcano, and leucitite suites all show age progression younging north to south from 28–7 Ma, 56–7 Ma, 34–6 Ma, and 18–9 Ma, respectively (Cohen et al., 2008; Mortimer et al., 2010; Cohen et al., 2013; Kalnins et al., 2015; Seton et al., 2019b). The lava fields, however, emplaced between 84 and 0 Ma, do not show the same variation in age with latitude (Vasconcelos et al., 2008). The most recent lava field eruptions were 7000 years ago in northern Queensland, and 4300 years ago in South

Australia (Cohen et al., 2017; Johnson, 2009), at opposite ends of the continent. As seen in the figure, almost all the continental volcanoes were emplaced in close proximity to the Great Dividing Range, indicating a possible link between the two. The timing of formation of the Great Divide is still under debate, but estimates vary from Mesozoic to Early Cenozoic (Johnson, 1989). What is clear is that the mountain range was in existence throughout the Cenozoic, as eroded Paleogene basalts are found as clasts in the Great Divide valleys formed prior to volcanism (Henderson and Johnson, 2016). Most fission track results place uplift in the Late Cretaceous (Henderson and Johnson, 2016).

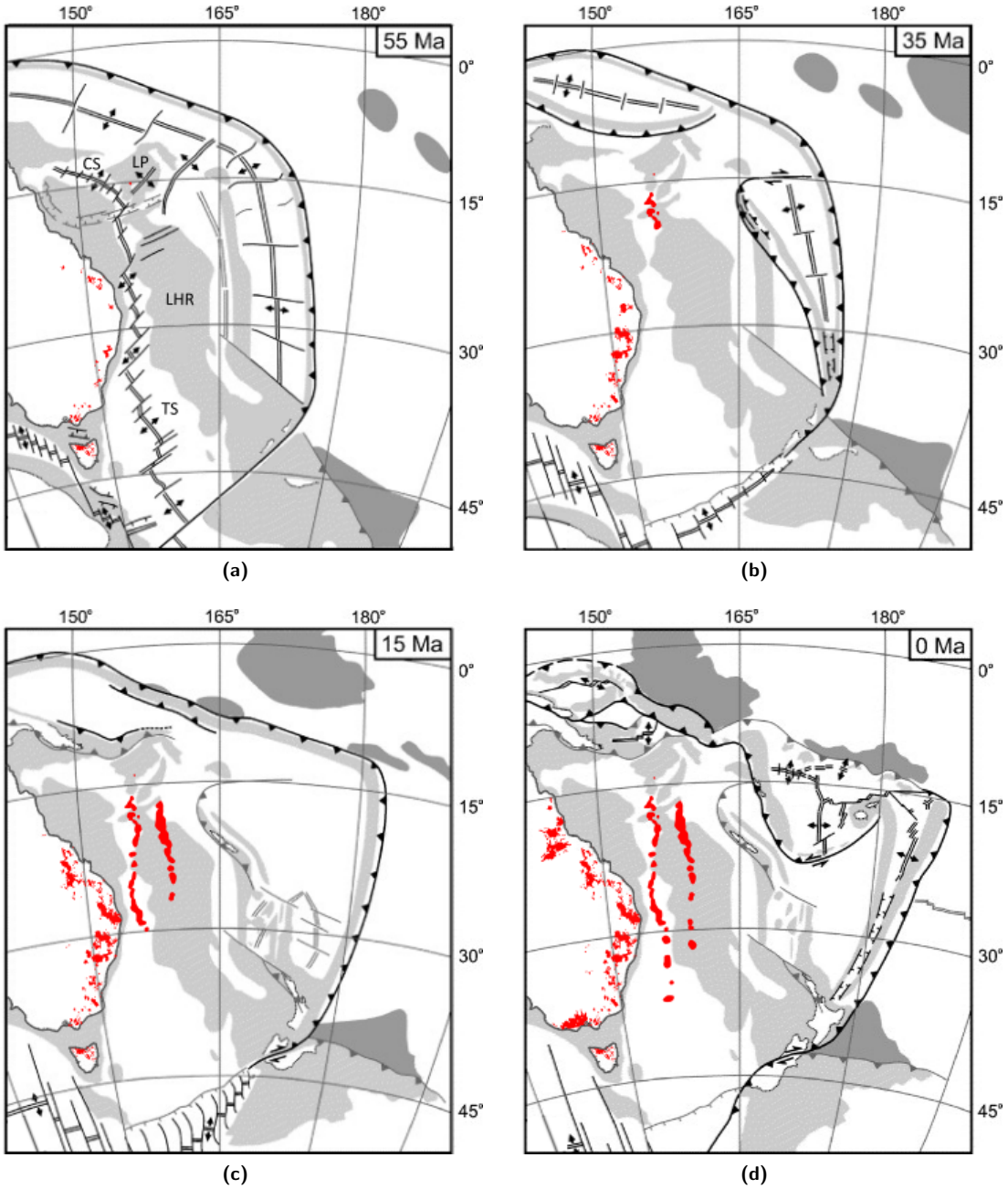

Figure 4.4: *Tectonic reconstructions of the east Australian plate from Schellart et al. (2006), modified to include Cenozoic intraplate volcanoes in red. (a) 55 Ma; (b) 35 Ma; (c) 15 Ma; and (d) 0 Ma. TS = Tasman Sea; CS = Coral Sea; LS = Louisiade Plateau; LHR = Lord Howe Rise. A more detailed explanation of both the diagrams and of Cenozoic tectonics may be found in Section 2.3 of this thesis.*

Around a similar time, as Australia rifted away from Antarctica, the Tasman Sea opened at 84 Ma and the Coral Sea farther north at 64 Ma (Gaina et al., 1998; Muller et al., 2000; White et al., 2013) (Figure 4.3a). From 56–7 Ma the Tasmantid seamount chain erupted almost directly along the Tasman spreading axis (Figure 4.4). At the top of this ridge sits the Louisiade Plateau; a poorly studied oceanic plateau which has been

suggested to represent a large igneous province formed by the arrival of the Tasmantid plume (Kalnins et al., 2015). To the east of the spreading ridge, the Lord Howe Rise represents a drowned continental fragment which broke off from Australia during rifting and through which the Lord Howe seamount chain was later erupted (Muller et al., 2000; White et al., 2013). Spreading in both the Tasman and Coral Seas ceased by 52 Ma, prior to the majority of volcanism, which continued throughout the rest of the Cenozoic in a relatively quiescent, intraplate setting (Gaina et al., 1999; Vasconcelos et al., 2008) (Section 2.3). The palaeogeographic reconstructions in Figure 4.4a show how minor lava field volcanism and the very first emplacement of the Tasmantids was taking place along the Australian coastline, and the Tasman Sea, respectively, prior to and during rifting of the Tasman and Coral Seas. From 52 Ma, the northern and eastern edge of the Australian plate saw numerous plate boundary configurations, discussed further in Section 2.3, but all continental and oceanic volcanoes emplaced after this time were erupted within-plate, onto variably thinned lithosphere.

Figures 4.3b and 4.4 show the Tasmantid seamounts were emplaced onto relatively young, thin, oceanic lithosphere, ~70–52 Ma and roughly 70–20 km thick (this study). Figure 4.3b also shows the locations of samples alongside continental lithosphere thickness estimates by Rawlinson et al. (2017). Moving on land, both the age and the thickness of the lithosphere increases from east to west towards the interior of the continent. This is roughly 200 km thick beneath Proterozoic cratonic areas and 100–50 km beneath Phanerozoic terranes where we find most Cenozoic volcanism. The composition of the lithosphere also varies in this direction, largely due to arc accretion events throughout the Phanerozoic (Section 2.1). The northernmost leucitites from the Byrock and El Capitan areas are situated on lithosphere thicker, ~130 km, than anywhere else along the East Australian chain. Lithosphere thickness has considerable effect on the chemistry of erupted lavas, whether asthenospheric or lithospheric in origin, and so it is important to quantify these differences (e.g. Davies et al., 2015). The location of all samples analysed in this study for major and trace element concentrations are shown in Figure 4.3b as white fill triangles. In addition to these, geochemical analyses of 1032 mafic samples have been assembled from the GEOROC database, shown in Figure 4.3b as coloured fill triangles (GEOROC, 1999). All samples are basaltic, *sensu lato*, ranging in composition from melilitites to tholeiitic basalt.

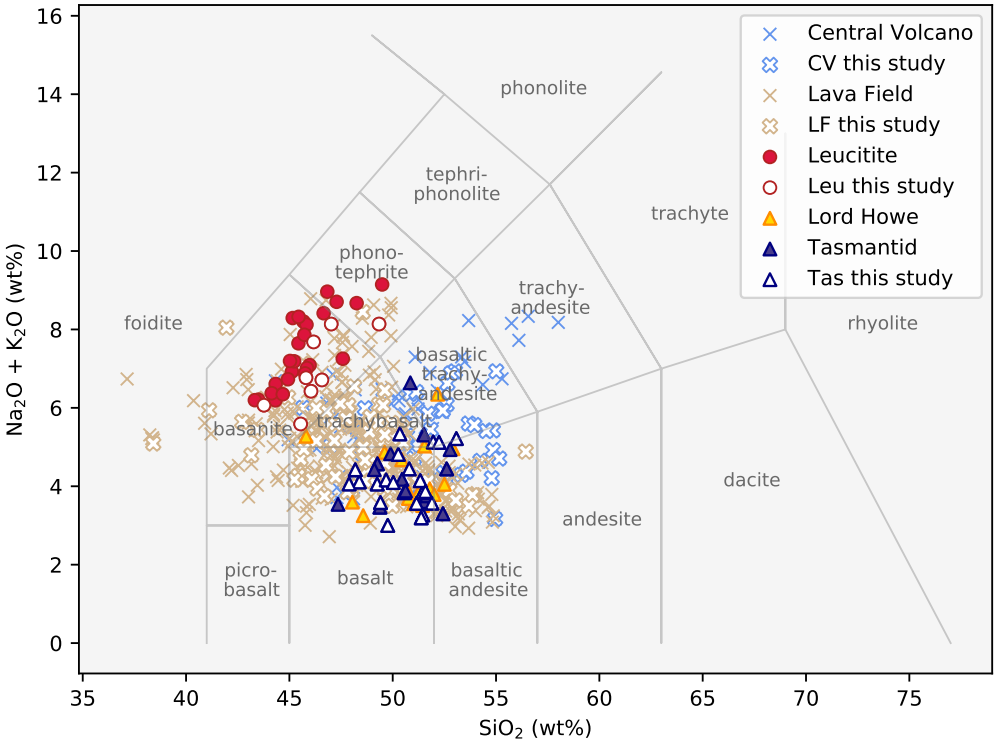

Figure 4.5: *Total alkali-silica (TAS) diagram of samples analysed in this study (white fill) including those taken from the GEOROC database (coloured fill) (GEOROC, 1999). Samples analysed in this study have been normalised to 100 wt% with Fe as FeO. Only samples with LOI < 2 wt% are plotted. Of note, seamount rocks are predominantly saturated with respect to silica. Leucitites are all undersaturated, occupying the basanite and phonotephrite fields. Lava field basalts span the greatest range in total alkali-silica, and include the most undersaturated samples from Tasmania. Central volcanoes also span a large range in composition and include the most evolved compositions.*

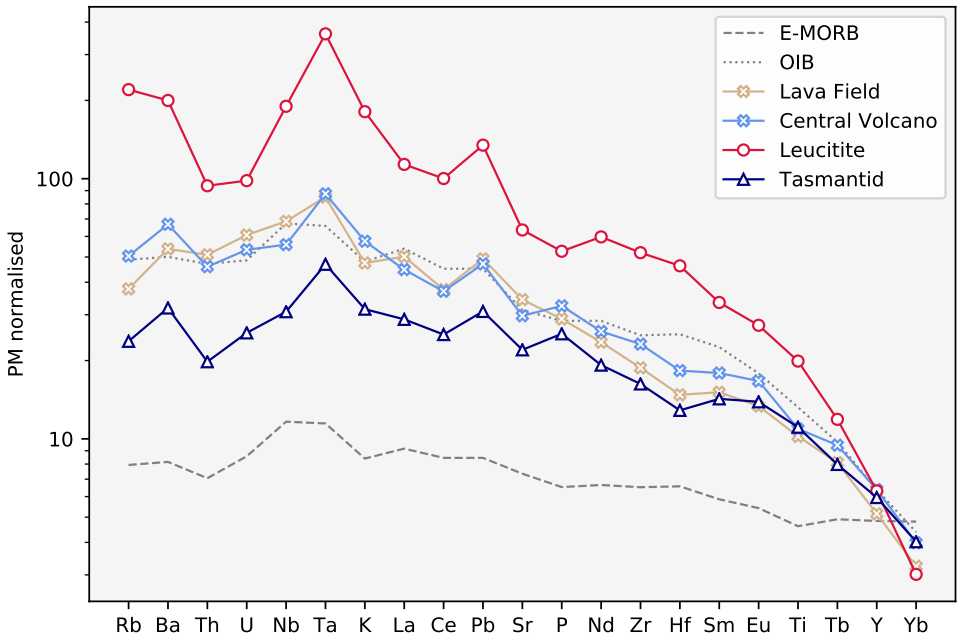

Figure 4.6: *Primitive mantle (PM)-normalised multi-element plot of incompatible elements. Element concentrations have been averaged across each suite and normalised to PM values from Sun and McDonough (1989). Average values for OIB and E-MORB also from Sun and McDonough (1989). Of note, the leucitites show the greatest enrichment in incompatible elements, followed by the lava fields and central volcanoes, and then the Tasmantids. The leucitite, central volcano and Tasmantid patterns all have similar shapes and crossovers, whilst the lava field pattern differs slightly, possibly owing to the greater range of rock types in this suite.*

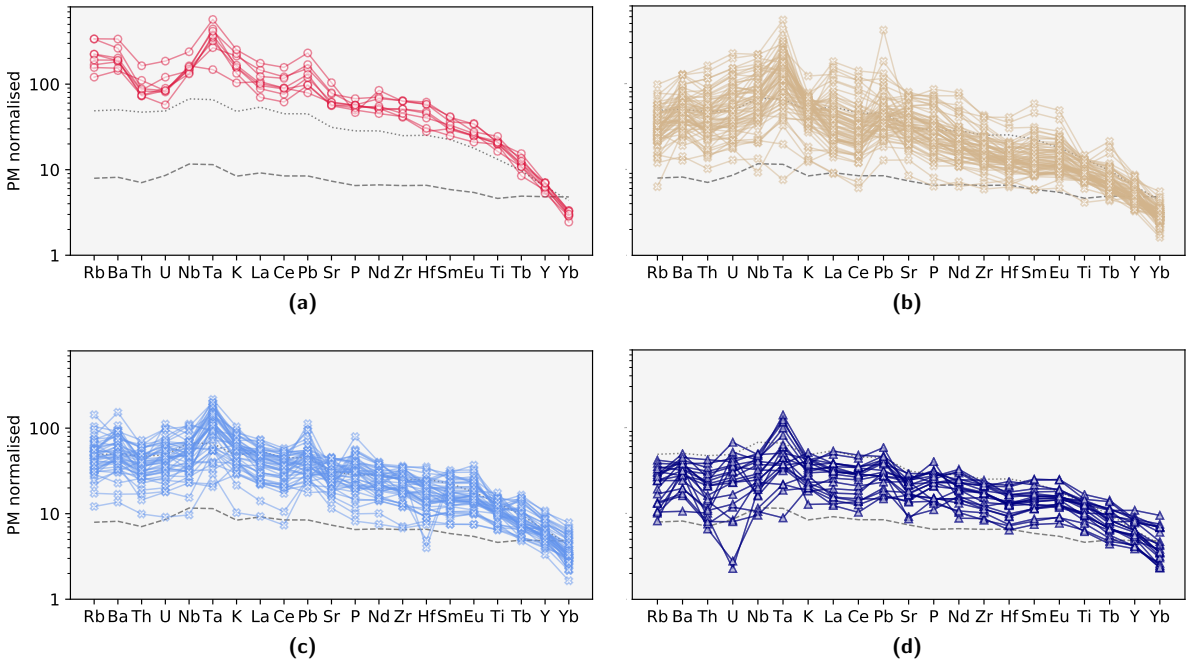

Figure 4.7: *PM-normalised multi-element plots of incompatible elements showing every sample analysed in this study, divided by suite (LOI < 2 wt%). (a) Leucitite samples; (b) lava field samples; (c) central volcano samples; and (d) Tasmantid seamount samples. Element concentrations have again been normalised to PM values from Sun and McDonough (1989). Average values for OIB and E-MORB also from Sun and McDonough (1989).*

Silica-saturation indices (SSI) have been calculated for each sample using the concentration of silica versus that of other major elements, as per the CIPW norm method. SSI values give the relative silica saturation of each rock where values greater than zero are saturated or oversaturated and values below zero are undersaturated with respect to silica. Several conclusions can be drawn from Figures 4.6, 4.7, and 4.8.

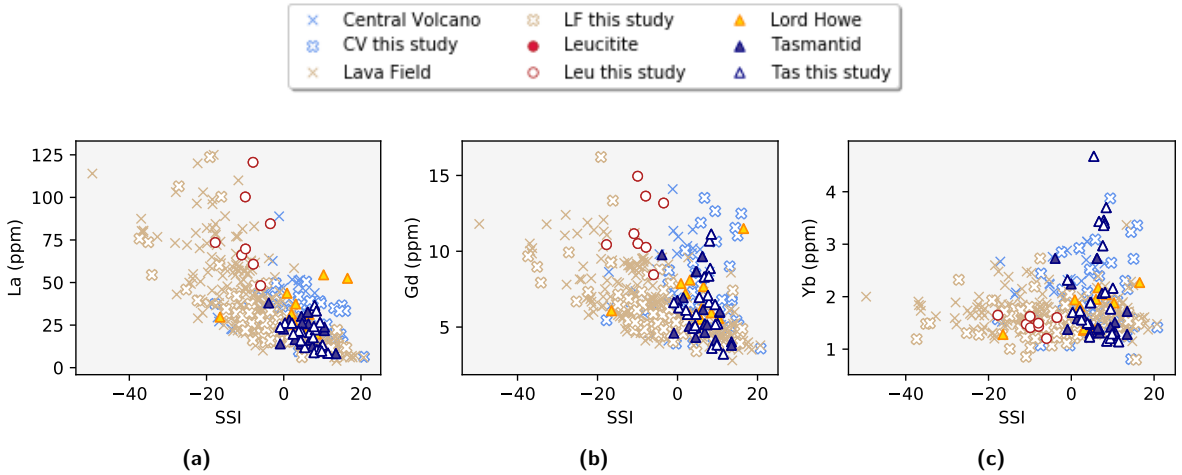

Figure 4.8: *SSI versus (a) La, (b) Gd, and (c) Yb for each suite. The most undersaturated samples with low SSI are the lava field and leucitite suites, which contain some of the highest levels of LREEs and consistently low levels of HREEs. In contrast, samples with the highest SSI from the central volcano and the Tasmantid suites have consistently low levels of LREEs but increasing levels of HREEs. This crossover pattern is reflected in all other LREE and HREE concentrations from Lanthanum through to Lutetium (see Appendix D).*

On average, the Tasmantid seamounts, usually silica saturated, have some of the lowest levels of incompatible elements (Figure 4.6). By contrast, the leucitites, consistently silica undersaturated, have some of the highest incompatible element concentrations (Figure 4.6). These trends may, in part, reflect differences in partial melting where small degrees of melting have produced the undersaturated, incompatible element enriched leucitites located on the thickest continental lithosphere. At the other end of the spectrum, relatively higher degrees of partial melting have produced the silica saturated Tasmantids, less enriched in incompatible element and located on the thinnest oceanic lithosphere. On average, most central volcano and lava field provinces plot between the Tasmantids and leucitites, except for samples from Tasmania which have some of the most undersaturated compositions and highest incompatible element concentrations recorded in this study (Figure 4.5, 4.7, and 4.8). As discussed in Section 2.2.3, these rocks display HIMU isotopic signatures not observed in any other samples and thus require a more comprehensive study of their own to accurately interpret.

Exceptions to these broad rules are found in elements compatible with garnet e.g. yttrium and the HREEs. The concentrations of these are highest in the Tasmantids and the central volcanoes and lowest in the majority of lava field and leucitite volcanism (Figure 4.8). This crossover between LREEs and HREEs across the suites is most likely due to varying degrees of melting within the garnet stability field. At pressures greater than 2.8 GPa, around roughly 70 km depth, garnet is present as a stable mantle phase and the bulk mantle may be modeled primarily as garnet peridotite (Wood et al., 2013). A small degree of melting at this depth would produce a melt depleted in Y and the HREEs as residual garnet preferentially incorporates these elements into its crystal structure. With greater degrees of melting, this effect is diluted as increasing amounts of Y and the HREEs enter the melt. This is often termed the "garnet signature" (Wood et al., 2013). Interestingly, in the Tasmantid suite, this change in LREEs relative to the HREEs appears to corresponds to latitude i.e the percentage of melting within the garnet stability field changes with latitude (discussed further in Figure 4.11).

Given the abundance of evolved rocks observed in the field, the central volcanoes, and to some extent the Tasmantids, are known to be considerably more affected by fractional crystallisation than the lava fields and leucitites (Cohen, 2007; Ruttor et al., 2018). Fractionation of olivine and clinopyroxene is evident in most samples from the MgO versus Ni and CaO/Al_2O_3 plots in Figure 4.9. Petrographic observations of Tasmantids, central volcanoes, and lava fields give a fractionating assemblage dominated by olivine, clinopyroxene, plagioclase and Fe-Ti oxides. Leucitite fractionation appears to be dominated by olivine, clinopyroxene, phlogopite, leucite and Fe-Ti oxides (Figure 4.9). The most primitive samples with limited fractionation occur in the lava field and leucitites (Figure 4.10c and 4.10d) some of which represent the most undersaturated and incompatible element enriched magmas. These observations are consistent with these being small degree melts that rose to the surface relatively rapidly, limiting crystallisation time. In the majority of Tasmantid and central volcano samples, plagioclase phenocrysts, up to 3 mm in length, make up a greater percentage of the rock (Figure 4.10a and 4.10b). These probably represent larger degree melts which stalled underground for longer periods of time prior to eruption, allowing for greater crystallisation. Both field observations and major

and trace element plots suggest that the central volcanoes are more evolved than the Tasmantids. This is possibly because magma was able to rise through the dense oceanic crust more easily. The Tasmantid lavas have also been shown to exploit pre-existing faults of the Tasman spreading ridge (Richards et al., 2018).

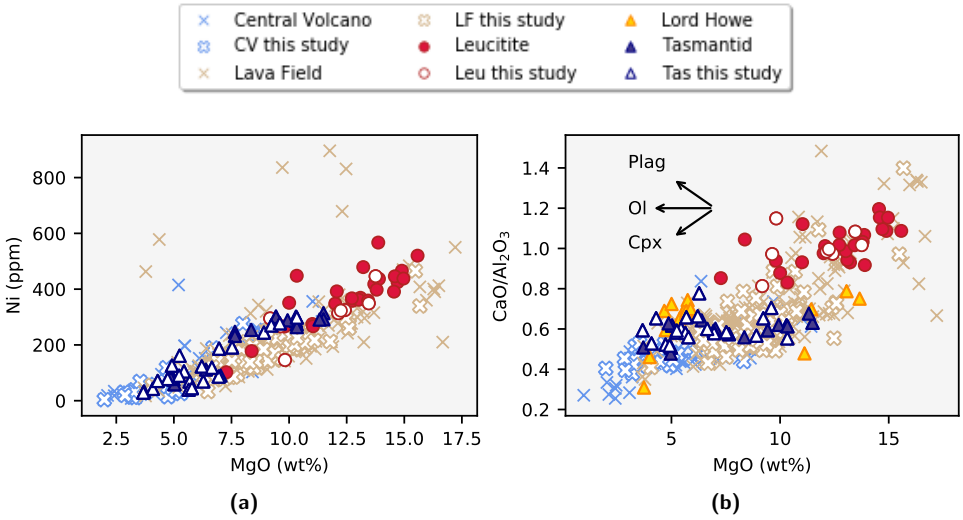

Figure 4.9: *(a) Ni and (b) CaO/Al_2O_3 plotted against MgO for each volcanic sample. All suites display some level of olivine and cpx fractionation, represented here by falling Ni and CaO/Al_2O_3, respectively, with MgO.*

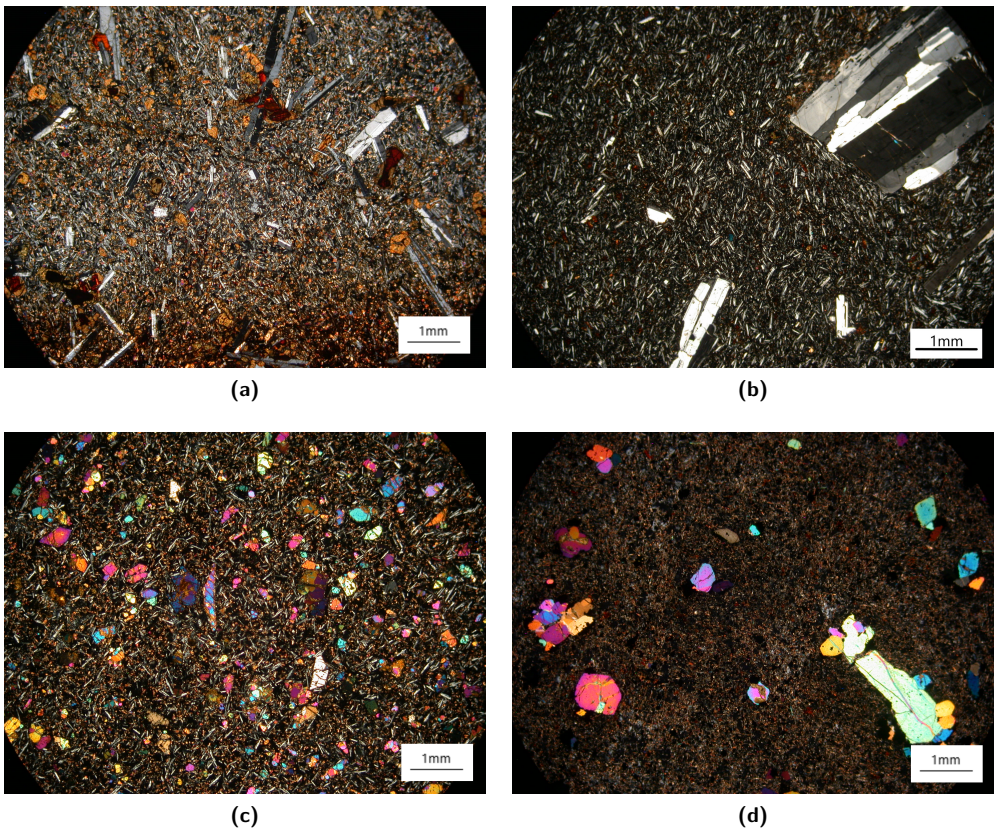

Figure 4.10: *Typical thin-section photomicrographs of each suite taken with crossed polars (XP). (a) Tasmantid sample 274-DR-41-E1 from Seamount C; (b) central volcano sample BC-48 from Cape Hillsborough; (c) lava field sample BC-62 from Bauhinia; and (d) leucitite sample E7980 from Cosgrove. All suites display some level of fractional crystallisation. However, the Tasmantids and central volcanoes contain a greater percentage of plagioclase phenocrysts, up to 3 mm in length. This is consistent with these being higher degree melts which stalled underground for longer periods of time where fractional crystallisation processes have influenced their composition to a greater extent.*

From recent Ar-Ar studies (Kalnins et al., 2015), the Tasmantid volcanoes are known to consistently young north to south, from 56 Ma at the Louisiade Plateau (Sample 274/DR17-H3) to 7 Ma at the Gascoyne Seamount (Sample 85-170) (Figure 4.11a). As spreading of the Tasman Sea ceased at 52 Ma, the seamounts were emplaced onto progressively older, colder, and thus thicker lithosphere. The seafloor age at the time of emplacement of the northern Tasmantids was only around 4 Ma, whilst the seafloor age at the time of emplacement of the Gascoyne Seamount was around 52 Ma. Within this time the thickness of the lithosphere would have greatly increased, and I have modeled this increase in order to assess how it might have affected the composition of erupted lavas. For this study, the depth to the base of the oceanic lithosphere has been defined as the depth to the 1100 °C isotherm, as was described by Watson and Mckenzie (1991) in their modeling of the Hawaiian plume (Fitton et al., 2021). The depth to the 1100 °C isotherm has then been estimated from seafloor ages using the plate model defined by McKenzie et al. (2005). Estimated lithosphere thicknesses at the time of eruption of individual seamounts are given in the supplementary data. My calculations show the lithosphere was around 20 km thick when the most northern Tasmantid sample was emplaced, compared to almost 70 km thick for the Gascoyne Seamount.

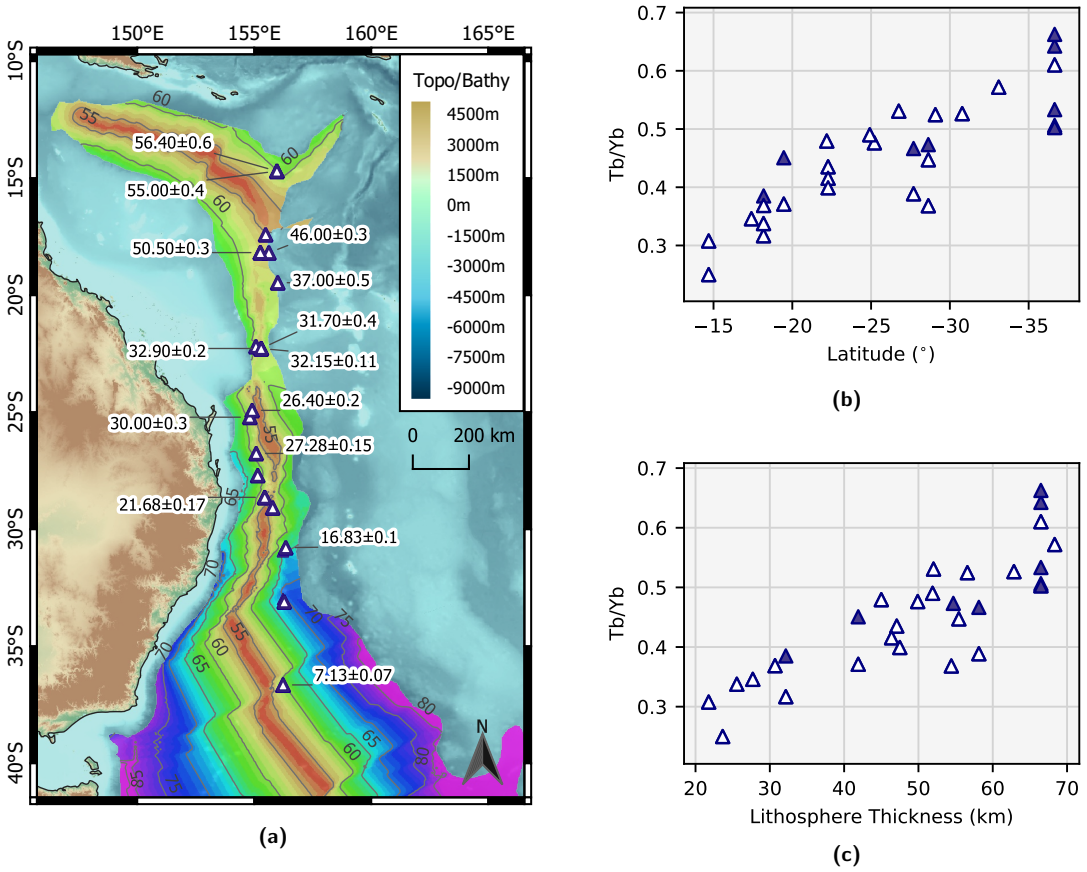

Figure 4.11: *(a) Tasmantid Ar-Ar sample ages (Ma) from Kalnins et al. (2015) are shown with associated errors; ages for samples with no Ar-Ar data have been interpolated from the Tasmantid age versus latitude trend ($y = 0.0457x^2 + 4.5085x + 112.05$); samples from Ruttor (2021) are shown as filled symbols, where ages have again been interpolated; contours show seafloor ages (Ma) from Muller et al. (2000). (b) Tasmantid samples with LOI < 2 wt% showing a clear increase in Tb/Yb with decreasing latitude. The Tasmantid seamounts contain very few primitive samples so all values of MgO have been included in these plots. However, REE ratios should be unaffected by low-P fractional crystallisation. (c) The same ratio plotted against lithosphere thickness estimates. Oceanic lithosphere thickness has been estimated as the depth to the 1100 °C isotherm, which in turn has been estimated from the age of the seafloor at the time of volcano emplacement using the plate model of McKenzie et al. (2005).*

Figure 4.11c shows how this increase in oceanic lithosphere thickness correlates remarkably well with an increase in Tb/Yb, as well as other LREE/HREE ratios. As discussed earlier, this likely relates to the amount of garnet in the source i.e. the final depth of melting or total melt fraction (F_{max}) occurs at a greater depth where a higher percentage of melt has been sourced from garnet peridotite in comparison to spinel peridotite. Thus, it appears that the Tasmantids are all sourced from a depth >70 km within the garnet stability field, where F_{max} varies along the chain and is controlled by lithosphere age and thickness.

Onshore, tomographic measurements by Rawlinson et al. (2017) and Fishwick et al. (2008) have allowed rough estimates of continental lithospheric thickness to be calculated and it is clear that the leucitites sit on the thickest lithosphere. Correspondingly, we see consistently high Tb/Yb ratios in this suite. A similar increase with thickness is actually found when plotting ratios of any incompatible element (Nb, Sr, Th, LREE, P) over any garnet-compatible element (Y, V, Sc, HREE) (Figure 4.12). Once again, these trends most likely relate to degrees and depths of melting i.e. small degrees of melt at greater depth concentrate incompatibles but leave garnet-compatible elements in the mantle residue. Therefore, the Tasmantids, erupting on relatively thin lithosphere, have undergone relatively greater degrees of partial melting whilst the leucitites, erupting on the thickest lithosphere, probably >110 km, have undergone considerably smaller degrees of melting.

The lava fields and central volcanoes sit on lithosphere between 70 and 100 km thick but exhibit considerable spread in incompatible/garnet-compatible ratios (Figure 4.12). The lava fields show the greatest range suggesting they are the product of both small and large degree partial melts. Given that these volcanoes sit on lithosphere of similar thickness it is unlikely they are explained fully by an asthenospheric source where F_{max} is controlled by lithosphere thickness. The central volcanoes generally trend down towards lower incompatible/garnet-compatible ratios suggesting almost all central volcano provinces are the product of relatively higher degrees of partial melting. This would explain the significant evolution of this suite as melt was stored in sizable magma chambers underground, allowing time for fractionation.

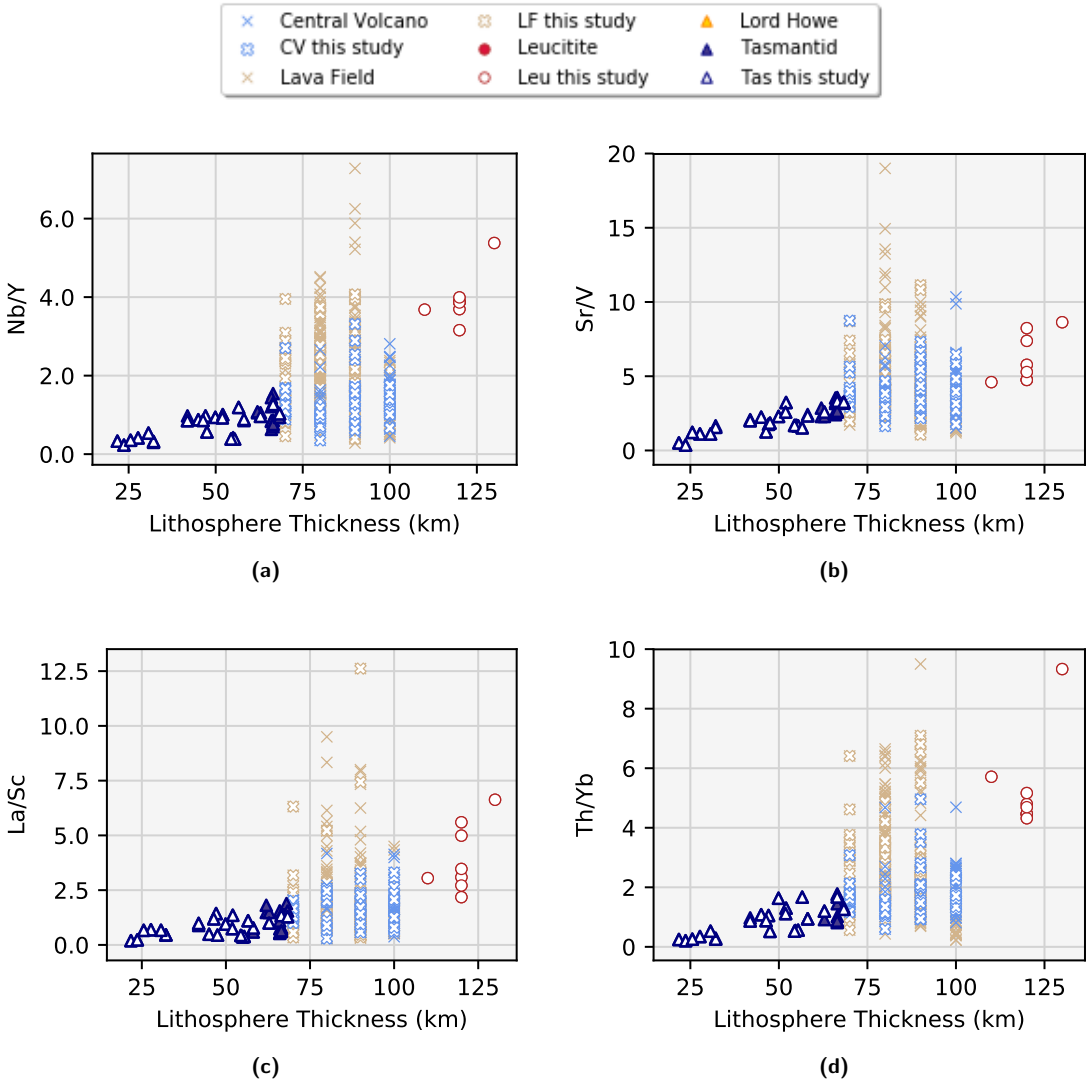

Figure 4.12: *Strongly incompatible/garnet-compatible element ratios versus estimated lithosphere thickness, highlighting relative degrees of melting; (a) Nb/Y, (b) Sr/V, (c) La/Sc, and (d) Th/Yb. All samples have LOI < 2 wt%.*

Using the decompression-melting model defined by Fitton et al. (2021), assuming simple equilibrium melting of a peridotite source (e.g., the OJP source from Hastie et al. (2016)), I have modeled the incompatible element and garnet-compatible element concentrations I would expect with increasing degrees of partial

melting along the 1300 °C, 1400 °C and 1500 °C isotherms (blue, green, red, respectively on Figure 4.13). Here increasing degrees of partial melting accompany reducing lithosphere thickness. Element concentrations have been calculated using Equation 4.1 (Shaw, 1970), where C_0 is the initial concentration of an element in the mantle source, C_L is its concentrations in the liquid, F is the melt fraction, D is the average distribution coefficient of mantle phases weighted by their respective mass fractions, and P is the average distribution coefficient of mantle phases weighted by their respective contribution to the melt.

$$C_L = \frac{C_O}{(D + F - P * F)} \tag{4.1}$$

Model details are outlined in Fitton et al. (2021). Distribution coefficients for spinel lherzolite and garnet lherzolite are presented in Table 4.1. D values from the GERM database (`https://earthref.org/KDD/`) have been averaged over a variety of pressures, temperatures and liquid compositions (Appendix D). Concentrations of La and Yb in the peridotite source have been assigned based on OJP values from Hastie et al. (2016). An OJP source is an appropriate estimate because it is thought to represent the head of a mantle plume which is potentially responsible for other intraplate volcanism within the Pacific Ocean (e.g. Fitton and Godard, 2004; Mahoney and Spencer, 1991). The source of the OJP has also been well modelled by Hastie et al. (2016) using observations from Herzberg (2004), Fitton and Godard (2004), and Tejada et al. (2004) that OJP basalts were produced by 30% melting of primitive mantle which has had around 1% mass removed of a small melt fraction (Fitton et al., 2021).

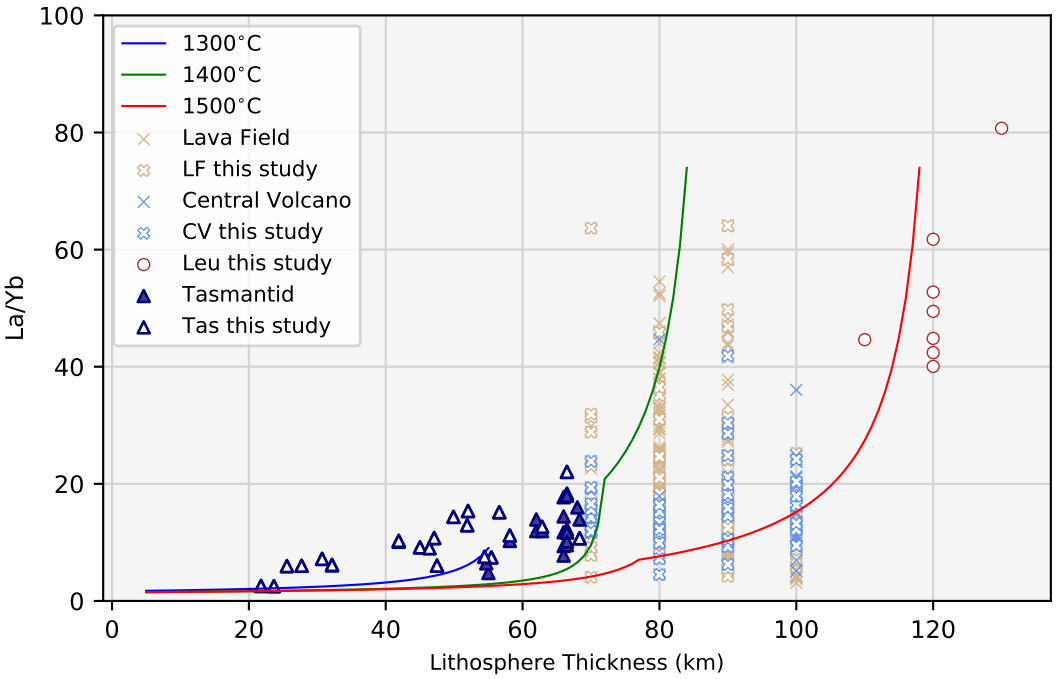

Figure 4.13: *Lithosphere thickness versus La/Yb concentration for each suite (point data). Blue, green, and red lines represent estimated La/Yb concentrations modelled by equilibrium melting of a peridotite source along the 1300 °C, 1400 °C and 1500 °C isotherms, respectively. Peridotite source composition from Hastie et al. (2016). D values taken from GERM (2002). The kinks in the green and red curve mark the position at which the garnet-spinel transition is crossed.*

	Ol	1σ	**Opx**	1σ	**Cpx**	1σ	**Sp**	1σ	**Gt**	1σ.
La	0.0040	0.0038	0.0033	0.0047	0.0464	0.0207	0.0100	-	0.0026	0.0031
Yb	0.0346	0.0236	0.1318	0.0657	0.4396	0.1490	0.0100	-	5.9131	1.0918

Table 4.1: *Distribution coefficients (D) with 1σ errors. Data complied from Adam and Green (2006); Elkins et al. (2008); Fujimaki et al. (1984); Green et al. (2000); Johnson (1994); Kelemen et al. (1993); McKenzie and O'Nions (1991); Salters and Longhi (1999) with full analytical values given in Appendix H.*

Figure 4.13 shows that, allowing for some error in source composition and D values, Tasmantid rocks may be reasonably modeled by non-modal batch partial melting of a peridotite source with potential temperatures (Tp) between 1300 °C and 1400 °C. However, melting beneath lithosphere > 100 km thick, as with the leucitites, would necessitate a considerably higher mantle Tp, or a more enriched and fertile source. From tomographic results, it is likely the central volcanoes and lava fields lie on lithosphere between 70–100 kms thick. Here, the spread in La/Yb between the suites is again difficult to model by simple equilibrium melting of an anhydrous peridotite source alone. A similar trend has been outlined by Regelous et al. (2003), and Fitton et al. (2021) using basalts along the Emperor Seamount chain. The Emperor Seamounts and the Tasmantid Seamounts both show a gradual increase in LREE/HREE ratios moving north to south through the chains. It should be noted that the age of the lithosphere at the time of emplacement of the Emperor Seamounts and the Tasmantids is very similar along both chains. It is likely this thickness variation is responsible for most of the chemical similarity between the Emperor and Tasmantid Seamounts as both are sourced from a depth > 70 km where F_{max} varies along the chains, primarily controlled by lithosphere age and thickness.

Whilst the change in LREE/HREE ratios along the Tasmantids is clear, Figure 4.13 shows appreciable scatter in the data which is particularly enhanced in the central volcanoes, lava fields, and leucitites. The observed spread in La/Yb values may be inherited from a number of factors including: (1) differing modal abundances of garnet in the residual source region; (2) variable partition coefficients (D); (3) AFC processes; (4) changing mantle Tp; and (5) heterogeneous mantle sources. In the case of the first two points, any adjustments to the input parameters of the model, such as mantle mineralogy and D values, change the position of the curves but not their form (Fitton et al., 2021). The model has been tested with a range of reasonable D values and modal ratios but it is not possible to encompass the full suite of continental rocks without the addition of either assimilation of continental crust, a change in mantle Tp or heterogeneous source regions. For example, in some cases lava fields sitting on lithosphere 70 and 100 km thick have the same La/Yb ratios which simply cannot be modeled with non-modal batch partial melting of a peridotite source along a single isotherm even with differing modal abundances of garnet in the residual source or with differing D values.

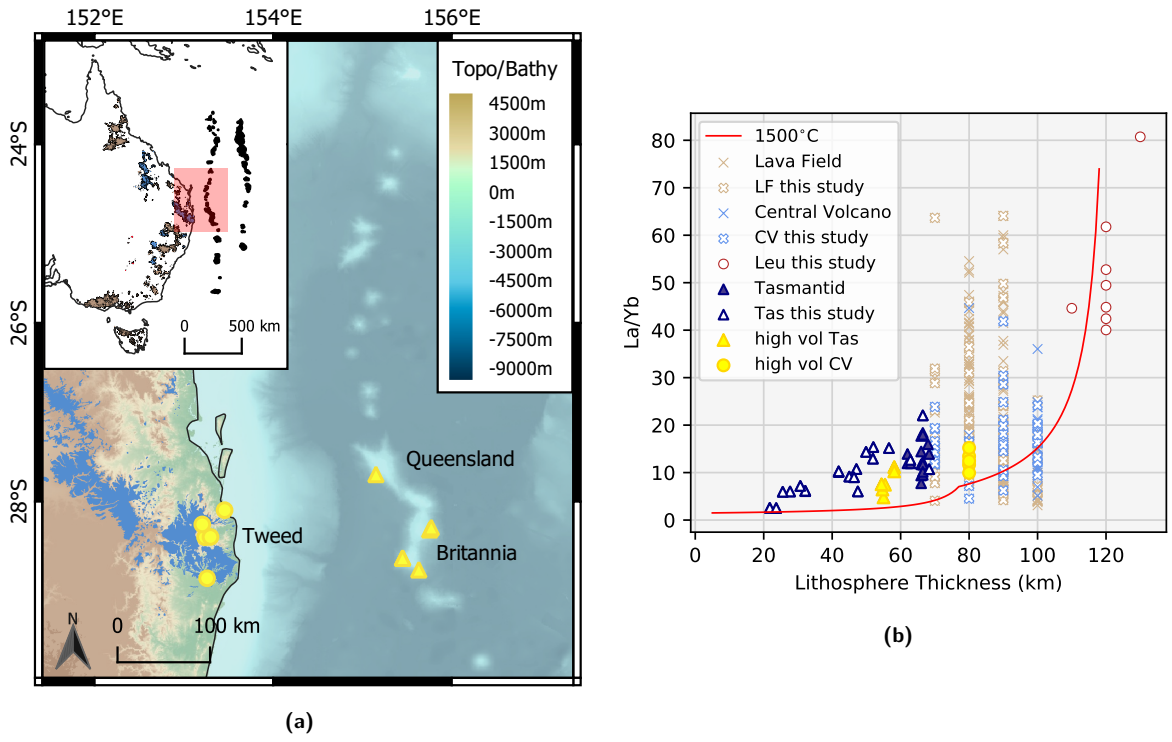

Figure 4.14: *(a) Map showing samples from the largest central volcano, the Tweed shield (yellow circles) alongside the largest Tasmantid seamounts, the Queensland and Britannia guyots (yellow triangles) which are all of similar age ~25–22 Ma. (b) Plot of La/Yb versus estimated lithosphere thickness (LOI < 2 wt%). The high volume Tweed shield, Queensland and Britannia guyots (yellow circle and triangles) have consistently low La/Yb ratios suggesting they are the product of higher degrees of melting. Given the thickness of lithosphere they sit on, this could be due to increasing mantle Tp. For reference, estimated La/Yb concentrations modelled by equilibrium melting of a peridotite source along the 1500° C isotherm is shown as a red line, taken from Figure 4.13. All samples from the Tweed shield, and the Queensland and Britannia guyots plot relatively close to this line.*

Given the greatest scatter is observed in continental samples, assimilation of crustal wall rock certainly must be considered. However, as discussed previously in Sections 2.2.1 and 2.2.3, assimilation of continental crust into both the central volcanoes and lava fields (where most scatter is observed) is expected to be minimal (Zhang et al., 2001; Ewart et al., 1988; Price et al., 1997; Crossingham et al., 2018). Also previously mentioned is the fact that, due to the relative difficultly in altering magma chemistry through crustal interaction as oppose to partial melting of the lithospheric mantle, the latter is presumed throughout this thesis to have had a greater influence on the continental east Australian rocks (Lum et al., 1989; Kempton et al., 1991; Wedepohl, 1995). With this, and the observation that La/Yb enrichments are found in the most primitive samples, AFC processes are not expected to account for the considerable spread in La/Yb with lithosphere thickness.

Another factor which may have played a role in inducing scatter across the dataset is the Tp of the mantle. The most voluminous of the central volcanoes, the Tweed shield (Wellman and McDougall, 1974a) lies 200 km east of two of the more voluminous Tasmantid seamounts, the Queensland and Britannia guyots (Seton et al., 2019b). The three volcanoes are of similar age ~25–22 Ma. It is unknown whether these larger volumes relate simply to melt building up over a long period of time or due to greater degrees of melting at these provinces i.e. an increase in mantle Tp. It is inferred that the motion of the Australian plate slowed down around the time the Tweed volcano was erupted, leading to greater volumes (Cohen et al., 2013). However, in Figure 4.14 samples from these high volume provinces have been highlighted in yellow, and all show fairly low values of La/Yb. Thus, there appears to be some evidence for higher degrees of partial melting, possibly a product of greater mantle Tp producing consistently low La/Yb which correlate with high SSI values. Changes in Tp may help to explain some of the finer variations in La/Yb and SSI along the Tasmantid, central volcano, and leucitite chains that do not fit the trend modeled in Figure 4.13. There are however other possibilities such as heterogenous mantle sources which could account for this change. Changes in Tp are unlikely to be the cause of the spread in La/Yb in the lava fields as to generate the range observed Tp would need to vary considerably across a single province e.g., the McBride which erupted over just 10 Ma and has La/Yb values ranging from of 10–36 which would require a change of 100 °C to explain just on the basis of Tp variation.

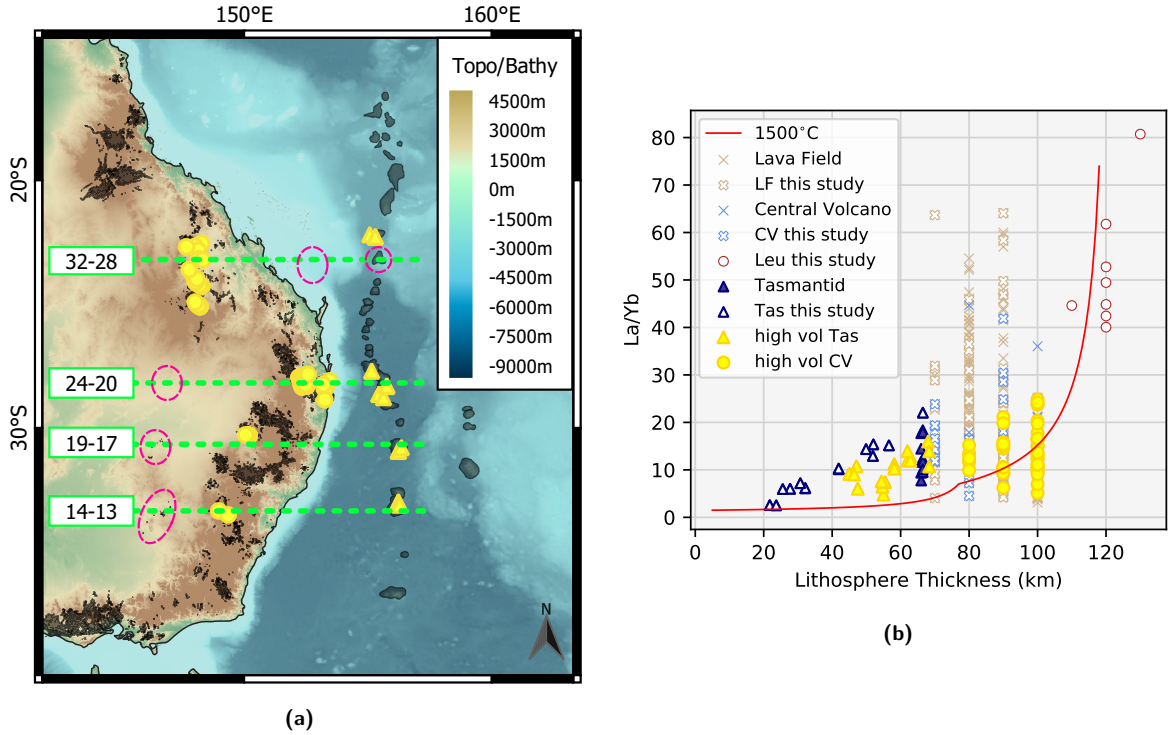

Figure 4.15: *(a) Map showing the locations of the Tasmantid seamounts (yellow triangles) and central volcanoes (yellow circles) with high volumes, and correspondingly low La/Yb. Similar trends are observed in other LREE/HREE pairs. Age ranges of volcanoes lying along the green dashed lines are given in the corresponding green boxes, ages are in Ma. Dashed pink circles represent areas where high volume and low La/Yb volcanoes may also be located but are potentially hidden beneath the Great Barrier Reef or were not analysed in this study i.e., Cato Reef. They also show the location of all leucitite samples, which whilst having high La/Yb and small volumes, lay on lithosphere of such great thickness that they may also be the product of high Tp melts. (b) The same high volume-low La/Yb volcanoes (yellow circles and triangles) shown on a plot of La/Yb versus lithosphere thickness. For reference, estimated La/Yb concentrations modelled by batch melting of a peridotite source along the 1500 °C isotherm is shown as a red line.*

If the Tp of a mantle source was considerably increased i.e., from 1300 °C to 1500 °C, one would expect a reciprocal increase in the degree of mantle melting, and this would be expressed in an increase in the volume of magma erupted and a decrease in LREE/HREE ratios. In Figure 4.15, all provinces which repeatedly show relatively low values of La/Yb and large volumes are highlighted. Given differences in lithosphere thickness moving between the ocean and the continent I have defined a large volume seamount to be anything greater than 2000 km^3, and a large volume continental volcano to be anything greater than 500 km^3. Seamount volumes are taken from Seton et al. (2019b), and continental volumes are from this study. Tasmantid provinces which consistently have low La/Yb values and large volumes include Wreck, Queensland, Britannia, Derwent-Hunter, Taupo, and Gascoyne. Continental provinces which consistently have low La/Yb values and large volumes are Peak Range, Springsure, Buckland, Main Range, Tweed, Nandewar, and Canobolas.

Considering Figure 4.15b, it is difficult to explain high volume and low La/Yb with variations in lithosphere thickness alone as these volcanoes are found on lithosphere anywhere between 45–100 km thick. Instead, these provinces would either require a higher mantle Tp or a more enriched and fertile source to produce the LREE/HREE values measured. Interestingly, many of these provinces appear to be of similar age and correspond to similar latitudes along the volcanic chains, as shown in Figure 4.15a. One explanation for these observations might be that the Tasmantids and some continental volcanoes share a common source which, at certain times (~32–28 Ma, 24–20 Ma, 19–17 Ma, and 14–13 Ma), underwent an elevation in Tp. Another explanation is that these differences are inherited from compositional changes in mantle sources or they may be coincidental and a product of under sampling at some volcanoes. Unfortunately, with such a vast area, these correlations are based on only a handful of samples from each province and so it is possible the La/Yb values collected do not represent each province in its entirety. More precise comparisons of LREE/HREE ratios versus volumes would require more rigorous sampling and may be considered for further work.

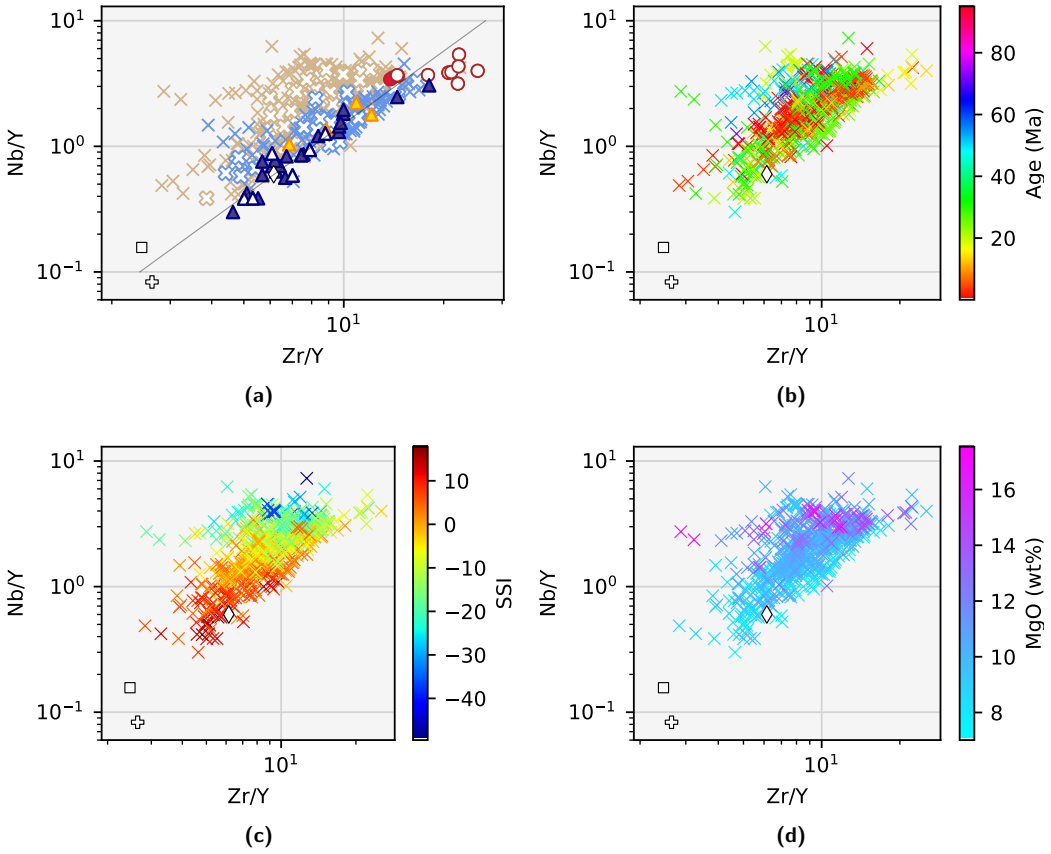

Figure 4.16: *(a) Nb/Y versus Zr/Y for all samples, coloured by (a) suite; (b) age; (c) SSI; and (d) MgO content. Data are filtered to show only primitive samples (MgO > 7 wt%). Black line = ΔNb=0 from Fitton et al. (1997); White diamond = average continental crust (Rudnick and Fountain, 1995); white plus = depleted mantle (DM) (Sun and McDonough, 1989); white square = primitive mantle (PM) (Sun and McDonough, 1989). The Tasmantid seamounts show the lowest Nb/Y whilst many of the lava fields and to some extent the central volcanoes show the highest Nb/Y. Leucitites appear more enriched in Zr. The most extreme enrichments in Nb correlate well with low SSI and high MgO. Also, samples of different ages define slightly different trends within the plot; this can be broken down further by considering the geographical location of each sample (Figure 4.20).*

In order to further evaluate the contribution from heterogeneous mantle sources, I studied immobile incompatible elements i.e. the high field strength elements (HFSE), across the four different suites (Figure 4.16). The Tasmantids have been shown to be well modeled by various degrees of melting beneath a thickening lithosphere, and on a plot of Nb/Y versus Zr/Y they define a trend very similar to the ΔNb=0 trend from Fitton et al. (1997), which was also shown to reflect various degrees of melting. However, many of the lava fields, and some central volcanoes, show unusually high Nb concentrations plotting away from the ΔNb=0 line and inconsistent with lithosphere thickness. Likewise, the leucitites appear to show enrichment in Zr that is unexplained by small degrees of partial melting alone. Variations between the four suites in silica saturation, fractionation and degree of melting appear to correlate to some degree with age. Not all samples included in this study have been dated and so, where necessary, sample ages have been taken from the age of the volcanic province from which it came. A full age review has been completed in Chapter 6, and the results are shown in Figure 4.17.

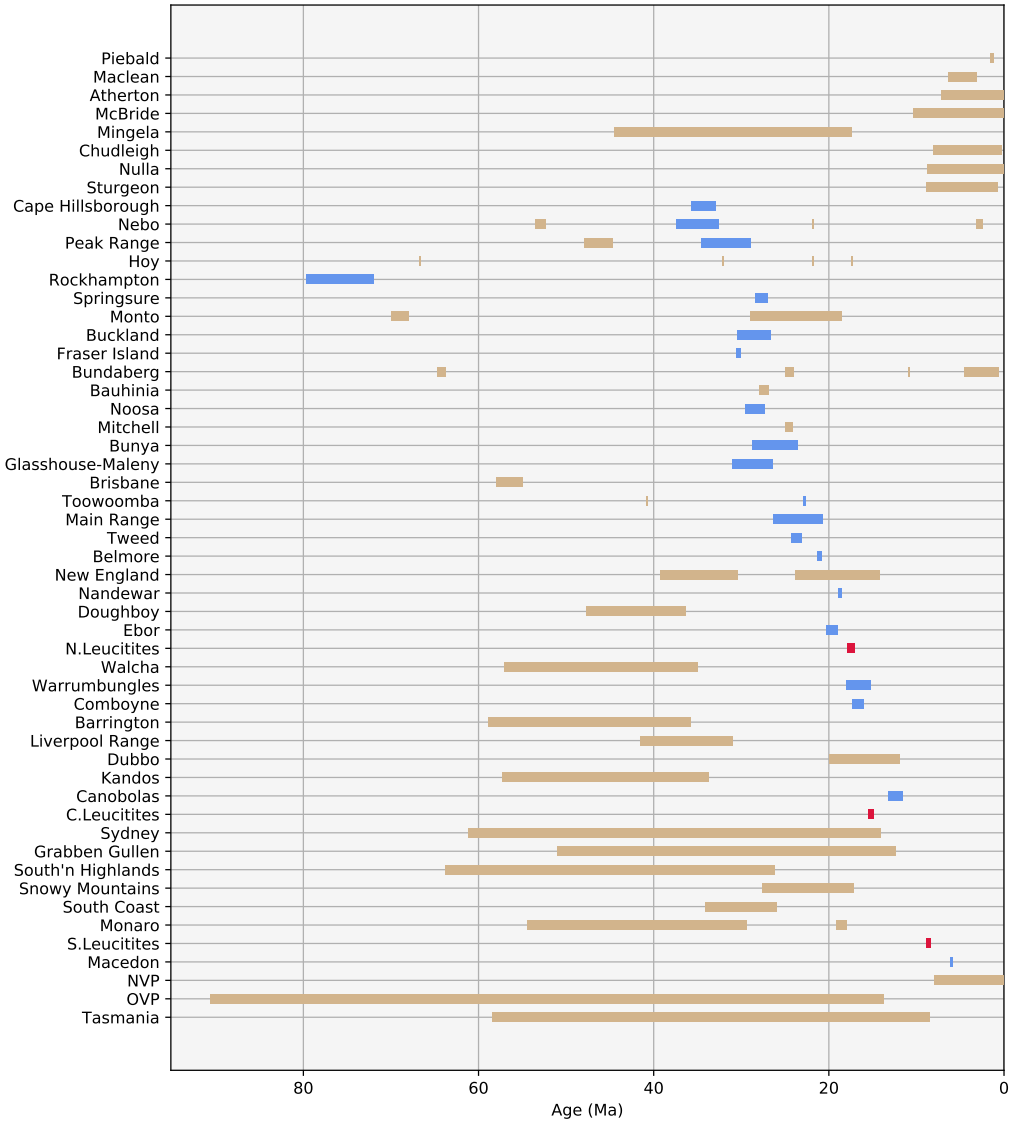

Figure 4.17: *Chronology of volcanic eruptions within the East Australian chain ordered by decreasing latitude. Location of individual provinces given in Figure 6.24. Central volcanoes are coloured blue, lava fields tan, and leucitites crimson.*

Given enrichments occur in the most primitive samples with MgO $>$ 7 wt%, distinctions in Nb-Zr-Y are unlikely to be a product of assimilation-fractional crystallisation (AFC) and instead may be explained by differences in source characteristics or interaction with the metasomatised SCLM. Also, considering these enrichments are only observed in continental samples, the simplest assumption, given a similar source to the Tasmantids, would be that these represent an influence of the SCLM. To better refine these variations, I have studied the temporal and spatial relationships of each continental province (Figure 4.18).

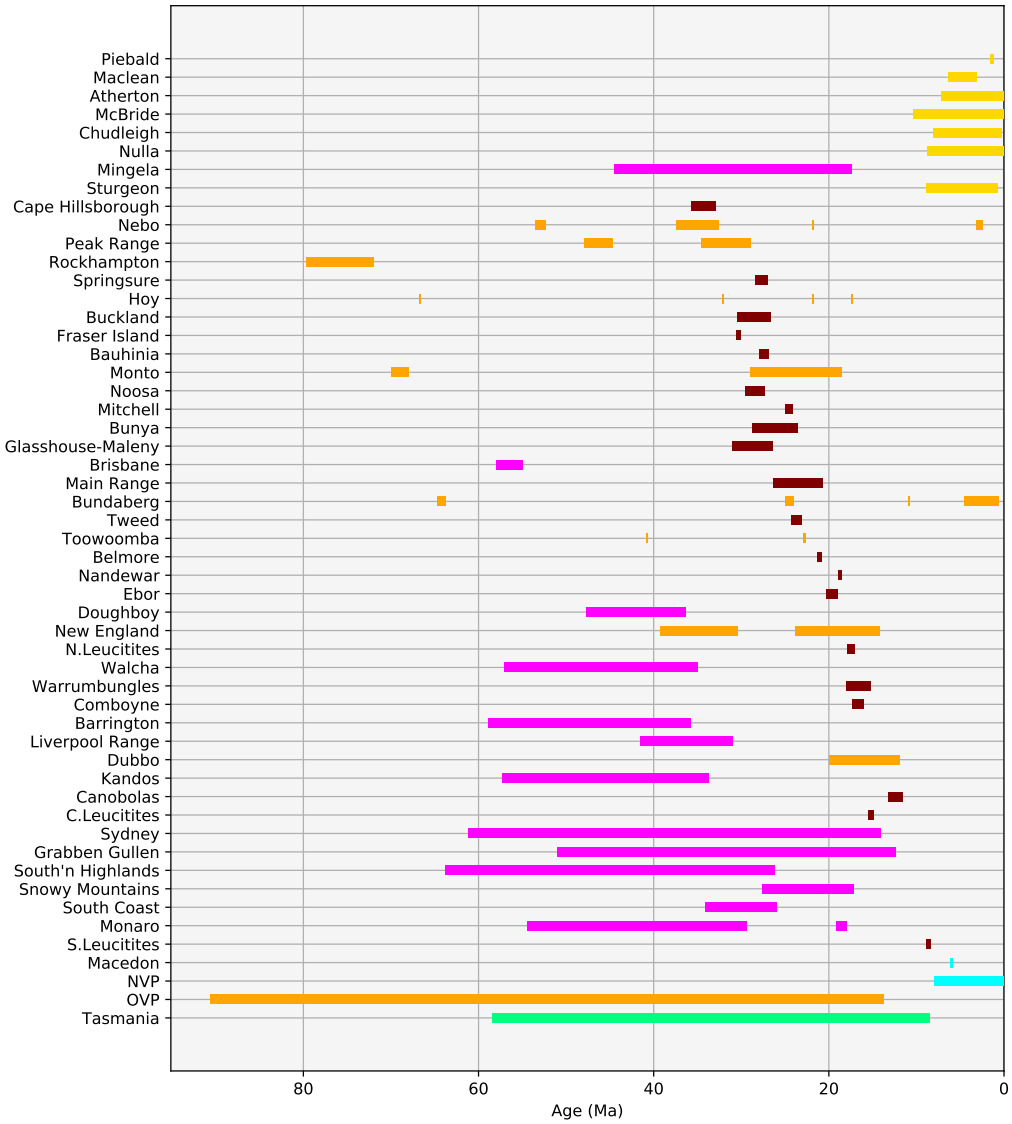

Figure 4.18: *Chronology of volcanic eruptions within the East Australian chain ordered by decreasing latitude and coloured by group: (1) multi-phase volcanism and volcanism > 66 Ma (orange); (2) continuous, lava field-type volcanism emplaced between 66–10 Ma (magenta); (3) HIMU Tasmania volcanism (green); (4) short-lived, age-progressive volcanism (maroon); (5) young volcanism from the NVP (cyan); and (6) young volcanism from far north Queensland (yellow). Location of individual provinces given in Figure 6.24.*

From Figures 4.17 and 4.18, the only provinces within eastern Australia to erupt prior to ∼66 Ma, based on current dating, were Hoy, Rockhampton, Monto, Bundaberg, and the OVP. Whilst OVP volcanism in Victoria persisted relatively continuously throughout the Cenozoic, volcanism around Hoy, Monto, and Bundaberg was much more sporadic and short-lived. The Rockhampton province appears to have only been active ∼80–72 Ma. This location has historically been catagorised as a central volcano because it produced bimodal lavas, although it was erupted almost 40 Ma earlier than all other central volcanoes and is very unlikely to be related to the same magmatic event. Interestingly, Rockhampton and Monto are two of the three provinces which have plagioclase megacrysts in particularly primitive samples (MgO ∼10 wt%), the other being the nearby Bunya province. It is possible these are sourced from the SCLM in southern Queensland.

Following this, abundant lava field-type volcanism started up along the length of the continent, mostly between ∼60–30 Ma, with much of it persisting up to around 10 Ma. The majority of these provinces are found in NSW but there are heavily eroded outcrops in Toowoomba, Brisbane, Mitchell, Bauhinia, Bundaberg, Monto, Hoy, and Mingela. Previous studies have attributed the occurrence of these volcanoes to rift-flank volcanism following opening of both the Tasman and Coral Seas, similar to Marie Byrd Land volcanism in Antarctica (e.g. Johnson, 1989). However, the longevity of eruptions poses a problem to this theory, as rifting

in the area ceased around 52 Ma (Gaina et al., 1999). Most provinces from this group erupted relatively continuously over long durations, except for the Nebo, Hoy, Monto, and Bundaberg provinces, which are instead defined by multiple, often short-lived, periods of activity. In the case of Nebo, this spans almost 60 Ma. Some of these provinces are likely to be the accumulation of both lava field and central volcano volcanism. This is again reflected in their geochemistry where, for example, the earliest flows of Nebo, Peak Range and Toowoomba are considerably more undersaturated with higher incompatible element concentrations compared to later volcanism, which is chemically more akin to other central volcanoes.

Around 35 Ma age-progressive central volcano volcanism begins at Cape Hillsborough. Moving south with time, other central volcanoes erupt defining a linear age versus latitude trend, typical of hotspot volcanism. Generally, these provinces have shorter age ranges, $\sim$1–4 Ma, although there are exceptions. A number of lava field provinces also show similar trends in age, location, and geochemistry, suggesting they may be more closely linked to the central volcanoes than previously thought. Examples include Bauhinia, Mitchell, and Dubbo, and parts of Hoy, Monto, Bundaberg, and New England.

The youngest volcanism across the East Australian chain has taken place at both the north and south extremities, with a few smaller volume eruptions in the Bundaberg and Nebo provinces in central Queensland. Geochemically, the high volume, far north Queensland and southern NVP volcanoes appear quite different to one another. Spatially and temporally, the NVP in Victoria may represent an extension of leucitite volcanism, an observation which has been discussed further in the following Chapter on leucitites. However there is no obvious genetic connection between age-progressive volcanism, or the older lava field-type volcanism, and the far north Queensland volcanoes.

Using these observations, rock samples from this study have been split into six distinct groups: (1) mixed, multi-phase volcanism and volcanism $>$66 Ma (orange); (2) single-pulse, lava field-type volcanism emplaced between 66–10 Ma (magenta); (3) HIMU Tasmania volcanism (green); (4) short-lived, age-progressive volcanism (maroon); (5) young volcanism from the NVP (cyan); and (6) young volcanism from far north Queensland (yellow). Each group is shown in terms of latitude versus age on Figure 4.18, and the geographic location of each group is shown on Figure 4.19.

On a plot of Nb/Y versus Zr/Y, each of these groups shows markedly different characteristics (Figure 4.20) and similar correlations are observed with SSI (Figure 4.21). Leucitite samples appear to extend towards the NVP, a trend that is seen in other plots and discussed in Chapter 5 (Figures 4.23, 5.6). They also follow a similar trend to the continental age-progressive samples and the Tasmantid samples. With high Zr concentrations, the leucitites themselves plot below the trend defined by the Iceland array, similar to the Western US lamproites studied by Fitton (2007). Fitton et al. (1991) and Kempton et al. (1991) have shown that these rocks probably inherited their chemical and isotopic characteristics from a lithospheric source. This is primarily because, whilst similar to other OIB-type rocks, their unique geochemical signatures are only ever found in continental samples. Work by Lum et al. (1989) and Kempton et al. (1991) revealed that it is much easier to inherit such chemical variations from the lithospheric mantle as oppose to the crust. It is therefore likely that the source of the leucitites is linked in some way to SCLM, enriched via metasomatism. The connection between the NVP and the leucitites is discussed more in Chapter 5 of this thesis and is thought to show mixing between an asthenospheric plume and the SCLM. For comparison, this trend has been included in other plots on Figure 4.20 as grey dots.

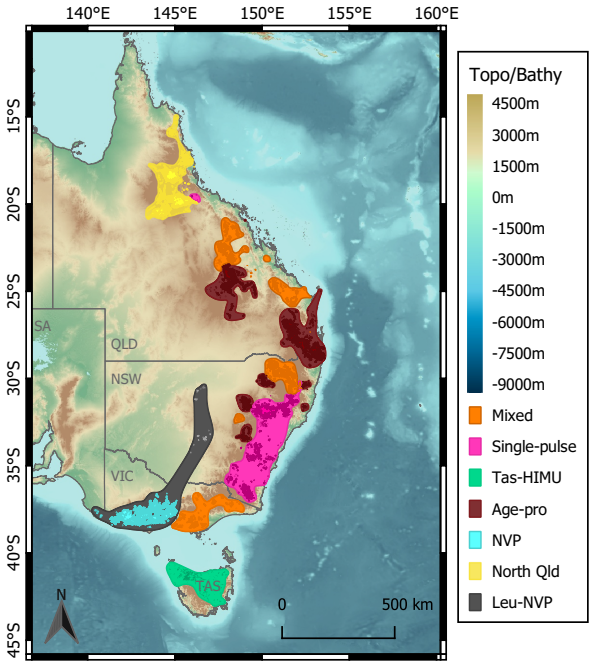

Figure 4.19: *Volcanic provinces split by the six groups outlined in Figure 4.18: (1) multi-phase volcanism and volcanism $>$ 66 Ma (orange); (2) continuous, lava field-type volcanism emplaced between 66–10 Ma (magenta); (3) HIMU Tasmania volcanism (green); (4) short-lived, age-progressive volcanism (maroon); (5) young volcanism from the NVP (cyan); and (6) young volcanism from far north Queensland (yellow). Grey shaded area shows the leucitite-NVP hotspot trend, also shown in Figure 4.20. SA = South Australia; QLD = Queensland; NSW = New South Wales; VIC = Victoria; TAS = Tasmania.*

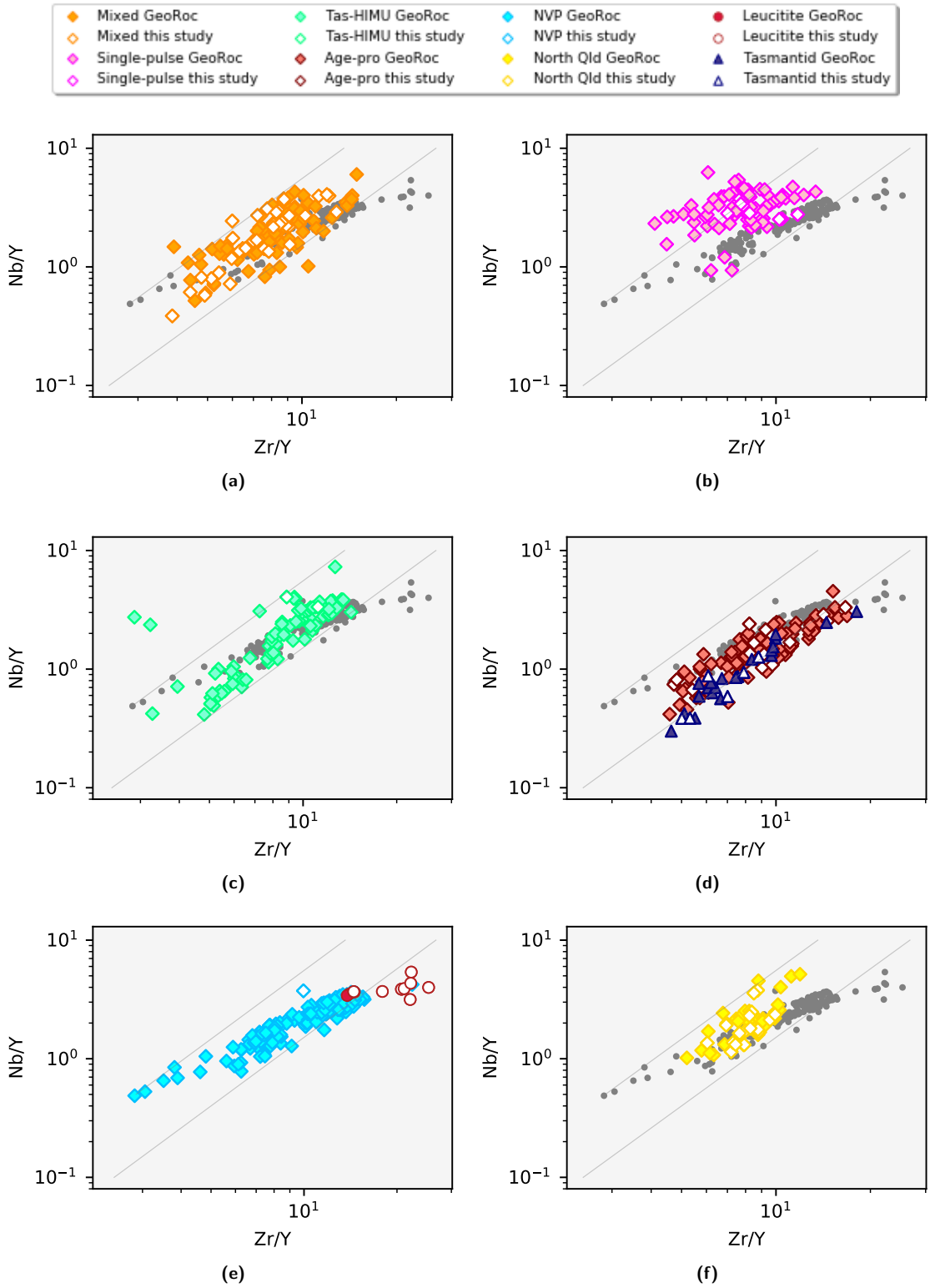

Figure 4.20: *Groups identified in Figures 4.19 and 4.18 on a plot of Nb/Y versus Zr/Y. Grey dots = leucitite-NVP trend. All data has MgO > 7 wt%. For comparison, grey lines represent the Iceland array from Fitton (2007). Almost all continental rocks show some level of relative Nb enrichment compared with the Tasmantids and it is likely these differences relate to influences of the SCLM. Of particular interest, the single-pulse group consistently has the highest Nb/Y which is not explained by varying degrees of melting and not observed in any other category or in the Iceland array. Recent volcanism in Victoria (NVP), age-progressive continental samples, and the Tasmantid seamounts all appear to trend towards the leucitite suite, potentially representing mixing between their respective sources. The leucitites themselves are the only samples to plot below the trend defined by the Iceland array. Also interestingly, age-progressive rocks are bound at the bottom by the Tasmantids and at the top by the leucitite-NVP trend, again possibly pointing to a connection in sources.*

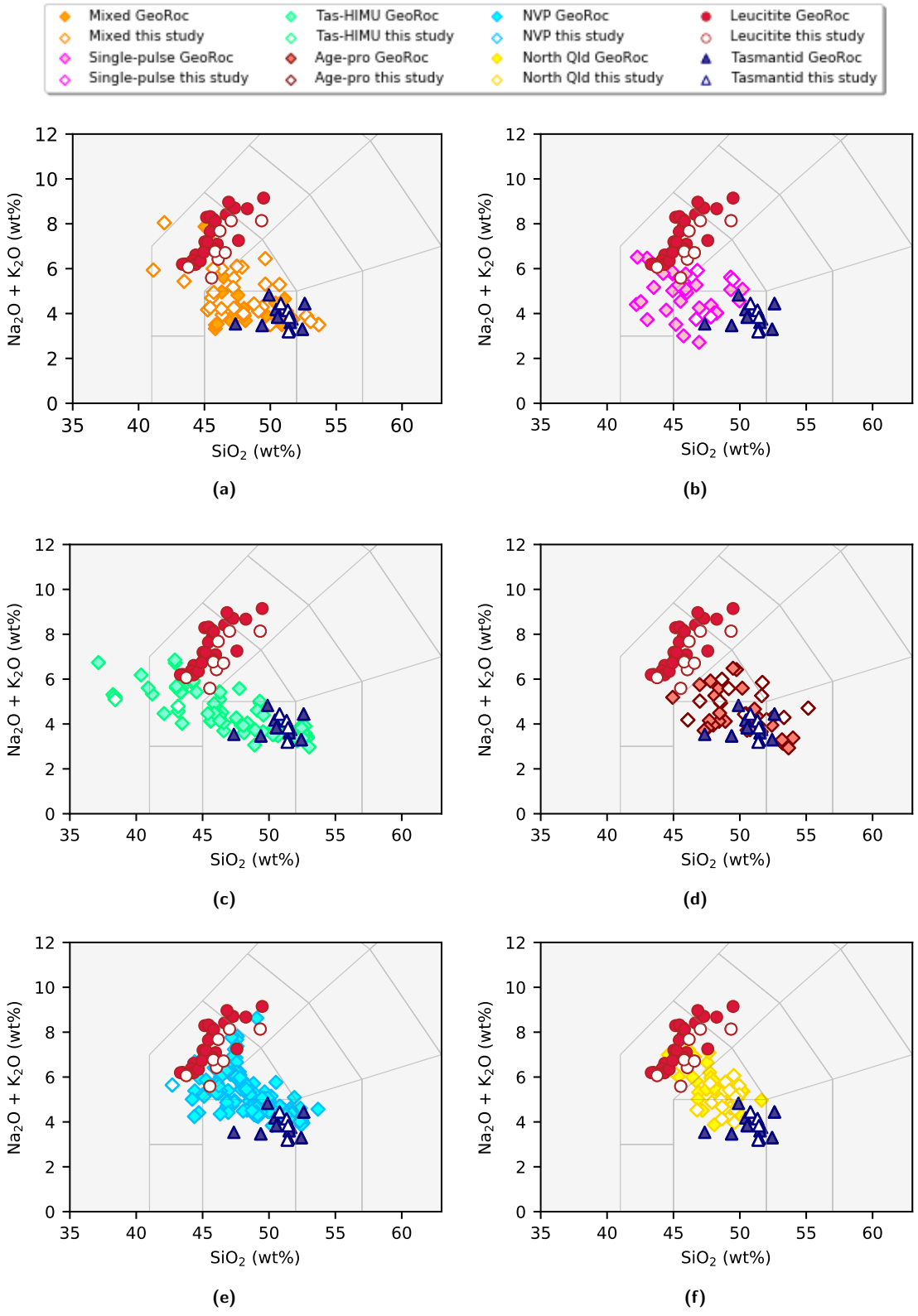

Figure 4.21: *TAS diagrams for data from the various geographical groups defined in Figure 4.19, data filtered with LOI < 2 wt% and MgO > 7 wt%, except for (d) where samples from the OVP have no LOIs reported (Price et al., 2014). Tasmantid data, representing the high-degree melt endmember, are plotted as navy triangles. Leucitite data, representing the low-degree melt endmember, are plotted as crimson circles. The only samples to show lower levels of silica saturation than the leucitites are from Tasmania (mint), Monto and Bundaberg (orange), and the Southern Highlands (magenta) and the only samples to show higher levels of saturation than the Tasmantids are again from Tasmania, the Monto, Bundaberg, Fraser Island and Noosa provinces (orange), and the Mitchell and Bauhinia provinces (maroon).*

The young oceanic lithosphere of the Tasman and Coral Seas is unlikely to have been considerably affected by metasomatism (McKenzie, 1989), which may explain why the Tasmantid seamounts do not show the same Nb/Y enrichments as seen on the continent, if they are in fact sharing a common source. In Figure 4.20d, the Tasmantids appear to follow the ΔNb=0 trend from Fitton et al. (1997), probably reflecting various degrees of partial melting from a plume-like source >70 km. Samples from the age-progressive provinces (maroon), plot neatly between these two end members i.e., the Tasmantids and the NVP-leucitite trend (Figure 4.20d). Given this and the similar age versus latitude trend of this group, they are probably derived from a similar source; that of an asthenospheric plume mixed with SCLM melts.

The single-pulse group has considerably elevated Nb/Y compared with other groups and plots almost exclusively above the NVP-leucitite trend. Given the long, relatively continuous duration of volcanism here (up to $\sim$50 Ma around Sydney) it is difficult to explain with a plume-like origin and much more likely these enrichments are also sourced from the SCLM. Since the onset of most magmatism was $\sim$60 Ma SCLM melts are perhaps the product of rift-flank volcanism following opening of the Tasman and Coral Seas (e.g. Johnson, 1989). Unfortunately, only one sample exists with Nb, Zr, Y data for the Mingela and Brisbane provinces, so whether this trend is representative of all lava field-type volcanism erupted between 60–10 Ma or whether it is just representative of southern, NSW lava field-type volcanism is difficult to say without further sampling. If the latter is true, Nb enrichment could be due to geographical differences in the composition of the SCLM underlying each area such as the Lachlan Fold Belt in NSW.

Much like this group, the recent north Queensland group (yellow) also plots exclusively within, or above the NVP-leucitite outline. Samples from the mixed, multi-phase group (orange) generally plot between the lines representing the Iceland array (Fitton, 2007) and as a mixture of old and young lava fields and central volcanoes, one would expect more scatter in this group. More detailed mapping and sampling of each province would be required to identify lava field-type flows from inherently central volcano-type flows to split this group further. Samples from Tasmania (mint) show a slightly different trend to other groups with moderate Nb enrichment. Coupled with the unusual HIMU isotopic signature in this group, it is possible they have an entirely different origin to other volcanoes in east Australia, although this is not discussed any further in this thesis.

Fitton et al. (1997) defined the parameter ΔNb (Equation 4.2), which expresses the excess or deficiency of Nb relative to the lower line of the Iceland array on the Nb/Y versus Zr/Y plot.

$$\Delta Nb = 1.74 + log(Nb/Y) - 1.92\, log(Zr/Y) \tag{4.2}$$

Figure 4.22 shows ΔNb versus Nb/La alongside Nb/Y versus Zr/Y, where (a) and (b) show all rock samples from age-progressive provinces, including the Tasmantids, age-progressive central volcano-type volcanoes (maroon), the NVP (cyan), and the leucitites (crimson), (c) and (d) show some provinces which exhibit unusually high Nb concentrations such as the single-pulse lava field-type volcanism emplaced between 66–10 Ma (magenta), old lava flows from the Buckland volcano identified by Crossingham et al. (2018), and rocks containing xenoliths or plagioclase megacrysts. Age-progressive provinces generally plot close to one another (Figure 4.22a) although there are slight differences when considering individual provinces in more detail.

Rocks from the Buckland central volcano have been analysed by Crossingham et al. (2018) who sampled, an older ($\sim$30 Ma) group, and a younger ($\sim$27 Ma) group. The authors attributed the earlier group to magmas derived from metasomatised SCLM, and the later group to deep-mantle-derived magmas. When including these results in our own plots (red squares in Figure 4.22c and 4.22d), the younger flows trace the same outline as the deep, plume-derived Tasmantid seamounts, and the older flows plot closer to the upper limits of the NVP and lower limits of the single-pulse group, both of which are thought to have some influence of SCLM derived melts.

In addition to this, included in Figures 4.22c and 4.22d are rock samples which were recorded in this study as containing lithosphere derived peridotite xenoliths (black crosses). Once again, these samples trace the upper limits of the NVP and lower limits of single-pulse group, suggesting Nb enrichment may well be linked to increased interaction with the SCLM. Similarly, primitive rock samples (MgO $\sim$10 wt%) containing plagioclase megacrysts which may also be derived from the lithospheric mantle, lie in a similar location on the Nb/Y vs Zr/Y plot. ΔNb vs Nb/La results plot closer to the single-pulse group than the NVP, perhaps due to La variations in compositionally different SCLM (Figure 4.22c).

To asses these distinctions further, I have complied all available isotopic data from each of our six groups, plus the leucitite and Tasmantid suites. The results are given in Figure 4.23. As with trace element data, basaltic rocks along the East Australian chain show a wide range in isotopic values with seemingly, some influence from DM, EMI, EMII and HIMU type reservoirs (Figure 4.23). However, a few trends can be picked out from the $^{206}Pb/^{204}Pb$ vs $^{208}Pb/^{204}Pb$ and εNd vs $^{87}Sr/^{86}Sr$ plots that again may be separated by the groups defined in Figure 4.19.

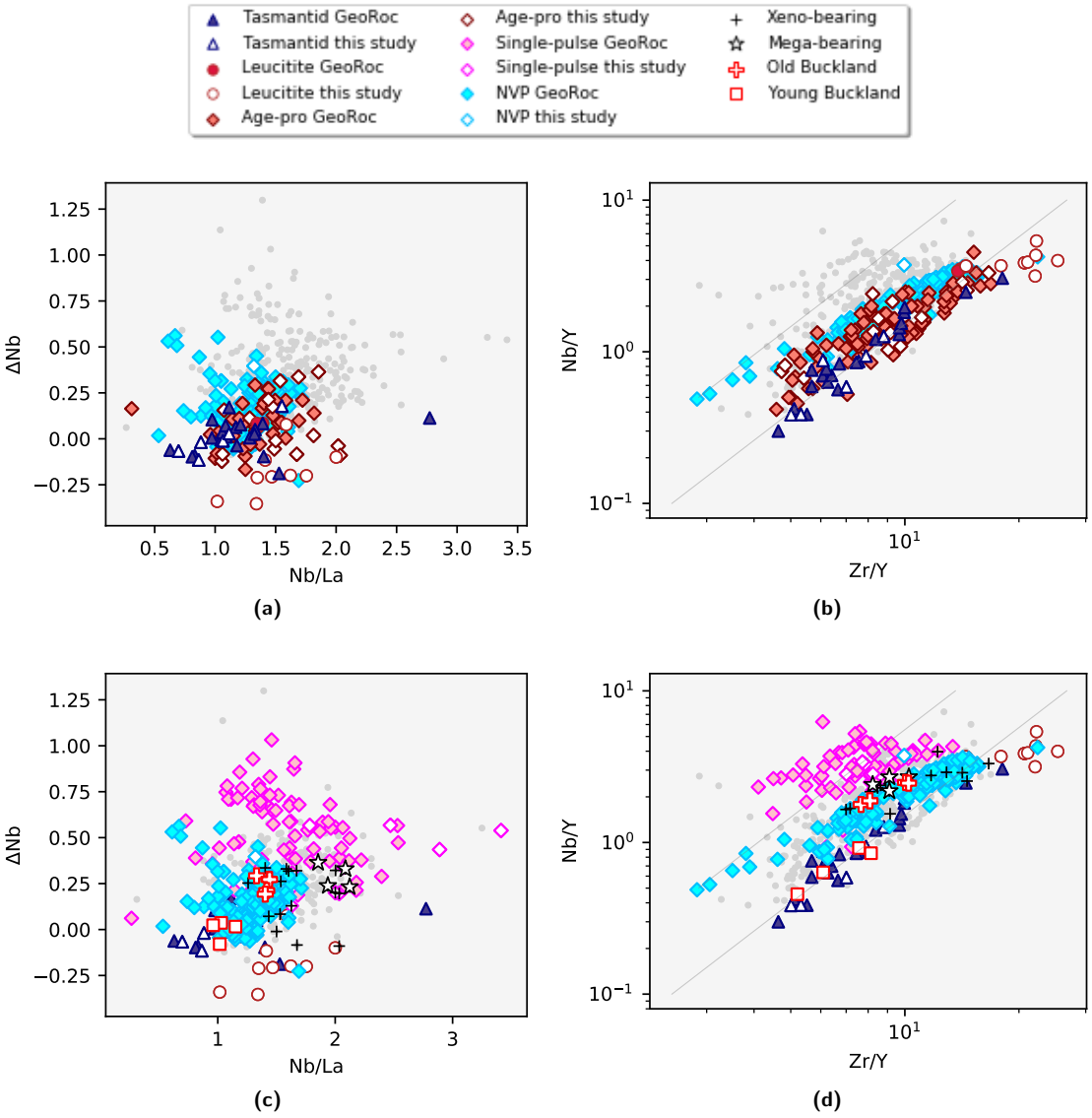

Figure 4.22: *(a) ΔNb vs Nb/La and (b) Nb/Y vs Zr/Y highlighting all samples from age-progressive provinces including the continental age-progressive group, the NVP, the leucitites, and the Tasmantids. (c) ΔNb vs Nb/La and (d) Nb/Y vs Zr/Y highlighting provinces with unusual Nb enrichment. Buckland volcano samples from Crossingham et al. (2018). Xenolith samples are from this study (Chudleigh, Mingela, Hoy, Mitchell, Monto, Bundaberg, New England, Walcha and the NVP provinces). Megacryst samples also from this study (Rockhampton, Monto, and Bunya provinces).*

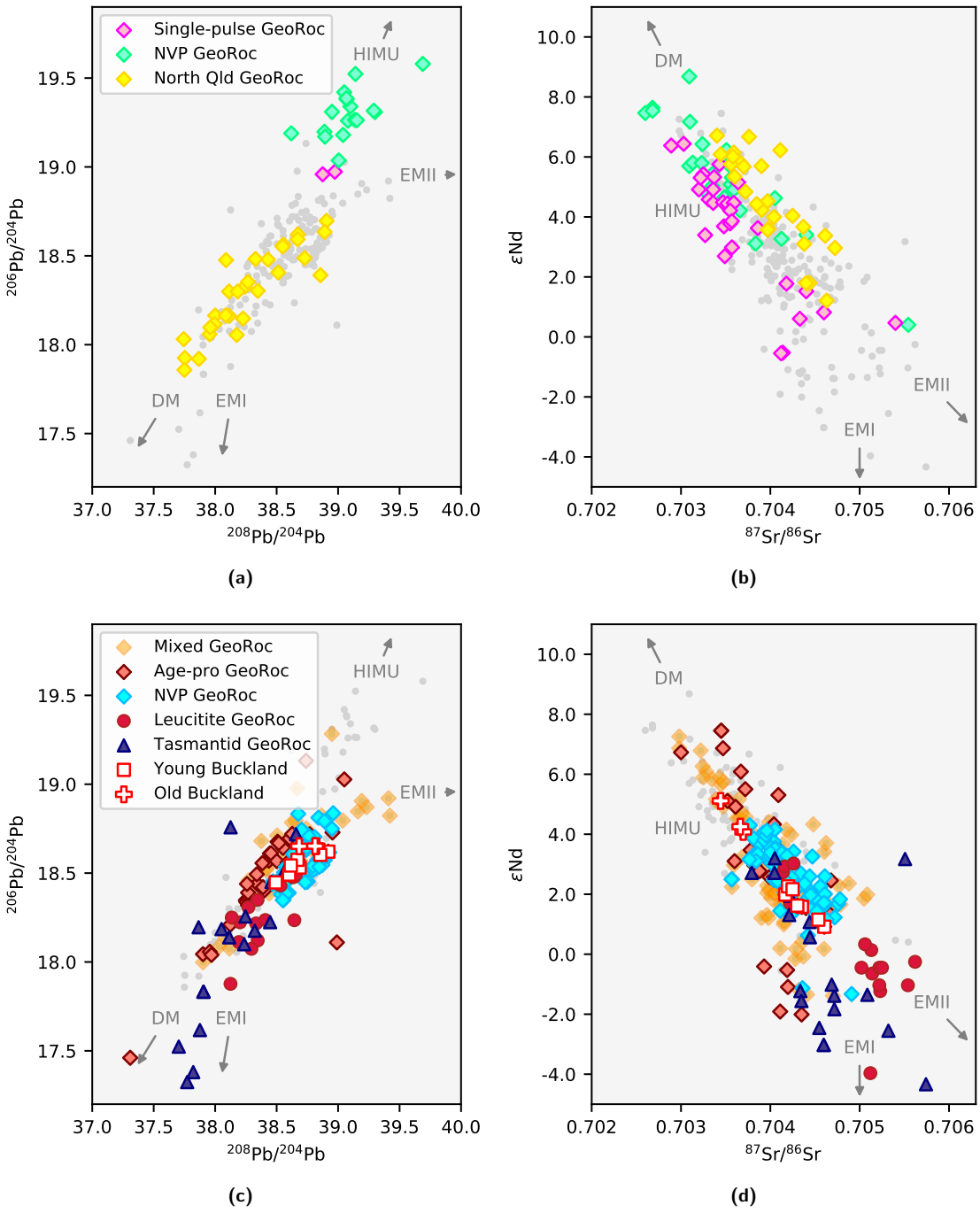

Figure 4.23: *(a) $^{206}Pb/^{204}Pb$ versus $^{208}Pb/^{204}Pb$ and (b) εNd versus $^{87}Sr/^{86}Sr$ for all samples split by group: (1) mixed, multi-phase volcanism and volcanism > 66 Ma (orange); (2) single-pulse, lava field-type volcanism emplaced between 66–10 Ma (magenta); (3) HIMU Tasmania volcanism (green); (4) age-progressive volcanism (maroon); (5) young volcanism from the NVP (cyan); and (6) young volcanism from far north Queensland (yellow) (Figure 4.19). DM, EMI, EMII, and HIMU mantle reservoir endmember compositions after Zindler and Hart (1986). Non-age-progressive samples (a, b) display different levels HIMU, EMI, and EMII enrichment but all contain a significant depleted mantle component, probably reflecting an upper mantle origin where enrichment is introduced by melting of metasomatised SCLM. These are the same samples which have the greatest Nb enrichment. Age-progressive samples, including the leucitites and Tasmantids, all extend towards the EMI reservoir, with the Tasmantid seamounts displaying the least-radiogenic Pb-isotope ratios (Figure 4.23c, 4.23d). These probably reflect varying degrees of melting within a EMI-like mantle plume. Consistently, these are the sample samples which have the least Nb enrichment. Samples from the mixed group cover the full data range from DM, EMI, EMII, and HIMU reservoirs, which is expected given the presence of both lava field-type volcanism and central volcano-type volcanism in this group.*

Non-age-progressive samples from the single-pulse and Tasmania-HIMU groups have the most-radiogenic Pb-isotope ratios, with Tasmania samples plotting close to the HIMU endmember (Figure 4.23a, 4.23b). εNd and $^{87}Sr/^{86}Sr$ results for Tasmania samples plot between DM and HIMU reservoirs. Unfortunately only two samples from the single-pulse have Pb-isotope values, not enough to accurately interpret, but on a plot of εNd vs $^{87}Sr/^{86}Sr$ they trend between DM, HIMU, and EMI reservoirs. By contrast, non-age-progressive samples from the far north Queensland group have some of the least-radiogenic Pb-isotope ratios, trending between DM and EMII on both $^{206}Pb/^{204}Pb$ vs $^{208}Pb/^{204}Pb$ and εNd vs $^{87}Sr/^{86}Sr$ plots (Figure 4.23a, 4.23b). Whilst all these provinces display different levels of HIMU, EMI, and EMII enrichment, all three appear to contain a significant component of depleted mantle. Considering the long duration in volcanic activity of each of these groups combined with the isotopic array observed here, the simplest explanation is that they are sourced from passive upper mantle processes, where enrichment is introduced by melting of metasomatised SCLM.

Almost all age-progressive samples appear to trend towards the EMI reservoir, with the Tasmantid seamounts displaying the least-radiogenic Pb-isotope ratios (Figure 4.23c, 4.23d). Exceptions to this include a few samples from the age-progressive group, including the lower Buckland lavas (red squares plotting above εNd=3), which generally have higher εNd, perhaps owing to a greater contribution from the depleted mantle in these rocks, i.e., a SCLM-DM-like origin similar to the non-age-progressive provinces of the single-pulse, Tas-HIMU, and north Queensland groups. Samples from the mixed, multi-phase group cover the full data range from DM, EMI, EMII, and HIMU reservoirs, which is again unsurprising given the mix of lava field-type volcanism and central volcano-type volcanism in this group. Samples from this set which extend towards the EMII reservoir are all from the OVP, a province which has been active since around 90 Ma. It is quite possible these have a different origin to the deep-plume and metasomatised SCLM sources discussed here but, due to time and sampling constraints, this is not discussed further in this thesis.

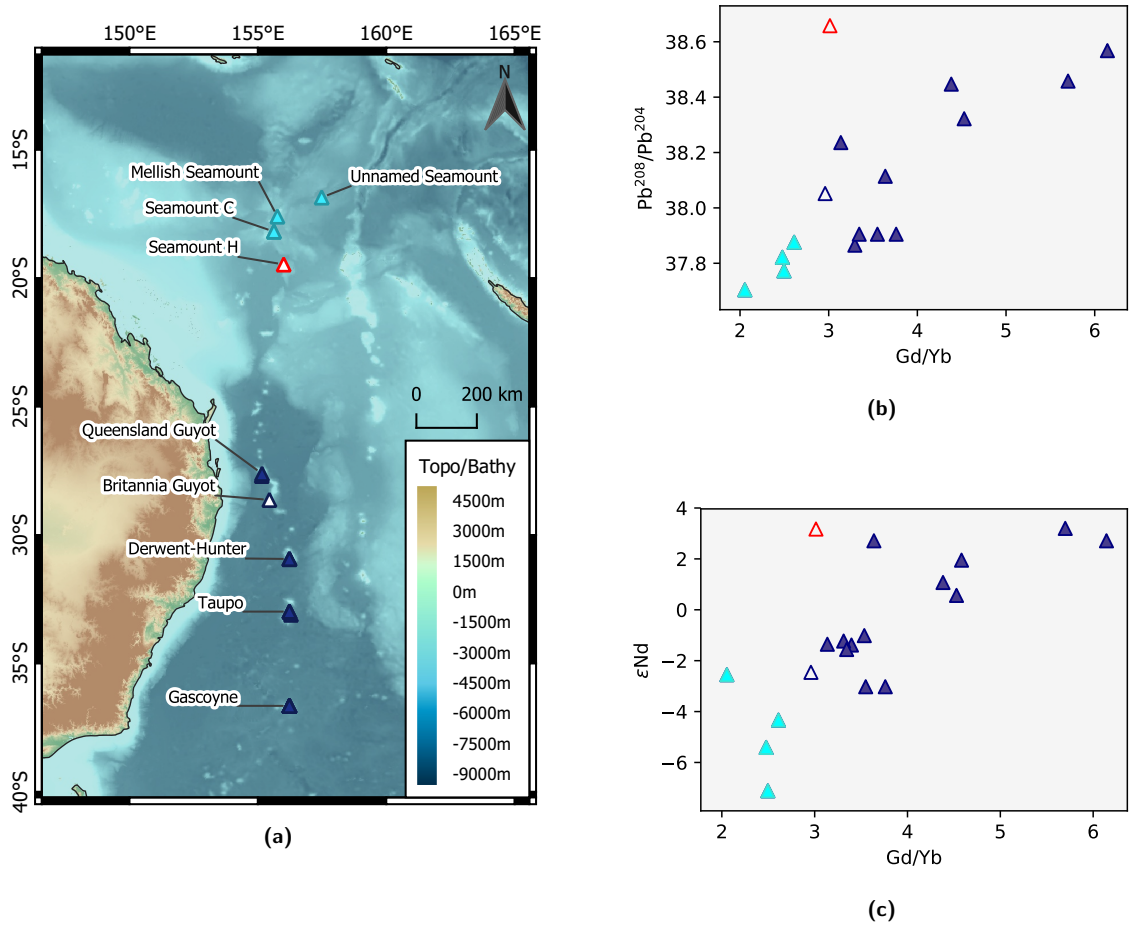

Figure 4.24: *(a) Map showing the Tasmantid samples analysed by Ruttor (2021) where cyan = northern Tasmantids, navy = southern Tasmantids, open navy = Britannia Guyot, red = Seamount H. The same samples are plotted showing an increase in Gd/Yb with (b) increasing $^{208}Pb/^{204}Pb$, and (c) increasing εNd. Samples which have undergone the highest degrees of melting primarily come from the northern end of the chain where lithosphere thickness was lowest at the time of emplacement, and also from the Britannia Guyot which may have been affected by a higher mantle Tp.*

The results discussed here are similar to those obtained by Zhang et al. (2001) where a deep EMI-like mantle plume appears responsible for most age-progressive volcanism across the East Australian chain alongside sporadic lava field-type eruptions from depleted mantle and varyingly metasomatised SCLM-derived melts. Here I have been able to compare these inferences with similar correlations in immobile Nb-Zr-Y concentrations, and with comparison to Tasmantid seamount isotope data from Ruttor (2021). To assess the EMI-plume-like source further one can consider the Tasmantid samples alone as they show a good correlation between depths of melting and isotopic ratios.

The locations of the Tasmantid seamounts analysed by Ruttor (2021) are shown in Figure 4.24a. Whilst there are some gaps in data sampling, a faint north versus south trend appears to be present when plotting pairs of isotope ratios against one another. This is consistent with evidence that the degree of melting decreases moving south through the Tasmantid chain. This trend is much better refined when plotting isotope results versus Gd/Yb, or any other LREE/HREE pair (Figures 4.24b and 4.24c). Samples with the lowest $^{208}Pb/^{204}Pb$ (along with other Pb-isotope ratios) and εNd include those from the north of the chain which were emplaced onto some of the thinnest oceanic lithosphere, and also one sample from the Britannia Guyot which is thought to have been the product of a higher mantle Tp (see Figure 4.14) i.e., both were produced by higher degrees of partial melting.

The same correlation with degree of melting is shown in Figure 4.25a where samples from the north of the chain and the Britannia Guyot trend towards EMI-type mantle. High degrees of partial melting correlate with low radiogenic Pb, low radiogenic Nd, lower ΔNb, lower Nb/La, and lower U/Pb (Figures 4.25 and 4.26). The most logical explanation for such results is that the Tasmantids are sourced from a deep EMI-type plume, isotopically enriched but compared with other OIB-type volcanism, less enriched in Nb. Higher degrees of partial melting of this source region then produces basalts with elevated Pb-Sr-enrichment and lower ΔNb and Nb/La. It is also possible, that the enrichment of the source region diminishes over time so that the older seamounts formed by high degrees of partial melting of the EMI-type plume have some of the highest Pb-Sr-enrichment, whilst the younger seamounts, formed later by lower degrees of partial melting of the same plume have considerably lower Pb-Sr-enrichment.

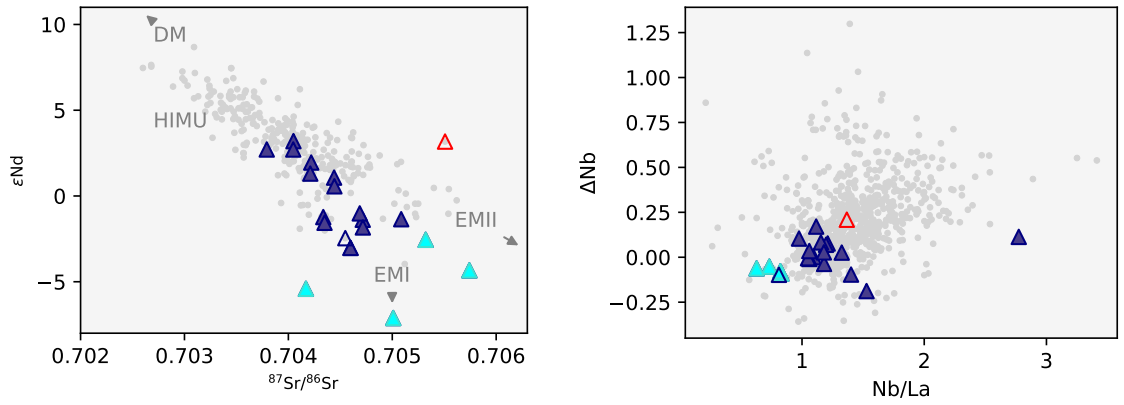

Figure 4.25: *(a) εNd versus $^{87}Sr/^{86}Sr$ and (b) ΔNb vs Nb/La showing the Tasmantid samples analysed by Ruttor (2021). High degrees of melting (low Gd/Yb) appear to correlate well with an EMI signature and also low Nb. One sample which does not follow this trend is from Seamount H which has Gd/Yb = 3.014, high radiogenic Pb, Nd, and Sr, and also high Nb (high ΔNb and Nb/La). One possible explanation might be that these melts have been influenced by the continental lithosphere of the nearby Lord Howe Rise.*

One sample which does not follow the trends identified here comes from Seamount H and has Gd/Yb = 3.014, higher radiogenic Pb, higher radiogenic Nd, and also higher Nb (ΔNb and Nb/La). One possible explanation for this anomalous result might be that these melts have been influenced by the continental lithosphere of the nearby Lord Howe Rise. This could perhaps be checked by analysing the sample alongside others from the Lord Howe chain, which should also show signs of interaction with the Lord Howe Rise continental lithosphere. This would be an interesting area for further work.

By converting U/Pb to $^{238}U/^{204}Pb$ and plotting $^{206}Pb/^{204}Pb$ versus $^{238}U/^{204}Pb$ I have calculated an age that derives from the EMI-type source (Figure 4.26a). The estimated age lies between 300–450 Ma but exactly what the age refers to is uncertain. Perhaps, if the EMI-type plume originated from a subducted slab

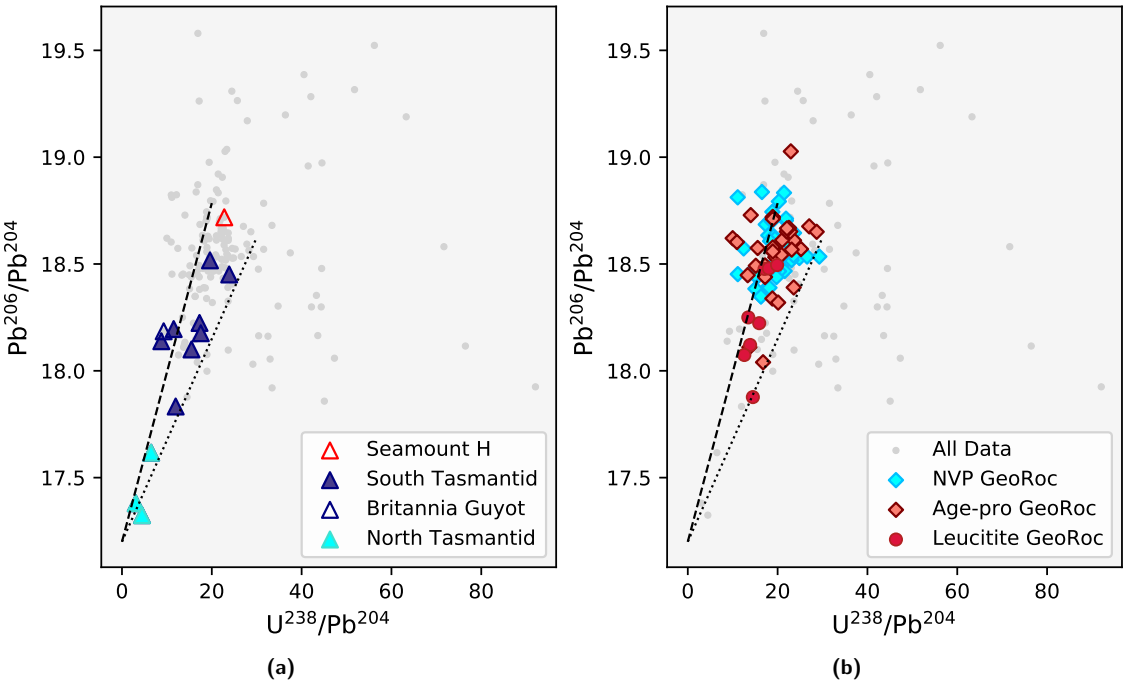

Figure 4.26: *(a) $^{206}Pb/^{204}Pb$ versus $^{238}U/^{204}Pb$ calculated for the Ruttor (2021) Tasmantid samples and corrected for degree of melting. The dashed black line represents 450 Ma and the dotted black line 300 Ma. Seamount locations given in Figure 4.24a. (b) $^{206}Pb/^{204}Pb$ versus uncorrected $^{238}U/^{204}Pb$ calculated for other age progressive provinces.*

then this may represent the age of the slab itself but this has not been assessed any further in this thesis and is instead left open for discussion. Interestingly, from Figure 4.26b, onshore age-progressive volcanoes have similar $^{206}Pb/^{204}Pb$ versus $^{238}U/^{204}Pb$ trends, suggesting they may come from a similar source with an age of around 300–450 Ma. Most other continental volcanoes plot outside these lines, where high $^{206}Pb/^{204}Pb$ samples derive from Tasmania, and high $^{238}U/^{204}Pb$ samples derive from far north Queensland.

4.3 Conclusions

Major element, trace element and isotopic modeling of Cenozoic basalts across east Australia suggest a complex range of source compositions involving DM, EMI, EMII and HIMU mantle reservoirs. The Tasmantid seamounts and continental central volcanoes are found to represent the highest degree melts. The continental lava field and leucitite suites generally represent smaller melt fractions. As modeled in Figures 4.13 and 4.25, the Tasmantid seamounts are likely sourced from an EMI-type mantle plume, originating >70 km depth, with moderate incompatible element enrichment, typical of OIB-type basalts, and where F_{max} is primarily controlled by lithosphere thickness and to a lesser extent, potentially by changes in mantle Tp. On a plot of Nb/Y vs Zr/Y, the Tasmantids plot along the ΔNb=0 line of Fitton et al. (1997) (Figure 4.27b). The simplest explanation for greater trace element enrichment and isotopic variations away from Tasmantid compositions, is that they relate to varying interaction with metasomatically enriched SCLM. Smaller variations in each suite may also be explained by changing mantle Tp over time or increased influence of the depleted mantle. When $Zr/Y < \sim 16$, increasing Nb/Y may be adequately explained by increased melt contribution from the SCLM. This has been highlighted in Figure 4.27b, where samples laying along the brown dotted line are thought to originate primarily from a deep plume-like source, i.e., the Tasmantid Seamounts, and samples laying along the red dotted line are thought to be derived primarily from SCLM melts, such as the single-pulse, lava field-type basalts. Between these two lines, samples appear to be a mix of asthenospheric and SCLM melts, such as the NVP basalts and the leucitites.

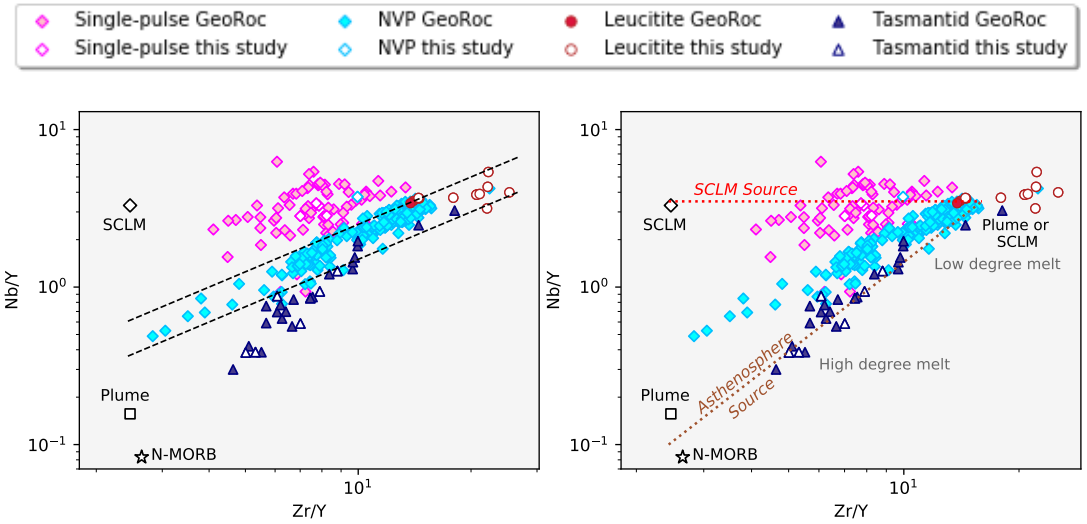

Figure 4.27: *Nb/Y versus Zr/Y showing three of the main groups identified in this study as having different sources including: (1) single-pulse, lava field-type volcanism emplaced between 66–10 Ma; (2) young volcanism from the NVP and the leucitite chain; (3) the Tasmantid Seamounts. Black symbols shows the rough position of mantle end-members where for high degree melts, an N-MORB source (star) is represented by the depleted mantle (DM) end-member from Sun and McDonough (1989); a plume-like source (square) is represented by the primitive mantle (PM) end-member from Sun and McDonough (1989); and an SCLM (diamond) source is arbitrarily placed using the results of this study. For low degree melts, the Nb/Y-Zr/Y signatures of basalts from both plume and SCLM sources have similar values but such high enrichments are not expected to originate from low degree melting of N-MORB. Figure (a) shows the bounds that best separate the three groups as dashed black lines. The lower bound has a gradient of 0.15, and the upper bound has a gradient of 0.25. Samples plotting between these two lines are expected to represent both plume and SCLM melts. Figure (b) shows the same plot annotated with inferred sources. Samples laying along the brown dotted line are thought to originate primarily from a deep plume-like source with an EMI isotopic signature. Samples laying along the red dotted line are thought to be derived primarily from SCLM melts. The placement of the red line is rather arbitrary, but the principle point stands that when $Zr/Y < 16$, increasing Nb/Y can be attributed to an increasing influence of both a plume source, and with more extreme values, the SCLM. Most samples plotting above $Zr/Y = 16$ are the highly enriched leucitites and these are also the only samples to plot below the $\Delta Nb{=}0$ line of Fitton et al. (1997), much like the Western US lamproites, studied by Fitton (2007).*

Chapter 5

The Leucitite Chain



Figure 5.1: *Leucitite sample from Byrock Quarry, NSW. Visible phlogopite phenocrysts up to 9mm in length.*

5.1 Introduction

The Cenozoic leucitite rocks of eastern Australia represent, rare leucite-phlogopite-bearing minor intrusions and flows that are found only in central New South Wales and Victoria (Wellman and McDougall, 1974a; Cundari, 1973; Nelson et al., 1986; Paul et al., 2005). K/Ar and $^{40}Ar/^{39}Ar$ results from the leucitites show a clear southward younging age trend, from Byrock in northern NSW to Cosgrove in northern Victoria (Figures 5.2 and 5.3), contemporaneous with the continental central volcanoes, and the Tasmantid and Lord Howe seamount chains (Wellman et al., 1970; Cohen et al., 2008, 2013; Kalnins et al., 2015; McDougall and Duncan, 1988; Seton et al., 2019a; Mortimer et al., 2010; Quilty, 1993). An extension of this linear chain can be traced further north to the central volcanoes of central Queensland and this belt has been collectively named the Cosgrove hotspot track by Davies et al. (2015). Here I present evidence that this track may extend further still to the southerly Macedon-Trentham central volcano and the Newer Volcanic Province (NVP) lava field in Victoria. The leucitites themselves record age progression from around 17.9–8.9 Ma (Cohen et al., 2008). The Macedon-Trentham central volcano has been dated at around 6.16–5.83 Ma and the NVP has been dated at around 7.93–0 Ma (Cohen, 2007; Ewart et al., 1985; Heath et al., 2020; Blackburn et al., 1982). The youngest volcanism within the NVP has taken place on its western edge at Mount Gambier (Blackburn et al., 1982).

The source of the leucitites remains a popular area of debate, although a lithospheric origin is generally preferred. Factors pointing towards subcontinental lithospheric mantle (SCLM) involvement include; (1) high enrichments which are only observed in continental samples; (2) good correlations (LILE enrichment, low εNd, high $^{87}Sr/^{86}Sr$) between the leucitites and lithospheric xenolith compositions (e.g. Griffin and O'Reilly, 1986; O'Reilly and Griffin, 1988; O'Reilly and Zhang, 1995); (3) significant LILE anomalies in the leucitites that lie on the thickest continental lithosphere; and (4) K > Na which cannot be achieved through partial melting of normal mantle or fractional crystallisation alone. The presence of these rocks above an interpreted Proterozoic rift system has also been described by Ewart et al. (1988) as evidence of a lithospheric source. However, the southward younging age trend coeval with other volcanism in eastern Australia has been suggested as evidence of an asthenospheric plume source. If this were the case, at least four plumes would be needed to explain the southward migration of the leucitites, the central volcanoes, and the Tasmantid and Lord Howe seamount chains, each separated by a lateral distance of ∼500 km.

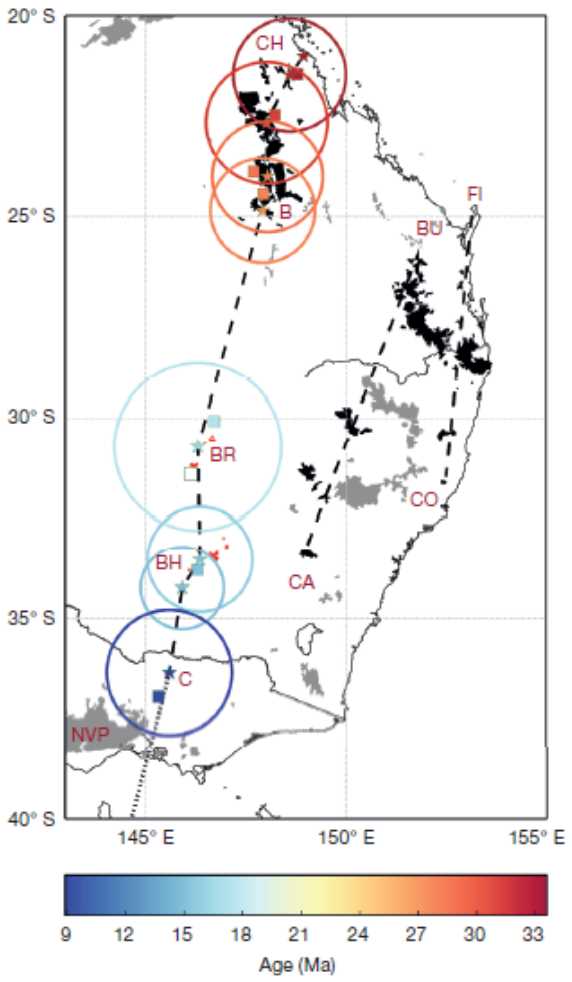

Figure 5.2: *The Cosgrove hotspot track from Davies et al. (2015). BR = Byrock, C = Cosgrove.*

The origin of the NVP is even less clear and incompatible element and Sr-Nd-Pb isotope results from various authors show complex patterns possibly representative of a number of mantle sources including: (1) a deep asthenospheric plume-like component (e.g. Davies et al., 2015; McDonough et al., 1985); (2) a shallow asthenospheric MORB-like component (e.g. Zhang et al., 2001; Sutherland, 2003); and (3) a metasomatised SCLM component (e.g. Ewart et al., 1988; Zhang et al., 2001) (Figure 2.6). More recently, a number of authors have suggested that the geochemical and geophysical characteristics of the NVP may relate to upwelling of the asthenosphere by edge-driven convection along the boundary between continental and oceanic lithosphere (Demidjuk et al., 2007; Price et al., 2014; Davies and Rawlinson, 2014; Boyce et al., 2015, e.g.). For this study I have gathered geochemical analyses, including samples collected during fieldwork in 2019, from across the leucitite chain, the Macedon-Trentham central volcano, and the NVP in order to compare their respective sources.

5.2 Results and Discussion

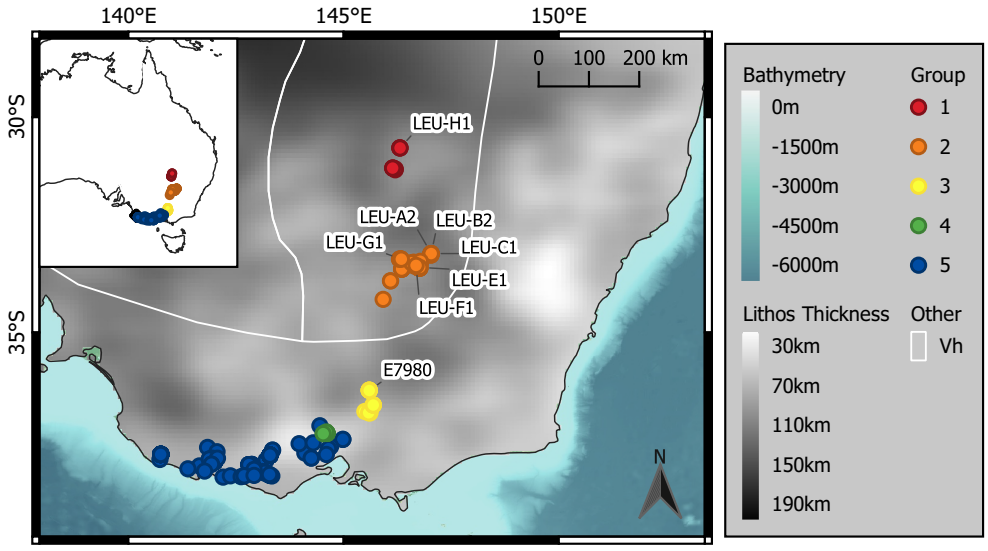

Figure 5.3: *Location of the leucitite, Macedon-Trentham central volcano and Newer Volcanic lava field samples. Leucitite samples analysed in this study are labelled, those collected on fieldwork in 2019 are labelled as LEU-. Samples not labelled are those collected from literature. Lithosphere thickness estimates (depth to the lithosphere-asthenosphere boundary, LAB) are derived from body wave tomography by Rawlinson et al. (2017). White lines mark distinct changes in lithospheric velocity (Vh) as defined by horizontal velocity gradients through the surface wave model of Fishwick et al. (2008). These probably relate to changes in age and composition of the underlying lithosphere. Temporally, spatially, and chemically, it appears that the leucitites may be related to recent lava field and central volcano eruptions throughout Victoria, as well as central volcano volcanism in central Queensland. In order to analyse this, I have split these rocks into five groups; (1) Red = northern leucitites located on the oldest, thickest lithosphere; (2) Orange = middle leucitites located close to the transition between older and younger lithosphere; (3) Yellow = southern leucitites and Euroa NVP basalts from Paul et al. (2005) both located on lithosphere of similar age and thickness; (4) Green = Macedon-Trentham central volcano, the only compositionally bimodal province in Victoria; (5) Blue = NVP lava fields. Bathymetry from GEBCO (2020). Data filtered to samples with MgO > 7 wt% and LOI < 3 wt%.*

The location of leucitite samples analysed in this study, and those samples taken from literature are shown in Figure 5.3. Geochemically, the leucitites are characterised by high K, Ti and Mg and low Si, Al and Na with a mineral assemblage consisting of olivine, clinopyroxene, leucite, phlogopite and Fe-Ti oxides with occasional amphibole, alkali feldspar, apatite, perovskite and nepheline (Cundari, 1973). They also contain the highest levels of incompatible elements of all Australian Cenozoic volcanism. There is, however, some variation in incompatible element concentrations moving north-south along the chain. These distinctions appear to continue into the Macedon-Trentham central volcano and the Newer Volcanics lava field provinces in Victoria. To analyse this, I have divided the samples into five groups moving north to south through the chain (Figure 5.3). Primitive-mantle-normalised incompatible element and chondrite-normalised REE plots of each group, with the leucitite samples analysed in this study, are given in Figures 5.4 and 5.5. Most samples plot above the average OIB composition identified by Sun and McDonough (1989), whilst the leucitites themselves show considerable enrichments in Rb, Ba, Nb, Ta, K, Sr, Zr, Hf, and Ti.

All eight of the leucitite samples analysed are fairly primitive, with MgO > 7 wt%, and unaltered, with LOI < 2.23 wt%. Therefore, variations between incompatible element concentrations should be unrelated to AFC processes or weathering and alteration. Whlist the leucitites have traveled through very thick lithosphere, their small volume (Chapter 6) necessitates the need to have risen up to the surface relatively rapidly before they froze within the subsurface. With this, and the fact that the greatest enrichments are found in the most primitive samples, assimilation is expected to be fairly low in the leucitite rocks. Differences in incompatible elements could be due to changes in the degree of partial melting, although similar trends are seen in major rock-forming elements (Na and Al), which should remain relatively unaffected by degree of partial melting. Partial melting will, however, have an effect on major element concentrations of the residual mantle. For example, Ca, Na, and Al will be removed through the generation of basalt, leaving the source depleted in these elements. The more partial melting takes place i.e., in older continental lithosphere, the greater the degree of depletion.

The unique, yet uniform, chemistry of the leucitite lavas suggests they derive from a common source region, which is mineralogically distinct to other east Australian volcanic sources. This is interpreted by Cundari et al. (1978) and Ewart et al. (1988) to be dominantly garnet-, clinopyroxene-, olivine-, and phlogopite-bearing and >100 km depth. The presence of phlogopite phenocrysts, up to 9mm long, coupled with Th-U depletions, and Rb, Ba, K enrichments, likely reflects melting of a phlogopite-rich source.

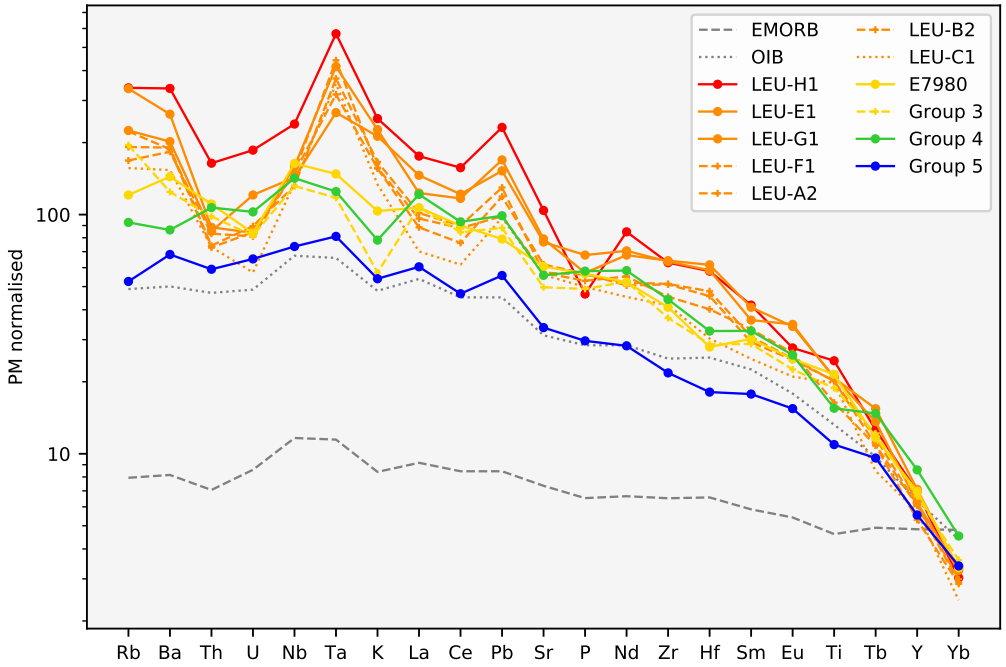

Figure 5.4: *Primitive mantle (PM)-normalised multi-element plot of incompatible elements for leucitite and Victoria samples. For groups 3, 4 and 5, element concentrations of all samples have been averaged and normalised to PM values from Sun and McDonough (1989). Average values for OIB and EMORB also from Sun and McDonough (1989). Samples collected on fieldwork in 2019 are labeled as LEU-.*

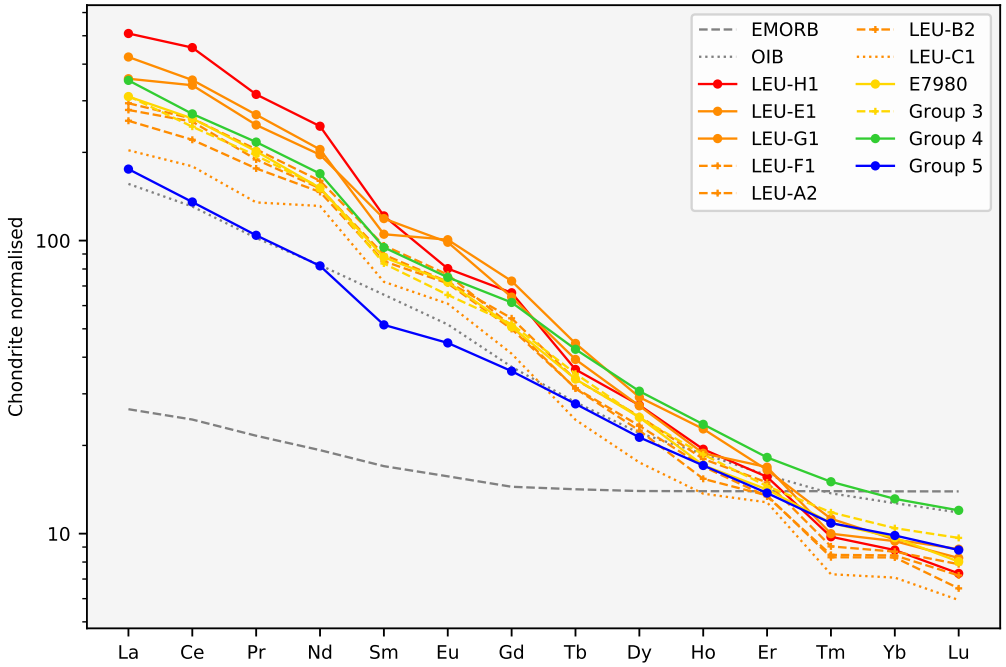

Figure 5.5: *Chondrite-normalised REE plot for leucitite and Victoria samples. Normalising values and average composition of OIB and EMORB from Sun and McDonough (1989).*

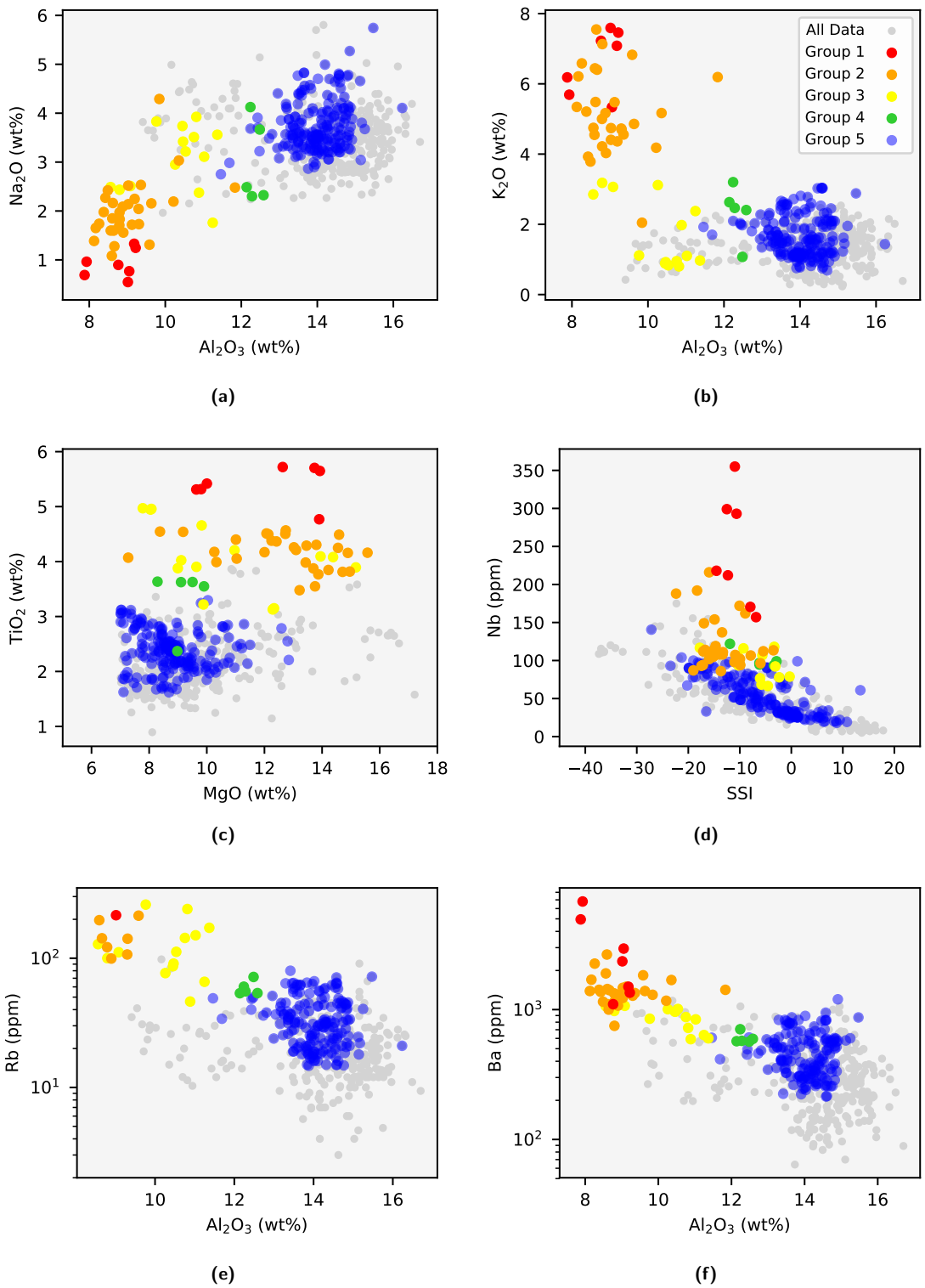

Figure 5.6: *(a) Na_2O vs Al_2O_3, (b) K_2O vs Al_2O_3, (c) TiO_2 vs MgO, (d) Nb vs SSI, (e) Rb vs Al_2O_3, and (f) Ba vs Al_2O_3; each showing the five groups identified in Figure 5.3 (groups 1-5 arranged from north to south). All samples have MgO $>$ 7 wt% and LOI $<$ 3 wt%. The north-south trend observed in Figures 5.4 and 5.5 are again mirrored in Na, Al, K, Ti and Mg concentrations. Generally, moving south through the chain, samples are consistently primitive (high MgO; although it does look like average MgO decreases slightly as you move south) whilst incompatible element concentrations gradually decrease (both in HFSEs and LILEs). As an incompatible HFSE, Ti also decreases. Interestingly, this correlates with a southward increase in Al and Na i.e. the leucitite source is showing progressive southward-enrichment in these elements. The most likely explanation is that, moving south, the rocks are increasingly sourced from the asthenosphere; the lithosphere is probably depleted via the removal of mafic partial melts.*

Within Figures 5.4, 5.5 and 5.6 there is a clear, progressive decrease in incompatible element concentrations moving south through the leucitite chain. Of note, this decrease also correlates with a increase in Na and Al (Figure 5.6a) and does not correlate with SSI and degree of melting (Figure 5.6d). The intrinsic difference between lithosphere and asthenosphere is that of depletion and enrichment and Griffin et al. (2009) have reported that older, thicker, lithospheric mantle is expected to be more depleted in clinopyroxene and garnet than younger counterparts, resulting in a depletion of Ca, Al and Na due to the ancient removal of mafic melts. As discussed in Section 2.1, the SCLM beneath Australia thins southwards along the leucitite chain to the exterior of the continent. It is possible the northernmost leucitites are situated on older, thicker, and more depleted lithosphere than the NVP at the edge of the continent, or the involvement of the asthenosphere may increase moving south, or both. The most likely explanation for the depletion in Na and Al is that the source of the leucitites is lithospheric, and that the SCLM has been depleted in these elements via partial melting and subsequently re-enriched in incompatible trace elements via mantle metasomatism.

It is quite possible the SCLM in Eastern Australia has been considerably altered by various forms of metasomatism over the course of its history, as discussed by numerous authors (e.g. Griffin et al., 1988; O'Reilly and Zhang, 1995; Yaxley et al., 1998). Such high concentrations of HFS and LIL elements in the leucitites (Figure 5.6e and 5.6f), which correlate with lithospheric thickness and Na-Al depletion, are likely to be the result of an initially depleted, then carbonate-metasomatised SCLM. Carbonate metasomatism is a plausible explanation because of the high concentrations of e.g. Nb and the lack of depletion of Ca, which would initially have been depleted in the SCLM. Small degrees of melting of these enriched areas at the base of thick, phlogopite-rich SCLM would produce primitive leucitite melts, small in volume, which were able to rise to the surface relatively rapidly (McKenzie, 1989). Moving south, melts become less Na, Al depleted and less enriched in incompatible elements, possibly due to greater dilution with less enriched asthenospheric melts as lithosphere thickness reduces. Similar trends are observed in Pb-Sr-Nd isotope data, as shown in Figure 5.7. On both plots, NVP-leucitite data trend towards more enriched endmembers following a parallel array to OIBs and continental basalts. In $^{206}Pb/^{204}Pb$–$^{208}Pb/^{204}Pb$ space leucitites trend towards the EMI endmember and in εNd–$^{87}Sr/^{86}Sr$ space they trend towards both EMI and EMII endmembers. Ancient depletion of the SCLM through melt removal would have resulted in a lowering of U/Pb and Th/Pb, meaning older lithosphere (northern leucitites) will have more unradiogenic Pb, and younger lithosphere (southern leucitites) will have less unradiogenic Pb. However, the trend towards unradiogenic Nd is difficult to explain by partial melting of the SCLM as Sm/Nd should increase with more prolonged melt removal. The northernmost leucitites, groups 1 and 2, actually have $^{143}Nd/^{144}Nd$ ratios less than bulk earth, i.e., εNd is less than 0.

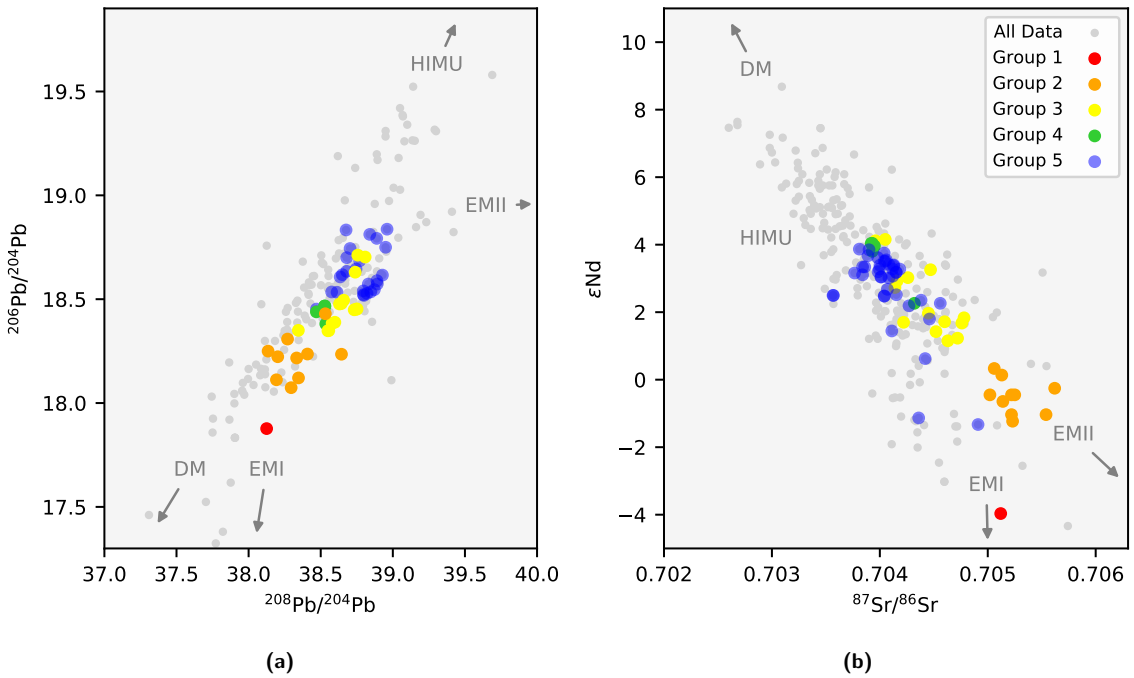

Figure 5.7: *(a) $^{206}Pb/^{204}Pb$ versus $^{208}Pb/^{204}Pb$ and (b) εNd versus $^{87}Sr/^{86}Sr$ for the five groups identified in Figure 5.3, again showing a S-N trend towards unradiogenic Pb and Nd in the NVP and leucitite rocks.*

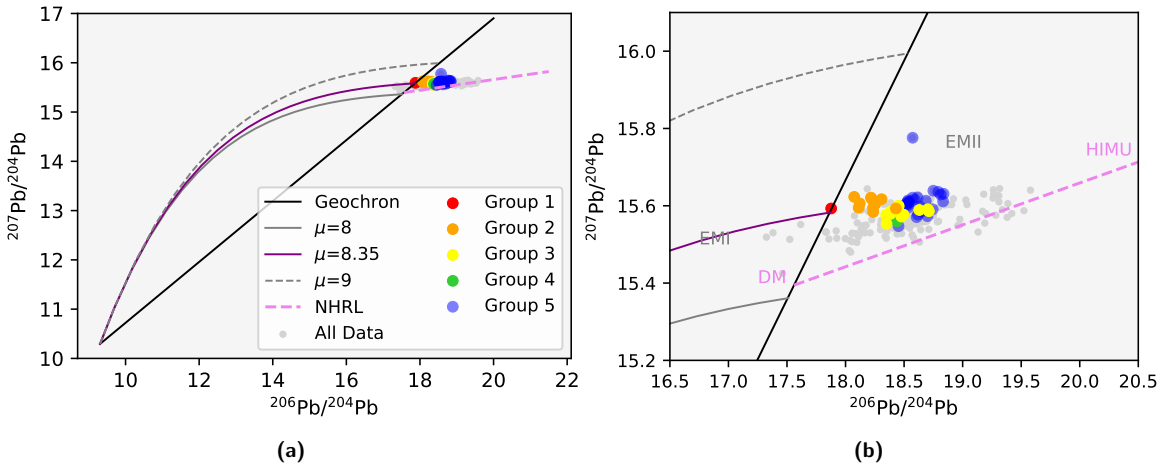

Figure 5.8: *(a) $^{207}Pb/^{204}Pb$ versus $^{206}Pb/^{204}Pb$ plotting each of the five groups alongside the Geochron, growth curves ($\mu = 8, 8.35, 9$), and the Northern Hemisphere Reference Line (NHRL). Moving south along the chain samples trend away from the Geochron, left to right, and appear to define a mixing array between EMI, EMII, and PREMA. All leucitite and NVP samples plot above the NHRL. (b) The same plot zoomed in.*

Figure 5.8 shows $^{207}Pb/^{204}Pb$ versus $^{206}Pb/^{204}Pb$ for each of the five groups plotted alongside the Geochron, three growth curves with $\mu = 8$, 8.35 and 9, and the Northern Hemisphere Reference Line (NHRL). The Geochron represents the simultaneous evolution of radiogenic ^{206}Pb and ^{207}Pb in a single-stage system where no disturbance or resetting of Pb has occurred since 4.55 Ga. Growth curves, given by Equations 5.1 and 5.2, relate to the change in $^{207}Pb/^{204}Pb$ and $^{206}Pb/^{204}Pb$ over time as defined by their decay rates (Equations 5.3 and 5.4). Different growth curves are plotted for different μ values which correspond to the amount of ^{238}U and ^{204}Pb in the system initially (Equation 5.5). If a Pb reservoir has remained closed for it's entire history then no matter what value of μ is used, samples of similar ages should plot along the same isochron, the 0 Ga isochron is given by the Geochron. As shown in Figure 5.8, samples from east Australia all have excess $^{206}Pb/^{204}Pb$, much like other OIBs. The NHRL represents a linear mixing line between DM and HIMU mantle reservoirs. For the below equations, T = initial age, t = age, λ_1 = the decay constant of ^{235}U to ^{207}Pb, and λ_2 = the decay constant of ^{238}U to ^{206}Pb.

$$\left(\frac{^{207}Pb}{^{204}Pb}\right)_t = \left(\frac{^{207}Pb}{^{204}Pb}\right)_T + \frac{\mu}{137.88}\left(e^{\lambda_1 T} - e^{\lambda_1 t}\right) \tag{5.1}$$

$$\left(\frac{^{206}Pb}{^{204}Pb}\right)_t = \left(\frac{^{206}Pb}{^{204}Pb}\right)_T + \mu(e^{\lambda_2 T} - e^{\lambda_2 t}) \tag{5.2}$$

$$\lambda_1 = 0.984850 \times 10^{-9} yr^{-1} \tag{5.3}$$

$$\lambda_2 = 0.155125 \times 10^{-9} yr^{-1} \tag{5.4}$$

$$\mu = \left(\frac{^{238}U}{^{204}Pb}\right) \tag{5.5}$$

Like other OIBs, none of the leucitite samples, bar one, fall along the Geochron. The position of the Group one leucitite on the Geochron is presumably fortuitous as other groups instead trend near-horizontally with little variation in $^{207}Pb/^{204}Pb$. This suggests that the samples do not define a stage two isochron, as very recent enrichment with a near-horizontal trend cannot produce an isochron. It is much more likely these samples define a mixing array between EMI, EMII and PREMA. This agrees with previous interpretations that the leucitite-NVP trend represents mixing between an EMI-PREMA-type mantle plume and metasomatised SCLM with an EMI-EMII-type signature. In this case, samples hailing from the PREMA reservoir appear to have elevated $^{207}Pb/^{204}Pb$ above the NHRL, much like the DUPAL anomaly of Hart (1984) and Dupré and Allègre (1983) which suggests the deep, prevalent mantle underlying much of eastern Australia is DUPAL-like. Similar hypotheses have been mentioned by other authors (e.g. Zhang et al., 2016).

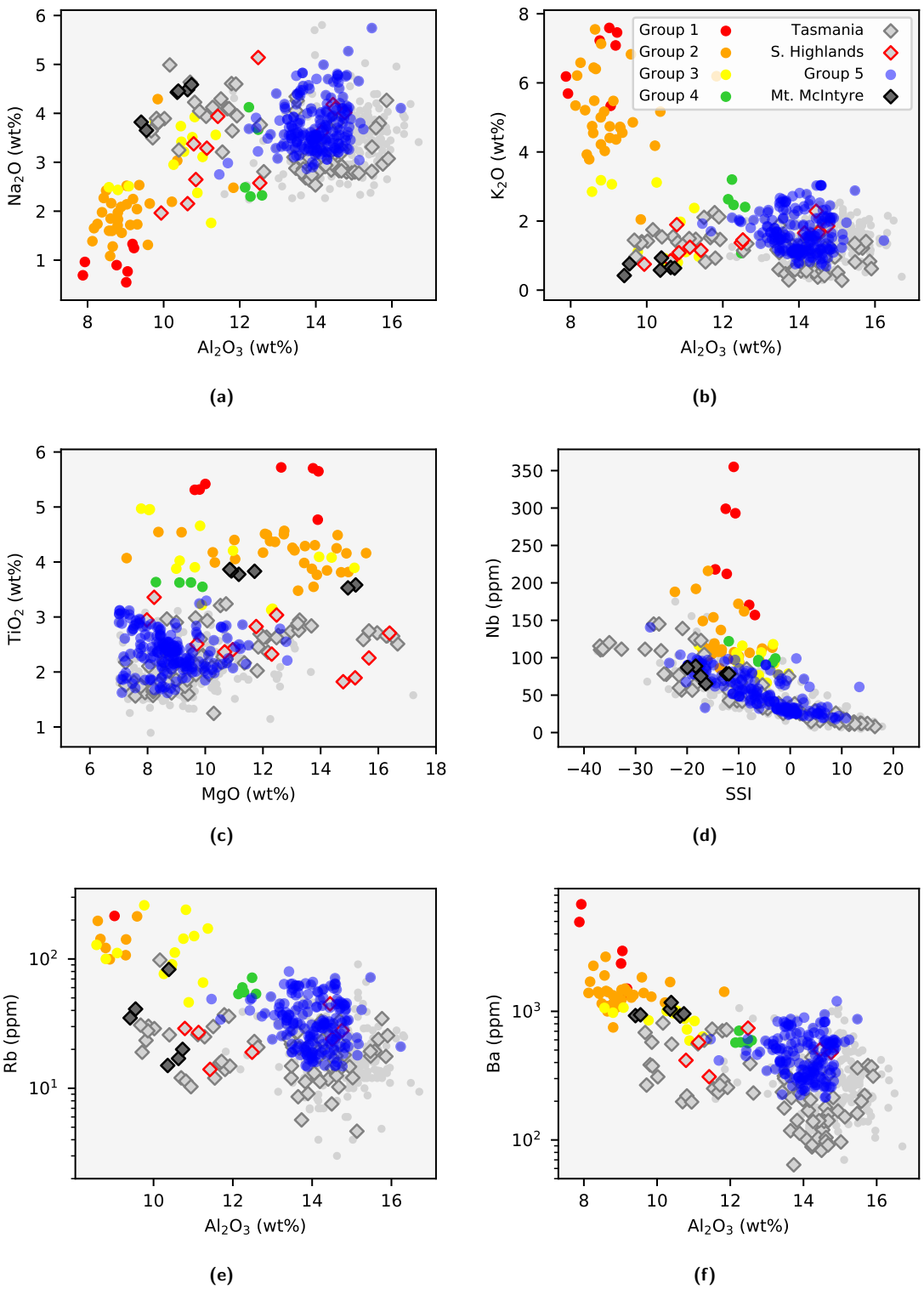

Figure 5.9: *Figure 5.6 with additional data added. (a) Na_2O vs Al_2O_3, (b) K_2O vs Al_2O_3, (c) TiO_2 vs MgO, (d) Nb vs SSI, (e) Rb vs Al_2O_3, and (f) Ba vs Al_2O_3; each showing the five groups identified in Figure 5.3 (groups 1-5 arranged from north to south). Also showing Tasmania samples as grey diamonds, samples from the Southern Highlands in NSW as red diamonds, and samples from Mount McIntyre in South Australia as black diamonds (Mount McIntyre analyses are from Foden et al. (2002) and McDonough et al. (1985)). All samples have $MgO > 7$ wt% and $LOI < 3$ wt%. Rocks from these locations show the same Al and Na depletion and the same Mg enrichment as the leucitites. Mt McIntyre samples also show considerable Ti enrichments, much like the leucitites. Mt McIntyre and Tasmania are also close to the boundary between the eastern Lachlan Fold Belt and the western Kanmantoo Fold Belt (e.g. Paul et al., 2005; Foden et al., 2002; Gaul et al., 2003; Kennett et al., 2004) and it is possible these differences are inherited from differences in SCLM composition between the two fold belts. Although this is less applicable to the Southern Highlands province.*

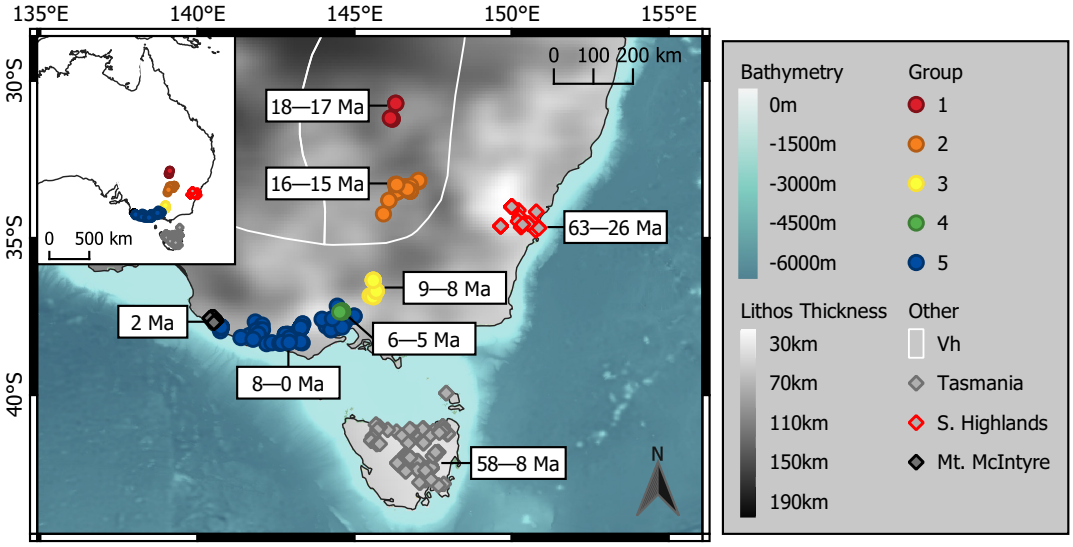

Figure 5.10: *Location of the five groups identified in Figure 5.3 alongside Mount McIntyre samples as black diamonds, Southern Highland as red diamonds, and Tasmania as grey diamonds. Age ranges of each group are displayed in the white boxes. All samples show considerable depletions in Al_2O_3 content and to some degree Na_2O, especially in high MgO samples (>12 wt%) (Figure 5.9). Most Southern Highland and Tasmania rocks were erupted much earlier than the leucitite, NVP, and Mt McIntyre volcanics and as such, these characteristics are most likely related to derivation of the lavas at different times, from an already Al-depleted SCLM. Mt McIntyre, Southern Highland, and Tasmania do not show quite the same LILE and HFSE enrichment as the leucitites and NVP, possibly owing to different levels of metasomatic enrichment in the underlying SCLM. Lithosphere thickness estimates are again from Rawlinson et al. (2017), horizontal velocity gradients (Vh) from Fishwick et al. (2008), and bathymetry from GEBCO (2020). Filtered to samples with MgO >7 wt% and LOI <3 wt%.*

Further evidence for an SCLM contribution is highlighted in Figure 5.9. Samples from Tasmania, the Southern Highlands in NSW, and Mount McIntyre in South Australia (Figure 5.10) show similar depletion in Al and Na, and enrichment in Mg and Ti as groups two, three and four. However, they do not show quite the same LILE and HFSE enrichment. $^{143}Nd/^{144}Nd$ and $^{87}Sr/^{86}Sr$ isotope data from Mt McIntyre are similar to other group three, four, and five samples (Figure 5.11). Isotope data from Tasmania trend between DM, HIMU, and PREMA reservoirs whilst data from the Southern Highlands trends between DM, and EMI. No Pb isotopes exist for Mt McIntyre or the Southern Highlands. Pb isotope data from Tasmania are highly radiogenic trending towards HIMU.

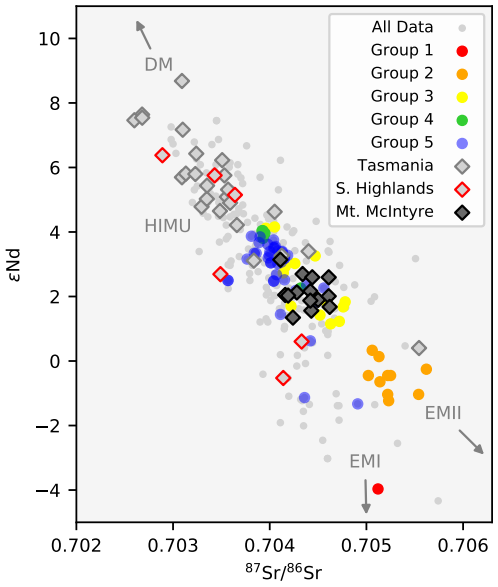

Figure 5.11: *εNd versus $^{87}Sr/^{86}Sr$ again showing the five groups identified in Figure 5.3, alongside samples from Tasmania, the Southern Highlands province, and Mount McIntyre in SA.*

Given such considerable changes in major and trace element geochemistry over relatively short distances, and given age correlations between these samples, it is difficult to account for these results with multiple different sources but much easier to relate to the changing composition of the SCLM locally. Marked changes in SCLM are likely to relate to variations in the overlying crust and throughout the Paleozoic the east coast of Australia underwent successive cycles of subduction, compression and arc volcanism, the products of which collectively make up the Tasman Fold Belt (TFB). The six main units of the TFB are shown in Figure 5.12 where the Tasman Line represents the boundary between Proterozoic and Phanerozoic lithosphere. The exact position of this and the contacts between each fold belt vary slightly between interpretations (e.g. Kennett et al., 2004). However, both Mt McIntyre and Tasmania samples are likely to lie very close the boundary between the Kanmantoo and Lachlan Fold Belts.

It is likely that the quantity of metasomatic melt that has frozen within the younger parts of the continental lithosphere is smaller than that beneath the Archaean cratons, with that beneath the oceans being smaller still (McKenzie, 1989). Therefore, depletions in Al and Na, and enrichments in incompatible elements through metasomatism may be more evident in rocks laying on older SCLM. This would include the leucitites which lie further into the interior of the continent on some of the oldest lithosphere, and the Mt McIntyre and Tasmania rocks which lie on the Kanmantoo Fold Belt. The same cannot be said for samples from the Southern Highlands, but it is certainly possible that the SCLM in this area has also been more affected by partial melting than surrounding provinces or other provinces incorporated more asthenospheric melts which would not be depleted in Al. Interestingly, a similar conclusion was reached by Foden et al. (2002), Wass (1980), Meeuws et al. (2019), Nasir et al. (2010), Adam (1990), and Price et al. (1997) who studied rocks from Tasmania, the Southern Highlands, and the NVP. Each author attributed variations in isotope and trace element data to influences of metasomatised SCLM. Here I have compared these provinces with other rocks from the East Australian volcanic chain and shown how the same variations are reflected in major element concentrations. All samples discussed here as showing unusual enrichment represent primitive, small degree melts, with MgO often greater than 12, and La/Yb $>$ 20.

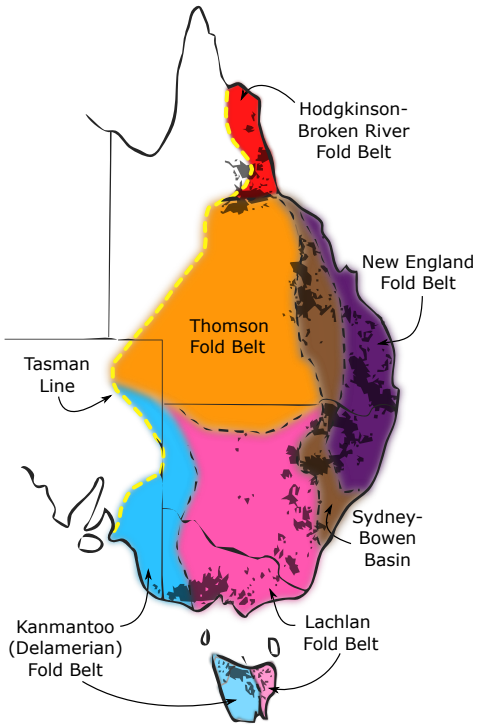

Figure 5.12: *The six main units of the TFB, modifed after Crawford et al. (2003).*

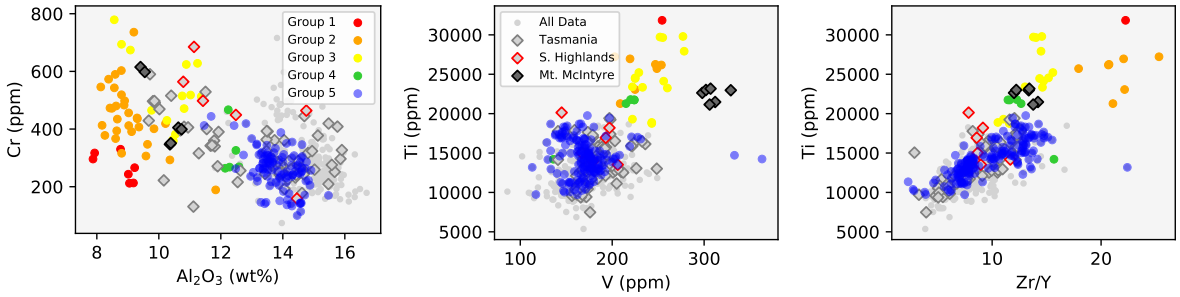

Figure 5.13: *(a) Cr vs vs Al_2O_3, (b) Ti vs V, and (c) Ti vs Zr/Y; each showing the five groups identified in Figure 5.3, Tasmania, Southern Highlands, and Mt McIntyre samples (MgO $>$ 7 wt% and LOI $<$ 3 wt%).*

Given the minimal evolution, degree of melting, and alteration (LOI $<$ 3wt%) of these samples, source heterogeneity is the most likely candidate for the observed differences in major element concentrations. The simplest way to lower Al and Na in the source region would be through partial melting with enrichment of incompatible elements, particularly the mobile LILEs, via metasomatism. A study by Gaul et al. (2003) show that older lithosphere in southeast Australia is paralleled by higher MgO, lower CaO, lower Al_2O_3, high Cr, high Ti and Zr/Y. High Cr, Ti and Zr/Y have been related to the role of Cr-pyrope garnet in the SCLM. Other papers have also identified a Ti enrichment of metasomatised zones which is sourced from opx or cpx (e.g. McKenzie, 1989; Niu et al., 2012). High MgO and low Al_2O_3 of the leucitites have been shown in Figure 5.6 but high Cr is only observed in Groups three and four (Figure 5.13a). Groups one to five and Mt McIntyre show enrichment in Ti that to some extent parallels an increase in V (Figure 5.13b) and Zr/Y (Figure 5.13c). Whether these trends are reflecting the involvement of pyroxene or garnet in the SCLM or whether they relate to the type of metasomatism the SCLM has been subject to remains uncertain.

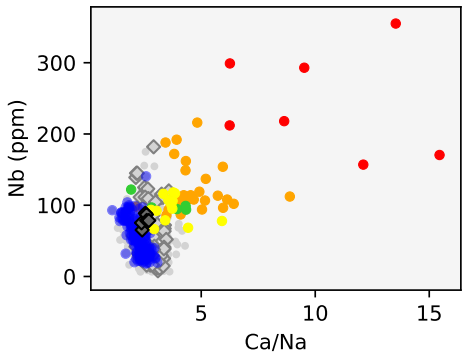

Figure 5.14: *Nb vs Ca/Na for each of the five groups identified in Figure 5.3, as well as Tasmania and Mt McIntyre samples (MgO > 7 wt% and LOI < 3 wt%).*

In Figure 5.14 there appears to be a clear distinction between Groups 1–2 and all other Groups in Nb and Ca/Na. It is likely this enrichment in Nb and Ca are the product of carbonate metasomatism which has had a greater influence on the northernmost leucitites situated on older, thicker lithosphere. Partial melting would have meant Ca, Na, and Al was originally depleted in the source of the leucitites. Subsequent carbonate metasomatism would have reintroduced Ca to the rock whilst Na and Al remain low, which is what we see in these samples. The generation of small, enriched metasomatised zones has been explained in detail by McKenzie (1989) who suggest these K-rich areas are the first thing to melt with passage of a plume or raised Tp. The melting of such zones would also explain why the highly enriched leucitite provinces in east Australia are considerably smaller volume than the extensive NVP lava field. The latter of which is likely to have a greater influence from asthenospheric melts as it lies on thinner lithosphere. An asthenospheric plume source for the NVP had been advocated by Paul et al. (2005) and McBride et al. (2001) based on Pb-Nd-Sr-Os isotope data although the authors also mention that the exact distinction between the involvement of lithospheric and asthenospheric mantle contributions remains a difficult undertaking as both can manifest as a variety of incompatible trace element and isotope compositions.

5.3 Conclusions

A stationary sublithospheric hotspot best explains the southward age-progression observed in the leucitites but extreme enrichments coupled with major element depletions are most easily explained by melting of a depleted SCLM, re-enriched by metasomatic fluids. The passing of an EMI-type plume beneath lithosphere >130 km, as is the case beneath the leucitites, may be too deep to induce melting of the plume itself but raised temperatures would melt small, enriched metasomatised zones that have been frozen at the base of the lithosphere. The resulting lavas may be small in volume, particularly K-rich owing to phlogopite in the source region, depleted in the major elements Na and Al due to partial melting of the lithosphere over time, and enriched in incompatible elements via multiple types of metasomatism. The lavas would also inherit very little, if any, melt from the plume itself, owing to the lack of a considerable EMI isotopic signature observed in the leucitites. On thinner lithosphere the asthenospheric-plume contribution would be greater and SCLM melts more diluted but on thicker lithosphere the asthenospheric-plume contribution would be less and SCLM melts more readily detected (e.g. Humphreys and Niu, 2009). The highly enriched leucitites and moderately enriched NVP probably represent the products of both depleted and re-enriched SCLM and an enriched plume, where the contribution of each is controlled by lithosphere thickness and depth of melting.

Chapter 6

Volume Estimates



Figure 6.1: *Cape Hillsborough National Park, Queensland.*

6.1 Introduction

In conjunction with the geochemistry of erupted lavas, the volume of lava is often indicative off the mechanism operating behind-the-scenes to drive volcanism. In this study, I have used reconstructions of present-day volcanic outcrops to model both the preserved and original volume of each continental volcano within eastern Australia. The results of my analyses are given in Appendix I and show the preferred method from which each volume was calculated. These have largely been split between the central volcanoes and the lava fields. Given the considerable morphological differences between the central volcanoes and the lava fields, reconstruction of the original volume of each would require different workings which are discussed in respect to each province in the latter half of this Chapter.

Present-day extents of volcanism were assessed initially using remote sensing to highlight basaltic and silicic lavas with multispectral satellite data. The preserved volume of volcanic rock at each province was then calculated with the selection of an appropriate base. Following this, simple reconstructions were carried out in QGIS to infer the original extent, top, and base of each volcano. Multiple iterations were run with each consecutive extent, top, or base created and the results of all iterations may be viewed in Appendix I. These are discussed in more detail at the end of this Chapter and compared to the volumes results of Wellman (1971), Jones and Verdel (2015), and Van den Hove et al. (2017) to see how they may differ and why.

6.2 Results and Discussion

6.2.1 Remote Sensing

Filtering data

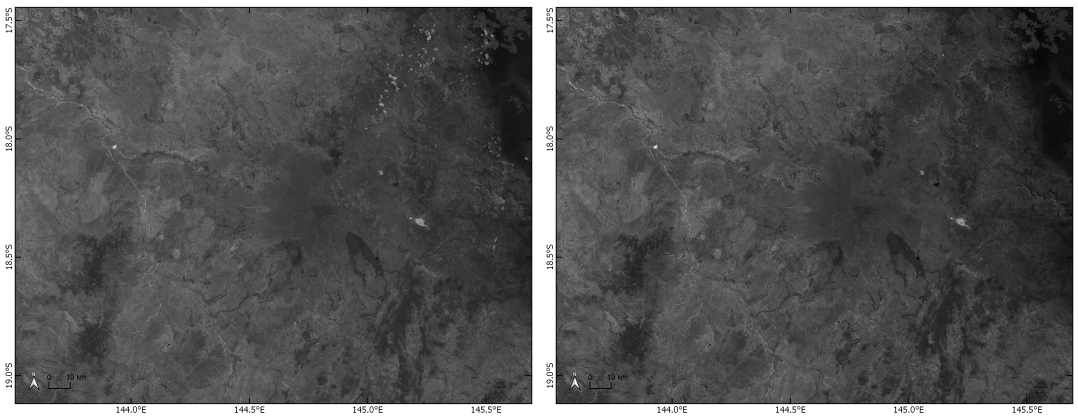

Figure 6.2: *(a) Landsat-8 band 1 mean reduction over the full age range with minor cloud visible in the NE of the image (b) Landsat-8 band 1 median reduction over the full age range with no cloud visible. Only scenes with cloud cover less than 1% have been reduced.*

As mentioned in the methods, to begin the remote sensing work Landsat-8, Sentinel-2, and ASTER collections were loaded into GEE and filtered to the appropriate constraints. The time of year in which satellite scenes are captured affects how the final images appear due changes in vegetation cover, industrialisation etc. Therefore, date filters were tested on a trial and error basis to see which range best represented geological rather than agricultural, or man-made variations. The size of Landsat-8 tiles are 170 km x 183 km, Sentinel-2 tiles are 100 km x 100 km, and ASTER tiles 60 x 60 km. Whilst Landsat-8 covers the greatest area of each volcano, no single scene is large enough to cover the whole region of interest and multiple tiles needed to be joined to create a complete image. By keeping cloud cover below 1% , adequate coverage of each volcano was only possible with a larger date range i.e., months to years, and I began by merging all scenes that have been collected to date with cloud cover below this threshold. Landsat-8, Sentinel-2, and ASTER have been collecting data since 2013, 2015, and 2000, respectively, and the final images were merged using the GEE reducer operator. The results of using a mean and a median reducer on Landsat-8 band 1 tiles, from 2013 to present at the McBride volcano, are shown in Figures 6.2a–b. Both images display little difference however,

it was noted that the median reducer did a better job at removing small areas of cloud and was thus chosen for this study.

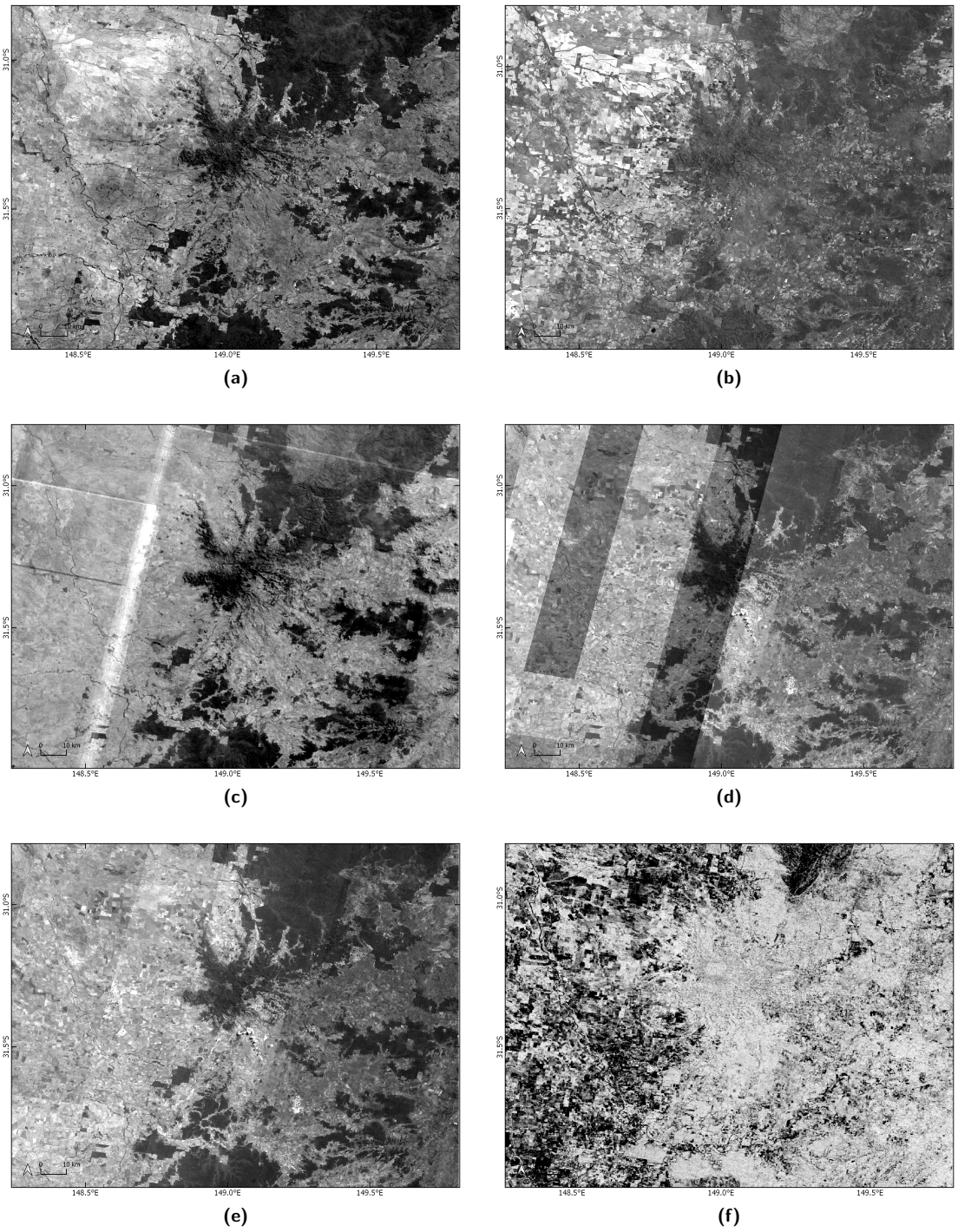

Figure 6.3: *(a) Landsat-8 band 1 median reduction over the full age range (b) Landsat-8 band 1 median reduction over the months of January, February, and March 2021 (c) Landsat-8 TIR band 10 median reduction over the full age range (d) ASTER band 1 median reduction over the full age range (e) ASTER band 1 median reduction in the years 2003–2006 (f) the pre-merged ASTER-GED grid. Only scenes with cloud cover less than 1% have been reduced. For the remainder of the workflow, Landsat-8 VNIR and SWIR bands have been reduced over the full age range, as shown in Figure (a) and ASTER-GED TIR bands have been included as a pre-merged grid, as shown in Figure (f).*

Figure 6.3a shows the median reduction on Landsat-8 band 1 scenes at the Warrumbungle volcano. Figure 6.3b shows the same Landsat-8 band 1 composite but filtered to show only a reduction of images collected in the months of January, February, and March in 2021. Different months were tested simply by moving backwards from the most recent images in 2021 to the first dates that showed consistent cloud-free days

that merged well. It was found that when using a smaller date range croplands appeared more pronounced, and geology and terrain more subdued. It was therefore decided that the full spread of dates gave the most seamless geological composite to use in the analyses. This was true for Landsat-8 and Sentinel-2 VNIR and SWIR bands but not for Landsat-8 TIR bands or the ASTER L1T Radiance product.

When reducing Landsat-8 TIR tiles, the boundaries between each scene are visible within the merged image, see Figure 6.3c. Severe contrast changes between scenes can often be caused by seasonal temperature fluctuations or various scattering effects. When the same method is tried with the ASTER L1T Radiance data overlapping zones are again visible, shown in Figure 6.3d. Figures 6.3e displays ASTER data collected between the years 2003–2006. In this image a narrower age range has reduced some of the boundary effects, but not completely and when narrowing the age range any further there are not enough cloud-free scenes to completely cover the Warrumbungle or McBride volcanoes. It was therefore, impossible to merge these bands seamlessly without further, more advanced, pre-processing. Fortunately, the other ASTER product available in GEE, the Global Emissivity Dataset (ASTER-GED), is provided as a pre-merged global grid derived from clear-sky pixels for all available ASTER data from 2000–2008 and includes all five of ASTERs TIR bands. Pre-processing and scaling between scenes has already been applied to this product to create a coherent grid that can be used directly in the remote sensing workflow, see Figure 6.3f. The only downside of this data set is that it has a slightly coarser resolution, 100 m, compared to the ASTER L1T Radiance TIR data, 90 m.

Because of the issues reducing the Landsat-8 TIR data and the ASTER L1T Radiance data, the rest of the analyses have focused on Landsat-8 (VNIR–SWIR) and ASTER-GED (TIR) data sets, with the occasional use of Sentinel-2 (VNIR–SWIR). The data products are provided as surface reflectance values, surface emissivity, and top-of-atmosphere reflectance, respectively. The computation and analysis of composite images, spectral ratios, and spectral response curves is possible using either of these radiation types and therefore, the data sets have been used for all processes throughout the workflow noting relative changes between bands rather than absolute values.

K-means clustering

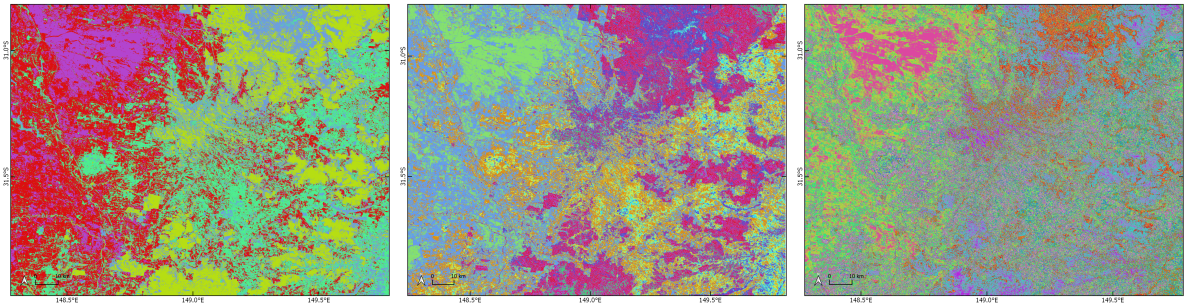

(a) **(b)** **(c)**

Figure 6.4: *K-means clustering on Landsat band 1 with k set to (a) 5 groups (b) 10 groups (c) 20 groups.*

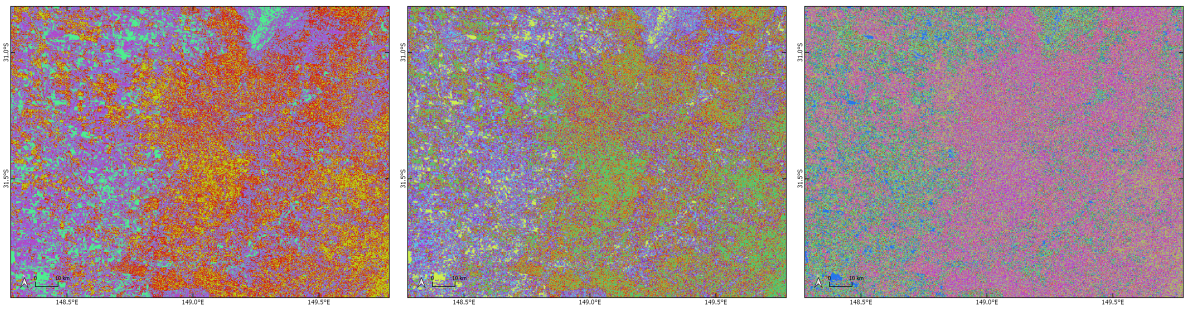

(a) **(b)** **(c)**

Figure 6.5: *K-means clustering on ASTER-GED band 10 with k set to (a) 5 groups (b) 10 groups (c) 20 groups.*

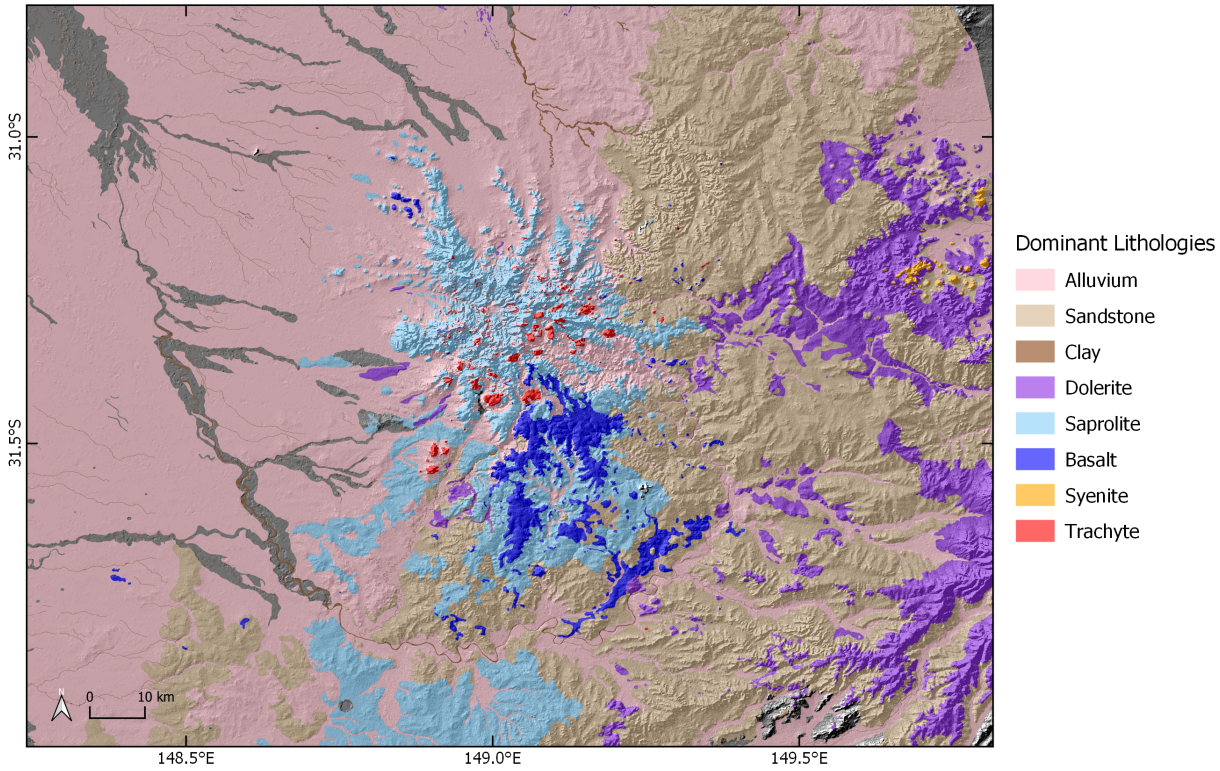

Figure 6.6: *Dominant lithologies of the Warrumbungle central volcano province.*

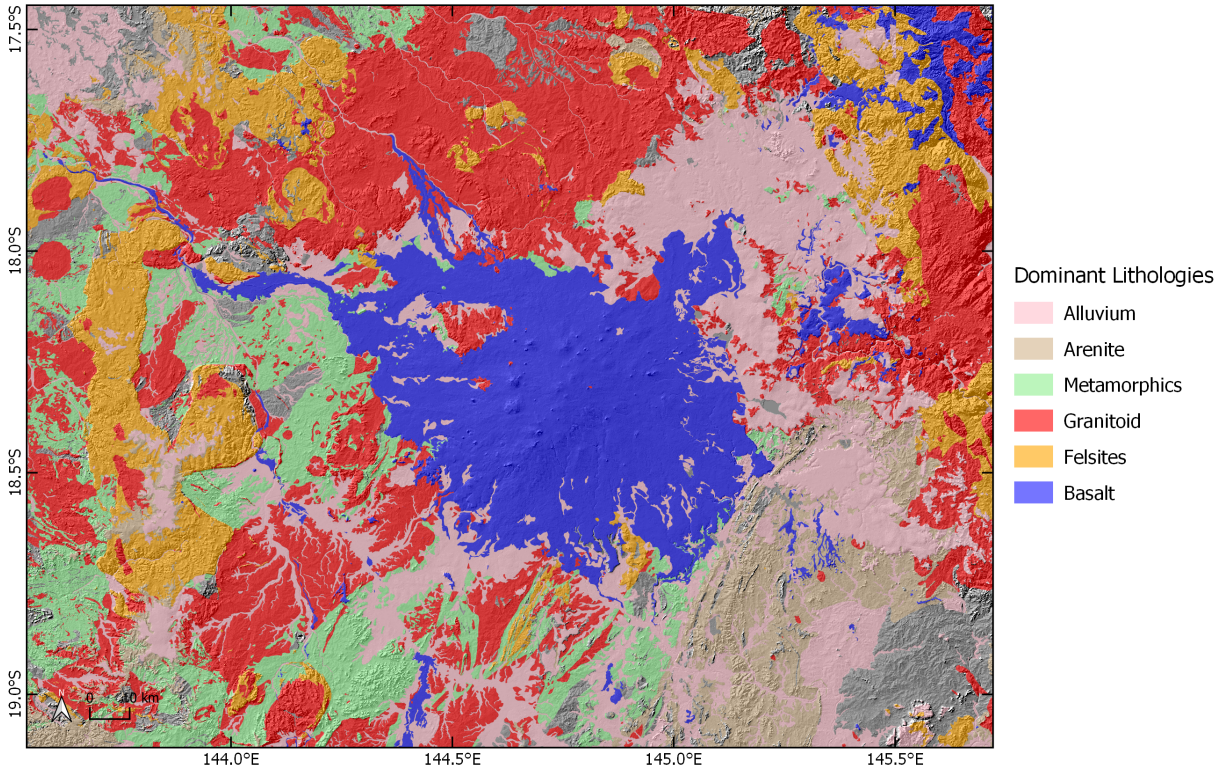

Figure 6.7: *Dominant lithologies of the McBride lava field province.*

K-means analysis was conducted on Landsat-8 bands 1–7 and ASTER-GED bands 10–14. Initially, the number of clusters was arbitrarily set to 5, 10, 20, and 30 (Figures 6.4 and 6.5). 10 clusters was deemed enough to identify distinct geological groups. The results of the k-means analysis have been compared to the

known geology at each location to assess which bands, if any, might be preferentially highlighting different geological units. For simplicity, the geology of each province has been reducted to the dominant lithologies which make up each unit. Dominant lithologies were already specified in each of the 2018 Queensland Detailed Surface Geology and 2021 New South Wales Seamless Geology data packages and are available as attributes in each shapefile.

The dominant lithologies of the Warrumbungle province comprise of alluvium, sandstone, clay, dolerite, saprolite, basalt, syenite, and trachyte (Figure 6.6). The Alluvium group includes Quaternary alluvium, colluvium and residual deposits of sand gravel, clay, calcrete, laterite, silcrete, silt, and minor evaporites. Sandstone primarily refers to the Jurassic Pilliga and Purlawaugh Sandstone Formations consisting of well sorted, quartzose sandstone and lithic sandstone, both interbedded with mudstone, siltstone, and coal, with common carbonaceous fragments. Clay encompasses the meander plain and channel facies of the Quaternary Marra Creek Formation which contain unconsolidated clayey silts and silty clays. Dolerite includes the Triassic-Jurassic Garrawilla Volcanics of dolerite, basalt, trachyte, tuff, and breccia, and the Cenozoic Liverpool Range Volcanics composed of basalt, dolerite, polymictic conglomerate, quartzose sandstone, gravel, and siltstone. Saprolite is defined by weakly-consolidated regolithic residuum, mostly containing poorly sorted mafic and trachytic sediments of the Warrumbungle Volcanic Complex. Basalt includes Warrumbungle lava deposits, primarily basalt and hawaiite with minor autobreccia. Syenite includes the Jurassic Bulga Complex of microsyenite, phonolitic trachyte and phonolite, emplaced primarily as lava domes. Finally, Trachyte encompasses the trachydacite, trachyte, quartz-trachyte and rhyolite intrusions and lava domes of the central Warrumbungle Volcanic Complex.

The dominant lithologies of the McBride province comprise of alluvium, arenite, metamorphics, granitoids, felsites, and basalt (Figure 6.7). Much like the Warrumbungles, the Alluvium group includes Quaternary sand, silt, clay, gravel and soil with some poorly consolidated sandstones, mudstones, and conglomerate. Arenite consists of Silurian-Devonian lithofeldspathic sandstone and mudstone turbidites with minor limestone, chert and altered basalt. Basalt refers to the McBride province which principally consists of olivine basalt flows. Felsites, and minor mafites, are made up of Carboniferous-Permian dominantly rhyolitic ignimbrite, breccia, and lava, with subordinate andesitic to basaltic lava and minor volcaniclastic sandstone and siltstone. Granitoids include Paleozoic, mainly I-type, biotite-granite, hornblende-granite, granodiorite, tonalite, microgranite, and leucogranite, with subordinate diorite and gabbro. Lastly, Metamorphics encompass quite a wide range of Paleoproterozoic-Paleozoic mixed metamorphic rocks, primarily, biotite gneiss, calc-silicate gneiss, mica schist, sillimanite-biotite schist, quartzite, migmatite, amphibolite, and granofels, with abundant leucogranite and pegmatite veins.

Whilst there are some crossovers i.e., altered basalt in the Arenite group, the mineralogy of most rock types are indicative of the dominant lithology describing them and this method does allow for a broad comparison between groups. To check whether either group was identifiable in a particular wavelength, simple k-means clustering was performed at each of the two locations. The results of the k-means analyses for each band in the Warrumbungle and McBride provinces are shown in Figures 6.8, 6.9, 6.10, and 6.11. The colours of each group have been selected at random and are not consistent between bands, they are simply highlighting differences within each image. For comparison, the Figures also include DEM, slope, FAA, and TMI grids.

In Figures 6.8 and 6.9, there are a few features from the Warrumbungle province that are noteworthy. Vegetation is mostly picked up in pinks and purples in bands 1 and 2, and faintly in other bands. Alluvium is visible in blue, green and orange in bands 1–4, particularly the Castlereagh River and associated sediments coming into the scene from the NW. Sandstone is one of the least well defined units, often very mottled and mixed up with alluvium, saprolite, and basalt deposits in all bands, it is also often obscured by vegetation. Clay is another poorly defined unit, usually grouped together with other alluvium, although finer grained deposits of the Castlereagh River are highlighted in bands 5, 6, and possibly 7. Dolerite and saprolite display similar footprints represented by steep, vegetated, dendrite-shaped lava flows of the Warrumbungle volcano, and the Liverpool Range volcano in the SE of the scene. Both groups are particularly well defined in bands 3, 4, 6, and 7 in reds and pinks, maybe due to higher moisture contents of the soil in these areas. The lower-lying Warrumbungle basalts are often merged with sandstone and alluvial deposits but are easiest to make out in bands 3, 4, and 6, and slightly in bands 1 and 2. Syenites and trachytes are difficult to reconcile in any band but may be seen slightly in band 5, possibly because all other groups are suppressed in this band. ASTER-GED results show less variation across the scene and the most prominent features in all five TIR bands appear to be elevated, vegetated hillsides, usually highlighted in greens in the centre and SW of the image. Bands 13 and 14 may be picking out basalts and dolerites in oranges and reds but this is difficult to confirm as the occurrences are small with blurred boundaries. Figures 6.9f–h show that some of the best differentiators between volcanic and non-volcanic units at the Warrumbungle volcano as well as the Liverpool Range and Mesozoic volcanics, are gravity free air anomalies and degree of slope.

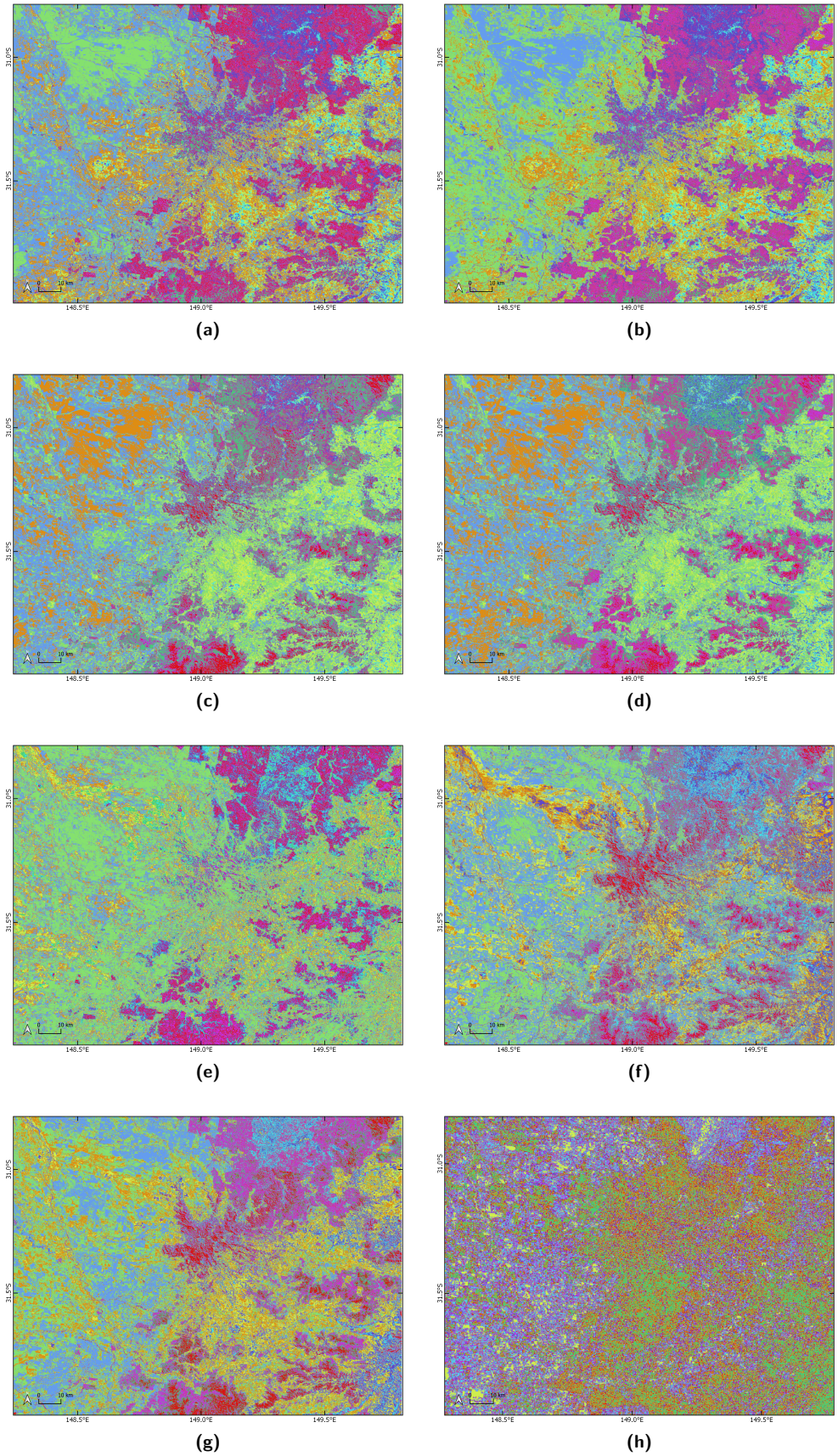

Figure 6.8: *Warrumbungle province k-means clustering on Landsat-8 bands (a) B1 (b) B2 (c) B3 (d) B4 (e) B5 (f) B6 (g) B7, and (h) ASTER-GED B10.*

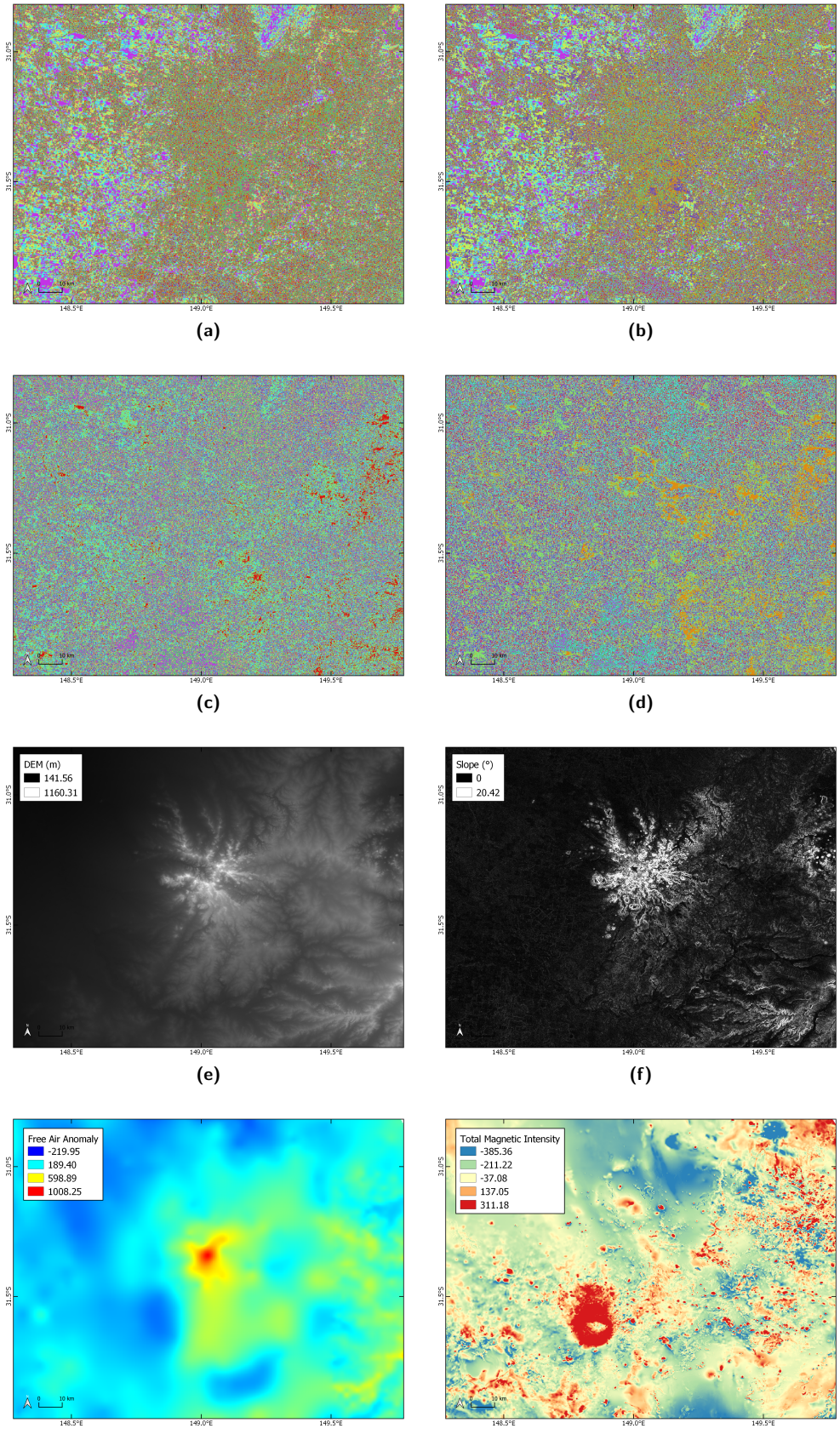

Figure 6.9: *Warrumbungle province k-means clustering on ASTER-GED bands (a) B11 (b) B12 (c) B13 (d) B14, including images of (e) DEM (f) slope (g) FAA (h) TMI.*

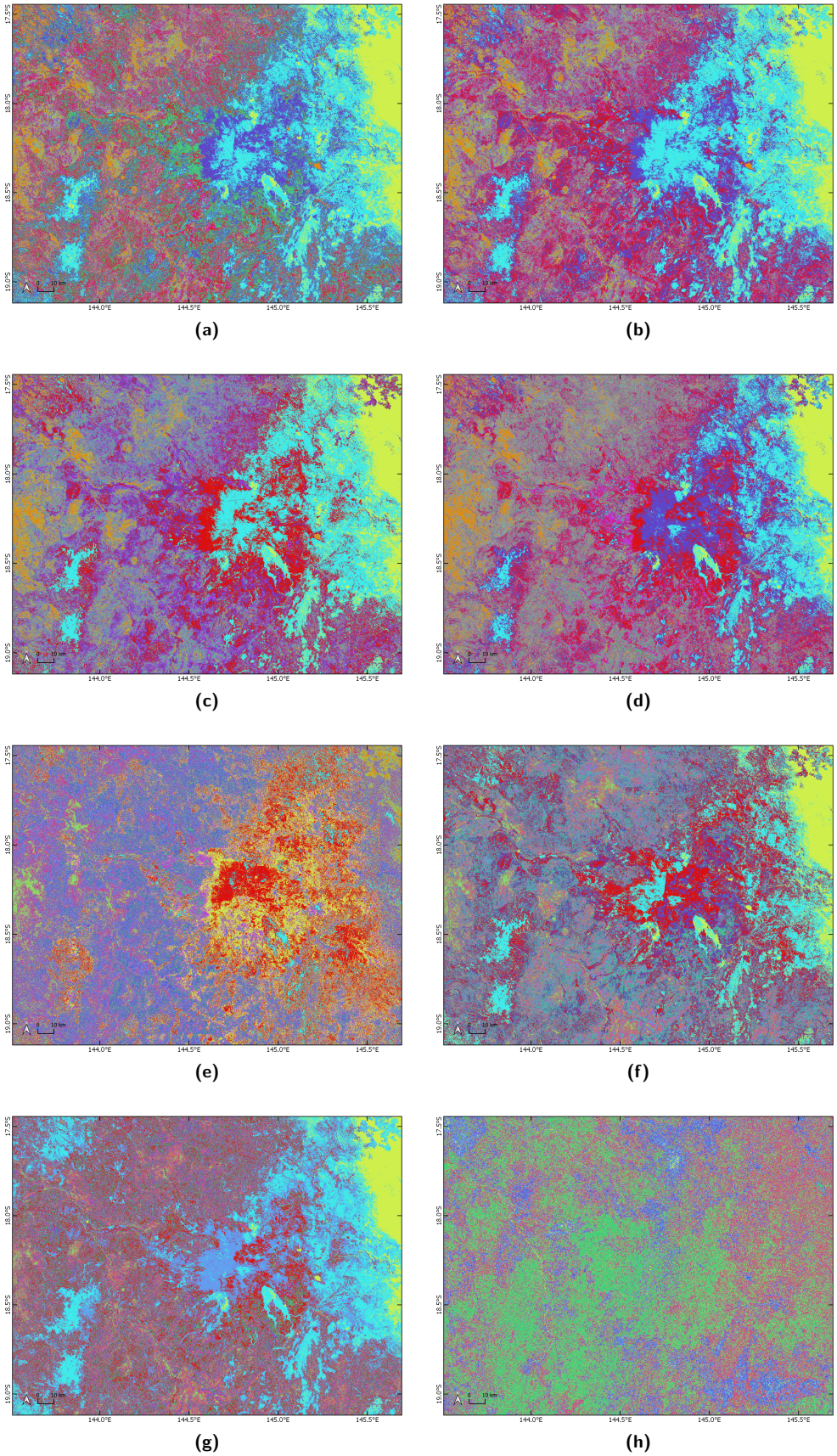

Figure 6.10: *McBride province k-means clustering on Landsat-8 bands (a) B1 (b) B2 (c) B3 (d) B4 (e) B5 (f) B6 (g) B7, and (h) ASTER-GED B10.*

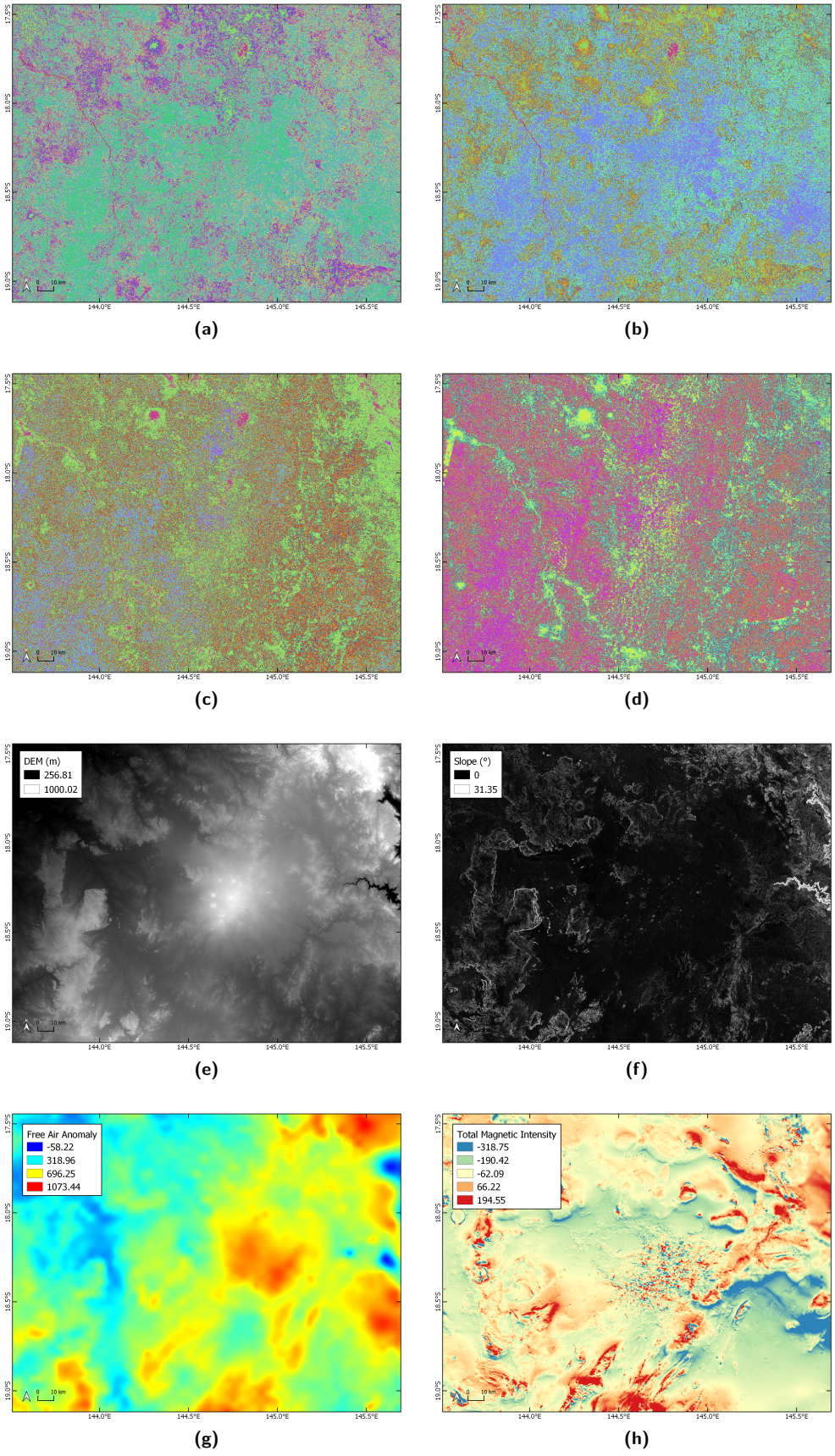

Figure 6.11: *McBride province k-means clustering on ASTER-GED bands (a) B11 (b) B12 (c) B13 (d) B14, including images of (e) DEM (f) slope (g) FAA (h) TMI.*

Figures 6.10 and 6.11 show the k-means results for the McBride province. The McBride province is situated in a more arid climate than the Warrumbungle but to the east lies the fertile hills of the Great Dividing Range, which is around 1000 m in elevation and covered in vegetation. This flora can be seen in all Landsat-8 images, except for Figure 6.10e, as a yellow, green, and blue band running along the eastern side of the scene. The McBride province itself lies on a vast plain to the west of the Great Divide uplands and a few geological features can be identified in this portion of the k-mean results. Alluvium is highlighted particularly well in the same bands as vegetation, shown in blues, but in some areas basalts of the McBride volcano have been included in the same class. The same is true for Arenite deposits, being grouped together with vegetation and alluvium in blues and greens in bands 1–4, and 6–7. Much of the reds and oranges in band 5 can also be attributed to vegetation, alluvium, and arenite. Metamorphics, Granitoids, and Felsites are represented by pinks, purples, and oranges in each of the Landsat-8 bands but neither group is distinctive enough to be entirely isolated from the others. This is unsurprising as the composition of these units are vey similar, being dominated by a high proportion of felsic minerals. The mafic basalts of the McBride province are visible in most bands as purples, greens, and reds. The greatest thickness of lava is visible as a circular mass in the centre of the image in bands 1, 2, 3, 4, 6, and 7. It is usually visible in the same blue as the vegetated uplands and alluvium. Thinner flows emanating from the centre to the west of the scene are again visible in bands 1, 2, 3, 4, 6, and 7, usually in greens, purples, and reds. Lava flows are most clearly visible in band 6, much like the Warrumbungle k-mean results and again perhaps due to the moisture content of basalt compared to the surrounding rocks. ASTER-GED bands 10 and 11 show the outline of the McBride basalt flows in green. Other rock types are included in this classification but as none of them are juxtaposed directly against the basalt, the outline is relatively clear. ASTER-GED bands 12, 13, and 14 are less clear. In the DEM and slope images the McBride volcano is not immediately obvious as it exists as a low-lying plain with few terrain changes except for very slight updoming in the centre. The thickest mass of the volcano is evident as a high in the free air anomaly grid and the same area exhibits a characteristic stippled, short-wavelength response on the magnetic intensity grid, which is often associated with shallow basaltic material (Van den Hove et al., 2017).

From the k-means results, the outline of Warrumbungle volcano appears most visible in Landsat-8 bands 1, 2, 3, 4, and 7, but particularly in Landsat-8 band 6 and in free air anomaly and slope images. The outline of the McBride volcano is most visible in Landsat-8 bands 1, 2, 3, 4, and 7, but again particularly in Landsat-8 band 6, ASTER-GED bands 10 and 11, and in free air anomaly and magnetic intensity images. The broad observations seen here have been used in the creation of composite images and to aid in the training of the random forest classifier.

Spectral response curves

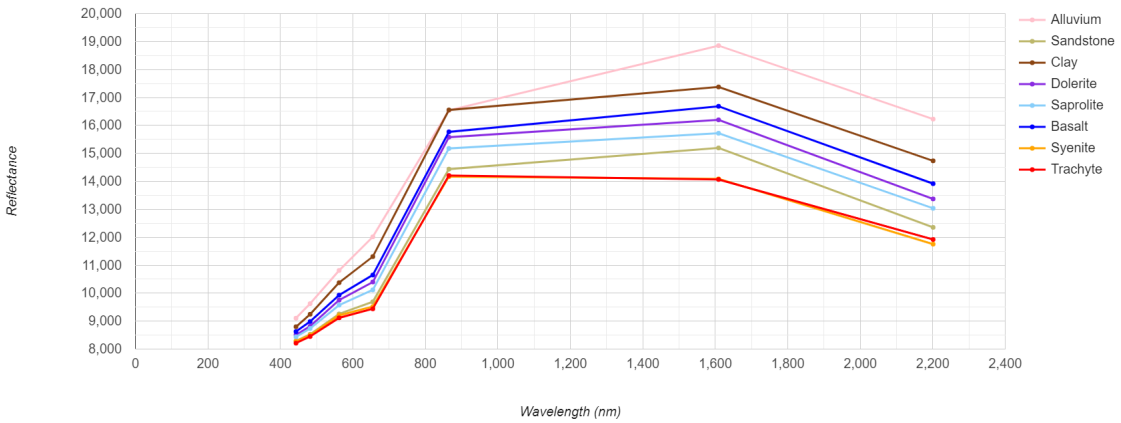

Figure 6.12: *Warrumbungle Landsat-8 reflectance spectra gathered from geological polygons.*

The surface reflectance curves for each of the Warrumbungle and McBride dominant rock units, at the central wavelength of each Landsat-8 band, are shown in Figures 6.12 and 6.14 and the emissivity curves at each ASTER-GED band, are shown in Figures 6.13 and 6.15. In order to compare the gathered spectra

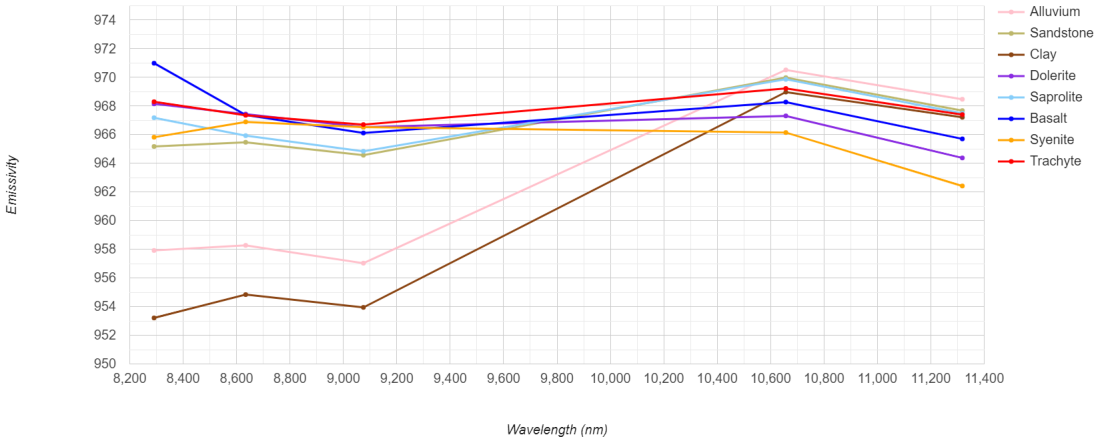

Figure 6.13: *Warrumbungle ASTER-GED emissivity spectra gathered from geological polygons.*

directly to laboratory measured spectra, the latter would need resampling to the resolution of the satellite data which is much coarser. Also, both Landsat-8 and ASTER-GED tiles contain mixed pixels, meaning each pixel represents a varying proportion of different materials. It is possible to use spectral mixing of different reflectance or emissivity signatures to isolate end-member rock types within each scene although this is notoriously difficult with intimate mixtures such as soil and rock and was thus not undertaken in this study. Therefore, instead of comparing gathered spectra to known rock libraries, the results were used to assess the broad differences between each of the geological groups and to identify any significant absorption features governing them.

From the two Warrumbungle spectra a few general characterisations can be made: (1) alluvium has the overall highest albedo in the VNIR and SWIR; (2) band 6 separates all units well, as confirmed by the k-means clustering; (3) the VNIR/SWIR spectrum of mafic rocks is a similar shape with the main difference being slight changes in overall albedo, decreasing from basalt, to dolerite, to saprolite; (4) the VNIR/SWIR spectrum of felsic rocks exhibits low slope between band 5 and band 6, and consistently low albedo; (5) dolerites, basalts, and some sedimentary units have similar VNIR/SWIR spectra and are likely to be difficult to discriminate with Landsat-8 reflectance data alone; (6) dolerites and volcanics also have similar TIR spectra, which is unsurprising given the similar composition of both units; (7) alluvium and clay may be isolated in ASTER bands 10, 11, and 12, where they display markedly low emissivity; (8) saprolite and sandstone have overlapping TIR spectra and are thus not easy to separate in any Landsat-8 or ASTER band; (9) syenites and trachytes are distinguished from each other only in ASTER bands 10, 13, and 14.

Broad observations from the McBride spectra include: (1) metamorphic, granitoid, and felsite units have similarly shaped spectra but are best separated in bands 6, 7 and the TIR; (2) basalt and arenite have directly overlapping VNIR/SWIR spectra, possibly owing to the high FeO content of either unit as a result of weathering; (3) alluvium displays consistently low albedo, where the opposite was true for the Warrumbungle volcano; (4) volcanic and sedimentary units have similar spectra and are likely to be difficult to discriminate with Landsat-8 VNIR/SWIR data alone; (5) both of these units are separated in all TIR bands; (6) metamorphic and granitoid units again have similar shapes in emissivity spectra; (7) whereas felsites have a similar shape to basalt; (8) alluvium and arenite also have comparable shapes in this spectrum.

In the aim of isolating the mafic and felsic rocks of the Cenozoic volcanoes along the entire East Australian chain, a few general observations can be made: (1) due to similar mineralogy remote sensing cannot distinguish between basalt and dolerite and both should be grouped together; (2) mafic rocks, and weathered mafic rocks, often have VNIR and SWIR spectra close to sandstone and sediments, probably due to the high FeO content of each rock type, and are thus difficult to separate in these bands; (3) the same rocks are easier to differentiate in TIR bands with sandstone, alluvium, and clay generally displaying lower emissivity in bands 10, 11, and 12; (4) in both provinces, felsic rocks display different VNIR/SWIR spectra to mafic rocks, sandstones, and sediments; (5) volcanic felsic rocks have the lowest reflectance in band 6, and a flat spectra between bands 5 and 6, and may be differentiated from plutonic felsic rocks and metamorphics using Landsat-8 bands 6, 7,

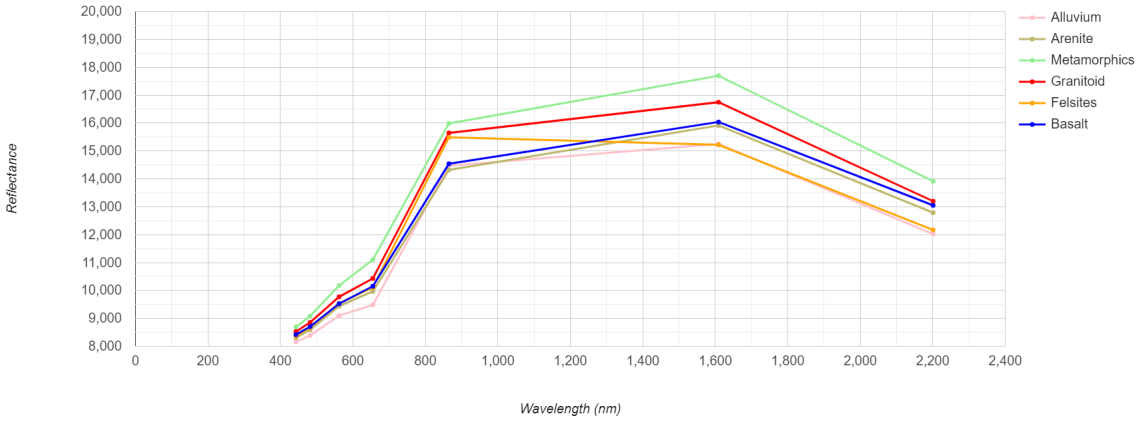

Figure 6.14: *McBride Landsat-8 reflectance spectra gathered from geological polygons.*

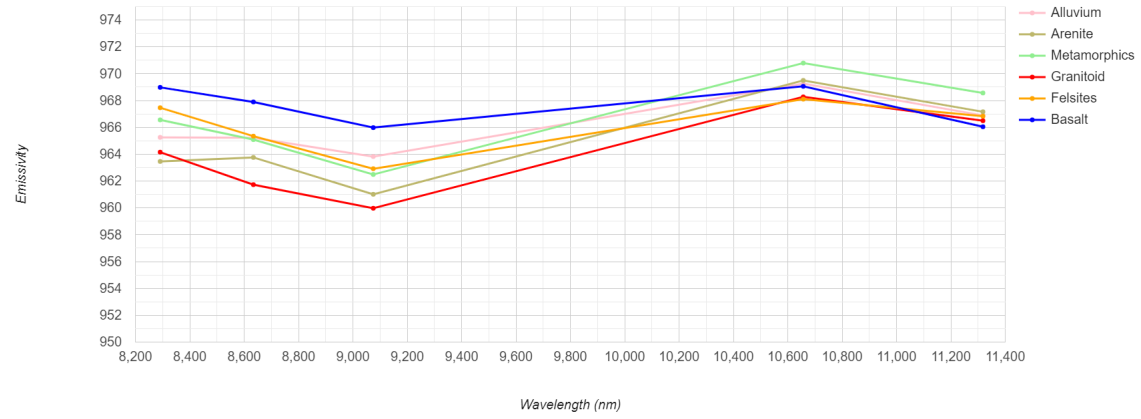

Figure 6.15: *McBride ASTER-GED emissivity spectra gathered from geological polygons.*

and ASTER bands 10–14. Mafic rocks should therefore be best isolated in using ASTER TIR bands and felsic rocks using Landsat-8 SWIR bands 5, 6, and 7, and ASTER TIR bands.

Composite analysis

To better isolate each of the geological groups, false colour composites (FCC) and band ratios were tested using Landsat-8 VNIR/SWIR and ASTER TIR bands. Band ratios measure the difference between the reflectance or emissivity of one band to the reflectance or emissivity of another band and in doing so, the effects of topography or grain size variation are reduced (Sultan et al., 1987). Band ratios are therefore extremely useful in lithology mapping and have been used in numerous rock and soil studies around the world, particularly in arid and semi-arid regions (e.g., Rowan and Mars, 2003; Gad and Kusky, 2006; Langford, 2015). To gain the best results, absorption features of different lithological units need to be distinct enough to appear in separate multispectral bands. An overview of Landsat and ASTER band indices typically used to identify different groups of minerals have been complied in Sabins (1999) and Kalinowski and Oliver (2004), and summarised in Van Der Meer et al. (2012) and Gupta (2017). The same principles have been applied here to isolate the volcanic rocks of eastern Australia.

From the k-mean and spectral response results of this study, the Landsat-8 bands which were found to best highlight the Warrumbungle and McBride volcanics include 3, 5, 6, 7. Bands 1, 2, and 4 gave reasonable

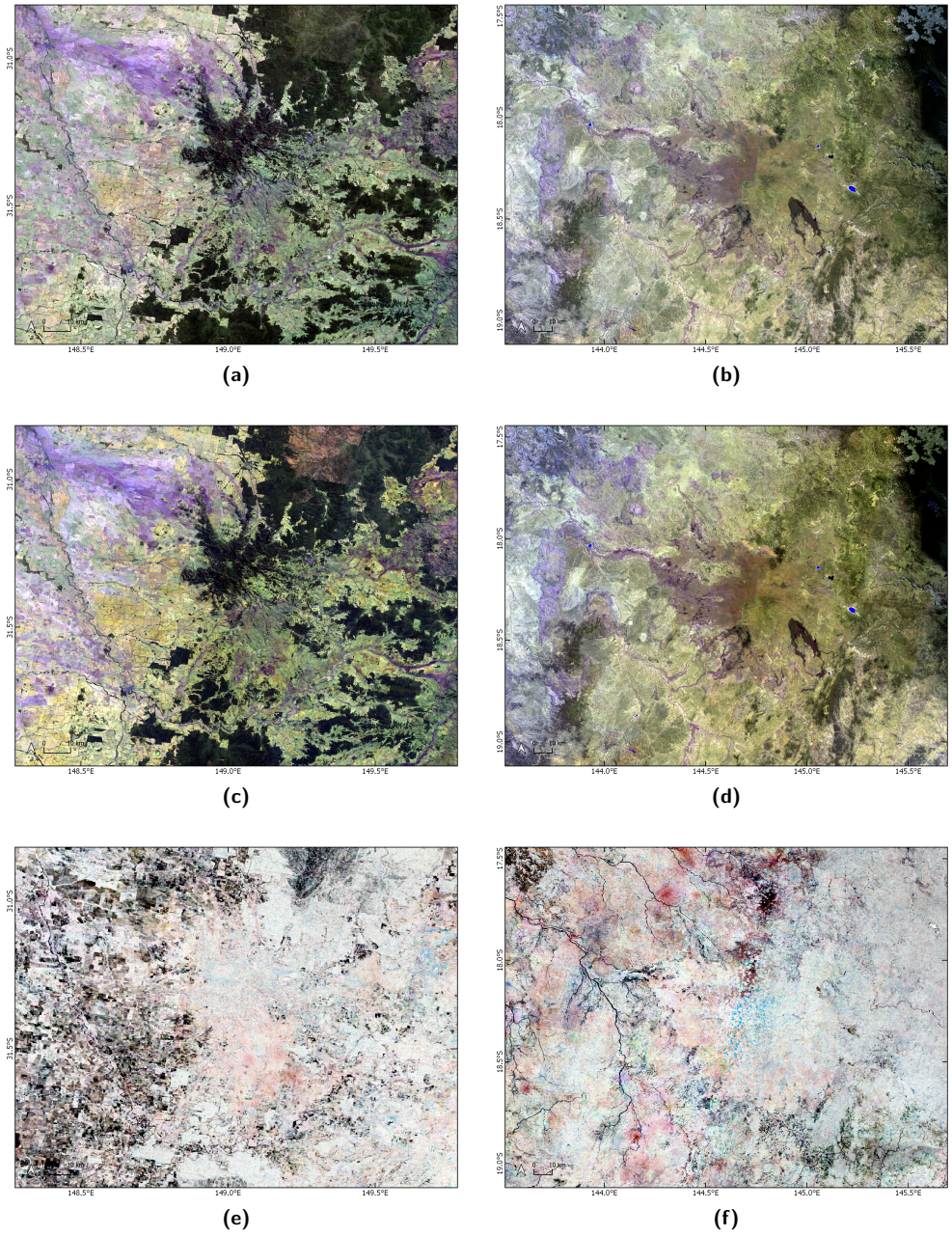

Figure 6.16: *The Landsat-8 7–6–3 FCC for the (a) Warrumbungle and (b) McBride provinces. The Sentinel-2 12–11–2 FCC for the (c) Warrumbungle and (d) McBride provinces. The ASTER 10–11–12 FCC for the (e) Warrumbungle and (f) McBride provinces.*

results but focus more on vegetation changes, although some composites were tested including these bands and a quality check. One of the best results came from the Landsat-8 7–6–3 composite, shown in Figures 6.16a–b. Within the Warrumbungle province, the deposits of the Castlereagh River in the NW of the scene are particularly visible in purples as well as areas of steep, high vegetation in dark green, this includes the Warrumbungle felsic volcanics in the centre of the image. Mafic rocks including saprolites, dolerites, and basalts making up the southern flanks of the Warrumbungle volcano, the Liverpool Range volcano, and Mesozoic volcanics, can be seen in the centre and east of the image but are also coloured purple, highlighting the difficulty isolating volcanics and sediments with Landsat-8 bands only. This is made particularly difficult near river channels as many rivers deposits will carry volcanic material from the volcanoes themselves. Within the McBride province lava flows to the north, west, and south of the volcano are highlighted well in the 7–6–3 composite but the boundaries are less well defined to the east where the elevation rises and vegetation increases.

The best results from Sentinel-2 data came from the 12–11–2 composite, however, band correlations

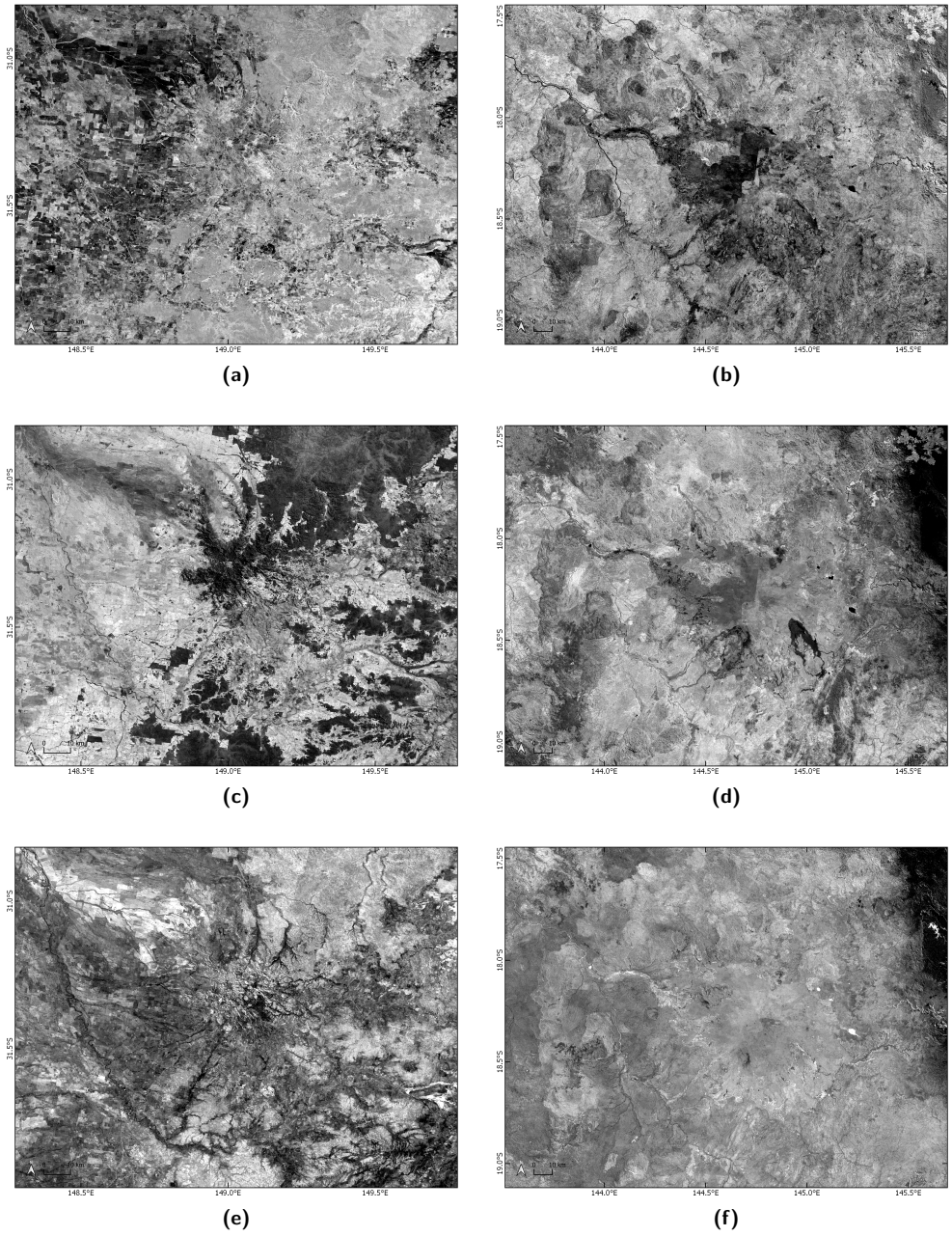

Figure 6.17: *The Landsat-8 6/7 ratio used to highlight clays in the (a) Warrumbungle and (b) McBride provinces. The Landsat-8 6/2 ratio used to isolate epidote and chlorite in the (c) Warrumbungle and (d) McBride provinces. The Landsat-8 2/5 ratio used to supress vegetation in the (a) Warrumbungle and (b) McBride provinces.*

between the Landsat-8 and Sentinel-2 sensors mean the Landsat-8 7–6–3 composite images almost the same wavelengths as Sentinel-2 12–11–2 composite which has previously been used for basic geology mapping (Van der Meer et al., 2014). Results between the two FCCs therefore look almost identical and highlight similar geological features (Figures 6.16c–d). It was decided that because of this similarity and because there was no need for enhanced spatial resolution at this stage of the classification, the Sentinel-2 data was not incorporated into any subsequent analysis as ancillary data.

From k-mean and spectral response results of the ASTER-GED data, bands 10, 11, and 12 were found to best differentiate between different rock types and the 10–11–12 FCC was preferred in this study for isolating volcanism (Figures 6.16e–f). Other TIR band composites were tested but volcanic boundaries were less clearly defined in these. In Figures 6.16e–f, the Cenozoic volcanoes are visible in the centre of the image in white/pale pink, although the volcano outline is much clearer in the McBride province probably due to the arid climate, lack of vegetation, and high volume of felsic rocks surrounding the volcano itself. All FCCs and band ratios found in this study to most precisely isolate volcanic rocks are shown in Figures 6.16–6.18.

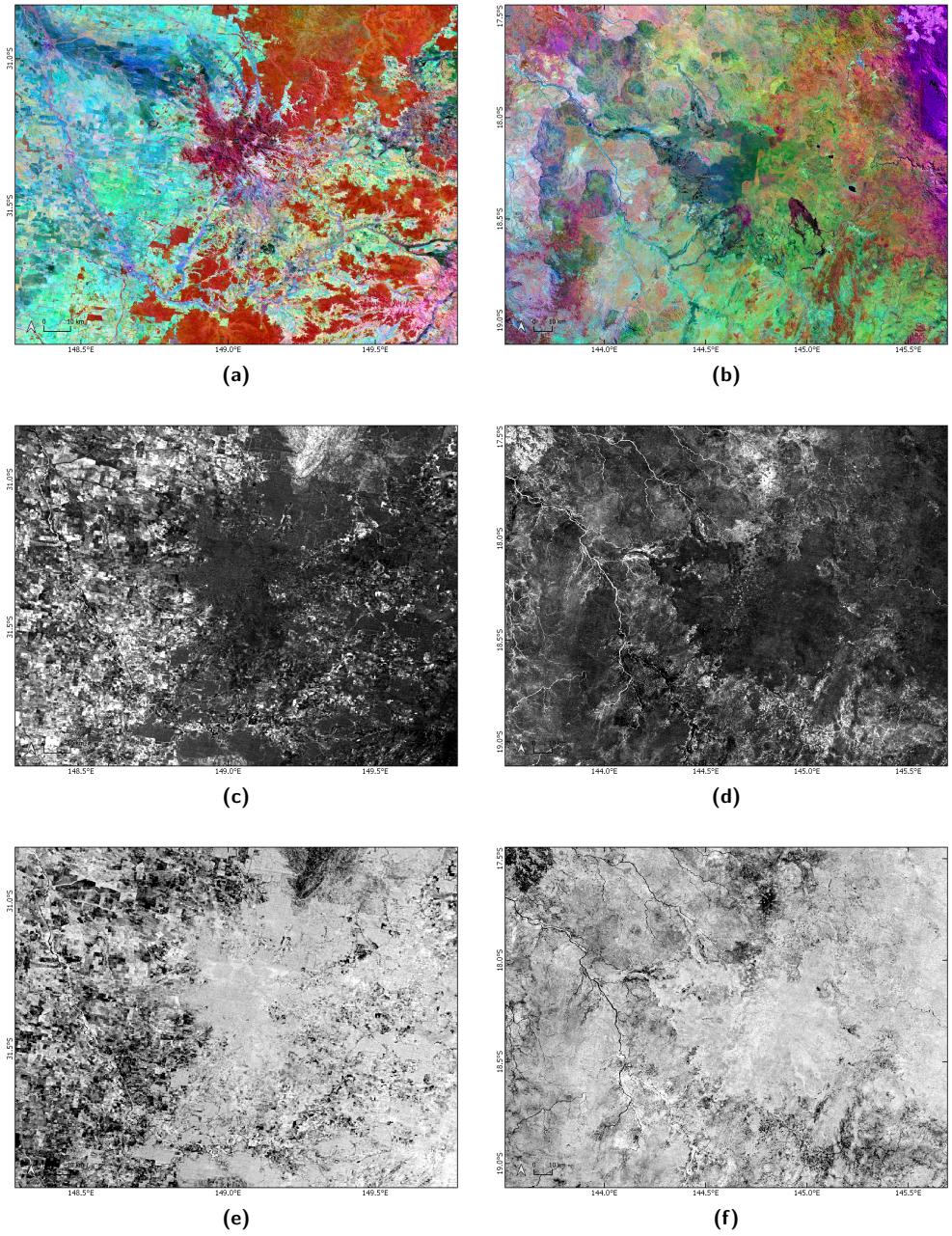

Figure 6.18: *The Landsat-8 FCC 6/7–6/2–5 at (a) Warrumbungle and (b) McBride. The ASTER empirical index of SiO_2 (%) from Watanabe and Matsuo (2003) at (c) Warrumbungle and (d) McBride. The ASTER Mafic Index from Ninomiya et al. (2005) at (e) Warrumbungle and (f) McBride.*

Because of the characteristic Al-OH absorption in many clay minerals, the Landsat-8 ratios 6/7 and 7/6 have been used by numerous authors to separate argillic from non-argillic materials (Van Der Meer et al., 2012). The results of the 6/7 ratio computed over the two study areas is shown in Figure 6.17a–b. In the Warrumbungles, clay-rich sediments and alluvium in darker shades can be distinguished from surrounding country-rock in lighter shades. In the McBride province the volcano itself displays a high proportion of clay-rich minerals in darker shades, probably due to greater weathering of the exposed basalt compared to the surrounding granitoid and metamorphic rocks. Reflectance features of iron oxide are present in all Landsat-8 VNIR bands and the ratios 4/2, 4/3, and 3/2 are a few that have been used in other studies for identification of FeO-rich rocks (e.g., Goetz and Rowan, 1981; Sabins, 1999; Gupta, 2017). Unfortunately the results of these ratios in this work were inconclusive and have not been used further. The band ratio 6/2 was instead found to best highlight mafic rocks in both the Warrumbungle and McBride provinces (Figure 6.17c–d). This is possibly due to the identification of minerals such as chorite or epidote which are common constituents of weathered mafic rocks. Chlorite and epidote both display high band 6 values due to their hydroxyl content

but have lower VNIR values than most clays due to their iron content. Finally, the Landsat-8 ratio 2/5 was used to suppress the effects of vegetation and to highlight structural trends across each of the provinces (Figure 6.17e–f). This ratio is particularly useful in identifying trachytes and syenites in the Warrumbungles which form small, isolated domes and the flat plain of the McBride volcano, particularly to the east where boundaries were previously obscured.

In a similar study, the Landsat-7 ETM+ composite 5/7–5/1–4 was used by Ramadan and Kontny (2004) for discriminating different volcanic and ophiolitic rocks and by Kaleliolu et al. (2009) for visualising dyke boundaries. The same bands correspond to 6/7–6/2–5 in Landsat-8 and this composite image is shown in Figure 6.18a–b for the two provinces. In both cases, the composite does a reasonable job highlighting volcanism in dark blues and greens, although in many places the same class is identified in streams and rivers. The trachytes of the Warrumbungle are isolated well in dark green and the more extensive saprolite rocks, representing weathered lava flows, are isolated well in dark red. Given the dense vegetation atop the Warrumbungle volcano, it is quite difficult in any composite or band ratio to separate these rocks from surrounding vegetation, which is also shown in red.

Band ratios in the ASTER TIR region are often used to assess the silica content of rocks and a wide variety of indices have been formulated by numerous authors using these bands (e.g., Papp and Cudahy, 2002; Ninomiya et al., 2005; Rowan et al., 2006; Rockwell and Hofstra, 2008). Many of these were tested in the study areas but the clearest results were observed with the ASTER empirical index of SiO_2 (%), defined by Watanabe and Matsuo (2003) with Equation 6.1, where Ems[n] = emissivity of ASTER band n.

$$SiO_2\,(\%) = 56.20 - 271.09 \times Log((Ems[10] + Ems[11] + Ems[12])/3/Ems[13]) \qquad (6.1)$$

The results are shown in Figures 6.18c–d where both the Warrumbungle and McBride volcanoes are visible in darker shades in the centre of the image. The inverse of the total silica content (ASTER band ratio 13/12) is known as the Mafic Index (MI), first described by Ninomiya et al. (2005) with the ASTER band ratio 12/13, where the value of MI should increase with increasing mafic character of the rock. The results of this ratio can be seen in Figures 6.18e–f and are similar to the SiO_2 (%) index but with the colours inverted. Both the mafic and SiO_2 (%) indices can be sensitive to vegetation changes or nearby carbonates, although there were limited carbonate rocks in both study areas. The best results from the two indices were both obtained in the McBride province and this is probably due to the semi-arid climate, lack of vegetation and the abundance of surrounding felsic rocks with considerably different silica contents to the volcano itself.

FCC and band ratios used by other authors for the identification of mafic and ultramafic rocks were tested in this study but gave results similar to those already found or inconclusive results and were thus not used in the final classification. These include Landsat TM composites 6–3–1, 5/7–3/1–5, 5/3–5/1–7/5, and 7/5–5/4–3/1 (e.g., Gad and Kusky, 2006; Khan et al., 2007; Kaleliolu et al., 2009). ASTER composites used to delineate volcanic rocks based on temperature and silica contents were also tested including 10–12–13, 12–13–14, (12 + 14)/(13 x 2) (e.g., Rowan and Mars, 2003; Rowan et al., 2005; Yamaguchi et al., 1998).

The final composite results do a reasonable job at highlighting the different lithologies in either study area. Small trachyte and syenite plugs in the Warrumbungles are visible in Landsat-8 composites but the resolution of ASTER data (100 m) is generally too coarse to identify them. Due to their unique structure these units are also visible with slope and other terrain tiles. The extensive, weathered lava flows of the central Warrumbungles, dominated by saprolite, are easily identifiable in most satellite images due to their dentritic shape, high elevation, and dense vegetation cover. The main problem in identifying this unit is that it is difficult to separate from other densely vegetated areas. Lower-lying mafic lavas of the Warrumbungle volcano flanks (including dolerite and basalt from the Liverpool Range volcano and some Mesozoic volcanism) are also best identified in Landsat-8 composites but are difficult to separate from alluvial fan and river sediments. The outline of the Warrumbungle may be observed slightly in TIR composite images. A more diagnostic feature of the Warrumbungle volcano is a considerable FAA gravity high, and magnetic data which displays a characteristic mottled appearance.

Basaltic lavas of the McBride province are more readily identifiable than the Warrumbungle volcanics due to the semi-arid environment in this part of eastern Australia. Landsat-8 and ASTER composite images both do a good job at highlighting individual flows of the McBride lava field. Landsat provides greater spatial resolution and finer detail to isolate thinner lava flows but the overall shape of the volcano is best identified in the ASTER TIR bands. Mafic and silicic index calculations worked particularly well, possibly due to the fact mafic lavas overlie silicic granites at this location so the contrast is more easily distinguished. The volcano again represents a high in FAA gravity, and displays a mottled appearance within the magnetic data, both of which are concentrated at the centre and east of the volcano where the thickest flows occur. Landsat-8 and ASTER composites, gravity data, magnetic data, and terrain grids were chosen to use in the classification of both provinces.

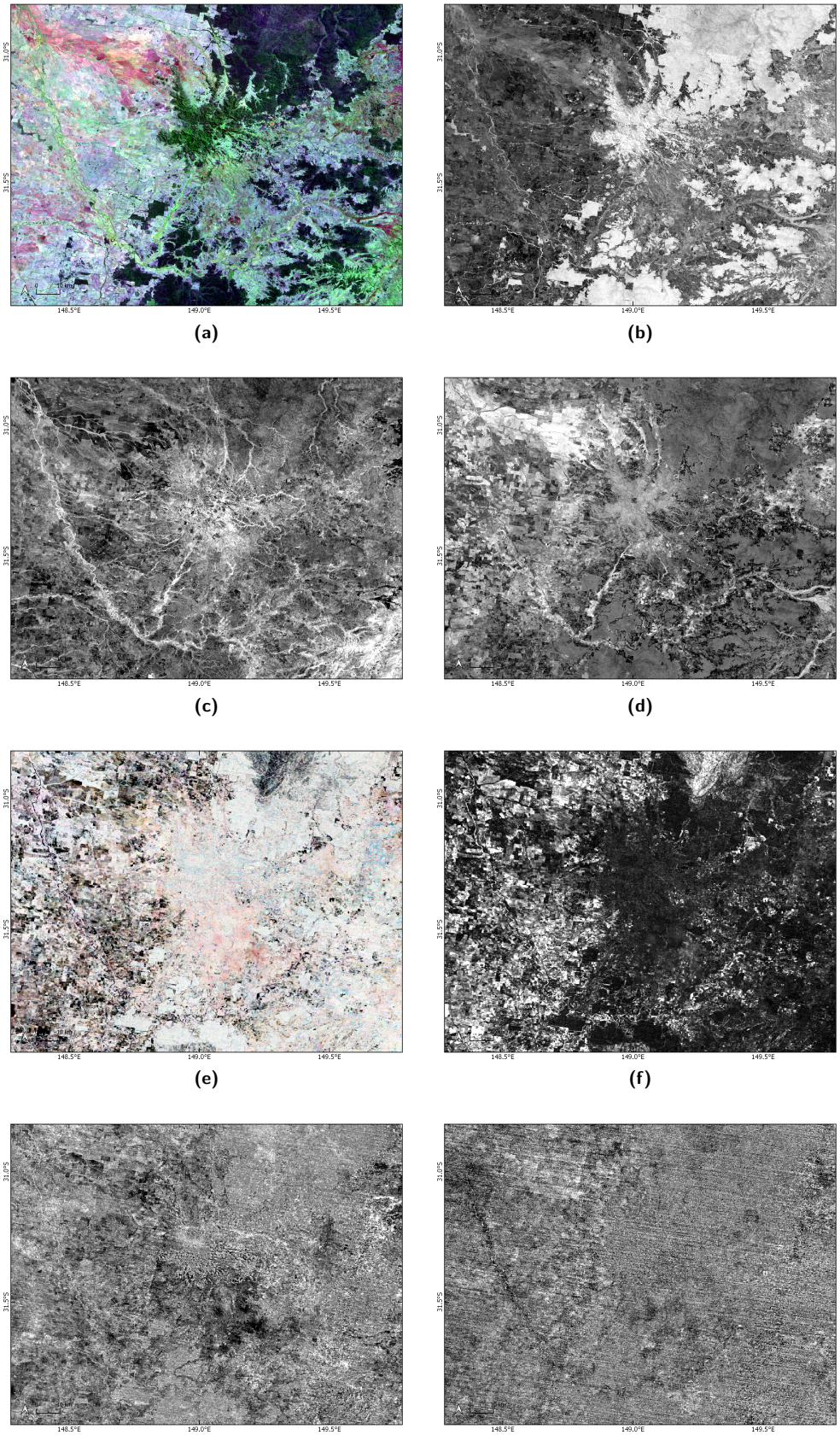

Figure 6.19: *Warrumbungle (a) Landsat-8 composite image including each of the seven components, followed by the calculated principle components (b) 1 (c) 2 (d) 3. Warrumbungle (e) ASTER composite image with each of the five components and principle components (f) 1 (g) 2 (h) 3.*

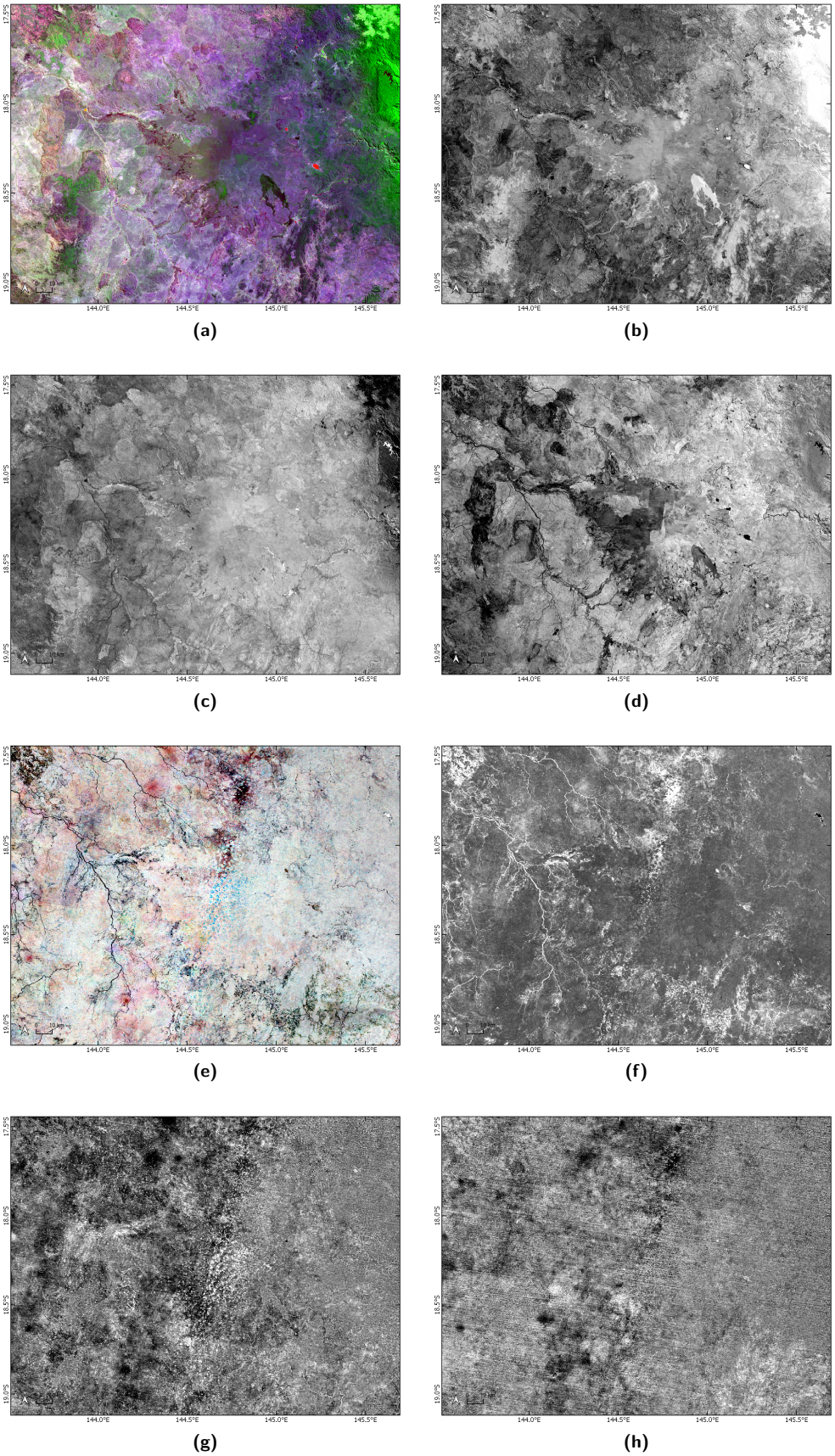

Figure 6.20: *McBride (a) Landsat-8 composite image including each of the seven components, followed by the calculated principle components (b) 1 (c) 2 (d) 3. McBride (e) ASTER composite image with each of the five components and principle components (f) 1 (g) 2 (h) 3.*

PCA

Following composite generation and the selection of data for the random forest classification, PCA was completed on all bands, including the new band ratios, in order to reduce all the input information into just a few uncorrelated output bands. In each province, 99% of the variance from the original images were captured in the first three principle components i.e., 3-bands calculated using the Landsat data and 3-bands calculated using the ASTER data. Using each of these PCA bands instead of the full composite sends a stronger signal to the classifier and improves accuracy by allowing it to distinguish between classes better. All PCA results are shown in Figures 6.19 and 6.20. The input to the Landsat PC analysis was a composite consisting of Landsat-8 bands 3, 5, 6, 7, and band ratios 6/7, 6/2, and 2/5, totaling seven components. The inputs into the ASTER PC analysis included ASTER bands 10, 11, 12, and the MI and SiO_2 (%) indices, totaling five components. The percentage variance of all bands in the Landsat-8 Warrumbungle data was PC1: 95.54, PC2: 3.01, PC3: 1.19, PC4: 0.26, PC5: 0.00, PC6: 0.00, PC7: 0.00 and the variance of all bands in the ASTER data was PC1: 96.93, PC2: 2.22, PC3: 0.68, PC4: 0.18, PC5: 0.00. The percentage variance of all bands in the Landsat-8 McBride data was PC1: 84.04, PC2: 14.55, PC3: 0.92, PC4: 0.48, PC5: 0.00, PC6: 0.00, PC7: 0.00 and the variance of all bands in the ASTER data was PC1: 93.03, PC2: 5.50, PC3: 1.14, PC4: 0.33, PC5: 0.00.

Classification

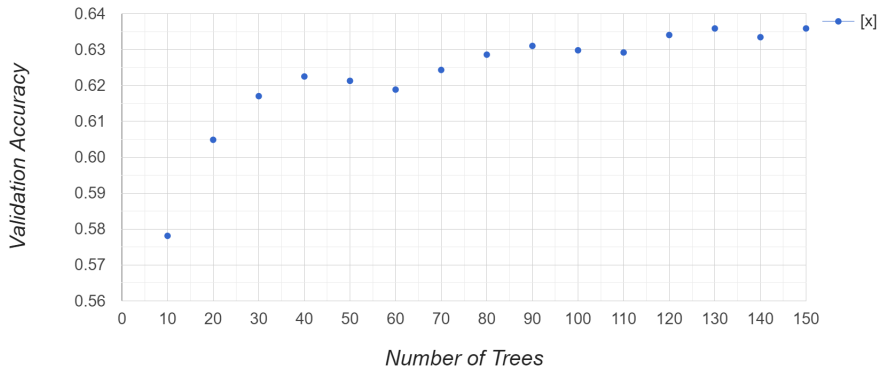

Figure 6.21: *Tuning results for the Warrumbungle province, showing the validation accuracy of the classification versus the number of decision trees specified in the random forest operator.*

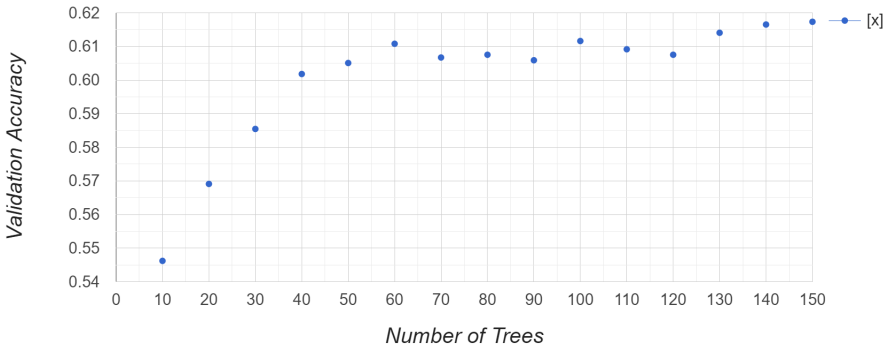

Figure 6.22: *Tuning results for the McBride province, showing the validation accuracy of the classification versus the number of decision trees specified in the random forest operator.*

The final PCA images, along with slope, gravity and magnetic data were normalised to values between 0 and 1 in order to help the classification run smoothly. The dominant geology polygons were then used

to randomly generate 300 points for each class, 70 % of these were used to train the classifier across the normalised input images, and the other 30 % were used to validate the output. The tuning results for the number of decision trees to be used in the classifier plateaued around 90 trees for the Warrumbungle province, and 60 trees for the McBride province (see Figures 6.21 and 6.22). The final results of each classification are shown in Figures 6.23a–b, with the corresponding geological maps shown in Figures 6.23c–d and the computed accuracy for the classifications was 0.63 for the Warrumbungle province and 0.61 for the McBride province.

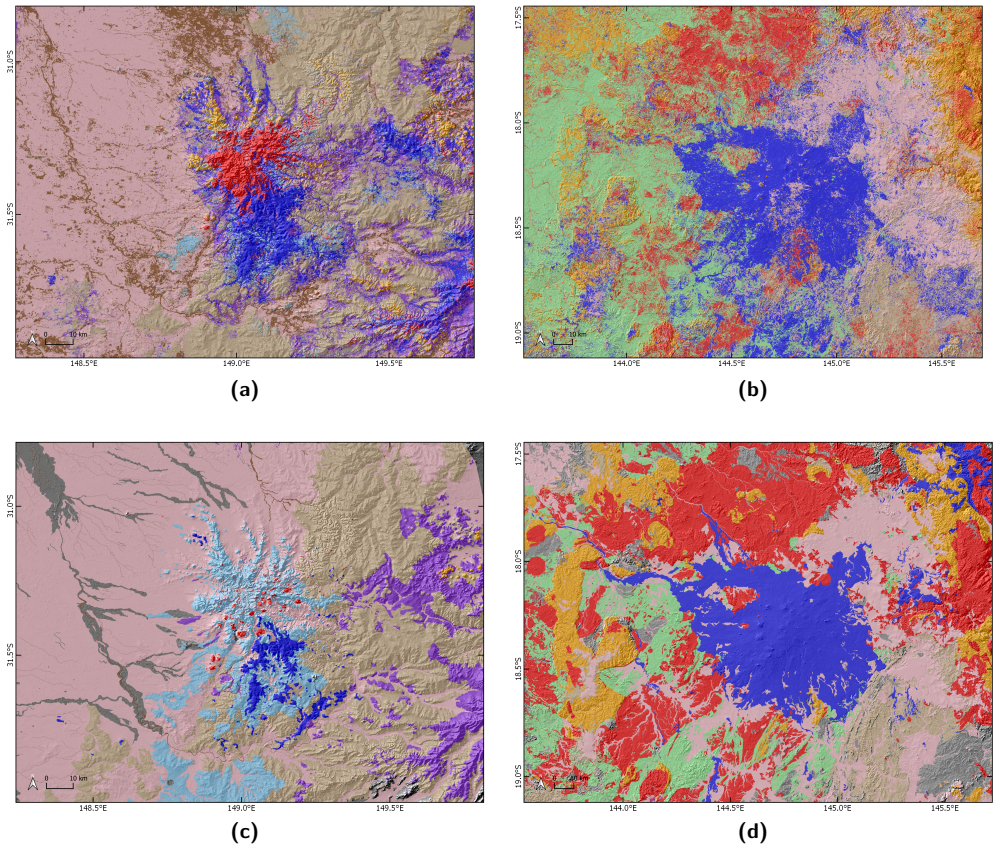

Figure 6.23: *(a) Warrumbungle and (b) McBride GEE classification. (c) Warrumbungle and (d) McBride dominant geology map.*

Classification results for the Warrumbungle province (Figure 6.23a) show that the basic outline of the volcano, as well as the Liverpool Range volcano and the Mesozoic volcanism to the east, are well defined by both mafic and felsic igneous rocks. Basalts and dolerites have been identified around the base of each volcano but the confusion matrix for the Warrumbungle classification (Figure 6.1) shows that, as expected from the spectral analyses, the mafic and sandstone classes were the most difficult to separate and thus occasionally show slightly irregular i.e., un-geological, shapes in the classification results. Furthermore, some rivers appear to have been incorrectly classified as mafic rocks, possibly due to the type of rock within the rivers i.e., eroded basalts. Trachyte and syenite rocks appear to have been over classified, making up a large portion of the upper Warrumbungle volcano which is unlike the mapping results of Bull et al. (2020). The spreading out of trachytes atop the Warrumbungle are probably due to their distinct spectral signature which consisted of high slope, highly vegetated samples, the same signature which is found surrounding most of the volcanic edifice. The same is true for the syenite group which has been classified along the steep ridgelines of lava flows which are actually composed of saprolite and more mafic rocks. This mis-classification is again probably due to the high slope of the pixels which correlate with the high slope of syenite plugs and domes.

Results for the McBride province are a bit better with the lava field outlined quite clearly in the centre of the image. There are a few discrepancies, for example, an area of basalt in south McBride, between the Murronga and Kinrara lava flows, has been incorrectly classified as granitoid and felsite rock in red and orange. Minor basalt has also been classified throughout the scene within all other geological groups. However, this is not necessarily incorrect as a number of the other geological groups are known to contain mafic units i.e., altered basalt in the Arenite group, mafites in the Felsite group, and mafic bands in the metamorphic rocks.

	Alluvium	Sandstone	Clay	Dolerite	Saprolite	Basalt	Syenite	Trachyte
Alluvium	**177**	6	39	10	16	2	5	0
Sandstone	6	**128**	8	21	19	9	13	2
Clay	8	7	**153**	4	8	4	5	1
Dolerite	5	25	9	**83**	12	30	7	6
Saprolite	2	17	7	7	**37**	12	2	8
Basalt	4	7	4	29	57	**132**	1	7
Syenite	0	11	2	23	22	2	**176**	14
Trachyte	0	5	2	16	45	7	7	**152**

Table 6.1: *Confusion matrix for the Warrumbungle random forest classification.*

	Alluvium	Arenite	Metamorphics	Granitoid	Felsites	Basalt
Alluvium	**159**	28	2	14	7	12
Arenite	13	**136**	14	14	14	10
Metamorphics	7	7	**129**	60	38	14
Granitoid	4	19	25	**66**	22	4
Felsites	7	5	11	45	**103**	5
Basalt	16	26	15	7	11	**154**

Table 6.2: *Confusion matrix for the McBride random forest classification.*

It is thus difficult to assess the accuracy of the classification further without fieldwork to ground truth results.

The computed accuracy for each classification were both deemed too low to accept this workflow as a success and the final outlines for both the Warrumbungle and McBride volcanoes did not particularly improve upon the present-day extents due to difficulties in precisely isolating basaltic and felsic igneous rocks from surrounding sandstone and vegetation. Better delineation of volcanic rocks using this process as a starter is instead suggested as further work to this thesis. Following this process, I adopted a quicker method for estimating the eroded extents of each volcano.

6.2.2 Continental Volumes

The two primary types of continental east Australian Cenozoic volcanoes are the central volcanoes and the lava fields. Central volcanoes typically contain a central cluster of silicic vents, often at high elevations, with thick sequences of mafic lavas and pyroclastic flow deposits radiating away from this central zone. The lava flows, dykes, and pyroclastic flow deposits are likely to have built up into large complexes, much of which has been subsequently eroded. Lava fields typically consist of diffuse fissure vent volcanism which have produced thin, extensive sheets of lava with small lava shields, scoria cones, lava cones (intermediate between a lava shield and scoria cone), and maars. All lava field deposits are mafic in composition, often contain lithospheric xenoliths, and are generally better preserved than the central volcanoes. In some lava field provinces individual flows have built up into thick lava piles more typical of the central volcanoes e.g., the Liverpool Range and the Barrington province.

Four of the most important variables affecting the levels of erosion in the East Australian volcanoes are age, climate, drainage, and composition (Wells et al., 1985). Generally speaking, older volcanism is more eroded than younger volcanism, older volcanoes such as the OVP and Tasmania now exists only as small, isolated outcrops of rock, whilst some of the most well preserved volcanoes are the young, inland, far north Queensland lava fields i.e., McBride, Chudleigh, Nulla, and Sturgeon. Volcanoes situated in the tropics, such as Piebald and Maclean, are likely to have experienced greater rates of erosion as have those along the Australian coastline i.e., Fraser Island and Cape Hillsborough, which have in some cases been reduced from large shield volcanoes to only a handful of small outcrops. The composition of central volcanoes, with thick ash blankets, pyroclastic deposits, and more silicic rock types, is expected to be more easily eroded than the flat-lying mafic lava fields and relatively few of the central volcanoes have retained their original broad, shield shape as pyroclastic deposits have been completely or partially removed.

In order to accurately calculate pre-erosive volumes, the present-day exposures at each province need reconstructing to their original volcanic shapes. For this study, the volumes of the original volcanoes have been estimated based on the two broad morphologies discussed above. Six different methods of volume estimation were tested for the lava fields (iterations 4–9 in the volume spreadsheet Appendix I), and nine different methods were tested for the central volcanoes (iterations 4–12, Appendix I). The results of each, along with the final volume estimates, are discussed below. As no detailed mapping was undertaken in this study, most volcanological descriptions are taken from Johnson (1989). The map of each province throughout the following section shows the present-day extent of volcanic rocks, footprint 1, footprint 2, and footprint 3, as white, blue, cyan, and purple lines, respectively. Samples collected during fieldwork are shown as red stars along with sample names, borehole locations are shown as red circles, and all data overlays a hillshade map created in QGIS from the SRTM DEM. The full methods for all volume surface calculations are discussed in Chapter 3. For each province the following footprints have been defined:

- Footprint 1: A tight geometry not connecting all exposures, using the concave hull tool in QGIS (number of neighbours = 3, and SNN clusters = 10), modified where needed to follow valley confines. This gives a lower estimate for the volcanic footprint.
- Footprint 2: A looser geometry connecting all exposures, using the concave hull tool in QGIS (number of neighbours = 3), modified where necessary to give a more geological shape. This gives a middle estimate for the volcanic footprint.
- Footprint 3: The minimum geometry bounding all exposures, using the convex hull tool in QGIS which gives a higher estimate for the volcanic footprint. Only the central volcanoes are expected to be adequately represented by this footprint.

Overview

To calculate the preserved, present-day volume of volcanic rocks three different methods were tested (iterations 1–3, Appendix I), the top surface was defined as the present-day DEM of volcanic rock exposures and the base surface was defined as (1) the local minima of the present-day DEM, (2) a surface interpolated across the present-day volcanic extent, and (3) a surface interpolated across the extent of footprint 1.

The local minima baseline method (1) generally works best on smaller, highly eroded volcanoes, which are now small mounds of rock e.g., Piebald; the most northerly volcano of the continental chain in far north Queensland. In these provinces masked baselines (2) and (3) tended to cut through present-day exposures, excluding deeper outcrops from the final volume. This is probably because they are buried by sediment so the elevation of outcrop edges is not very representative of the elevation of the base. In part, larger volcanoes will also have their volume underestimated in this way but probably by a lower percentage. By using the

local minima estimation, all of the deepest exposures of volcanic rocks were included in the final volume estimate. Because of this reasoning, where the local minima estimate produced a greater volume than the masked baseline estimate, the prior result was chosen as the most likely volume of preserved volcanic rock. This was mostly the case for very small scattered rocks, or where volcanoes are located in a depression from the surrounding footprint e.g., Fraser Island, GMN, Leucitite, Piebald, and Rockhampton provinces.

Volcanoes which form prominent hills above surrounding plains, either as thick lava packages or thick shield remnants e.g., Barrington, Buckland, were all likely underestimated with the local minima baseline as small minima at the top of thick lava packages were taken as the baseline. A more accurate estimation was produced using a baseline interpolated across the present-day extent of volcanism (2). As proven by the need for the local minima baseline, the edges of the present-day DEM are not always a good representation of the base of each volcano and so this process was also repeated with the edges extracted from the larger footprint 1 boundary (3). Most preferred estimates of preserved rock volume have been produced by this method except for results which were higher using the local minima baseline i.e., in the heavily eroded volcanoes which now exist as small, scattered outcrops.

To calculate the original volume of volcanic rocks six different methods were tested for the lava fields (iterations 4–9, Appendix I), and nine different methods for the central volcanoes (iterations 4–12, Appendix I). Iterations 4–6 use a top surface defined by the present-day DEM and a base surface defined by an interpolated surface across footprints 1, 2, and 3, respectively. Iterations 7–9 use a top surface defined by resurfaced ridgelines to the extents of footprints 1, 2, and 3, and a base surface again defined by an interpolated surface across footprints 1, 2, and 3, respectively. Iterations 10–12 then use the top surface as a pyramid which encompasses 80, 90, and 100% of all preserved outcrops, and a base surface interpolated across footprint 3 i.e., the convex hull extent. This was only estimated for the central volcanoes as in keeping with the morphology of the lava fields, single plugs and vents are not expected to have formed a large, pyramidal shield.

For most lava fields the combination of surfaces which give the most appropriate estimate for the minimum pre-eroded volume was defined as the ridgeline resurfacing of footprint 1 and the interpolated footprint 1 base (iteration 7, Appendix I). In areas where greater connectivity of present-day exposures was assumed the preferred method was defined as the ridgeline resurfacing of footprint 2 and the interpolated footprint 2 base (iteration 8, Appendix I). In some cases, usually in young, low-lying volcanoes which have not been subjected to large amounts of erosion e.g., far north Queensland, ridgelines were not well defined and the extrapolations were likely to be overestimating the pre-erosive volume of rock. In this case, the present-day DEM actually worked better for defining the upper surface of volcanism and the minimum eroded volume was best defined by a combination of the present-day DEM of footprint 1 and the interpolated footprint 1 base (iteration 4, Appendix I).

For all lava fields the maximum eroded volume was produced by combining the ridgeline resurfacing of footprint 3 and the interpolated footprint 3 base (iteration 9, Appendix I). As discussed in the text, this volume is likely a significant overestimate for each province but was included to show how volume calculations may vary between suites and to show what effect the resurfaced ridgelines and increased connectivity of outcrops are having on the final results. The preferred estimate for the original, pre-erosion volumes of each volcano are given in the volume spreadsheet and discussed in the following text (Appendix I).

For the central volcanoes the minimum eroded volumes were produced using the same method as the lava fields but the maximum eroded volumes were calculated using the top surface as a pyramid which covers 100% of the preserved outcrops, and using the interpolated footprint 3 baseline (iterations 10–12, Appendix I). The preferred estimate for the original, pre-erosion volumes of each central volcano are given in the volume spreadsheet and discussed in the following text (Appendix I). All ages discussed in the following Chapter include available $^{40}Ar/^{39}Ar$ analyses, K-Ar analyses, U-Pb analyses, fission track (FT) dating, radiocarbon (C-14) dating, cosmogenic nuclide (CN) dating, thermoluminescence (TL), and U-Th analyses. The subsections below are split into the geochemical groups described in Chapter 4, and provinces are arranged north to south within each group.

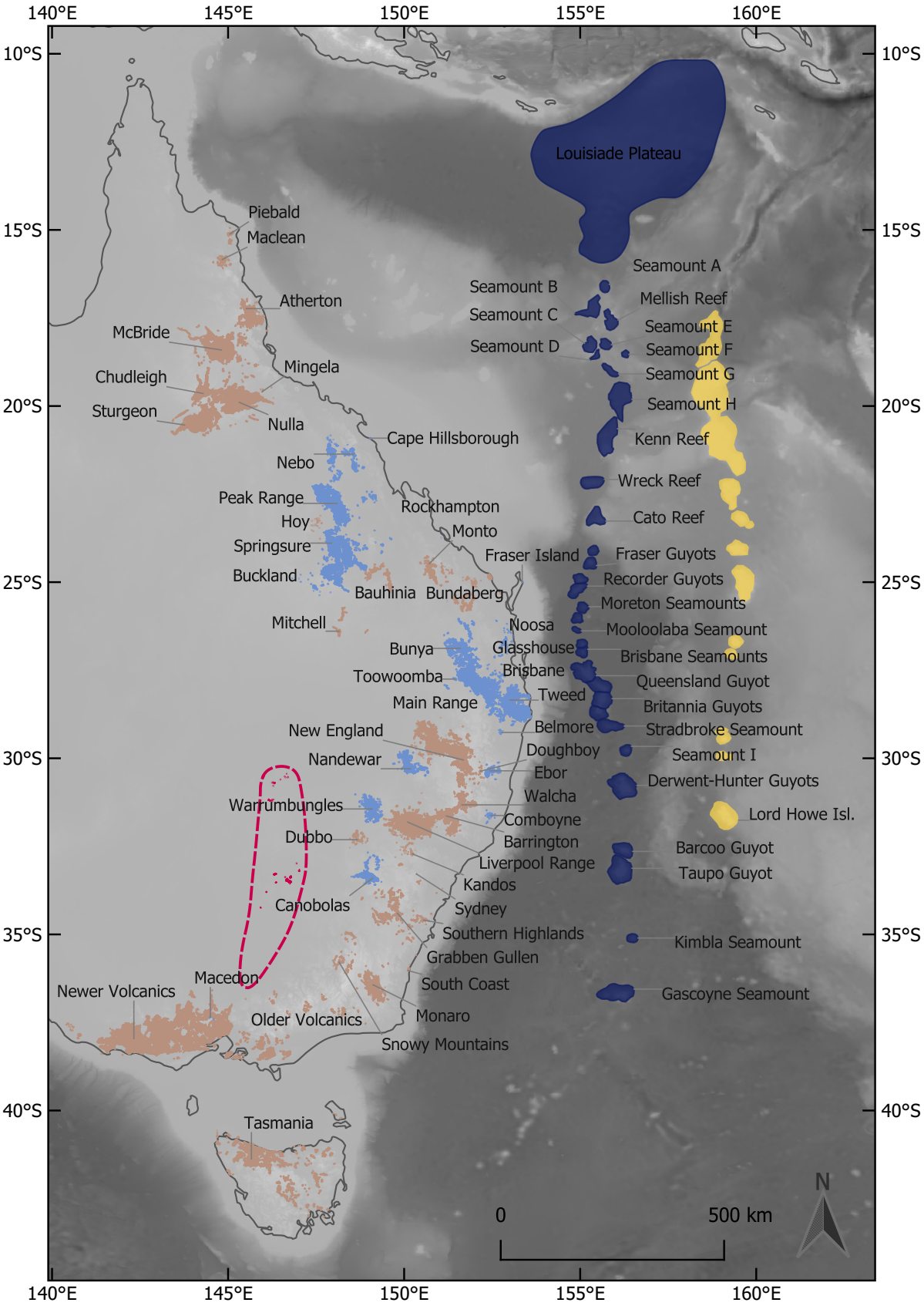

Figure 6.24: *Individual volcanic provinces within the five volcanic suites. Tasmantid seamounts marked in navy; Lord Howe seamounts in yellow; central volcanoes in light blue; lava fields in tan; and leucitites within the dashed crimson area. Topographic and Bathymetric grid from GEBCO (2020).*

6.2.3 Recent Northern Queensland Volcanism

Piebald (1.62–1.20 Ma)

The Piebald lava field is made up of around 14 vents within residual basaltic hills that are likely to have been small, low-lying, shield volcanoes, and dissected pyroclastic cones (Johnson, 1989). Only two K-Ar ages exist for the Piebald province itself and these range from ∼1.62–1.20 Ma (Cohen et al., 2017). Despite a lack of age data, volcanism here is much like other far north Queensland provinces, erupting within the last 10 Ma, and given the small size of the present-day lava field, volcanism is likely to have been fairly short-lived. Piebald now exists as three, isolated lava fields and the pre-erosion volumes estimate here vary considerably depending on how connected each of the fields were originally. Since many outcrops in Piebald consist of valley filling lava flows the original extent is not assumed to extend over hills and ridges between the three fields. I have therefore taken the preferred pre-erosion extent as footprint 1 which roughly encloses each of the three fields but keeps flows isolated and within the valley confines. Given the young age of the province, erosion is expected to be quite low and thus the present-day DEM was taken as the preferred pre-erosion top surface. However, it is possible significantly more material has been eroded when considering the location of Piebald by the coastline and in a tropical climate, so the estimate made here may be an underestimation.

- Estimated Preserved Volume; 1 km^3.
- Estimated Original Volume; 3 km^3.
- Oldest Age; 1.62 Ma (no errors reported) K-Ar (Cohen et al., 2017) (no comment on sample quality); mafic lava from Bald Hills, 5 km west of Mount Piebald.
- Youngest Age; 1.20 Ma (no errors reported) K-Ar (Cohen et al., 2017) (no comment on sample quality); mafic lava from Mount Piebald crater edge.

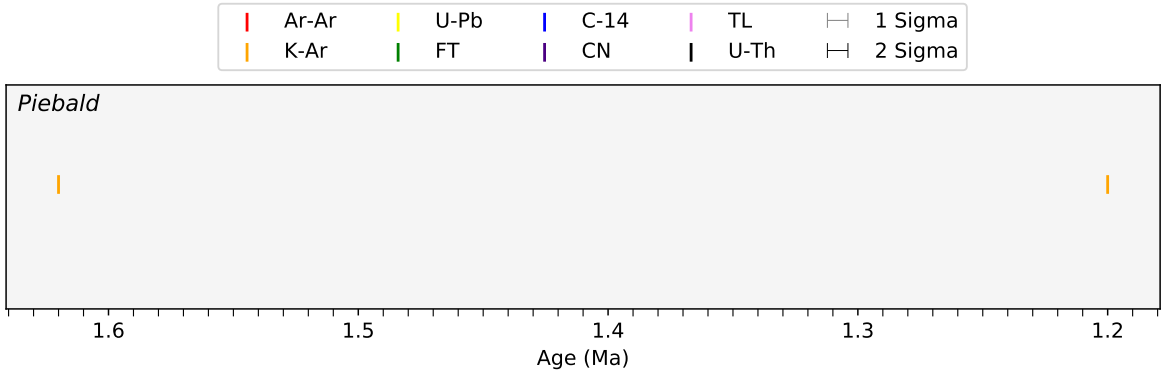

Figure 6.25: *Age data for the Piebald province.*

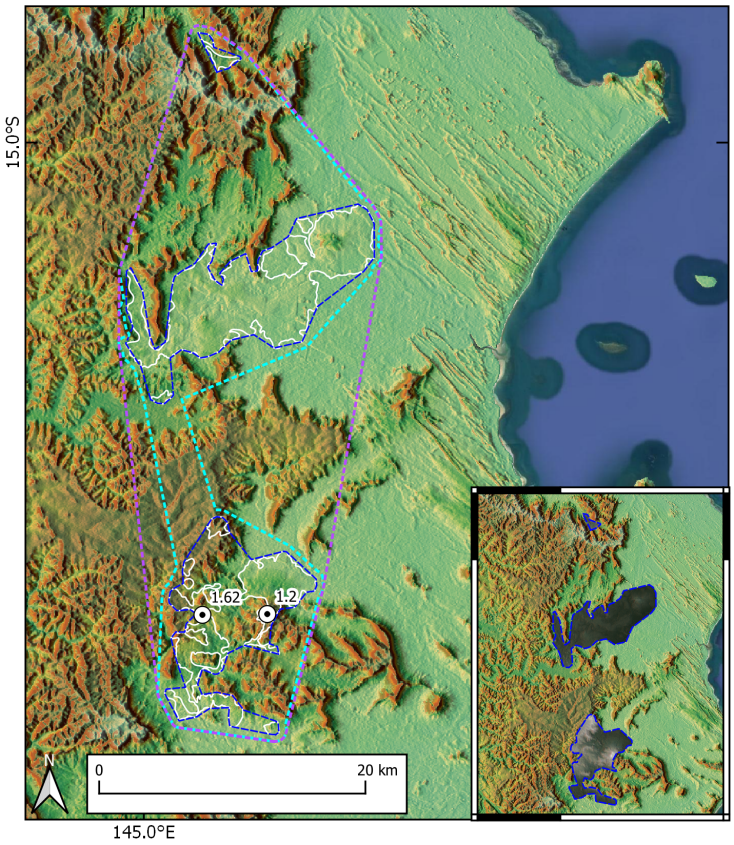

Figure 6.26: *The Piebald volcanic province.*

Maclean (6.29–3.08 Ma)

The Maclean province is closely associated with the Piebald province and contains similar scattered and isolated lava field remnants (Johnson, 1989). The province consists of moderately-preserved scoria cones, lava cones, small composite volcanoes, and valley-floor lava fields (Johnson, 1989). 18 vents have been identified by Johnson (1989). The only dates recorded for the Maclean province are nine K-Ar ages by Cohen et al. (2017), Sutherland et al. (1998), and Barron et al. (1996). Again, despite there being few dates available, results are very similar to others in North Queensland, erupting towards the end of the Cenozoic Era and within the last 10 Ma. Whilst larger than the Piebald province, Maclean does display similar volcanological features which are best represented as low-lying lava plains and the same method of volume estimation was used for this province where flows are only moderately connected between fields. The present-day DEM was again the preferred top surface for the pre-erosion estimate as this relatively young province should not have been considerably affected by erosion. However, given the coastal location this may again be an underestimate.

- Estimated Preserved Volume; 8 km^3.
- Estimated Original Volume; 10 km^3.
- Oldest Age; 6.29 Ma (no error reported) K-Ar (Cohen et al., 2017) (no comment on sample quality); mafic lava from Racecourse Mountain, Spring Gully.
- Youngest Age; 3.08 Ma (no error reported) K-Ar (Cohen et al., 2017) (no comment on sample quality); mafic lava from a volcanic cone, west of Normanby River.

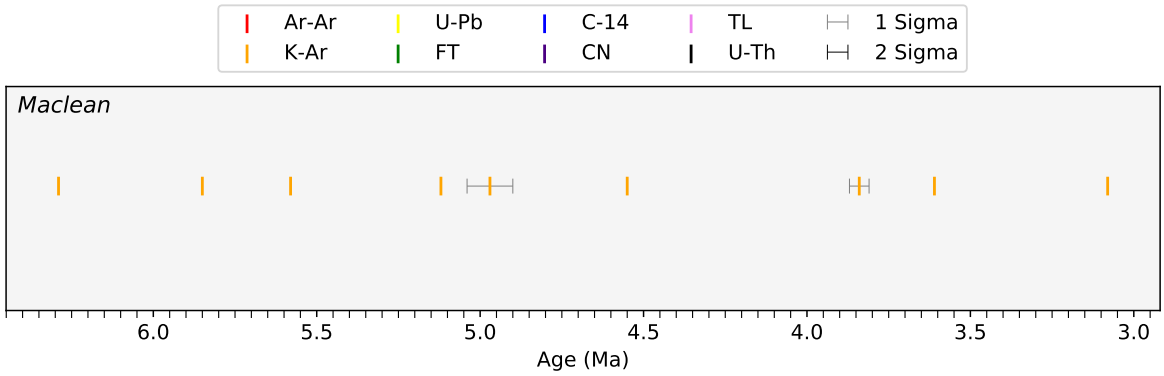

Figure 6.27: *Age data for the Maclean province.*

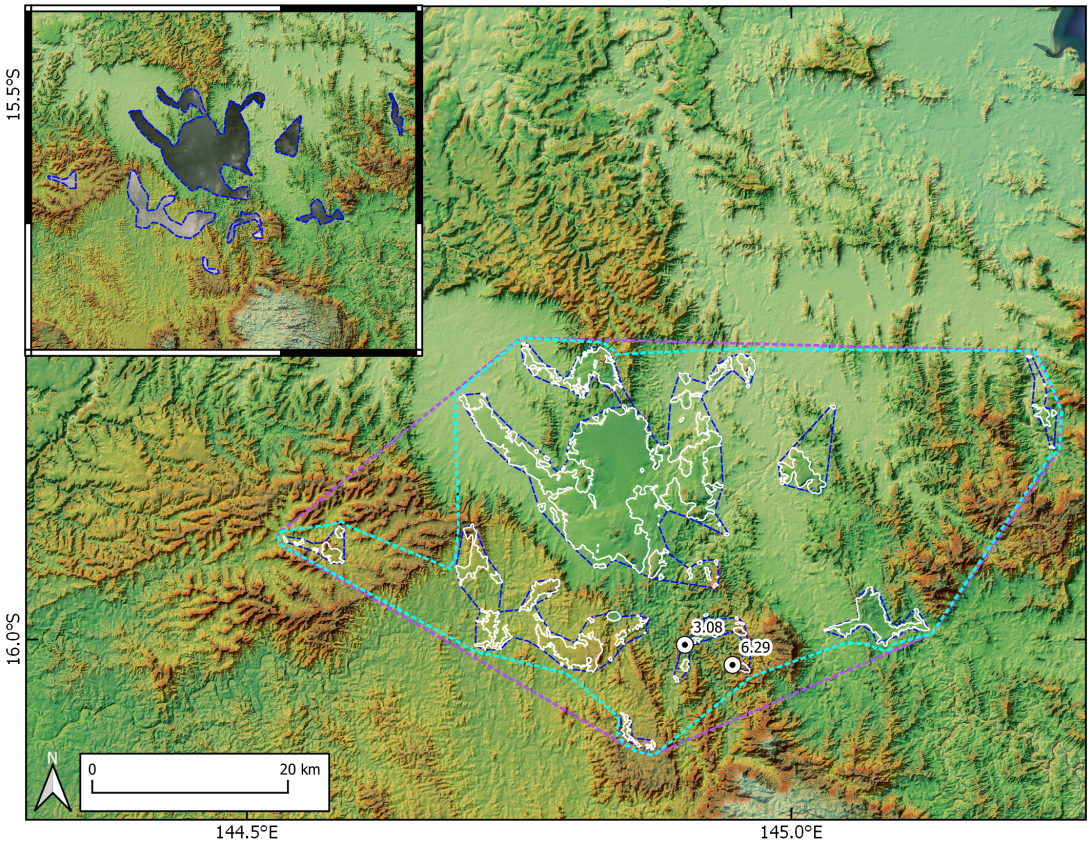

Figure 6.28: *The Maclean volcanic province.*

Atherton (7.10–0.00725 Ma)

Covering much of the Atherton Tableland and adjacent areas are at least 65 eruption centres forming a range of volcano types, previously named the Quincan province by Wellman (1971). The province generally consists of broad lava plains where the most extensive and voluminous flows were produced from two shield volcanoes, the Jensenville and Malanda (Whitehead et al., 2007). In some areas lava flows reach thicknesses of up to 300 m (Johnson, 1989). Later volcanism is comprised of less voluminous alkaline lavas, cinder cones, maars, and one phreatomagmatic diatreme (Johnson, 1989). The generation of maars in this province, unlike elsewhere in Queensland, is possibly due to the wetter, tropical climate adjacent to the coastline. The most recent summaries of chronology from Atherton are reported in Whitehead et al. (2007) and Cohen et al. (2017). From K-Ar analysis of 47 samples Whitehead et al. (2007) identified six main periods of volcanism; (1) the Western Creek 7 Ma period; (2) the Jensenville 3.90–2.82 Ma and (3) Malanda 3.39–3.01 Ma period; (4) the 2 Ma period; (5) the 1.8–1.5 Ma period; and (6) the 1.5–0.8 Ma period. Whilst several eruption centres remain undated, volcanism again took place within the last 10 Ma. U-Th and radiocarbon ages, by previous workers and compiled in Whitehead et al. (2007), give ages of $\sim$350–7.25 Ka and represent the youngest volcanism at Atherton. Despite having two, sizable shield volcanoes, Jensenville and Malanda, the morphology of the province as a whole is best represented by the extrapolation of present-day ridgelines and not as a pyramidal structure covering all present-day deposits. A flatter volume is preferred because the shields did not cover the whole province and valley floor lavas make up a large proportion of the rest of the Atherton deposits. Atherton deposits have relatively good connectivity and the preferred pre-erosion estimates again uses the present-day DEM as the upper surface and footprint 1 as the extent.

- Estimated Preserved Volume; 67 km^3.
- Estimated Original Volume; 130 km^3.
- Oldest Age; 7.10 ± 0.14 Ma (1σ) K-Ar (Whitehead et al., 2007) (minor mesostasis or glass in the groundmass, provided this material had minimal alteration, samples were accepted for dating); mafic lava from an isolated remnant flow near Western Creek.
- Youngest Age; 7.25 Ka (no error reported) C-14 (Whitehead et al., 2007) (minimum age of eruption); sediment from Mt Quincan.

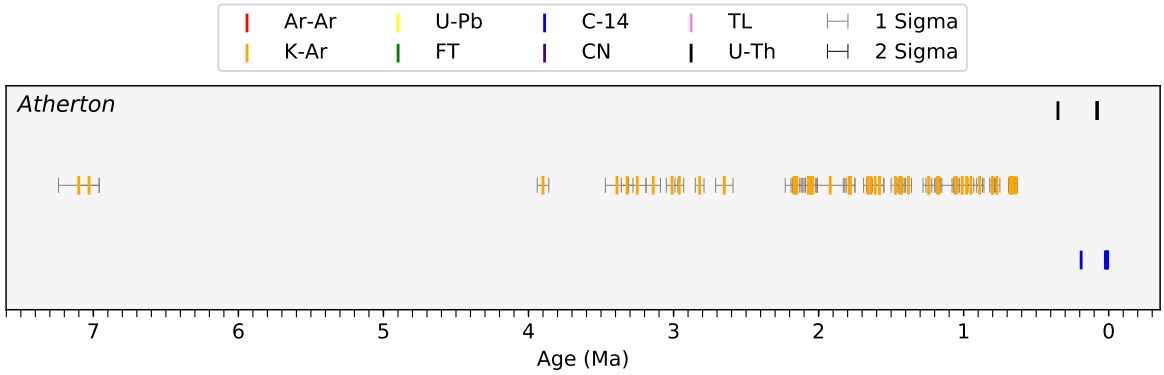

Figure 6.29: *Age data for the Atherton province.*

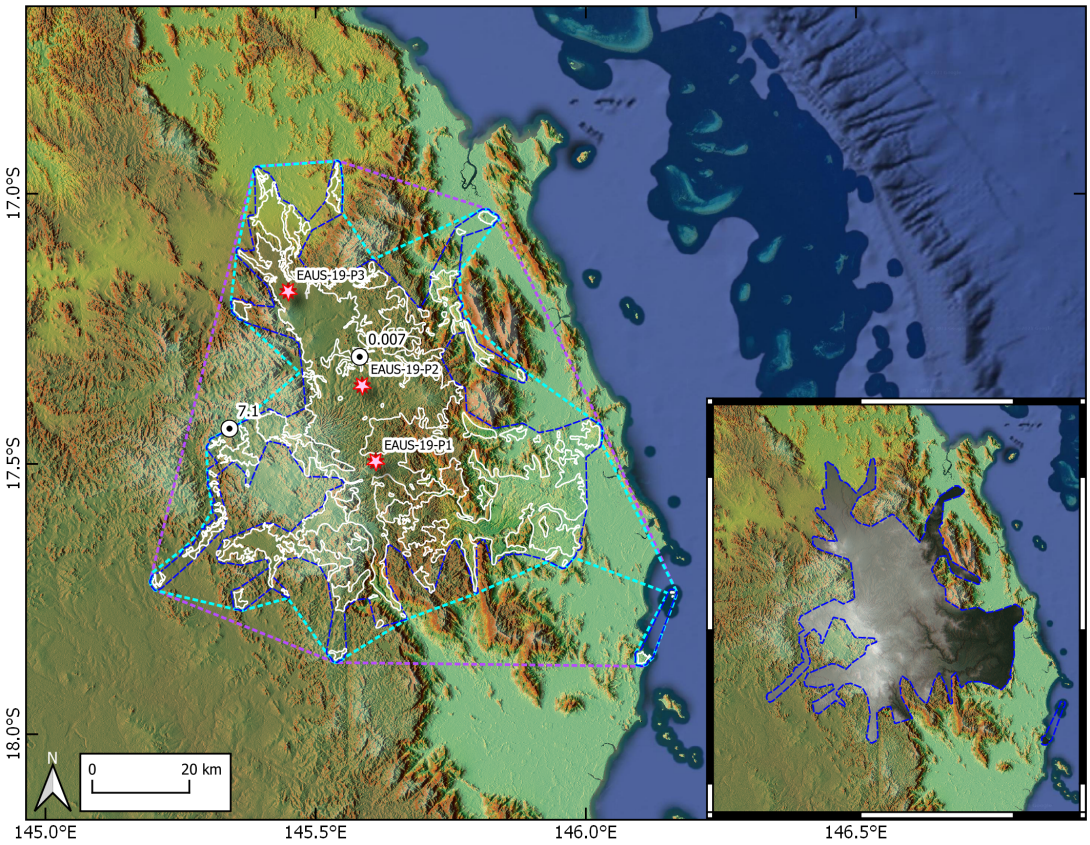

Figure 6.30: *The Atherton volcanic province.*

McBride inc. Wallaroo (10.3–0.007 Ma)

The McBride province is composed mostly of broad basaltic lava flows with thickness estimates reaching a maximum of 600 m (Griffin and McDougall, 1975; Ransley et al., 2020). The central area forms a gentle topographic dome and contains numerous small shields, pyroclastic cones, and scoria cones (Johnson, 1989). Griffin (1977) identified 164 volcanic centres and the whole province covers an area of 5500 km^2. Older McBride volcanism outcrops as plugs, mesas and plateaux in north and southwest of the province. Younger basalts, along with those from Chudleigh, Sturgeon and Nulla, are noteworthy for the length of some flows such as the 160 km flow from the Undara Crater (Johnson, 1989; Cohen et al., 2017; Stephenson, 2009). To the east lies the smaller Wallaroo province which, given similarities in age and morphology, have here been included in the McBride volume calculations. Wallaroo contains valley-filling lava flows up to 50 m thick (Johnson, 1989). Flows from the two provinces have been relatively well preserved due to the young age and semi-arid climate of the localities. K-Ar results from the McBride province range from $\sim$8.41–0.051 Ma and appear to show two stages of volcanism, one $\sim$8.41–6.53 Ma, and the other $\sim$3.26–0.051 Ma. Unfortunately, only the younger flows of this volcano have been Ar-Ar dated by Cohen et al. (2017) and Jones (2018). The total age range is again consistent with the onset of the most recent volcanism in Northern Queensland, erupting within the last 10 Ma. K-Ar analysis of the Wallaroo show that it was probably active during the first stage of McBride volcanism, $\sim$10.3–5.53 Ma. There is no publicly available borehole data from the McBride area but data from a drilling program conducted by the Queensland Government Department of Environment and Science in 2017–2018 (Hansen et al., 2020) was acquired by Ransley et al. (2020) who produced a 3D surface of the base of the McBride basalts. The same surface has been used in the volume calculations in this study. Like other far north Queensland volcanism, the McBride deposits have relatively good connectivity and limited erosion and so the present-day DEM and footprint 1 were again used as the preferred original top and extent.

- Estimated Preserved Volume; 283 km^3.
- Estimated Original Volume; 327 km^3.
- Oldest Age; 10.3 (no error reported) K-Ar (Cohen et al., 2017) (no comment on sample quality); mafic lava from the easternmost mesa, north of Herbert Gorge; Wallaroo province.
- Youngest Age; 7.00 $\pm$ 2.00 Ka (2σ) Ar-Ar (Cohen et al., 2017) (little or no appreciable excess or inherited argon); basanite from Kinrara lava; this is the flow with the most youthful geomorphology and least weathering, representing the last eruption in the area.

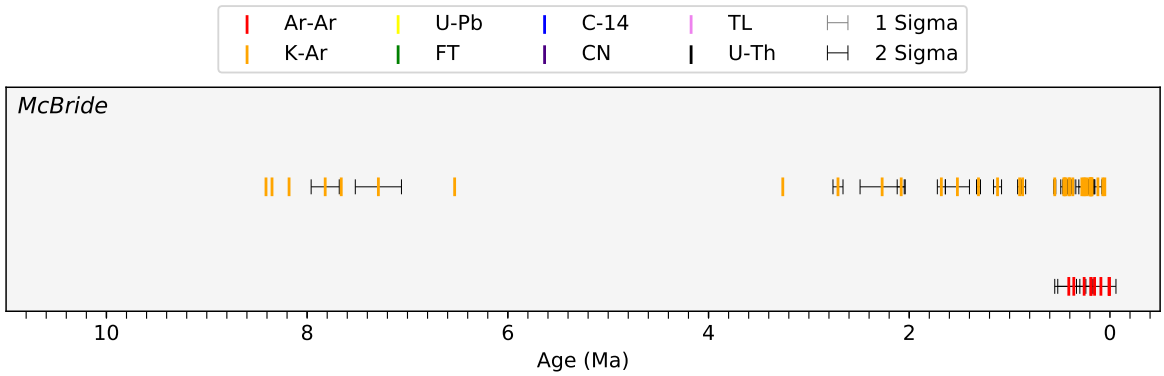

Figure 6.31: *Age data for the McBride province.*

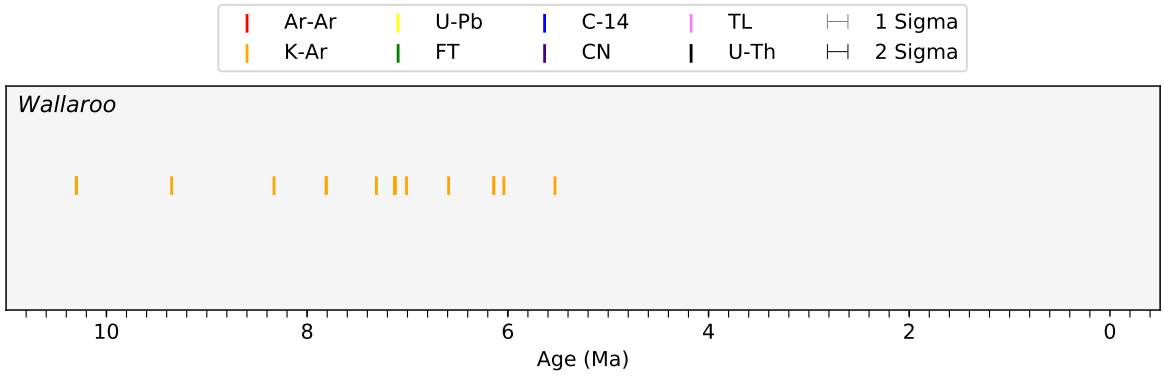

Figure 6.32: *Age data for the Wallaroo province.*

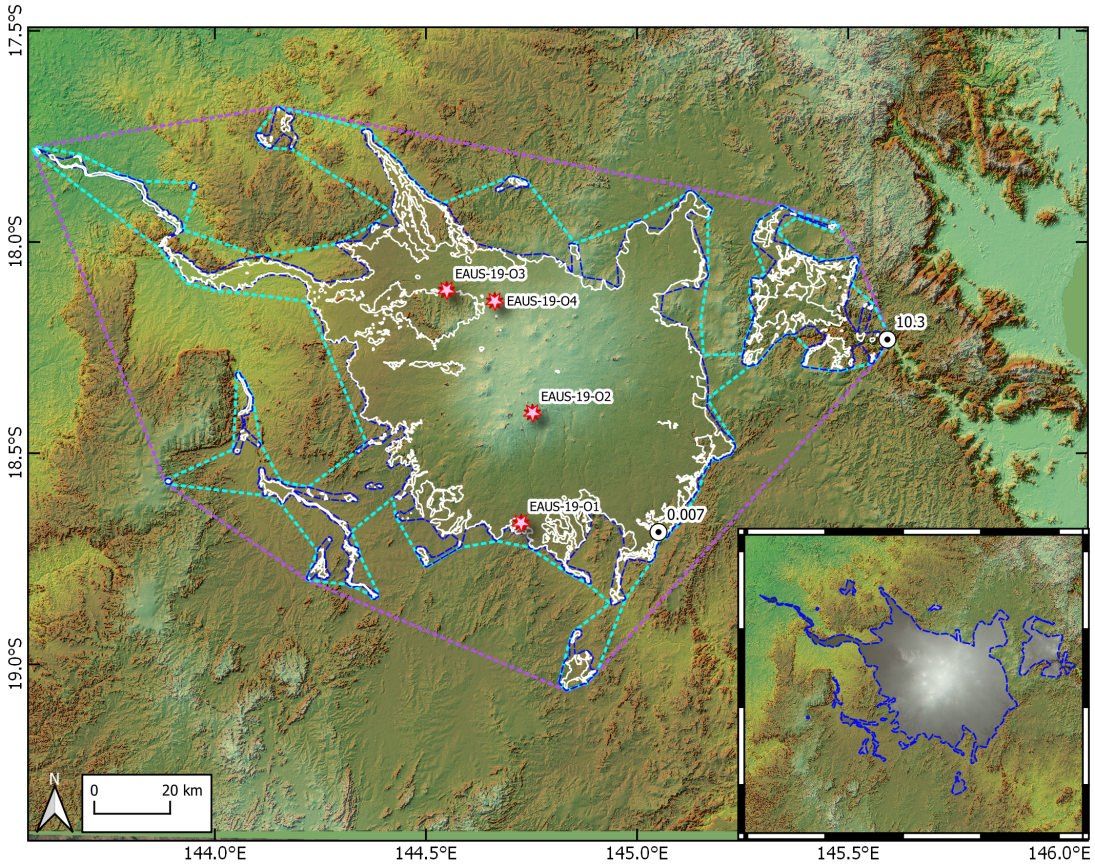

Figure 6.33: *The McBride volcanic province. The 3D baseline by Ransley et al. (2020) has been created using the results of a drilling program conducted by the Queensland Government Department of Environment and Science in 2017–2018 (Hansen et al., 2020)*

Chudleigh (8.03–0.23 Ma)

The Chudleigh province consists of 46 known volcanic centres within a continuous basalt plateau (Johnson, 1989). Like other lava field provinces Chudleigh is characterised by broad, partly dissected lava plains with numerous pyroclastic cones, composite cones, and several lava shields (Johnson, 1989; Cohen et al., 2017; Stephenson, 2009). Individual lava flows extend up to 100 km. The only available ages for the Chudleigh province are K-Ar results complied in Cohen et al. (2017). Whilst little detail on quality and freshness of the samples is given, there is a very good coverage of ages from across the volcano and they also correlate well with other volcanism in Northern Queensland, with frequent activity over the last 10 Ma. Between the Chudleigh, Sturgeon, and Nulla provinces there are numerous, discontinuous basaltic mesas which suggest the three regions may once have been connected. This also points to a substantial amount of erosion around Clarke Hills and Wando Vale, between the provinces. This area has been accounted for within the estimated pre-erosion footprints of Chudleigh, Sturgeon and Nulla collectively. Chudleigh again has good connectivity and the pre-erosion volume was defined by the present-day DEM and footprint 1. The base of the Chudleigh province was much more difficult to constrain as the centre of the volcano is surrounded by relatively high basement, meaning the edges of the present-day extent give a base much too shallow. The base was instead constrained by excluding these central areas from the masked baseline calculation.

- Estimated Preserved Volume; 159 km^3.
- Estimated Original Volume; 267 km^3.
- Oldest Age; 8.03 Ma (no error reported) K-Ar (Cohen et al., 2017) (no comments on sample quality); mafic lava from Umbrella Mountain.
- Youngest Age; 0.23 Ma (no error reported) K-Ar (Cohen et al., 2017) (no comments on sample quality); mafic lava from Barkers Crater.

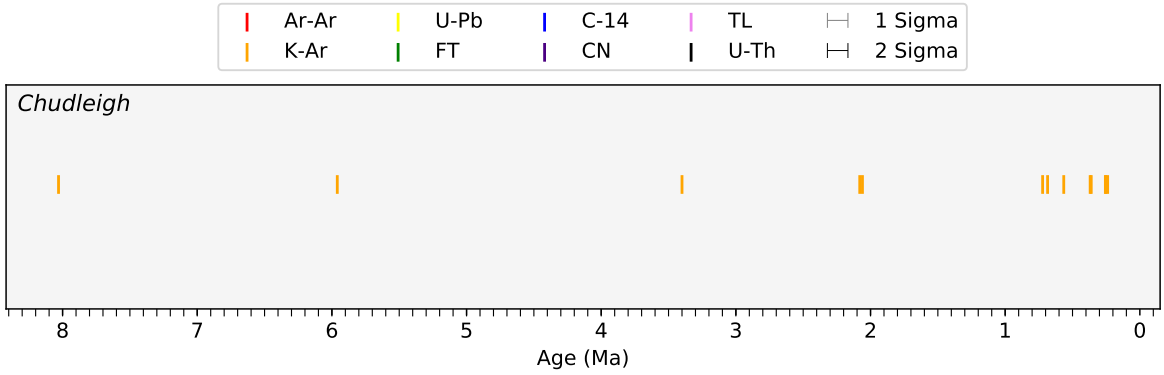

Figure 6.34: *Age data for the Chudleigh province.*

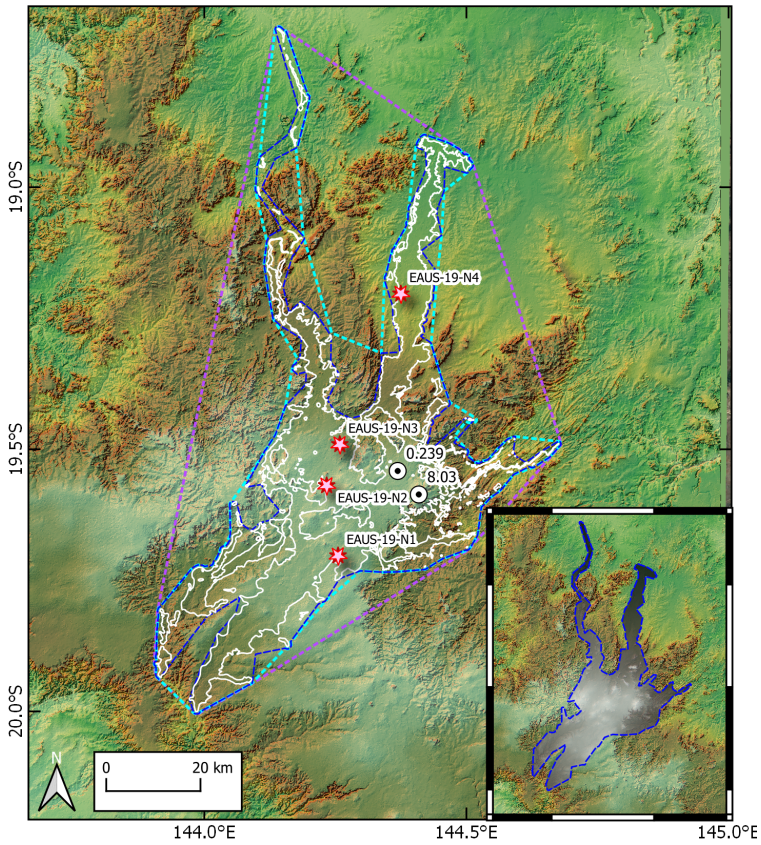

Figure 6.35: *The Chudleigh volcanic province.*

Nulla (8.81–0.01994 Ma)

The Nulla lava field has 46 recognised vents in a complex of fissures and minor pyroclastic cones which produced mafic lavas that flowed east towards the Burdekin Valley (Johnson, 1989). K-Ar ages by Wyatt and Webb (1971) and Cohen et al. (2017) range from ∼8.81–0.044 Ma, with the oldest samples collected from the west of the province at the boundary with Chudleigh and Sturgeon. Volcanism is thought to have been continuous from around 5 Ma up to 0.021 Ma when the youngest volcano, Toomba, was erupted (Cohen et al., 2017; Stephenson, 2009), this represents the stratigraphically highest unit. Like other North Queensland volcanism, the Toomba basalt flow is noted for its exceptional length of 120 km (Whitehead and Stephenson, 1998). Upper age limits have been refined further with Ar-Ar ages from Cohen et al. (2017) and C-14 ages from Mishra et al. (2019). Radiocarbon ages from Stephenson et al. (1978) have issues with carbon contamination which is discussed in detail in Cohen et al. (2017). For this reason, these ages have been excluded from the overall age range at Nulla. Most of the Nulla province has well preserved flow morphology and connectivity of lavas and as such the preferred pre-erosion volume estimate has again been taken from present-day DEM and the extent of footprint 1. The basal surface is well constrained with borehole data from (Hansen et al., 2020), which was gridded by Ransley et al. (2020) and the resultant 3D surface used in this study.

- Estimated Preserved Volume; 274 km^3.
- Estimated Original Volume; 330 km^3.
- Oldest Age; 8.81 Ma (no error reported) K-Ar (Cohen et al., 2017) (no comments on sample quality); mafic lava from the northwestern limit of Nulla; unsure if this is the stratigraphic base.
- Youngest Age; 0.01994 ± 0.00021 Ma (2σ) C-14 (Mishra et al., 2019) (good agreement with Ar-Ar ages of same location); charcoal sample from beneath the Toomba lava flow at Big Bend.

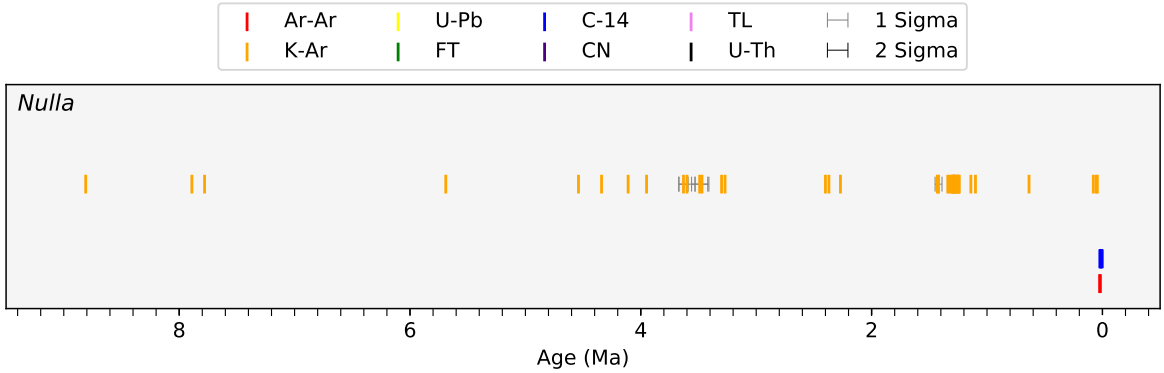

Figure 6.36: *Age data for the Nulla province.*

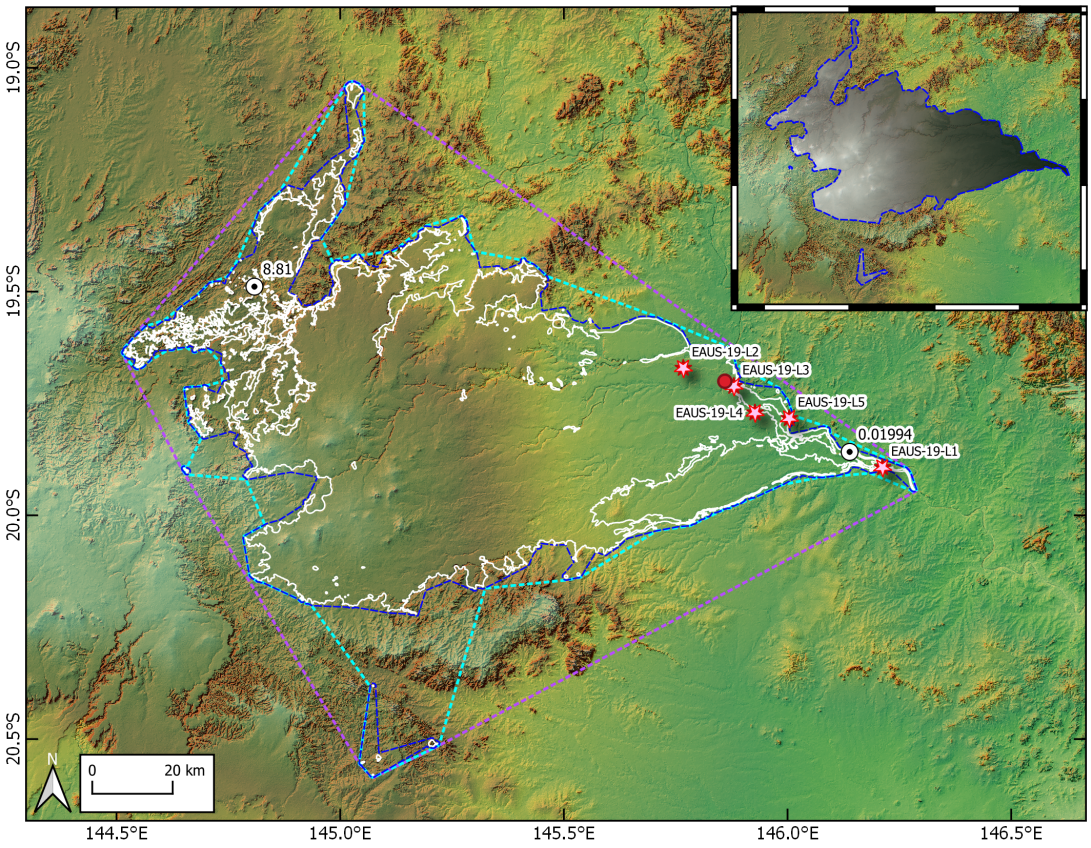

Figure 6.37: *The Nulla volcanic province. The red dot shows the location of the only freely available borehole from Queensland Government (2022). The 3D baseline by Ransley et al. (2020) has instead been created using the results of a drilling program conducted by the Queensland Government Department of Environment and Science in 2017–2018 (Hansen et al., 2020).*

Sturgeon (8.90–0.68 Ma)

The Sturgeon volcano consists of wide lava plains that form a broad topographic dome across the province (Johnson, 1989). To date, around 46 volcanic centres have been recognised with lava flows again reaching up to 120 km long (Stephenson, 2009). Correlation among the multitude of flow remnants is difficult and as such stratigraphical constraints of K-Ar data is limited (Coventry et al., 1985). The only available ages for Sturgeon are K-Ar data from Coventry et al. (1985) and Cohen et al. (2017) which range from ∼8.90–0.68 Ma. K-Ar samples provide particularly good coverage across the province and again ages are similar to other provinces in northern Queensland, with volcanism taking place in the last 10 Ma. The oldest ages come from the northeast of the province, at the boundary with the Chudleigh and Nulla volcanic areas. As with other far north Queensland volcanoes, the Sturgeon field exhibits good connectivity of outcrops and minimal erosion of the lava field. However, ridgelines were not well defined in this province and the volumes calculated from resurfacing ridgelines were lower than the estimated preserved volume of rock. Again, the volume calculated using the present-day DEM as the upper surface provided a much better estimate of the top, pre-erosive volcanic surface. The base was well constrained by masking the footprint 1 extent downslope to the SW. Unfortunately, no freely available borehole data exists for the Sturgeon province, or indeed any of the far north Queensland volcanoes, but the volumes produced with the masking method are consistent with those produced for the McBride and Nulls fields using the 3D baseline from Ransley et al. (2020).

- Estimated Preserved Volume; 210 km^3.
- Estimated Original Volume; 254 km^3.
- Oldest Age; 8.90 Ma (no error reported)K-Ar (Cohen et al. (2017)) (no comments on sample quality); mafic lava from an old mesa 3.5 km ENE of Clarke Hills.
- Youngest Age; 0.68 Ma (no error reported) K-Ar (Cohen et al. (2017)) (no comments on sample quality); mafic lava from Fresh Crater, east of Shelly Mountain.

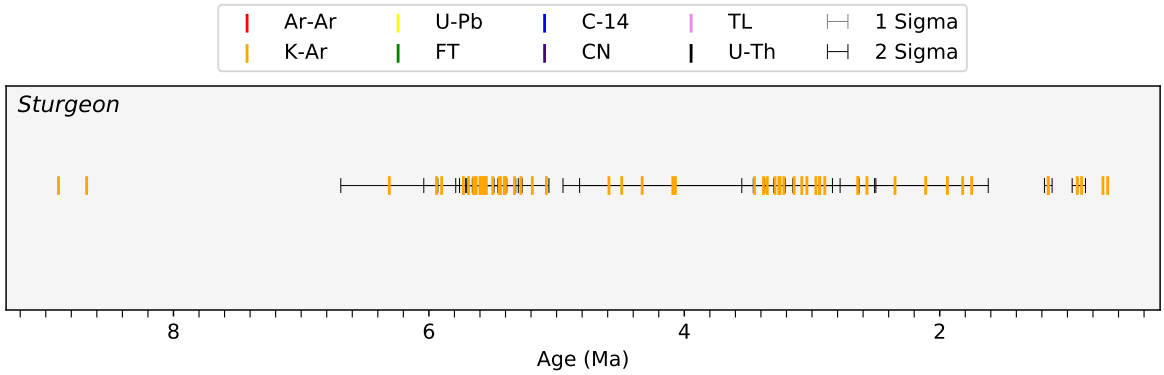

Figure 6.38: *Age data for the Sturgeon province.*

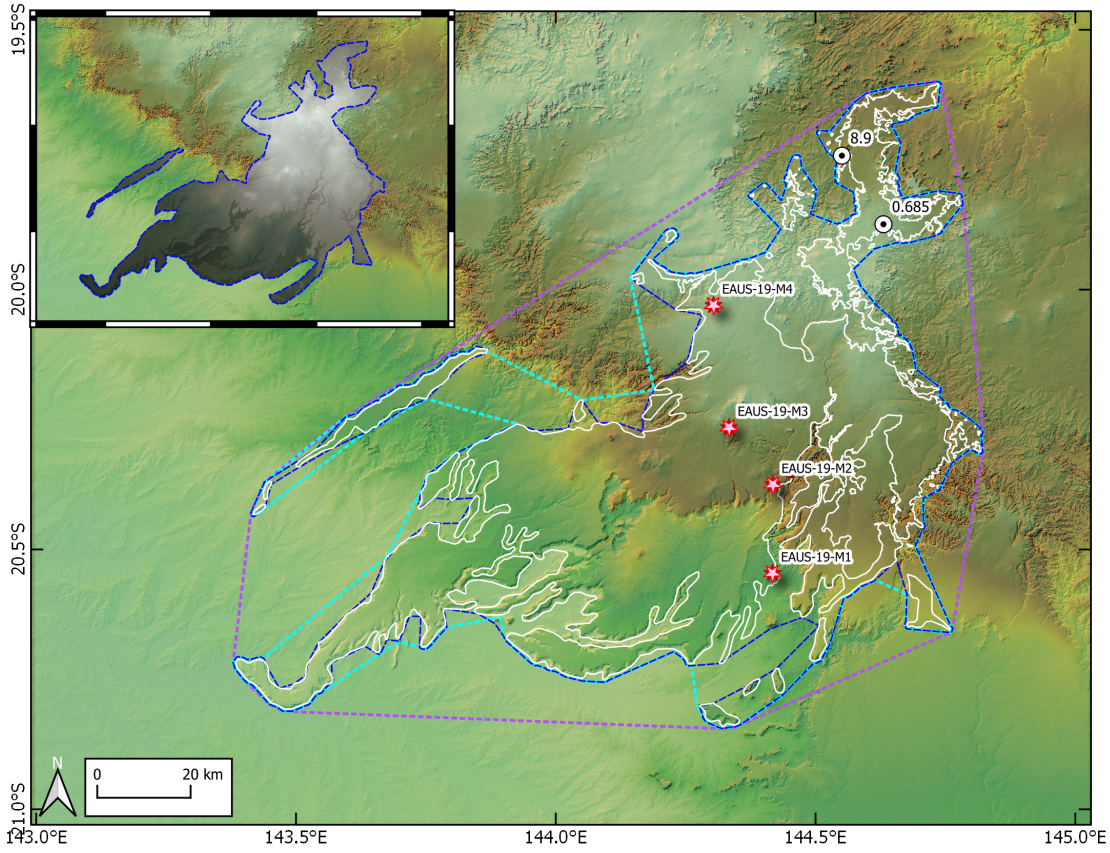

Figure 6.39: *The Sturgeon volcanic province.*

6.2.4 Leucitites, Macedon & the NVP

Leucitite Chain (17.9–8.90 Ma)

The East Australian leucitite chain extends roughly 600 km from potentially as far north as Bokhara River in NSW to Cosgrove in Victoria (Cohen et al., 2008) (the single outcrop at Cosgrove is not shown on the maps provided). Outcrops comprise leucitite-bearing flows and rarely, small intrusions. Most localities along the length of the chain have been K-Ar and Ar-Ar dated by a variety of authors. K-Ar ages by Wellman et al. (1970) and Sutherland (1985) are dated at $\sim$16.8–5.7 Ma, from Byrock to Cosgrove, respectively. The same areas were re-analysed by Ar-Ar dating by Cohen et al. (2008) who defined a more accurate age range of $\sim$17.9–8.90 Ma, from El Capitan (just south of Byrock) to Cosgrove, respectively. The lower K-Ar ages given by Wellman et al. (1970) are likely to be the result of considerable argon loss following alteration of the samples. Despite the differences in accuracy, both K-Ar and Ar-Ar results display a southward younging age trend which is comparable to the southward younging trend observed in the East Australian central volcanoes, the Tasmantid seamounts, and the Lord Howe seamounts. Fission track data by Cundari et al. (1978) have been excluded from the overall age range as there is less accuracy with this method and the same locations were dated by the Ar-Ar method. In this study, all individual leucitite volcanoes have been grouped into a single province meaning there is quite a large distance between very small, isolated outcrops. For this reason, the ridgeline resurfacing does not make much sense in this province. Even slightly connecting the province, using footprint 1, the volume is increased quite considerably from just 5 km^3 to 15 km^3. This value is based upon 15 separate fields between Byrock and Cosgrove ($\sim$600 km) suggesting each singular leucitite volcano has an average volume of just 1 km^3. Exposures are therefore much smaller, and lower volume, than other age-progressive volcanoes across the East Australian chain which is to be expected given the thickness of lithosphere at this location. Because of the limited exposure and problems associated with ridgeline resurfacing, the upper surface was taken as the present-day DEM and footprint 1 as the preferred areal extent.

- Estimated Preserved Volume; 5 km^3.
- Estimated Original Volume; 15 km^3.
- Oldest Age; 17.9 ± 0.3 Ma (2σ) Ar-Ar (Cohen et al., 2008) (near-ideal flat spectra); olivine leucitite from El Capitan.
- Youngest Age; 8.90 ± 0.2 Ma (2σ) Ar-Ar (Cohen et al., 2008) (saddle-shaped spectra for grain two, possible excess argon); olivine leucitite from Cosgrove Quarry.

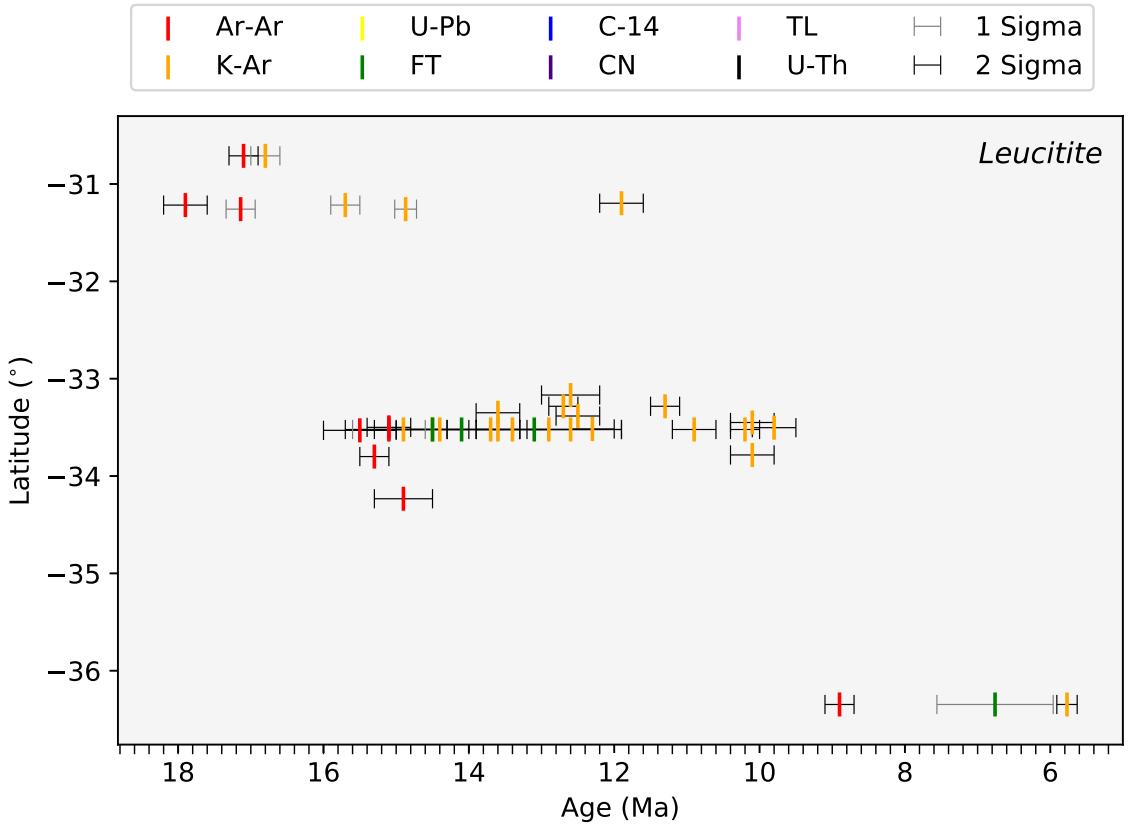

Figure 6.40: *Age data for the Leucitite chain.*

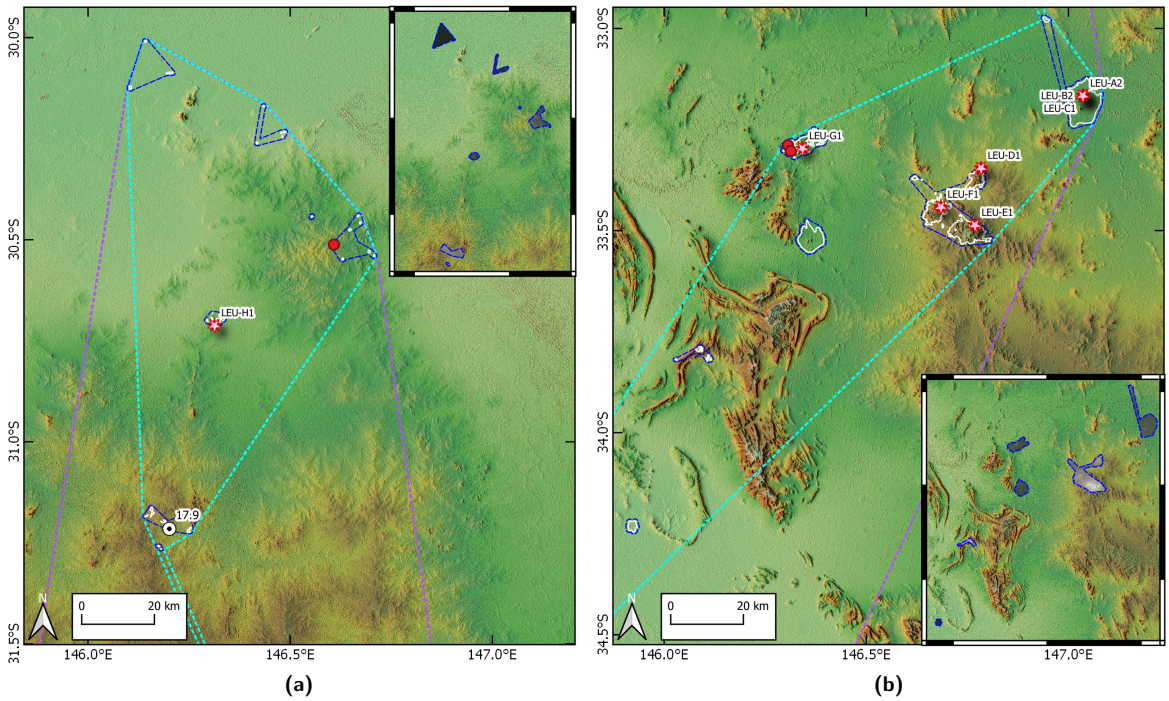

Figure 6.41: *(a) Northern Leucitite volcanic province (b) Central Leucitite volcanic province. Red dots show the locations of freely available borehole data obtained from New South Wales Government (2022).*

Macedon-Trentham (6.16–5.83 Ma)

The Macedon-Trentham province contains the only felsic volcanic rocks of Cenozoic age in the state of Victoria, and are also the most southerly silicic lavas in eastern Australia. The province is represented by small trachytic flows, domes, plugs, and spines in the Lancefield, Macedon, Gisborne, Trentham, and Blackwood areas (Johnson, 1989). Within the Macedon-Trentham province K-Ar ages of silicic rocks dated by Ewart et al. (1985) range from ∼6.13–5.83 Ma. The oldest ages come from the Macedon-Lancefield area and the younger ages from the Trentham-Blackwood area. Ar-Ar dating of silicic rocks around Macedon-Lancefield by Cohen (2007) yield ages of ∼6.16–6.10 Ma, where all three results were indistinguishable within analytical error. Unfortunately, none of the mafic units from the area have been K-Ar or Ar-Ar dated, but this is critical for precise age assignment, as stratigraphic constraints in this area are often ambiguous (Cohen, 2007). For this reason the full duration of mafic and silicic volcanism is yet to be discovered. For the age range presented here, the more precise Ar-Ar data has been used to define older volcanism around Macedon and Lancefield and, in the absence of Ar-Ar analyses, K-Ar data has been used to define slightly younger volcanism around Trentham and Blackwood. The preserved volume of rock in the Macedon-Trentham province is just 7 km^3. However, assuming these rocks are the product of a single shield volcano, as is the case with most central volcanoes, then the original volume of the shield is likely to reach around 66 km^3. In this case, given the extent of current outcrops the shield has been made to encompass the northeastern outcrops, which form a domed mass, rather than the southern and western outcrops which appear to represent low-lying, valley lava flows. For this, I found the ridgeline resurfacing of all outcrops to the Footprint 1 extent worked the most appropriately to extrapolate exposures whilst maintaining their general morphology.

- Estimated Preserved Volume; 7 km^3.
- Estimated Original Volume; 66 km^3.
- Oldest Age; 6.16 ± 0.1 Ma (2σ) Ar-Ar (Cohen, 2007) (concordant results); peralkaline trachyte from Hanging Rock, between Macedon and Lancefield.
- Youngest Age; 5.83 ± 0.06 Ma (1σ) K-Ar (Ewart et al., 1985) (no comment on sample quality); trachyte from the summit of Babbingtons Hills, 6 km west of Trentham.

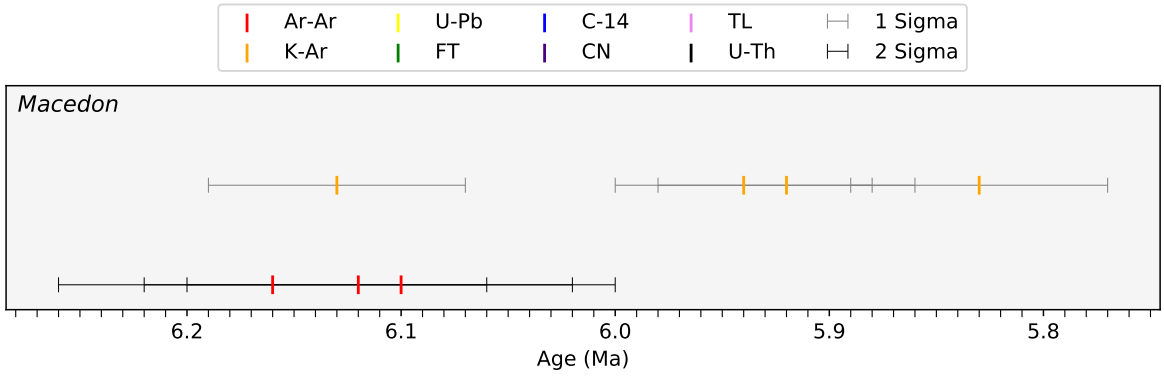

Figure 6.42: *Age data for the Macedon-Trentham province.*

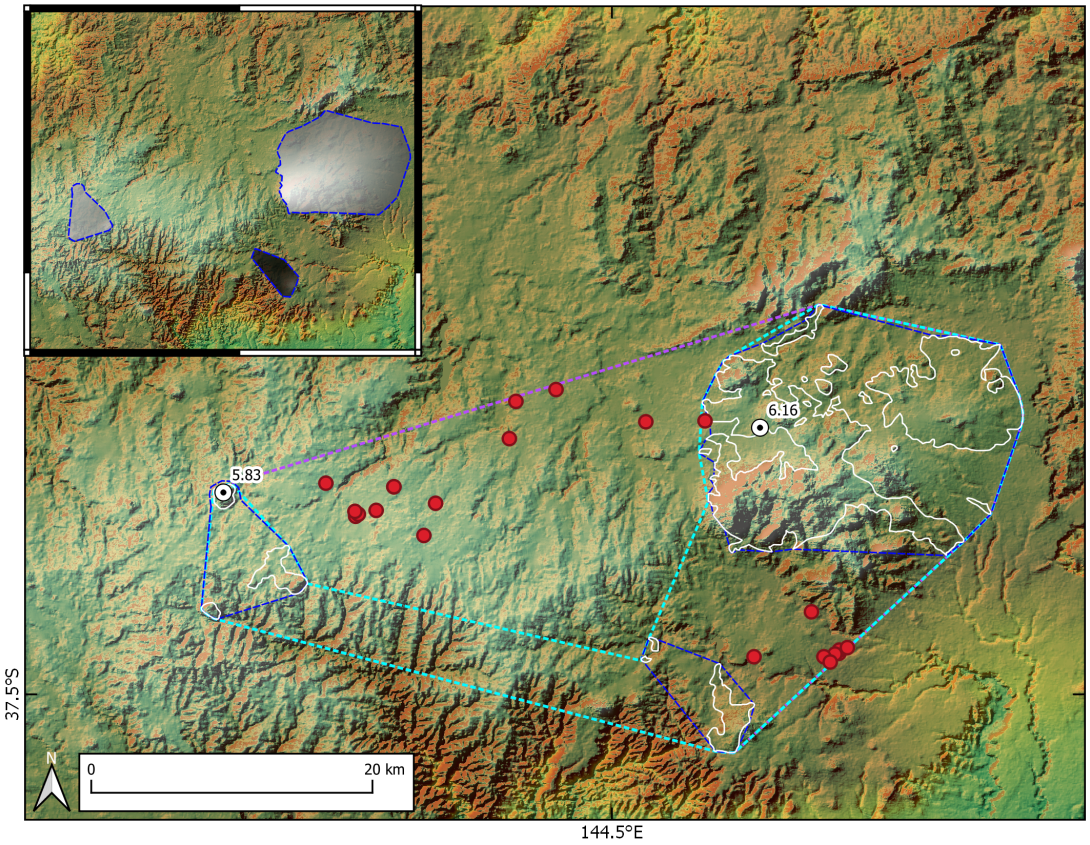

Figure 6.43: *The Macedon-Trentham volcanic province. Red dots show the locations of freely available borehole data obtained from Victoria State Government (2022).*

Newer Volcanic Province (NVP) (7.93–0.00403 Ma)

The Newer Volcanic Province (NVP) covers around 19,000 km^2 and contains over 416 known eruption centres (Boyce, 2013). It may be subdivided into three sub-provinces; the Central Highlands, the Western Plains, and Mount Gambier (Johnson, 1989). Maars and composite volcanoes are common in the Western Plains and Mount Gambier region, due to the presence of aquifers in underlying sediments (Heath et al., 2020). In the Central Highlands, low-lying lava shields and scoria cones dominate, with lava flows filling narrow valleys (Heath et al., 2020). K-Ar results from across the Central Highlands and Western Plains by numerous authors range almost continuously from ∼7.80–0.26 Ma. This is within the limits of the more precise Ar-Ar data by Heath et al. (2020), Matchan et al. (2018), and Oostingh et al. (2017) which range from ∼7.93–0.098 Ma. There have been a number of cosmogenic nuclide, thermoluminescence and radiocarbon dating studies, particularly in the Mount Gambier region, all of which plot below 1 Ma. Some of these studies have been discarded as the effects of weathering, bleaching, and location within the sediment pile mean not all samples give a true age of volcanism. However, numerous C-14 samples analysed by Blackburn et al. (1982) suggest that the most recent volcanism occurred at Mount Gambier around 4300 years before present. The oldest eruption dated is from the eastern Central Highlands at Bald Hill (Heath et al., 2020). Despite this east-west maxima and minima, there is no simple age trend across the NVP (Heath et al., 2020). NVP rocks generally outcrop in a broad belt which curves at the east and west edges, meaning the extent of the convex hull footprint includes a large area which contains no NVP outcrops. The volume calculated from this footprint is therefore probably a considerable overestimation. The overall morphology of the NVP is typical of other lava fields, and given the young age of the province, erosion is again expected to be relatively minimal and the preferred method for the pre-erosion volume is using the present-day DEM as the top and footprints 1 as the areal extent. The preserved volume of rock across the entire NVP is calculated as 649 km^3 but the original volume is estimated to be roughly 1190 km^3. The base of the NVP is well constrained by numerous boreholes across the region. The results calculated here are very similar to those by Van den Hove et al. (2017) who calculated a preserved dense rock equivalent of erupted NVP volcanics of least 680 km^3 and a total pre-erosion volume between 930–1000 km^3. In this case, the authors used a rate of erosion for basalt of between 1.7 mm/ka and 5mm/ka for a semi-arid environment (Sims et al., 2007) to estimate the volume loss of NVP lavas. This study instead uses simple extrapolations of preserved rock outcrops to estimate the volume loss.

- Estimated Preserved Volume; 649 km^3.
- Estimated Original Volume; 1190 km^3.
- Oldest Age; 7.93 ± 0.038 Ma (2σ) Ar-Ar (Heath et al., 2020) (no comments on sample quality); mafic lava from Bald Hill, one of the most easterly points of the NVP.
- Youngest Age; 4.03 ± 0.29 Ka (1σ) C-14 (Blackburn et al., 1982) (no comments on sample quality); charcoal from inner zone of ash-fall 2.5 km north of Blue Lake, Mount Gambier, one of the most westerly points of the NVP.

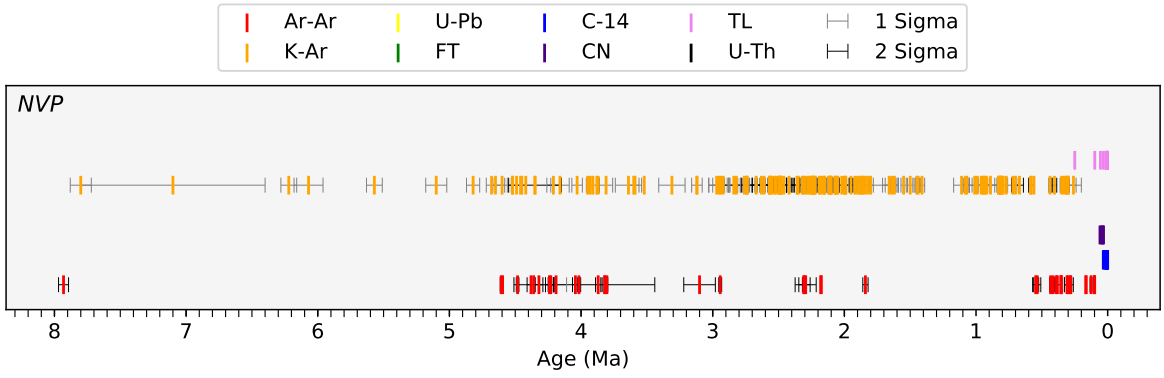

Figure 6.44: *Age data for the Newer Volcanic Province.*

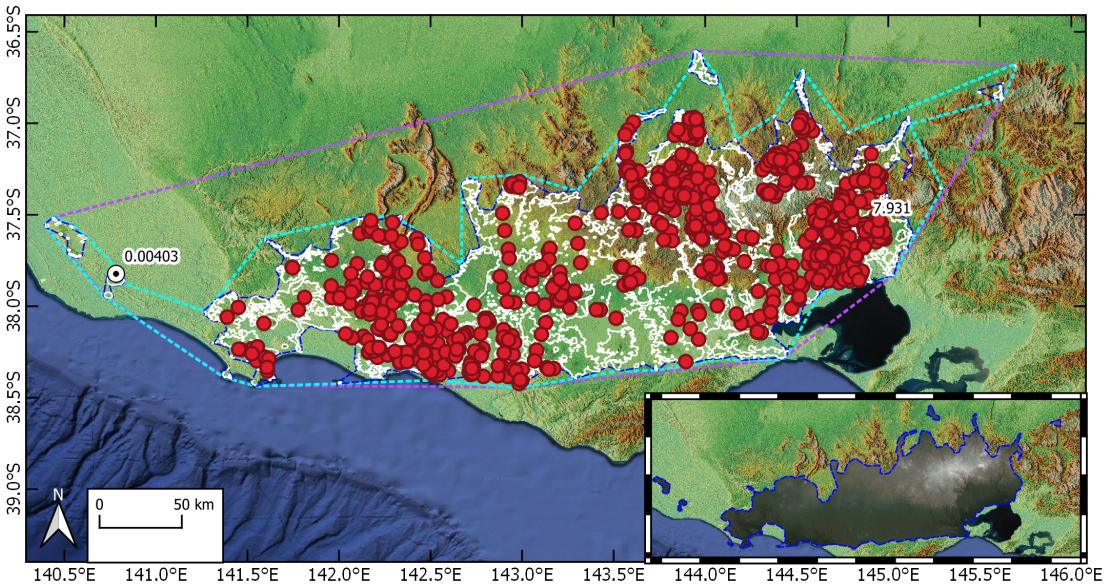

Figure 6.45: *The Newer Volcanic Province. Red dots show the locations of freely available borehole data obtained from Victoria State Government (2022).*

6.2.5 Age Progressive Volcanism

Cape Hillsborough (35.7–32.9 Ma)

Cape Hillsborough is the northernmost central volcano on the Australian mainland. The province has been highly eroded, removing any indications of a former volcanic shield (Johnson, 1989). All that now remains is a fault-bound sequence of lavas and dykes up to 300 m thick at Cape Hillsborough, their intrusive equivalents at Mount Jukes and Mount Blackwood, and a few minor silicic plugs (Johnson, 1989). McDougall and Slessar (1972) analysed samples from the Cape Hillsborough Beds, Mount Blackwood and a silicic plug at Pinnacle Rock. Their results gave a total K-Ar age range of $\sim$33.2–30.3,Ma, however the two youngest samples were defined as minimum ages. For this reason, the Ar-Ar ages of the same units from McDougall and Roksandic (1974) were deemed more accurate, with an age range from $\sim$35.7–32.9 Ma. U-Pb dating by Sutherland et al. (2012) of a sample at Mount Blackwood gave a corroborating age of 33.9 ± 1.1 Ma (1σ). Also, Cohen et al. (2013) Ar-Ar dated a sample of alkaline granite from Mount Jukes giving an age of 33.6 ± 0.5 Ma (2σ). Both analyses suggest the lavas and intrusive complexes are of similar age. The volume estimate for preserved rocks is just 3 km^3, but the volume of the original volcano, assuming all intrusive and extrusive rocks are encompassed within a single shield, is around 58 km^3. However, results from this area are likely to be a significant underestimation due to two main reasons: (1) this volume is based only on a single fault-bound block of lava and intrusive rocks, and (2) the location of the Cape Hillborough volcano along the coastline means it has probably been heavily eroded over 35 Ma.

- Estimated Preserved Volume; 3 km^3.
- Estimated Original Volume; 58 km^3 (underestimate).
- Oldest Age; 35.7 ± 0.5 Ma (1σ) Ar-Ar (McDougall and Roksandic, 1974); trachyte lava from the Cape Hillsborough Beds; close to the exposed stratigraphic base, but this is a fault-bounded block, so older lavas may be present elsewhere.
- Youngest Age; 32.9 ± 0.9 Ma (1σ) Ar-Ar (McDougall and Roksandic, 1974); trachyandesite lava from the Cape Hillsborough Beds; close to stratigraphic top.

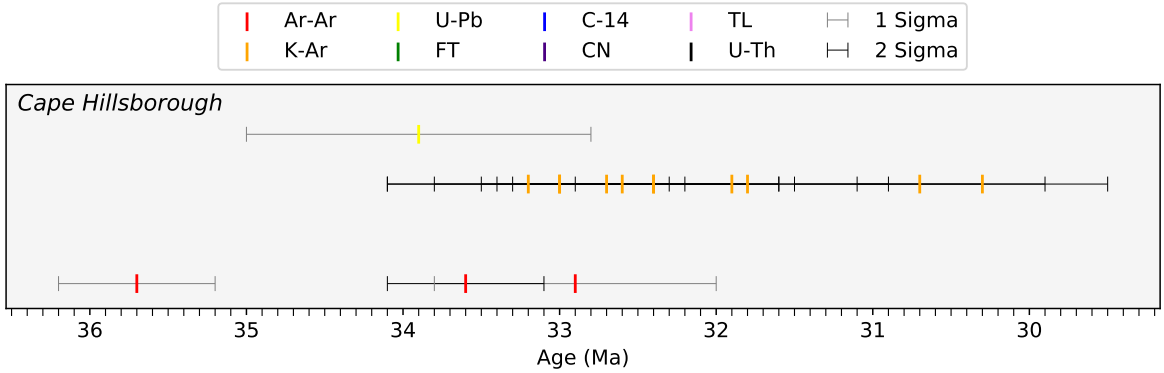

Figure 6.46: *Age data for the Cape Hillsborough province.*

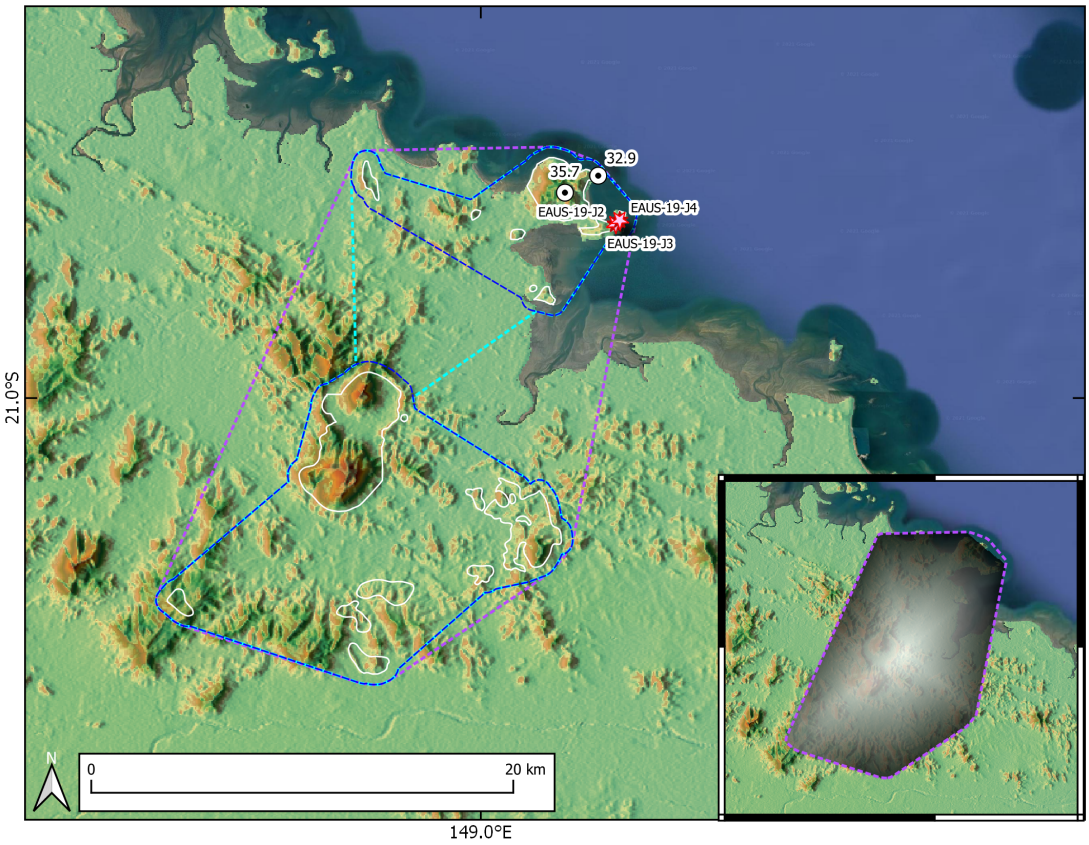

Figure 6.47: *The Cape Hillsborough volcanic province.*

Nebo Central Volcano (37.5–32.6 Ma)

Within the Nebo region, there are numerous occurrences of eroded mafic lavas often weathered to form lateritic profiles, with a subordinate volume of silicic plugs and flows (Sutherland, 1977; Cohen, 2007). The relationships between each of the many isolated outcrops display a long, complex, and protracted history of volcanism in the Nebo province. A detailed K-Ar study was completed by Sutherland (1977) who identified three, separate volcanic episodes. Some of these areas were Ar-Ar dated by Cohen (2007) and Jones (2018) who were able to refine the accuracy of the middle ages to identify another separate event. For the purpose of this study, the Nebo area has been split into three distinct provinces: (1) the bimodal, Nebo central volcano; (2) the Dalrymple-Yatton mafic only lava field; and (3) the Fort Cooper-St Martin mafic only lava field. Events (2) and (3) are discussed further on in this Chapter along with other lava field volcanism. The Nebo central volcano emplacement took place from $\sim$37.5–32.6 Ma. The volcano consists of a large number of mafic and silicic flows in the central Nebo region, with plugs and intrusions concentrated around Sydney Heads, some of which protrude through earlier lava flows. U-Pb ages by Sutherland et al. (2012) give similar ages of $\sim$33.6–31.4 Ma. The age of this is consistent with other proposed hotspot-related activity throughout the region (Cohen, 2007). Due to the difficulty in isolating earlier and later lava field volcanism from the main central volcano volcanism, all outcrops have been included in the final shield volume calculation but the location of the pyramid sits over the Sydney Heads region where most most silicic plugs are found. The resulting volume is still likely to be an overestimate as outlying lavas are included in the shield. Further field mapping would be required to define the true extent of the central volcano lavas in more detail.

- Estimated Preserved Volume; 26 km^3.
- Estimated Original Volume; 2454 km^3 (overestimate).
- Oldest Age; 37.5 $\pm$ 0.4 Ma (2σ) Ar-Ar (Cohen, 2007) (minor recoil for low-temperature steps); alkali olivine basalt west of Sydney Heads; basalt flow underlying rhyolite capping.
- Youngest Age; 32.6 $\pm$ 0.4 Ma (2σ) Ar-Ar (Cohen et al., 2013) (concordant results); trachyte dyke cutting pyroclastic rocks, 1 km from Mount Britton summit.

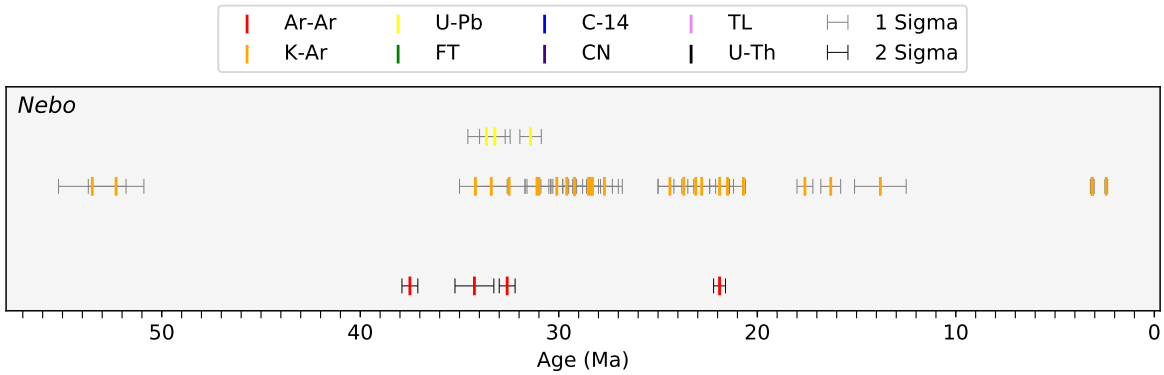

Figure 6.48: *Age data for the Nebo province.*

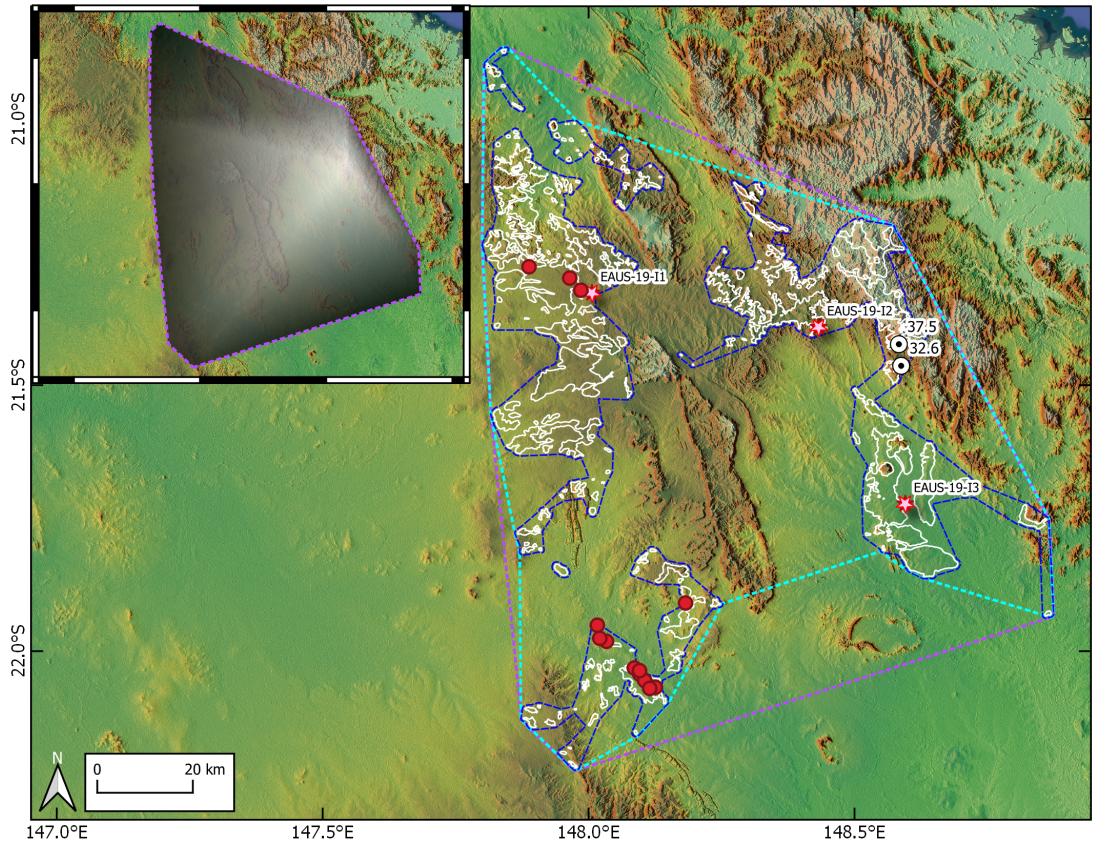

Figure 6.49: *The Nebo volcanic province. Red dots show the locations of freely available borehole data obtained from Queensland Government (2022).*

Peak Range Central Volcano (34.6–29.0 Ma)

The Peak Range forms a prominent line of hills around 100 km long in the central highlands of Queensland (Cohen, 2007). The range consists of three segments: a group of silicic plugs in the north, residual peaks and mesas of mafic lavas in the centre, and a group of silicic plugs in the south (Cohen, 2007). The central Peak Range mesas reach up to 389 m in thickness and removal of a large volume of basalt surrounding them is implied. To the east of the province lies scattered lavas of the East Clermont province, emplaced at a similar time, and surrounding the higher peaks are gently sloping mafic lava plains, typically 30 m in thickness and extending 15–30 km east and west of the range (Cohen, 2007; Wellman and McDougall, 1974b). Numerous dykes cut through these lower lavas in the centre of the Peak Range and based on field relationships mafic magmatism is found to have preceded felsic magmatism (Johnson, 1989). K-Ar ages by Wellman and McDougall (1974b) range from $\sim$40.9–25.8 Ma and U-Pb ages by Sutherland et al. (2012) range from 31.3–30.7 Ma. More extensive Ar-Ar dating by Cohen (2007), Cohen et al. (2013) and Jones et al. (2020) give a total age range of $\sim$47.9–26.0 Ma and highlight two distinct phases of activity; $\sim$47.9–44.6 Ma, and $\sim$34.6–26.0 Ma. The 26.0 ± 0.2 Ma (2σ) Ar-Ar age from Mount McLaren were reported by Jones et al. (2020) as an anomalous result. The spectra for this result indicates some disturbance to the Ar-Ar system, also this analysis is lower resolution than that by Cohen (2007). For this reason, the Ar-Ar age of 29.0 ± 0.4 Ma (2σ) by Cohen (2007) with a near-ideal flat spectra has been taken as the minimum age of this volcano. Most silicic activity appears to have begun around 31 Ma, almost 17 Ma later than the earliest mafic lava analysed. Cohen (2007) suggests this may represent an earlier event (e.g., a lava-field eruption) unrelated to the Peak Range central volcano. Supporting this theory, sample EAUS-19-H1 collected during this study from the base of the volcano at Shepton Quarry is full of peridotite xenoliths and chemically similar to other lava fields from across the region. Johnson (1989) suggest the lavas of the East Clermont province are more reminiscent of earlier lava field volcanism due to their morphology, and thus the deposits have not been included in the final shield volume calculation, as shown by the smaller convex hull extent (footprint 3). The pre-erosion volume of the shield therefore estimated at 1459 km^3. The volume stated here still includes the lava field lying directly beneath the central volcano. Unfortunately, without more precise mapping the two could not be separated for this study. There was no freely available borehole data for the Peak Range province but Jones and Verdel (2015) acquired thickness data from open coal mines across the region. The authors were able to create an isopach map across the province to show that lavas in the central Peak Range reach a considerable thickness, around 389 m, and the resulting volume calculation based on the generation of a simple conical volume, was 2600 km^3. The authors have again included the underlying lava field deposits in their estimates. Using the same method, with the perimeter value calculated from the footprint 3 extent and a thickness of 389 m, this study estimates a similar volume of 2498 km^3. However, this is probably an overestimate as the final values stated here all resolve earlier lava field volcanism and later central volcano volcanism into a single large shield across the province.

- Estimated Preserved Volume; 108 km^3.
- Estimated Original Volume; 1459 km^3 (overestimate).
- Oldest Age; 34.6 ± 0.4 Ma (2σ) Ar-Ar (Jones et al., 2020) (no comment on sample quality); mafic lava from central Peak Range; road cutting along Huntley Road.
- Youngest Age; 29.0 ± 0.4 Ma (2σ) Ar-Ar (Cohen et al., 2013) (near-ideal flat spectra); metaluminous trachyte from Malvern Hill, south Peak Range.

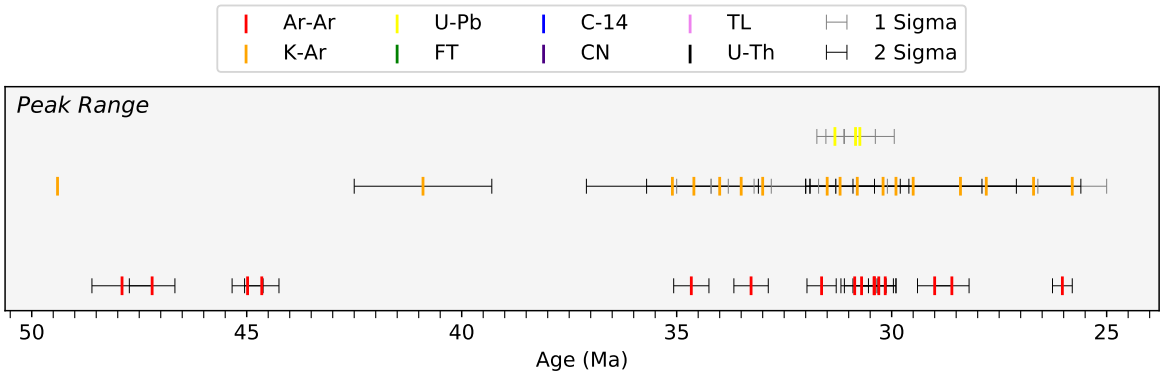

Figure 6.50: *Age data for the Peak Range province.*

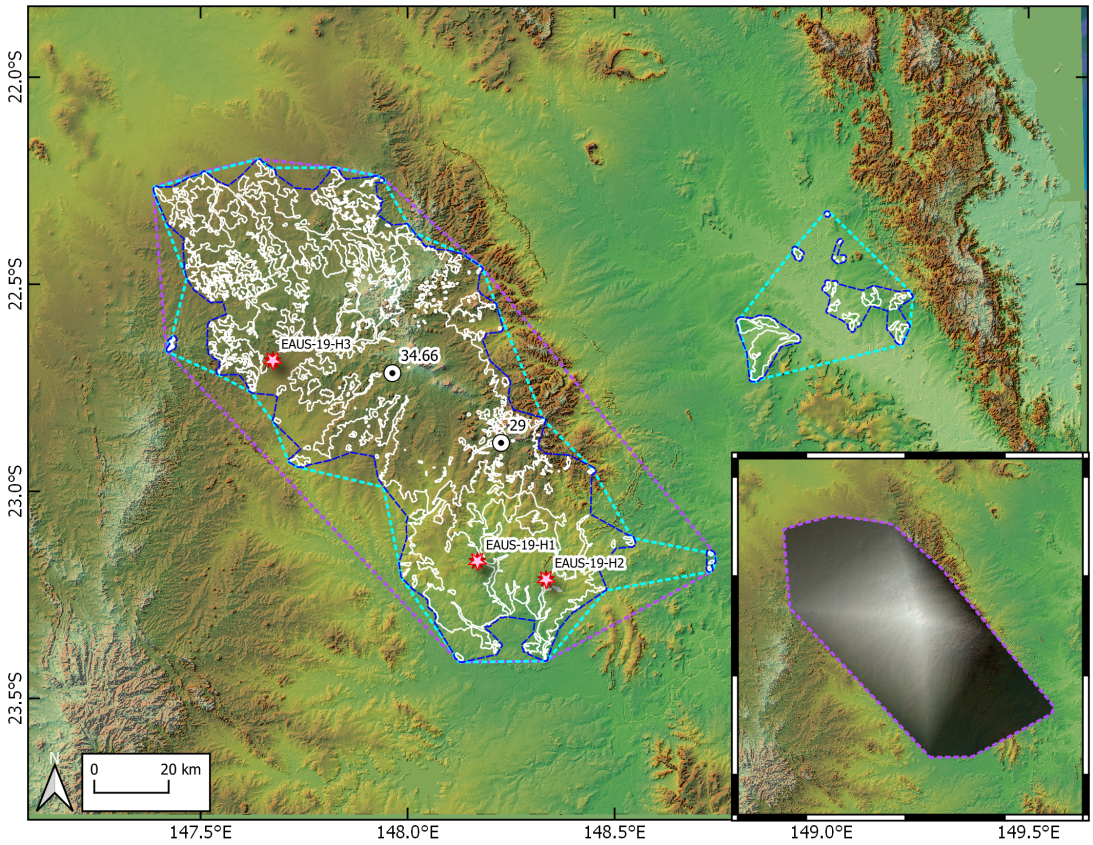

Figure 6.51: *The Peak Range volcanic province.*

Springsure (28.4–27.0 Ma)

The Springsure central volcano has a central zone of silicic plugs, dykes, mesas, pyroclastic deposits and flow remnants (the Minerva Hills Volcanics) surrounded by a large apron of mafic lavas with a preserved maximum thickness of around 330 m (Johnson, 1989). The felsic peaks exhibit a rugged relief, domed at the centre due to a vast intrusive complex, and the basaltic lavas generally dip away from this centre with stepped relief, the result of considerable erosion. K-Ar ages for the Springsure province by Webb and McDougall (1967) range from $\sim$32.8–18.3 Ma however most locations were re-analysed by Ar-Ar dating by Cohen (2007) and Jones et al. (2020) with results instead ranging from $\sim$28.4–27.0 Ma. Due to the high viscosity of sanidine the youngest K-Ar samples did not fully release radiogenic Ar during analysis so yielded minimum ages (Webb and McDougall, 1967). Older K-Ar ages are likely the result of excess argon (Webb and McDougall, 1967). The youngest Ar-Ar age of 24.9 ± 1.6 Ma (2σ) from Jones et al. (2020), sample IJS07, is considered incorrect due to extensive alteration producing a high error in this sample. U-Pb ages from Sutherland et al. (2012) correlate well with Ar-Ar analyses ranging from $\sim$28.1–26.7 Ma. Considering the size of the volcano, ages here span a very short range, although, it is unlikely the lowest mafic lavas of this volcano have been analysed as there are a few extensive sections of exposed flows resulting in poor stratigraphic control across the province (Cohen, 2007). For the calculation of the original volume of a shield, the easternmost exposures have been excluded from the final convex hull (footprint 3) outline, as these appear to represent particularly elongated lava flows, rather than the central mass of the shield. From my calculations, 90% of exposures are covered by a pyramid with height 400 m, giving a volume of 1409 km^3 but to cover 100% of exposures the height rises abruptly to 720 m, with a volume of 2695 km^3. This dramatic change is primarily due to the incorporation of the central silicic plugs into the top surface. However, these are known be elevated at present-day due to the intrusion of a vast intrusive complex at the centre of the volcano and this present-day height is unlikely to be representative of the original volcano height. For this locality a volume between 1408–2695 km^3 is therefore preferred. Jones and Verdel (2015) estimated a total volume of 1460 km^3 for the Springsure volcano based on a simple conical volume with a thickness of 330 m. Using the same thickness, with the perimeter value calculated from the convex hull extent, this study estimated a conical volume of 1328 km^3 for the Springsure volcano.

- Estimated Preserved Volume; 155 km^3.
- Estimated Original Volume; 2695 km^3 (overestimate).
- Oldest Age; 28.4 ± 0.14 Ma (2σ) Ar-Ar (Jones, 2018) (relatively flat spectra); mafic lava from a road cutting in northern Springsure, close to Mount Wills.
- Youngest Age; 27.0 ± 0.24 Ma (2σ) Ar-Ar (Jones, 2018) (relatively flat spectra); mafic lava from a road cutting in southern Springsure, NW of Mount Hope.

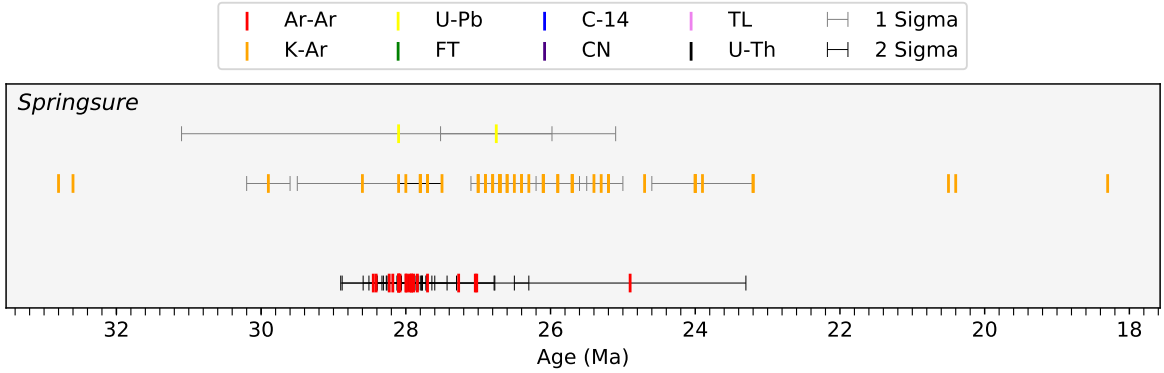

Figure 6.52: *Age data for the Springsure province.*

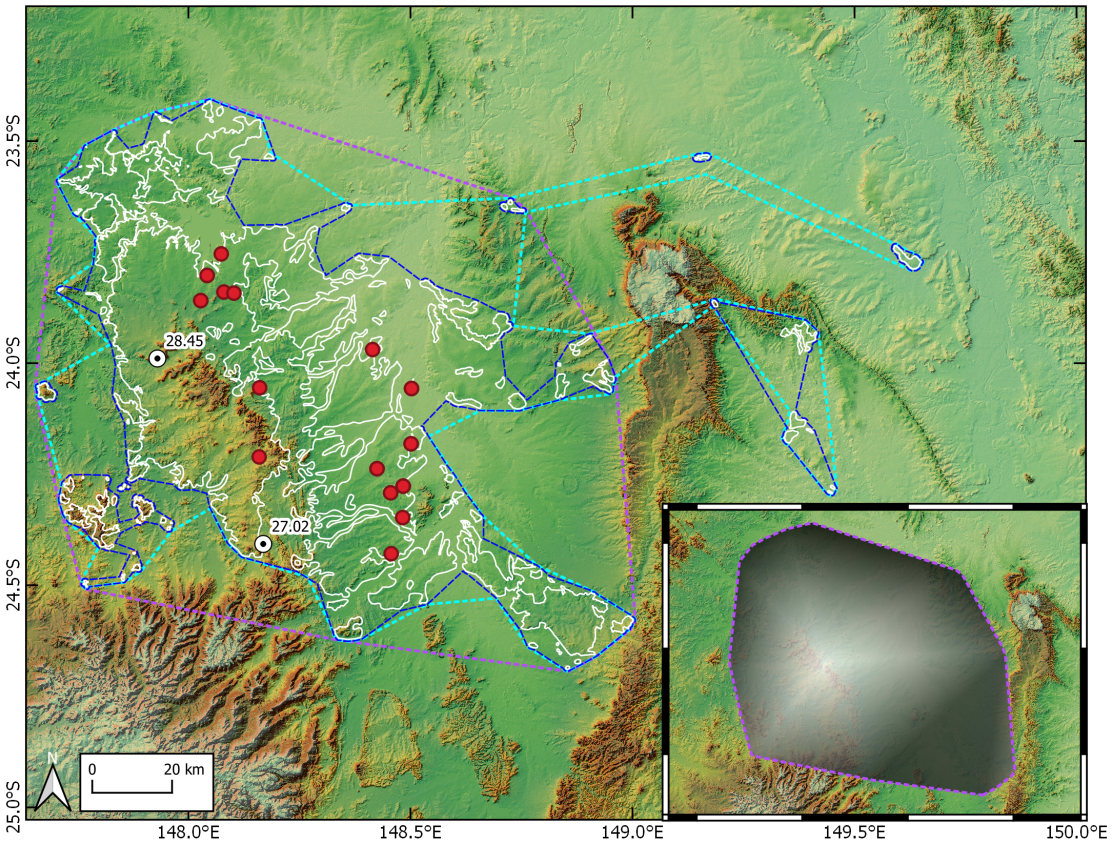

Figure 6.53: *The Springsure volcanic province. Red dots show the locations of freely available borehole data obtained from Queensland Government (2022).*

Buckland (30.4–26.6 Ma)

The Buckland province consists of two distinct parts, a large eroded shield to the northeast with at least three silicic plugs near the volcano centre, and a sparse scattering of intrusive and flow remnants to the southwest (Cohen, 2007). The main shield contains radially extending lavas, the most well-preserved of which are probably valley fills. Today the flows form sequences up to 300 m thick with numerous cross-cutting dykes and plugs (Jones and Verdel, 2015). The west Buckland region contains roughly 120 intrusive bodies and dissected flow remnants (Johnson, 1989). Outcrops in this region are more reminiscent of the multi-episode Hoy province, and have therefore not been included in the total extent of the shield. Sutherland et al. (2012) produced K-Ar ages of ~29.9–25.1 Ma and one U-Pb age of 27.9 ± 0.47 Ma (1σ) from the Buckland volcano. However, the same upper and lower flows were re-analysed by Ar-Ar dating by Cohen (2007) and Crossingham et al. (2018). These analyses gave a more accurate age range of ~30.4–26.6 Ma. Crossingham et al. (2018) noted two separate stages of volcanism around 30 Ma and 27 Ma from the southern Buckland flows at Carnarvon Gorge. This location is situated on the flanks of the shield so the lavas sampled are probably not at the absolute earliest or latest eruptions of the volcano, but should be reasonable approximations. Also, flows and plugs from the centre of the volcano analysed by Cohen et al. (2013) yielded similar ages around 30 and 27 Ma. It is thus likely the Buckland volcano had two main periods of volcanism, separated by almost 2 Ma. For the purpose of this analysis both episodes have been included in the final volume calculations. The volume of the original Buckland shield is estimated at 1918 km^3. Jones and Verdel (2015) calculated the volume of the Buckland volcano as 860 km^3, using a thickness of 300 m and a radius of 52 km. Using the same thickness with the perimeter defined from the extent of the convex hull footprint, the volume calculated in this study from a simple conical model is 992 km^3.

- Estimated Preserved Volume; 409 km^3.
- Estimated Original Volume; 1918 km^3.
- Oldest Age; 30.4 ± 0.4 Ma (2σ) Ar-Ar (Crossingham et al., 2018); mafic lava; sampled from the base of Transect A at Carnarvon Gorge, southern Buckland shield.
- Youngest Age; 26.6 ± 0.2 Ma (2σ) Ar-Ar (Crossingham et al., 2018); mafic lava; sampled from the top of Transect B at Carnarvon Gorge, southern Buckland shield.

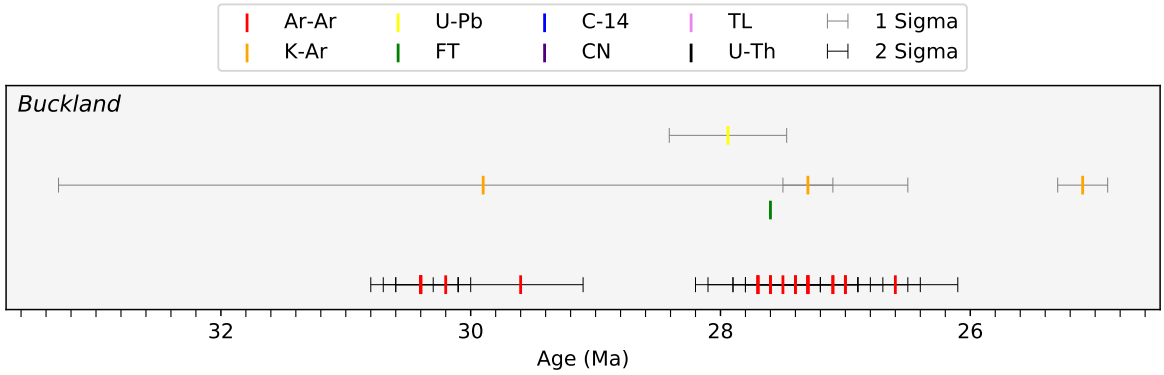

Figure 6.54: *Age data for the Buckland province.*

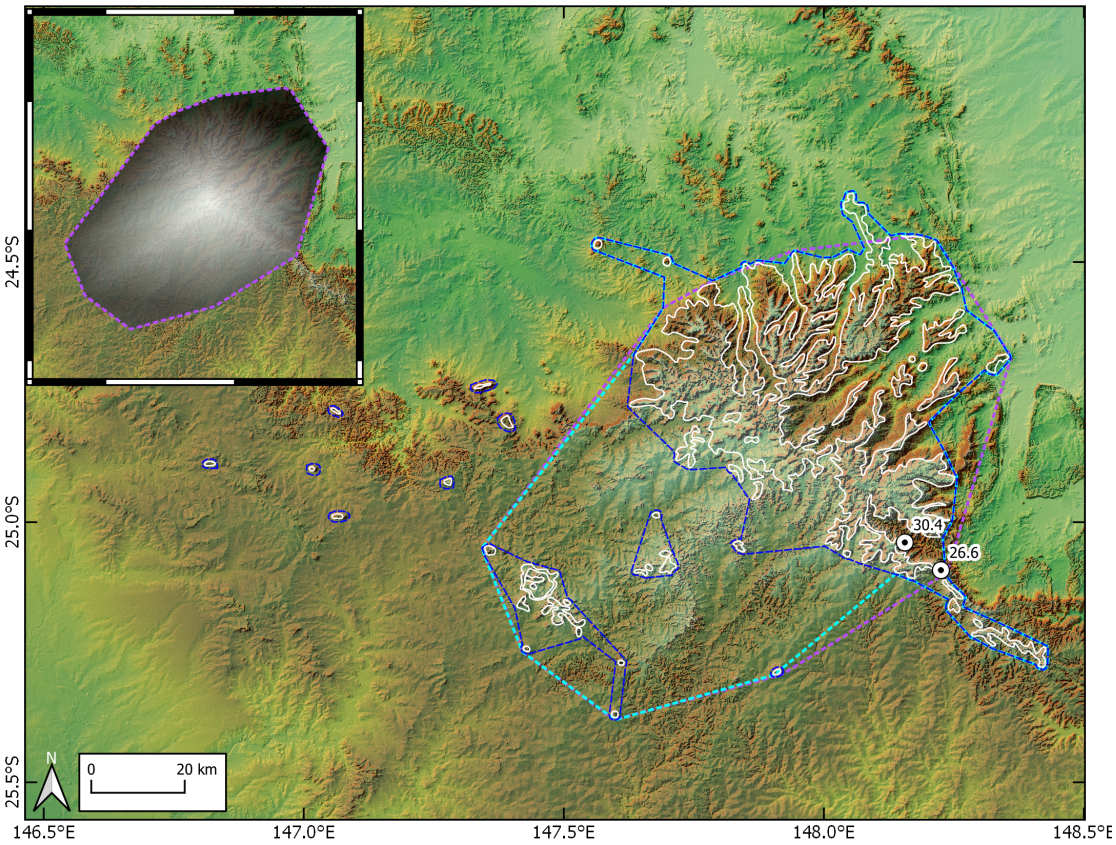

Figure 6.55: *The Buckland volcanic province.*

Fraser Island (30.6–30.1 Ma)

Cenozoic volcanism from Fraser Island includes the Waddy Point Volcanics and lavas from the Sandy Cape borehole on the northern end of the island. The Waddy Point Volcanics are composed of subaerial trachytic lavas and agglomerate surrounded by Quaternary sand deposits (Cohen, 2007). Mafic dykes have been observed cross-cutting the trachytes and have been correlated with subaerial mafic lavas from the drillhole Sandy Cape, 30 km north. Mafic lavas were encountered at 450 m in the drill hole. To date, no samples from Sandy Cape have been dated but fossils interbedded with volcanic formations are Late Oligocene (33.9–23.03 Ma) in age (Palmieri, 1984). K-Ar ages from the Waddy Point Volcanics range from $\sim$30.9–19.6 Ma. However, the same locations were re-dated by Cohen et al. (2007) to give a more limited Ar-Ar age range of $\sim$30.6–30.1 Ma. The inaccurate, younger K-Ar ages are possibly caused by argon loss via partial weathering or devitrification (Cohen et al., 2007). The volume of volcanic remnants at Waddy Point are just 0.01 km^3 but the original shield was at least 1–3 km^3 so as to encompass the Sandy Cape volcanics. Unfortunately, due to the location of Fraser Island on the Australian coastline, the vast majority of the original shield has been eroded away and this volume is probably still a vast underestimate.

- Estimated Preserved Volume; 0.01 km^3.
- Estimated Original Volume; 3 km^3 (underestimate).
- Oldest Age; 30.6 ± 0.3 Ma (2σ) Ar-Ar (Cohen et al., 2007) (near-ideal flat spectra); porphyritic metaluminous trachyte from the south side of Middle Rocks; part of the Waddy Point Volcanics.
- Youngest Age; 30.1 ± 0.3 Ma (2σ) Ar-Ar (Cohen et al., 2007) (near-ideal flat spectra); porphyritic metaluminous trachyte from the south side of Indian Head; part of the Waddy Point Volcanics.

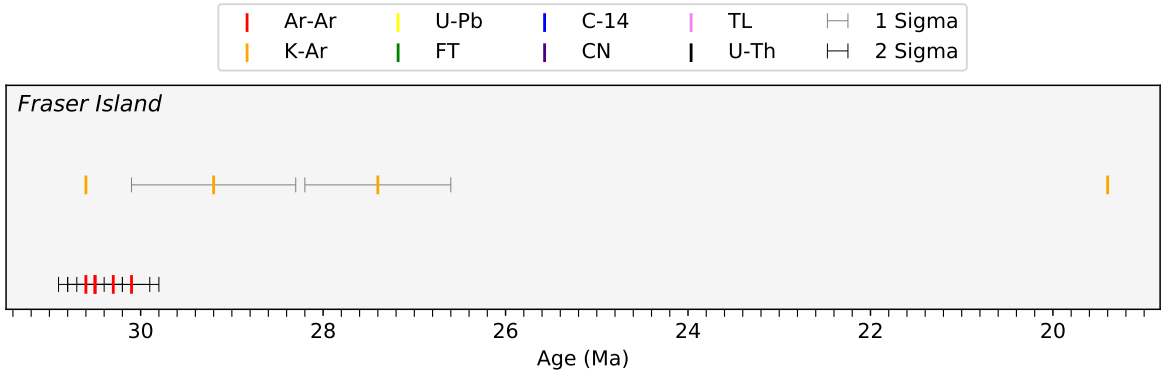

Figure 6.56: *Age data for the Fraser Island province.*

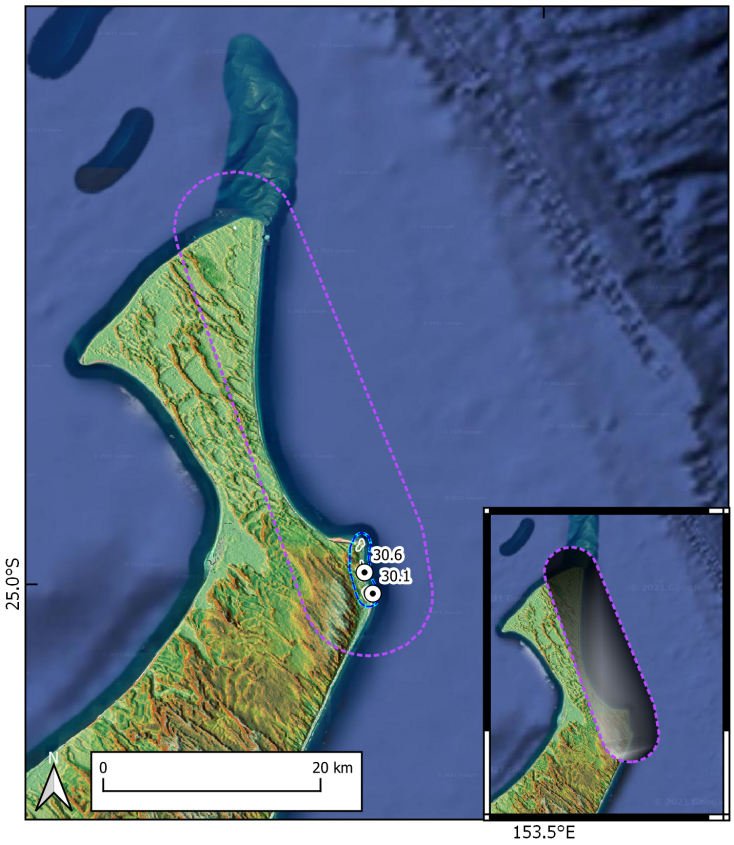

Figure 6.57: *The Fraser Island volcanic province.*

Bauhinia (27.9–26.8 Ma)

The Bauhinia volcano lies immediately east of the much more voluminous Springsure and Buckland central volcanoes. The area contains several scattered outcrops of plugs, dykes, and lavas reaching up to 310 m thick in the western Expedition Range and often infilling incised channels (Johnson, 1989). The province is morphologically simlar to the nearby Mitchell province. The Bauhinia province has been Ar-Ar and K-Ar dated by Jones (2018), Sutherland (2003), and Harding (1969). Ar-Ar ages range from ∼27.9–22.5 Ma and K-Ar ages range from ∼26.5–20.4 Ma. These dates are close to those given for the Springsure and Buckland provinces, ∼28–26 Ma, possibly relating to genetic links between the three areas. The more recent Ar-Ar ages by Jones (2018) are considered more accurate than K-Ar ages which are likely subject to Ar loss. However, despite covering a considerable area, none of the outcrops around Stonecroft, southeast of Bauhinia Downs, have been Ar-Ar dated, only lavas and plugs closer to the Springsure and Buckland volcanoes. The step heating data from the youngest Ar-Ar age, sample 8421 (Jones, 2018), shows a descending spectrum and no plateau - a spectrum that is typical of recoil. For this province the more accurate Ar-Ar ages have been taken to represent the upper and lower limits of volcanism. Depsite the similar age of the Bauhinia province to nearby central volcanoes, based on relatively thin, mafic lava flows reminiscent of lava field volcanism, it is unlikely the province ever formed a large shield volcano but instead consisted of isolated lava flows. The age of the province suggests it will have been more eroded than the far north Queensland volcanoes, over 28 Ma, and the pre-erosion volume of the Bauhinia province has therefore been estimated by extrapolating present-day peaks and ridgelines to the extent of footprint 2. Footprint 2 has been modified slightly to ensure most flows remain confined to preexisting valleys.

- Estimated Preserved Volume; 12 km^3.
- Estimated Original Volume; 121 km^3.
- Oldest Age; 27.9 ± 0.27 Ma (2σ) Ar-Ar (Jones, 2018) (near-ideal flat spectra); mafic lava within Expedition Range.
- Youngest Age; 26.8 ± 0.35 Ma (2σ) Ar-Ar (Jones, 2018) (near-ideal flat spectra); mafic lava within Expedition Range.

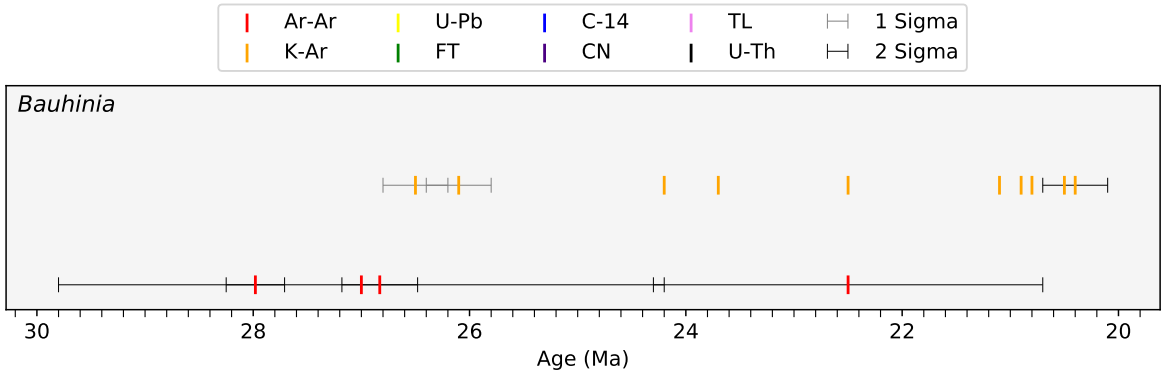

Figure 6.58: *Age data for the Bauhinia province.*

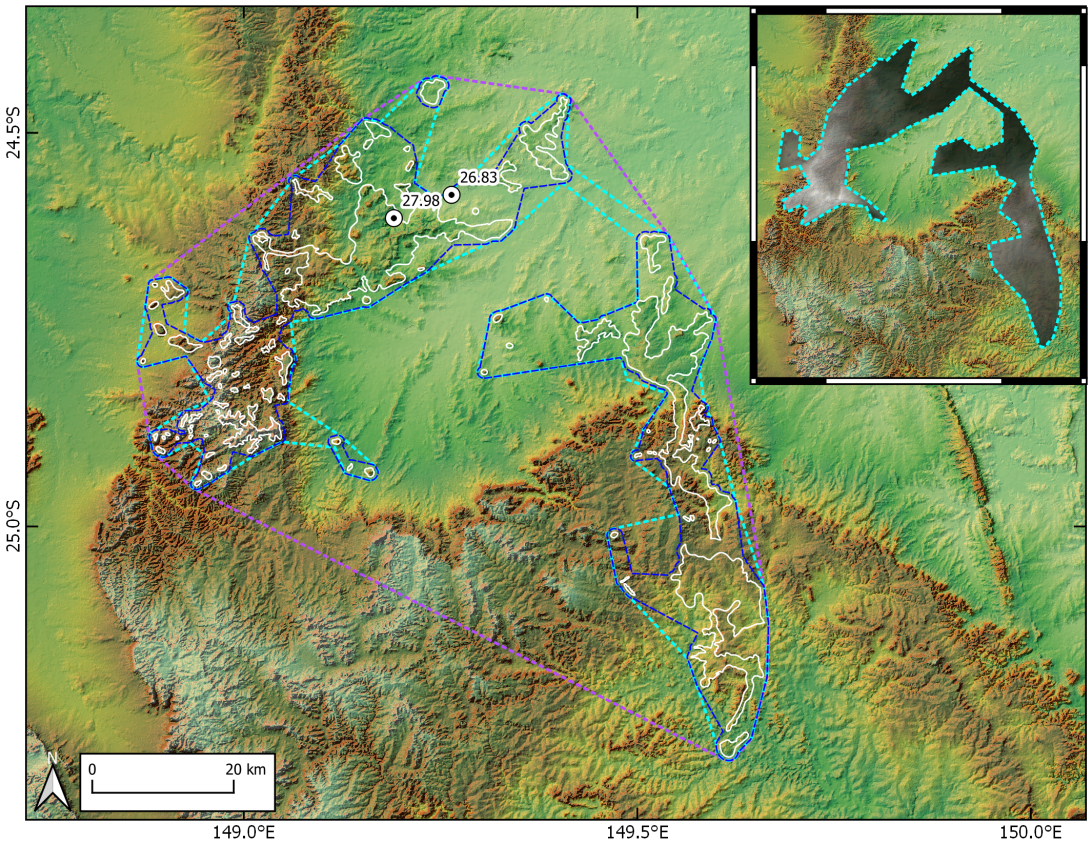

Figure 6.59: *The Bauhinia volcanic province.*

Mitchell (25.0–24.2 Ma)

South of the Buckland shield is the Mitchell province. Many lavas flowed along former river valleys, and erosion of surrounding country rock has formed prominent examples of inverted relief (Johnson, 1989). Individual lavas range from 6–30 m thick and total thicknesses are around 30–80 m (Exon et al., 1970). Both alkaline and tholeiitic mafic lavas are present, as well as one doleritic intrusion in a small quarry near Roma (Cohen, 2007). K-Ar ages from the Mitchell province by Exon et al. (1970) range from ∼23.2–20.0 Ma, however the authors noted that argon loss was expected due to the partially weathered mineralogy of the samples. Re-analysis of one younger sample by Ar-Ar dating produced a much older age. Ar-Ar ages by Cohen (2007), McDougall and Roksandic (1974), and Jones (2018) instead produced an age range of ∼25.0–24.2 Ma which is deemed more accurate. This is within the expected age of hotspot volcanism at this latitude suggesting this province may be more related to the central volcanoes than previously thought (Cohen, 2007). Exon et al. (1970) noted that the base of the basalt outcrops south of Amby and the top outcrops north of Kilmorey Homestead. Both of these locations, along with many others, were K-Ar dated. Unfortunately, the same locations were not re-analysed by Ar-Ar and it is unlikely that the stratigraphic top and base of the province have been dated by this method. This may explain the very short range of ages observed here. As with the nearby Bauhinia province, the Mitchell province is represented by isolated lava flows which are unlikely to have formed a large shield. The extrapolation of ridgelines however, did not work particularly well at this province, probably due to the flat, low-lying nature of most exposures. Therefore, original volumes were calculated using the present-day DEM as the upper surface, clipped to the extent of footprint 2.

- Estimated Preserved Volume; 14 km^3.
- Estimated Original Volume; 67 km^3.
- Oldest Age; 25.0 ± 0.7 Ma (2σ) Ar-Ar (Cohen, 2007) (minor Ar loss for low-temperature steps); dolerite from Roma Quarry; same as the Ar-Ar age from McDougall and Roksandic (1974).
- Youngest Age; 24.2 ± 1.1 Ma (2σ) Ar-Ar (Jones et al., 2017) (no comments on sample quality); valley filling basalt from Kilmorey Falls.

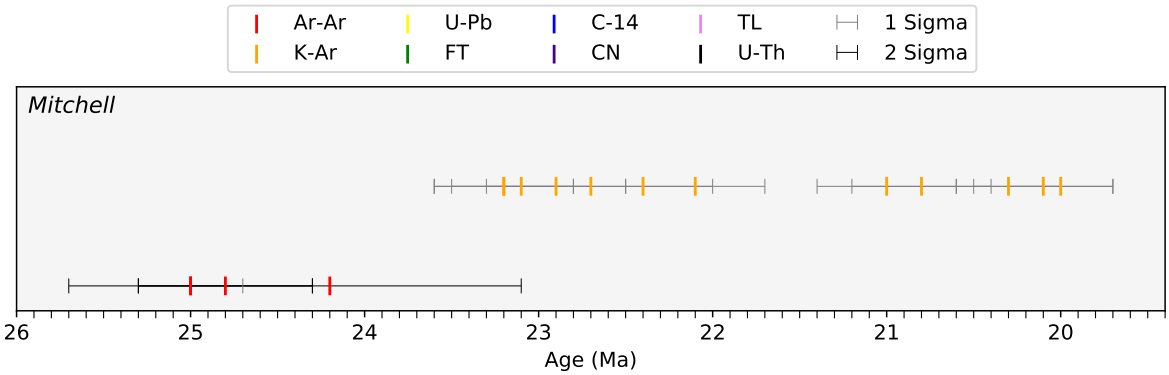

Figure 6.60: *Age data for the Mitchell province.*

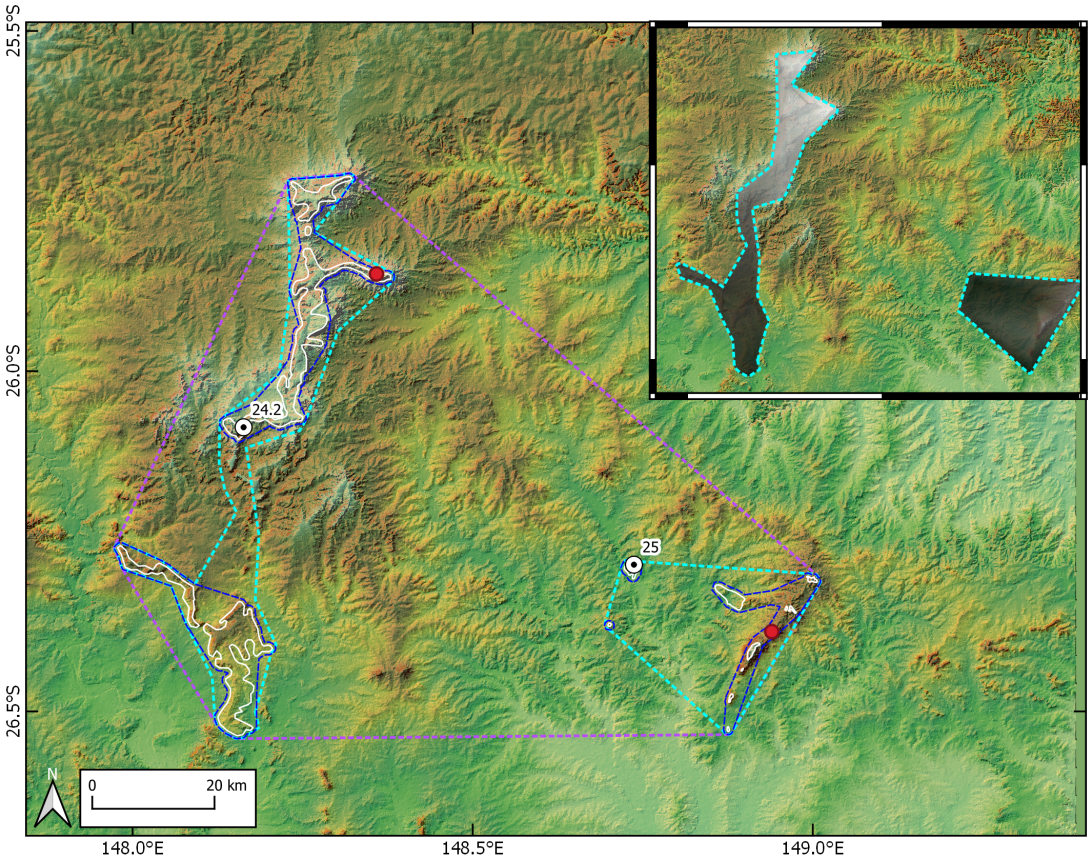

Figure 6.61: *The Mitchell volcanic province. Red dots show the locations of freely available borehole data obtained from Queensland Government (2022).*

Glasshouse-Maleny-Noosa (31.0–26.4 Ma)

The Noosa-Maleny-Glasshouse provinces, named the Glass Houses province in Wellman (1971), are thought to represent the remains of a either single, or two, large shield volcanoes, which have been heavily eroded leaving only a few scattered intrusive and extrusive rocks behind. The Noosa province consists of small dome-shaped hills and spine-like peaks of hypabyssal silicic rocks, and the Allandale Granite, along with minor mafic lavas around the Noosa Heads area(Johnson, 1989; Cohen, 2007). The Glasshouse-Maleny area includes the northerly Maleny volcanic field where lavas reach a maximum thickness of 180 m forming a dissected tableland, the numerous dome-shaped hills and spine-like peaks of rhyolitic and trachytic plugs, laccoliths, sills and dyke dotted around Glasshouse National Park, and the more southerly Mount Mee lava (Johnson, 1989; Cohen and Vasconcelos, 2007). No pyroclastic rocks have been recognised in the area which is unusual for this type of central volcano, and suggests a considerable volume of rock has been eroded from the area. K-Ar ages from the Noosa province range from $\sim$32.0–23.3 Ma but samples were re-dated by Cohen (2007) to give a more accurate Ar-Ar age range of $\sim$29.5–27.3 Ma. The oldest K-Ar age was 32.0 ± 1.0 Ma (1σ) from the Allendale arfvedsonite granite (Green, 1974); however this K-Ar age can be discarded as the same locality was re-dated by Ar-Ar, yielding an age of 27.6 ± 0.4 Ma (2σ) (Cohen and Vasconcelos, 2007). The younger K-Ar ages are possibly caused by argon loss via partial weathering or devitrification (Cohen, 2007). Since the Noosa province is dominated by plugs there is little stratigraphical control across the ages. However, most major outcrops have been dated including Mt Cooran, Mt Cooroora, Mt Tinbeerwah, Mt Cooroy, Allandale Granite, Mt Peregian, Mt Coolum, Mt Pinbarren. K-Ar ages from the Glasshouse-Maleny area range from $\sim$41.7–24.7 Ma but the same samples were re-dated by Cohen (2007) to give an Ar-Ar age range of $\sim$31.0–26.4 Ma, which is within the age range of Noosa volcanism. Were the province to have encompassed a single shield, then the original volume is calculated at 813 km^3. However, were the province to exist as two separate shields, one covering the Noosa deposits, and the other encompassing the Glasshouse-Maleny deposits then the volume of the original shields are calculated at just 347 km^3. Given the the slight separating of the Noosa deposits from the Glasshouse-Maleny deposits, a two shield model was preferred for this study.

- Estimated Preserved Volume; 7 km^3.
- Estimated Original Volume; 347 km^3.
- Oldest Age; 31.0 ± 0.8 Ma (2σ) Ar-Ar (Cohen et al., 2007) (slightly non-atmospheric initial argon 300 ± 2); basaltic andesite from the base of the Maleny lava sequence.
- Youngest Age; 26.4 ± 0.2 Ma (2σ) Ar-Ar (Cohen et al., 2007) (near-ideal flat spectra, highly reproducible age between grains); porphyritic metaluminous trachyte from Mount Beerburrum.

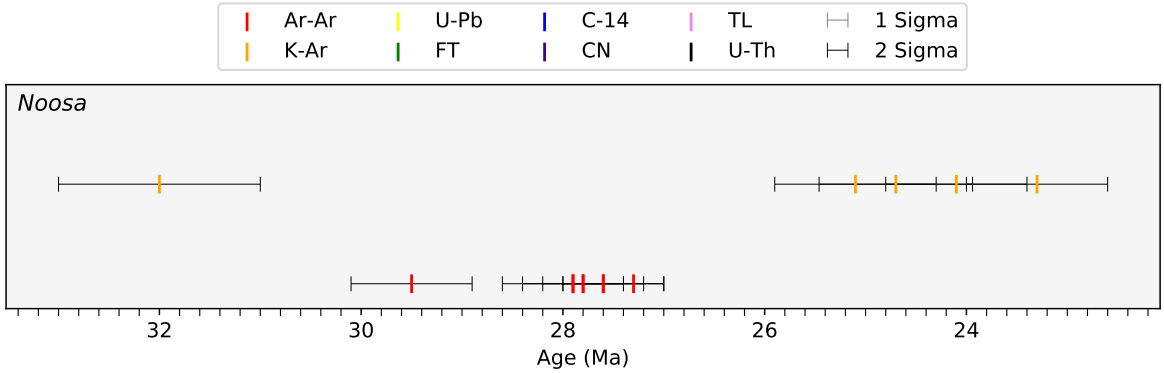

Figure 6.62: *Age data for the Noosa province.*

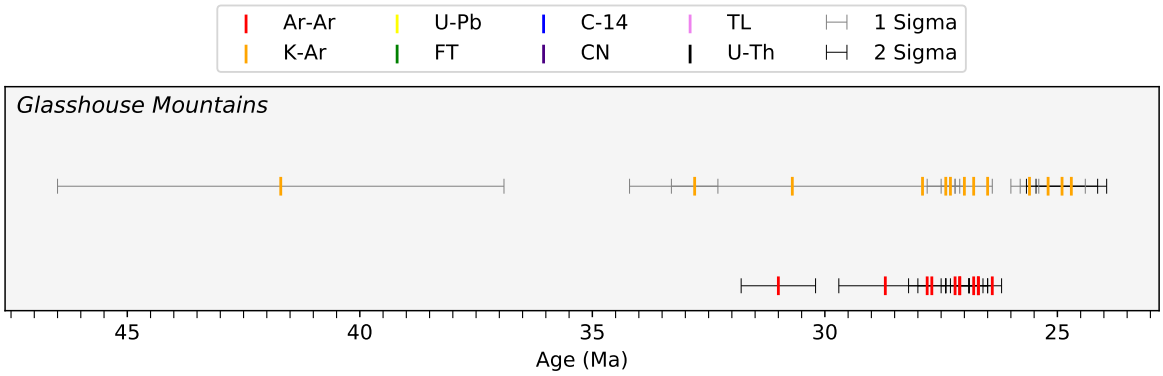

Figure 6.63: *Age data for the Glasshouse-Maleny province.*

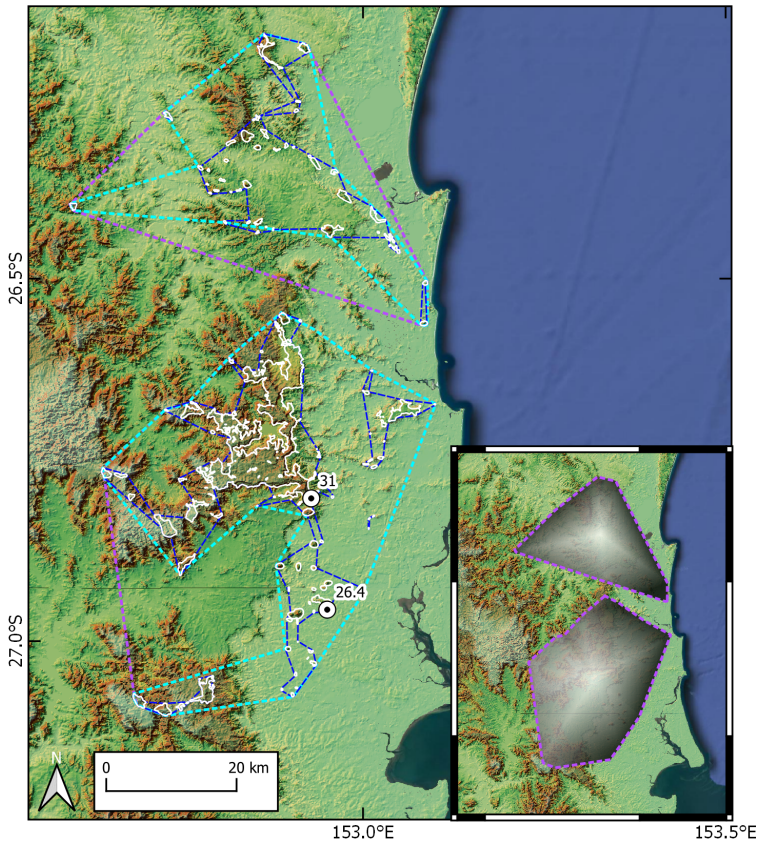

Figure 6.64: *The Glasshouse-Maleny-Noosa volcanic province.*

Bunya (28.8–23.6 Ma)

The Bunya central volcano is considered to be the eroded remnants of a volcanic shield (Johnson, 1989). The centre of the province is domed and lava flows dip away from the summit. Gravity highs across the range may be the result of an extensive intrusive complex. The maximum thickness of lava is expected to have exceeded 600 m (Johnson, 1989). Only a handful of evolved rock types have been recorded within the province. However, no detailed mapping or geochemical sampling has been undertaken on the Bunya volcano and as such, there is the possibility for additional undiscovered units (Cohen, 2007). The Bunya province has been K-Ar dated by numerous authors with results ranging from $\sim$29.4–22.0 Ma. The province has also been dated by Cohen (2007) using Ar-Ar analysis. Results from the authors range from $\sim$28.8–23.6 Ma and include the oldest unit dated by the K-Ar method. K-Ar of the youngest units from Ewart (1982) are also in agreement with the youngest Ar-Ar ages, around 23 Ma, although no specific coordinates are reported for these samples. The more accurate Ar-Ar ages from Cohen (2007) are presumed to be close to the stratigraphical base and top of this volcano. To the north of the province, from Kingaray to Proston lies numerous scattered exposures of low, lateritised basalt which are thought to represent a single, unusually long, lava flow from the Bunya central volcano. For this study, these outcrops have not been included in the calculation of the original shield volume as the convex hull geometry needed to confine them adds a big area to the volcano that is unlikely to represent the true extent.

- Estimated Preserved Volume; 160 km^3.
- Estimated Original Volume; 1343 km^3.
- Oldest Age; 28.8 $\pm$ 0.4 Ma (2σ) Ar-Ar (Cohen, 2007) (low T steps are slightly irregular so age is from the high T steps); mafic lava north of the Bunya Mountains considered to represent an older volcanic episode; more detailed stratigraphy is lacking from this area.
- Youngest Age; 23.6 $\pm$ 0.4 Ma (2σ) Ar-Ar (Cohen, 2007) (near-ideal flat spectra); mafic lava from Mount Kiangarow in the Bunya Mountains; given the high elevation, 1120 m, this is considered to represent the highest stratigraphical unit.

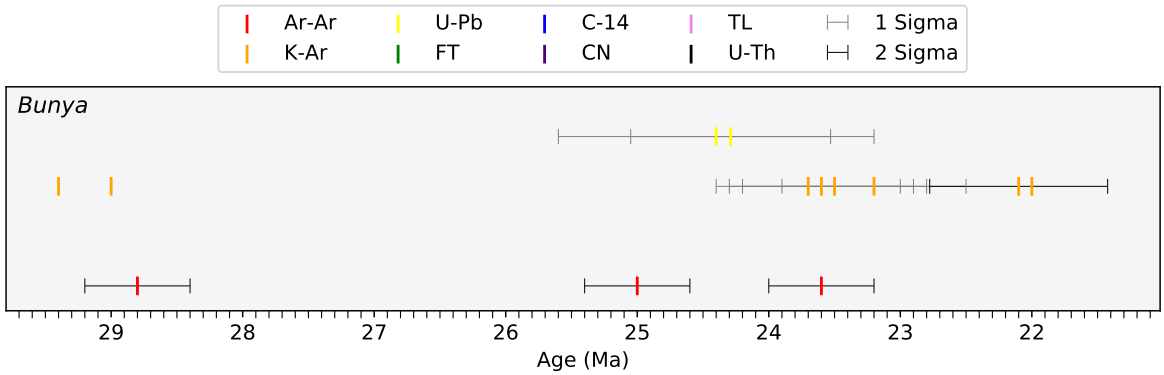

Figure 6.65: *Age data for the Bunya province.*

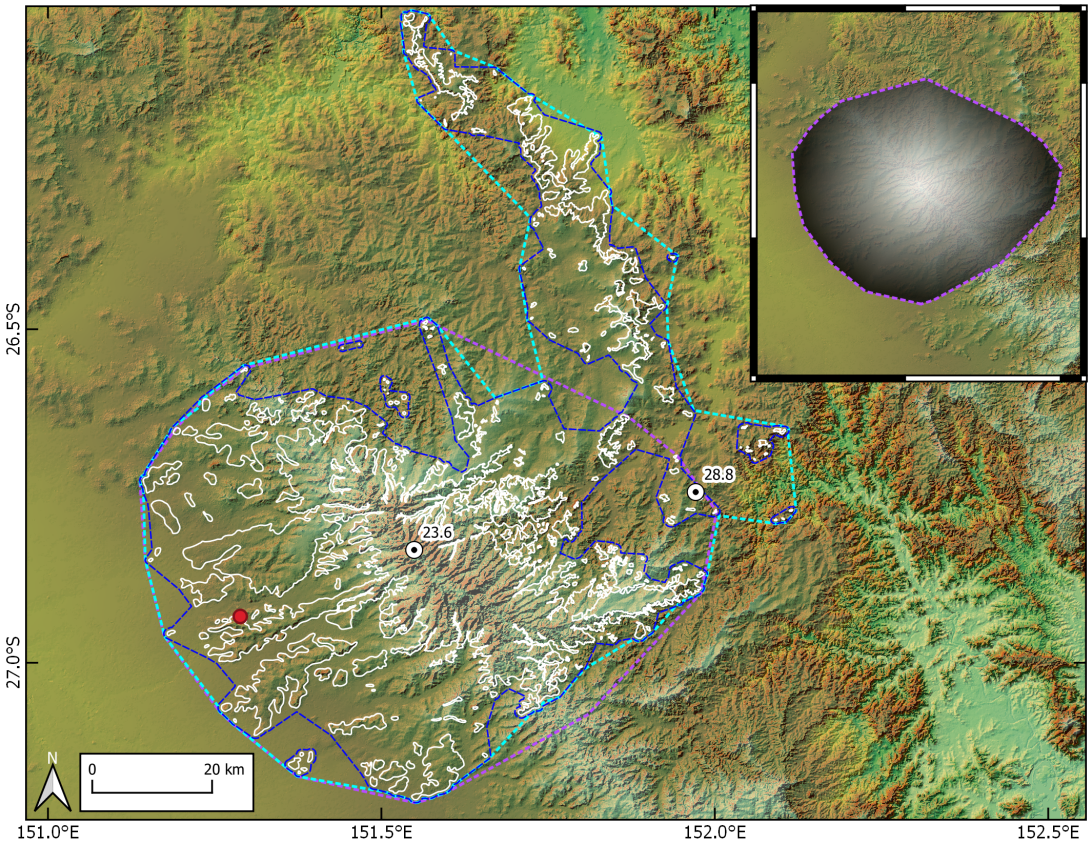

Figure 6.66: *The Bunya volcanic province. The red dot shows the location of the only freely available borehole obtained from Queensland Government (2022).*

Toowoomba Central Volcano (22.9–22.6 Ma)

The Toowoomba central volcano is located between the larger Bunya and Main Range shields to the north and south, respectively. Lavas, pyroclastic rocks, and some sediments have built up to create a plataeu of mesas around 250 m thick (Johnson, 1989; Cohen, 2007). Lavas are divided into two main stratigraphic units; the lower Meringandan Volcanics and the upper Toowoomba Basalt (Johnson, 1989). At the top of the sequence are a number of lava pools formed by explosive phreatic eruptions which crosscut and overlie all other volcanic units (Johnson, 1989). Rocks of the Meringandan Volcanics mostly include hawaiites and mugearites whilst the Toowoomba Basalt is primarily composed of hawaiite with sporadic occurrences of ne-normative rocks (Johnson, 1989). Only one silicic unit is known, a trachyte flow at Cooby Creek (Cohen, 2007). Ar-Ar ages for the Toowoomba province range from $\sim$40.9–22.6 Ma and K-Ar ages by Grenfell (1984) range from $\sim$34.8–18.1 Ma. Re-analysis of two samples by Ar-Ar dating show K-Ar values are slightly lower than expected. The lower Toowoomba lava was dated at 27.4 ± 0.7 Ma (2σ) by K-Ar analysis, and 40.9 ± 1.0 Ma (2σ) by Ar-Ar analysis. Similarly, the upper Harlaxton Quarry lava pool was dated at 20.5 ± 0.7 Ma (2σ) by K-Ar analysis, and 22.6 ± 0.4 Ma (2σ) by Ar-Ar analysis. Cohen (2007) suggest these discrepancies are likely due to an abundance of zeolites in the samples and Ar loss during the K-Ar analyses. U-Pb ages by (Sutherland et al., 2012) range from $\sim$41.6–22.2 Ma, consistent with Ar-Ar ages although the errors given are larger. Given such a spread of ages, the basal Toowoomba flow dated here at 40.9 ± 1.0 Ma (2σ) is likely to represent an earlier, previously unrecognised lava field eruption, subsequently buried by hotspot-derived lavas (Cohen, 2007). This theory is consistent with the geochemistry of these lavas as the lower flows generally display higher incompatible-element concentrations, lower SSI, and higher MgO, more typical of the East Australian lava fields than central volcanoes. Unfortunately, due to the lack of a clear, mapped boundary between the lower lava field and upper central volcano, both have been included in the final volume estimation of the province. Similar to the Peak Range, the volume estimate given here is probably an overestimation as it includes both lava field and central volcano deposits. The volume of a shield covering all present-day outcrops is estimated to be 1075 km^3. One 25 km^2 area of lava to the southwest of the province increases the convex hull footprint quite extensively but it is not entirely clear whether this outcrop was part of the central volcano shield or the lower lava field. Including this outcrop in the final shield calculation the volume is estimated at 1202 km^3.

- Estimated Preserved Volume; 233 km^3.
- Estimated Original Volume; 1075 km^3 (overestimate).
- Oldest Age; 22.9 ± 0.9 Ma (2σ) Ar-Ar (Macphail and Gibson, 2014) (weighted mean age); basalt chips from lava flows enclosing a lignitic claystone at Toowoomba Bypass pilot tunnel.
- Youngest Age; 22.6 ± 0.4 Ma (2σ) Ar-Ar (Cohen, 2007) (minor argon loss); hawaiite from Harlaxton Quarry lava pool; this is one of the youngest units based on stratigraphic relationships; dated by K-Ar at 20.5 ± 0.7 Ma (2σ).

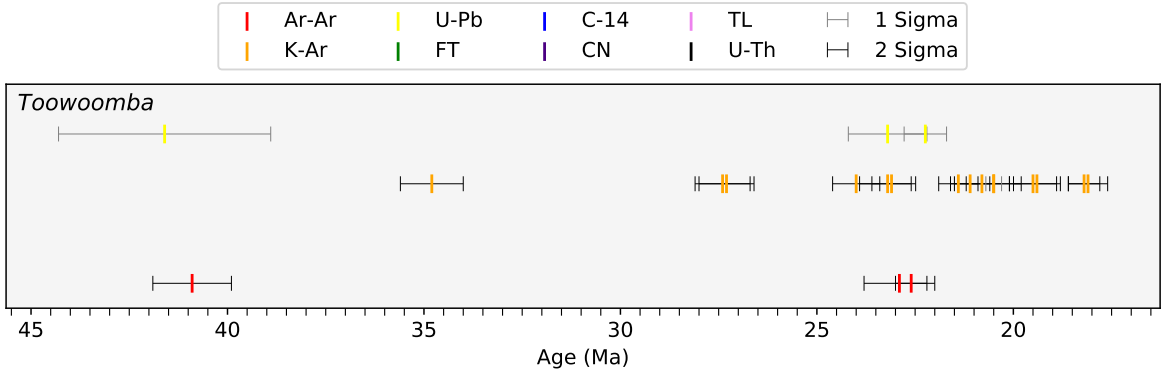

Figure 6.67: *Age data for the Toowoomba province.*

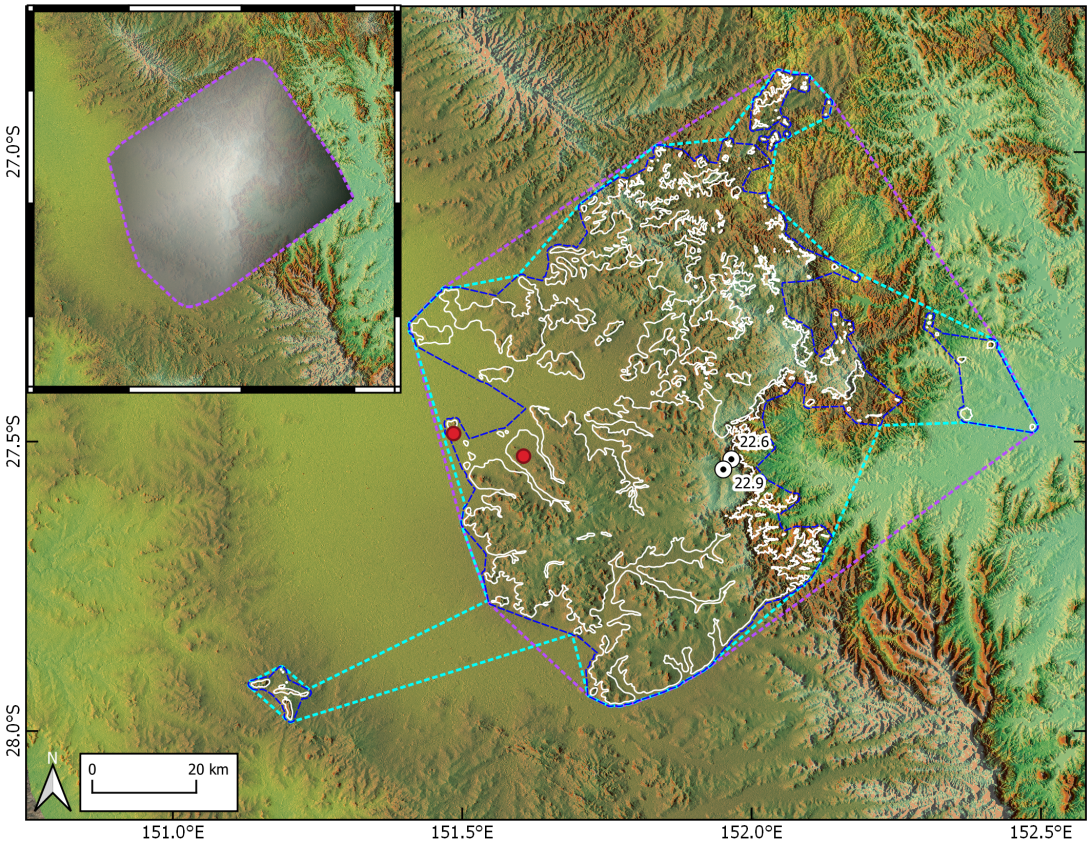

Figure 6.68: *The Toowoomba volcanic province. Red dots show the locations of freely available borehole data obtained from Queensland Government (2022).*

Main Range (26.3–20.7 Ma)

The Main Range edifice is the second largest central volcano in eastern Australia with a maximum preserved thickness of around 900 m (Johnson, 1989). The volcano appears strongly dissected on the western slopes and contains a few remnant pyroclastic rocks, both suggesting a considerable volume of material has been eroded from the original shield. Main Range is comprised of two formations; the lower Governors Chair Volcanics, and the upper Superbus Basalt. The Governors Chair Volcanics contains numerous mafic flows in the lower parts of the formation and several silicic members in the upper part (Grenfell, 1984). The Superbus Basalt is comprised of mafic flows only (Grenfell, 1984). Within this thesis, the Main Range volcano is taken to include the thick mafic lavas of southern Main Range as well as the silicic plugs of Fassifern Valley and Flinders Peak to the northeast. Main Range has particularly good constraints on the oldest and youngest flows within the volcano as the area was well mapped by Grenfell (1984). Stratigraphically, the oldest flows are found at Mistake Mountain and the youngest at Mount Mitchell. These locations also gave the oldest and youngest Ar-Ar ages, ranging from $\sim$26.3–20.7 Ma. K-Ar ages range from $\sim$35.3–19.1 Ma although most samples date between 26–21 Ma. The oldest K-Ar age came from a sample in Fassifern Valley, however the same location was re-analysed by Ar-Ar to give an age of only 25.9 ± 0.6 Ma (2σ) which is within the main period of Main Range volcanism. The youngest K-Ar age came from Mount Mitchell which was re-dated by Ar-Ar analysis and found to be 20.7 ± 0.5 Ma (2σ). The younger K-Ar ages are probably the result of argon loss. The preserved volume of volcanic material, including those of Fassifern Valley and Flinders Peak, is 466 km^3 and the estimated volume of the original shield is around 3807 km^3.

- Estimated Preserved Volume; 466 km^3.
- Estimated Original Volume; 3807 km^3.
- Oldest Age; 26.3 ± 0.4 Ma (2σ) Ar-Ar (Cohen et al., 2007) (near-ideal flat spectra); hawaiite from the base of Mistake Mountain; Governors Chair Volcanics; stratigraphic base.
- Youngest Age; 20.7 ± 0.5 Ma (2σ) Ar-Ar (Cohen et al., 2007) (excess argon indicated from isochron, intercept of 331 ± 9); nepheline benmoreite from the top flow of Mount Mitchell; Superbus basalt; stratigraphic top; this is likely a late stage or rejuviunated eruption.

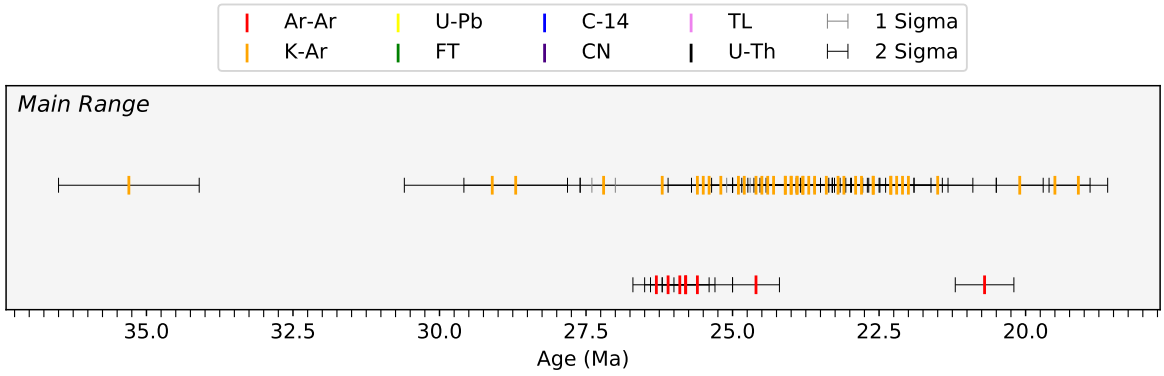

Figure 6.69: *Age data for the Main Range province.*

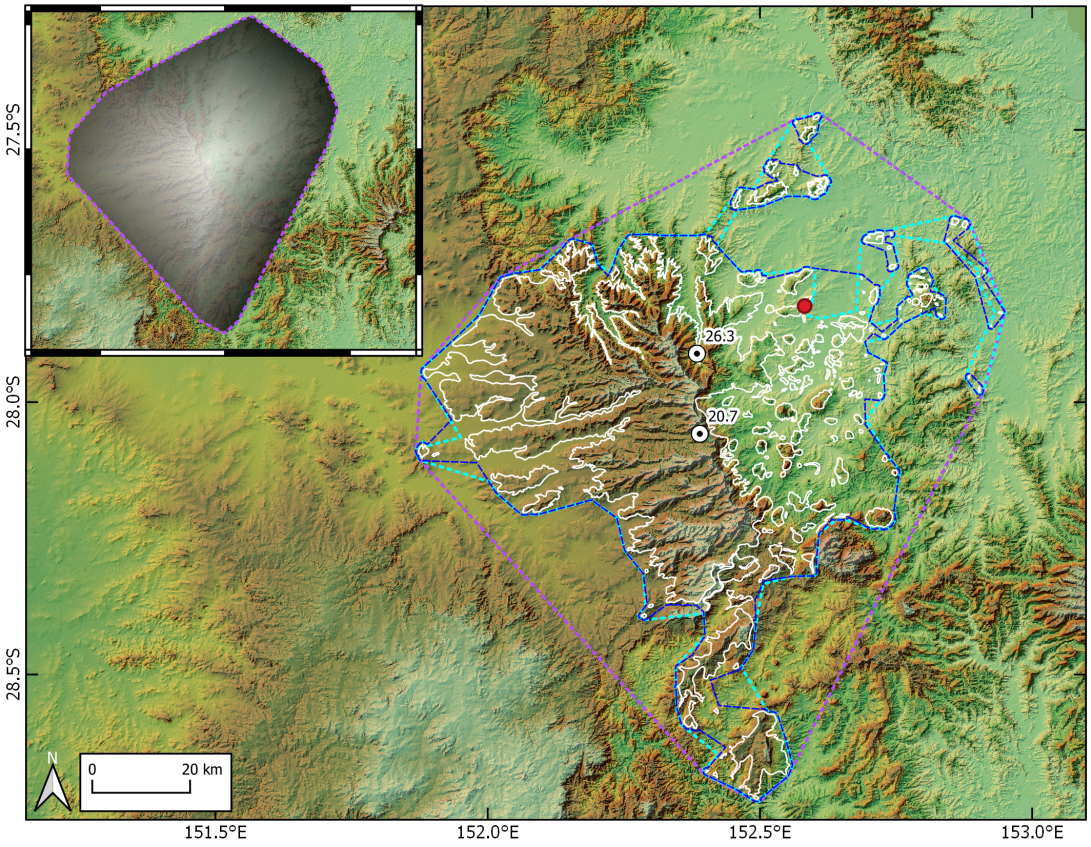

Figure 6.70: *The Main Range volcanic province. The red dot shows the location of the only freely available borehole obtained from Queensland Government (2022).*

Tweed (24.3–23.1 Ma)

Tweed is a major, 100 km-wide, shield volcano with a maximum present day thickness of around 900 m (Johnson, 1989). The shield on the Queensland side of the volcano has been separated into three main units: the lower Beechmont Basalt, the middle Binna Burra and Springbrook Rhyolites, and the upper Hobwee Basalt. The New South Wales side of the shield comprises the Lismore Basalt, Nimbin Rhyolite, and Blue Knob Basalt, which are the correlative equivalents of the units in Queensland. At the centre of the volcano lies the high-level, intrusive complex of Mount Warning (Johnson, 1989). The complex consists of gabbro, monzonite, syenite, quartz diorite, trachyandesite, basaltic dykes, and comendite dykes (Cohen, 2007). K-Ar ages from the Tweed volcano range from $\sim$34.5–12.7 Ma. However, most of the young K-Ar results clearly suffered from Ar loss, as many of the results from the lava flows, (i.e., the Binna Burra Rhyolite, Albert Basalt, Hobwee Basalt, Beechmont Basalt, and Hillview Rhyolite) are younger than the central intrusive complex (Mt Warning), and therefore fail the stratigraphic principle of cross-cutting relationships. More precise Ar-Ar ages by (Cohen, 2007), from the same locations, range from $\sim$24.3–23.1 Ma where the youngest ages are represented by the Mount Warning complex. The Ar-Ar ages have thus been used to define the total range of volcanism at the Tweed shield. Due to the location of the Tweed shield on the coastline, a huge portion of the volcano has been subject to erosion, both around the central complex and along the flanks of the volcano. The preserved volume of Tweed volcanic rocks is around 638 km^3 but the volume of the original shield is likely to be as high as 5199 km^3, making it the most voluminous volcano in the East Australian chain.

- Estimated Preserved Volume; 638 km^3.
- Estimated Original Volume; 5199 km^3.
- Oldest Age; 24.3 $\pm$ 0.4 Ma (2σ) Ar-Ar (Cohen, 2007) (possibly very minor argon loss from low T steps); mafic lava from Burleigh Heads Flow; this is from the lowest stratigraphical unit, the Lower Beechmont Basalt, contemporaneous with the southerly Lismore Basalt; however Burleigh Heads is not necessarily the basal flow of the Beechmont Basalt.
- Youngest Age; 23.1 $\pm$ 0.3 Ma (2σ) Ar-Ar (Cohen, 2007) (near-ideal flat spectra); comendite dyke and layered gabbro from Mount Warning Intrusive Complex; considered the youngest unit; erosion has removed all of the lavas from around the Mt Warning complex.

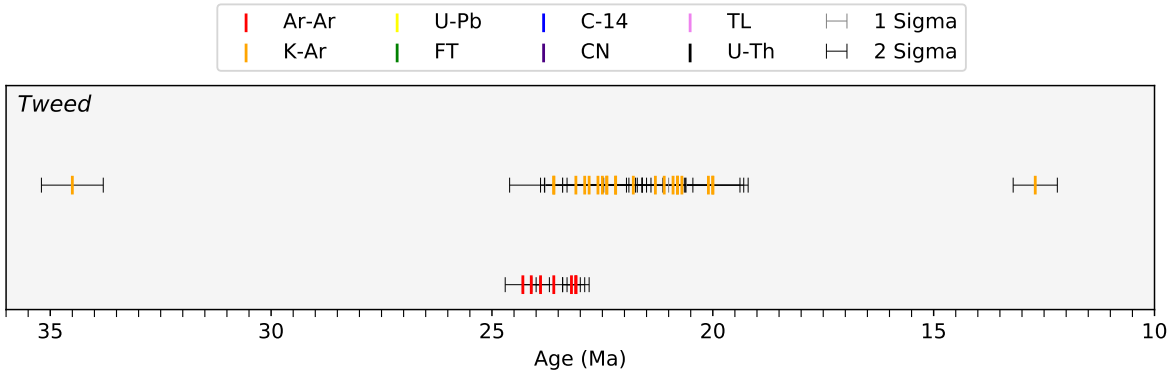

Figure 6.71: *Age data for the Tweed province.*

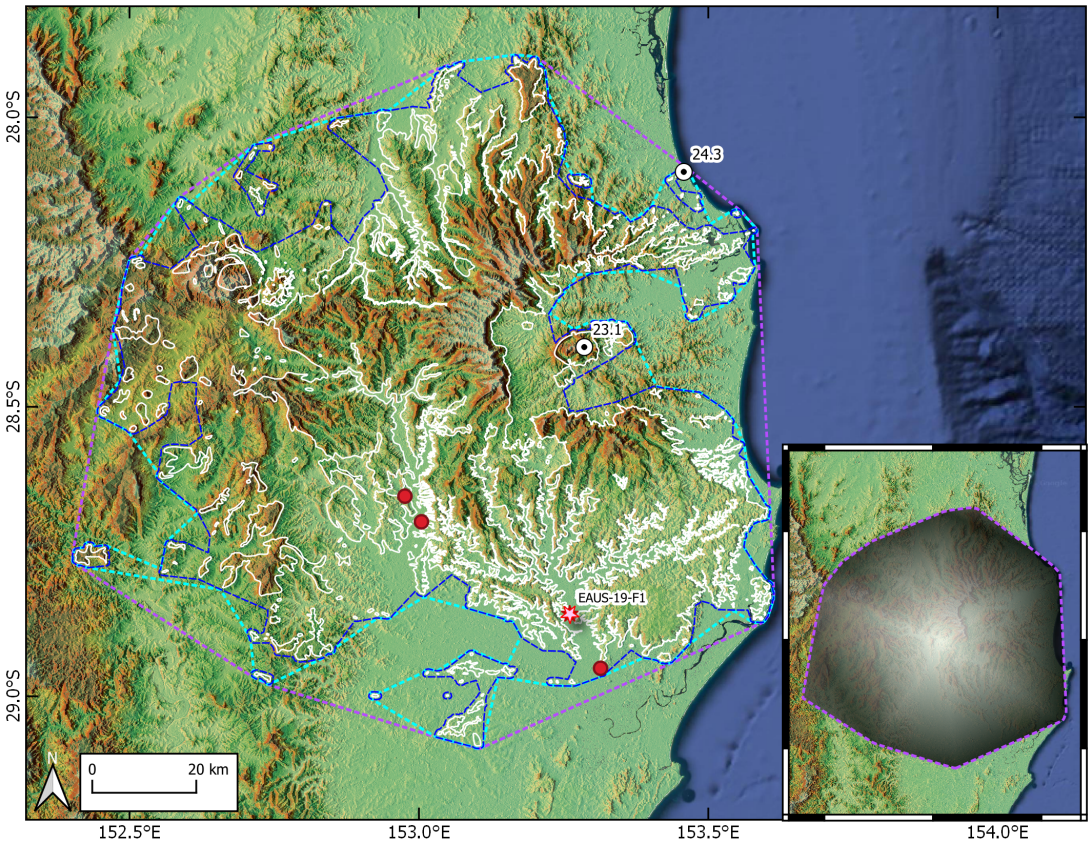

Figure 6.72: *The Tweed volcanic province. Red dots show the locations of freely available borehole data obtained from New South Wales Government (2022).*

Belmore (21.3–20.8 Ma)

The Belmore province is dominated by small flow remnants with several intrusions below and within flows (Sutherland et al., 2005). Outcrops reach over 350 m in thickness but average some 100 m and total an area of around 60 km^2 (Sutherland et al., 2005). Twenty two individual trachyte bodies have been identified but mafic rocks are primarily present as dykes with only one flow in the southeast, sandwiched within a sequence of silicic lavas, implying a substantial volume of rock has been eroded (Sutherland et al., 2005). Cohen (2007) Ar-Ar dated three silicic rocks from the Belmore area, yielding ages of $\sim$21.3–20.8 Ma. These are similar to, but more precise than, the K-Ar and U-Pb SHRIMP dates of the same silicic units analysed by Sutherland et al. (2005) who produced values of $\sim$31.2–18.0 Ma and $\sim$19.6 Ma, respectively. It should be noted however, that no mafic dykes have been dated by the Ar-Ar method as well as none of the outcrops northwest of Dobie Mountain, see Sutherland et al. (2005). It is unlikely the full range of ages have been analysed at this province, especially given considerable erosion of the Belmore volcano. For the same reason, the estimate volume of the original Belmore shield is likely to be a considerable underestimation but without further outcrop data the volume cannot be constrained any further. The volume estimate for the remnants of the Belmore province are a mere 2 km^3 but the origin of the original shield should be at least greater than 30 km^3. Using a maximum thickness of 350 m (Sutherland et al., 2005), the volume of the Belmore province using the simple conical model of Jones and Verdel (2015), is estimated at around 23.4 km^3. This uses the same extent as is used for the pyramidal estimation.

- Estimated Preserved Volume; 2 km^3.
- Estimated Original Volume; 30 km^3.
- Oldest Age; 21.3 $\pm$ 0.3 Ma (2σ) Ar-Ar (Cohen, 2007); trachyte from the top of Dome Mountain, Upper Fine Flower.
- Youngest Age; 20.8 $\pm$ 0.8 Ma (2σ) Ar-Ar (Cohen, 2007); peralkaline trachyte from Barretts Creek between Coaldale and Upper Fine Flower.

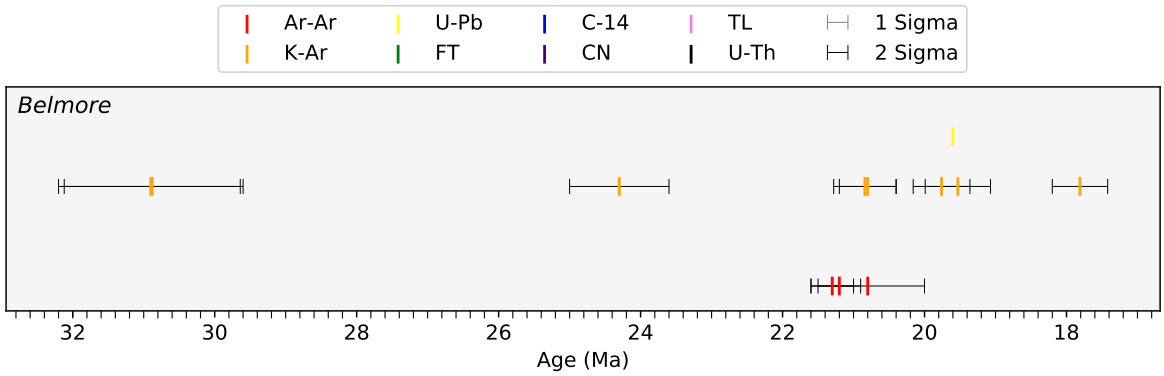

Figure 6.73: *Age data for the Belmore province.*

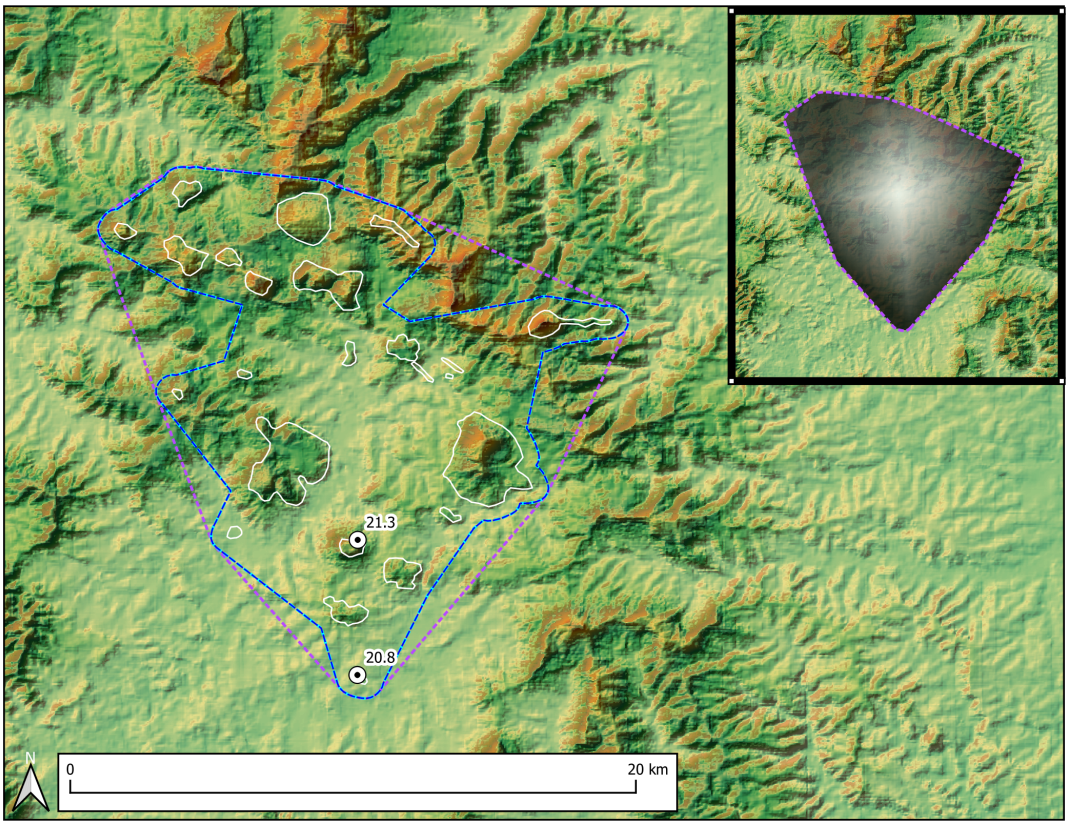

Figure 6.74: *The Belmore volcanic province.*

Ebor (20.3–19.0 Ma)

Ebor is a medium-sized, dominantly tholeiitic, shield volcano in northern New South Wales (Cohen, 2007). The northern and western parts of the shield are preserved as a semicircular arc extending from Point Lookout to Dorrigo, but only scattered outcrops of mafic lavas remain from the southern side. Lava piles vary in thickness from 100–400 m but erosion of the escarpment is calculated to have removed almost 90 % of the original volume, mostly from the eastern and southern sides of the volcano (Ashley et al., 1995). The original diameter of the shield was estimated by Johnson (1989) to be around 50 km. Ar-Ar ages for the Ebor volcano range from ∼20.3–19.0 Ma and K-Ar age range from ∼52.9–17.7 Ma. The K-Ar age of 52.9 ± 0.5 Ma (1σ) for the central Crescent intrusive complex by Gleadow and Ollier (1987) is clearly erroneous and probably due to excess argon in this sample. An apatite fission track age of 18.2 ± 2.2 Ma (1σ) by the same authors for the same unit is much closer to the Ar-Ar ages of ∼20.0–19.6 Ma by Knesel et al. (2008). The short age span of this volcano may indicate that there are older flows present that have not been dated (Cohen, 2007). The preserved volume of volcanic rock is estimated at 126 km^3 but the volume of the original shield is estimated to be considerably more substantial, at around 723 km^3. This estimated would suggest that around 83% of the volcano has been eroded which is close to similar estimates made by Ashley et al. (1995) of 90%. Including some of the more far-flung outcrops, such as a single isolated exposure in the south of the region, in this final estimate would increase the volume further but it is difficult to say whether this was part of the main shield or a single, elongated lava flow.

- Estimated Preserved Volume; 126 km^3.
- Estimated Original Volume; 723 km^3.
- Oldest Age; 20.3 ± 0.09 Ma (2σ) Ar-Ar (Jones, 2018) (no comments on sample quality); no rock type mentioned; roadside cutting collected 3.5 km northeast of Ebor.
- Youngest Age; 19.0 ± 0.18 Ma (1σ) Ar-Ar (Ashley et al., 1995) (some groundmass deuteric alteration); ryholite from shield lavas at Point Lookout; the location of the thickest lava sequences, around 400 m; unlikely to truly represent the youngest unit due to considerable erosion of this volcano.

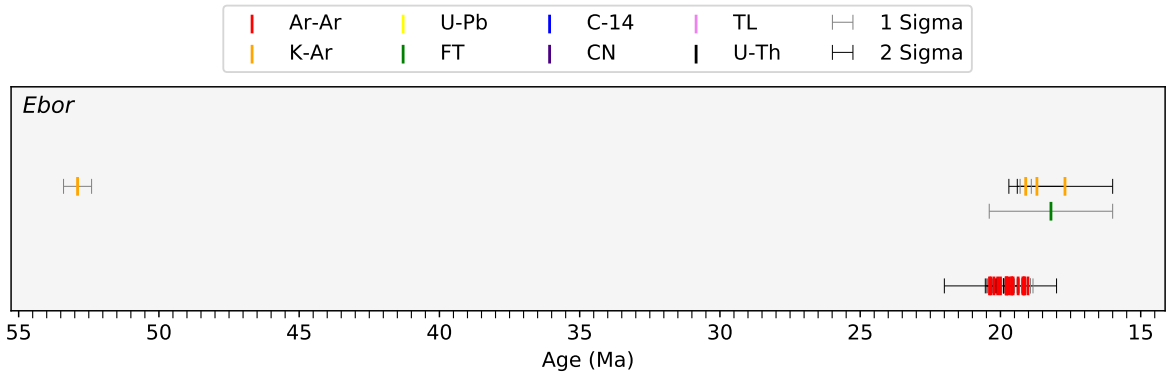

Figure 6.75: *Age data for the Ebor province.*

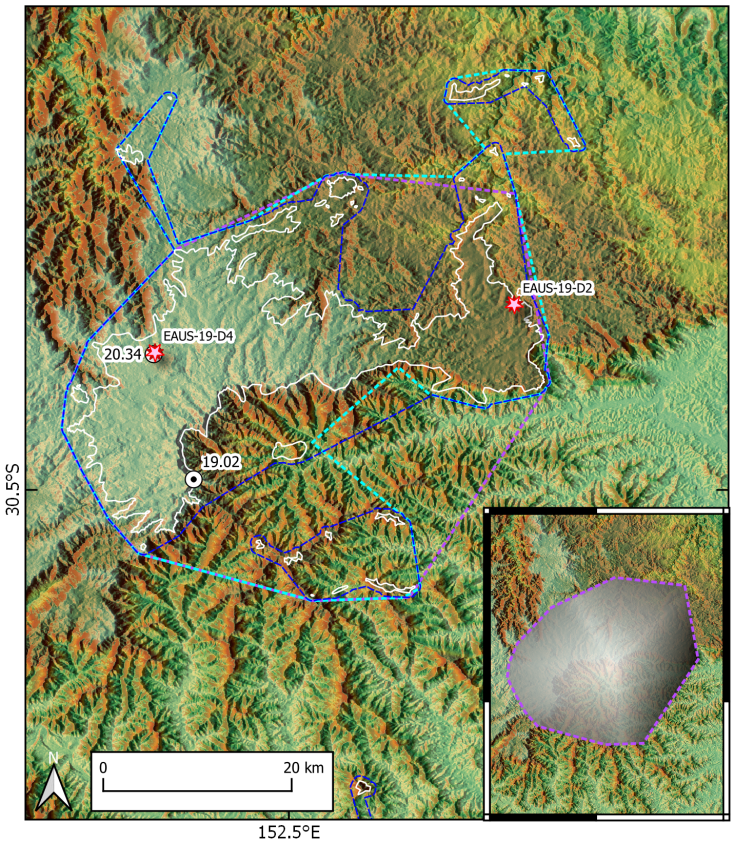

Figure 6.76: *The Ebor volcanic province.*

Comboyne (17.3–16.0 Ma)

Comboyne is a relatively small central volcano where mafic and trachytic lavas cover roughly 110 km^2 on the Comboyne Plateau, along with some high level intrusions. To the south in the Lansdowne Valley, and southeast in Lorne Basin there are approximately a dozen silicic plugs and one mafic plug (Cohen, 2007). The original diameter of the shield volcano was estimated by Johnson (1989) to be around 20 km, but this study estimates a greater value of 35 km based on numerous isolated exposures to the north, south, and east of the main plateau. K-Ar ages from the Comboyne volcano range from $\sim$19.6–13.3 Ma Sutherland et al. (2012); Wellman and McDougall (1974a); McDougall and Wilkinson (1967). The same units were re-analysed by Knesel et al. (2008), Sutherland et al. (2012), and Crossingham et al. (2018) who produced more accurate age estimates with Ar-Ar dating. The resultant Ar-Ar age range suggests volcanic activity within the Comboyne province was fairly short-lived from $\sim$17.3–16.0 Ma. The preserved volume of volcanic rock at Comboyne is around 23 km^3 and the volume of the original shield is estimated to be around 230 km^3. Again, given the position of the volcano on the Australian coastline it is difficult to be sure whether the small volume of the Comboyne volcano is due to limited magma emplacement or extremely high levels of erosion.

- Estimated Preserved Volume; 23 km^3.
- Estimated Original Volume; 230 km^3.
- Oldest Age; 17.3 ± 0.5 Ma (1σ) Ar-Ar (Sutherland et al., 2012) (no comments on sample quality); trachyte plug from Juhle Mountain.
- Youngest Age; 16.0 ± 0.5 Ma (2σ) Ar-Ar (Crossingham et al., 2018) (sample yielded large errors in each step as a result of low radiogenic % 40Ar); no rock type mentioned; sample collected 6 km northwest of Comboyne; whilst errors were reported in each step, the resultant age is similar to other samples nearby.

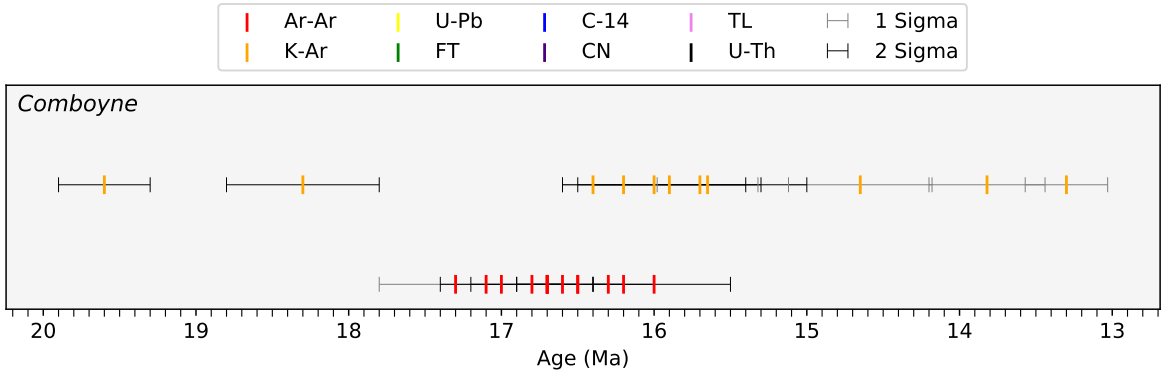

Figure 6.77: *Age data for the Comboyne province.*

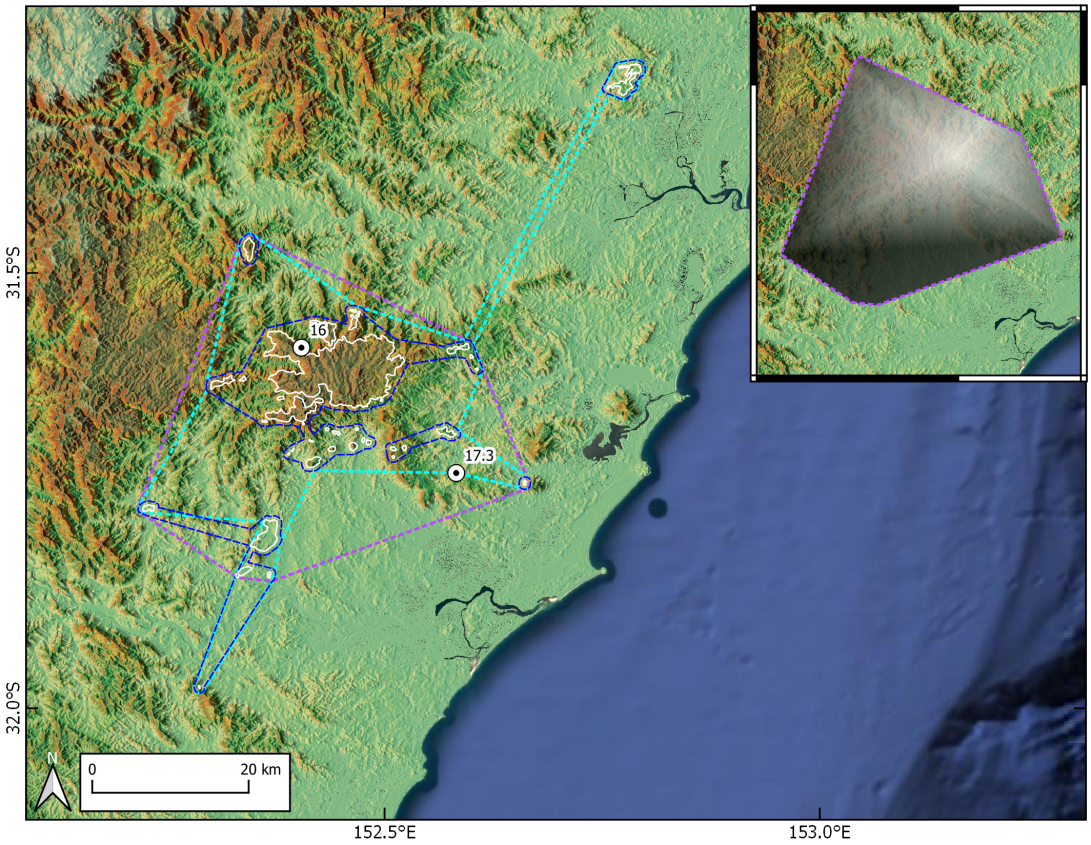

Figure 6.78: *The Comboyne volcanic province.*

Nandewar (18.9–18.5 Ma)

The Nandewar central volcano has a present day thickness of around 800 m but the original thickness is considered to be greater based on an intrusive plug outcropping at one of the highest locations in the complex (Johnson, 1989). Deposits represent isolated flows, plugs, and massive shield forming lavas, often intercalated with pyroclastic rocks (Johnson, 1989; Cohen, 2007). Occasional lavas to the northwest of the province, now covered by Quaternary sediments, have been identified in sparse borehole data. Unfortunately, no base depths have been recorded as the holes are only a few meters deep and whether or not they correlate directly to the Nandewar volcano is still unknown. For this reason, these lavas have not been included in the final volume estimate of the Nandewar volcanic rocks. K-Ar ages from the Nandewar province range from $\sim$22.1–14.9 Ma. They were re-analysed by Ar-Ar by Cohen (2007) to give a much narrower range of $\sim$18.9–18.5 Ma. The reportedly "older" rhyolite lavas from Stipp and McDougall (1968) were re-dated by Cohen (2007) to give a younger Ar-Ar age of 18.9 Ma. Unfortunately, none of the oldest K-Ar samples from the stratigraphically lower mafic lavas (such as the basalt flows immediately overlying the Mesozoic Pilliga Sandstone) have been analysed by the Ar-Ar method so the oldest age is still to be determined. Also, the youngest K-Ar age was recorded at Mount Kaputar just south of Barraba, a location that also remains un-dated by Ar-Ar analysis. This possibly accounts for the very short range of ages at Nandewar volcano, and further Ar-Ar analysis is required to estimate the full duration of activity here, especially given the larger size of the volcano. The volume of the original shield is estimated to be around 2103 km^3. Isolated lava flows to the southeast of the province have also not been included in the final volume estimate as they are likely to represent singular, elongated lava flows and not the bulk mass of the central shield.

- Estimated Preserved Volume; 218 km^3.
- Estimated Original Volume; 2103 km^3.
- Oldest Age; 18.9 $\pm$ 0.2 Ma (2σ) Ar-Ar (Cohen, 2007) (concordant results); metaluminous trachyte from an unnamed bluff 1.5 km north of Killarney Gap; this is the same unit that gave the second oldest K-Ar age.
- Youngest Age; 18.5 $\pm$ 0.2 Ma (2σ) Ar-Ar (Cohen, 2007) (near-ideal flat spectra); peralkaline trachyte plug from the western face of Mount Deriah; this is the same unit that gave the second youngest K-Ar age.

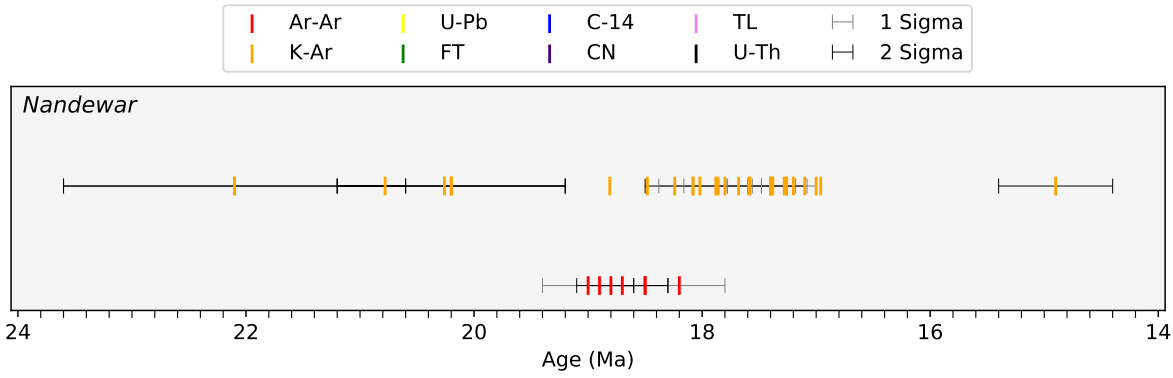

Figure 6.79: *Age data for the Nandewar province.*

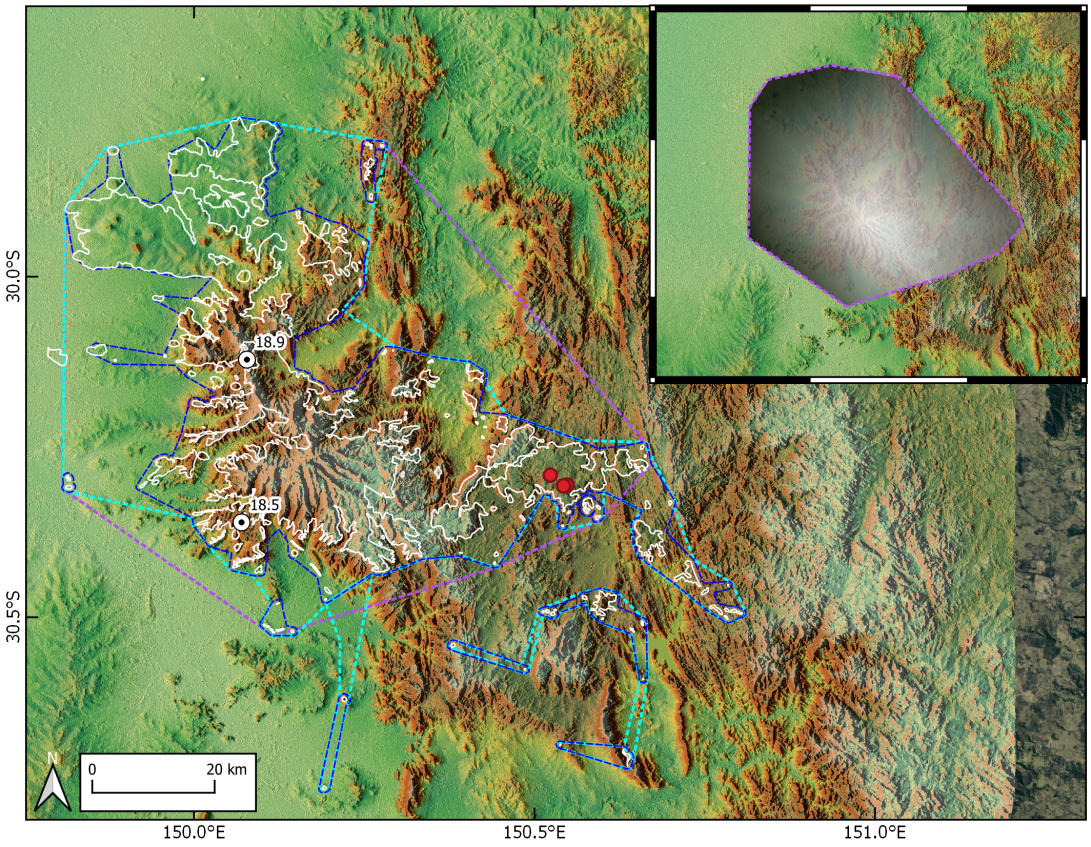

Figure 6.80: *The Nandewar volcanic province. Red dots show the locations of freely available borehole data obtained from New South Wales Government (2022).*

Warrumbungles (18.0–15.2 Ma)

Warrumbungle is a deeply dissected, low-lying, shield volcano that is likely to originally have reached a height close to 1000 m above the surrounding basement (Johnson, 1989). A considerable portion of the province has been very recently, and very comprehensively mapped by Bull et al. (2020). As with most central volcanoes, silicic rocks, mostly trachytes, are situated in the centre of the volcano, and mafic lavas, mostly hawaiites and mugearites, are dominant on the shield flanks, often interbedded with pyroclastic rocks (Cohen, 2007). The palaeotopography is now represented by a central high around 600 m, as suggested by Bull et al. (2020) and Johnson (1989), and dips smoothly to the outskirts of the volcano to a lower depth of around 200 m so as to encompass all present-day outcrops. The Warrumbungles province has been very well dated by Cohen et al. (2017) giving an Ar-Ar age range of $\sim$18.0–15.2 Ma. K-Ar ages range from $\sim$17.2–13.3 Ma but are deemed less precise as the same flows were re-analysed by Cohen (2007). Palaeomagnetic measurements from the same province displaying normal polarity, to transitional polarity, to reversed polarity suggesting the entire sequence of lavas must have been erupted over a relatively protracted length of time (Cohen, 2007). Ar-Ar ages by Crossingham et al. (2018) agree with those by Cohen et al. (2017), with magmatism taking place over a relatively short period of time between $\sim$18.0–15.2 Ma. Exposures across the Warrumbungle province form a relatively uniform shield shape and the volume of the original shield is estimated to be around 1269 km^3, excluding any small, isolated, far-flung exposures.

- Estimated Preserved Volume; 171 km^3.
- Estimated Original Volume; 1269 km^3.
- Oldest Age; 18.0 ± 0.2 Ma (2σ) Ar-Ar (Cohen, 2007) (relatively flat spectra); mafic lava from the northern Warrumbungles on the western side of Goorianwa Gap; from the lowest section of the lowest flow.
- Youngest Age; 15.2 ± 0.3 Ma (2σ) Ar-Ar (Cohen, 2007) (excess argon, intercept of 320 ± 15); peralkaline trachyte from the southern end of a 600 m long dyke known as "The Breadknife"; this youngest age is consistent with stratigraphy as the dyke crosscuts all other units in the vicinity.

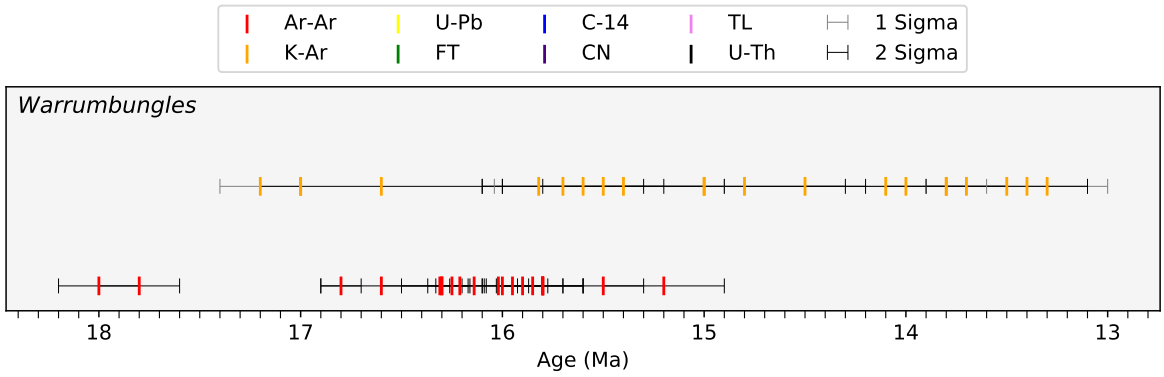

Figure 6.81: *Age data for the Warrumbungles province.*

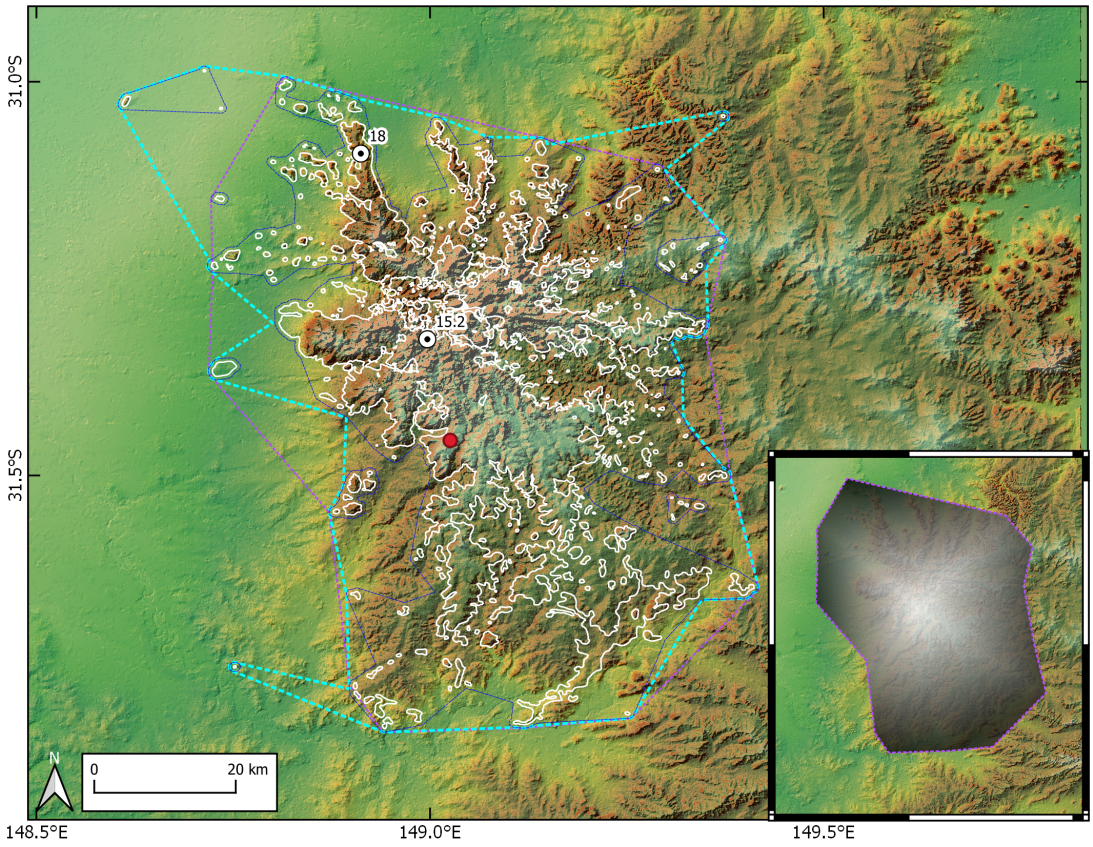

Figure 6.82: *The Warrumbungles volcanic province. The red dot shows the location of the only freely available borehole obtained from New South Wales Government (2022).*

Canobolas (13.2–11.5 Ma)

Canobolas is a moderately preserved, low-angle shield volcano where mildly alkaline to transitional magma evolved within a large, high level magma chamber (Johnson, 1989). The original diameter of the volcano was estimated by Johnson (1989) to be around 50 km and is here estimated to be around 60 km along the E-W axis but just 30 km along the N-S axis. Canobolas is the youngest central volcano of considerable volume and with a recognisable shield shape (Cohen, 2007). Within the centre of the volcano there are numerous pyroclastic units, silicic domes, dykes and plugs (Johnson, 1989). The shield flanks are dominated by hawaiite lavas, although minor palaeosols, pyroclastic beds, and diatomaceous sediments are present between flows (Middlemost, 1981). The Canobolas province has been K-Ar dated by Wellman and McDougall (1974a) and Ar-Ar dated by Cohen (2007) and Jones et al. (2017). As the same units have been analysed by both methods, the Ar-Ar ages are used here to define the age range as they are deemed more accurate. K-Ar ages by Wellman and McDougall (1974a) range from $\sim$12.7–10.9 Ma, very similar to Ar-Ar ages of $\sim$13.2–11.5 Ma. However, this is unlikely to be the full duration of activity as the stratigraphically lower mafic flows have not been analysed by either method. The volume of the original shield is estimated to be around 513 km^3, although this estimate excludes considerable flows to the north of the inferred shield as these are again thought to represent singular, elongated lava flows and not the bulk mass of the central shield.

- Estimated Preserved Volume; 55 km^3.
- Estimated Original Volume; 513 km^3.
- Oldest Age; 13.2 $\pm$ 0.3 Ma (2σ) Ar-Ar (Cohen, 2007) (excess argon, intercept of 370 $\pm$,40); basalt from an early valley filling flow on the southeast side of the Canobolas volcano; whilst this is the same lava flow which gave the oldest K-Ar age, it does not represent the oldest flow of the volcano.
- Youngest Age; 11.5 $\pm$ 0.05 Ma (2σ) Ar-Ar (Jones et al., 2017) (no comments on sample quality) mafic lava near the summit of Mount Canobolas; this is the same location that gave the youngest K-Ar age at the top of the stratigraphy.

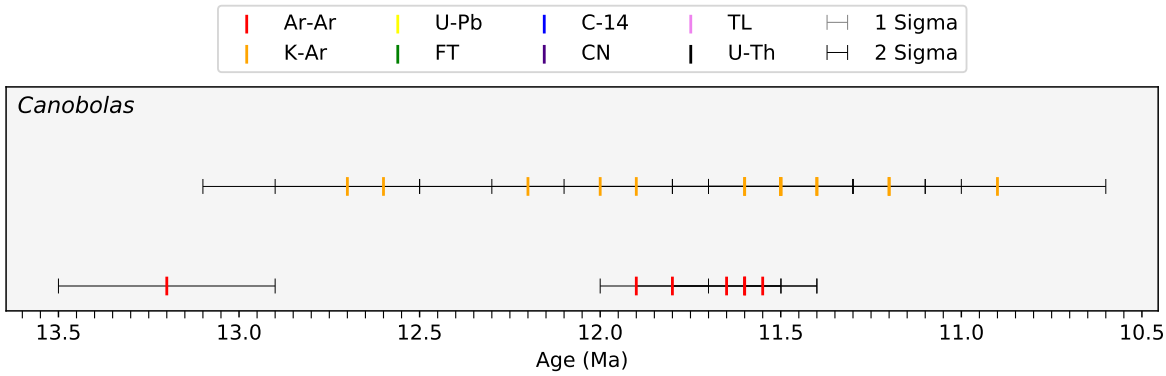

Figure 6.83: *Age data for the Canobolas province.*

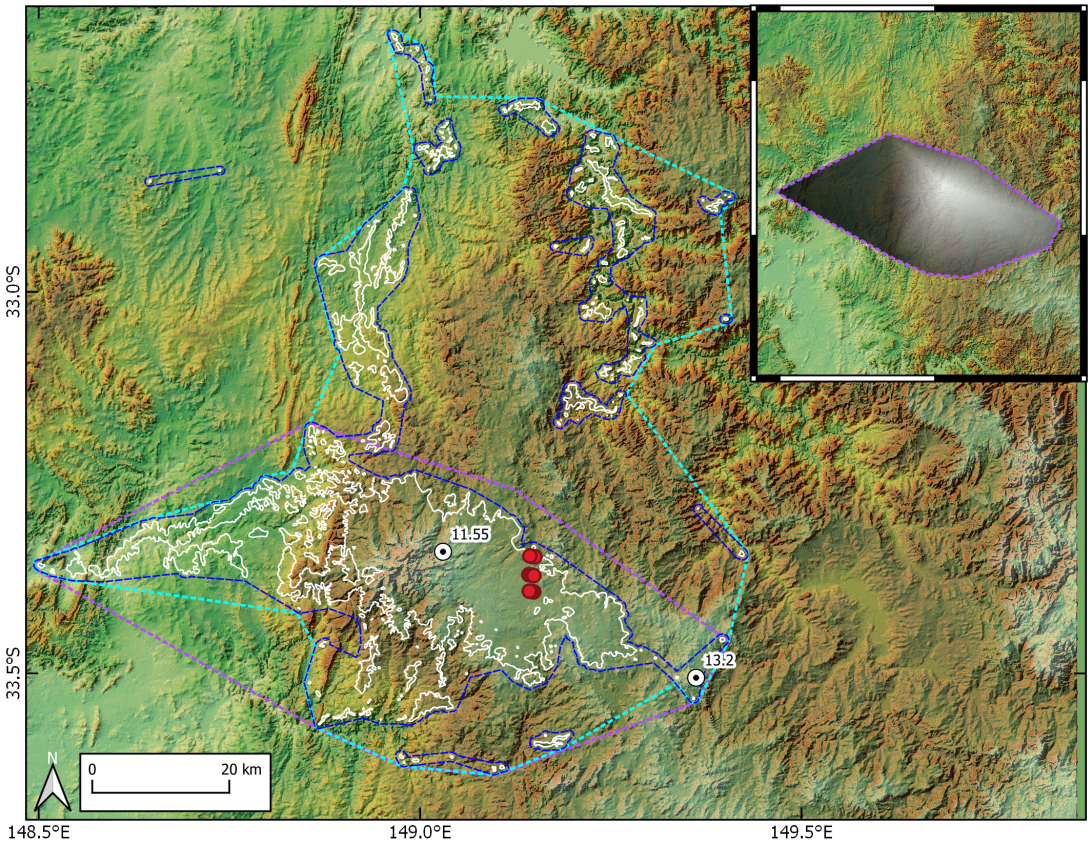

Figure 6.84: *The Canobolas volcanic province. Red dots show the locations of freely available borehole data obtained from New South Wales Government (2022).*

6.2.6 Prolonged 60–10 Ma Volcanism

Mingela (44.5–17.4 Ma)

The Mingela province, as described by Johnson (1989), contains around 22 known plugs and several dykes that are concentrated in the Arthur Peak and Mingela areas. For this study, the Mingela province is taken to include all scattered plugs and remnants that form a roughly 100 km southeast-trending belt from Mingela to Greenvale. Flows are absent from the south of the province, implying substantial amounts of erosion has taken place here. This is unsurprising given the older age of the volcanoes, the tropical climate, and the location next to one of Australia's largest rivers, the Burdekin. Plugs generally form small hills and reach up to 400 m in diameter, the most prominent of which, Arthur Peak, frequently contains peridotite and pyroxenite xenoliths (Johnson, 1989). The only age data for the numerous small, isolated plugs of the Mingela province come from K-Ar analyses compiled in Cohen et al. (2017). Around twenty plugs across the province produce a fairly continuous range of ages from 44.9–17.4 Ma. This data confirms geological observations that the Mingela province is older than the surrounding lava field provinces of Nulla, Sturgeon, Chudleigh, McBride, Atherton, Maclean and Piebald, which all erupted in the last 10 Ma. The estimated pre-erosion volume varies greatly but is likely to be between 6–150 km^3 depending on how connected the present-day exposures were originally. For the preferred estimate made here, the volume has been calculated using extrapolated ridgelines as the top surface across the extent of footprint 1. This is to assume that most outcrops were erupted as separate, isolated volcanoes, rather than one huge lava field. This was deemed more likely when considering the vast age range over which the lavas have been emplaced.

- Estimated Preserved Volume; 2 km^3.
- Estimated Original Volume; 19 km^3.
- Oldest Age; 44.5 Ma (no error reported) K-Ar (Cohen et al., 2017) (no comments on sample quality); mafic lava from plug M6 near Townsville.
- Youngest Age; 17.4 Ma (no error reported) K-Ar (Cohen et al., 2017) (no comments on sample quality); mafic lava from the summit of Nome Hill.

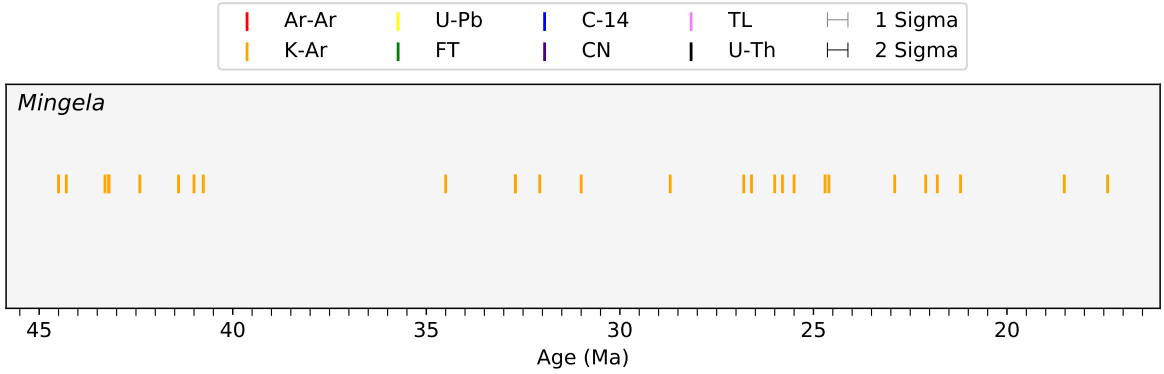

Figure 6.85: *Age data for the Mingela province.*

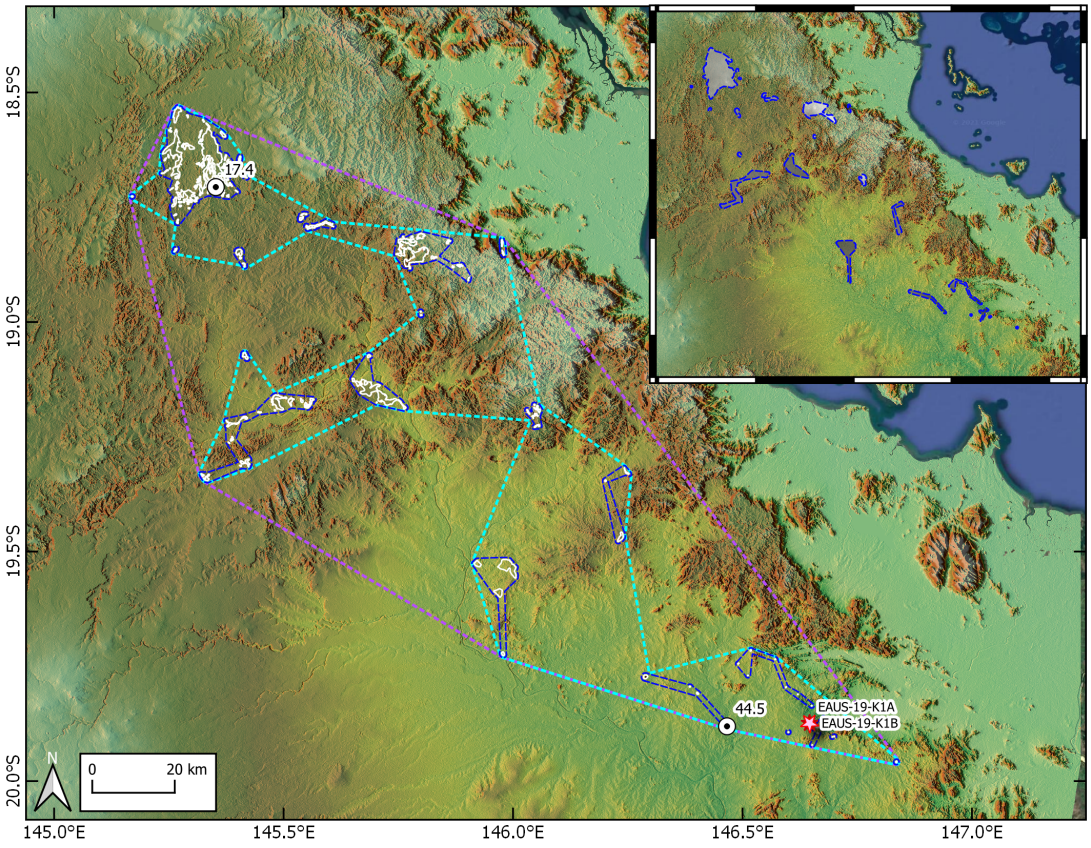

Figure 6.86: *The Mingela volcanic province.*

Peak Range Lava Field (47.9–44.6 Ma)

Surrounding the high summits of the Peak Range are gently sloping mafic lava plains, typically 30 m in thickness which extend around 15–30 km east and west of the range along with small, scattered outcrops in the East Clermont area (Cohen, 2007). Geochronology, field relationships, the abundance of peridotite xenoliths and geochemical results from this study all suggest the lower Peak Range lavas represent an earlier phase of lava field volcanism prior to the eruption of the Peak Range central volcano around 34 Ma. Unfortunately, it is difficult to resolve the true extent and thickness of the underlying lava field whilst it remains obscured by the Peak Range central volcano. For this study the volume of the lava field has been included in the central volcano volume calculation. Ar-Ar dating by Cohen (2007), Cohen et al. (2013) and Jones et al. (2020) give a total age range of the Peak Range lava field volcanism from $\sim$47.9–44.6 Ma.

- Oldest Age; 47.9 ± 0.7 Ma (2σ) Ar-Ar (Cohen, 2007) (near-ideal flat spectra); mafic lava obtained close to the tholeiitic basalt sample that yielded the oldest K-Ar age of 40.9 ± 1.6 Ma (2σ); also similar to the oldest Ar-Ar age of 47.2 ± 0.53 Ma (2σ) from (Jones et al., 2020); unlikely to represent the true stratigraphic base if there are additional earlier lava field flows present beneath the Peak Range central volcano.
- Youngest Age; 44.6 ± 0.4 Ma (2σ) Ar-Ar (Jones et al., 2020) (no comment on sample quality); mafic lava from central Peak Range; road cutting along Huntley Road.

Toowoomba Lava Field (40.9 Ma)

The lower Toowoomba lavas are thought to be the remnants of an earlier phase of lava field volcanism, prior to the onset of central volcano magmatism. This basal flow, the Meringandan Lava Field, was dated at 27.4 ± 0.7 Ma (2σ) by K-Ar analysis, and 40.9 ± 1.0 Ma (2σ) by Ar-Ar analysis. Unfortunately, no age data is available to constrain the upper limit of the Toowoomba lava field. It is also difficult to reconcile a volume of the lava field as it is obscured and buried by later central volcano deposits. For this study the volume of the lava field has been included in the central volcano volume calculation.

- 40.9 ± 1.0 Ma (2σ) Ar-Ar (Cohen, 2007) (minor argon loss); mafic lava from the lowermost basalt within the Toowoomba escarpment; likely to be close to the stratigraphic base; dated by K-Ar at 27.4 ± 0.7 Ma (2σ) (discrepancy due to considerable Ar loss).

Brisbane (65.3–55.0 Ma)

Around Brisbane and Ipswich there are several small low-lying sedimentary deposits, including the Petrie, Oxley, Booval, Amberley, Beaudesert, and Pomona Basins. (Cohen, 2007). These are typically less than 10 km wide, but can be several kilometers deep and occasionally contain mafic lavas interbedded with lacustrine and fluvial sediments (Johnson, 1989). Thicknesses reach up to 300 m in places but outcrops are often strongly weathered forming lateritised profiles (Johnson, 1989). Each of the six sedimentary basins are included in the Brisbane province, previously named the Ipswich province by Wellman (1971). K-Ar ages by Webb and McDougall (1967) and Green and Stevens (1975) range from $\sim$65.3–46.6 Ma with basalt samples obtained from the Booval Basin, the Oxley Basin, and the Amberley Basin. The younger K-Ar ages have been discarded from this analysis due to the strong likelihood of Ar loss in these samples. Ar-Ar ages by Cohen (2007) from three mafic lavas in the Petrie and Oxley Basins range from $\sim$58.0–55.0 Ma. All three samples yielded low K/Ca ratios with low amounts of gas released, the resulting plateau and isochron ages are consequently imprecise, with $2\,\sigma$ errors of between 2–6 Ma (Cohen, 2007). All three samples yielded indistinguishable ages between $\sim$55–58 Ma. These ages fall within the period of seafloor spreading in the Coral and Tasman Seas, which ceased around 52 Ma. The numerous basins along the eastern coast of Queensland may therefore represent the onshore products of this tensional stress regime (Cohen, 2007). To date, only the Amberley, Booval, Oxley, and Petrie Basins have been dated. No ages exist for volcanic outcrops in the Beaudesert Basin or the more northerly Pomona Basin. Lavas throughout the Brisbane province are found interbedded with sediments and often observed only in drillcores meaning the true extent of the lavas are difficult to define. For this study, the pre-erosion volume is estimated, using ridgeline resurfacing across footprint 1, to be between 10–58 km^3 but this does include interbedded sediments and the base is poorly defined due to limited access to borehole data. The preferred pre-erosion volume is 31 km^3, which assumes volcanism is strictly confined to the six basins. The results mentioned here could be improved upon greatly by the addition of more borehole data.

- Estimated Preserved Volume; 3 km^3.

- Estimated Original Volume; 31 km^3.
- Oldest Age; 65.3 ± 1.9 Ma (1σ) K-Ar (Webb and McDougall, 1967) (no comments on sample quality); olivine basalt from Mount Walker Creek, Cunningham Highway; unlikely to be the base of stratigraphy.
- Youngest Age; 55.0 ± 2.0 Ma (2σ) Ar-Ar (Cohen, 2007) (imprecise results due to the low amounts of gas released); mafic lava from the Corinda drillcore; unlikely to be the top of stratigraphy.

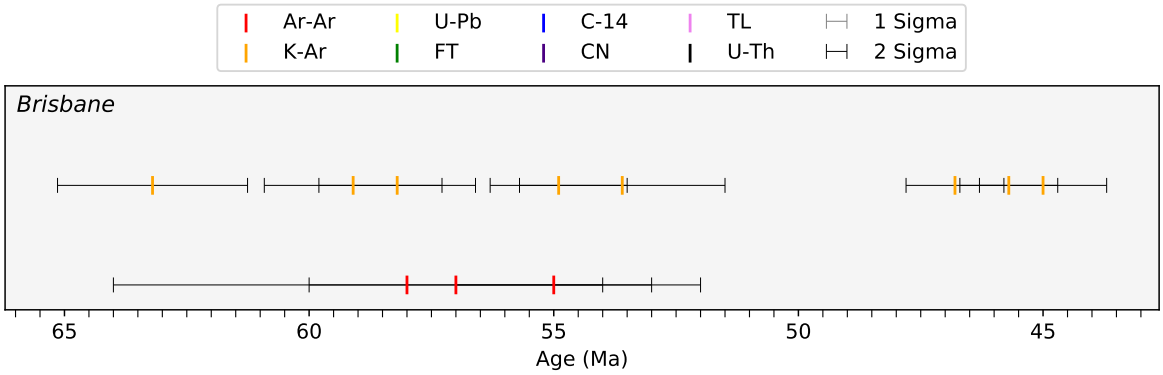

Figure 6.87: *Age data for the Brisbane province.*

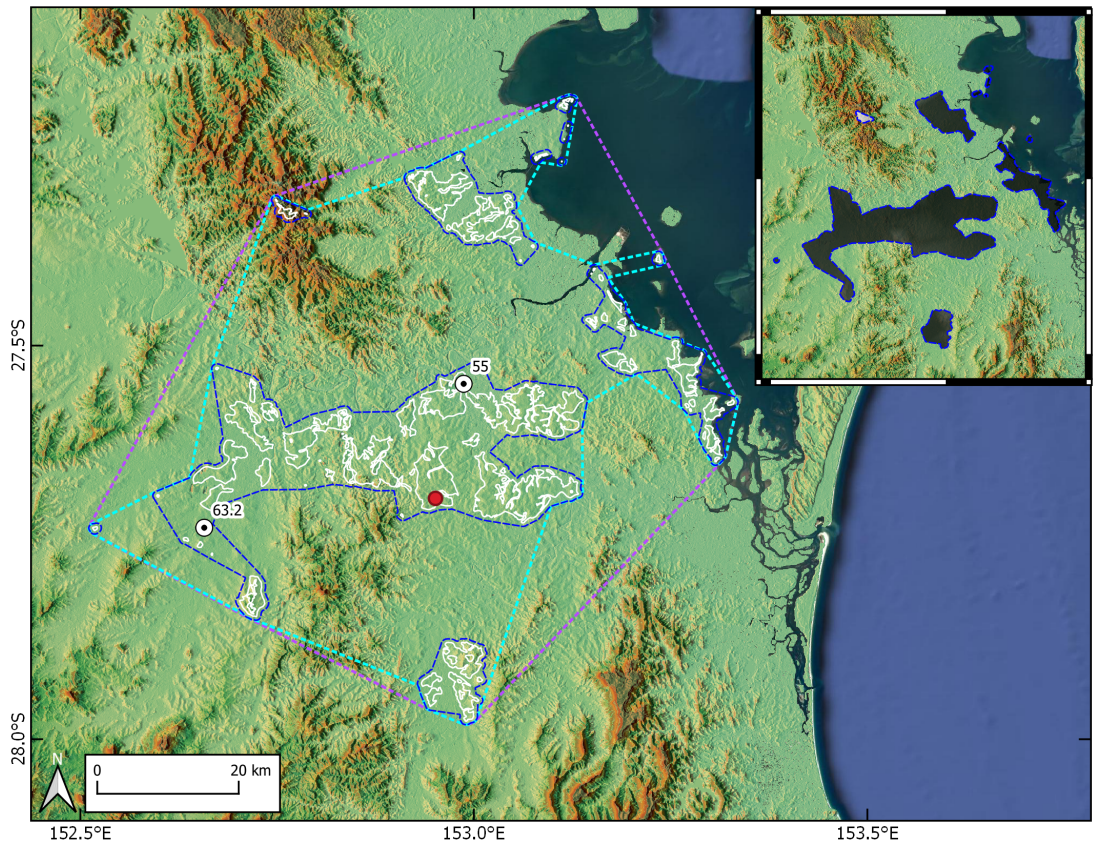

Figure 6.88: *The Brisbane volcanic province. The red dot shows the location of the only freely available borehole obtained from Queensland Government (2022).*

Doughboy (47.7–36.3 Ma)

The Doughboy lava field is similar to the nearby New England province albeit smaller in size, consisting of flat-lying, relatively thin lava flows (Johnson, 1989). Basalts are fairly heavily eroded but remnants reach around 150 m in thickness (Johnson, 1989). Only four K-Ar ages from Wellman and McDougall (1974a) and one Ar-Ar age from Ashley et al. (1995) exist for the Doughboy province. These range from $\sim$47.7–36.3 Ma although the youngest ages are from relatively altered samples and probably represent a minimum age. Without more detailed mapping from this area it is difficult to say if these represent the top and base of the Doughboy volcano. The extrapolation of ridgelines here did not work particularly well, presumably due to the flat, low-lying nature of most exposures. Therefore, original volumes were calculated using the present-day DEM as the upper surface, clipped to the extent of footprint 2, assuming all, relatively close, exposures were originally connected as a single lava field.

- Estimated Preserved Volume; 4 km^3.
- Estimated Original Volume; 32 km^3.
- Oldest Age; 47.7 ± 0.45 Ma (1σ) Ar-Ar (Ashley et al., 1995) (evidence of groundmass deuteric alteration); basanite near the summit of Round Mountain within Cathedral Rock National Park.
- Youngest Age; 36.3 ± 1.4 Ma (2σ) K-Ar (Wellman and McDougall, 1974a) (fairly altered sample, probably a minimum age); alkali olivine basalt from the Doughboy Range, north of Cathedral Rock National Park. The true youngest age of the Doughboy volcano is not yet determined as the K-Ar analyses discussed here are likely affected by Ar loss.

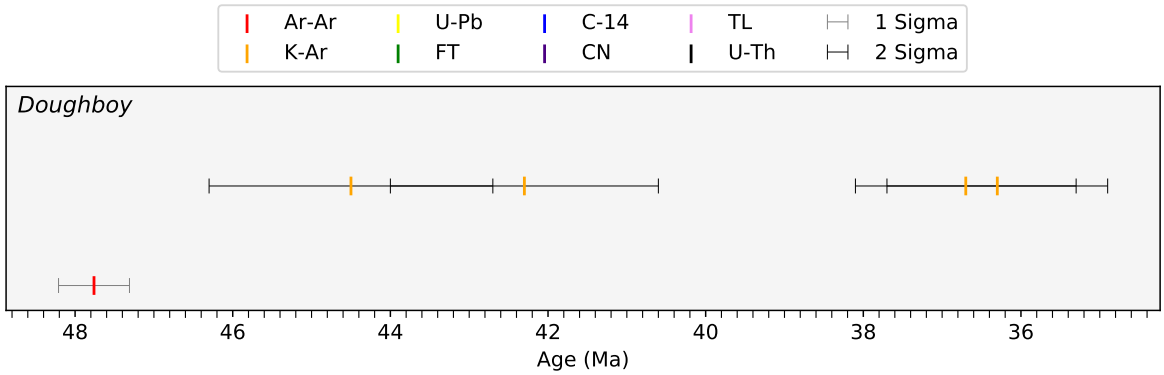

Figure 6.89: *Age data for the Doughboy province.*

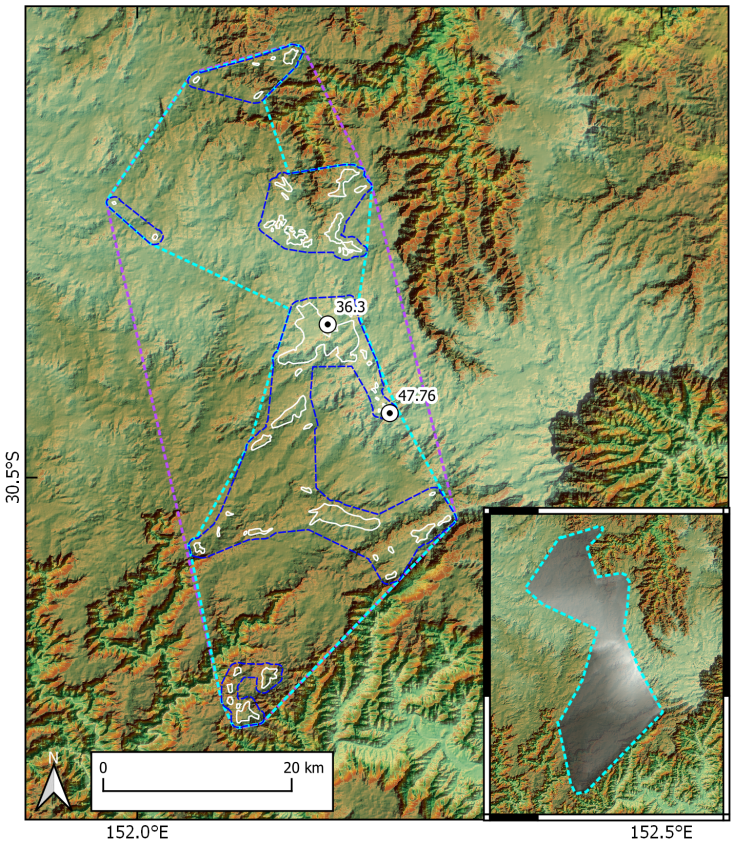

Figure 6.90: *The Doughboy volcanic province.*

Walcha (57.1–35.0 Ma)

The Walcha province represents relatively thin residual lava field which outcrops between Walcha and Nowendoc (Wellman and McDougall, 1974b). For this study, small exposures between Walcha and Piallaway have been included in the province but further mapping is required to confirm if these lavas originate from the same volcano. To date, no detailed geological studies have been conducted across the Walcha lava field. Lava sequences are typically less than 100 m thick around Walcha but reach up to 600 m thick further south along the Great Divide and Tia Range (Johnson, 1989). The only available dates for the Walcha province are K-Ar ages by Wellman and McDougall (1974b) and Sutherland (1991), some of which have relatively high errors (up to 2.3 Ma 2σ). From the limited analyses available, ages date from $\sim$57.1–35.0 Ma with fairly sizable hiatuses in between although this is likely the result of poor sampling. Interpretation of these ages is difficult as no detailed mapping of Walcha has been completed so stratigraphic relations are unclear (Wellman and McDougall, 1974b). Despite a lack of precise ages, older dates are coeval with the Barrington volcano 30 km to the southwest, and younger dates are coeval with the New England volcano 30 km to the north. The extrapolation of ridgelines at Walcha did not manage to isolate the upper volcanic surface well and the preferred original estimate for the Walcha province has instead been calculated using using the present-day DEM as the upper surface, clipped across the extent of footprint 2, assuming all exposures were originally connected as a single lava field. The older age of the volcano suggests it has been subject to a considerable amount of erosion and in using the present-day DEM this volume is likely to be an underestimate. This may explain the sizeable difference between this volume and that estimated by Wellman (1971), of 700 km^3.

- Estimated Preserved Volume; 82 km^3.
- Estimated Original Volume; 472 km^3 (underestimate).
- Oldest Age; 57.1 ± 2.3 Ma (2σ) K-Ar (Wellman and McDougall, 1974b) (no comments on sample quality); mafic lava 1 km NW of Yarrowitch; stratigraphic relationship unclear.
- Youngest Age; 35.0 ± 0.2 Ma (1σ) K-Ar (Sutherland, 1991) (no comments on sample quality); nepheline mugearite from a dyke at Brickclay Creek, 16 km SW of Walcha; stratigraphic relationship unclear.

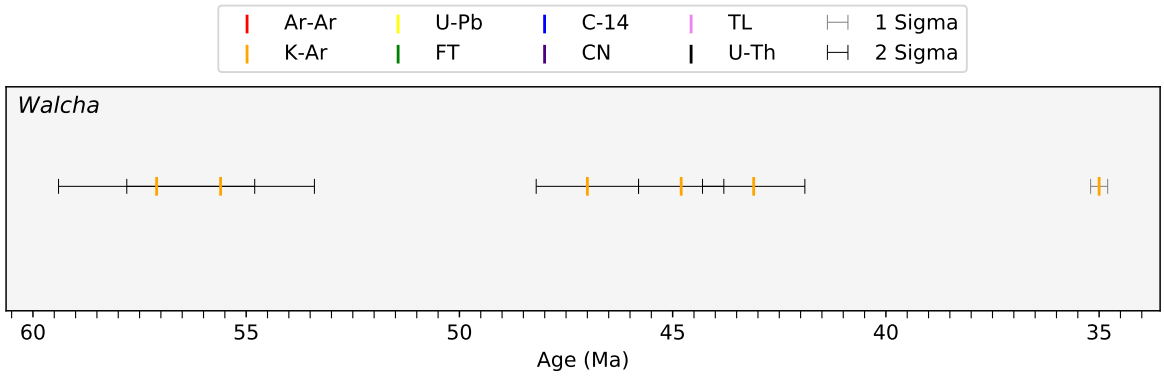

Figure 6.91: *Age data for the Walcha province.*

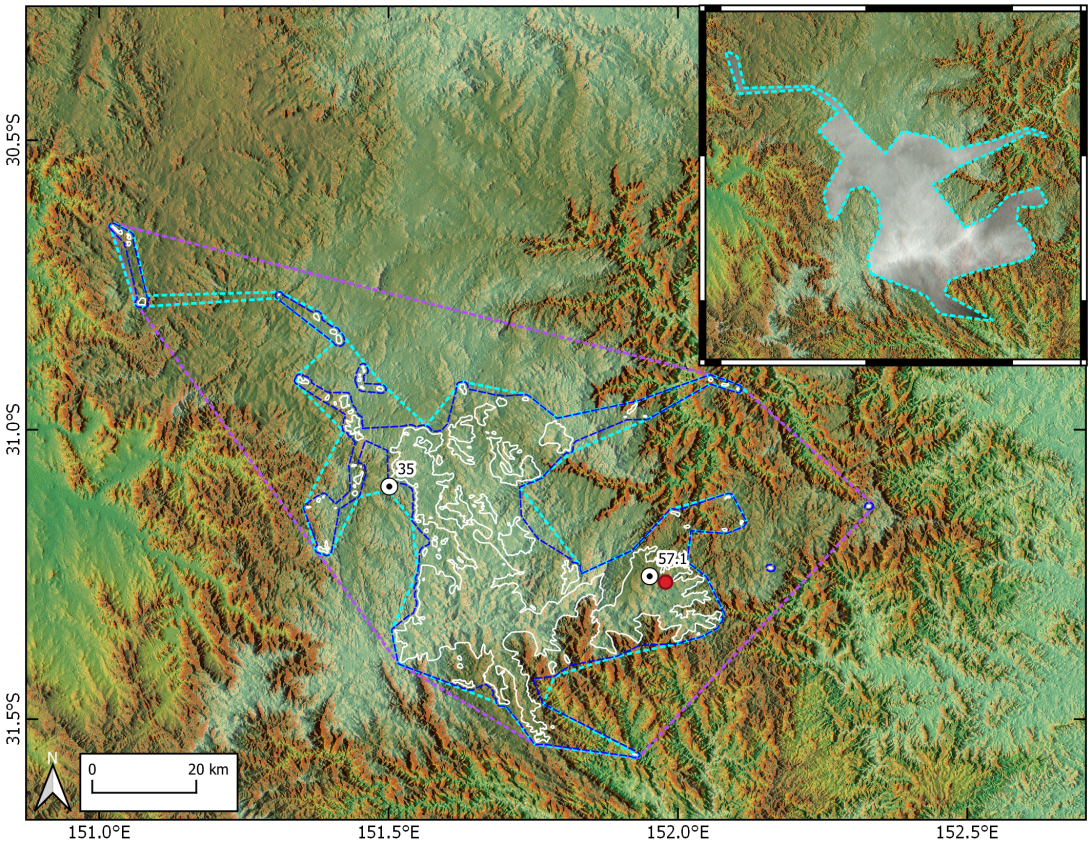

Figure 6.92: *The Walcha volcanic province. The red dot shows the location of the only freely available borehole obtained from New South Wales Government (2022).*

Barrington inc Mount Royal (58.9–35.8 Ma)

The Barrington volcano represents an eroded, low-angle, mafic shield which today forms an isolated plateau, around 700 m thick across the Barrington Tops National Park (Wellman et al., 1969; Sutherland and Fanning, 2001). For this study, the province has also included the mafic lavas north of Barrington near Nundle, which display similar morphology although without more detailed mapping it is not entirely clear whether or not these were formed by the same volcanic events. Both areas are defined by thick lava piles intruded by numerous plugs and sills (Johnson, 1989). Ar-Ar, K-Ar and U-Pb SHRIMP dating suggest the main eruptive period at Barrington volcano peaked between $\sim$58.9–35.8 Ma, marked by voluminous, tholeiitic basalt flows (Jones, 2018; Wellman et al., 1969; Sutherland and Fanning, 2001). Ar-Ar results by Jones (2018) only range from $\sim$58.9–52.7 Ma, although these samples are all collected from one 13 km stretch of road running through the northeast of Barrington Tops. Ages from 69.2 ± 4.3 to 3.5 ± 0.7 Ma (1σ) have been determined by fission track analyses on alluvial zircons Sutherland and Fanning (2001). Zircon fission tracks have a closure temperature of 230–250 °C (Garver, 2008), therefore alluvial zircons are susceptible to thermal resetting, e.g., by bushfires (Bernet and Garver, 2005). As no young eruption sites have been discovered, these young ages have not been used in this study. There is also, one K-Ar age of 20.7 ± 0.3 Ma (1σ). However, younger K-Ar dates could represent radiogenic argon loss from minor alteration of the basalts. Given there is no mention of sample quality and freshness in Sutherland (1991), this sample has also been discarded from the overall age range. Barrington lavas are relatively well connected and the preferred original estimate, using extrapolated ridgelines as the top surface across the extent of footprint 2 assuming all exposures were originally connected as a single lava field, is 1535 km^3. This makes Barrington one of the two largest lava fields across the continent, the other being the Liverpool Range. The older age of the volcano suggests it has been subject to a considerable amount of erosion and the resurfaced ridgeline is probably an appropriate upper surface with which to model the volcano on.

- Estimated Preserved Volume; 433 km^3.
- Estimated Original Volume; 1535 km^3.
- Oldest Age; 58.9 ± 0.58 Ma (2σ) Ar-Ar (Jones, 2018) (no comment on sample quality); mafic lava from Barrington Tops; age consistent with the oldest K-Ar age and U-Pb age by Sutherland and Fanning (2001) (recognisance analysis) also from Barrington Tops, although the U-Pb age has an error of 4.5 Ma (2σ).
- Youngest Age; 35.8 ± 5.1 Ma (2σ) U-Pb (Sutherland and Fanning, 2001) (no comment on sample quality); swamp on the west side of Mt McKenzie, Gloucester Tops; quite a large error but age consistent with K-Ar age from Pain (1983).

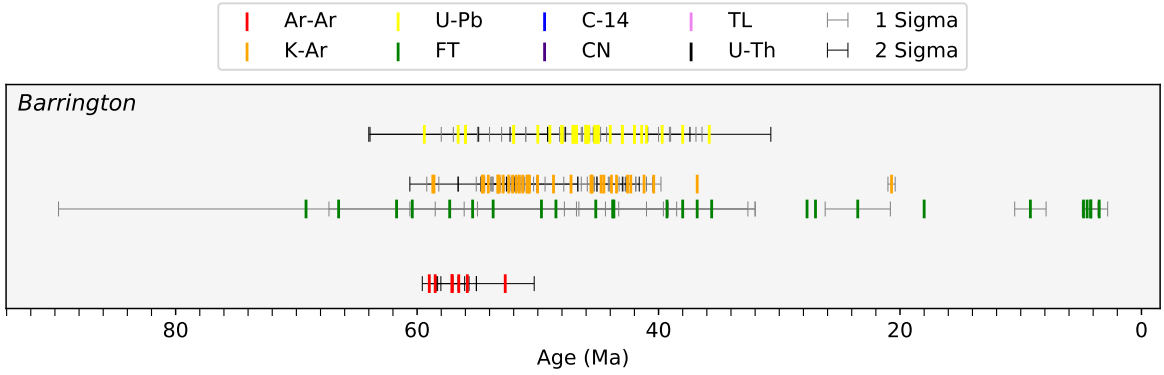

Figure 6.93: *Age data for the Barrington province.*

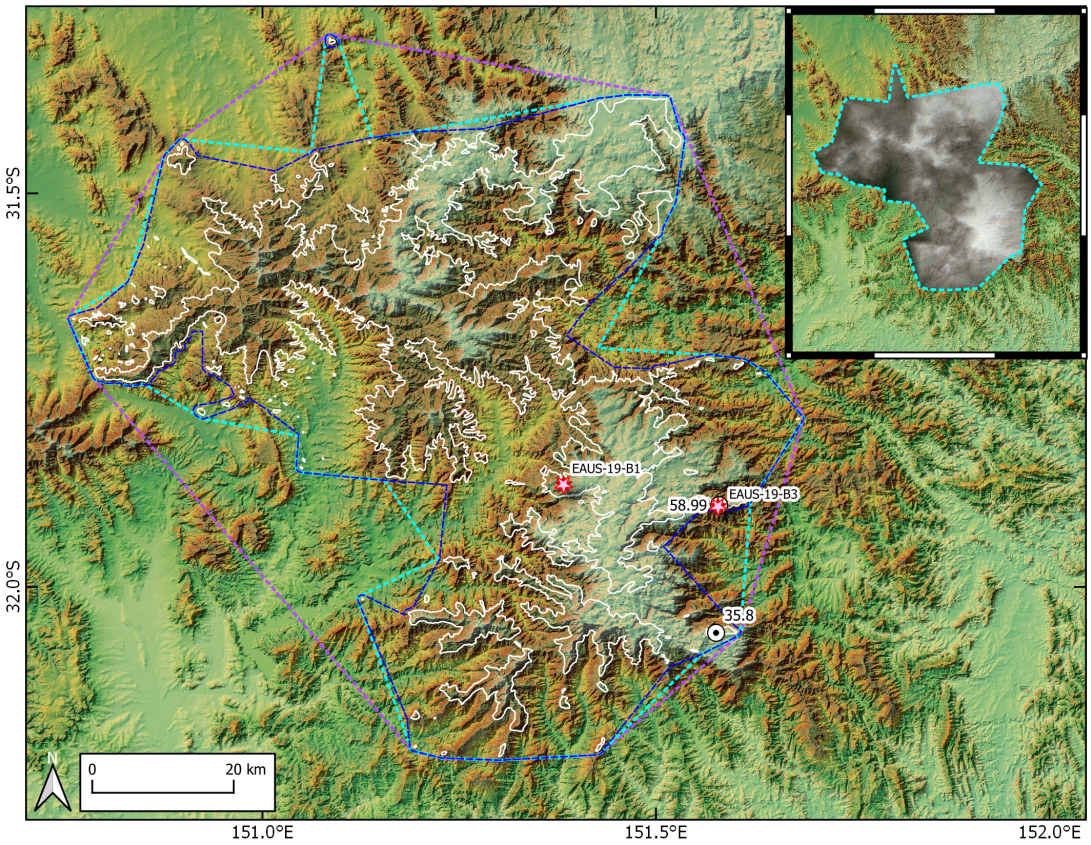

Figure 6.94: *The Barrington volcanic province.*

Liverpool Range (41.6–31.0 Ma)

Liverpool Range deposits cover a surface area of around 6000 km^2, making it one of the largest volcanoes in New South Wales (Johnson, 1989). Three types of extrusive events have been recognised here; (1) massive lava flows 2–4 m thick; (2) columnar layers totaling 200 m thick; and (3) massive units up to 15 m thick (Johnson, 1989). Numerous remnant lava flows are also exposed around the margins of the range which suggests a considerable volume of the volcano has also been eroded (Johnson, 1989). The Liverpool Range includes both the Liverpool East and the Liverpool West provinces described by Wellman and McDougall (1974b). Detailed fieldwork is still required to clarify if the Liverpool Ranges were built as two volcanoes or one, for the purpose of this study I initially defined it as one. A number of K-Ar ages are available for the Liverpool Range, primarily by Wellman and McDougall (1974b). Ages range from $\sim$41.6–31.0 Ma. There appears to be a slight younging trend across the province as ages from Liverpool East range from $\sim$41.6–37.3 Ma and ages from Liverpool West range from $\sim$35.3–31.0 Ma. Liverpool lavas are again well connected and the preferred original estimate, using extrapolated ridgelines as the top surface across the extent of footprint 2 assuming all exposures were originally connected as a single lava field, is 2612 km^3. This volume is at least twice as large as all other lava fields. Whether this high volume is due to two separate provinces being classified as one, or whether it is due high rates of magma emplacement are still to be determined.

- Estimated Preserved Volume; 1186 km^3.
- Estimated Original Volume; 2612 km^3.
- Oldest Age; 41.6 $\pm$ 1.1 Ma (2σ) K-Ar (Wellman and McDougall, 1974b) (no comment on sample quality); mafic lava 13 km northeast of Mount Tingaroo at Ardglen.
- Youngest Age; 31.0 $\pm$ 0.4 Ma (1σ) K-Ar (Wellman et al., 1969) (possible Ar loss as the age is inconsistent with stratigraphy, average age of duplicate analysis is 31.8 Ma); alkali olivine basalt from 955 m elevation at the Yarraman Creek section.

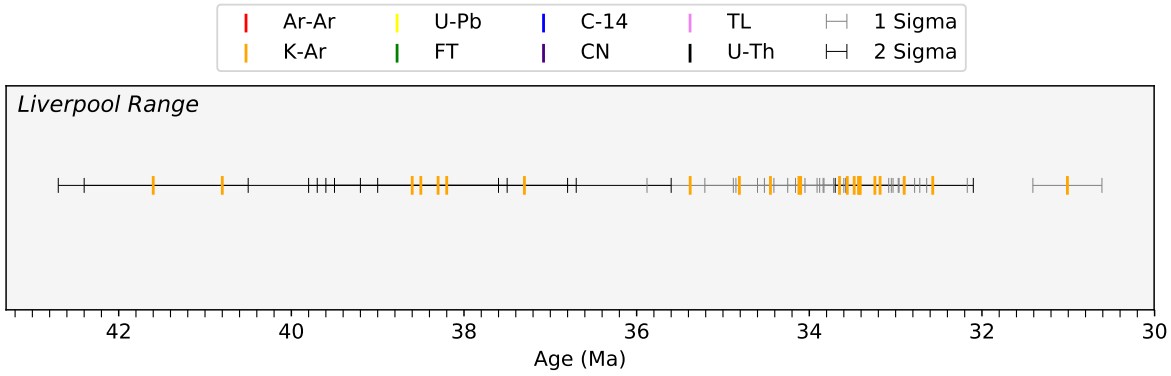

Figure 6.95: *Age data for the Liverpool Range province.*

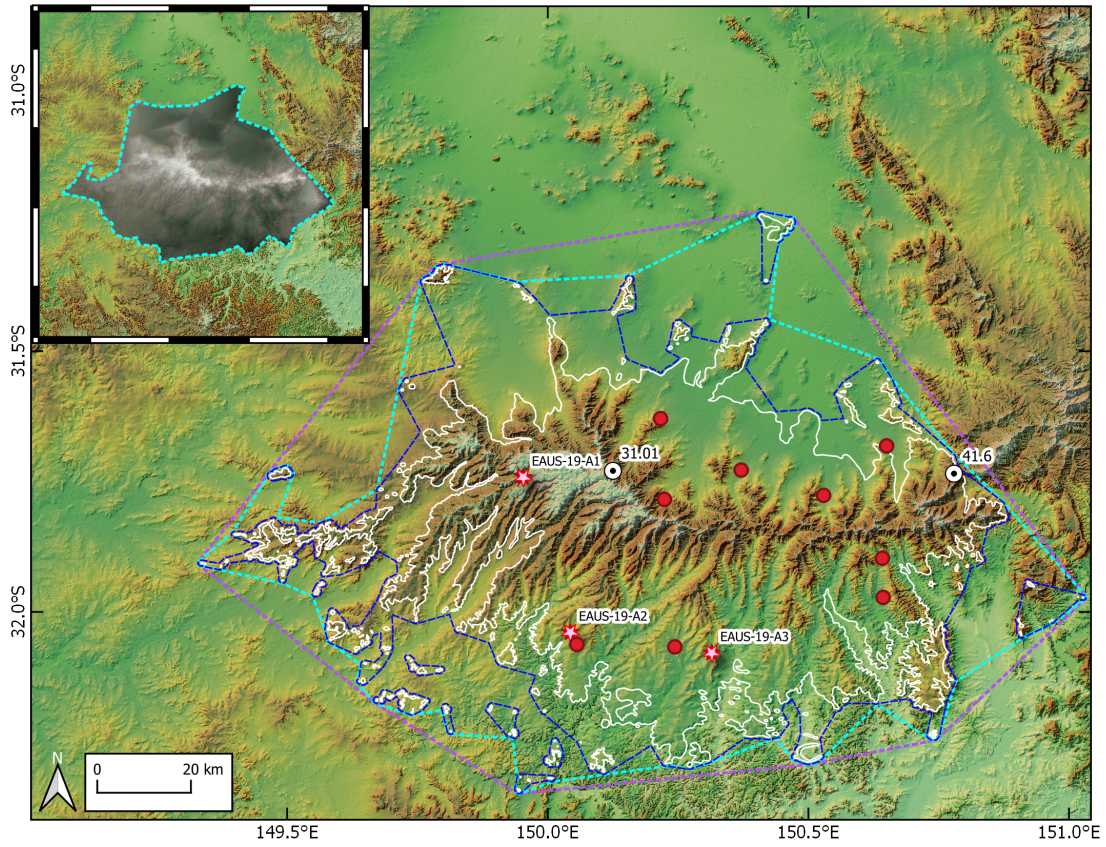

Figure 6.96: *The Liverpool Range volcanic province. Red dots show the locations of freely available borehole data obtained from New South Wales Government (2022).*

Kandos (57.3–33.7 Ma)

The Kandos province represents a lava field within the Permian Sydney Basin where mafic rocks are found most commonly as columnar-jointed, high-level vent fillings that form topographic highs (Johnson, 1989). Small flows, dykes, sills, and diatremes are also present (Johnson, 1989). Much like other older lava fields in New South Wales, thicker flow sequences or longer flows are exposed only rarely suggesting erosion has been considerable in this area (Johnson, 1989). K-Ar ages by Embleton et al. (1985) suggest a bimodal distribution of ages for the Kandos province including Jurassic volcanism from ∼190–170 Ma, as well as Tertiary volcanism from ∼57.3–43.6 Ma (Johnson, 1989). K-Ar ages from Wellman and McDougall (1974b) (who name the Kandos province the Airly province) and Dulhunty (1973) range instead from ∼41.6–33.7 Ma. Taken together, the overall K-Ar age range for the small fows, dykes, sills, and diatremes around Kandos are ∼57.3–33.7 Ma. Depending on how the numerous scattered remnants were originally connected, pre-erosion volumes are estimated to be between 63–429 km^3. For the preferred estimate made here, the volume has been calculated using extrapolated ridgelines as the top surface across the extent of footprint 1. This is to assume that most outcrops were erupted as separate, isolated volcanoes, rather than one huge lava field.

- Estimated Preserved Volume; 14 km^3.
- Estimated Original Volume; 121 km^3.
- Oldest Age; 57.3 ± 0.8 Ma (1σ) K-Ar (Embleton et al., 1985) (no comment on sample quality); mafic plug from Mount Touwouwan.
- Youngest Age; 33.7 ± 2.1 Ma (1σ) K-Ar (Dulhunty, 1973) (no comment on sample quality); basalt flow near Mount Vernon.

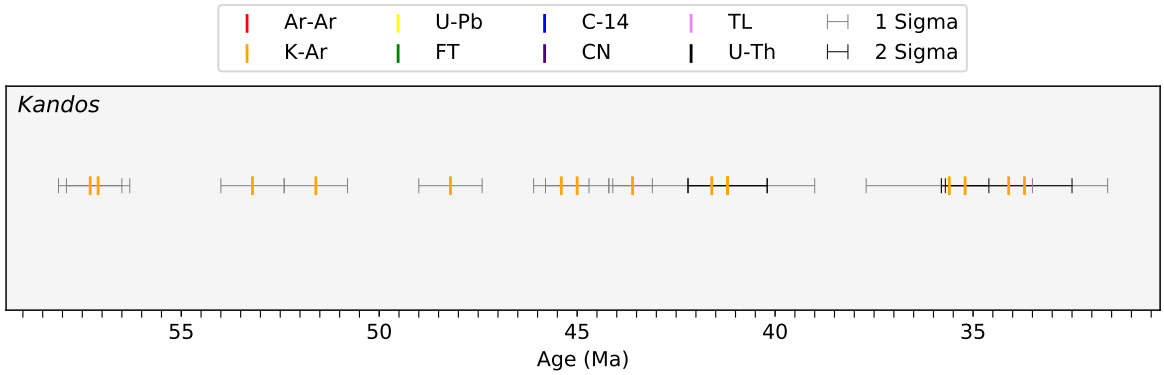

Figure 6.97: *Age data for the Kandos province.*

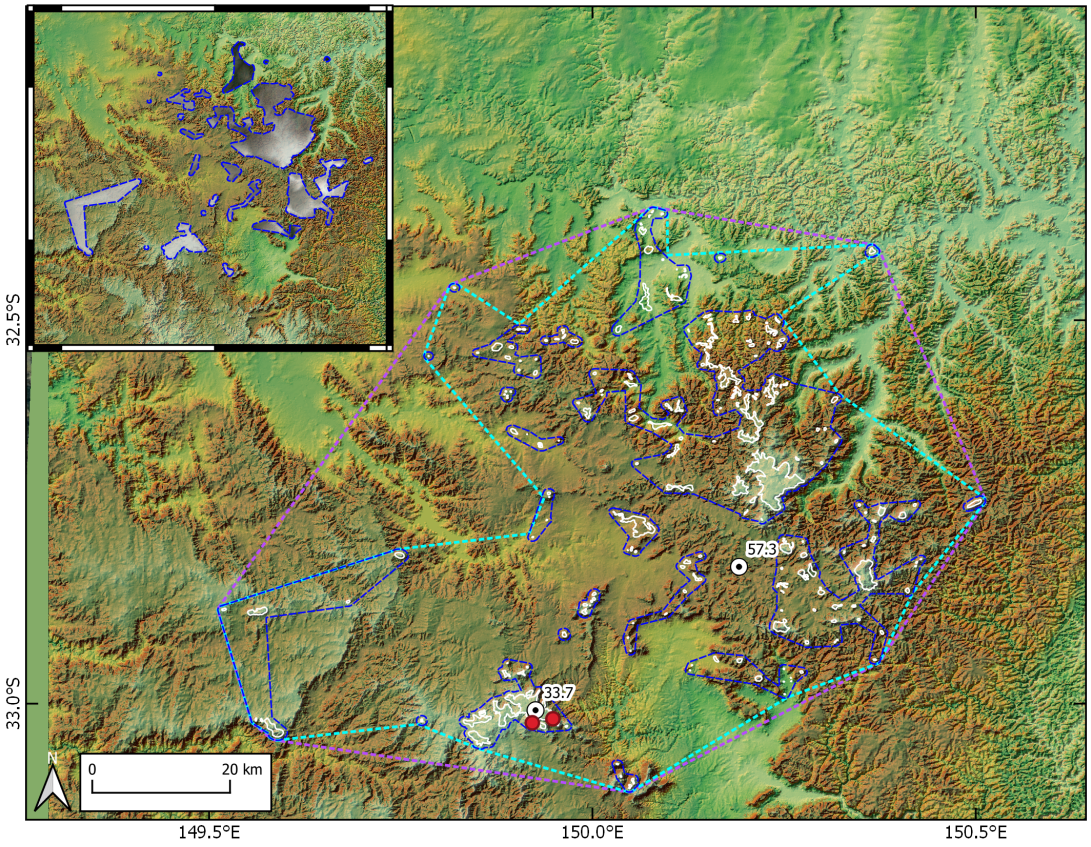

Figure 6.98: *The Kandos volcanic province. Red dots show the locations of freely available borehole data obtained from New South Wales Government (2022).*

Sydney (61.2–14.1 Ma)

The Sydney province is taken to include all the basaltic volcanic rocks and intrusions within the southern Sydney Basin, excluding those provinces otherwise specifically defined (i.e. Kandos, Barrington etc.) that also lie within the Sydney Basin (Johnson, 1989). Diatremes are particularly abundant within the province and along with dykes, plugs, and small flows are scattered over an area roughly 120 km in length (Johnson, 1989). Like many older, long-lived lava fields, present-day exposures are generally small, isolated, and heavily eroded, typical of other coastal provinces. K-Ar ages for the Sydney province are primarily provided by Van Der Beek et al. (2001), Wellman and McDougall (1974b), and Embleton et al. (1985). Results suggest the Sydney Basin has been subject to fairly small, isolated, and sporadic episodes of volcanism throughout most of the Cenozoic. The oldest volcanism occurs as isolated lavas outcropping throughout the Sydney Basin from Wollemi National Park to the coastline between $\sim$64.4–30.9 Ma. The most recent volcanism primarily occurred further south in the Blue Mountains from $\sim$20.4–14.1 Ma (Van Der Beek et al., 2001; Wellman and McDougall, 1974b). The connectivity of exposures is again difficult to constrain but with such a large span in ages across the province, it is most likely individual exposures were erupted as separate, isolated volcanoes. The preferred original volume estimate has therefore been calculated using extrapolated ridgelines as the top surface across the extent of footprint 1.

- Estimated Preserved Volume; 2 km^3.
- Estimated Original Volume; 55 km^3.
- Oldest Age; 61.2 Ma (no error reported) K-Ar (Harding, 1969) (minimum age); volcanic breccia from the Umbrella Creek Pipe, north of Gospers Mountain, Wollemi NP.
- Youngest Age; 14.1 $\pm$ 0.2 Ma (1σ) K-Ar (Van Der Beek et al., 2001) (age consistent with stratigraphy); mafic lava from Mount Banks, Blue Mountains.

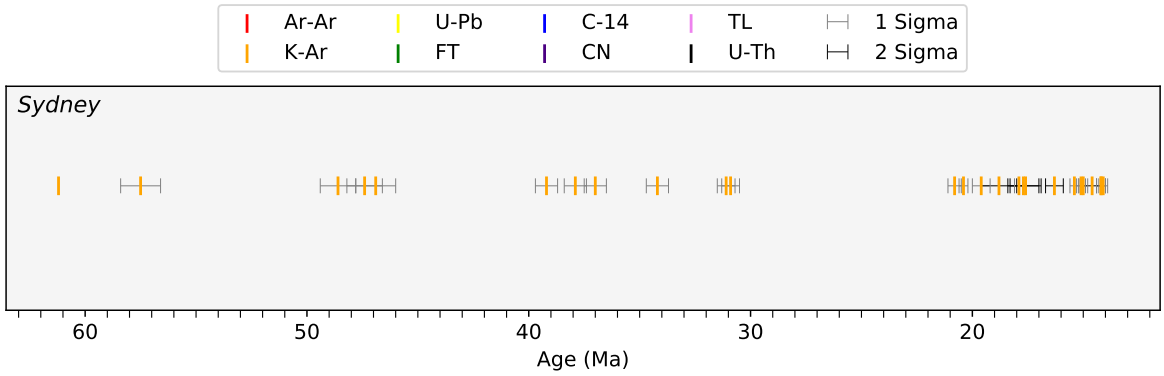

Figure 6.99: *Age data for the Sydney province.*

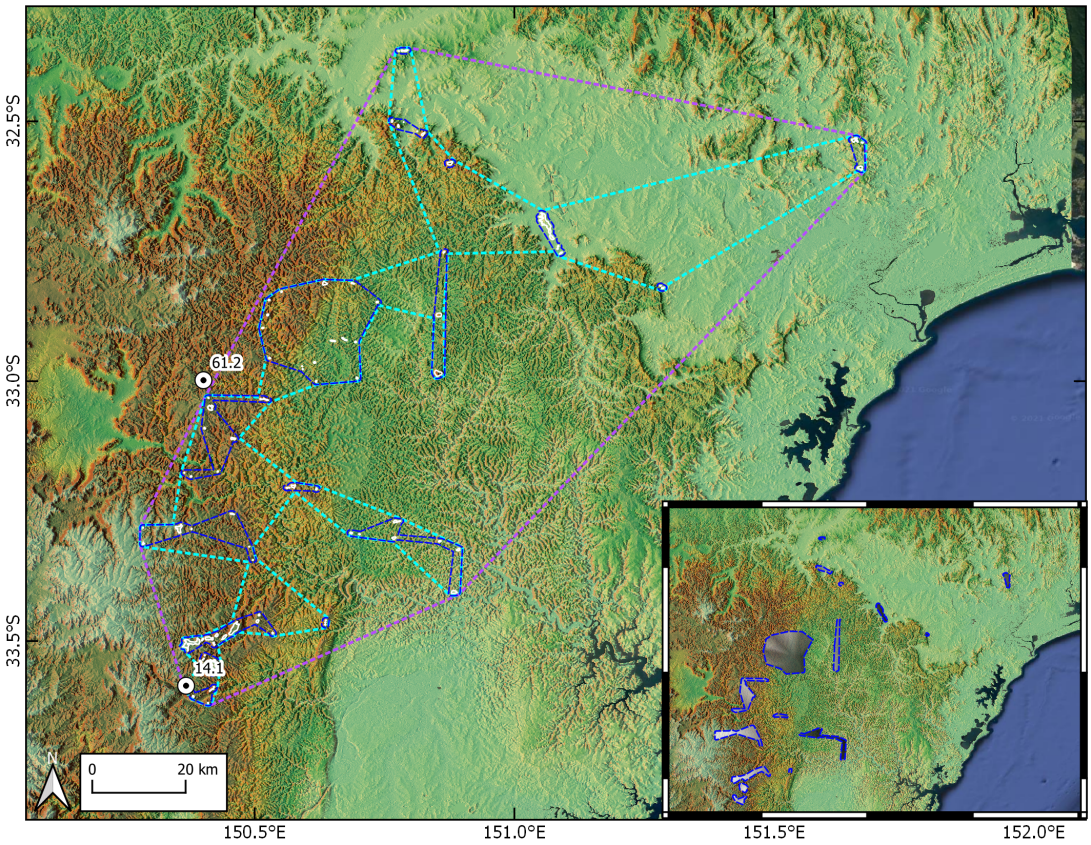

Figure 6.100: *The Sydney volcanic province.*

Grabben Gullen (51.0–12.4 Ma)

In this thesis, the Grabben Gullen province includes the many valley filling lava fields around Crookwell, Taralga, Bathurst, and the Abercrombie River National Park, previously described by Wellman (1971) as the Abercrombie region. Basalts from this region include longer, valley-filling lava flows, as well as small, isolated lava flows with associated necks and diatremes (Johnson, 1989). Stratigraphic relationships from Bishop and Young (1980) and Bishop (1984) suggest an age of $\sim$26–15 Ma for the Grabben Gullen volcanics. However K-Ar ages from Wellman and McDougall (1974b), who cover a greater area, report ages of $\sim$51.0–12.4 Ma. Two fission track ages from Sutherland et al. (1993) of $\sim$9.4–8.6 Ma are presumed to be erroneous and subject to later resetting of zircon grains. Although there is good coverage of K-Ar samples across the province, it is unclear whether these represent the true stratigraphic top and base due to limited mapping of the area. Again, given such a large span in ages across the province, it is most likely individual exposures were erupted as separate, isolated volcanoes. The preferred original volume estimate has therefore been calculated using extrapolated ridgelines as the top surface across the extent of footprint 1.

- Estimated Preserved Volume; 31 km^3.
- Estimated Original Volume; 153 km^3.
- Oldest Age; 51.0 ± 2.5 Ma (1σ) K-Ar (Dulhunty, 1973) (no comments on sample quality); mafic lava from Big Brother Hill, 30 km southwest from Bathurst.
- Youngest Age; 12.4 ± 0.9 Ma (1σ) K-Ar (Dulhunty, 1973) (no comments on sample quality); mafic lava from quarry on the outskirts of Bathurst.

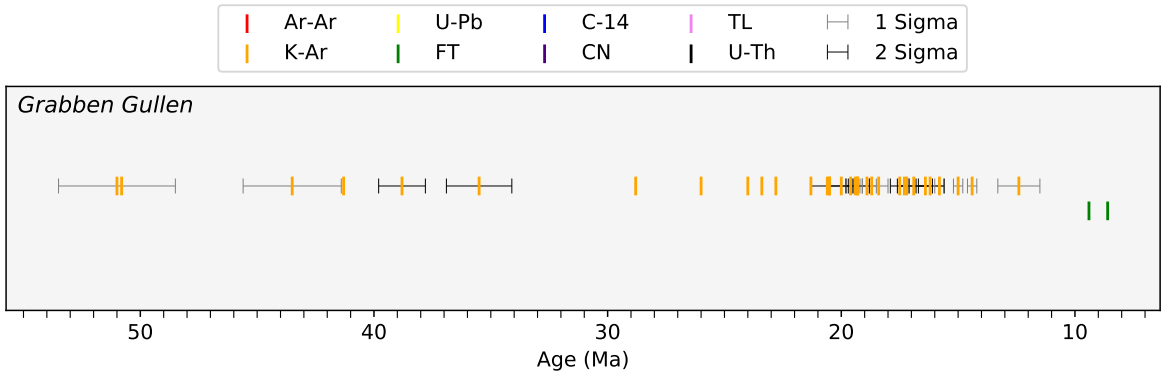

Figure 6.101: *Age data for the Grabben Gullen province.*

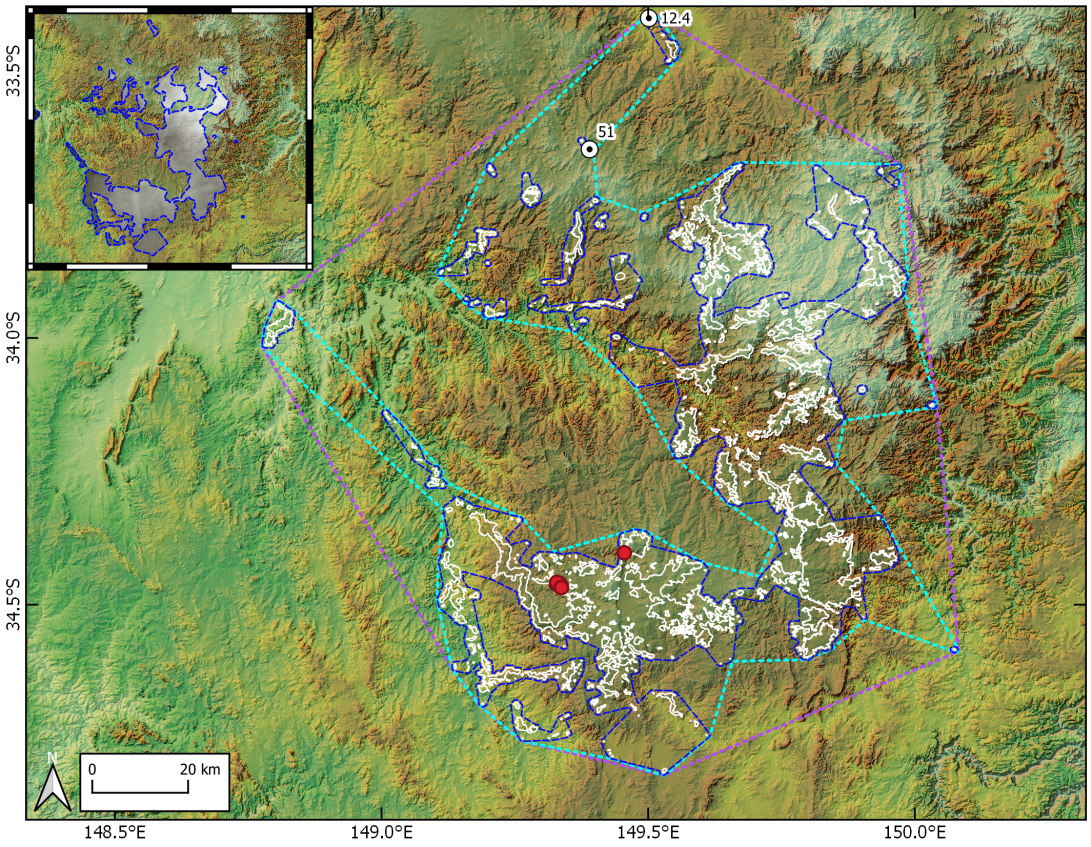

Figure 6.102: *The Grabben Gullen volcanic province. Red dots show the locations of freely available borehole data obtained from New South Wales Government (2022).*

Southern Highlands (63.8–26.2 Ma)

The Southern Highlands province includes both the Nerriga and Mittagong provinces of Wellman (1971). The province contains isolated flows, necks, dykes, and rare sills of mafic rocks (Johnson, 1989). Individual flows are short in length and rarely exceed a few meters in thickness (Johnson, 1989). However, rare flows up to 2 km long are preserved as hill cappings and thicker flow sequences are found at eruption centres such as Rileys Peak, Mount Wayo, and Mount Wanganderry (Johnson, 1989). These both suggest erosion has been fairly intense across the entire Southern Highland province, much like other coastal provinces. The only age estimates for the area are K-Ar ages from Wellman and McDougall (1974b); Nott et al. (1996); Ruxton and Taylor (1982). All suggest that volcanic activity in the area was prolonged through most of the Cenozoic, similar to the nearby Grabben Gullen and Sydney provinces. The majority of volcanic activity appears to have occurred between 50–40 Ma. One Ar-Ar age from a mafic lava at Endrick River by McDougall and Roksandic (1974) gave an age of 48.5 ± 0.6 Ma (1σ). The same lava analysed by K-Ar gave an age of 45.5 ± 1.5 Ma (2σ), suggesting at least some K-Ar results may be slightly younger than their actual age. Unfortunately no other Ar-Ar ages exist from the region to constrain ages further. Once again, the large span in ages across the province suggest exposures were erupted as separate, isolated volcanoes and the preferred original volume estimate has been calculated using extrapolated ridgelines as the top surface across the extent of footprint 1.

- Estimated Preserved Volume; 11 km^3.
- Estimated Original Volume; 81 km^3.
- Oldest Age; 63.8 ± 3.2 Ma (2σ) K-Ar (Facer and Carr, 1979) (no comments on sample quality); Robertson dolerite near Wattamolla.
- Youngest Age; 26.2 ± 3.0 Ma (2σ) K-Ar (Facer and Carr, 1979) (no comments on sample quality); teschenite from the Cordeaux drillcore, 5 km west of Wollongong.

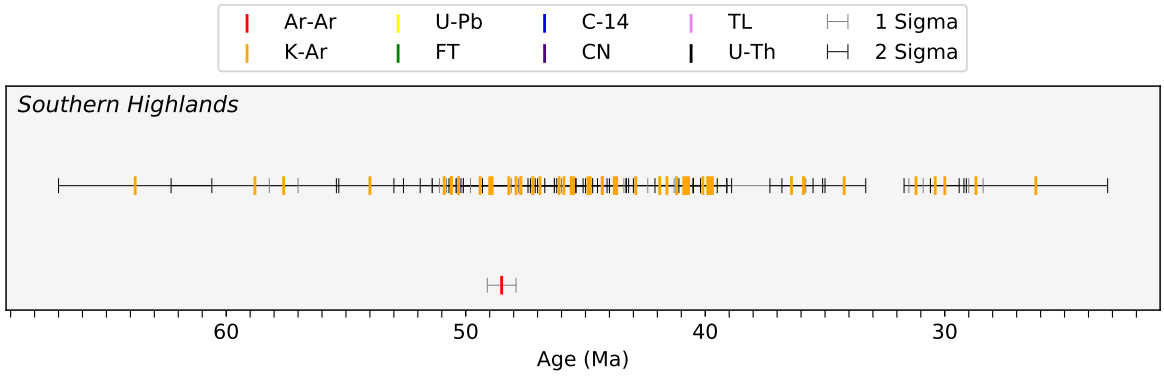

Figure 6.103: *Age data for the Southern Highlands province.*

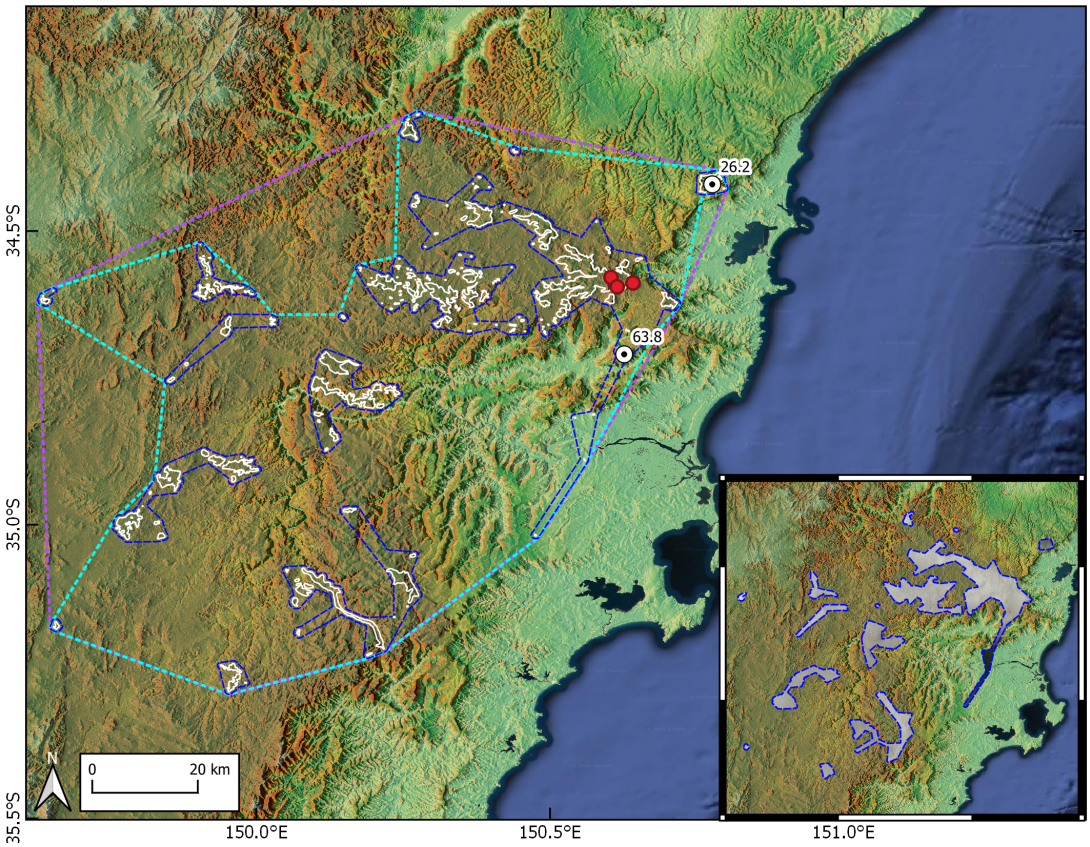

Figure 6.104: *The Southern Highlands volcanic province. Red dots show the locations of freely available borehole data obtained from New South Wales Government (2022).*

Snowy Mountains (27.6–17.2 Ma)

The Snowy Mountains province consists of relatively small, isolated, mafic lavas in the Tumut, Kiandra, and Tumbarumba areas of southern New South Wales (Johnson, 1989). In both the north and south of the province flows rest on plateaus with partly filled former valleys cut in this highland (Wellman and McDougall, 1974b). Lavas from across the region range from 1–10 m thick with some showing excellent columnar jointing (Young and McDougall, 1993). K-Ar ages by Wellman and McDougall (1974b), Young and McDougall (1993), and Sutherland et al. (2002) range from ∼23.7–17.2 Ma whilst U-Pb and fission track ages of alluvial grains also from Sutherland et al. (2002) have similar ranges of ∼27.6–22.6 Ma and ∼26.0–18.6 Ma, respectively. No Ar-Ar ages exist from the Snowy Mountains province. Taken together, the overall age range for the province is ∼27.6–17.2 Ma. All U-Pb SHRIMP ages from Sutherland et al. (2002) lie within the eruptive range of zircon megacrysts and basalts from elsewhere in the region. The preferred original volume estimate for the Snowy Mountains has been calculated using extrapolated ridgelines as the top surface, expanded across the extent of footprint 1.

- Estimated Preserved Volume; 27 km^3.
- Estimated Original Volume; 110 km^3.
- Oldest Age; 27.6 ± 0.3 Ma (1σ) U-Pb (Sutherland et al., 2002) (age for this inclusion in sapphire lies within the eruptive range of zircon megacrysts and basalts from the region); alluvial sapphire from the Tumbarumba gemfield.
- Youngest Age; 17.2 ± 0.5 Ma (2σ) K-Ar (Wellman and McDougall, 1974a) (relatively fresh sample); mafic lava from a dyke at Jugiong, north of Tumut.

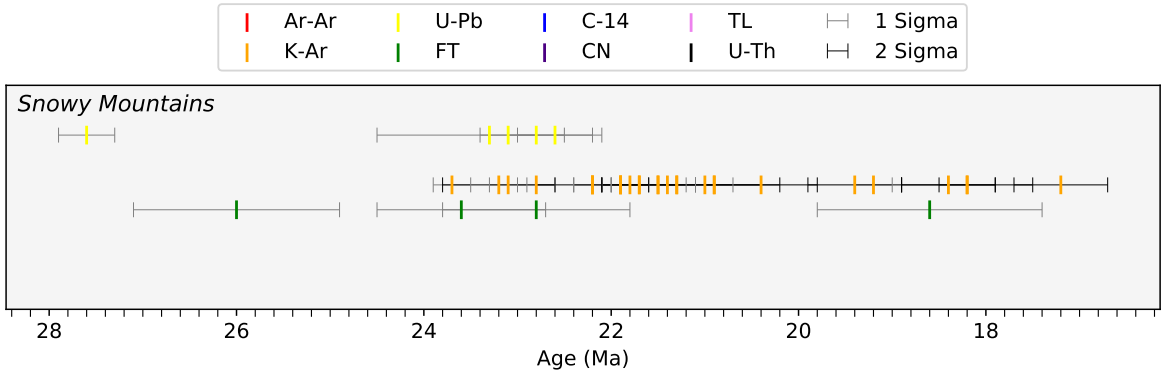

Figure 6.105: *Age data for the Snowy Mountains province.*

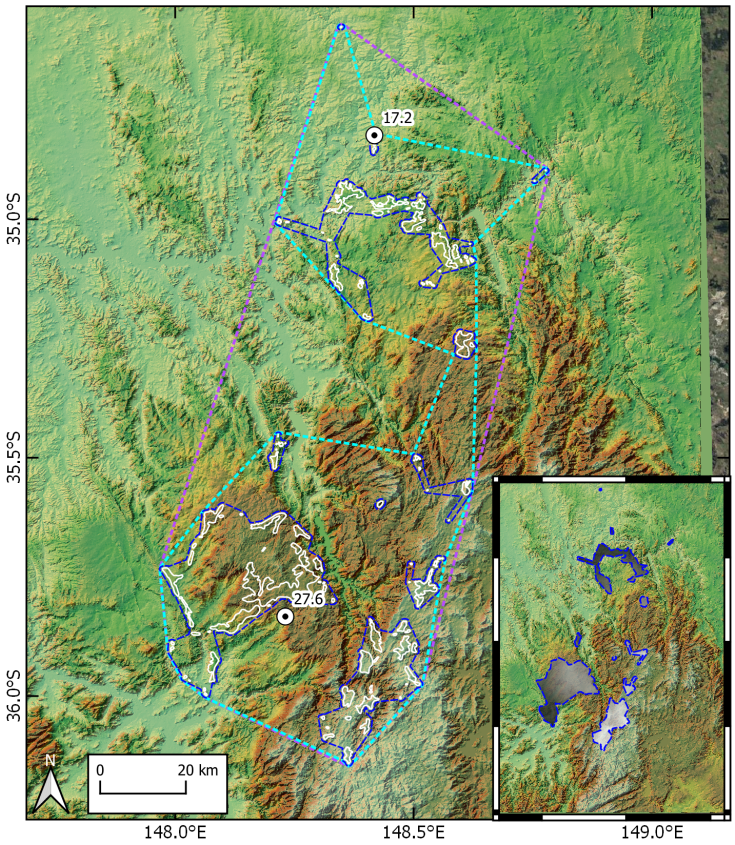

Figure 6.106: *The Snowy Mountains volcanic province.*

South Coast (34.1–25.9 Ma)

The South Coast province consists of only a few, small, scattered basaltic flows, typically just 30 m thick, outcropping along the coast of southern New South Wales (Johnson, 1989; Wellman and McDougall, 1974b). The South Coast province was previously named the Moruya province by Wellman (1971). Age estimates for the area are K-Ar ages from Young and McDougall (1985), Spry et al. (1999), and Wellman and McDougall (1974b), which produce a range of $\sim$34.1–25.9 Ma. The upper age limit has been estimated from mafic lavas showing considerable alteration with an error of 3 Ma. Unfortunately, no other analyses are available to constrain this date further. These ages are however, consistent with other provinces nearby such as the Southern Highlands, Grabben Gullen, and Sydney. With such limited data and mapping, it is unlikely the upper and lower age limits of this province have been sampled. Pre-erosion volumes are estimated to be between 2–59 km^3. Individual fields in the east and west of the South Coast province are unlikely to have ever been connected due to the considerable change in elevation, across the Great Dividing Range, where no other lava flows are found in between. For this reason, exposures were modeled as separate, isolated volcanoes and the preferred original volume estimate has been calculated using extrapolated ridgelines as the top surface across the extent of footprint 1.

- Estimated Preserved Volume; 1 km^3.
- Estimated Original Volume; 6 km^3.
- Oldest Age; 34.1 ± 3.0 Ma (2σ) K-Ar (Wellman and McDougall, 1974b) (considerable alteration of sample but no better analyses are available); mafic lava 10 km north of Moruya.
- Youngest Age; 25.9 ± 0.5 Ma (2σ) K-Ar (Wellman and McDougall, 1974b) (relatively fresh sample probably reflects a slightly younger age of extrusion); mafic lava 10 km north of Ulladulla.

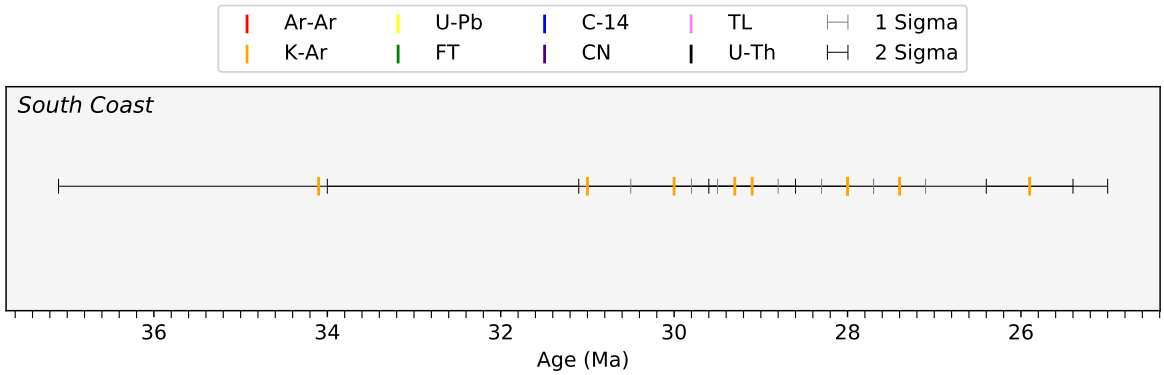

Figure 6.107: *Age data for the South Coast province.*

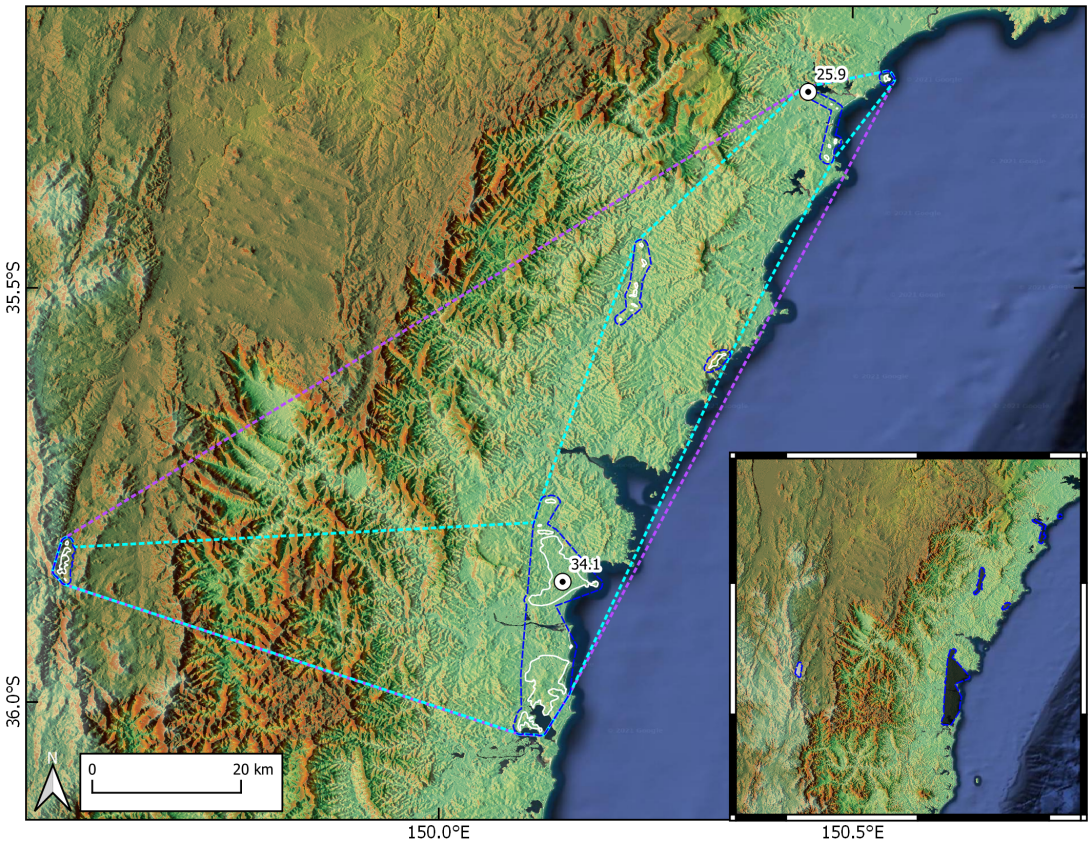

Figure 6.108: *The South Coast volcanic province.*

Monaro (54.5–29.4, and 19.2–18.0 Ma)

The Monaro province is made up of around 65 eruption centres and contains numerous, stacked basaltic lava flows covering an area of 4000 km^2 and with an aggregate thickness of up to 400 m (Johnson, 1989; Wellman and McDougall, 1974b; Kesson, 1973; O'Reilly and Zhang, 1995). K-Ar ages for the Monaro volcano from Sharp (2004), Owen and Wyborn (1979), and Wellman and McDougall (1974a) range from $\sim$54.4–15.2 Ma and Ar-Ar ages from Matchan et al. (2018) range from $\sim$54.5–54.0 Ma. The more precise Ar-Ar ages have here been taken as the onset of Cenozoic volcanism but with limited Ar-Ar sample coverage, the more widespread K-Ar data has had to be used to define the youngest age. The age of 15.2 ± 0.3 Ma (2σ) is cited by Owen and Wyborn (1979) as probably erroneous due to argon loss so we have instead used the next youngest age. The full suite of K-Ar data suggest there were multiple periods of activity at Monaro, one $\sim$54–29 Ma, and another $\sim$19–18 Ma. Early Miocene deposits became known in northern Monaro when Owen and Wyborn (1979) dated small basalt outcrops near Shannons Flat and noted that sediments underlying or interbedded with these basalts were clearly Miocene (Sharp, 2004). Following this, Sharp (2004) found that the hiatus, $\sim$29–19 Ma, prior to Miocene volcanism not only represented a lull in volcanic activity, but also erosion, tectonism and widespread sedimentation. Given this, and the longevity of volcanism, it may be that Monaro is the product of multiple volcanic processes operating at different times throughout the Cenozoic. Pre-erosion volumes are estimated have been calculated using extrapolated ridgelines as the top surface, guided across the extent of footprint 1 where most far-flung exposures, including those near Shannons Flat, are not connected to the main lava mass.

- Estimated Preserved Volume; 68 km^3.
- Estimated Original Volume; 210 km^3.
- Oldest Age; 54.5 ± 0.6 Ma (2σ) Ar-Ar (Matchan et al., 2018) (no comments on sample quality); mafic lava from Thompson Pit Quarry in southern Monaro; likely close to stratigraphic base; only Ar-Ar results from this location.
- Youngest Age; 18.0 ± 0.4 Ma (2σ) K-Ar (Owen and Wyborn, 1979) (no comments on sample quality); mafic lava from nearby Shannons Flat in northern Monaro; likely close to stratigraphic top.

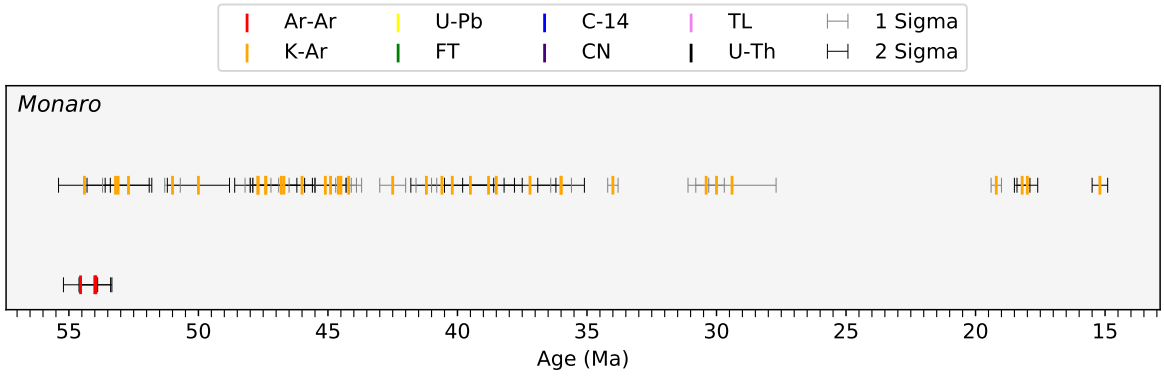

Figure 6.109: *Age data for the Monaro province.*

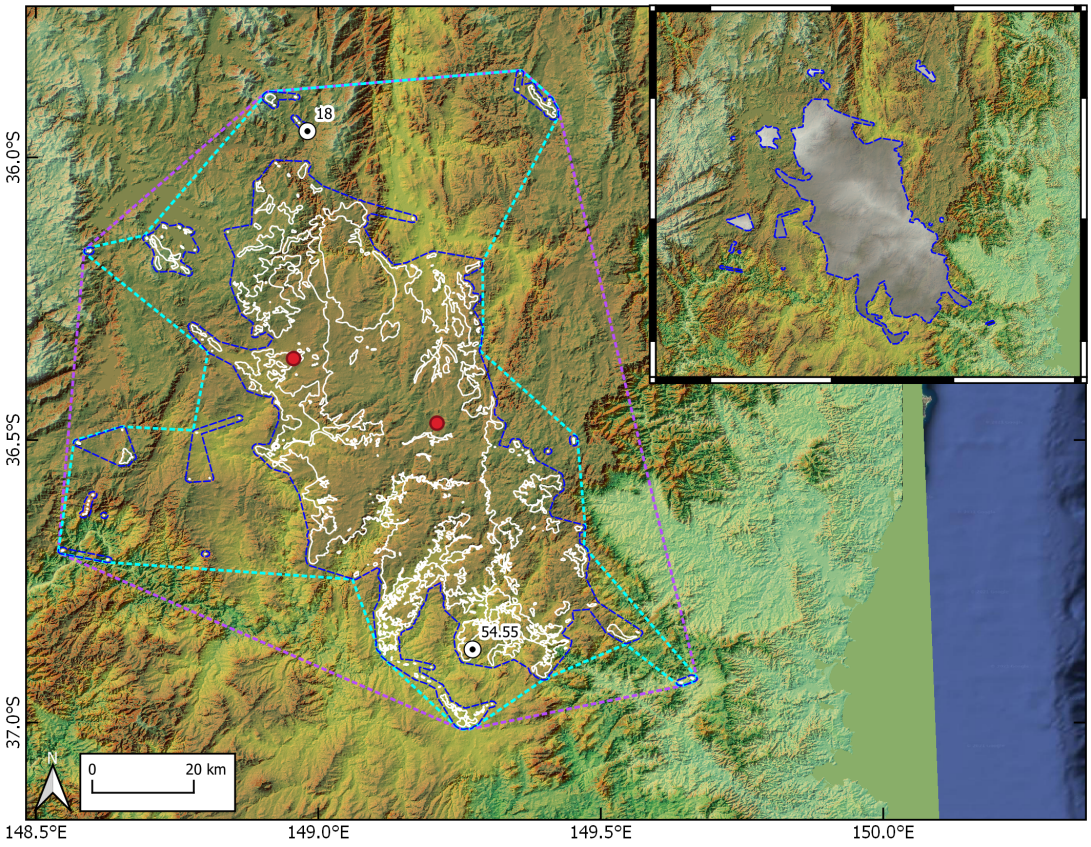

Figure 6.110: *The Monaro volcanic province. Red dots show the locations of freely available borehole data obtained from New South Wales Government (2022).*

6.2.7 Older, Multi-phase Volcanism

Dalrymple-Yatton (Nebo) (53.5–52.3 Ma)

The Dalrymple-Yatton (Nebo) province is represented by a plateau of mafic lavas in northeast of the Nebo region, often deeply weathered to form lateritic profiles, and a small outcrop around 100 km SSE of Nebo at Yatton Creek (Sutherland, 1977; Cohen, 2007). K-Ar results from Sutherland (1977) suggest that Dalrymple-Yatton volcanism took place $\sim$53.5–52.3 Ma but the analysis consists of only two small mafic outcrops at Mount Dalrymple and Yatton Creek. Sutherland (1977) interpreted this to relate to the rifting of the Coral Sea, much like older magmatism around Monto, Bundaberg, and Rockhampton. These observations rely only on K-Ar ages which show varying amounts of alteration and argon loss and so more detailed mapping and Ar-Ar dating is still required to refine these dates. As lava fields are difficult to isolate from the later central volcano deposits, the volume of the lava field has instead been included in the central volcano volume calculation.

- Oldest Age; 53.5 ± 1.7 Ma (1σ) K-Ar (Sutherland, 1977) (possible minimum age); hawaiite from flow cap at Mount Dalrymple, west of Nebo.
- Youngest Age; 52.3 ± 1.4 Ma (1σ) K-Ar (Sutherland, 1977) (reliable minimum age); hawaiite flow cap 6 km west of Mount Dalrymple.

Fort Cooper-St Martin (Nebo) (21.9, and 3.14–2.42 Ma)

The Fort Cooper-St Martin province in the east of the Nebo region contains numerous occurrences of deeply weathered and eroded mafic lavas (Sutherland, 1977; Cohen, 2007). The province has been K-Ar dated by Sutherland (1977) and Ar-Ar dated by Cohen (2007). A single Ar-Ar age of 21.9 ± 0.3 Ma (2σ) was produced for a tholeiitic flow at Mount Fort Cooper. K-Ar ages of the same flow were much younger, probably owing to argon loss in these samples. Cohen (2007) suggest this flow may represent an unrecognised lava field eruption in this area. Another, final volcanic episode, identified by K-Ar dating, took place around $\sim$3.14–2.42 Ma and consists solely of a small cone of feldspathoidal olivine trachyandesite at Mount St Martin. Given such a young age, it is thought the origin of this volcanism may be related to the other young volcanoes in far northern Queensland. The latter of these observations rely only on K-Ar ages which show varying amounts of alteration and argon loss and so more detailed mapping and Ar-Ar dating is still required to refine each volcanic episode more accurately. Once again, as the lava fields are difficult to isolate from the Nebo central volcano deposits, their volume has been included in the final central volcano volume calculation.

- Oldest Age; 21.9 ± 0.3 Ma (2σ) Ar-Ar (Cohen, 2007) (some argon loss from low-temperature steps); Mount Fort Cooper basalt body, chilled basalt base.
- 3.14 ± 0.08 Ma (1σ) K-Ar (Sutherland, 1977) (possible minimum age); trachyandesite from flow cap north side of Mount St Martin.
- Youngest Age; 2.42 ± 0.07 Ma (1σ) K-Ar (Sutherland, 1977) (possible minimum age); pyroclastic beds from the west side of Mount St Martin.

Rockhampton (79.7–72.0 Ma)

The Rockhampton province contains isolated lava flows and plugs, petrologically similar to other central volcanoes but almost twice as old (Cohen, 2007). The province is split into two primary regions: (1) NE Rockhampton, containing a group of around 20 plugs mostly comprised of peralkaline rhyolite or trachyte, but peraluminous rhyolites are also present (Cohen, 2007). There are also some minor low-lying mafic plugs (Cohen, 2007); and (2) SW Rockhampton, including minor outcrops of the Eulogie Peak mafic plug and the Mt Ramsay nepheline syenite (Cohen, 2007). The Rockhampton province contains isolated lava flows and plugs, petrologically similar to other central volcanoes, however, numerous Ar-Ar, K-Ar, and U-Pb ages from the region place volcanism as occurring within the Late Mesozoic Era. K-Ar ages range from $\sim$70.1–65.6 Ma, although most of these locations were re-dated by the more accurate Ar-Ar method producing an older age range of $\sim$79.7–72.0 Ma. U-Pb SHRIMP ages are similar, ranging from $\sim$80.0–73.0 Ma. Younger K-Ar ages are probably due to sample alteration and argon loss. Based on the preserved deposits, the Rockhampton province is more typical of the central volcanoes and has thus been reconstructed as a shield volcano. However, given a lateral separation of almost 40 km between the primary Rockhampton exposures, it was decided that two small shields may better describe the pre-erosion volcanic morphology, as oppose to one single shield.

The pre-erosion volumes for a single shield covering all outcrops is around 992 km^3 and the volume for two small shields is much lower, at just 213 km^3.

- Estimated Preserved Volume; 3 km^3.
- Estimated Original Volume; 213 km^3.
- Oldest Age; 79.7 ± 0.8 Ma (2σ) Ar-Ar (Cohen, 2007) (Ar loss and recoil for low-T steps, age from plateau steps only); alkali basalt with ultramafic xenoliths from Eulogie Peak, WSW Rockhampton; location also sampled by K-Ar dating.
- Youngest Age; 72.0 ± 1.0 Ma (2σ) Ar-Ar (Cohen, 2007) (flat spectra); nepheline syenite from Mount Ramsay, SW Rockhampton; location also sampled by K-Ar dating.

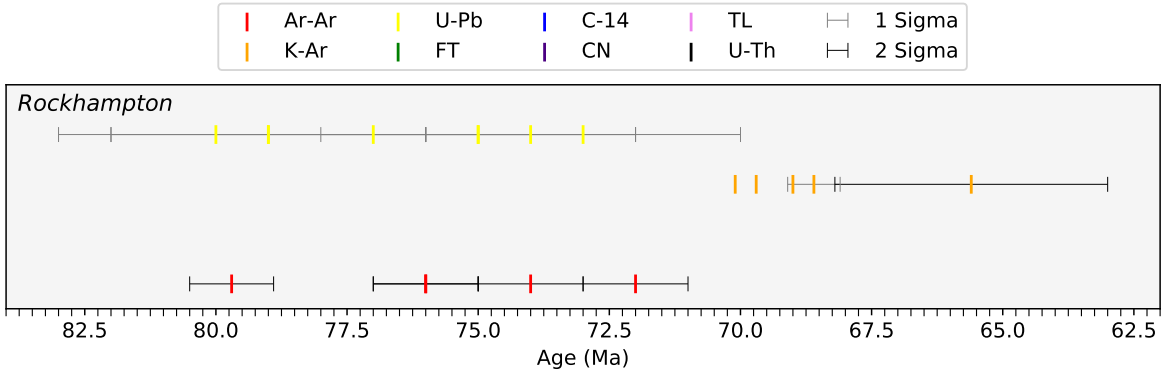

Figure 6.111: *Age data for the Rockhampton province.*

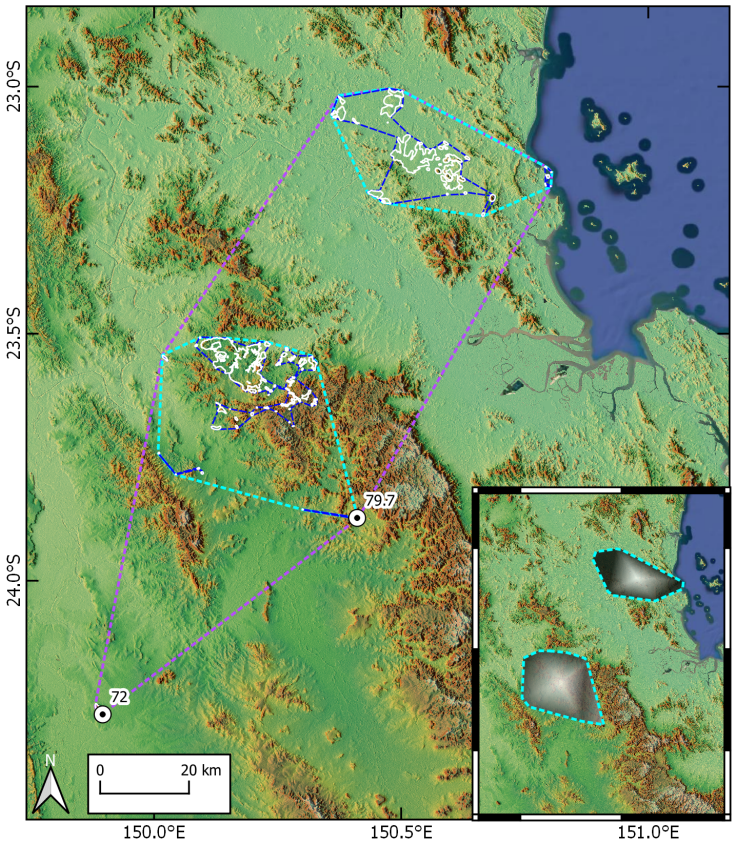

Figure 6.112: *The Rockhampton volcanic province.*

Hoy (66.8, 32.2, 21.9, and 17.5 Ma)

The Hoy lava field contains over 70 alkali basalt plugs, characterised by prominent conical hills, low rises, and even small depressions, all within an area covering less than 50 km in diameter (Johnson, 1989; Cohen, 2007). Plugs average a height of around 50–100 m above the surrounding plain and the largest plug, Mount Leura, reaches 240 m (Johnson, 1989). The area is also notable for the occurrence of alluvial sapphires, zircons, and more rarely, diamonds (Johnson, 1989). Multiple periods of activity are recorded in the Hoy province, evident from Ar-Ar and K-Ar results. K-Ar ages suggest five main periods of activity (Robertson and Sutherland, 1992) although all of these, bar one, were re-dated by Ar-Ar analysis. The five stages include; (1) 56 Ma (Policemans Knob) (Ar-Ar age of 66.8 Ma); (2) 31 Ma (Silver Hills lava, Mount Newsome) (no Ar-Ar age); (3) 28–25 Ma (Sheepstation Knob, Mount Llandillo) (Ar-Ar age of 32.2 Ma); (4) 20–18 Ma (Black Mountain, Mount Leura, Mount Ball, Mount Scholfield, Chinaman Peak) (Ar-Ar age of 21.9 Ma); and (5) 14.5 Ma (Anakie Hill) (Ar-Ar age of 17.5 Ma). Fission track results of Reward-Rubyvale alluvial zircons by Robertson and Sutherland (1992) have high errors of $\sim$1–5 Ma (1σ) but again suggest there were multiple periods of activity at Hoy between the period $\sim$66.8–17.5 Ma. For this study we have used the more accurate Ar-Ar data to define the age range at Hoy. However, only a total of 5 out of 70 plugs were analysed at this province. One sample from Policemans Knob was Ar-Ar dated by Jones (2018) at 53.3 Ma but with an error of $\pm$8.9 Ma (2σ). With considerable secondary alteration of the sample and disturbed Ar-Ar spectra, this result has been discarded from the overall age range. In keeping with other lava field provinces, the original volume of the Hoy lava field was estimated by extrapolating ridgelines, or in this case the tops of the plugs, to the boundaries of footprints 1, 2, and 3. As with other province exhibiting prolonged, yet sporadic volcanism, the large span in ages suggests individual exposures were erupted as separate, isolated volcanoes. The preferred original volume estimate has therefore been calculated using extrapolated ridgelines as the top surface across the extent of footprint 1. In this case, many of the central, older plugs have been grouped into a single lava field.

- Estimated Preserved Volume; 1 km^3.
- Estimated Original Volume; 29 km^3.
- Oldest Age; 66.8 $\pm$ 0.9 Ma (2σ) Ar-Ar (Cohen, 2007) (Ar loss for low-temperature steps); alkali basalt from north side of Policemans Knob; oldest K-Ar age location; difficult to say with so many plugs if this is the oldest age; only 5 out of 70 plugs were analysed by Ar-Ar dating.
- Youngest Age; 17.5 $\pm$ 0.5 Ma (2σ) Ar-Ar (Cohen, 2007) (probable excess Ar); alkali basalt from Anakie Hill trigonometry station; youngest K-Ar age location; again difficult to say if this is the youngest age, but from mapping done by the Geological Survey of Queensland, and the morphology of the flow, we can be fairly confident this is the youngest unit.

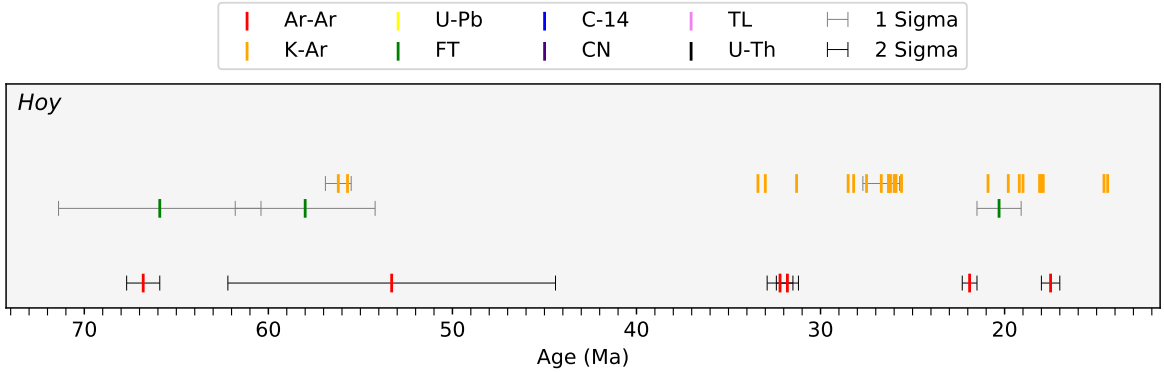

Figure 6.113: *Age data for the Hoy province.*

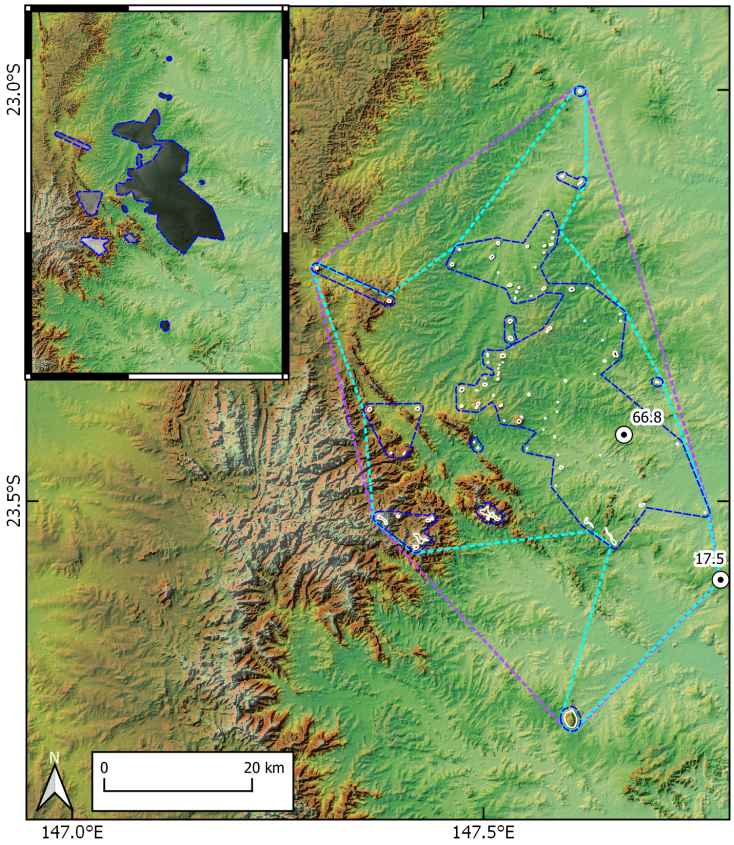

Figure 6.114: *The Hoy volcanic province.*

Monto (70.0–68.0, and 29.0–18.5 Ma)

The area around Monto and Mundubbera consists of long, channel-filling basalt flows, flow remnants, and several scattered plugs and minor intrusions (Johnson, 1989). These dissected remnants of basaltic lava flows are thought to have once formed extensive flow systems that originated from small shield volcanoes, similar to the volcanoes in far north Queensland (Johnson, 1989). In the north, relatively fresh basalts have built up into sequence up to 270 m thick and are intruded or overlain by small plugs, dykes, and flows. In the south, these intrusions form isolated bodies (Johnson, 1989). At present, exposures across the Monto province are situated in a structurally complex and strongly faulted region (Johnson, 1989). Rocks range from saturated to highly undersaturated (e.g., olivine melilitite from Mt Coppin) and many flows and plugs contain ultramafic xenoliths (Cohen, 2007; Ewart et al., 1988), again showing similarities with the more recent, far north Queensland volcanism. Much like the neighbouring Bundaberg province, Monto records multiple periods of activity separated by long hiatuses. K-Ar ages range from 70–18 Ma but some dates are not fully published (i.e., no analytical details, errors, or grid references) (Cohen, 2007). Peak activity looks to have occurred during the Oligocene around 29–18 Ma which is when the inferred hotspot was beneath this part of Australia (Cohen, 2007). It is possible lavas of this age are the products of the East Australian hotspot although no silicic rocks have been recorded in the area (Cohen, 2007). The province contains only two Ar-Ar results of 68.0 ± 1.0 Ma (2σ) (Binjour Plateau) and 29.0 ± 0.3 Ma (2σ) (Callide Mine) analysed by Cohen (2007) and Jones (2018), respectively. Further Ar-Ar dating is required to fully constrain the full duration of volcanism at Monto and whether or not this is a true lava field, central volcano, or both. The results do however concur with K-Ar results that volcanism occurred primarily in two stages, the Late Cretaceous and the Mid Cenozoic. The presence of channel-filling lava flows suggests this province did not form a single, large volcanic field covering all exposures but is expected to have a small shield-type volcano towards the centre of the province. For this reason, and again due to a large range in the ages of rock samples at Monto, the province was modeled using extrapolated ridgelines as the top surface, and the areal extent as footprint 1. Using the ridgeline extrapolation the shape of a small shield was relatively well constructed in the centre of the province.

- Estimated Preserved Volume; 39 km^3.
- Estimated Original Volume; 85 km^3.
- Oldest Age; 70.0 ± 2.0 Ma (σ not specified) K-Ar (Green, 1974) (no comments on sample quality); nepheline hawaiite from Mount Runsome.
- Youngest Age; 18.5 ± 1.3 Ma (σ not specified) K-Ar (Jones, 2002) (no comments on sample quality); trachybasalt from 30 km west of Camboon State Forest; between Monto and Bauhinia provinces.

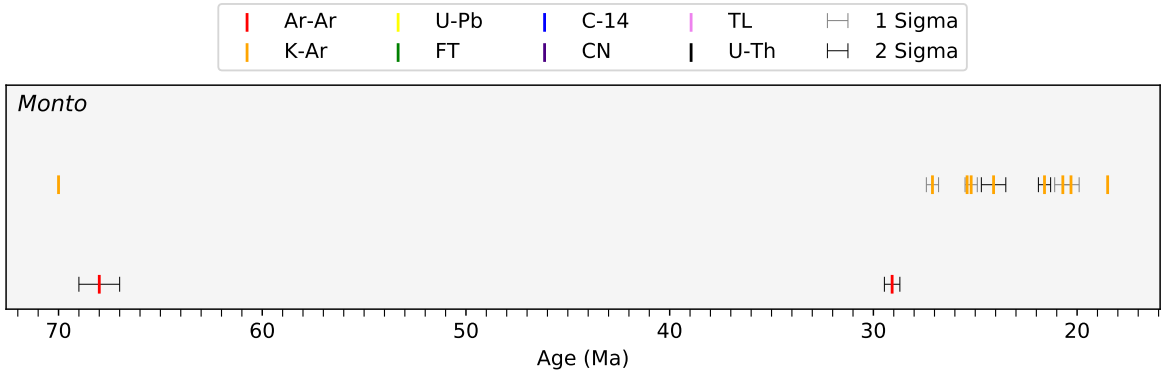

Figure 6.115: *Age data for the Monto province.*

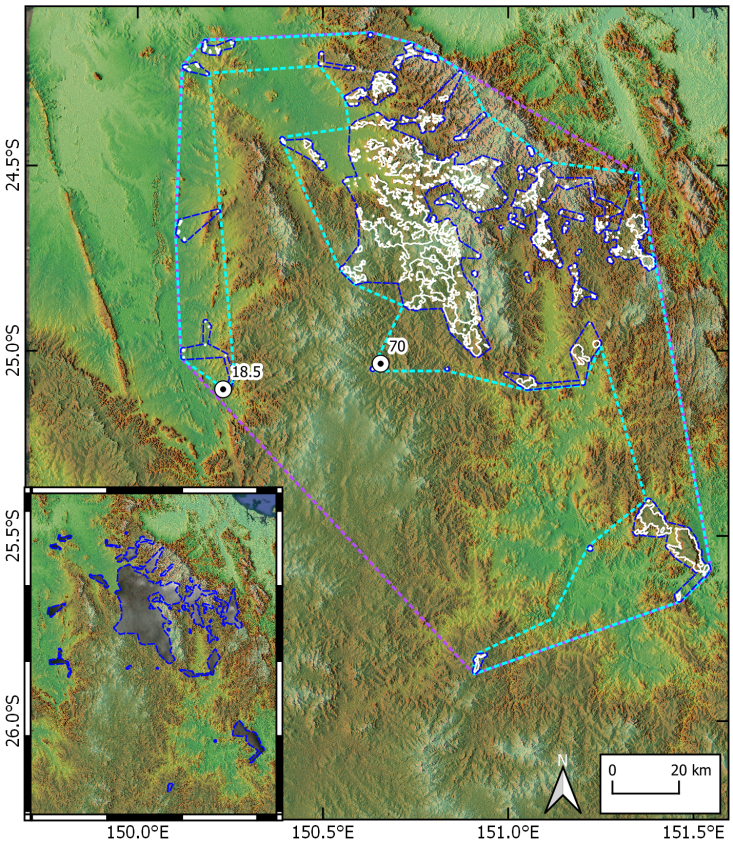

Figure 6.116: *The Monto volcanic province.*

Bundaberg (64.7–0.60 Ma)

The Bundaberg area has been the site of a diverse range of sporadic mafic eruptions spanning the entire Cenozoic and is the only known area outside far north Queensland and Victoria where Pleistocene volcanoes are present in Australia (Cohen, 2007). Today, Palaeocene–Pliocene units are represented by small plugs and flow remnants of restricted extent and thickness within small basins, and Pleistocene units are represented by longer, valley-filling, lava flows (Johnson, 1989). Units of the Bundaberg area include the Gin Gin Basalt, the Pemberton Grange Basalt, the Dundowran Basalt, the Childers Basalt, the Tararan Basalt, the Hummock Basalt, the Berrembea Basalt, and the Barambah Basalt. K-Ar ages generated by multiple authors for the Bundaberg province span a large range from $\sim$65.3–0.62 Ma. The oldest age comes from the Palaeocene Gin Gin basalt which is stratigraphically the lowest formation in the area. This is overlain by what are presumed to be Eocene-Oligocene volcanics, although these units remain undated (Robertson, 1979). The younger Miocene-Pliocene-Pleistocene units have had considerably more attention and the youngest K-Ar age comes from the Barambah basalt and it appears volcanism around Bundaberg has been fairly sporadic throughout the Cenozoic. Two Ar-Ar ages were determined by Cohen et al. (2007). 10.9 ± 0.3 Ma (2σ) for a hawaiite sample from Childers, and 4.5 ± 0.2 Ma (2σ) for a nephelinite sample from Kolan South. The Bundaberg province consists of many restricted and isolated flow remnants, separated by very large age ranges. For these reasons, footprint 1 was deemed the most appropriate extent with which to model the many isolated fields. The extrapolation of ridgelines at the Bundaberg province did not work particularly well, probably due to the flat, low-lying nature of most exposures. Therefore, original volumes were calculated using the present-day DEM as the upper surface. This estimation is probably reasonable for younger Pleistocene volcanics which will have been less subject to erosion but it is likely to be a little low for the older Paleocene–Oligocene volcanics.

- Estimated Preserved Volume; 4 km^3.
- Estimated Original Volume; 11 km^3.
- Oldest Age; 64.7 ± 0.3 Ma (1σ) K-Ar (Robertson, 1993) (no comments on sample quality); Gin Gin basalt from Sheepstation Creek, near Gin Gin.
- Youngest Age; 0.60 ± 0.02 Ma (2σ) K-Ar (Wellman, 1978) (age consistent with normal magnetic polarity of the flow); Barambah basalt from Barambah Creek Bridge.

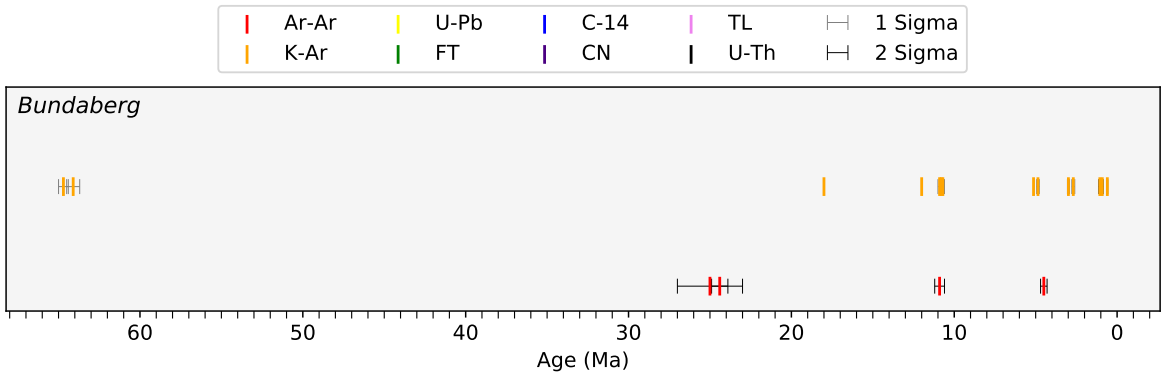

Figure 6.117: *Age data for the Bundaberg province.*

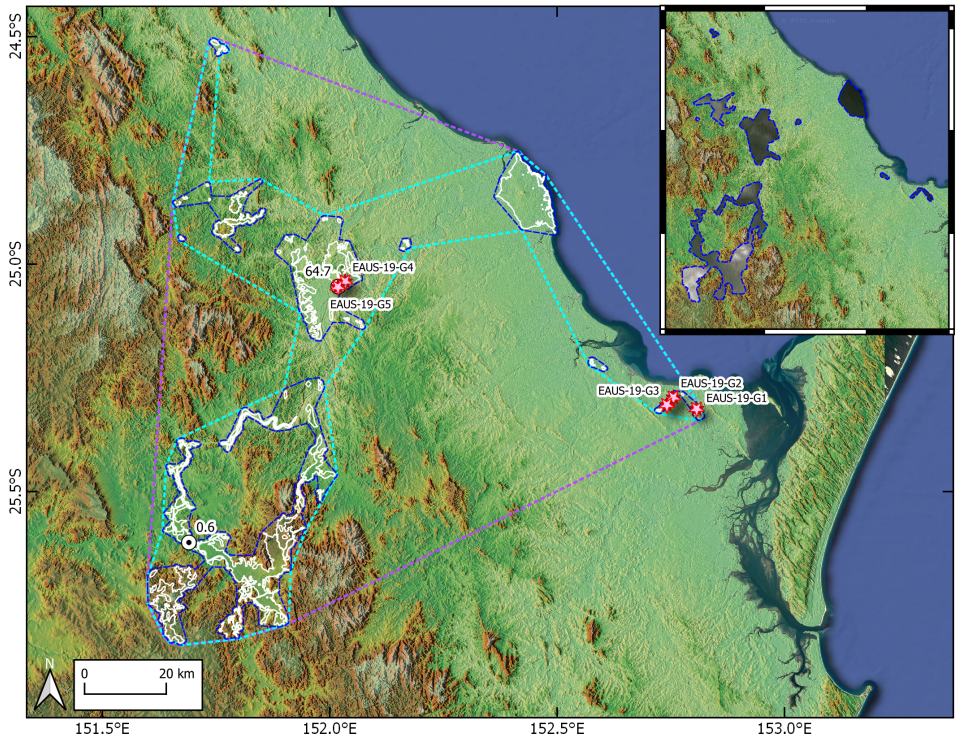

Figure 6.118: *The Bundaberg volcanic province.*

New England (39.2–30.4, and 23.9–14.2 Ma)

The 200 km long New England lava field was previously named the Central province by Wellman (1971). The province is preserved as a relatively thin but elongate belt of alkaline lavas overlying the New England tablelands (Johnson, 1989). Lava flows are flat-lying and usually below 100 m thick, although in some areas they are thought to reach up to 300 m (Johnson, 1989). Minor intrusives are also found across the province as well as alluvial sapphires, zircons to the east, as well as a few rare diamonds, the source of which is still widely debated (Barron et al., 1996; Sutherland, 2003). K-Ar ages primarily by McDougall and Wilkinson (1967) and Vickery et al. (2007) range from ∼39.2–14.2 Ma. U-Pb ages by Sutherland et al. (1993) give a similar range from ∼39.4–20.6 Ma but with much greater errors ∼5 Ma (no σ given). Fission track ages by Sutherland et al. (1993) range from ∼55.6–2.2 Ma but again have errors up to 13 Ma (no σ given). For this reason the age range defined here is based on K-Ar ages. To check the quality of the K-Ar data the youngest sample by McDougall and Wilkinson (1967) was re-dated by Cohen (2007) using the Ar-Ar method which yielded an age of 21.3 ± 0.4 Ma (2σ) compared to 18.5 ± 1.0 Ma (2σ), just slightly older suggesting the K-Ar age range is relatively accurate. From K-Ar data there appears to be two clusters of dates; one around 40–30 Ma and the other around 24–14 Ma. Because of this, it has been suggested that the New England lava field is actually comprised of two distinct overlapping volcanoes, active at different times, which have been combined into a single province (Johnson, 1989). Alternatively, the relatively few dates from surface outcrops may not cover the full age range of volcanism, which may have been quasi-continuous from around 40–14 Ma. The majority of younger ages come from the western, sapphire-poor, part of the volcano which, with ages of ∼21 Ma, is the correct age for a central volcano at this latitude. However, no silicic rocks have been recognised in this region to confirm the status as a central volcano here (Cohen, 2007). The large spread in ages of rocks across the New England province suggest it was not erupted as a single, large lava field. The original volume estimate of the New England province has therefore been estimated using extrapolated ridgelines as the top surface, and the areal extent as footprint 1. Borehole data suggest the thickness of lava across the region rarely exceeds 100 m and thus the total original volume is relatively small given the total surface area, at just 451 km^3.

- Estimated Preserved Volume; 291 km^3.
- Estimated Original Volume; 451 km^3.
- Oldest Age; 39.2 ± 0.5 Ma (1σ) K-Ar (Vickery et al., 2007) (no comments on sample quality); transitional basalt from the roadside 800 m north of Swan Peak; part of the Maybole Volcanic Suite.
- Youngest Age; 14.2 ± 0.2 Ma (1σ) K-Ar (Vickery et al., 2007) (no comments on sample quality); hawaiite from the roadside 2.8 km ENE of Kerosene Peak; part of the Langari Hill Volcanics.

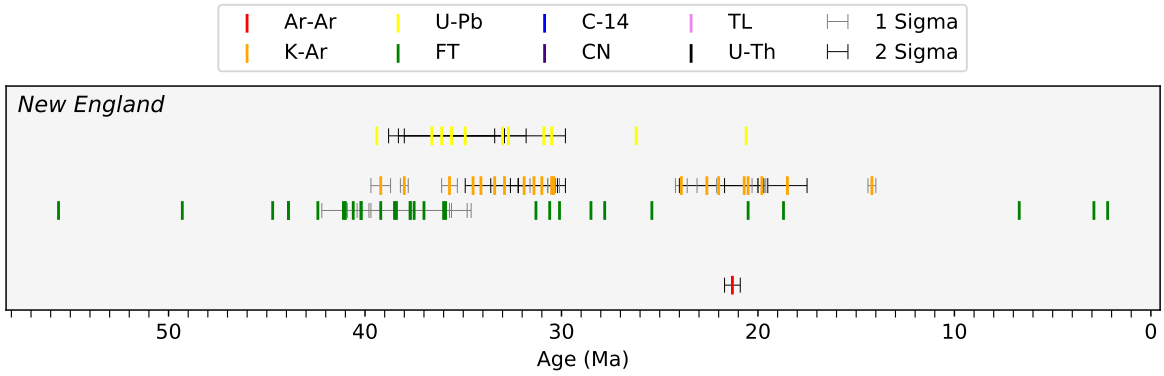

Figure 6.119: *Age data for the New England province.*

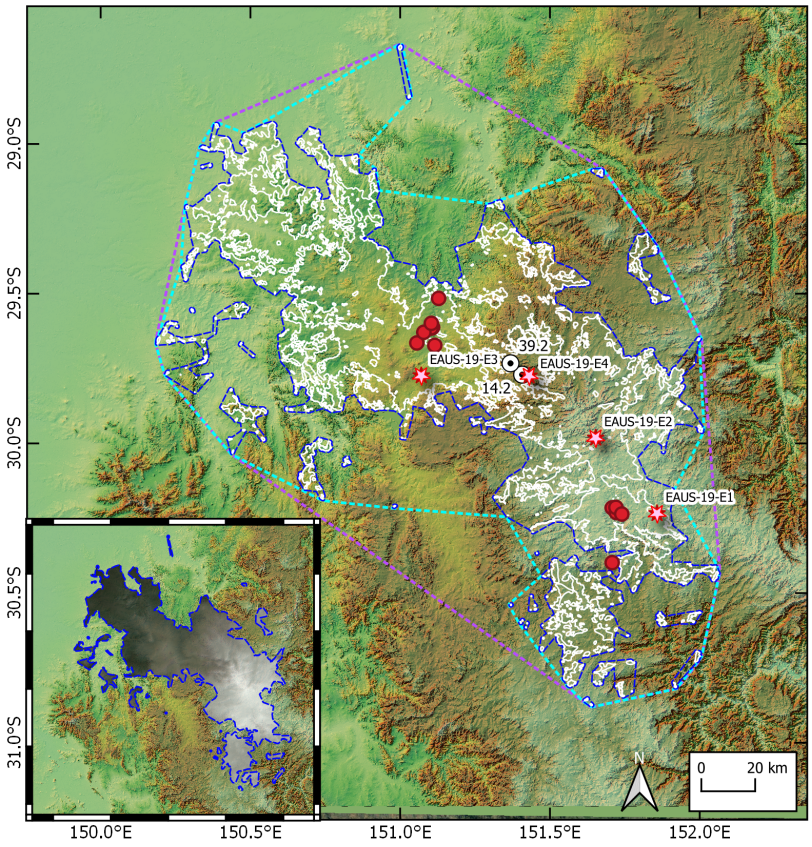

Figure 6.120: *The New England volcanic province. Red dots show the locations of freely available borehole data obtained from New South Wales Government (2022).*

Dubbo (20.0–11.9 Ma)

The Dubbo province consists entirely of isolated flow remnants, intrusions, and domes, outcropping between Dubbo and Goulburn River (Wellman and McDougall, 1974b). Older deposits generally occupy topographic highs whilst younger flows are found filling-in topographic lows caused by extensive erosion (Johnson, 1989). The only available dates for the Dubbo province are K-Ar ages by Wellman and McDougall (1974b), Dulhunty (1973) and Sutherland (2003). All of whom, also report an abundance of Mesozoic volcanism in this area, similar to the nearby Kandos province. Cenozoic K-Ar ages range from $\sim$20.0–11.9 Ma. Many of the Wellman and McDougall (1974b) samples show significant alteration which may have led to considerable Ar loss, however, fresher samples analysed by Dulhunty (1973) produced similar ages. It is unlikely the stratigraphic base and top of this volcano have been analysed. As with the Bundaberg province, the extrapolation of ridgelines at Dubbo did not work particularly well, presumably due to the flat, low-lying nature of most exposures and the change in elevation across the province. Therefore, original volumes were calculated using the present-day DEM as the upper surface. The original volume estimates for the Dubbo volcanic field are likely between 6–46 km^3 (footprint 1–2 using the present-day DEM as the upper surface), depending on how well connected the preserved isolated lava fields were originally. A volume of 6 km^3, has here been given as a minimum estimate.

- Estimated Preserved Volume; 2 km^3.
- Estimated Original Volume; 6 km^3 (minimum).
- Oldest Age; 20.0 $\pm$ 0.8 Ma (2σ) K-Ar (Sutherland, 2003) (no comments on sample quality); olivine basalt from hillside northwest of Wongarbon.
- Youngest Age; 11.9,$\pm$ 0.5 Ma (2σ) K-Ar (Wellman and McDougall, 1974b) (minor alteration); mafic lava 8 km north of Bylong.

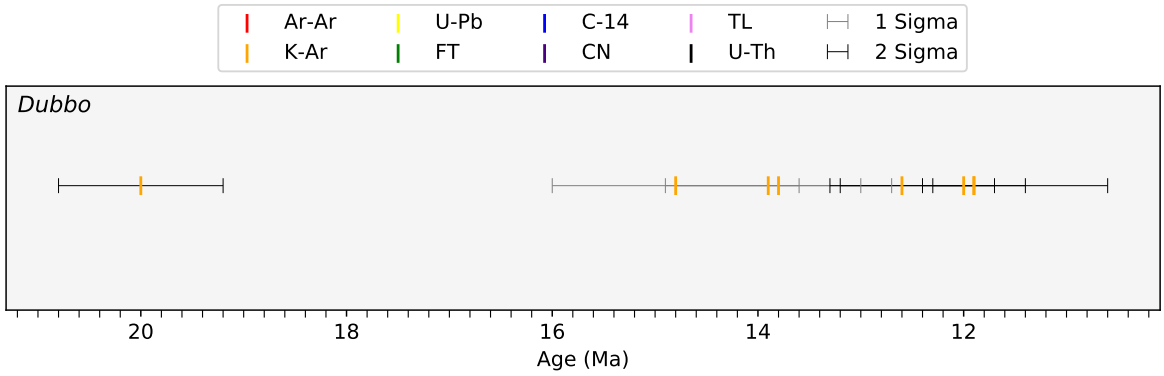

Figure 6.121: *Age data for the Dubbo province.*

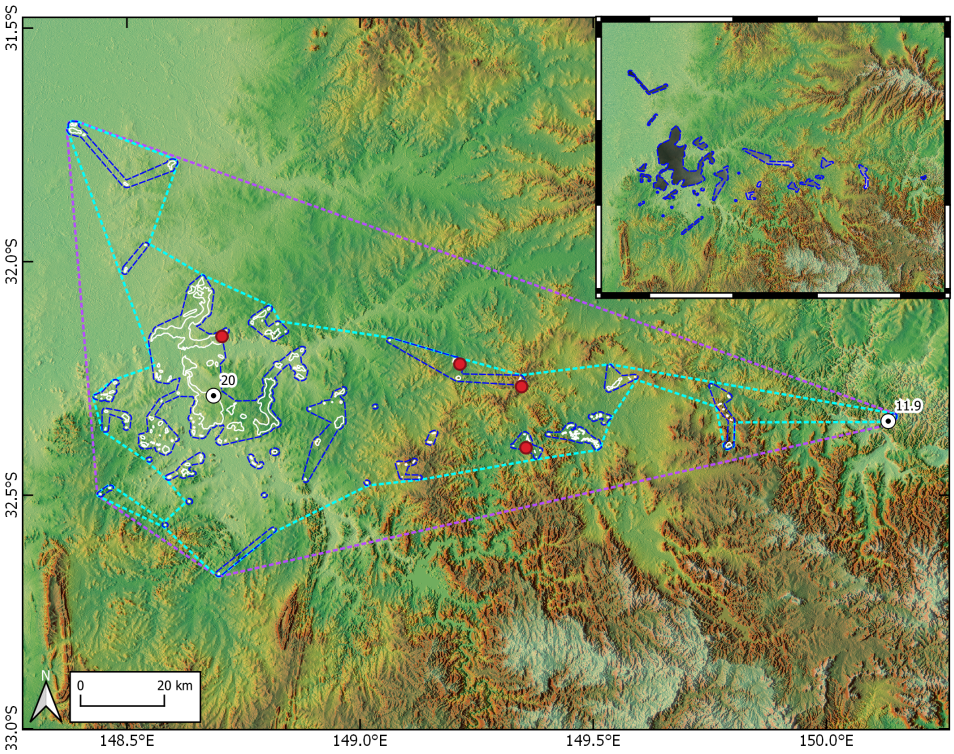

Figure 6.122: *The Dubbo volcanic province. Red dots show the locations of freely available borehole data obtained from New South Wales Government (2022).*

Older Volcanics (OVP) (90.6–13.7 Ma)

A total of 15 separate fields have been identified within the Older Volcanic Province (OVP) extending 700 km east to west across Victoria (Johnson, 1989). Most of these are lava fields 10–130 km across and old valley-filling flows where dykes and small plugs are prominent only locally (Johnson, 1989). There is a continuum of compositions from nephelinite to quartz tholeiitic basalt but ranges and relative proportions differ widely between volcanic fields (Johnson, 1989). Regionally, there is no correlation between basalt type and either age or location (Johnson, 1989). Day (1983) compiled a list of seventy-three K-Ar ages from across the OVP and was able to identify four distinct groups on the basis of age and location: (1) Group 1 (95–55 Ma) Poowong, Bacchus Marsh; (2) Group 2 (59–38 Ma) La Trobe, Flinders, Otway Basin; (3) Group 3 (44-31 Ma) Toombullup, Howitt, Bogong, Gelantipy; and (4) Group 4 (29–19 Ma) Gellibrand, Aberfeldy, Neerim, Thorpdale, Melborne (Johnson, 1989). Unfortunately, the thesis from Day (1983) was not available to this study. K-Ar ages which were freely available include those by McKenzie et al. (1984), Wellman and McDougall (1974a), Abele and Page (1974), and Henley and Webb (1990) and range from $\sim$90.6–13.7 Ma. The broad geographic locations of these ages correlate well with the four groups identified by Day (1983), suggesting volcanism has been quasi-continuous from $\sim$90.6–13.7 Ma across much of Victoria. Only two Ar-Ar ages by McLaren et al. (2009) from the Eagle Rock sea stack, Angahook Formation basalt, are available and plot within the limits of the much broader K-Ar data. The preserved volume of rock across the entire OVP is calculated as 78 km^3 but accounting for erosion the original volume is estimated to be around 174 km^3. The vast distances, and indeed ages, over which the OVP erupted make it extremely unlikely that this province exists as one single lava field and thus the preferred original volume has been estimated from the extrapolation of ridgelines as the top surface, and the areal extent as footprint 1.

- Estimated Preserved Volume; 78 km^3.
- Estimated Original Volume; 174 km^3.
- Oldest Age; 90.6 $\pm$ 1.5 Ma (1σ) K-Ar (McKenzie et al., 1984) (no comments on sample quality); basalt from the Parish of Narracan.
- Youngest Age; 13.7 $\pm$ 0.3 Ma (2σ) K-Ar (Wellman and McDougall, 1974a) (minimum age); basalt 4 km east of Mount Howitt.

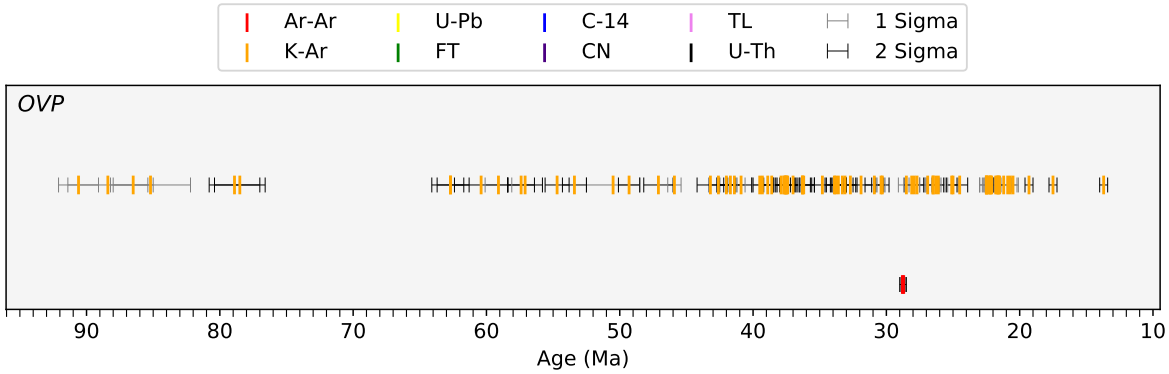

Figure 6.123: *Age data for the Older Volcanic Province.*

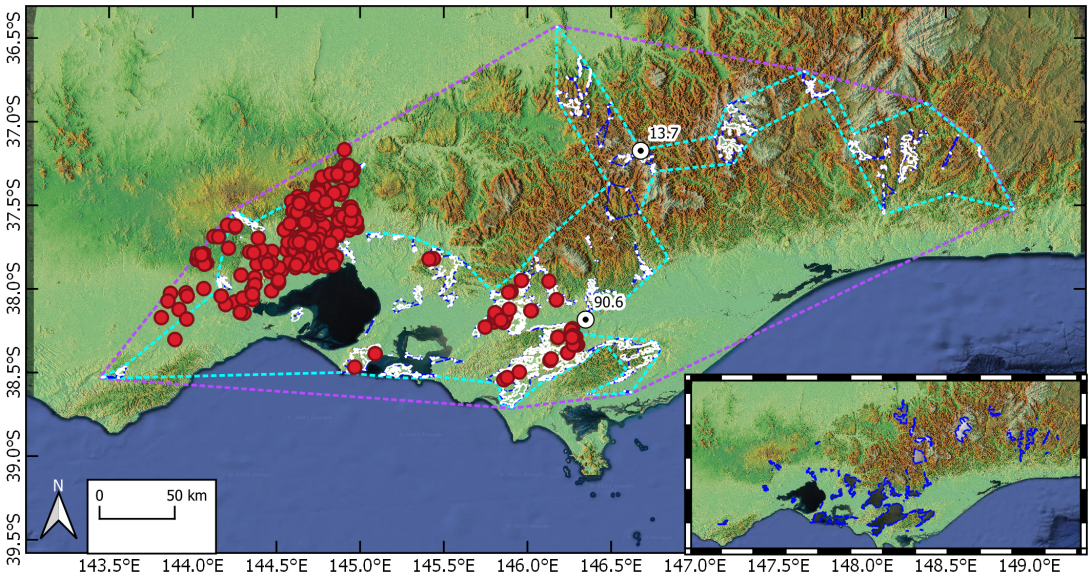

Figure 6.124: *The Older Volcanic Province. Red dots show the locations of freely available borehole data obtained from Victoria State Government (2022).*

6.2.8 Tasmania

Tasmania (58.5–8.50 Ma)

Tasmania hosts two prominent Meso-Cenozoic mafic magmatic provinces: abundant Jurassic dolerites that belong to the Ferrar Magmatic Province that formed during Gondwana break-up; and Cenozoic, mainly mafic volcanics, which represent intraplate magmatism, post-Gondwana break-up (Meeuws et al., 2019). Cenozoic basalts outcrop as lava fields, eroded valley fills, and other scattered remnants (Johnson, 1989). Basalts mainly extend diagonally so that they are absent in the southwest and form only minor outcrops on the larger Bass Strait islands (Johnson, 1989). The compositions of the Cenozoic lavas span a wide range from highly silica-undersaturated olivine melilitites and nephelinites to basanites, nehawaiites, olivine basalts and quartz-tholeiites (Meeuws et al., 2019). There are numerous K-Ar ages from Tasmania all of which cover a good spread of outcrops across the island (e.g. Sutherland and Wellman, 1986; Sutherland et al., 2006). Ar-Ar data is limited to just three ages from Sutherland et al. (2006) and Meeuws et al. (2019), all plotting within the K-Ar range. Fission track data from Sutherland et al. (1996) again plots within the total K-Ar age range. Similar to other provinces in New South Wales and Victoria, such as the Southern Highlands, Grabben Gullen, Sydney, and the OVP, lava field-type mafic volcanism across Tasmania occurred sporadically throughout much of the Cenozoic. Mesozoic volcanism in Tasmania occurred in the Jurassic and Cretaceous, but these eruptions formed from separate processes than the Cenozoic volcanoes, so are not considered in this thesis. In the Jurassic, the Karoo-Ferrar LIP was responsible for widespread dolerite intrusions across Tasmania, while in the mid-Cretaceous there are minor intrusions associated with the breakup of Australia and Antarctica. Much like the OVP, the vast distances and ages over which Tasmanian lavas have erupted make it extremely unlikely that this province exists as one single lava field and thus the preferred original volume has again been estimated from the extrapolation of ridgelines as the top surface, and the areal extent as footprint 1. The base of the Tasmania lavas are relatively well constrained by a number of boreholes.

- Estimated Preserved Volume; 312 km^3.
- Estimated Original Volume; 652 km^3.
- Oldest Age; 59.0 ± 0.7 Ma (1σ) K-Ar (Baillie, 1987) (no comments on sample quality); alkali olivine basalt from a scree deposit on the Kellevie Bream Creek Road, SE Tasmania; rocks generally age north to south across the island so we would expect the oldest ages to outcrop in the SE; this is likely close to the stratigraphic base.
- Youngest Age; 8.50 ± 0.1 Ma (1σ) K-Ar (Baillie, 1986) (no comments on sample quality); porphyritic basalt from Green Hills, northern end of Godfreys Beach, NW Tasmania; rocks generally age north to south across the island so we would expect the youngest ages to outcrop in the NW; this is likely close to the stratigraphic top.

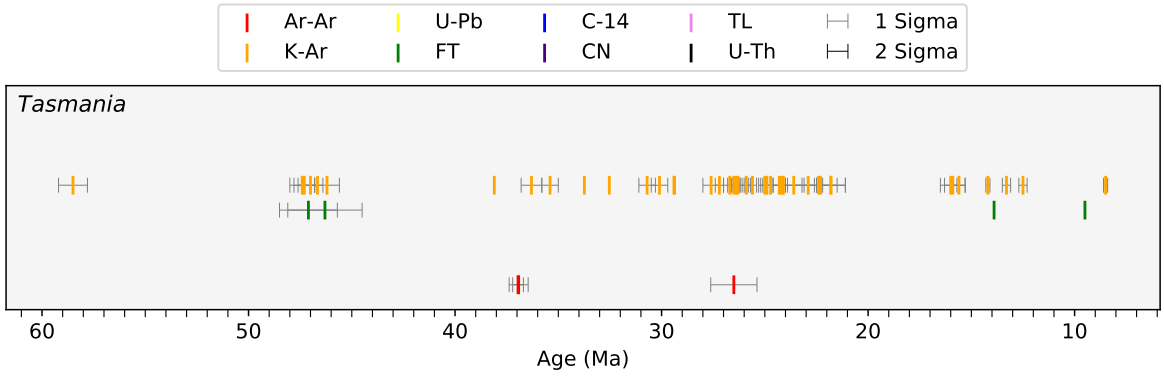

Figure 6.125: *Age data for the Tasmania province.*

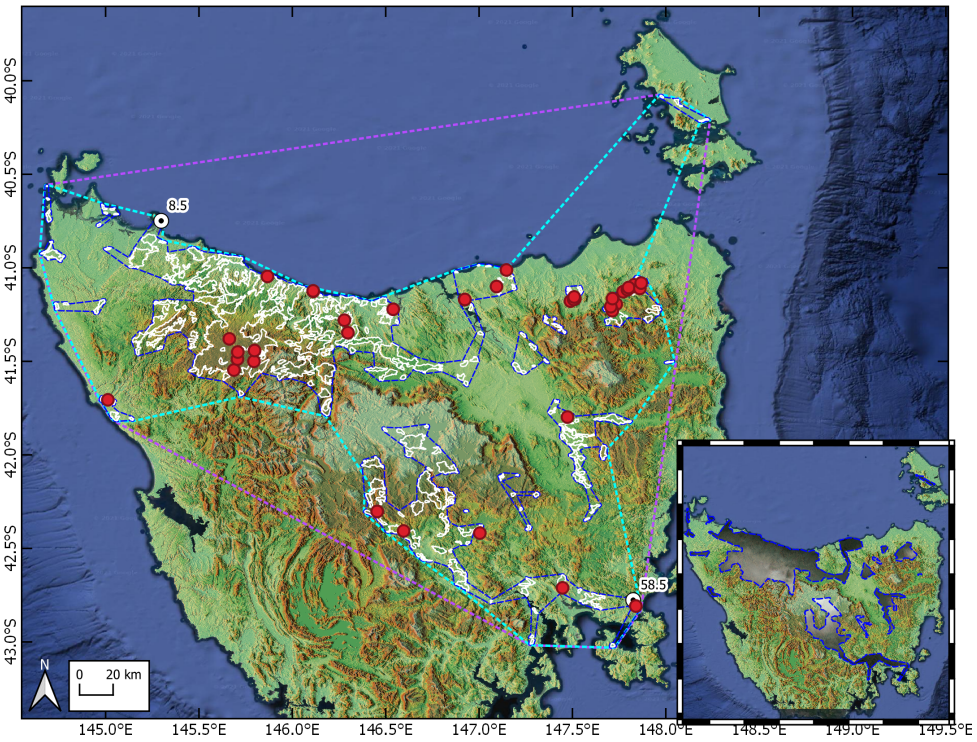

Figure 6.126: *The Tasmania volcanic province. Red dots show the locations of freely available borehole data obtained from Mineral Resources Tasmania and Tasmanian Government (2022).*

6.2.9 Seamounts

Tasmantid Chain (56.4–7.13 Ma)

The Tasmantid Seamounts have been K-Ar dated by McDougall and Duncan (1988) but these results have been superseded by the more accurate Ar-Ar data, although both studies show a clear southward younging age trend along the chain. Ar-Ar ages by Kalnins et al. (2015) and Crossingham et al. (2018) sample the length of the chain from the Louisaide Plateau in the north to the Gascoyne Seamount in the south and the total age span is ∼56.4–7.13 Ma, similar to the parallel East Australian central volcanoes and the Lord Howe seamount chain. Ar-Ar analyses by Crossingham et al. (2018) have not been used here to define the total age range across the chain simply because the same seamounts were analysed by Kalnins et al. (2015) who yielded more precise results. Kalnins et al. (2015) also sampled the full chain, while Crossingham et al. (2018) only sampled the central portion. Volume estimates for the Tasmantid seamounts have been produced by Crossingham et al. (2018) and Seton et al. (2019a). Crossingham et al. (2018) calculated an average extrusive volume for individual volcanoes of $2587 \pm 3078\,km^3$ ($1\,\sigma$), and also showed that the chain exhibits a general increase in volume southwards, excluding the Britannia Guyot, which produced an anomalously high volume of $11374\,km^3$ within the centre of the chain, adjacent to the onshore Tweed volcano. This result was found by Seton et al. (2019a) to be fairly anomalous, and the authors instead calculated an average extrusive volume of individual volcanoes of $\sim 2000\,km^3$. The bathymetry data used by Crossingham et al. (2018) did not include the lower flanks of the volcanoes and so there are limitations when considering these volume estimates. What is clear from both studies, is that on average, the Tasmantid seamounts have a greater volume than the average continental central volcanoes and lava fields.

- Oldest Age; 56.4 ± 0.6 Ma (2σ) Ar-Ar (Kalnins et al., 2015); mafic sample from the southern spur of the Louisaide Plateau at the northern end of the Tasmantid chain.
- Youngest Age; 7.13 ± 0.07 Ma (2σ) Ar-Ar (Kalnins et al., 2015); mafic sample from the Gascoyne seamount at the southern end of the Tasmantid chain.

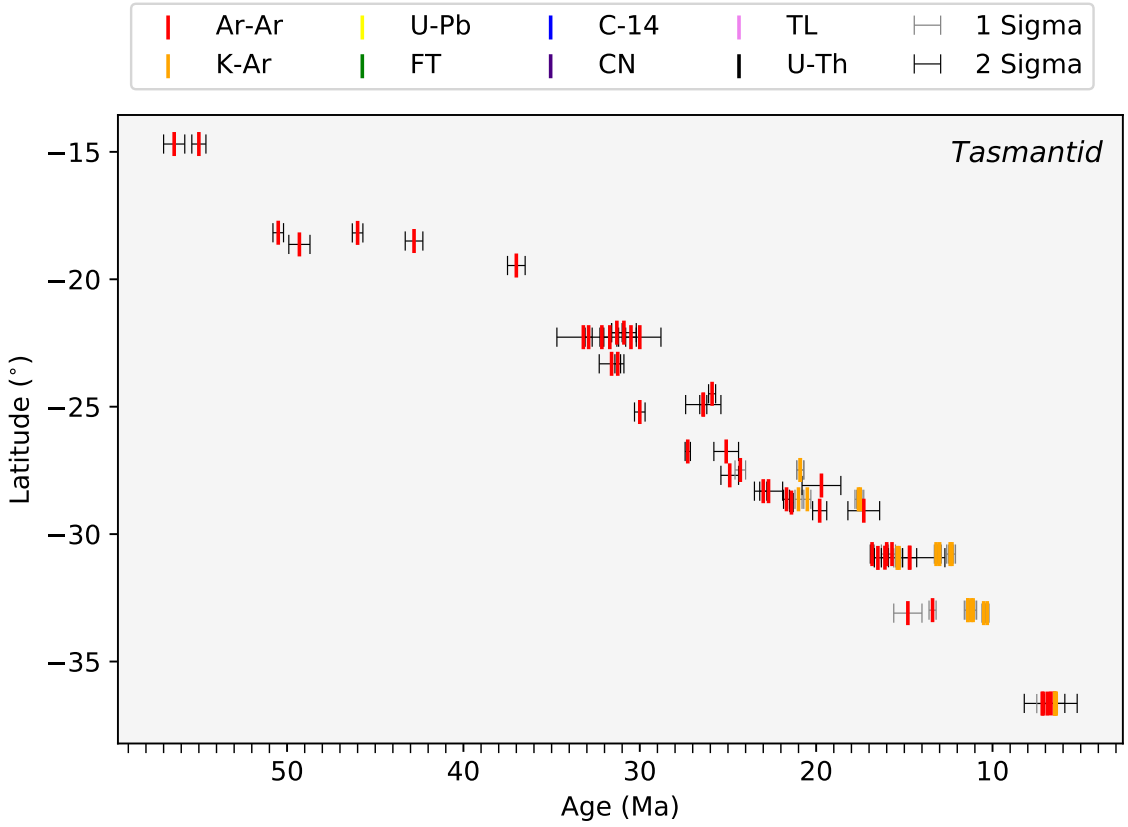

Figure 6.127: *Age data for the Tasmantid chain.*

Lord Howe Chain (28.1–6.38 Ma)

The Lord Howe seamount chain extends as far as 2400 km from Horsehead Seamount (although there may be further as yet unstudied seamounts further north) to Lord Howe Island, and potentially even further south to Flinders Seamount (Seton et al., 2019a). The chain was erupted onto the Lord Howe Rise, a drowned continental fragment (part of Zelandia) which lies through parts of the Coral Sea and Tasman Sea. Only three seamounts along the Lord Howe chain have been Ar-Ar dated (Mortimer et al., 2010, 2017), another three have rough ages from biostratigraphy (Quilty, 1993), and the Lord Howe Island itself has numerous K-Ar ages (McDougall et al., 1981). Whilst only a few ages exist, together they show a southward younging trend, similar to the Tasmantid Seamounts and the East Australian central volcano and leucitite suites. Unfortunately, no volume estimates exist for the Lord Howe seamounts but this would be a good area for further work.

- Oldest Age; 28.1 ± 1.0 Ma (2σ) Ar-Ar (Mortimer et al., 2017) (minor influence of argon loss and recoil); basalt from Chesterfield Island, Lord Howe chain; not the northernmost point in the chain but Horsehead Seamount further north gave a similar age of 27.2 Ma.
- Youngest Age; 6.38 ± 0.1 Ma (1σ) K-Ar (McDougall et al., 1981) (the spread in apparent age obtained from the samples at Mount Lidgebird is somewhat greater than might be expected from the geology, and no systematic variation in age is found with stratigraphic position; however, multiple samples yield ages which agree at 6.38 Ma); various mafic lavas from the Mount Lidgebird Basalt, Lord Howe Island.

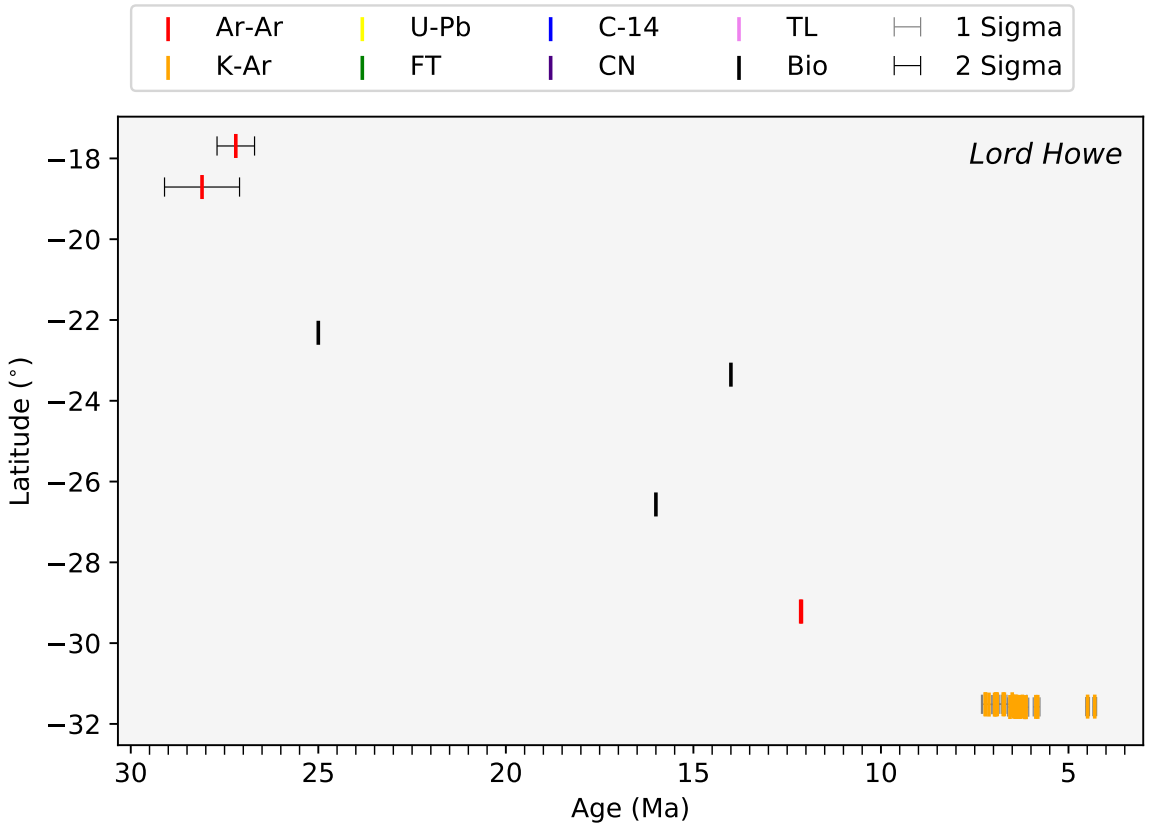

Figure 6.128: *Age data for the Lord Howe chain.*

6.3 Conclusions

The results of the preferred original volume estimates for both the central volcanoes and lava fields are shown in Figure 6.129, alongside volume estimates of the Tasmantid seamounts from Crossingham et al. (2018).

Central volcanoes have an average volume of 1405 km^3 and lava fields an average of 315 km^3. These compare to Wellman (1971) volumes of 500 km^3 and 200 km^3 for the central volcanoes and lava fields, respectively. Tasmantid seamount volumes from Crossingham et al. (2018) and Seton et al. (2019a) average 2587 ± 3078 km^3 ($1\,\sigma$), and $\sim$2000 km^3, respectively. This larger volume, along with the smaller total volume of all leucitite volcanoes calculated in this study (5 km^3) are consistent with broad changes in lithospheric thickness.

Central volcanoes in Queensland show consistently high volumes, although the volume gathered for the Nebo volcano is expected to be an overestimate as it includes lava fields with the central volcano. The volumes of Peak Range, Springsure, and Buckland volcanoes are estimated at 1459 km^3, 2695 km^3, and 1918 km^3, which are relatively different from Jones and Verdel (2015) volume of 2600 km^3, 1460 km^3, and 860 km^3. Peak Range may be slightly smaller as the lavas of East Clermont have been excluded from the final calculation. Springsure and Buckland estimates are almost double those by Jones and Verdel (2015) suggesting the preserved maximum thicknesses may not be an accurate representation of original volcanic thickness. The Cape Hillsborough central volcano in central Queensland has a characteristically small volume of 58 km^3 which is to be expected of volcanoes located directly along the coastline due to high erosion rates.

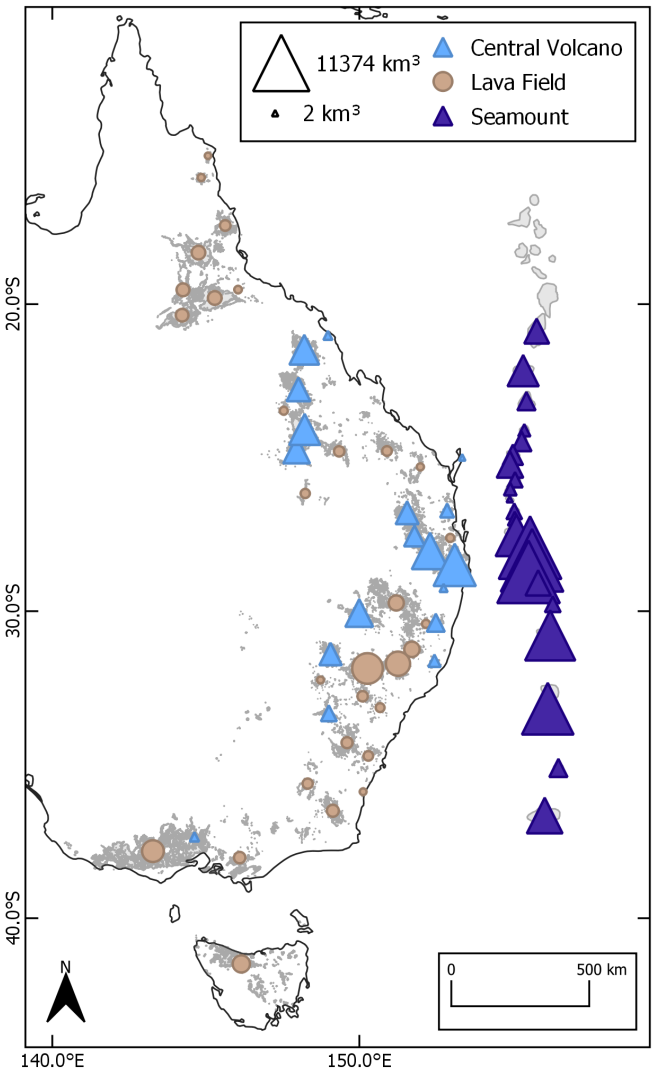

Figure 6.129: *Graphical depiction of central volcano and lava field preferred original volume estimates. For comparison, volume estimates of the Tasmantid seamounts from Crossingham et al. (2018) are included but results should be used with caution given the bathymetry data used did not include the lower flanks of the volcanoes.*

Central volcano provinces along the eastern side of the East Australian chain i.e., from Fraser Island to Comboyne, also have characteristically smaller volumes compared with the other central volcanoes. Whether this is due to a reduced supply of magma along this branch of the chain or due to intense erosion of the volcanoes along the Australian coastline, is unclear. Given the trajectory of this chain, it may also include deposits of the Focal Peak volcano (Mount Barney) which lies on the western flank of the Tweed shield but is almost completely eroded leaving only vent deposits and intruded plutonic rocks visible at present-day. Due to the limited coverage and unknown extent of the volcano, this was not included in this study of volume estimates.

The central volcanoes in southern Queensland including Bunya, Main Range, and Tweed, show a systematic increase in volume versus age moving south through the chain from 1343 km^3, to 3807 km^3, to 5199 km^3. This is a much higher estimate for the volume of the Tweed shield than has previously been suggested by Wellman (1971) but given the location of this volcano on the Australian coastline it is likely a huge portion of the Tweed volcano has been lost through erosion and this estimate is therefore deemed reasonable. The Toowoomba volcano has a slightly smaller volume than others in this chain, at 1075 km^3, although the boundary of this volcano is often obscured by the Bunya and Main Range volcanics, plus those of inferred underlying lava fields and it is thus difficult without further mapping to confirm the accuracy of this volume.

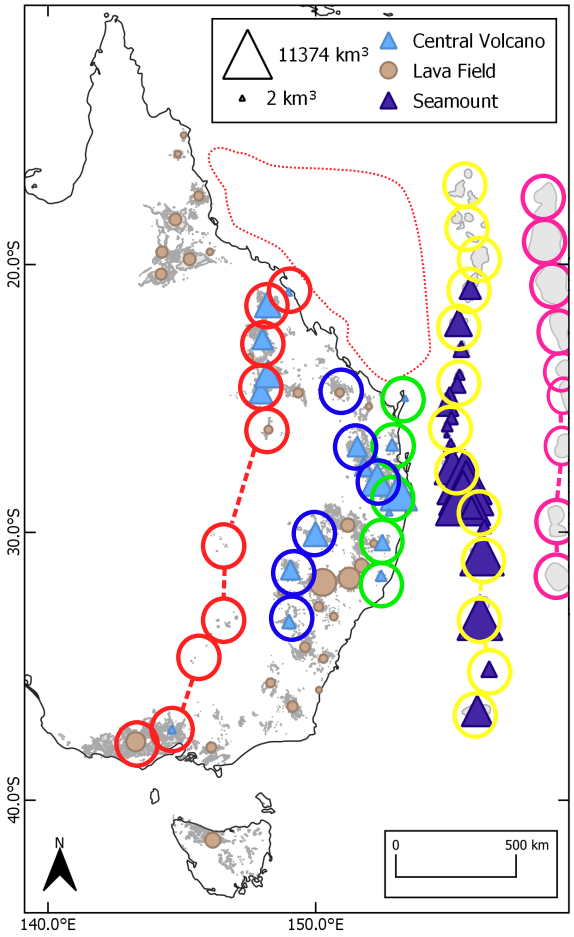

Figure 6.130: *Estimated paths of multiple mantle plumes (red, blue, green, yellow and pink circles) overlaying central volcano, lava field and Tasmantid seamount volume estimates from Figure 6.129. The red dotted line shows the area of the Australian continental slope which is obscured by the Great Barrier Reef and associated sediments.*

Central volcanoes in central New South Wales i.e., Nandewar, Warrumbungle, and Canobolas, have decreasing volume estimates from 2103 km^3, to 1269 km^3, to 513 km^3, respectively, which fits with the Jones and Verdel (2015) interpretation of a waning mantle plume. Moving further south still, the Macedon-Trentham central volcano in Victoria has an unusually small volume of just 66 km^3. Situated in the central highlands of the NVP and being relatively close to the coastline it is possible this area has suffered from high erosion rates, or the extent of mafic lavas radiating from the shield may be buried by more recent NVP volcanism, or the volume is displaying the further effects of a waning mantle plume.

From the observations made in this Chapter, it is clear the majority of central volcanoes have volumes greater than the lava fields but these results are primarily modeled off the assumption that huge volumes of ash, scoria, and pyroclastic deposits have been removed from the central volcanoes through weathering and erosion. This is not an unreasonable assumption and these observations tie in nicely with geochemical results which suggest that the central volcanoes of eastern Australia are the product of higher degree partial melting when compared to the lava fields. Were these high degree partial melts to be sourced from a mantle plume, as has been hypothesised in this thesis, then at least five distinct plumes, or plumelets, would be required to cover the swath of age-progressive volcanism found on both the continent and offshore. The location of each of these plumes can be seen in Figure 6.130 where each chain is separated by a distance of around 300 km. All plumes follow similar trends and whilst the Tasmantid chain appears to be the longest it is possible additional volcanoes at the north of the continent have been obscured by the Great Barrier Reef and associated continental shelf sediments (dotted red line). The mechanism responsible for producing such an array has not been clearly identified within this work but favoured mechanisms include: (1) interaction with a remnant oceanic slab beneath the Tasman Sea (Kalnins et al., 2015) (see tomographic studies by Matthews et al. (2012) and Schellart et al. (2009) in Section 2.3.1); (2) a plume pooling at the 660 km discontinuity with separate conduits to the surface (Saki et al., 2015; Ballmer et al., 2013); (3) edge-driven convection (EDC) (Davies and Rawlinson, 2014; Rawlinson et al., 2017); and (4) small-scale convection (SSC) beneath the lithosphere (Ballmer et al., 2009, 2011). Further modeling work is required to assess which of these processes, plus others, may most feasibly explain age-progressive volcanism across eastern Australia.

All lava fields, except for Liverpool Range, Barrington, and the NVP have estimated volumes below 1000 km^3 which is consistent with their derivation from an SCLM source where lower degrees of melting, compared with the inferred age-progressive plume volcanism, are expected. Of the lava fields not fitting this trend, most have been suggested as being the product of multiple different volcanic episodes, for example the Liverpool Range is thought to both represent two provinces in one (Wellman and McDougall, 1974b). The Barrington province appears to be the result of relatively continuous, long-lived volcanism, suggesting the high volumes found here are not the result of high degrees of partial melting but of prolonged build up of smaller degree melts. In keeping with the results of the geochemical analysis, this would suggest that lava field volcanism is likely the result of lower degree SCLM and DM partial melting, produced through passive plate tectonic processes. The NVP is slightly anomalous as a high volume of lavas appear to have built up here in a relatively short space of time (<8 Ma), although the interaction of SCLM melts with an asthenospheric plume, as discussed in Chapter 4 of this thesis, may help to explain this.

Chapter 7

Summary



Figure 7.1: *Noosa National Park, Queensland.*

7.1 Conclusions

The results gathered in this thesis show that the age-progressive, Tasmantid seamounts represent relatively high degree partial melts, usually silica saturated and with relatively low incompatible/garnet-compatible element ratios e.g., LREE/HREE. The volume of the Tasmantid seamounts is generally much larger than continental volcanoes (Seton et al., 2019a), primarily due to their location on thinner lithosphere ($\sim$20–70 km). These relatively high degree, high volume partial melts were probably stored in sizable chambers underground allowing time for significant fractionation of olivine, clinopyroxene, and plagioclase. Incompatible element ratios for the Tasmantids may be adequately modeled by non-modal batch partial melting of a peridotite source along the 1300 °C isotherm. Trace element and isotopic results also show that the Tasmantid seamounts are probably sourced from garnet-bearing, EMI-type asthenosphere where F_{max} is primarily controlled by lithosphere age and thickness which increases southwards along the length of the chain, and to a lesser extent by changes in mantle Tp.

Rocks from the nearby leucitite chain represent small degree partial melts, consistently silica undersaturated with the highest incompatible/garnet-compatible element ratios, e.g., LREE/HREE, across the area. The leucitites lie on the thickest lithosphere of any suite ($>$130 km) and small degree partial melting has produced lavas of low volume and limited fractionation, as they rose to the surface relatively rapidly. The leucitites are likely sourced from metasomatically enriched, Al-Na depleted SCLM that underwent partial melting following the passing of an asthenospheric mantle plume. Factors pointing towards SCLM involvement include: (1) a unique chemistry that is globally only observed in continental rocks (2) a good correlation between leucitite compositions and lithospheric xenolith compositions (3) K$>$Na which cannot be achieved through partial melting of normal mantle or fractional crystallisation alone and (4) a systematic increase in major element depletion, LILE enrichment, Pb isotope enrichment, and Nb and Ca/Na enrichment moving north through the chain from relatively thin, young lithosphere to thicker and older lithosphere.

Like the Tasmantids, the continental central volcanoes represent higher degree partial melts. On a PM-normalised multi-element plot of incompatible elements the central volcanoes display a similar pattern to the Tasmantids and the leucitites but overall values plot between the two. The same trend is observed in incompatible/garnet-compatible element ratios which plot marginally higher than the Tasmantids but lower than the leucitites. In many plots, the continental lava fields display a distinctly different character to each of the other three suites. Lava fields represent smaller melt fractions and fractionation is often limited, but this suite has the widest range of silica saturation, incompatible element concentrations, and incompatible/garnet-compatible element ratios. Diagnostic characteristics of the lava fields are therefore difficult to define as they represent as considerable range in trace element and isotope results.

Based on results for the Tasmantid and leucitite suites, a deep, EMI-type plume and metasomatised SCLM likely represent the two enriched mantle endmembers from which volcanism across eastern Australia has been sourced. The simplest explanation for greater trace element enrichment and isotopic variations away from Tasmantid compositions, is that they relate to varying interaction with metasomatically enriched SCLM. Given that geochemical compositions of the central volcanoes and lava fields often plot between both the Tasmantid and leucitite suites, it seems most likely the central volcanoes and lava fields are the product of both EMI-plume and SCLM melts, with varying contribution from the depleted mantle. The age-progressive, high degree partial melt central volcanoes probably have a greater contribution of EMI-type plume melts whilst the non-age-progressive, primitive, undersaturated and incompatible element enriched lava fields probably have a greater contribution of SCLM derived melts.

Volumes estimated in this study tend to agree with these interpretations. Central volcanoes have an average volume of 1405 km^3 which is consistent with their derivation from a deep seated plume and high degree partial melts. The lava fields have an average of 315 km^3 which is consistent with their derivation from an SCLM source where lower degrees of partial melting are implied. Of the lava fields not fitting this trend, most have been suggested as being the product of multiple different volcanic episodes, for example the Liverpool Range. The Barrington province appears to be the result of relatively continuous, long-lived volcanism, suggesting the high volumes found here are not the result of high degrees of partial melting but of prolonged build up of smaller degree melts. The NVP is slightly anomalous as a high volume of lava appear to have built up here in a relatively short space of time ($<$8 Ma), although the interaction of SCLM melts with an asthenospheric plume within this province may help to explain this province.

Considering these interpretations alongside volcanic ages, the central volcano and lava field suites may be separated into six different groups including: (1) mixed, multi-phase volcanism and volcanism $>$ 66 Ma; (2) single-pulse, lava field-type volcanism emplaced between 66–10 Ma; (3) HIMU Tasmania volcanism; (4) short-lived, age-progressive volcanism; (5) young volcanism from the NVP; and (6) young volcanism from far north Queensland (Figures 7.2 and 7.3).

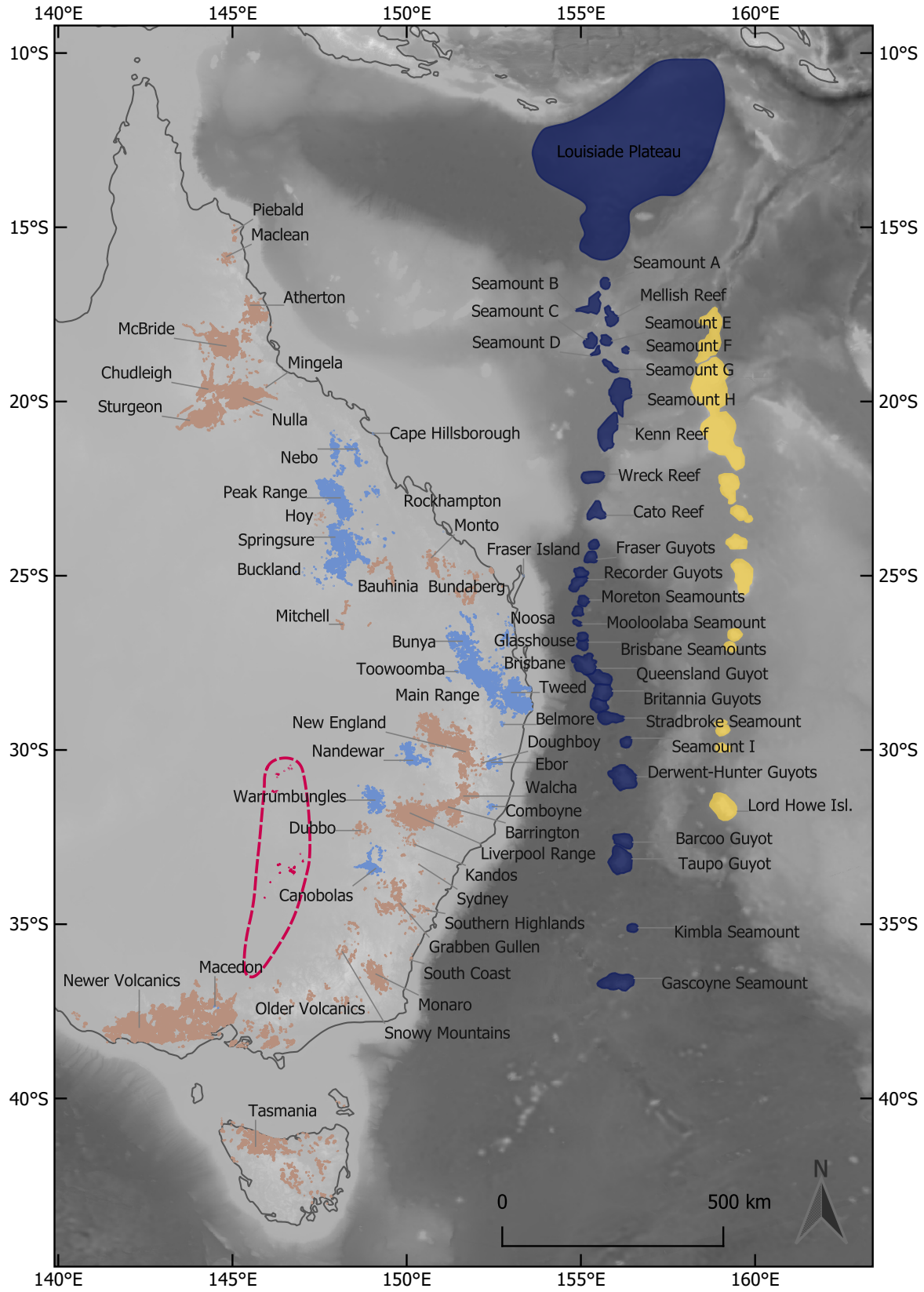

Figure 7.2: *Individual volcanic provinces within the five volcanic suites. Tasmantid seamounts marked in navy; Lord Howe seamounts in yellow; central volcanoes in light blue; lava fields in tan; and leucitites within the dashed crimson area. Topographic and Bathymetric grid from GEBCO (2020).*

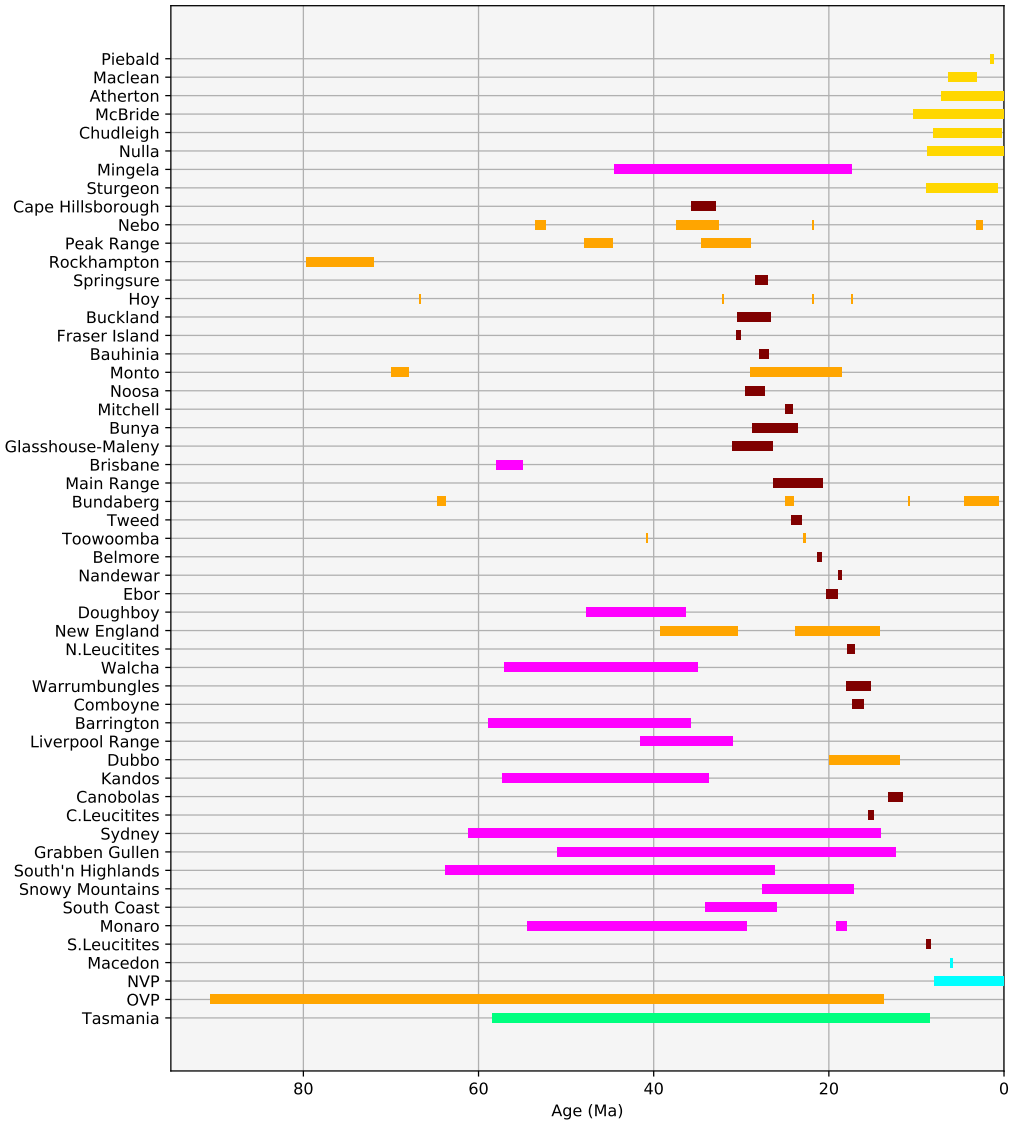

Figure 7.3: *Chronology of continental volcanic eruptions ordered by decreasing latitude and coloured by group: (1) mixed, multi-phase volcanism and volcanism > 66 Ma (orange); (2) single-pulse, lava field-type volcanism emplaced between 66–10 Ma (magenta); (3) HIMU Tasmania volcanism (green); (4) short-lived, age-progressive volcanism (maroon); (5) young volcanism from the NVP (cyan); and (6) young volcanism from far north Queensland (yellow).*

(1) Volcanism erupting prior to ∼66 Ma includes the Hoy, Rockhampton, Monto, Bundaberg, and the OVP (Figure 7.4). OVP volcanism persisted relatively continuously throughout the Cenozoic but began at a similar time to the opening of the Tasman Sea. Volcanism around Hoy, Monto, and Bundaberg was much more sporadic and short-lived, yet reoccurred over a period greater than 40 Ma, beginning around 60 Ma. Given the proximity of these volcanoes to the coastline of Victoria and Queensland, where rifting took place, it is possible these are a product of rift-flank volcanism where small degree partial melting of enriched lithosphere were produced following changes in the stress regime of the Australian plate. The Rockhampton province appears to have only been active ∼80–72 Ma. This location has historically been catagorised as a central volcano because it produced bimodal lavas, although it was erupted almost 40 Ma earlier than all other central volcanoes and is very unlikely to be related to the same magmatic event but instead appears to match more closely with melts derived from the SCLM. Rockhampton, Monto, and Bundaberg all have some of the most undersaturated rocks across the region, and are also the only provinces containing plagioclase megacrysts which, chemically, showed a good correlation with an SCLM source. To add to this, these three provinces are all situated within the New England Fold Belt which represents a complex collage of continental margin terranes now represented by a series of fault-bound blocks (Veevers, 1984). It is possible such faults have acted as conduits to transport SCLM melts through the lithosphere.

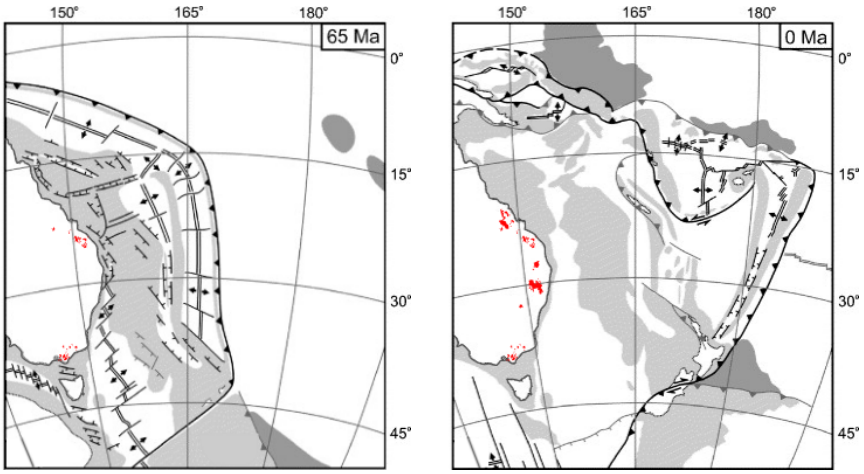

Figure 7.4: *Tectonic reconstructions of the east Australian plate from Schellart et al. (2006), modified to include mixed, multi-phase volcanism and volcanism > 66 Ma in red. (a) 65 Ma; (b) 0 Ma.*

The Peak Range and Toowoomba provinces fall within the "mixed" catagory as they are likely to be the products of earlier lava field volcanism and later central volcano volcanism. However, without more accurate mapping it was not possible to definitively say which volcanic event the samples collected for this study belonged to and this would instead be a good area for further work. Similarly, certain events within the Nebo, Monto, Bundaberg, New England and Dubbo provinces fit the trend of the age-progressive volcanoes and it is possible some of these lava fields contain SCLM melts derived from the passing of a mantle plume. Again, to confirm this theory further much more detailed mapping of each of these provinces would be required.

(2) Similar to OVP and multi-phase volcanism, prolonged, single-pulse volcanism emplaced between 66–10 Ma requires a passive, long-lived mechanism to explain (Figure 7.5). Given most provinces in this group occur close to the coast of NSW they again may be best described as rift flank volcanism but the longevity of the group poses a problem as rifting only took place from 84–52 Ma. The development of self-perpetuating small-scale sub-lithospheric convection (SSC) (Van Hunen and Zhong, 2006; Ballmer et al., 2009) might help to explain the longevity of these groups but further work outside of this thesis would be needed to confirm this. Around 61 Ma the velocity of the Australian plate increased rapidly from ~10–70 Ma which could potentially have induced volcanism via shear-driven upwelling (SDU) (Shankar and Deshpande, 2000; Conrad et al., 2010). Also, Johnson (1989) propose a genetic link of these lava fields and the creation of the Great Dividing Range where gravitational instability of the deep lithospheric root may have induced volcanism. The mechanism involved in the creation of these volcanoes is highly recommended as an area of further work to this thesis as they also display some of the most interesting geochemical characteristics i.e., high Nb/Y.

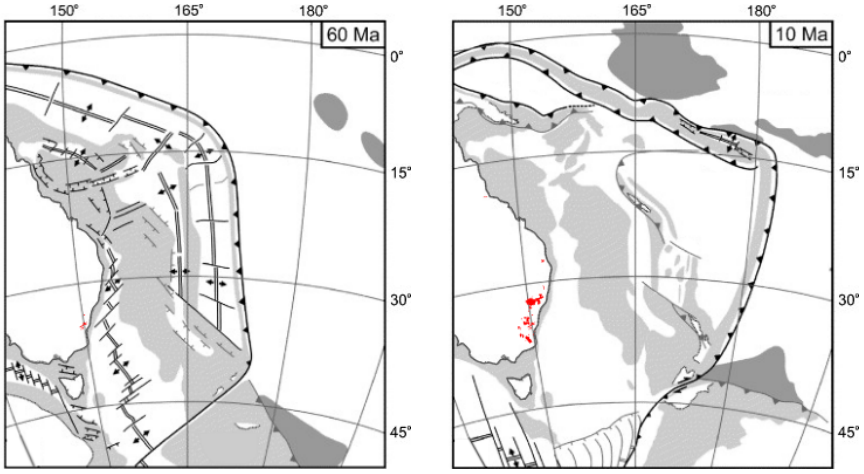

Figure 7.5: *Tectonic reconstructions of the east Australian plate from Schellart et al. (2006), modified to include single-pulse, lava field-type volcanism emplaced between 66–10 Ma in red. (a) 60 Ma; (b) 10 Ma.*

(3) HIMU volcanism in Tasmania also began relatively early on, around 60 Ma. The geochemistry of Tasmania lavas show considerable range, including highly silica undersaturated to silica saturated samples with a range of incompatible element concentrations. Isotopic results from the province almost always plot towards a HIMU composition which has been tentatively explained by the arrival of the Balleny plume in eastern Tasmania. Given the different chemistry it is certainly possible these lavas have an entirely different origin to that of other volcanoes in east Australia and further analysis of these samples, possibly alongside those of the OVP, is again recommended as further work to this study.

(4) Southward younging, age-progressive volcanism is best explained chemically and mechanically by a plume source with an EMI-type signature that has interacted with the SCLM upon ascent. The steady progression of each of the five possible chains is shown in Figure 7.6 (see Chapter 4 for full conclusions).

(5) Given similarities in age and composition to the nearby Macedon-Trentham central volcano and leucitite chain, young volcanism within the NVP appears to be well explained by the melting of a mantle plume mixed with SCLM melts, with a greater contribution of the latter (Figure 7.6d) (see Chapter 5 for full conclusions).

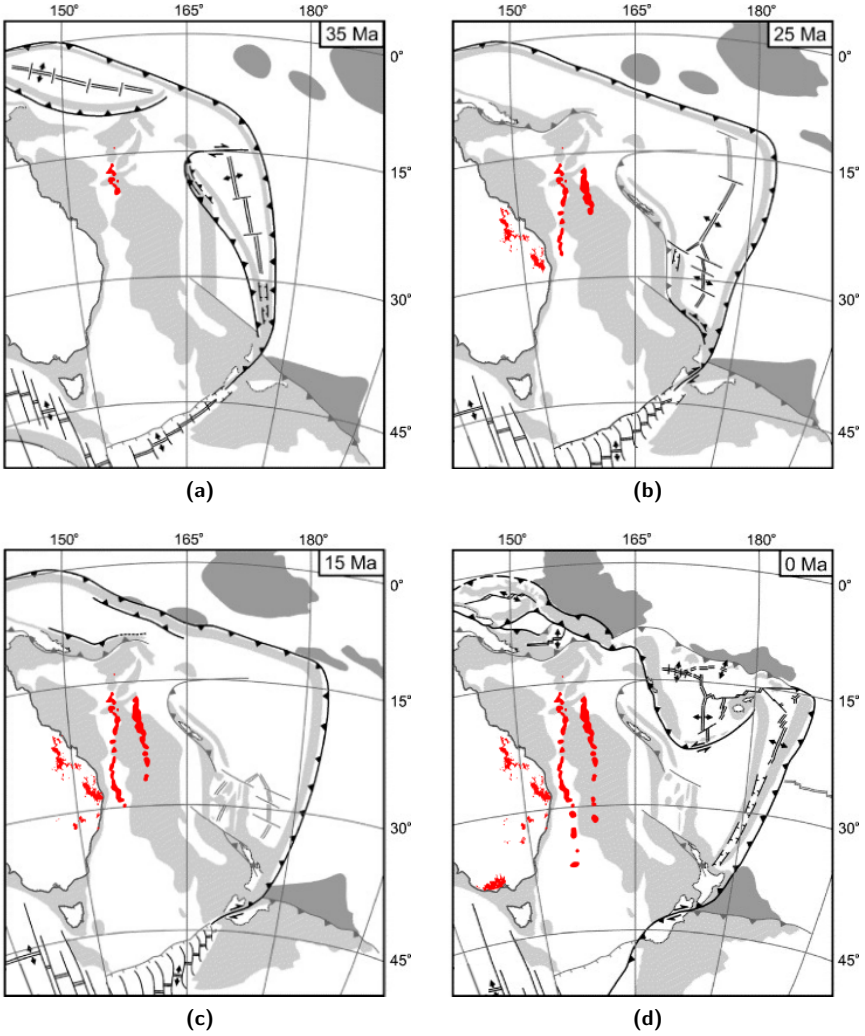

Figure 7.6: *Tectonic reconstructions of the east Australian plate from Schellart et al. (2006), modified to include short-lived, age-progressive volcanism and NVP volcanism in red. (a) 35 Ma; (b) 25 Ma; (c) 15 Ma; and (d) 0 Ma.*

(6) SCLM melting in far north Queensland requires a passive process to induce volcanism which has only activated in the last 10 Ma but has been continuous since then. One possibility is that this is due to blocking and compression following OJP collision along the north Australian plate (Petterson et al., 1997; Wessel and Kroenke, 2000). This event resulted in a flip in subduction polarity and the opening of the Lau, North Fiji, and Woodlark Basins as back-arc basins (Hall, 2002) as this area moved from a compressional to extensional regime. It is possible the volcanoes in far north Queensland are the result of these changing plate stresses in the north of the continent where major faults between the Hodgkinson-Broken River Fold Belt, the Thompson Fold Belt, and the Georgetown Inlier may have aided the flow of magma through the lithosphere.

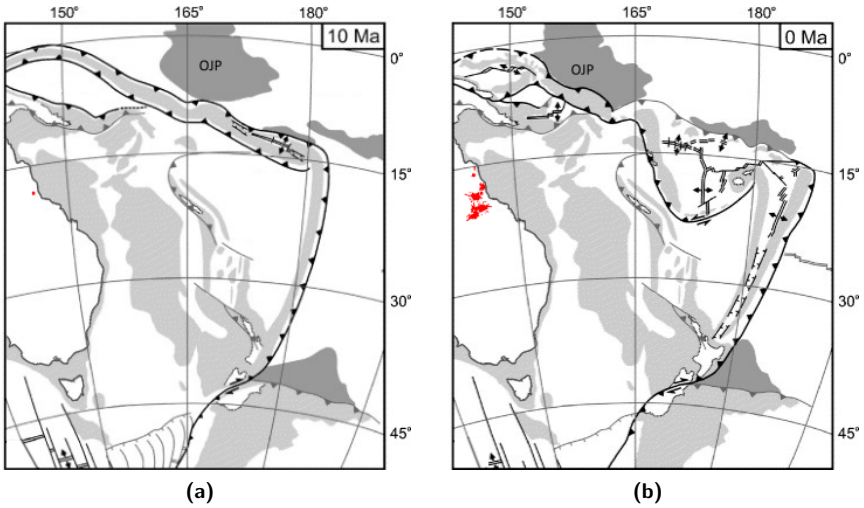

Figure 7.7: *Tectonic reconstructions of the east Australian plate from Schellart et al. (2006), modified to include young volcanism from far north Queensland in red. (a) 10 Ma; (b) 0 Ma. OJP = Ontong Java Plateau.*

From all results gathered in this thesis, three different volcanic sources may be used to explain the suite of Cenozoic volcanoes found in eastern Australia today: (1) oceanic, high volume, age-progressive volcanism from a deep, EMI-type mantle plume; (2) continental, age progressive volcanism from the same plume mixed with metasomatised SCLM melts where volume is controlled by lithosphere thickness and the contribution of the plume versus the SCLM; and (3) continental, low volume, non-age-progressive volcanism related to passive melting of the DM and metasomatised SCLM. The Nb/Y versus Zr/Y plot from Fitton (2007) appears to differentiate very well between each of these groups, where, when Zr/Y is $<\sim$16, Nb/Y increases with increased contribution of melt from an enriched plume, or an enriched SCLM source. These results also comply with those by Zhang et al. (2001) who suggested the east Australian volcanoes could be explained by mixing of a plume, SCLM, and DM (Pacific MORB and Indian MORB) source however their results were based mostly on isotopic values. In this study the same variations have been identified through the analysis of major element and immobile trace element data.

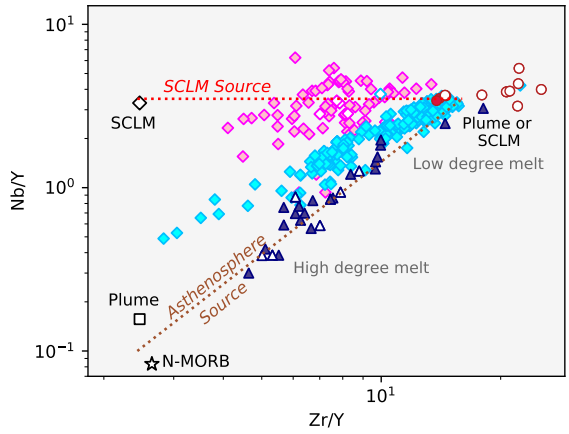

Figure 7.8: *Nb/Y versus Zr/Y showing three of the main groups identified in this study as having different sources including: (1) single-pulse, lava field-type volcanism emplaced between 66–10 Ma (magenta diamonds); (2) young volcanism from the NVP and the leucitite chain (cyan diamonds and crimson circles, respectively); (3) the Tasmantid Seamounts (navy triangles). Black symbols shows the rough position of mantle end-members where for high degree melts, an N-MORB source (star) is represented by the depleted mantle (DM) end-member from Sun and McDonough (1989); a plume-like source (square) is represented by the primitive mantle (PM) end-member from Sun and McDonough (1989); and an SCLM (diamond) source is arbitrarily placed using the results of this study. For low degree melts, the Nb/Y-Zr/Y signatures of basalts from both plume and SCLM sources have similar values but such high enrichments are not expected to originate from low degree melting of N-MORB. Samples laying along the brown dotted line are thought to originate primarily from a deep plume-like source with an EMI isotopic signature. Samples laying along the red dotted line are thought to be derived primarily from SCLM melts.*

7.2 Future Work

- One of the primary findings of this work is that when $Zr/Y < 16$, increasing Nb/Y of intraplate basalts in eastern Australia can be attributed to an increasing influence of a plume source, and with more extreme values, the SCLM. The exact source of this Nb enrichment would therefore be an interesting area for further work as this is the main differentiator between MORB-derived, plume-derived, and SCLM-derived OIB rocks. A thorough study of xenoliths across each terrane in the Tasman Fold Belt may help to better characterise the SCLM beneath east Australia, with a particularly focus on the SCLM beneath New South Wales where we see the highest levels of Nb enrichment. If high Nb does appear to correspond to lithospheric involvement then it would be interesting to find out why, what mechanism might be responsible for concentrating a relatively immobile element in the lithosphere?

- On the same topic, another area of further work would be to look into where both the EMI signature and the Nb enrichment from the plume-like source might originate, although this can be complicated by contamination of plumes with SCLM-like melts which also have an EMI-like signature and high Nb, as has been shown in this work. Another unknown regarding both the continental and oceanic plume sources is the depth of origin. Within this thesis age-progressive volcanoes have been defined as having an asthenospheric origin sourced at a depth at least 70 km within the garnet stability field but the total depth of origin has not been identified any further. To date, seismic tomography results, such as those from Montelli et al. (2004), have only traced Tasmantid plume-like volcanism down to the middle mantle. Further geochemical studies on all age-progressive rocks but particularly the Tasmantid seamounts would help to fully define their source depth and petrogenetic evolution.

- In addition to a more in-depth geochemical review, geodynamic modeling of the mechanisms potentially responsible for the emplacement of the age-progressive volcanoes would also be a very useful area of research. How feasible would it be to maintain five different plumes, or plumelets, separated laterally by only 300 km? Could splitting of a plume emerge through interaction with a stagnant slab or pooling at the 660 km discontinuity? And how might EDC or SSC aid in self-perpetuating such volcanism?

- Evidence for the involvement of the lithosphere in generating the leucitite rocks is outlined fairly clearly in Chapter 5 of this study. If this is the case, then a comprehensive review of how the leucitites correlate with the SCLM moving north to south through the chain would be a good area for future work. Ideally, a study of lithospheric xenoliths from older, thicker lithosphere in the north, to younger thinner lithosphere in the south would be undertaken. The results may then be analysed to assess potential signs of metasomatism and whether or not the identification of an originally depleted, then carbonate metasomatised lithosphere is a suitable source for the northern-most leucitites.

- On the Nb/Y versus Zr/Y plot, samples from Tasmania have a slightly different trend to other groups with moderate Nb enrichment. Coupled with the unusual HIMU isotopic signature of this group, it is possible they have a different origin to other volcanoes in east Australia. The source of the Tasmania lava fields would therefore be an interesting area for further work and given the age range through which they were erupted ($\sim$58–8 Ma) a similar mechanism may be responsible for the 66–10 Ma single-pulse volcanism in NSW. Similarly, the OVP rocks in Victoria are the only province to extend towards the EMII reservoir and have been active since around 90 Ma. It would be good to confirm whether these differences are all able to be derived through changes in the composition of the SCLM.

- Another advantageous area of research would be detailed mapping of each continental province, particularly for provinces such as Nebo, Peak Range and Toowoomba which are thought to contain both lava field and central volcano suites of volcanism. For this study, only a handful of samples were collected from each area and one of the main difficulties in grouping the results was knowing whether or not the samples were truly representative of the entire province or just a subsection. More in-depth fieldwork would eliminate the need for a "mixed" group, as has been the case in this thesis. Better mapping would also help refine volume estimates further as distal outcrops may be assigned to the correct volcano. In line with this, further Ar-Ar dating, particularly of the lava fields, would be useful to resolve the rate of volcanism as oppose to a single volume. In the reconstructions of this thesis a single province (sometimes quite large) is quite simply assigned to a single age of emplacement.

- More work could also be done to model the intrusive volumes of both the continental and oceanic provinces e.g., using seismic data or flexure modeling. The volume results could also be enhanced with an improved remote sensing classifications which is able to isolate basaltic and felsic igneous rocks more accurately, perhaps using ground truthing to better tune the remote sensing parameters.

References

Abele, C. and Page, R. W. (1974). Stratigraphic and Isotopic Ages of Tertiary Basalts at Maude and Aireys Inlet, Victoria, Australia. *Proceedings of the Royal Society of Victoria*, 86:143–150.

Abrams, M., Hook, S., and Ramachandran, B. (2002). *ASTER user handbook, version 2*. Jet propulsion laboratory, 4800.

Abrams, M. J., Brown, D., Lepley, L., and Sadowski, R. (1983). Remote sensing for porphyry copper deposits in southern Arizona. *Economic Geology*, 78(4):591–604.

Adam, J. (1990). The Geochemistry and Experimental Petrology of Sodic Alkaline Basalts from Oatlands, Tasmania. *Journal of Petrology*, 31:1201–1223.

Adam, J. and Green, T. (2006). Trace element partitioning between mica- and amphibole-bearing garnet lherzolite and hydrous basanitic melt: 1. Experimental results and the investigation of controls on partitioning behaviour. *Contributions to Mineralogy and Petrology*, 152(1):1–17.

Aitchison, J. C., Clarke, G. L., Meffre, S., and Cluzel, D. (1995). Eocene arc-continent collision in New Caledonia and implications for regional southwest Pacific tectonic evolution. *Geology*, 23(2):161–164.

Ali, J. R. and Aitchison, J. C. (2000). Significance of palaeomagnetic data from the oceanic Poya Terrane, New Caledonia, for SW Pacific tectonic models. *Earth and Planetary Science Letters*, 177:153–161.

Allegre, C. J. (1982). Chemical geodynamics. *Tectonophysics*, 81:109–132.

Anderson, D. L. (2002). Plate Tectonics as a Far- From- Equilibrium Self-Organized System. *Geodynamics*, 30.

Anderson, D. L. (2007). *New theory of the Earth*. Cambridge University Press.

Armstrong, R. L. (1968). A Model for the Evolution of Strontium and Lead Isotopes in a Dynamic Earth. *Reviews of Geophysics*, 6(2).

Ashley, P. M., Duncan, R. A., and Feebrey, C. A. (1995). Ebor volcano and crescent complex, northeastern new south wales: Age and geological development. *Australian Journal of Earth Sciences*, 42(5):471–480.

Baillie, P. W. (1986). Radiometric ages for Circular Head and the Green Hills basalt, north-western Tasmania. *Unpublished Report Department of Mines Tasmania*, 39.

Baillie, P. W. (1987). A Palaeocene radiometric age for basalt at Bream Creek, south-eastern Tasmania. *Unpublished Report Department of Mines Tasmania*, 21.

Baldridge, A., Hook, S., Grove, C., and Rivera, G. (2009). The ASTER spectral library version 2 . 0. *Remote Sensing of Environment*, 113:711–715.

Ballmer, M. D., Hunen, J. V., Ito, G., Bianco, T. A., and Tackley, P. J. (2009). Intraplate volcanism with complex age-distance patterns: A case for small-scale sublithospheric convection. *Geochemistry, Geophysics, Geosystems*, 10(6).

Ballmer, M. D., Ito, G., Van Hunen, J., and Tackley, P. J. (2011). Spatial and temporal variability in Hawaiian hotspot volcanism induced by small-scale convection. *Nature Geoscience*, 4(6):457–460.

Ballmer, M. D., Ito, G., Wolfe, C. J., and Solomon, S. C. (2013). Double layering of a thermochemical plume in the upper mantle beneath Hawaii. *Earth and Planetary Science Letters*, 376:155–164.

Ballmer, M. D., van Hunen, J., Ito, G., Tackley, P. J., and Bianco, T. A. (2007). Non-hotspot volcano chains originating from small-scale sublithospheric convection. *Geophysical Research Letters*, 34(23):1–5.

Barron, B. J., Sutherland, F. L., and Robertson, A. D. (1996). Olivine leucitites', their xenolith and megacryst suites, Hoskings Peaks, north Queensland. *Australian Journal of Earth Sciences*, 43(3):231–244.

Bernet, M. and Garver, J. I. (2005). Fission-track analysis of detrital zircon. *Reviews in Mineralogy and Geochemistry*, 58:205–238.

Bird, P. (1979). Continental Delamination and the Colorado Plateau. *Journal of Geophysical Research*, 84.

Bird, P. (2003). An updated digital model of plate boundaries. *Geochemistry, Geophysics, Geosystems*, 4(3).

Bishop, P. (1984). Oligocene and Miocene Volcanic Rocks and Quartzose Sediments of the Southern Tablelands, New South Wales: Definitions of Stratigraphic Units. *Journal and proceedings of the Royal Society of New South Wales*, 117:113–113.

Bishop, P. and Young, R. W. (1980). Discussion: On the Cainozoic uplift of the southeastern Australian highland. *Journal of the Geological Society of Australia*, 27(1-2):117–119.

Blackburn, G., Allison, G. B., and Leaney, F. W. (1982). Further evidence on the age of tuff at Mount Gambier, South Australia. *Transactions of the Royal Society of South Australia*, 106:163–167.

Blewett, R. (2012). *Shaping a Nation: A Geology of Australia*. Geoscience Australia and ANU E Press, Canberra.

Bonatti, E. and Harrison, C. G. (1976). Hot lines in the Earth's mantle. *Nature*, 263(5576):402–404.

Boyce, J. (2013). The Newer Volcanics Province of southeastern Australia: A new classification scheme and distribution map for eruption centres. *Australian Journal of Earth Sciences*, 60(4):449–462.

Boyce, J. A., Nicholls, I. A., Keays, R. R., and Hayman, P. C. (2015). Variation in parental magmas of Mt Rouse, a complex polymagmatic monogenetic volcano in the basaltic intraplate Newer Volcanics Province, southeast Australia. *Contributions to Mineralogy and Petrology*, 169(11).

Bull, K. F., Troedson, A. L., Bodorkos, S., Blevin, P. L., Bruce, M. C., and Waltenberg, K. (2020). Warrumbungle Volcano: facies architecture and evolution of a complex shield volcano. *Australian Journal of Earth Sciences*, 0(0):1–39.

Chavez, P., Sides, S. C., and Anderson, J. A. (1991). Comparison of three different methods to merge multiresolution and multispectral data- Landsat TM and SPOT panchromatic. *Photogrammetric Engineering and remote sensing*, 57(3):295–303.

Churikova, T., Dorendorf, F., and Wörner, G. (2001). Sources and fluids in the mantle wedge below Kamchatka, evidence from across-arc geochemical variation. *Journal of Petrology*, 42(8):1567–1593.

Class, C. and Goldstein, S. L. (1997). Plume-lithosphere interactions in the ocean basins: constraints from the source mineralogy. *Earth and Planetary Science Letters*, 150:245–260.

Cohen, B. (2002). Geochronology and geochemistry of southeast Queensland Tertiary volcanism. *BSc Thesis, University of Queensland*.

Cohen, B. and Vasconcelos, P. (2007). 40Ar/39Ar Geochronology of Bundaberg Samples from DME Fairymead NS1, RUN 78. *Queensland Geological Record 2008/02*, pages 43–58.

Cohen, B. E. (2007). High-Resolution 40Ar/39Ar Geochronology of Intraplate Volcanism in Eastern Australia. *PhD Thesis, The University of Queensland*.

Cohen, B. E. (2018). Personal Communication.

Cohen, B. E., Knesel, K. M., Vasconcelos, P. M., and Schellart, W. P. (2013). Tracking the Australian plate motion through the Cenozoic: Constraints from 40Ar/39Ar geochronology. *Tectonophysics*, 32:1371–1383.

Cohen, B. E., Knesel, K. M., Vasconcelos, P. M., Thiede, D. S., and Hergt, J. M. (2008). 40Ar/39Ar constraints on the timing and origin of Miocene leucitite volcanism in southeastern Australia. *Australian Journal of Earth Sciences*, 55(3):407–418.

Cohen, B. E., Mark, D. F., Fallon, S. J., and Stephenson, P. J. (2017). Holocene-Neogene volcanism in northeastern Australia: Chronology and eruption history. *Quaternary Geochronology*, 39:79–91.

Cohen, B. E., Vasconcelos, P. M., and Knesel, K. M. (2007). 40Ar/39Ar constraints on the timing of Oligocene intraplate volcanism in southeast Queensland. *Australian Journal of Earth Sciences*, 54(1):105–125.

Conrad, C. P. (2000). Convective instability of thickening mantle lithosphere. *Geophysical Journal International*, 143(1):52–70.

Conrad, C. P., Behn, M. D., and Silver, P. G. (2007). Global mantle flow and the development of seismic anisotropy: Differences between the oceanic and continental upper mantle. *Journal of Geophysical Research: Solid Earth*, 112(7):1–17.

Conrad, C. P. and Molnar, P. (1997). The growth of Rayleigh-Taylor-type instabilities in the lithosphere for various rheological and density structures. *Geophysical Journal International*, 129(1):95–112.

Conrad, C. P., Wu, B., Smith, E. I., Bianco, T. A., and Tibbetts, A. (2010). Shear-driven upwelling induced by lateral viscosity variations and asthenospheric shear: A mechanism for intraplate volcanism. *Physics of the Earth and Planetary Interiors*, 178(3-4):162–175.

Córdoba, A. M. C. and Ballmer, M. D. (2021). The role of edge-driven convection in the generation of volcanism - Part 1: A 2D systematic study. *Solid Earth*, 12(3):613–632.

Courtillot, V., Davaille, A., Besse, J., and Stock, J. (2003). Three distinct types of hotspots in the Earth's mantle. *Earth and Planetary Science Letters*, 205(3-4):295–308.

Coventry, R. J., Stephenson, P. J., and Webb, A. W. (1985). Chronology of landscape evolution and soil development in the upper Flinders River area, Queensland, based on isotopic dating of Cainozoic basalts. *Australian Journal of Earth Sciences*, 32(4):433–447.

Crawford, A. J., Meffre, S., and Symonds, P. A. (2003). 120 to 0 Ma tectonic evolution of the southwest Pacific and analogous geological evolution of the 600 to 220 Ma Tasman Fold Belt System. *Geological Society of Australia Special Publication*, 22:377–397.

Crossingham, T. J., Ubide, T., Vasconcelos, P. M., Knesel, K. M., and Mallmann, G. (2018). Temporal constraints on magma generation and differentiation in a continental volcano: Buckland, eastern Australia. *Lithos*, 302-303:341–358.

Crosta, A. P., De Souza Filho, C. R., Azevedo, F., and Brodie, C. (2003). Targeting key alteration minerals in epithermal deposits in Patagonia, Argentina, using ASTER imagery and principal component analysis. *International Journal of Remote Sensing*, 24(21):4233–4240.

CSIRO (2012). Tasmantid Seamounts: volcanic, tectonic, and carbonate record (TMD2012). Technical report, Australia's Marine National Facility.

Cundari, A. (1973). Petrology of the leucitebearing lavas in New South Wales. *Journal of the Geological Society of Australia*, 20(4):465–492.

Cundari, A., Renard, J. G., and Gleadow, A. J. (1978). Uranium-Potassium relationship and apatite fission-track ages for a differentiated leucitite suite from New South Wales (Australia). *Chemical Geology*, 22(C):11–20.

Davies, D. R. and Rawlinson, N. (2014). On the origin of recent intraplate volcanism in Australia. *Geology*, 42(12):1031–1034.

Davies, D. R., Rawlinson, N., Iaffaldano, G., and Campbell, I. H. (2015). Lithospheric controls on magma composition along Earth's longest continental hotspot track. *Nature*, 525:511–514.

Dawson, J. B. (1984). Contrasting types of upper-mantle metasomatism. *Kimberlites II: The Mantle and Crust-Mantle Relationships*, pages 289–294.

Day, R. A. (1983). *Petrology and geochemistry of the Older Volcanics, Victoria*. PhD thesis.

DeMets, C., Gordon, R. G., and Argus, D. F. (2010). Geologically current plate motions. *Geophysical Journal International*, 181:1–80.

Demidjuk, Z., Turner, S., Sandiford, M., George, R., Foden, J., and Etheridge, M. (2007). U-series isotope and geodynamic constraints on mantle melting processes beneath the Newer Volcanic Province in South Australia. *Earth and Planetary Science Letters*, 261:517–533.

DePaolo, D. J. (1981). Trace element and isotopic effects of combined wallrock assimilation and fractional crystallization. *Earth and Planetary Science Letters*, 53:189–202.

Downes, H. (2001). Formation and modification of the shallow sub-continental lithospheric mantle: A review of geochemical evidence from ultramatic xenolith suites and tectonically emplaced ultramafic massifs of Western and Central Europe. *Journal of Petrology*, 42(1):233–250.

Ducart, D. F., Silva, A. M., Toledo, C. L. B., and De Assis, L. M. (2016). Mapping iron oxides with Landsat-8/OLI and EO-1/Hyperion imagery from the Serra Norte iron deposits in the Carajás Mineral Province, Brazil. *Brazilian Journal of Geology*, 46(3):331–349.

Dulhunty, J. A. (1973). Potassium-argon basalt ages and their significance in the Macquarie Valley, New South Wales. *Journal and Proceedings of the Royal Society of New South Wales*, 106:104–110.

Dumoulin, C., Doin, M. P., Arcay, D., and Fleitout, L. (2005). Onset of small-scale instabilities at the base of the lithosphere: Scaling laws and role of pre-existing lithospheric structures. *Geophysical Journal International*, 160(1):345–357.

Duncan, R. A. and Kulm, L. D. (1989). Plate tectonic evolution of the Cascades arc-subduction complex. In Winterer, E. L., Hussong, D. M., and Decker, R. W., editors, *The Eastern Pacific Ocean and Hawaii*. The Geological Society of America, Inc.

Dupré, B. and Allègre, C. J. (1983). Pb-Sr isotope variation in Indian Ocean Basalts and mixing phenomena. *Nature*, 303(5913):142–146.

EarthByte (2006). GPlates Age Grid.

Eggins, S., Green, D. H., and Falloon, T. J. (1991). The Tasmantid Seamounts: shallow melting and contamination of an EM1 mantle plume. *Earth and Planetary Science Letters*, 107:448–462.

Eklundh, L. and Singh, A. (1993). A comparative analysis of standardised and unstandardised principal components analysis in remote sensing. *International Journal of Remote Sensing*, 14(7):1359–1370.

Elkins, L. J., Gaetani, G. A., and Sims, K. W. (2008). Partitioning of U and Th during garnet pyroxenite partial melting: Constraints on the source of alkaline ocean island basalts. *Earth and Planetary Science Letters*, 265(1-2):270–286.

Elkins-Tanton, L. T. (2007). Continental magmatism, volatile recycling, and a heterogeneous mantle caused by lithospheric gravitational instabilities. *Journal of Geophysical Research: Solid Earth*, 112(3):1–13.

Elkins Tanton, L. T., Van Orman, J. A., Hager, B. H., and Grove, T. L. (2002). Re-examination of the lunar magma ocean cumulate overturn hypothesis: Melting or mixing is required. *Earth and Planetary Science Letters*, 196(3-4):239–249.

Embleton, B. J. J., Schmidt, P. W., Hamilton, L. H., and Riley, G. H. (1985). Dating volcanism in the Sydney Basin: evidence from KAr ages and palaeomagnetism. *Volcanism in Eastern Australia with Case Histories in New South Wales*, 1:59–72.

Ewart, A. (1982). Petrogenesis of the Tertiary Anorogenic Volcanic Series of Southern Queensland, Australia, in the Light of Trace Element Geochemistry and O, Sr and Pb Isotopes*. *Journal of Geophysical Research: Solid Earth*, 23:344–382.

Ewart, A., Baxter, K., and Ross, J. A. (1980). The Petrology and Petrogenesis of the Tertiary Anorogenic Mafic Lavas of Southern and Central Queensland, Australia - Possible Implications for Crustal Thickening. *Contributions to Mineralogy and Petrology*, 75:129–152.

Ewart, A., Chappell, B. W., and Le Maitre, R. W. (1985). Aspects of the mineralogy and chemistry of the intermediate-silicic Cainozoic volcanic rocks of eastern Australia. Part 1: Introduction and geochemistry. *Australian Journal of Earth Sciences*, 32(4):359–382.

Ewart, A., Chappell, B. W., and Menzies, M. A. (1988). An Overview of the Geochemical and Isotopic Characteristics of the Eastern Australian Cainozoic Volcanic Provinces. *Journal of Petrology*, pages 225–273.

Exon, N. F., Langford-Smith, T., and McDougall, I. (1970). The age and geomorphic correlations of deep-weathering profiles, silcrete, and basalt in the roma-amby region, Queensland. *Journal of the Geological Society of Australia*, 17(1):21–30.

Facer, R. A. and Carr, P. F. (1979). K-Ar dating of Permian and Tertiary igneous activity in the southeastern Sydney Basin, New South Wales. *Journal of the Geological Society of Australia*, 26(1-2):73–79.

Farr, T. G., Rosen, P. A., Caro, E., Crippen, R., Duren, R., Hensley, S., Kobrick, M., Paller, M., Rodriguez, E., Roth, L., Seal, D., Shaffer, S., Shimada, J., Umland, J., Werner, M., Oskin, M., Burbank, D., and Alsdorf, D. (2007). The Shuttle Radar Topography Mission. *Reviews of Geophysics*, 45:1–33.

Farrington, R. J., Stegman, D. R., Moresi, L. N., Sandiford, M., and May, D. A. (2010). Interactions of 3D mantle flow and continental lithosphere near passive margins. *Tectonophysics*, 483:20–28.

Finn, C. A., Muller, R. D., and Panter, K. S. (2005). A Cenozoic diffuse alkaline magmatic province (DAMP) in the southwest Pacific without rift or plume origin. *Geochemistry, Geophysics, Geosystems*, 6(2).

Fishwick, S., Heintz, M., Kennett, B. L. N., Reading, A. M., and Yoshizawa, K. (2008). Steps in lithospheric thickness within eastern Australia, evidence from surface wave tomography. *Tectonics*, 27:1–17.

Fitton, J. G. (2007). The OIB paradox. *The Geological Society of America Special Paper*, 430:387–412.

Fitton, J. G. (2018). Personal Communication.

Fitton, J. G. and Dunlop, H. M. (1985). The Cameroon line, West Africa, and its bearing on the origin of oceanic and continental alkali basalt. *Earth and Planetary Science Letters*, 72(1):23–38.

Fitton, J. G. and Godard, M. (2004). Origin and evolution of magmas on the Ontong Java Plateau. In Fitton, J. G., Mahoney, J. J., Wallace, P. J., and Saunders, A. D., editors, *Origin and Evolution of the Ontong Java Plateau*, volume 229, pages 151–178. Geological Society, London, Special Publications.

Fitton, J. G. and James, D. (1986). Basic Volcanism Associated with Intraplate Linear Features. *Philosophical Transactions of the Royal Society of London*, 317:253–266.

Fitton, J. G., James, D., and Leeman, W. P. (1991). Basic magmatism associated with late Cenozoic extension in the western United States: compositional variations in space and time. *Journal of Geophysical Research*, 96(B8).

Fitton, J. G., Saunders, A. D., Norry, M. J., Hardarson, B. S., and Taylor, R. N. (1997). Thermal and chemical structure of the Iceland plume. *Earth and Planetary Science Letters*, 153(3-4):197–208.

Fitton, J. G., Williams, R., Barry, T. L., and Saunders, A. D. (2021). The role of lithospheric thickness in the formation of ocean islands and seamounts: contrasts between the Louisville and Emperor-Hawaiian hotspot trails. *Journal of Petrology*.

Foden, J., Song, S. H., Turner, S., Elburg, M., Smith, P. B., Van der Steldt, B., and Van Penglis, D. (2002). Geochemical evolution of lithospheric mantle beneath SE South Australia. *Chemical Geology*, 182:663–695.

Foulger, G. R. (2005). *Plates, plumes, and paradigms*. Geological Society of America.

Foulger, G. R. (2010). *Plates vs. Plumes: A Geological Controversy*. Blackwell Publishing Ltd.

Fujimaki, H., Tatsumoto, M., and Aoki, K.-i. (1984). Partition coefficients of Hf, Zr, and REE between phenocrysts and groundmasses. *Journal of Geophysical Research*, 89:662–672.

Gad, S. and Kusky, T. (2006). Lithological mapping in the Eastern Desert of Egypt, the Barramiya area, using Landsat thematic mapper (TM). *Journal of African Earth Sciences*, 44(2):196–202.

Gad, S. and Kusky, T. (2007). ASTER spectral ratioing for lithological mapping in the Arabian-Nubian shield, the Neoproterozoic Wadi Kid area, Sinai, Egypt. *Gondwana Research*, 11(3):326–335.

Gaina, C., Muller, R., Royer, J., Stock, J., Hardebeck, J., and Symonds, P. (1998). The tectonic history of the Tasman Sea : A puzzle with 13 pieces. *Journal of Geophysical Research*, 103:413–433.

Gaina, C., Muller, R. D., Brown, B. J., and Ishihara T (2003). Microcontinent formation around Australia. In Hillis, R. R. and Muller, R. D., editors, *Evolution and Dynamics of the Australian Plate*. The Geological Society of America, Inc.

Gaina, C., Muller, R. D., Royer, J.-Y., and Symonds, P. (1999). Evolution of the Louisiade triple junction. *Journal of Geophysical Research*, 104:927–939.

Gale, A., Dalton, C. A., Langmuir, C. H., Su, Y., and Schilling, J. G. (2013). *The mean composition of ocean ridge basalts*, volume 14.

Garver, J. I. (2008). Fission-track dating. In Gornitz, V., editor, *Encyclopedia of Paleoclimatology and Ancient Environments*, pages 247–249. Kluwer Academic Press.

Gaul, O. F., O'Reilly, S. Y., and Griffin, W. L. (2003). Lithosphere structure and evolution in southeastern Australia. In Hillis, R. R. and Muller, R. D., editors, *The Evolution and Dynamics of the Australian Plate*. The Geological Society of America, Inc.

GEBCO (2020). General Bathymetric Chart of the Oceans. *https://download.gebco.net/*.

GeoReM (2005). Geological and Environmental Reference Materials, Max Planck Institute for Chemistry, Mainz, Germany. *http://georem.mpch-mainz.gwdg.de/*.

GEOROC (1999). Geochemistry of Rocks of the Oceans and Continents, Max Planck Institute for Chemistry, Mainz, Germany. *http://georoc.mpch-mainz.gwdg.de/georoc/*.

GERM (2002). Geochemical Earth Reference Model. *https://earthref.org/KDD/*.

Ghorbani, M. R. and Middlemost, E. A. (2000). Geochemistry of pyroxene inclusions from the Warrumbungle Volcano, New South Wales, Australia. *American Mineralogist*, 85:1349–1367.

Gleadow, A. J. and Ollier, C. D. (1987). The age of gabbro at The Crescent, New South Wales. *Australian Journal of Earth Sciences*, 34(2):209–212.

Goetz, A. F. and Rowan, L. C. (1981). Geologic remote sensing. *Science*, 211(4484):781–791.

Google (2022a). Google Earth Engine Datasets.

Google (2022b). Google Earth Engine Guides.

Gorczyk, W., Hobbs, B., and Gerya, T. (2012). Initiation of Rayleigh-Taylor instabilities in intra-cratonic settings. *Tectonophysics*, 514-517:146–155.

Gordon, R. G. and Jurdy, D. M. (1986). Cenozoic global plate motions. *Journal of Geophysical Research: Solid Earth*, 91(B12):12389–12406.

Green, D. C. (1974). Isotope Geology Laboratory Report No 2. *University of Queensland, Department of Geology and Mineralogy*.

Green, D. C. and Stevens, N. C. (1975). Age and Stratigraphy of Tertiary Volcanic and Sedimentary Rocks of the Ipswich District, Southeast Queensland. *Queensland Government Mining Journal*, 76:148–150.

Green, T. H., Blundy, J. D., Adam, J., and Yaxley, G. M. (2000). SIMS determination of trace element partition coefficients between garnet, clinopyroxene and hydrous basaltic liquids at 2-7.5 GPa and 1080-1200C. *Lithos*, 53(3-4):165–187.

Grenfell, A. T. (1984). The stratigraphy, geochronology and petrology of the volcanic rocks of the Main Range, southeastern Queensland. *PhD Thesis, The University of Queensland*.

Griffin, T. (1977). The geology, mineralogy and geochemistry of the McBride basaltic province, Northern Queensland. *PhD Thesis, James Cook University of North Queensland*.

Griffin, T. J. and McDougall, I. (1975). Geochronology of the cainozoic mcbride volcanic province, Northern Queensland. *Journal of the Geological Society of Australia*, 22(4):387–396.

Griffin, W. L. and O'Reilly, S. Y. (1986). The lower crust in eastern Australia: xenolith evidence. *Geological Society Special Publication*, 24:363–374.

Griffin, W. L., O'Reilly, S. Y., Afonso, J. C., and Begg, G. C. (2009). The composition and evolution of lithospheric mantle: A re-evaluation and its tectonic implications. *Journal of Petrology*, 50(7):1185–1204.

Griffin, W. L., O'Reilly, S. Y., and Stabel, A. (1988). Mantle metasomatism beneath western Victoria, Australia: II. Isotopic geochemistry of Cr-diopside lherzolites and Al-augite pyroxenites. *Geochimica et Cosmochimica Acta*, 52(2):449–459.

Gupta, R. P. (2017). *Remote sensing geology: Third edition*. Springer US.

Hall, R. (2002). Cenozoic geological and plate tectonic evolution of SE Asia and the SW Pacific: Computer-based reconstructions, model and animations. *Journal of Asian Earth Sciences*, 20(4):353–431.

Hall, R. and Spakman, W. (2002). Subducted slabs beneath the eastern Indonesia-Tonga region: Insights from tomography. *Earth and Planetary Science Letters*, 201(2):321–336.

Halliday, A. N., Lee, D.-c., Tommasini, S., Davies, G. R., Paslick, C. R., Fitton, J. G., and James, D. E. (1995). Incompatible trace elements in OIB and MORB and source enrichment in the sub-oceanic mantle. *Earth and Planetary Science Letters*, 133:379–395.

Hansen, J. W. L., Muller, C. B., White, T. T., and Leach, L. M. (2020). Exploring for the Future Upper Burdekin Project: Stratigraphic and monitoring bore drilling programme. *Queensland Department of Environment and Science, Brisbane*.

Harding, R. (1969). Catalogue of Age Determinations on Australian Rocks. *Bureau of Mineral Resources, Geology and Geophysics*, 117.

Hart, S. R. (1984). A large-scale isotope anomaly in the Southern Hemisphere mantle. *Nature*, 309:753–757.

Hart, S. R., Hauri, E. H., Oschmann, J. A., and Whitehead, J. A. (1992). Mantle Plumes and Entrainment: Isotopic Evidence. *Science*, 256:517–520.

Harte, B., Hunter, R. H., and Kinny, P. D. (1993). Melt geometry, movement and crystallization, in relation to mantle dykes, veins and metasomatism. *Philosophical Transactions - Royal Society of London, A*, 342(1663):1–21.

Hassouna, H., Melgani, F., and Mokhtari, Z. (2015). Spatial contextual Gaussian process learning for remote-sensing image classification. *Remote Sensing Letters*, 6(7):519–528.

Hastie, A., Fitton, J. G., Bromiley, G., Butler, I., and Odling, N. (2016). The origin of Earth's first continents and the onset of plate tectonics. *Geology*.

Haxby, W. F. and Weissel, J. K. (1986). Evidence for Small-Scale Mantle Convection From Seasat Altimeter Data. *Journal of Geophysical Research: Solid Earth*, 91:3507–3520.

Heath, M., Phillips, D., and Matchan, E. L. (2020). Basalt lava flows of the intraplate Newer Volcanic Province in south-east Australia (Melbourne region): 40Ar/39Ar geochronology reveals ˜8 Ma of episodic activity. *Journal of Volcanology and Geothermal Research*, 389:106730.

Henderson, R. and Johnson, D. (2016). *The Geology of Australia*. Cambridge University Press, 3rd edition.

Henley, K. J. and Webb, A. (1990). Radiometric dating on various granites and Newer Volcanics basalts. *Geological Survey of Victoria Unpublished Report 1990/27*.

Hernlund, J. W., Tackley, P. J., and Stevenson, D. J. (2008). Buoyant melting instabilities beneath extending lithosphere: 1. Numerical models. *Journal of Geophysical Research: Solid Earth*, 113(4):1–17.

Herzberg, C. (2004). Partial crystallization of mid-ocean ridge basalts in the crust and mantle. *Journal of Petrology*, 45(12):2389–2405.

Hewson, R., Cudahy, T., and Huntington, J. (2001). Geologic and alteration mapping at Mt Fitton, South Australia, using ASTER satellite-borne data. *IEEE International Geoscience and Remote Sensing Proceedings*, pages 724–726.

Hill, K. C. and Hall, R. (2003). Mesozoic-Cenozoic evolution of Australia's New Guinea margin in a west Pacific context. In Hillis, R. R. and Muller, R. D., editors, *The Evolution and Dynamics of the Australian Plate*. The Geological Society of America, Inc.

Hillis, R. R. and Muller, R. D. (2003). Evolution and Dynamics of the Australian Plate. *Geological Society of Australia Special Publication*, 22.

Hofmann, A. W. (1997). Mantle geochemistry: the message from oceanic volcanism. *Nature*, 385:219–229.

Hofmann, A. W., Jochum, K. P., Seufert, M., and White, W. M. (1986). Nb and Pb in oceanic basalts: new constraints on mantle evolution. *Earth and Planetary Science Letters*, 79(1-2):33–45.

Hofmann, A. W. and White, W. M. (1982). Mantle plumes from ancient oceanic crust. *Earth and Planetary Science Letters*, 57:421–436.

Holm, R. J., Rosenbaum, G., and Richards, S. W. (2016). Post 8 Ma reconstruction of Papua New Guinea and Solomon Islands: Microplate tectonics in a convergent plate boundary setting. *Earth-Science Reviews*, 156:66–81.

Houseman, G. A. and Molnar, P. (1997). Gravitational (Rayleigh-Taylor) instability of a layer with non-linear viscosity and convective thinning of continental lithosphere. *Geophysical Journal International*, 128(1):125–150.

Huang, J. and Zhong, S. (2005). Sublithospheric small-scale convection and its implications for the residual topography at old ocean basins and the plate model. *Journal of Geophysical Research: Solid Earth*, 110(5):1–17.

Humphreys, E. and Dueker, K. (1994). Western U.S. upper mantle structure. *Journal of Geophysical Research*, 99:9615–9634.

Humphreys, E. R. and Niu, Y. (2009). On the composition of ocean island basalts (OIB): The effects of lithospheric thickness variation and mantle metasomatism. *Lithos*, 112:118–136.

Ionov, D. A., Bodinier, J. L., Mukasa, S. B., and Zanetti, A. (2002). Mechanisms and sources of mantle metasomatism: Major and trace element compositions of peridotite xenoliths from Spitsbergen in the context of numerical modelling. *Journal of Petrology*, 43(12):2219–2259.

Ito, E., White, W. M., and Göpel, C. (1987). The O, Sr, Nd and Pb isotope geochemistry of MORB. *Chemical Geology*, 62(3-4):157–176.

Ito, G. and Mahoney, J. J. (2005). Flow and melting of a heterogeneous mantle: 1. Method and importance to the geochemistry of ocean island and mid-ocean ridge basalts. *Earth and Planetary Science Letters*, 230:29–46.

Iwamori, H. and Nakamura, H. (2015). Isotopic heterogeneity of oceanic, arc and continental basalts and its implications for mantle dynamics. *Gondwana Research*, 27(3):1131–1152.

Johnson, D. (2009). *The Geology of Australia*. Cambridge University Press.

Johnson, K. (1994). Experimental cpx/ and garnet/melt partitioning of REE and other trace elements at high pressures; petrogenetic implications. *Mineralogical Magazine*, 58:454–455.

Johnson, R. W. (1989). *Intraplate Volcanism in Eastern Australia and New Zealand*.

Jones, I., Ubide, T., Crossingham, T., Wilding, B., and Verdel, C. (2020). Evidence of a common source component for east Australian Cenozoic mafic magmatism. *Lithos*, 354-355:105254.

Jones, I. and Verdel, C. (2015). Basalt distribution and volume estimates of Cenozoic volcanism in the Bowen Basin region of eastern Australia : Implications for a waning mantle plume. *Australian Journal of Earth Sciences*, 62(2):255–263.

Jones, I., Verdel, C., Crossingham, T., and Vasconcelos, P. (2017). Animated reconstructions of the late cretaceous to cenozoic northward migration of Australia, and implications for the generation of east Australian mafic magmatism. *Geosphere*, 13(2).

Jones, I. M. (2018). Evolution and migration of Cenozoic Australia: Precision 40Ar/39Ar geochronology, geochemistry and paleomagnetic data from east Australian Cenozoic magmas. *PhD Thesis, The University of Queensland*.

Jones, J. (2002). *UQ Hons Thesis*. PhD thesis.

Kaleliolu, Ö., Zorlu, K., Kurt, M. A., Gül, M., and Güler, C. (2009). Delineating compositionally different dykes in the Ulukla basin (Central Anatolia, Turkey) using computer-enhanced multi-spectral remote sensing data. *International Journal of Remote Sensing*, 30(11):2997–3011.

Kalinowski, A. and Oliver, S. (2004). ASTER Mineral Index Processing Manual. *Remote Sensing Applications, Geoscience Australia*, 37(36).

Kalnins, L. M., Cohen, B. E., Fitton, J. G., and Mark, D. E. (2020). Volcanism in east Australia and the Tasman Sea: Mechanisms behind three parallel hotspot trails. *Workshop: Feedbacks between mantle composition, structure, and evolution*, 14-16(online).

Kalnins, L. M., Cohen, B. E., Fitton, J. G., Mark, D. F., Richards, F. D., and Barfod, D. N. (2015). The East Australian, Tasmantid, and Lord Howe Volcanic Chains: Possible mechanisms behind a trio of hotspot trails. *AGU Abstract*.

Kelemen, P. B., Shimizu, N., and Dunn, T. (1993). Relative depletion of niobium in some arc magmas and the continental crust: partitioning of K, Nb, La and Ce during melt/rock reaction in the upper mantle. *Earth and Planetary Science Letters*, 120:111–134.

Kempton, P. D., Fitton, J. G., Hawkesworth, C. J., and Ormerod, D. S. (1991). Isotopic and Trace Element Constraints on the Composition and Evolution of the Lithosphere Beneath the Southwestern United States. *Journal of Geophysical Research*, 96.

Kennett, B. L., Fishwick, S., Reading, A. M., and Rawlinson, N. (2004). Contrasts in mantle structure beneath Australia: Relation to Tasman Lines? *Australian Journal of Earth Sciences*, 51(4):563–569.

Kennett, B. L. N. (2003). Seismic structure in the mantle beneath Australia. In Hillis, R. R. and Muller, R. D., editors, *The Evolution and Dynamics of the Australian Plate*. The Geological Society of America, Inc.

Kesson, S. E. (1973). The Primary Geochemistry of the Monaro Alkaline Voleanics, Southeastern Australia - Evidence for Upper Mantle Heterogeneity. *Contributions to Mineralogy and Petrology*, 42:93–108.

Khan, S., Mahmood, K., and Casey, J. (2007). Mapping of Muslim Bagh ophiolite complex (Pakistan) using new remote sensing, and field data. *Journal of Asian Earth Sciences*, 30:333–343.

King, S. D. and Anderson, D. L. (1998). Edge-driven convection. *Earth and Planetary Science Letters*, 160(3-4):289–296.

King, S. D. and Ritsema, J. (2000). African hot spot volcanism: Small-scale convection in the upper mantle beneath cratons. *Science*, 290(5494):1137–1140.

Knesel, K., Cohen, B., Vasconcelos, P., and Thiede, D. (2008). Rapid change in drift of the Australian plate records collision with Ontong Java plateau. *Nature*, 454:754–757.

Knipling, E. B. (1970). Physical and physiological basis for the reflectance of visible and near-infrared radiation from vegetation. *Remote sensing of environment*, 1(3):155–159.

Kokaly, R. F., Clark, R. N., Swayze, G. A., Livo, K. E., Hoefen, T. M., Pearson, N. C., and Klein, A. J. (2017). *Usgs spectral library version 7 data: Us geological survey data release*. United States Geological Survey (USGS): Reston, VA, USA.

Korenaga, J. and Jordan, T. H. (2002). Onset of convection with temperature- and depth-dependent viscosity. *Geophysical Research Letters*, 29(19):10–13.

Kroenke, L. W., Wessel, P., and Sterling, A. (2004). Motion of the Ontong Java Plateau in the hot-spot frame of reference: 122 Ma-present. In Fitton, J. G., Mahoney, J. J., Wallace, P. J., and Saunders, A. D., editors, *Origin and Evolution of the Ontong Java Plateau*, volume 229, pages 9–20. Geological Society, London, Special Publications.

Laat, J. I. D., Lebedev, S., Celli, N. L., Bonadio, R., Melo, B. C. D., and Rawlinson, N. (2021). Structure and evolution of the Australian Plate and underlying upper mantle from waveform tomography with massive datasets. pages 1–73.

Lane, R., Wynne, P., Poudjom Djomani, Y., Stratford, W.R. Barretto, J., and Caratori Tontini, F. (2019). 2019 Australian National Gravity Grids: Free Air Anomaly, Complete Bouguer Anomaly, De-trended Global Isostatic Residual.

Langford, R. L. (2015). Temporal merging of remote sensing data to enhance spectral regolith, lithological and alteration patterns for regional mineral exploration. *Ore Geology Reviews*, 68:14–29.

Langmuir, C. H., Goldstein, S. L., Donnelly, K., and Su, Y. J. (2005). No Title. *American Geophysical Union, Fall Meeting*.

Lanyon, R., Varne, R., and Crawford, A. J. (1993). Tasmanian Tertiary basalts, the Balleny plume, and opening of the Tasman Sea (southwest Pacific Ocean). *Geology*, 21:555–558.

Le Pourhiet, L., Gurnis, M., and Saleeby, J. (2006). Mantle instability beneath the Sierra Nevada Mountains in California and Death Valley extension. *Earth and Planetary Science Letters*, 251(1-2):104–119.

Li, C., van der Hilst, R. D., Engdahl, E. R., and Burdick, S. (2008). A new global model for P wave speed variations in Earth's mantle. *Geochemistry, Geophysics, Geosystems*, 9(5).

Lloyd, F. and Bailey, D. (1975). *Light Element Metasomatism of the Continental Mantle: the Evidence and the Consequences*. Pergamon Press Ltd.

Lum, C. C., Leeman, W. P., Foland, K. A., Kargel, J. A., and Fitton, J. G. (1989). Isotopic variations in continental basaltic lavas as indicators of mantle heterogeneity: examples from the western US Cordillera. *Journal of Geophysical Research*, 94(B6):7871–7884.

Luth, R. W. (2003). Mantle Volatiles-Distribution and Consequences. *Treatise on Geochemistry*, 2-9:319–361.

Macphail, M. and Gibson, D. (2014). Testing the Gippsland Basin zonation in northern Australia: Palynostratigraphical analysis of a 23 Ma 40Ar/39Ar dated claystone from Toowoomba, southeast Queensland. *Palynology*, 38(1):117–128.

MacQueen, J. (1967). Some methods for classification and analysis of multivariate observations. *Proceedings of the fifth Berkeley symposium on mathematical statistics and probability*, 1(14):281–297.

Mahoney, J. J. and Spencer, K. J. (1991). Isotopic evidence for the origin of the Manihiki and Ontong Java oceanic plateaus. *Earth and Planetary Science Letters*, 104(2-4):196–210.

Mann, P. and Taira, A. (2004). Global tectonic significance of the Solomon Islands and Ontong Java Plateau convergent zone. *Tectonophysics*, 389:137–190.

Martinez, F. and Taylor, B. (1996). Backarc spreading, rifting, and microplate rotation, between transform faults in the Manus Basin. *Marine Geophysical Researches*, 18(2):203–224.

Matchan, E. L., Honda, M., Barrows, T. T., Phillips, D., Chivas, A. R., Fifield, L. K., and Fabel, D. (2018). Production of 21Ne in depth-profiled olivine from a 54 Ma basalt sequence, Eastern Highlands (37 S), Australia. *Geochimica et Cosmochimica Acta*, 220:276–290.

Matthews, K. J., Seton, M., Flament, N., and Müller, R. D. (2012). Late Cretaceous to present-day opening of the southwest Pacific constrained by numerical models and seismic tomography Southwest Pacific plate model. *Eastern Australasian Basins Symposium IV*, pages 10–14.

McBride, J. S., Lambert, D. D., Nicholls, I. A., and Price, R. C. (2001). Osmium Isotopic Evidence for CrustMantle Interaction in the Genesis of Continental Intraplate Basalts from the Newer Volcanics Province, Southeastern Australia. *Journal of Petrology*, 42(6):1197–1218.

McDonough, W. F., McCulloch, M. T., and Sun, S. S. (1985). Isotopic and geochemical systematics in Tertiary-Recent basalts from southeastern Australia and implications for the evolution of the sub-continental lithosphere. *Geochimica et Cosmochimica Acta*, 49:2051–2067.

McDougall, I. and Duncan, R. A. (1988). Age progressive volcanism in the Tasmantid Seamounts. *Earth and Planetary Science Letters*, 89:207–220.

McDougall, I., Embleton, B. J. J., and Stone, D. B. (1981). Origin and evolution of Lord Howe Island, Southwest Pacific Ocean. *Journal of the Geological Society of Australia*, 28:155–176.

McDougall, I. and Roksandic, Z. (1974). Total fusion 40Ar/39Ar ages using hifar reactor. *Journal of the Geological Society of Australia*, 21(1):81–89.

McDougall, I. and Slessar, G. C. (1972). Tertiary volcanism in the cape hillsborough area, North Queensland. *Journal of the Geological Society of Australia*, 18(4):401–408.

McDougall, I. and Wilkinson, J. F. (1967). Potassiumargon dates on some cainozoic volcanic rocks from northeastern new south wales. *Journal of the Geological Society of Australia*, 14(2):225–233.

McKenzie, D. (1989). Some remarks on the movement of small melt fractions in the mantle. *Earth and Planetary Science Letters*, 95:53–72.

McKenzie, D., Jackson, J., and Priestley, K. (2005). Thermal structure of oceanic and continental lithosphere. *Earth and Planetary Science Letters*, 233(3-4):337–349.

McKenzie, D. and O'Nions, R. K. (1991). Partial melt coefficients from inversion of rare earth element concentrations. *Journal of Petrology*, 32:1021–1091.

McKenzie, D. A., Nott, R. J., and Bolger, P. F. (1984). Radiometric age determinations. Victorian Geological Survey Report #74. *Geological Survey of Victoria*.

McLaren, S., Wallace, M. W., Gallagher, S. J., Dickinson, J. A., and McAllister, A. (2009). Age constraints on Oligocene sedimentation in the Torquay Basin, southeastern Australia. *Australian Journal of Earth Sciences*, 56(4):595–604.

Meeuws, F., Foden, J., Holford, S., and Marnie, A. (2019). Geochemical constraints on Cenozoic intraplate magmatism and their relation to Jurassic dolerites in Tasmania, using Sr-Nd-Pb isotopes. *Chemical Geology*.

Menzies, M. A. and Wass, S. Y. (1983). CO 2- and LREE-rich mantle below eastern Australia: a REE and isotopic study of alkaline magmas and apatite-rich mantle xenoliths from the Southern Highlands Province, Australia. *Earth and Planetary Science Letters*, 65:287–302.

Middlemost, E. A. (1981). The Canobolas complex, N.S.W., an alkaline shield volcano. *Journal of the Geological Society of Australia*, 28(1-2):33–49.

Mineral Resources Tasmania and Tasmanian Government (2022). TIGER Database.

Mishra, A. K., Placzek, C., Wurster, C., and Whitehead, P. W. (2019). New radiocarbon age constraints for the 120 km-long Toomba flow, north Queensland, Australia. *Australian Journal of Earth Sciences*, 66(1):71–79.

Montelli, R., Nolet, G., Dahlen, F. A., Masters, G., Engdahl, E. R., and Hung, S. (2004). Finite-Frequency Tomography Reveals a Variety of Plumes in the Mantle. *Science*, 303:338–343.

Morency, C., Doin, M. P., and Dumoulin, C. (2002). Convective destabilization of a thickened continental lithosphere. *Earth and Planetary Science Letters*, 202(2):303–320.

Morgan, W. (1971). Convection Plumes in the Lower Mantle. *Nature*, 230:42–43.

Mortimer, N., Gans, P. B., Meffre, S., Martin, C. E., Seton, M., Williams, S., Turnbull, R. E., Quilty, P. G., Micklethwaite, S., Timm, C., Sutherland, R., Bache, F., Collot, J., Maurizot, P., Rouillard, P., and Rollet, N. (2017). Regional volcanism of northern Zealandia: Post-Gondwana break-up magmatism on an extended, submerged continent. *Geological Society Special Publication*, 463(1):199–226.

Mortimer, N., Gans, P. B., Palin, J. M., Meffre, S., Herzer, R. H., and Skinner, D. N. (2010). Location and migration of Miocene-Quaternary volcanic arcs in the SW Pacific region. *Journal of Volcanology and Geothermal Research*, 190:1–10.

Mortimer, N., Herzer, R., Gans, P., Parkinson, D., and Seward, D. (1998). Basement geology from Three Kings Ridge to West Norfolk Ridge, southwest Pacific Ocean: evidence from petrology, geochemistry and isotopic dating of dredge samples. *Marine Geology*, 148:135–162.

Muller, R. D., Gaina, C., and Clark, S. (2000). Seafloor spreading around Australia. In Veevers, J. J., editor, *Billion-year earth history of Australia and neighbours in Gondwanaland*.

Muller, R. D., Royer, J. Y., and Lawver, L. A. (1993). Revised plate motions relative to the hotspots from combined atlantic and indian-ocean hotspot tracks. *Geology*, 21:275–278.

Myers, J. S., Shaw, R. D., and Tyler, I. M. (1996). Tectonic evolution of Proterozoic Australia. *Tectonics*, 15(6):1431–1446.

NASA Jet Propulsion Laboratory (JPL) (2022). Shuttle Radar Topography Mission.

Nasir, S. J., Everard, J. L., Mcclenaghan, M. P., Bombardieri, D., and Worthing, M. A. (2010). The petrology of high pressure xenoliths and associated Cenozoic basalts from Northeastern Tasmania. *Lithos*, 118:35–49.

Nelson, D. R., McCulloch, M. T., and Sun, S. S. (1986). The origins of ultrapotassic rocks as inferred from Sr, Nd and Pb isotopes. *Geochimica et Cosmochimica Acta*, 50:231–245.

New South Wales Government (2022). MinView Regional NSW.

Ninomiya, Y., Fu, B., and Cudahy, T. J. (2005). Detecting lithology with Advanced Spaceborne Thermal Emission and Reflection Radiometer (ASTER) multispectral thermal infrared radiance-at-sensor" data. *Remote Sensing of Environment*, 99:127–139.

Niu, Y. and O'Hara, M. J. (2003). Origin of ocean island basalts: A new perspective from petrology, geochemistry, and mineral physics considerations. *Journal of Geophysical Research: Solid Earth*, 108(B4).

Niu, Y., Wilson, M., Humphreys, E., and O'Hara, M. J. (2012). A trace element perspective on the source of ocean island basalts (OIB) and fate of subducted ocean crust (SOC) and mantle lithosphere A trace element perspective on the source of ocean island basalts (OIB) and fate of subducted ocean crust (SOC). *Episodes*, 35(June):310–327.

Nott, J., Young, R., and McDougall, I. (1996). Wearing down, wearing back, and Gorge extension in the long-term denudation of a highland mass: Quantitative evidence from the Shoalhaven catchment, southeast Australia. *Journal of Geology*, 104(2):224–232.

O'Neill, C., Moresi, L., Lenardic, A., and Cooper, C. M. (2003). Inferences on Australia's heat flow and thermal structure from mantle convection modelling results. In Hillis, R. R. and Muller, R. D., editors, *The Evolution and Dynamics of the Australian Plate*. The Geological Society of America, Inc.

Oostingh, K., Jourdan, F., Matchan, E., and Phillips, D. (2017). 40Ar/39Ar geochronology reveals rapid change from plume-assisted to stress-dependent volcanism in the Newer Volcanic Province, SE Australia. *Geochemistry, Geophysics, Geosystems*, 18:1065–1089.

Oostingh, K. F., Jourdan, F., Merle, R., and Chiaradia, M. (2016). Spatio-temporal Geochemical Evolution of the SE Australian Upper Mantle Deciphered from the Sr, Nd and Pb Isotope Compositions of Cenozoic Intraplate Volcanic Rocks. *Journal of Petrology*, 57(8):1509–1530.

O'Reilly, S. and Griffin, W. (1984). Sr isotopic heterogeneity in primitive basaltic rocks , southeastern Australia : correlation with mantle metasomatism. *Contributions to Mineralogy and Petrology*, 87:220–230.

O'Reilly, S. and Griffin, W. (1988). Mantle metasomatism beneath western Victoria , Australia : I . Metasomatic processes in Cr-diopside lherzolites. *Geochimica et Cosmochimica Acta*, 52:433–447.

O'Reilly, S. and Griffin, W. (2013). Mantle metasomatism. In *Metasomatism and the chemical transformation of rock*, pages 471–533. Springer, Heidelberg.

O'Reilly, S. Y. and Zhang, M. (1995). Geochemical characteristics of lava-field basalts from eastern Australia and inferred sources: connections with the subcontinental lithospheric mantle? *Contributions to Mineralogy and Petrology*, 121:148–170.

Owen, M. and Wyborn, D. (1979). Geology and Geochemistry of the Tantangara and Brindabella 1: 100000 Sheet Areas. New South Wales and Australian Capital Territory. *Bureau of Mineral Resources Bulletin*, 204.

Pain, C. F. (1983). Geomorphology of the barrington tops area, New South Wales. *Journal of the Geological Society of Australia*, 30(1-2):187–194.

Palmieri, V. (1984). Neogene Foraminiferida from GSQ Sandy Cape 1-3R Bore, Queensland: A Biostratigraphic Appraisal. 46:165–183.

Papp, E. and Cudahy, T. (2002). Hyperspectral remote sensing. *Geophysical and Remote Sensing Methods for Regolith Exploration*, 144:13–21.

Parson, L. M., Rothwell, R. G., and MacLeod, C. J. (1994). Tectonics and sedimentation in the Lau Basin (southwest Pacific). *Proceedings of the Ocean Drilling Program, Scientific Results*, 135:9–21.

Paul, B., Hergt, J., and Woodhead, J. (2005). Mantle heterogeneity beneath the Cenozoic volcanic provinces of central Victoria inferred from trace-element and Sr, Nd, Pb and Hf isotope data. *Australian Journal of Earth Sciences*, 52(2):243–260.

Petersen, K. D., Schiffer, C., and Nagel, T. (2018). LIP formation and protracted lower mantle upwelling induced by rifting and delamination. *Scientific Reports*, 8(1):1–11.

Petterson, M. G., Babbs, T., Neal, C. R., Mahoney, J. J., Saunders, A. D., Duncan, R. A., Tolia, D., Magu, R., Qopoto, C., Mahoa, H., and Natogga, D. (1999). Geological-tectonic framework of Solomon Islands, SW Pacific: crustal accretion and growth within an intra-oceanic setting. *Tectonophysics*, 301:35–60.

Petterson, M. G., Neal, C. R., Mahoney, J. J., Kroenke, L. W., Saunders, A. D., Babbs, T. L., Duncan, R. A., Tolia, D., and McGrail, B. (1997). Structure and deformation of north and central Malaita, Solomon Islands: tectonic implications for the Ontong Java Plateau-Solomon arc collision, and for the fate of oceanic plateaus. *Tectonophysics*, 283:1–33.

Pigram, C. J. and Davies, H. L. (1987). Terranes and the accretion history of the New Guinea orogen. *AGSO Journal of Australian Geology & Geophysics*, 10(3).

Pilet, S., Baker, M., and Stolper, E. (2008). Metasomatized Lithosphere and the Origin of Alkaline Lavas. *Science*, 320(May):916–920.

Pilet, S., Baker, M. B., Müntener, O., and Stolper, E. M. (2011). Monte Carlo simulations of metasomatic enrichment in the lithosphere and implications for the source of alkaline basalts. *Journal of Petrology*, 52(7-8):1415–1442.

Poudjom Djomani, Y. and Minty, B. (2019). Total Magnetic Intensity (TMI) Grid of Australia with Variable Reduction to Pole (VRTP) 2019 - seventh edition.

Price, R. C., Gray, C. M., and Frey, F. A. (1997). Strontium isotopic and trace element heterogeneity in the plains basalts of the Newer Volcanic Province, Victoria, Australia. *Geochimica et Cosmochimica Acta*, 61(1):171–192.

Price, R. C., Nicholls, I. A., and Day, A. (2014). Lithospheric influences on magma compositions of late Mesozoic and Cenozoic intraplate basalts (the Older Volcanics) of Victoria, south-eastern Australia. *Lithos*, 206-207:179–200.

Quarles van Ufford, A. and Cloos, M. (2005). Cenozoic tectonics of New Guinea. *AAPG Bulletin*, 89(1):119–140.

Queensland Government (2022). Queensland Spatial Catalogue.

Quigley, M. C., Clark, D., and Sandiford, M. (2010). Tectonic geomorphology of Australia. In Bishop, P. and Pillans, B., editors, *Australian Landscapes*, volume 346, pages 243–265. Geological Society, London, Special Publications.

Quilty, P. G. (1993). Tasmantid and Lord Howe seamounts: biostratigraphy and palaeoceanographic significance. *Alcheringa*, 17(1):27–53.

Raddick, M. J., Parmentier, E. M., and Scheirer, D. S. (2002). Buoyant decompression melting: A possible mechanism for intraplate volcanism. *Journal of Geophysical Research: Solid Earth*, 107(B10).

Ramadan, T. M. and Kontny, A. (2004). Mineralogical and structural characterization of alteration zones detected by orbital remote sensing at Shalatein District, SE Desert, Egypt. *Journal of African Earth Sciences*, 40(1-2):89–99.

Ransley, T. R., Dixon-jain, P., Cook, S. B., Lai, E. C. S., Kilgour, P., Wallace, L., Dunn, B., Hansen, J. W. L., and Herbert, G. (2020). Hydrogeology of the McBride and Nulla basalt provinces in the Upper Hydrogeology of the McBride and Nulla basalt provinces in the Upper Burdekin region , north Queensland. *Geoscience Australia*, (July).

Rawlinson, N., Davies, D. R., and Pilia, S. (2017). The mechanisms underpinning Cenozoic intraplate volcanism in eastern Australia: Insights from seismic tomography and geodynamic modeling. *Geophysical Research Letters*, 44.

Regelous, M., Hofmann, A. W., Abouchami, W., and Galer, S. J. (2003). Geochemistry of lavas from the Emperor Seamounts, and the geochemical evolution of Hawaiian magmatism from 85 to 42 Ma. *Journal of Petrology*, 44(1):113–140.

Richards, F. (2014). The Origin, Structural Evolution and Potential Field Signatures of the Tasmantid Seamount Chain. *MSc Thesis, University of Oxford*.

Richards, F. D., Kalnins, L. M., Watts, A. B., Cohen, B. E., and Beaman, R. J. (2018). The Morphology of the Tasmantid Seamounts: Interactions Between Tectonic Inheritance and Magmatic Evolution. *Geochemistry, Geophysics, Geosystems*, 19(10):3870–3891.

Richter, F. M. and Parsons, B. (1975). On the Interaction of Two Scales of Convection in the Mantle. *Journal of Geophysical Research*, 80(17).

Ringwood, A. E. (1974). The petrological evolution of island arc systems. *Journal of the Geological Society*, 130(3):183–204.

Ritsema, J. and Allen, R. M. (2003). The elusive mantle plume. *Earth and Planetary Science Letters*, 207(1-4):1–12.

Roach, I. C., Hill, S. M., and Lewis, A. C. (2008). Evolution of a small intraplate basaltic lava field: Jerrabattgulla Creek, upper Shoalhaven River catchment, southeast New South Wales. *Australian Journal of Earth Sciences*, 55(8):1049–1061.

Robertson, A. D. (1979). Origin of the'mystery craters' of south Kolan, Bundaberg area. *Queensland Government Mining Journal*, 80:448–449.

Robertson, A. D. (1993). *Bundaberg volcanic province. Queensland Geology*. PhD thesis.

Robertson, A. D. C. and Sutherland, F. L. (1992). Possible origins and ages for sapphire and diamond from the central Queensland gem fields. *Records of the Australian Museum, Supplement*, 15(1992):45–54.

Rockwell, B. W. and Hofstra, A. H. (2008). Identification of quartz and carbonate minerals across northern Nevada using aster thermal infrared emissivity data-implications for geologic mapping and mineral resource investigations in well-studied and frontier areas. *Geosphere*, 4(1):218–246.

Rowan, L. C. and Mars, J. C. (2003). Lithologic mapping in the Mountain Pass, California area using Advanced Spaceborne Thermal Emission and Reflection Radiometer (ASTER) data. *Remote Sensing of Environment*, 84:350–366.

Rowan, L. C., Mars, J. C., and Simpson, C. J. (2005). Lithologic mapping of the Mordor, NT, Australia ultramafic complex by using the Advanced Spaceborne Thermal Emission and Reflection Radiometer (ASTER). *Remote Sensing of Environment*, 99:105–126.

Rowan, L. C., Schmidt, R. G., and Mars, J. C. (2006). Distribution of hydrothermally altered rocks in the Reko Diq, Pakistan mineralized area based on spectral analysis of ASTER data. *Remote Sensing of Environment*, 104(1):74–87.

Rudnick, R. L. and Fountain, D. M. (1995). Nature and Composition of the Continental Crust: A Lower Crustal Perspective. *Reviews of Geophysics*, (95):1–43.

Ruttor, S. (2021). Personal Communication.

Ruttor, S., Nebel, O., Nebel-Jacobsen, Y., Smethurst, A., Cohen, B., and Eggins, S. (2018). On the depth of melting of enriched components in the Tasmantid mantle plume. *Abstract*.

Ruxton, B. P. and Taylor, G. (1982). The Cainozoic geology of the Middle Shoalhaven Plain. *Journal of the Geological Society of Australia*, 29(1-2):239–246.

Sabins, F. F. (1999). Remote sensing for mineral exploration. *Ore Geology Reviews*, 14:157–183.

Saki, M., Thomas, C., Nippress, S., and Lessing, S. (2015). Topography of upper mantle seismic discontinuities beneath the North Atlantic: The Azores, Canary and Cape Verde plumes. *Earth and Planetary Science Letters*, 409:193–202.

Salisbury, J. and D'Aria, D. (1992). Emissivity of Terrestrial Materials in the 8-14 / tm Atmospheric Window. *Remote Sensing of Environment*, 42:83–106.

Salisbury, J. W., D'Aria, D. M., and Jarosewich, E. (1991). Midinfrared (2.513.5 μm) reflectance spectra of powdered stony meteorites. *Icarus*, 92(2):280–297.

Salters, V. J. and Longhi, J. (1999). Trace element partitioning during the initial stages of melting beneath mid-ocean ridges. *Earth and Planetary Science Letters*, 166(1-2):15–30.

Schellart, W. P. (2007). Northeastward subduction followed by slab detachment to explain ophiolite obduction and Early Miocene volcanism in Northland, New Zealand. *Terra Nova*, 19(3):211–218.

Schellart, W. P., Kennett, B. L. N., Spakman, W., and Amaru, M. (2009). Plate reconstructions and tomography reveal a fossil lower mantle slab below the Tasman Sea. *Earth and Planetary Science Letters*, 278:143–151.

Schellart, W. P., Lister, G. S., and Toy, V. G. (2006). A Late Cretaceous and Cenozoic reconstruction of the Southwest Pacific region: Tectonics controlled by subduction and slab rollback processes. *Earth-Science Reviews*, 76:191–233.

Schilling, J.-G. (1973). Iceland mantle plume: geochemical evidence along Reykjanes Ridge. *Nature*, 242(5400):565–571.

Sdrolias, M., Muller, R., and Gaina, C. (2003). Tectonic evolution of the SW Pacific using constraints from back-arc basins. In Hillis, R. R. and Muller, R. D., editors, *The Evolution and Dynamics of the Australian Plate*, pages 343–359. The Geological Society of America, Inc.

Sdrolias, M., Müller, R. D., and Gaina, C. (2001). Plate tectonic evolution of eastern Australian marginal ocean basins. *PESA Eastern Australian Basins Symposium*, (November):25–28.

Sdrolias, M., Muller, R. D., Mauffret, A., and Bernardel, G. (2004). Enigmatic formation of the Norfolk Basin, SW Pacific: A plume influence on back-arc extension. *Geochemistry, Geophysics, Geosystems*, 5(6).

Sella, G. F., Dixon, T. H., and Mao, A. (2002). REVEL: A model for Recent plate velocities from space geodesy. *Journal of Geophysical Research*, 107.

Seton, M., Muller, R. D., Zahirovic, S., Gaina, C., Torsvik, T., Shephard, G., Talsma, A., Gurnis, M., Turner, M., Maus, S., and Chandler, M. (2012). Global continental and ocean basin reconstructions since 200Ma. *Earth-Science Reviews*, 113:212–270.

Seton, M., Williams, S., Mortimer, N., and Meffre, S. (2019a). Magma production along the Lord Howe Seamount Chain, northern Zealandia. *Geological Magazine*.

Seton, M., Williams, S., Mortimer, N., Meffre, S., Micklethwaite, S., and Zahirovic, S. (2019b). Magma production along the Lord Howe Seamount Chain, northern Zealandia. *Geological Magazine*, 156(9):1605–1617.

Shankar, P. and Deshpande, M. (2000). Fluid Mechanics in the Driven Cavity. *Annual Review of Fluid Mechanics*, 32:93–136.

Shao, F., Niu, Y., Regelous, M., and Zhu, D.-c. (2015). Petrogenesis of peralkaline rhyolites in an intra-plate setting: Glass House Mountains, southeast Queensland, Australia. *Lithos*, 216-217:196–210.

Sharp, K. R. (2004). Cenozoic volcanism, tectonism and stream derangement in the Snowy Mountains and northern Monaro of New South Wales. *Australian Journal of Earth Sciences*, 51(1):67–85.

Sharp, W. D. and Clague, D. A. (2006). 50-Ma Initiation of Hawaiian-Emperor Bend Records Major Change in Pacific Plate Motion. *Science*, 313:1281–1284.

Shaw, D. M. (1970). Trace element fractionation during anatexis. *Geochimica et Cosmochimica Acta*, 34(2):237–243.

Shaw, R. D., Wellman, P., Gunn, P., Whittaker, J., Tarlowski, C., and Morse, M. (1996). Australian Crustal Elements. *Australian Geological Survey Organisation Record 1996/30*.

Silver, P. G. and Holtz, W. E. (2002). The mantle flow field beneath Western North America. *Science*, 295(5557):1054–1057.

Simmons, N. A., Forte, A. M., Boschi, L., and Grand, S. P. (2010). GyPSuM: A joint tomographic model of mantle density and seismic wave speeds. *Journal of Geophysical Research: Solid Earth*, 115(B12).

Sims, K. W., Ackert, R. P., Ramos, F. C., Sohn, R. A., Murrell, M. T., and DePaolo, D. J. (2007). Determining eruption ages and erosion rates of Quaternary basaltic volcanism from combined U-series disequilibria and cosmogenic exposure ages. *Geology*, 35(5):471–474.

Spandler, C., Rubatto, D., and Hermann, J. (2005). Late Cretaceous-Tertiary tectonics of the southwest Pacific: Insights from U-Pb sensitive, high-resolution ion microprobe (SHRIMP) dating of eclogite facies rocks from New Caledonia. *Tectonics*, 24(3):1–16.

Spry, M. J., Gibson, D. L., and Eggleton, R. A. (1999). Tertiary evolution of the coastal lowlands and the Clyde River palaeovalley in southeast New South Wales. *Australian Journal of Earth Sciences*, 46(2):173–180.

Stephenson, J. (2009). Personal Communication.

Stephenson, P. J., Polach, H., and Wyatt, D. H. (1978). The age of the Toomba basalt, north Queensland. *Abstract Program, 3rd Australian Geological Convention*, 62.

Stipp, J. J. and McDougall, I. (1968). Potassiumargon ages from the Nandewar volcano, near Narrabri, New South Wales. *Australian Journal of Science*, (31):84–85.

Stolz, A. J. (1985). The role of fractional crystallization in the evolution of the Nandewar Volcano, north-eastern New South Wales, Australia. *Journal of Petrology*, 26(4):1002–1026.

Sultan, M., Arvidson, R. E., Sturchio, N. C., and Guinness, E. A. (1987). Lithologic mapping in arid regions with Landsat thematic mapper data: Meatiq dome, Egypt. *Geological Society of America Bulletin*, 99(6):748–762.

Sun, S. and McDonough, W. F. (1989). Chemical and isotopic systematics of oceanic basalts: implications for mantle composition and processes. *Geological Society Special Publication*, 42:313–345.

Sun, S. S. and Hanson, G. N. (1975). Evolution of the mantle: Geochemical evidence from alkali basalt. *Geology*, 4(10):625–626.

Sutherland, F. (1977). Cainozoic basalts of the Mt Fox area, north Queensland. *Records of the Australian Museum*, 30(19):532–543.

Sutherland, F. L. (1985). Regional controls in eastern Australian volcanism. *Volcanism in Eastern Australia with Case Histories in New South Wales*, pages 13–31.

Sutherland, F. L. (1991). Cainozoic volcanism, eastern Australia: a predictive model based on migration over multiple'hotspot'magma sources. *Special Publication of the Geological Society of Australia*, 18:15–43.

Sutherland, F. L. (2003). Boomerang' migratory intraplate Cenozoic volcanism, eastern Australian rift margins and the Indian-Pacific mantle boundary. In Hillis, R. R. and Muller, R. D., editors, *The Evolution and Dynamics of the Australian Plate*. The Geological Society of America, Inc.

Sutherland, F. L. and Fanning, C. M. (2001). Gem-bearing basaltic volcanism, Barrington, New South Wales: Cenozoic evolution, based on basalt K-Ar ages and zircon fission track and U-Pb isotope dating. *Australian Journal of Earth Sciences*, 48(2):221–237.

Sutherland, F. L., Graham, I. T., Forsyth, S. M., Zwingmann, H., and Everard, J. L. (2006). The Tamar Trough revisited : correlations between sedimentary beds, basalts, their ages and valley evolution, north Tasmania. *Papers and Proceedings of the Royal Society of Tasmania*, 140.

Sutherland, F. L., Graham, I. T., Hollis, J. D., Meffre, S., Zwingmann, H., Jourdan, F., and Pogson, R. E. (2014). Multiple felsic events within post-10 Ma volcanism, Southeast Australia: inputs in appraising proposed magmatic models. *Australian Journal of Earth Sciences*, 61(2):241–267.

Sutherland, F. L., Graham, I. T., Meffre, S., Zwingmann, H., and Pogson, R. E. (2012). Passive-margin prolonged volcanism, East Australian Plate: outbursts, progressions, plate controls and suggested causes. *Australian Journal of Earth Sciences*, 59(7):983–1005.

Sutherland, F. L., Graham, I. T., Pogson, R. E., Schwarz, D., Webb, G. B., Coenraads, R. R., Fanning, C. M., Hollis, J. D., and Allen, T. C. (2002). The Tumbarumba Basaltic Gem Field, New South Wales: In Relation to Sapphire-Ruby Deposits of Eastern Australia. *Records of the Australian Museum*, 54(2):215–248.

Sutherland, F. L., Graham, I. T., Zwingmann, H., Pogson, R. E., and Barron, B. J. (2005). Belmore Volcanic Province, northeastern New South Wales, and some implications for plume variations along Cenozoic migratory trails. *Australian Journal of Earth Sciences*, 52(6):897–919.

Sutherland, F. L., Hendry, D. F., Barron, B. J., Matthews, W. L., and Hollis, J. D. (1996). An unusual Tasmanian Tertiary basalt sequence, near Boat Harbour, Northwest Tasmania. *Records of the Australian Museum*, 48:131–162.

Sutherland, F. L., Hoskin, W. O. P., Fanning, C. M., and Coenraads, R. R. (1998). Models of corundum origin from alkali basaltic terrains: a reappraisal. *Contributions to Mineralogy and Petrology*, 133:356–372.

Sutherland, F. L., Pogson, R. E., and Hollis, J. D. (1993). Growth of the central New England basaltic gemfields, New South Wales, based on zircon fission track dating. *NEO '93 Conference*, pages 1–680.

Sutherland, F. L. and Wellman, P. (1986). Potassium-Argon Ages of Tertiary Volcanics Rocks, Tasmania. *Papers and Proceedings of the Royal Society of Tasmania*, 120:77–86.

Tackley, P. and Stevenson, D. (1993). A mechanism for spontaneous self-perpetuating volcanism on the terrestrial planets. In Stone, D. and Runcorn, S., editors, *Flow and Creep in the Solar System: Observations, Modeling and Theory*, pages 307–321. Kluwer Academic Publishers.

Taylor, B., Goodliffe, A., Martinez, F., and Hey, R. (1995). Continental rifting and initial sea-floor spreading in the Woodlark Basin. *Nature*, 374(6522):534–537.

Tejada, M. L., Mahoney, J. J., Castillo, P. R., Ingle, S. P., Sheth, H. C., and Weis, D. (2004). Pin-pricking the elephant: Evidence on the origin of the Ontong Java Plateau from Pb-Sr-Hf-Nd isotopic characteristics of ODP Leg 192 basalts. *Geological Society Special Publication*, 229:133–150.

Till, C. B., Elkins-Tanton, L. T., and Fischer, K. M. (2010). A mechanism for low-extent melts at the lithosphere-asthenosphere boundary. *Geochemistry, Geophysics, Geosystems*, 11(10):1–22.

Tregoning, P. (2003). Is the Australian Plate deforming? A space geodetic perspective. In Hillis, R. R. and Muller, R. D., editors, *The Evolution and Dynamics of the Australian Plate*. The Geological Society of America, Inc.

Turcotte, D. and Schubert, G. (2002). *Geodynamics*. Cambridge University Press.

USGS Landsat Program (2017). Comparison of Landsat 7, 8, Sentinel 2, ASTER & MODIS bands.

Valentine, A. and Kalnins, L. (2016). An introduction to learning algorithms and potential applications in geomorphometry and Earth surface dynamics. *Earth Surface Dynamics*, 4(2):445–460.

Van den Hove, J., Grose, L., Betts, P. G., Ailleres, L., Van Otterloo, J., and Cas, R. A. F. (2017). Spatial analysis of an intra-plate basaltic volcanic field in a compressional tectonic setting: South-eastern Australia. *Journal of Volcanology and Geothermal Research*, 335:35–53.

Van Der Beek, P., Pulford, A., and Braun, J. (2001). Cenozoic landscape development in the blue mountains (SE Australia): Lithological and tectonic controls on rifted margin morphology. *Journal of Geology*, 109(1):35–56.

Van Der Lee, S. and Frederiksen, A. (2005). Surface wave tomography applied to the North American upper mantle. *Geophysical Monograph Series*, 157:67–80.

Van Der Meer, F. D., D, Vaner Werff, H. M. A., Van Ruitenbeek, F. J. A., Hecker, C. A., Bakker, W. H., Noomen, M. F., Van der Meijde, M., Carranza, E. J. M., Smeth, J. B. D., and Woldai, T. (2012). Multi- and hyperspectral geologic remote sensing: A review. *International Journal of Applied Earth Observation and Geoinformation*, 14:112–128.

Van der Meer, F. D., van der Werff, H. M., and van Ruitenbeek, F. J. (2014). Potential of ESA's Sentinel-2 for geological applications. *Remote Sensing of Environment*, 148:124–133.

Van Hunen, J. and Zhong, S. (2006). Influence of rheology on realignment of mantle convective structure with plate motion after a plate reorganization. *Geochemistry, Geophysics, Geosystems*, 7(8).

Vasconcelos, P. M., Knesel, K. M., Cohen, B. E., and Heim, J. A. (2008). Geochronology of the Australian Cenozoic: a history of tectonic and igneous activity, weathering, erosion, and sedimentation*. *Australian Journal of Earth Sciences*, 55(6-7):865–914.

Veevers, J. J. (1984). *Phanerozoic earth history of Australia*. Oxford University Press.

Veevers, J. J. (1986). Breakup of Australia and Antarctica estimated as mid-Cretaceous from magnetic and seismic data at the continental margin. *Earth and Planetary Science Letters*, 77(1):91–99.

Veevers, J. J. (2000). Change of tectono-stratigraphic regime in the Australian plate during the 99 Ma (mid-Cretaceous) and 43 Ma (mid-Eocene) swerves of the Pacific. *Geology*, 28(1):47–50.

Veevers, J. J., Powell, C., and Roots, S. R. (1991). Review of seafloor spreading around Australia. I. synthesis of the patterns of spreading. *Australian Journal of Earth Sciences*, 38(4):373–389.

Vickery, N. M., Dawson, M. W., Sivell, W. J., Malloch, K. R., and Dunlap, W. J. (2007). Cainozoic igneous rocks in the Bingara to Inverell area, northeastern New South Wales. *Quarterly Notes: Geological Survey of New South Wales*.

Victoria State Government (2022). Geovic Earth Resources.

Wass, S. Y. (1980). Geochemistry and origin of xenolith-bearing and related alkali basaltic rocks from the Southern Highlands, New South Wales, Australia. *American Journal of Science*, 280:639–666.

Watanabe, H. and Matsuo, K. (2003). Rock type classification by multi-band TIR of ASTER. *Geosciences Journal*, 7(4):347–358.

Watson, S. and Mckenzie, D. (1991). Melt generation by plumes: A study of Hawaiian volcanism. *Journal of Petrology*, 32(3):501–537.

Webb, A. W. and McDougall, I. (1967). A comparison of mineral and whole rock potassium-argon ages of tertiary volcanics from central Queensland, Australia. *Earth and Planetary Science Letters*, 3(C):41–47.

Wedepohl, K. H. (1995). The composition of the continental crust. *Geochimica et Cosmochimica Acta*, 59(7):1217–1232.

Weissel, J. K. and Hayes, D. E. (1977). Evolution of the Tasman Sea reappraised. *Earth and Planetary Science Letters*, 36(1):77–84.

Wellman, P. (1971). The age and palaeomagnetism of the Australian Cenozoic volcanic rocks. *PhD Thesis, Australian National University*.

Wellman, P. (1978). Potassium-argon ages of Cainozoic volcanic rocks from the Bundaberg, Rockhampton and Clermont areas of eastern Queensland. *Proceedings of the Royal Society of Queensland*, 89:59–64.

Wellman, P., Cundari, A., and McDougall, I. (1970). Potassium-argon ages for leucite-bearing rocks from New South Wales, Australia. *Journal and proceedings of the Royal Society of New South Wales*, 103.

Wellman, P. and McDougall, I. (1974a). Cainozoic igneous activity in eastern australia. *Tectonophysics*, 23:49–65.

Wellman, P. and McDougall, I. (1974b). Potassium-argon ages on the cainozoic volcanic rocks of New South Wales. *Journal of the Geological Society of Australia*, 21(3):247–272.

Wellman, P., McElhinny, M. W., and McDougall, I. (1969). On the PolarWander Path for Australia during the Cenozoic. *Geophysical Journal of the Royal Astronomical Society*, 18(4):371–395.

Wells, S. G., Dohrenwend, J. C., McFadden, L. D., Turrin, B. D., and Mahrer, K. D. (1985). Late Cenozoic landscape evolution on lava flow surfaces of the Cima volcanic field, Mojave Desert, California. *Geological Society of America Bulletin*, 96(12):1518–1529.

Wessel, P. and Kroenke, L. W. (2000). Ontong Java Plateau and late Neogene changes in Pacific plate motion. *Journal of Geophysical Research*, 105:255–277.

White, L. T., Gibson, G. M., and Lister, G. S. (2013). A reassessment of paleogeographic reconstructions of eastern Gondwana: Bringing geology back into the equation. *Gondwana Research*, 24:984–998.

White, R. and McKenzie, D. (1989). Magmatism at rift zones: the generation of volcanic continental margins and flood basalts. *Journal of Geophysical Research: Solid Earth*, 94(B6):7685–7729.

White, W. M. (2015). Isotopes, DUPAL, LLSVPs, and Anekantavada. *Chemical Geology*, 419:10–28.

Whitehead, P. W. and Stephenson, P. J. (1998). Lava rise ridges of the Toomba basalt flow, north Queensland, Australia. *Journal of Geophysical Research: Solid Earth*, 103(B11):27371–27382.

Whitehead, P. W., Stephenson, P. J., Mcdougall, I., Hopkins, M. S., Collerson, K. D., Johnson, D. P., Stephenson, P. J., Mcdougall, I., and Hopkins, M. S. (2007). Temporal development of the Atherton Basalt Province , north Queensland. *Australian Journal of Earth Sciences*, 54(5):691–709.

Wood, B. J., Kiseeva, E. S., and Matzen, A. K. (2013). Garnet in the earth's mantle. *Elements*, 9(6):421–426.

Wright, N. M., Dietmar Müller, R., Seton, M., and Williams, S. E. (2015). Revision of Paleogene plate motions in the Pacific and implications for the Hawaiian-Emperor bend. *Geology*, 43(5):455–458.

Wyatt, D. H. and Webb, A. W. (1971). K/Ar ages of some north Queensland basalts and an interpretation of late Cainozoic history. *Geological Society of Australia Journal*, 17:39–51.

Wyllie, P. J. (1988). Solidus curves, mantle plumes, and magma generation beneath Hawaii. *Journal of Geophysical Research*, 93(85):4171–4181.

Yamaguchi, Y., Kahle, A., Tsu, H., Kawakami, T., and Pniel, M. (1998). Overview of Advanced Spaceborne Thermal Emission and Reflection Radiometer (ASTER). *Transactions on Geoscience and Remote Sensing*, 36(4):1062–1071.

Yamaguchi, Y. and Naito, C. (2003). Spectral indices for lithologic discrimination and mapping by using the ASTER SWIR bands. *International Journal of Remote Sensing*, 24(22):4311–4323.

Yan, C. and Kroenke, L. W. (1993). A plate tectonic reconstruction of the Southwest Pacific 0-100 Ma. In Berger, W., editor, *Proceedings of the Ocean Drilling Program, Scientific Results*. Ocean Drilling Program, College Station.

Yaxley, G. M., Green, D. H., and Kamenetsky, V. (1998). Carbonatite Metasomatism in the Southeastern Australian Lithosphere. *Journal of Petrology*, 39(11):1917–1930.

Yesou, H., Besnus, Y., and Rolet, J. (1993). Extraction of spectral information from Landsat TM data and merger with SPOTpanchromatic imagery a contribution to the study of geological structures. *Journal of Photogrammetry & Remote Sensing*, 48(5):23–36.

Young, R. and McDougall, I. (1993). Long-term landscape evolution: early Miocene and modern rivers in southern New South Wales, Australia. *Journal of Geology*, 101(1):35–49.

Young, R. W. and McDougall, I. (1985). The age, extent and geomorphological significance of the sassafras basalt, South-Eastern New South Wales. *Australian Journal of Earth Sciences*, 32(4):323–331.

Zahirovic, S., Müller, R. D., Seton, M., and Flament, N. (2015). Tectonic speed limits from plate kinematic reconstructions. *Earth and Planetary Science Letters*, 418:40–52.

Zhang, M., O'Reilly, S. Y., and Chen, D. (1999). Location of Pacific and Indian mid-ocean ridge-type mantle in two time slices: Evidence from Pb, Sr, and Nd isotopes for Cenozoic Australian basalts. *Geology*, 27(1):39–42.

Zhang, M., Stephenson, P. J., Reilly, S. Y. O., Mcculloch, M. T., and Norman, M. (2001). Petrogenesis and Geodynamic Implications of Late Cenozoic Basalts in North Queensland, Australia: Trace-element and SrNdPb Isotope Evidence. *Journal of Petrology*, 42(4):685–719.

Zhang, Z., Li, S., Suo, Y., Somerville, I. D., and Li, X. (2016). Formation mechanism of the global Dupal isotope anomaly. *Geological Journal*, 51:644–651.

Zhao, S. and Muller, R. D. (2003). Three-dimensional finite-element modelling of the tectonic stress field in continental Australia. In Hillis, R. R. and Muller, R. D., editors, *The Evolution and Dynamics of the Australian Plate*. The Geological Society of America, Inc.

Zindler, A. and Hart, S. (1986). Chemical Geodynamics. *Annual Review of Earth and Planetary Sciences*, 14:493–571.

Zoback, M. and Zoback, M. (1989). Stress in the earth's lithosphere. In *Geophysics Encyclopedia of Earth Science*. Springer, Boston, MA.